Degradation of persistent organic pollutants (pharmaceuticals & dyes) by combined dielectric barrier electrohydraulic discharge system and photo catalysts

By

Emile Salomon Massima Mouele

BSc (Chemical Science), BSc Honours (Chemistry), MSc cum Laude (Chemistry), University of the Western Cape, South Africa

A thesis submitted in fulfilment of the requirements for the degree of Doctor of Philosophy in Chemistry, Department of Chemistry, University of the Western Cape, South Africa

Supervisor: Prof L F. Petrik

Co-supervisor: Dr O. Fatoba

June 2019

ABSTRACT

Water pollution problems have continued to increase not only in South Africa but worldwide due to human activities. The presence of organic toxins and bacteria in water sources is mostly due to population growth, industrial development and agricultural run-off. The accumulation of persistent organic pollutants (POPs) in water and wastewater sources has raised various questions on the safety of potable water used for drinking, households and other activities. Traditional mechanical, biological, physical, and chemical methods such as flocculation, coagulation, reverse osmosis, filtration, ultrafiltration, adsorption and active sludge treatment methods have failed to remove these new xenobiotic from aquatic media. This is due to the fact that instead of degrading the toxins, the methods listed above often transform organic contaminants from one form another. Also, the post treatment of by-products resulting from these methods is costly. In addition, this new generation of contaminants, often referred to as compounds of emerging concern (CECs), exist in tiny concentrations (ng) and conventional techniques have not been designed for these low levels of pollutants which consequently pass through during treatment processes and end up in the treated effluents at minute concentrations (ug/L to ng/L). However, complete remediation of chemical toxins in wastewater treatment plants has not been achieved. A better option involves the direct oxidation of the pollutants in the effluent but so far their complete mineralisation has not been achieved. Advanced oxidation processes (AOPs) have emerged in recent years as adequate techniques for the complete removal of POPs. AOPs focus more on the production of non-selective hydroxyl radicals ($OH^{\cdot}$) which have been considered as the most powerful oxidants (2.8 V) that directly or indirectly mineralise the organic pollutant into dissolved CO_2, H_2O and harmless end-products. However, the use of excessive chemicals, corrosion of catalyst supports, wasted UV, ozone escapes and the cost associated with AOPs often limit their application for the removal of POPs from water and wastewater treatment facilities. The principal aim of this study was to optimise a double cylindrical barrier discharge (DBD) system for the removal of low concentration persistent organic pollutants (POPs). The efficiency of the DBD system was initially confirmed by quantification of three main reactive oxygen species including ozone (O_3), hydrogen peroxide (H_2O_2) and hydroxyl radicals ($\cdot OH$) among others. These three active species were successfully detected and quantified using indigo, per titanyl sulphate and terephthallic acid (TA) spectroscopy methods, respectively. Thereafter, the DBD reactor was optimised by assessing the effect of electrophysico-chemical parameters on the removal efficiencies of two selected pollutants including orange II sodium salt dye (O.II) and sulfamethoxazole (SMX), a

pharmaceutical, as model persistent organic pollutants. The electrophysico-chemical factors investigated included initial concentration (mg/L), solution pH, air flow rate (L/min) and peak voltage (kV). For each model pollutant, each of the aforementioned parameters was varied at a time while other parameters were kept constant. The optimised conditions were used to evaluate the performance of the DBD configuration on O.II and SMX degradation. The following analytical techniques: UV-vis, FT-IR, LC-MS, HPLC, etc. were used to investigate the degradation of the model pollutants. The degradation mechanistic pathways of the contaminants were established. To enhance the performance and utilise UV light of the optimised DBD reactor, C-N-TiO_2 co-doped nano catalyst was synthesised by a sol gel method. The immobilised C-N-TiO_2 on stainless steel (SS) (SS/C-N-TiO_2) and pure Ti (Ti/C-N-TiO_2) mesh by dip coating was incorporated into the system to induce photo catalysis with the UV-light generated by the DBD reactor. To overcome the support corrosion occurring during DBD experiments, the SS support was coated with various transition metal (Cr, Ti, Zr and Si) based anticorrosion layers prepared by cathodic arc evaporation (CAE) principle and the following coated supports SS/TiON, SS/CrN/CrON, SS/ZrON and SS/ZrSiN/ZrSiON were identified as the most corrosion resistant coatings. After evaluating the corrosion resistance of the obtained coatings, the supports were coated with C-N-TiO_2 nano catalyst and their photo catalytic ability was tested upon the removal of O.II under UV light. Furthermore, the sol gel precursor for C-N-TiO_2 was also deposited on a glass support by the spin coating technique. The adhesion of C-N-TiO_2 to the glass support and the stability of glass/C-N-TiO_2 films were investigated during the degradation of O.II exposed to UV light. During the sol gel spin coating process, the effect of coating speed and sol gel to solvent ratio, on the thickness of films were investigated at the indicated conditions. The C-N-TiO_2 was deposited on glass as an alternative option in case the catalyst would not adhere to SS mesh when introduced into the DBD system. Its direct immobilisation on glass support implied that synthesised C-N-TiO_2 could be directly deposited on the outer side of the inner tube of the DBD reactor to induce photo catalytic process and hence improve the decomposition of the targeted contaminants. During treatment of model solutions, the physico-chemical parameters: pollutant concentrations (10 - 60 mg/L for O.II and 20 – 100 mg/L for SMX), solution pH (2.5 - 10.5 for both O.II and SMX) and air flow rate (3 – 9 L/min for both pollutants) were altered at the corresponding conditions. The peak voltage was also varied from 6.8, 8 to 10 kV for both pollutants, at the applied experimental conditions. The optimum electro physico-chemical parameters obtained for both model contaminants include a concentration of 60 mg/L for O.II and 40 mg/L for SMX, pH 2.5, air flow rate 3 L/min, and peak voltage 8 kV for O.II and 6. 8 kV for SMX. For both O.II

and SMX, the following factors, initial concentration, solution pH and air flow rate significantly affected the removal of the model contaminants compared to the peak voltage that proved to be an insignificant parameter during degradation of the two pollutants. In the case of O.II dye, all experiments conducted at the indicated conditions showed that complete decolouration of the dye was mostly reached after 30 min of reaction time. Moreover, total degradation of O.II was achieved after 20 minutes at the optimum conditions. This demonstrated that the optimised DBD reactor reduced the treatment time from 30 to 20 min that was further reduced to 10 min upon incorporation of the C-N-TiO_2 nano composites into DBD (DBD + C-N-TiO_2) system for complete detoxification of O.II. Besides, at the optimum conditions, the high (99%) O.II degradation percentage observed after 20 min was however countered by the low (15.38%) TOC removal showing the refractory behaviour of the six degradation intermediate metabolites. These metabolites were detected by LC-MS, and were later mineralised to CO_2, H_2O and inorganic salts by electrophilic and nucleophilic attacks of O_3 and $OH^{\cdot}$ as dictated by the amount of nitrates + nitrites that increased from < 0.1 to 8 mg/L after 60 minutes of treatment time. Unlike TOC, the chemical oxygen demand (COD) decreased from 70 before to 27 mg/L after the DBD experiment, respectively, which indicated that the toxicity of O.II was removed by 61%. Furthermore, the UV-vis investigation of the untreated and treated O.II samples confirmed the full degradation of O.II that was attained within 20 min of reaction time which was due to the fragmentation of the azo (–N=N-) and sulfonate (SO_3^-) groups in the orange II structure that induced colour fading of the dye during the experiment. The presence of these functional groups along with O-H, =C-H, C=C, C=O, CH=CH, S=O CO_3^{2-}, SO_4^{2-} fragments among others, were further evidenced by FT-IR spectroscopy. Furthermore, the HPLC results showed that the degradation of O.II by DBD + C-N-TiO_2/SS or DBD + C-N-TiO_2/Ti systems resulted in four or ten degradation intermediate by-products, respectively that were all oxidised into dissolved CO_2, H_2O and simpler inorganics. As for SMX pharmaceutical residue, its total removal was achieved between 20 and 30 minutes of reaction time. This showed the recalcitrance of the six SMX degradation intermediate metabolites identified by LC-MS, which were likely converted to CO_2, H_2O and other aqueous chemical entities by nucleophilic and electrophilic reactions of O_3 and $\cdot OH$. Moreover, the HPLC results for the degradation of SMX by DBD with catalyst showed that four degradation intermediate by-products were generated with DBD + C-N-TiO_2/SS system while seven degradation intermediate by-products were obtained with DBD + C-N-TiO_2/Ti combination. These compounds were further converted through electrophilic and nucelophilic attack of O_3 and $OH^{\cdot}$ into H_2O, CO_2 and simpler aqueous entities. Hence an optimised DBD

system is an adequate technology for water and wastewater treatment. The incorporation of a catalyst in the DBD configuration significantly improves the conversion of POPs into H_2O, CO_2 and simpler inorganics. Suitable new anticorrosion layers prevent support corrosion in the harsh oxidative environments of the DBD system were successfully developed.

Keywords: DBD, organic pollutants, oxygen based species, persistent organic pollutant

DECLARATION

I hereby declare that "Degradation of persistent organic pollutants (Pharmaceuticals & dyes) by combined dielectric barrier electrohydraulic discharge system and photo catalysts
" is my own work, that it has not been submitted for any degree or examination in any other university, and that all the sources I have used or quoted have been defined and accredited by complete references.

Emile Salomon Massima Mouele June 2019

Signed……

ACKNOWLEDGEMENTS

I would like first to thank God for giving me life, to believing and trusting in him in good and tough times. Thank you almighty for your love and support. You are my defender, with you I am secured and I have no fear. Thank you Lord for keeping me protected, motivated and energised during my PhD degree curricula.

Special thanks go to my supervisor, Prof Leslie Petrik, for the chance she gave me to be part of the Environmental and Nanoscience research group (ENS) at UWC. Thank you Prof for all the workshops, trainings and mostly for your guidance, patience and inspiration.

I personally thank my co-supervisor, Dr. O. Fatoba for all his advice and contributions towards my project.

Many thanks go to Prof Mariana Braic and the whole ReCAST group in Magurelle Romania for the collaborative project and for hosting me safely in 2017 and 2018 in Romania.

Extreme warm thanks are directed towards my friend and collaborator Dr Mihaela Dinu for the positive assistance in corrosion studies and warm endorsement in Romania. Extended thanks are directed to Dr Omotola. O. Babajide, to my friend, Mr Jimoh. O. Tijani, for their support.

Lots of thanks go to Mama Vanessa Kellerman, Ilse Wells, Rallston Richards, and Mr Denzil Bent, and to all colleagues and friends at ENS. Also I would like to thank Mr Petrus and Timo for the power supply, Mr Andre de Jager at UCT for all technical inputs with designs and glass blowing for the experimental set up.

Further thanks go to Prof Christopher Arendse, Mr Siphelo Ngqoloda, Dr Franscious Cummings, and Mr All at Physics Department UWC for their assistance in spin coating and SEM and TEM analysis.

Kind acknowledgments are addressed to all in-service training students at ENS namely Mr Jonathan Kiangani, Deborah Kalume, Evral Ntsa, Method Rosicki Kalombe, Vinny Ndjate, Ninette Irakoze, Natacha Kakama, etc. who have assisted me in plotting reactor configurations using Engineering advanced soft ware and laboratory experiments.

Individual thanks are directed to the Water Research Commission (WRC), NRF, etc. for financial support. I personally thank the Government of Gabon for providing support and giving me an opportunity to pursue my studies in South Africa.

Finally, warm thanks go to my dearly loved family members including my mother, Odette Boukangou; my grandmother, Mathilde Kanga, my uncles, Nicolas Boukangou and Barnabe Boukangou for all the support and love that empowered my dedication.

TABLE OF CONTENTS

LIST OF TABLES

LIST OF FIGURES

LIST OF ABBREVIATIONS

DBD: Dielectric barrier discharge

DCDBD: Double cylindrical dielectric barrier discharge

TA: Terephthallic acid

UV-vis: Ultraviolet spectroscopy

FT-IR: Fourier transforms infrared spectroscopy

LC-MS: Liquid chromatography- Mass spectroscopy

HPLC: High performance liquid spectroscopy

CAE: Cathodic arc evaporation

O.II: Orange II sodium salt dye

SMX: Sulfamethozole drug

TOC: Total organic carbon

COD: Chemical oxygen demand

DOC: dissolve organic carbon

BOD: Biological oxygen demand

POPs: Persistent organic pollutants

AOPs: Advanced oxidation processes

EDCs: Endocrine disrupting compounds

PPCPs: Pharmaceuticals and personal care products

PhACs: Pharmaceutically active compounds

EHD: Electrohydraulic discharge

SS: Stainless steel

WWTPs: Wastewater treatment plants

STPs: Sewage treatment plants

ROS: Reactive oxygen species

DWTPs: Drinking water treatment plants

DMF: N, N-dimethylformamide

EDS: Energy dispersive spectroscopy

FT-IR: Fourier Transform Infrared Spectroscopy

SEM: Scanning Electron Microscopy

HRSEM: High Resolution Scanning Electron Microscopy

HRTEM: High Resolution Transmission Electron Microscopy

PAN: Polyacrylonitrile

SAED: Selected Area Electron Diffraction (SAED)

TGA: Thermo gravimetric analysis/Defferential Scanning Calorimetric

XRD: X-ray diffraction

ANTPs: Atmospheric non-thermal plasma

NTP: Non-thermal plasma

HAAs: Haloacetic acids

HOMO: Highest occupied molecular orbitals

NIOE National Institute of Opto-Electronics, Bucharest, Romania

CAE: cathodic arc evaporation

EAS: Electro active species

EDL: Electrical double layer

OCP: Open circuit potential (mV)

ROS: Reactive oxygen species

ORP-EIS: Odd random phase multisine electrochemical impedance spectroscopy

PP-EIS: Potentiodynamic polarization and electrochemical impedance spectroscopy

CL: Chemiluminescence

ICM-iopromide: A nonionic iodinated, water-soluble, radiographic contrast medium which is available in three stable, ready-to-use solutions of different concentrations.

LIST OF THE TERMS USED IN EQUATIONS

hv: light (photon) used for photo catalysis

e^-_{cb}: electrons on the conducting band

h^+_{vb}: Positive holes on the valence band surface

E_{cb}: Conducting band potential

h^+_{tr}: Charge transfer in positive holes

h^+_{vb}: Positive holes on the valence band surface

ΔE: Change in potential (mV)

ΔI: Change in current density (nA /cm^2)

$\Delta E/\Delta I$: Slope = linear polarisation/polarisation resistance

R_p: Polarisation resistance/linear polarisation (mV.cm^2/nA)

I_{corr}: Corrosion current density (nA/cm^2)

P: Porosity

R_q: Linear polarisation factor

P_e: Protection efficiency (%)

E_{corr}: Corrosion potential (mV)

E^o: Initial potential (mV)

ACADEMIC OUTPUTS, PRESENTATIONS AND PUBLICATION HISTORY ACHIEVED IN THIS STUDY

The output highlighted below directly resulted from this study

Oral presentations

Emile S. Massima Mouele, Olanrewaju Ojo. Fatoba, Leslie Petrik, (2017). Presentation of various projects run at ENS research group at UWC: Water research workshop 26 -28th March 2017 organised by the Council for Scientific and Industrial Research (CSIR), South Africa. Auditorium, room A2, Building 19B CSIR campus, Pretoria, South Africa

Mihaela Dinu, ***Emile S. Massima Mouele***, Anca C.Parau, Alina Vladescu, Leslie Petrik and Mariana Braic, (2018). Enhancement of the corrosion resistance of 304 stainless steel by Cr-N and Cr (N, O) coatings. Nanosmat-Africa conference, Lord Charles Hotel, Stellenbosch, Summerset West, Cape Town, South Africa 19 – 23rd November, 2018.

List of publications

Emile S. Massima Mouele, Olanrewaju Ojo. Fatoba, Omotola Babajide, Kassim O. Badmus, Leslie F. Petrik, (2018). Review of the methods for determination of reactive oxygen species and suggestion for their application in advanced oxidation induced by dielectric barrier discharges. *Environmental Science and Pollution Research,* 25(10):9265-9282 https://doi.org/10.1007/s11356-018-1392-9 [Published]

Emile S. Massima Mouele, Jimoh O. Tijani, Ojo O. Fatoba, Leslie. F. Petrik, (2015). Degradation of organic pollutants and microorganisms from wastewater using different dielectric barrier discharge configurations — a critical review. *Environ Sci Pollut Res* 22:18345–18362, DOI 10.1007/s11356-015-5386-6 [Published]

Mihaela Dinu, Emile S. Massima Mouele, Anca C. Parau, Alina Vladescu, Leslie F. Petrik, Mariana Braic, (2018). Enhancement of the Corrosion Resistance of 304 Stainless Steel by Cr–N and Cr (N, O) Coatings. Coatings, 8, 132; doi:10.3390/coatings8040132 [Published]

Jimoh O Tijani, Massima E. S. Mouele, Ojo O Fatoba, Omotola O Babajide and Leslie F Petrik, (2017). Degradation of bisphenol-A by dielectric barrier discharge system: influence of polyethylene glycol stabilized nano zero valent iron particles. *Adv. Nat. Sci.: Nanosci. Nanotechnoly*. 8 035013

Kassim Olasunkanmi Badmus & Jimoh Oladejo Tijani & Emile Massima, Leslie Petrik, (2018). Treatment of persistent organic pollutants in wastewater using hydrodynamic cavitation in synergy with advanced oxidation process. *Environmental Science and Pollution Research* 25:7299–7314

J. O. Tijani, M. E. S. Mouele, T. C. Tottito, O. O. Fatoba, L. F. Petrik, Degradation of 2-Nitrophenol by Dielectric Barrier Discharge System: The Influence of Carbon Doped TiO_2 Photo catalyst Supported on Stainless Steel Mesh. Plasma Chem Plasma Process (2017) 37:1343–1373 DOI 10.1007/s11090-017-9824-8

Manuscripts under review

Massima, Emile Salomon, Dinu Mihaela, Franscious Cummings, Fatoba Olanrewaju, Parau Anca, Vladescu Alina, Braic Mariana, Petrik Leslie, (2018). Synthesis, characterization and photo catalytic application of carbon-nitrogen co- doped TiO_2 Nano photo catalysts: Part I Submitted to "*Journal of Materials Science & Engineering B"* (in collaboration with Romania)

Emile S. Massima Mouele, Jimoh. O. Tijani, Kassim O. Badmus, Jonathan O. Kiangani, Kalume D.Wa., Ninette Irakoze, Natacha K. Kakama, Omotola O. Babajide, Olanrewaju Ojo. Fatoba, Omoniyi Pereao, Chris Bode-Aluko, Cosmas Uche, Oluseyi Omoniyi, Alechine Emmanuel Ameh, Adong O. Raissa, Leslie. F. Petrik, (2018). A critical review on generation of ozone and derivatives, reaction mechanisms in dielectric barrier induced advanced oxidation technologies for water and wastewater treatment. Submitted to *Environmental science: Water Research and Technology*.

Mihaela Dinu, Emile S. Massima Mouele, Anca C. Parau, A. Vladescu, Leslie F. Petrik, Mariana Braic, (2018). Enhancement of the corrosion resistance of 304 stainless steel by Ti nitride and oxynitride coatings. Submitted to *Journal of coatings*. (In collaboration with Romania)

Emile S. Massima Mouele, MSc; Mihaela Dinu; Roland Missengue; Anca C. Parau; Alina Vladescu; Olanrewaju O. Fatoba; Mariana Braic, 2018. The Photo catalytic activity of stainless steel and anticorrosion meshes coated with carbon-nitrogen doped TiO_2 Nano catalyst. Submitted to *Applied Surface Science*. (In collaboration with Romania)

Emile S. Massima Mouele[1], Jimoh .O.Tijani[2], O. Babajide[3], Ojo. O. Fatoba[1], Leslie. F. Petrik[1], (2018). Removal of Pharmaceutical Remains from Water using Dielectric Barrier Discharge methods – A Review, Submitted to *Environmental Chemistry Letters.*

Emile S. Massima Mouele, Tijani Oladejo Jimoh, Ojo. O. Fatoba, Chuks P. Eze, Omotola Babajide, Leslie Petrik. (2018). Degradation of Methylene blue by double cylindrical dielectric barrier discharge advanced technoloy. Submitted to *Water*

Manuscripts in preparation

Emile S. Massima Mouele, Siphelo Ngqoloda, Christopher Arendse, Ojo. O. Fatoba, Leslie F. Petrik, (2018). Spin coating immobilization of C-N-TiO_2 gel on glass and application for photocatalytic removal of orange II sodium salt dye.

Emile S. Massima Mouele, Jimoh .O.Tijani, O. Babajide, Ojo. O. Fatoba, Leslie. F. Petrik, (2018). Quantification of free reactive oxygen species in double cylindrical dielectric barrier discharge advance oxidation technology for water and wastewater treatment.

Emile S. Massima Mouele, Jimoh .O.Tijani, O. Babajide, Ojo. O. Fatoba, Leslie. F. Petrik, (2018). Degradation of orange II sodium salt dye by double cylindrical dielectric barrier discharge technology combined with C-N-TiO_2 immobilised on SS and pure Ti meshes.

Emile S. Massima Mouele, Jimoh .O.Tijani, O. Babajide, Ojo. O. Fatoba, Leslie. F. Petrik, (2018). Degradation of sulfamethoxaole drug by double cylindrical dielectric barrier discharge technology combined with C-N-TiO_2 immobilised on SS and pure Ti meshes.

Mihaela Dinu, Emile S. Massima Mouele, Anca C. Parau, Alina Vladescu, Leslie F. Petrik, Mariana Braic, (2018). Corrosion study for beginners: A critical review.

CHAPTER ONE

1 INTRODUCTION

Chapter 1 presents the background to the occurrence of persistent organic pollutants (POPs) in water effluents, their origins and impacts on humans and their surrounding ecosystems. This chapter also highlights the different conventional methods used for water and wastewater remediation and points out the benefits of employing advanced oxidation processes (AOPs) mainly dielectric barrier discharges (DBDs) for total removal of POPs from contaminated water. Next, chapter 1 is subdivided into concise headings including problem statement, aims and objectives, research approach and research hypothesis. The scope and delimitations of the study as well as the chapter outlines are also presented.

1.1 BACKGROUND

Water remains a vital necessity of life as well as a crucial requirement for industries. However, its contamination has become an alarming situation for consumers, the environment and aquatic ecosystems. Endocrine disrupting compounds (EDCs), pharmaceuticals and personal care products (PPCPs) represent typical groups of water pollutants that are usually considered worldwide as emerging micro pollutants or compounds of emerging concern. The presence of these contaminants in drinking and wastewater has shown serious environmental impacts which have attracted global attention (Farré *et al.*, 2005; Zhihui, Peng and Xiaohua, 2005). A number of these compounds originate from human and animal urine sewage and escape through wastewater treatment plants (WWTPs) and then disseminated in surface waters. The improper disposal of these compounds in water sources poses a potential health concern to humans mostly through the consumption of contaminated drinking water and thus necessitates urgent mitigation (Wu, Doan and Upreti, 2008). The development of alternative treatment methods for water reuse and drinking water production has therefore increasingly become a global challenge. The resistance to degradation of these contaminants in water during conventional treatment is mainly based on their high chemical stability and/or low biodegradability and hence their lipophilic or resistant characteristic (Yang et al. 2009). Recently, advanced oxidation processes (AOPs) have been identified as a new generation of techniques for water reuse and water treatment. This is because AOPs have been found capable of removing contaminants that are not remediable by conventional treatment methods. Previous studies

mentioned that AOPs can not only be used as pre-treatment or post-treatment stages in water treatment processes but they can also be used in combination with biological treatment methods for water decontamination (Lapertot *et al.*, 2006; Pérez *et al.*, 2006; Oller, Malato and Sánchez-Pérez, 2011). Based on these physical and chemical advantages, a large number of studies based on water treatment using AOPs have been conducted (de Souza, Bonilla and de Souza, 2010; Volmajer Valh *et al.*, 2012).

1.1.1 Dielectric barrier discharges, promising advanced oxidation processes for water and wastewater treatment

Conventional treatment methods such as coagulation, flocculation filtration, etc. have failed to totally purify the contaminated water due to their limitations based on the cost, availability, efficiency as well as their feasibility (Volmajer Valh *et al.*, 2012). In recent decades, advanced oxidation processes (AOPs) including dielectric barrier discharges (DBDs) have been established and used as suitable, alternative water treatment technologies. In fact, DBDs processes are based on the plasma concept which originates from the interaction of a feed gas with highly energised electrons, generated by a small amount of current induced on a conductive electrode. This is usually accompanied by the generation of electric and magnetic fields. The dissociation of the feed gas by energetic electrons in the plasma region leads to various excitation, ionising and recombination chemical reactions. More often, electrode arrangements, known as reactor configurations play an important role in DBDs processes used as water purification methods. Indeed, various DBD reactor configurations have been reviewed in the literature. However, the most common of these include single/double planar and single/double cylindrical dielectric barrier discharges (Lapertot *et al.*, 2006). A considerable number of studies have been conducted using single/planar DBD configurations and high degradation of organic pollutants has been achieved (Lukeš 2001). However, in most of those studies, various chemical additives were used. The reviewed literature also mentioned that the addition of chemicals in DBD treatment processes usually resulted in unwanted by-products in the treated effluents and their removal is problematic (de Souza, Bonilla and de Souza, 2010). Conversely, only a few of the single and double cylindrical DBD configurations have been used in water treatment processes and considerable decomposition percentages were also achieved (Oller, Malato and Sánchez-Pérez, 2011). The advantage of cylindrical DBD configuration over the planar electrode geometry remains the fact that in single or double cylindrical systems, the electrode is protected by one or more dielectric materials separating it

from the effluent and hence avoiding electrode corrosion. Moreover, the existence of the electric and magnetic fields associated with the inner electrode facilitates the free circulation and even distribution of the highly energised electrons around the anode making the system continuously safer (Gogate and Pandit, 2004a). Unlike the single and double cylindrical DBD configurations, the single/double planar configuration is mostly dominated by the electric field that accelerates the high energy electrons in one direction. In the DBD systems, the excited atomic and molecular species tend to return to their ground state emitting light commonly known as UV- radiations. In return, exposure of the chemical species produced in DBD systems to UV- radiations enhances the generation of free active radicals that mineralise the contaminants to the desired end-products. The plasma generated in DBD systems is characterised by its physical and chemical properties. The physical properties usually refer to the production of UV-radiation and shock waves while the chemical properties involve the generation of highly reactive species such as ozone, atomic oxygen, superoxide, hydrogen peroxide and hydroxyl radicals, etc., (Gogate and Pandit, 2004b). which act as oxidants and selectively or non-selectively attack the target pollutants. In most research studies on water treatment using DBDs, the free reactive species mainly O_3, H_2O_2 and $^{\cdot}OH$ have been identified using Indigo, Eisenberg and terphtallic acid methods, respectively. In the case of ozone, scientists such as Galindo & Kalt (1998) stated that O_3 is a strong oxidising agent and mainly reacts with chemical compounds as an electron transfer acceptor that can oxidise metal ions, or an electrophile that induces the oxidation of phenol and other stimulated aromatics. Then ozone can act as a dipole addition reagent when added to carbon–carbon multiple bonds. However, organic pollutants such as aromatic azo dyes are very stable when exposed to ozone; the reactivity of these compounds with ozone is very low compared to an olefinic or azomethine group (Gogate and Pandit, 2004a). On the other hand, hydrogen peroxide is typically considered as a weak acid. A recombination product of hydroxyl radicals induces reduction in acidic medium and has the ability to oxidize itself at room temperature (Kirk & Othmer 1996). Furthermore, the production of hydroxyl radicals remains the common factor in most advanced oxidation processes highlighted in the literature as water treatment techniques (Lukeš 2001). Indeed, literature sustains that the most powerful oxidant, namely the hydroxyl radical, acts through three different ways during the reaction with organic compounds. These include abstraction of a hydrogen atom, electrophilic addition to double/triple bonds and electron transfer (Gogate and Pandit, 2004a, 2004b). As a result, all these free reactive species mentioned above are produced in the DBD reactor and their combination with the UV-vis radiations generated in the DBD system shows a promising way of decomposing organic

contaminants. In this context, attention has been focussed on degradation of pharmaceutical and personal care products (PPCPs) due to their diversity and persistence in the environment and in living ecosystems (Gogate and Pandit, 2004b).

1.2 PROBLEM STATEMENT

The existence of persistent organic pollutants (POPs), also referred to as emerging micro pollutants in the environment and aquatic ecosystems, is an issue of great concern. Emerging micro-pollutants usually include pharmaceuticals, pesticides, hormones herbicides and surfactants, etc. The presence of pharmaceutically active compounds (PhACs) in aquatic ecosystems could have adverse impacts on living organisms. Up to date, hundreds of contaminants including pharmaceuticals, as well as several drug intermediates have been identified worldwide in aquatic environments (Heberer, 2002). However a particular attention has been focussed on pharmaceutical and personal care products (PPCPs) due to their variety in the environment. Indeed PPCPs are a group of diverse chemical substances including drugs, food supplements, ingredients in cosmetics and other personal care products, as well as their respective intermediates and conversion products (Auriol *et al.*, 2006). These substances have been designed to achieve pharmacological effects on humans and animals in trace concentrations. PPCPs found in water and wastewaters derive mainly from agricultural and veterinary activities, industry, medical treatment in hospitals and common households. PPCPs are extremely resistant to biological degradation processes and generally escape integrally from conventional treatment plants and end up in water distribution systems. Their presence in minute concentrations in the initial and treated water effluents pose serious toxic and other effects to humans and other living organisms. These effects are suspected to induce a complete extinction of these populations with time (Klavarioti, Mantzavinos and Kassinos, 2009). Based on these observations, more sophisticated and less laborious analytical tools for their accurate determination and removal are required.

1.3 AIM AND OBJECTIVES OF THE STUDY

The main purpose of this study is to degrade two selected pollutants including O.II dye and sulfamethoxazole (SMX) pharmaceutical drug using an optimised double cylindrical dielectric barrier discharge (DBD) system at ambient conditions. In order to reach this goal, the following objectives need to be achieved:

Optimise the electrohydraulic discharge (EHD) reactor to a new sealed double cylindrical dielectric barrier discharge (DBD) system.

Quantify the reactive species mainly O_3, H_2O_2 and $^{\cdot}OH$ produced in the DBD reactor using distilled water as model pollutant.

Optimise the DBD reactor using orange II sodium salt dye (O.II) as a model compound whereby the effect of physical, chemical and electrical parameters on O.II dye could be assessed individually.

Optimise the DBD reactor using the selected sulfamethoxazole (SMX) drug as a second model contaminant and establishment the degradation mechanistic pathways. During this process, the impact of physical, chemical and electrical factors on the removal of SMX could be evaluated separately.

Compare the DBD advanced oxidation process with DBD+ catalysts for the degradation of the selected pollutants.

Develop anticorrosion layers for durable catalytic supports in the harsh oxidative DBD environment.

1.4 RESEARCH HYPOTHESIS

Persistent organic pollutants such as pharmaceutical residues and textile dyes can be totally oxidised and mineralised into dissolved CO_2, H_2O and harmless inorganics by an optimised DBD configuration. The incorporation of a supported photo catalyst in the optimised DBD system may improve pollutants removal efficiencies in a short treatment time. The coating of stainless steel (SS) with anticorrosion layers may not only protect SS catalyst support from corrosion but may assist in developing solid and adequate photo catalytic supports that can be employed in the DBD geometry. Furthermore, the immobilisation of catalyst on solid supports may help to overcome the post separation issues when powder catalysts are used in water and wastewater treatment.

1.5 RESEARCH QUESTIONS

A large number of organic and inorganic contaminants in water and wastewater present an endocrine activity. The existence of these pollutants in water effluents and the failure of conventional and some novel treatment methods for their remediation have led to many unresolved questions.

What is the benefit of DBDs and how do they work?
What are their best configurations?
What active species do they produce?
How can one test for the active species?
Are DBDs effective for the removal of dyes and pharmaceuticals from water and wastewater?
What are the degradation mechanistic pathways of pollutants?
Can the process be intensified by catalysis or photo catalysis?
What materials are stable in the harsh oxidative environment of DBD system?

1.6 EXPERIMENTAL RESEARCH APPROACH OF THE CURRENT STUDY

An in depth review on the degradation of POPs, mainly pharmaceutical and textile dyes, has been prepared. The review showed that multiple methods have been employed for the removal of POPs from contaminated waters. However, their refractory tendency implies that some of these xenobiotics are resistant to conventional treatment techniques. This necessitates development of novel procedures for their complete oxidation ideally into dissolved CO_2, H_2O and inorganic salts. AOPs based on non-thermal plasma technologies mainly DBD configurations have recently been proved effective for the removal of POPs and related contaminants from water. Of interest, in our previous studies (Mouele 2014; Tijani et al. 2017), an open DBD system was used for the decomposition of various pollutants including methylene blue (MB) dye, Bisphenol A and 2-nitrophenol. The results of these investigations demonstrated that the DBD is a promising technology that could be employed as an efficient integrative method for the removal of recalcitrant organic pollutants. However, the evaporation of ozone during experiments suggested that DBD should be reconfigured to a closed semi-batch geometry that can trap more ozone and hence boost the formation of various oxygen based species. Thereafter, the optimisation of the newly reconfigured reactor and incorporation of a photo catalyst could lead to a total oxidation and mineralisation of the targeted pollutants.

So the achievement of these goals required coherent experimental steps that were subdivided into 4 sections as described below.

Section I: Quantification and optimisation of the reconfigured DBD reactor

In section I, the free reactive species mainly O_3, H_2O_2 and $^{\cdot}OH$ radicals generated in the DBD system were subsequently quantified using Indigo, pertitanyl sulphate and terephtallic acid spectroscopy techniques, respectively. The effect of pH on the production of each species was investigated. The effect of scavengers and that of the amount of chemical probe on the generation of the active species in the reconfigured DBD configuration were also examined. In addition, section I incorporates the optimisation of the reconfigured DBD reactor using O.II and SMX as model persistent organic pollutants. Furthermore, the degradation intermediate metabolites of the two contaminants and their degradation mechanistic pathways in the optimised DBD reactor were also determined.

Section II: Sol gel synthesis and characterisation of a co-doped powder C-N-TiO_2 Nano catalyst and photo catalytic activity test is presented in section II. A co-doped C-N-TiO_2 nano catalyst was prepared by a sol-gel method. In order to assess the effect of pyrolysis time on the electronic and structural properties of the catalyst, the C-N-TiO_2 sol-gel was pyrolysed at three different holding times, 105, 120 and 135 min. Then the photocatalytic activity of the ground powder nano catalyst was evaluated for the removal of O.II under UV-light irradiation at the indicted conditions.

Section III: Preparation of anticorrosive coatings and corrosion study

In section III, various transition metals namely Cr, Ti, Zr and Si nitride and oxynitride anticorrosive coatings were prepared by cathodic arc evaporation methods. The anticorrosion performance of the coatings was examined by potentio dynamic polarisation process. The characterisation of the anticorrosive coatings before and after corrosion is also disclosed.

Section IV: Immobilisation of the C-N-TiO_2 nano catalyst on SS, pure Ti meshes and on anticorrosive coatings and photocatalytic application

In section IV, the C-N-TiO_2 nano catalyst was deposited on the various supports, namely tainless steel (SS) mesh, Ti mesh and on anticorrosion coated SS by dip coating at room temperature. The catalyst coated supports were calcined at 350 ^{o}C at a ramping rate of 50 ^{o}C /min for a holding time of 105 min. The photo catalytic performance of the C-N-TiO_2 coated upon anticorrosion coatings was assessed up on the degradation of O.II dye under UV-light at the applied conditions. Alternatively, the same C-N-TiO_2 sol gel was spin coated on glass and annealed at 350^{o}C, at a ramping rate of 10 ^{o}C /min for 105 min holding time. The adhesion of

the prepared films was tested upon the photocatalytic degradation of O.II under UV light at the corresponding conditions.

1.7 SCOPE AND DELIMITATION OF THE STUDY

1.7.1 Scope

The typical dielectric barrier discharge open semi batch advanced treatment system was earlier initiated by Okolongo, Petrik and Perold (2013) for water and wastewater remediation at UWC and was later optimised by Mouele (2014) during degradation of synthetic MB defined dye wastewater. However, during the optimisation process, it was noticed that the O_3 produced in the open reactor escaped and was evidenced by an irritating smell of ozone that needed to be resolved. Therefore, this actual study focuses on reconfiguring a closed double cylindrical dielectric barrier discharge (DBD) system whose optimisation using O.II dye and SMX pharmaceutical drug as model pollutants led to improved efficiency. To achieve the optimisation process, the effect of physico-electrochemical parameters such as pollutants initial concentrations (mg/L), solution pH, air flow rate (L/min) and the peak voltage (kV) on the degradation efficiencies of the targeted contaminants were successively evaluated. Nevertheless, before the optimisation process, the major free active species mainly O_3, H_2O_2 and OH were quantified by spectroscopy techniques to determine the effectiveness of the newly reconfigure DBD reactor. Next, the synthesis and characterisation of C-N-TiO_2 photo catalyst and its incorporation in the newly redesigned DBD configuration was achieved in the actual study. Furthermore, the development of anticorrosive coatings and the determination of their corrosion resistance to oxidation in the current system were also conducted. Thereafter, the catalysts on supports were compared by photocatalytic tests.

1.7.2 Delimitation

Despite of the results obtained in this study, the measurement of UV-light generated inside the newly reconfigured DBD reactor is still a challenging task to achieve. Apart from this, the up scaling of the current DBD reactor to an industrial level and related costs were not part of this study.

1.8 SUMMARY OF THE SUBSEQUENT CHAPTERS

All aspects covered in this study resulted in nine chapters that were subsequently outlined as shown below:

Chapter two: This chapter presents the literature review of the overall study focussing on various aspects including the quantification of reactive oxygen species (ROS) in advanced oxidation processes and electrical discharges during water and wastewater treatment. Moreover, the occurrence of pharmaceuticals and dyes in effluents and their removal by AOPs among which DBDs are also highlighted. Chapter 2 further outlines the incorporation of C-TiO_2 and C-N-TiO_2 in AOPs and mostly in DBDs for the removal of dye and pharmaceutical toxins from water and wastewater. Chapter II also outlines corrosion measurement principle and the exploration of crucial factors that were extracted to define corrosion behaviour in harsh environments. Finally various analytical methods/ procedures, and characterisation techniques used in this study have also been reviewed.

Chapter three: This chapter details all experimental protocols used to achieve the aims and objectives of the study previously highlighted in section 1.3. As described in the study flow diagram, chapter 3 discloses the sequential experimental techniques used for analysis, characterisation starting from the quantification of free reactive species in the DBD reactor and its optimisation. This chapter also shows methodical procedures employed in corrosion measurement, catalyst synthesis and its immobilisation on various supports including SS, pure Ti and anticorrosive meshes and glass. The photocatalytic protocols for the degradation of O.II are also outlined.

Chapter four: This chapter covers all results based on the quantification of reactive species, mainly O_3, H_2O_2 and $^{\cdot}OH$ using indigo, pertitanyl sulphate and terephtallic acid spectroscopic techniques, respectively. The impact of solution pH on the formation of each species is defined. Finally, the effect of scavengers, and the influence of the amount of chemical probe on the production of OH radical in the reconfigured DBD are successfully investigated.

Chapter five: In this chapter, the results on optimisation of the newly designed DBD reactor are presented and discussed. That is, the effect of physico electrochemical parameters such as initial concentration, solution pH, and air flow rate and peak voltage on the degradation efficiencies of O.II dye and SMX pharmaceutical pollutant are evaluated. The pollutant degradation intermediates by-products are successfully detected and their degradation mechanistic pathways are also defined.

Chapter six: This chapter presents the results on the synthesis and characterisation of C-N-TiO_2 co-doped nano catalyst prepared by sol gel method. The effects of calcination holding time on physical, chemical and electronic properties on the synthesised catalyst are surveyed. The influence of calcination time on the morphology, shape and band gap of the C-N-TiO_2 nano composites is clarified. Furthermore, chapter six discloses the results and discussion of the photocatalytic degradation of O.II and SMX achieved with the combination of the optimised DBD and C-N-TiO_2/SS and C-N-TiO_2/Ti films prepared by dip coating of SS and pure Ti meshes substrates in C-N-TiO_2 sol gel. Apart from these, the photo catalytic degradation intermediate metabolites of O.II dye and SMX drug achieved with DBD + C-N-TiO_2/SS and DBD + C-N-TiO_2/Ti films advanced combinations were successfully determined by LC-MS analysis and their decomposition mechanistic pathways were also proposed.

Chapter seven: This chapter deals with the results and discussion on the corrosion study. For this purpose, Cr and Ti nitride and oxynitride based coatings were obtained by cathodic arc evaporation (CAE) and their corrosion resistance was assessed by potentio dynamic polarisation technique. The following parameters: open circuit potential (E_{oc}), polarisation resistance (R_p), corrosion potential (E_{corr}), corrosion current (i_{corr}), porosity (P) and protection efficiency (P_e) were used to define the corrosion performance of each coating in acidic oxidative environment. Upon discussion, chapter seven demonstrates that the most corrosion resistant coating should have a highly increasing E_{oc} and E_{corr} with low icorr and P but may exhibit a high P_e, respectively.

Chapter eight: In this chapter, the results on immobilisation of C-N-TiO_2 on anticorrosive coatings and their application in the photo catalytic removal of O.II under UV-light are discussed. In addition to these, chapter eight also discloses the results and discussion of the deposition of C-N-TiO_2 on glass support by the spin coating method. Consequently, the effects of coating speed and sol gel to solvent ratio on the thickness of the films are investigated. The adhesion of C-N-TiO_2 catalyst on the glass substrate was tested by the photo catalytic degradation of O.II dye under UV-light at the applied conditions.

Chapter nine: This chapter gives the overall conclusions and recommendation of the study. In fact, the results obtained from all experimental protocols were compared in accordance with the hypotheses highlighted in section 1.4. In addition, the experimental results compared in chapter nine demonstrate whether the aims and objectives of the study were achieved. Hence the summarised results provide direct answers to research questions stated in section 1.5. Chapter nine further points out challenges/limitations encountered during the study and importantly possible solutions and future recommendations.

CHAPTER II: LITERATURE REVIEW

2 INTRODUCTION

The scarcity of clean and fresh water across the globe has been an urgent burden that requires direct remediation. Water contamination and treatment has become the most studied subject in environmental research worldwide. Indeed, wastewater denotes any water whose quality has been undesirably modified by human activities or natural causes. The mixture of industrial, domestic, agricultural or commercial activities, stormwater or surface runoff and infiltration or sewer outflow has been recognised as the principal sources of wastewater (Tilley *et al.*, 2014). Municipal wastewater often referred to as sewage, is generally transported in a collective or clean drain straight to a water and wastewater treatment plant (WWTP) where it gets gradually cleaned. However, the occurrence of prescription and non-prescription pharmaceutical drugs in surface water streams has drawn global attention in recent years. Though the effect of these pollutants on humans and aquatic species are still unknown or under investigation, preliminary genotoxic and immunotoxic effects of pharmaceuticals on fish have been reported (Liney *et al.*, 2006) after exposure to wastewater containing estrogenic and alkylphenolic compounds. Hence the presence of pharmaceutical drugs in water and wastewater treatment plants (WWTPs) and distribution systems show the inefficiency of the sewage treatment plants (STPs) for their complete removal. Apart from political campaigns, green environmental awareness, conventions, etc., pharmaceutical toxic discharge monitoring processes still necessitate more practical methods for environmental remediation. This, therefore, entails the reduction of toxins or cleaning of waste before being discharged into the environment. To alleviate water pollution problems, numerous conventional treatment methods such as flocculation, filtration, electrocoagulation, chlorination, sedimentation, biological digestion, etc. have been established (Saracino et al. 2015). Although these conventional remedies have been proved suitable for the removal of many contaminants from water, emerging organic pollutants (EOPs) escape these treatment techniques and end up in the treated effluents. In addition to this, biological digestion has not been able to remove many biorecalcitrant pollutants as these technologies were not designed for removal of recalcitrant pollutants. Lately, advanced oxidation processes (AOPs) such as ultraviolet disinfection and photolysis, photolysis of H_2O_2 or O_3, photo-catalysis, electron-beam, plasma technologies, supercritical water oxidation, wet air oxidation, water sonolysis, sonolysis by ultrasound cavitation, electrochemical oxidations and sonoelectrochemistry have been developed to remove organic

contaminants from water matrices by converting them into harmless end products without any separation or post-treatment processes (Ivancev-Tumbas, 2014). AOPs are based on the production of powerful non-toxic and nonselective hydroxyl radical ($OH^{\cdot}$) oxidants that completely oxidises and mineralises organic pollutants. The abundance of dyes in wastewater and their removal by AOPs have been reviewed in our previous study (Massima, 2014). This chapter presents a review on the occurrence of pharmaceutical (and dyes to some extent) pollutants in water and wastewater, and their removal by various AOPs such as the dielectric barrier discharge (DBD) system, photocatalysis, or by a combination of both. In addition to this, methods on detection and quantification of free radicals produced in DBD systems and their effect on pollutants are also presented. Furthermore, various analytical and characterisation techniques employed during the treatment of water and wastewater have also been reviewed.

2.1 Sources of pharmaceutical substances in aquatic environment

For the past decades, pharmaceutical drugs have increasingly been consumed around the globe for various purposes including recreation health, cleaning, beauty maintenance, etc. For instance, (Khetan et al. (2007) and Magureanu et al. (2015) emphasised that in recent years, the population growth has triggered the disproportionate utilisation of numerous types of pharmaceuticals substances. This consequently has increased the direct or indirect contamination of water sources. Apart from that, human excretions containing defecated pharmaceuticals circulate through the sewage system and end up in wastewater treatment plants (WWTPs). Research studies on surface water treatment have shown that pharmaceuticals are non-biodegradable in sewage treatment plants and trace amounts of these toxins have been detected in different water sources (Esplugas *et al.*, 2007; Trovó, Melo and Nogueira, 2008; Rizzo *et al.*, 2009). These have also been viewed as one of the principal sources of water pollution. Literature sustains that some of the evacuated pharmaceuticals are not totally removed (Thomas et al. 2009; Magureanu et al. 2015). Since WWTPs technologies have not been designed for removal of such compounds, these contaminants escape through the treatment and are therefore transferred to surface and even to drinking water. In agriculture, the emitted veterinary pharmaceuticals initially infect soil mostly by fertiliser spread on the soil followed by run-off and leaching, further contaminating ground and surface water. Moreover, WWTP sludge containing nondegradable pharmaceuticals are also often utilised as

manure in agriculture and contaminate surface water following the same routes as previously described. In addition to this, veterinary pharmaceuticals employed in aquaculture and unutilised medicines discarded in landfills might also contaminate groundwater by leaching. Furthermore, the discharge of pharmaceutical remains from the manufacturing industries, or leaks during production or delivery processes can also contribute to water pollution. In turn, even if contaminated ground and surface water reach drinking water treatment plants (DWTPs) for purification purpose before distribution, the minute recalcitrant and nonbiodegradable pharmaceuticals might still pass through during that treatment stage and end up in tap water (Mouele *et al.*, 2018). The water contamination sources described above were summarised by Magureanu et al. (2015)and are presented in Figure 2-1.

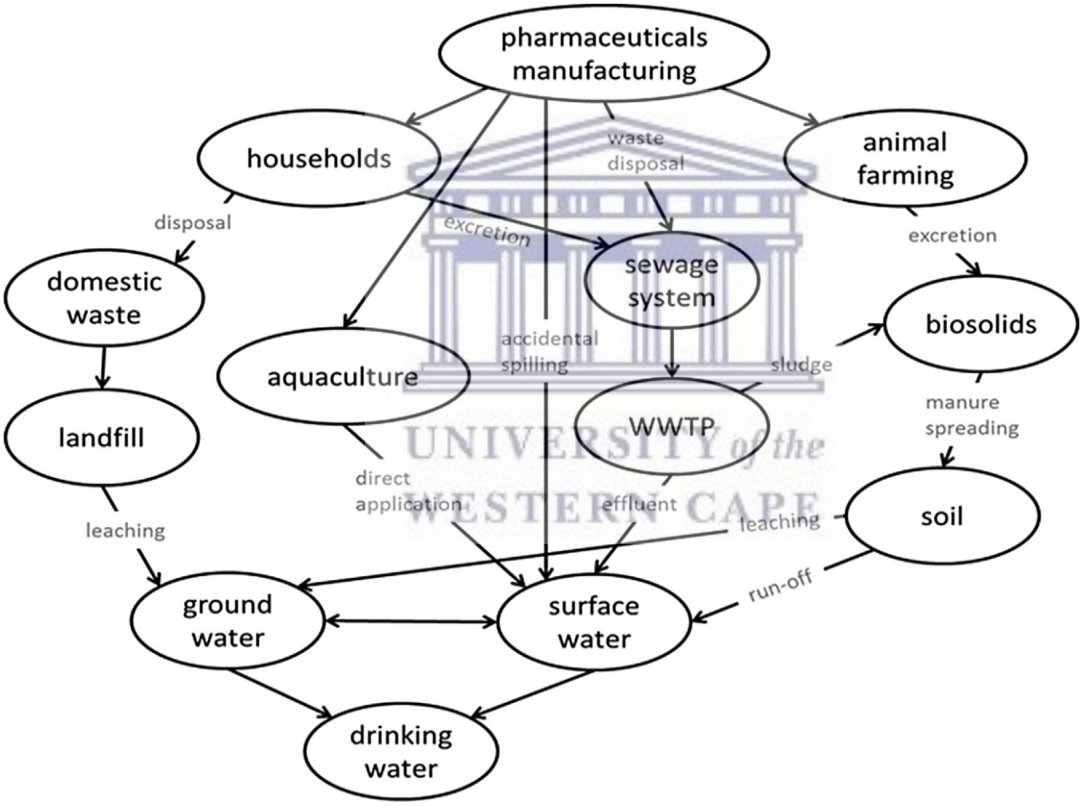

Figure 2-1: Sources of pharmaceutical products in the environment. (Magureanu, Mandache and Parvulescu, 2015).

2.1.1 Different types of pharmaceutical compounds

Various authors ((Evgenidou et al.2015; Homem et al. 2010; Lopez-Serna et al. 2012; Van Doorslaer et al. 2015; Swartz et al. 2017) confirmed that diverse pharmaceutical contaminants have been detected in influents and effluents of WWTP. These pollutants are often divided into

various groups. To begin with antibiotics, their occurrence in the environment was reported in high mg/L quantities in hospital sewage with minor mg/L concentrations found in municipal effluents and ng/L level reported in surface, ground wastewater and in tap water, respectively (Loraine et al. 2006; Yiruhan et al. 2010; Magureanu et al. 2015) This particular group of pharmaceuticals has attracted environmental scientist's attention due to their ability to cause resistance in bacteria in WWTPs (Daughton and Ternes, 1999). For instance Homem et al. (2010), Chahbane *et al.*, (2007) and Van Doorslaer et al. (2014) showed that antibiotics such as sulfonamides and fluoroquinolones may be toxic to aquatic species and their phytotoxicity might be problematic to the environment. Trovó et al. (2008) emphasised that recent scientific attention has been devoted to antibiotics due to their causing resistance in bacteria. In addition to antibiotics, Non-Steroidal Anti-Inflammatory Drugs (NSAIDs) is another class of pharmaceuticals that exhibit pain-relieving, antipyretic and anti-inflammatory properties. Various authors highlighted that the high consumption of NSAIDs results in their presence in WWTPs streams where they have been identified in tens of mg/L (Lopez-Serna et al. 2012; Evgenidou et al. 2015).. Likewise, their concentration expressed in tens to hundreds ng/L in WWTPs was reported by other authors (Rabiet et al. 2006; Lopez-Serna et al. 2015). Moreover, it has been reported that pharmaceuticals such as aspirin, acetaminophen, diclofenac, ibuprofen, naproxen, ketoprofen, are present in drinking water (Rabiet et al. 2006; Houtman, 2014; Petrovic et al. 2014; Petrik *et al.*, 2017).

In addition, clofibric acid commonly used as blood lipid regulator has recurrently been reported in the environment. This active metabolite has been detected in wastewater treatment plants, ground and water and in tap water in concentrations of tens of mg/L (Heberer and Stan 1997; Heberer 2002; Postigo and Barcelo 2015; Evgenidou et al. 2015; Luo et al. 2014; Lopez-Serna et al. 2012; Wen et al. 2014; Houtman, et al. 2014). This is probably due to its persistent characteristic and high mobility in the aquatic environment as highlighted by Khetan and Collins, (2007). Furthermore, various authors recalled that in addition to clofibric acid, gemfibrozil and bezafibrate have also identified in surface water (Vieno et al. 2005; Lopez-Serna et al. 2012; Petrovic et al. 2014).

An additional group of pharmaceuticals is antihypertensives often used to lower blood pressure include beta blockers such as metoprolol, atenolol and propranolol. These antihypertensives followed by the diuretic furosemide, ACE inhibitors, calcium channel blockers, beta blockers, and angiotensin II receptor antagonists have repeatedly been detected in tens of ng/L in the ground, surface and drinking water (Lopez-Serna et al. 2012; Petrovic et al. 2014; Postigo and Barcelo, 2015). An additional pharmaceutically active compound is carbamazepine, though

used for various purposes; (Humme et al. 2006; Petrovic et al. (2014) reported that this anticonvulsant is mainly used for epilepsy treatment.

Its presence in groundwater and drinking water sources is estimated to about tens of ng/L. However, Rabiet et al. (2006), Zhang et al. (2008), Hu *et al.* (2011) and Luo et al. (2014) claimed that the removal of this chemical is extremely low and might fall below 10 %. The authors indicated that this might be due to its biodegradability resistance at low concentration. Besides, Miao et al. (2005), Petrovic et al. (2014) and Evgenidou et al. (2015) sustained that carbamazepine metabolites are also stubborn in WWTPs, consequently, these toxins often end up in few mg/L in drinking water supplies (Petrovic et al. 2014). Beyond carbamazepine, Heberer, (2002) and Hummel et al. (2006) informed that primidone is another antiepileptic detected in surface water and drinking water. In addition to this, Heberer, (2002) and Hummel et al. (2006) claimed that estrogenic drugs have widely been utilised in hormone-replacement therapy, oral contraceptive as well as in veterinary medicine focusing on growth enhancement. A number of authors Santos et al. (2010) clarified that even at low quantities the aforementioned hormones may cause serious effects. Typical examples of these are 17b-Estradiol, estrone and 17a-ethinylestradiol that have been identified in a few ng/L in river, ground and drinking water (Kolpin et al. 2002; Benotti *et al.,* 2009; Gorga, et al. 2015). Likewise, the impact of these endocrine disruptive compounds (EDCs) on aquatic organisms have been already been summarised by Santos et al. (2010). The pharmaceutical compounds reviewed above have considered as the principal types of water contaminants and have they been summarised by Magureanu et al. (2015) and are presented in Figure 2-2. As a consequence of the growing accumulation of persistent organic pharmaceuticals in the environment, their removal from different water sources using advanced oxidation process constitutes an essential component of research and development in the water and wastewater treatment sector (Arslan-Alaton and Dogruel, 2004a). Their presence in aquatic media has been reported to have significant health effects on humans and ecosystems (Trovó et al. 2008). Some of the various effects of human exposures to POPs include the neurotoxic and behavioural effects in newborns, reduced birth weight and length of growth; reduced seminal parameters; impaired semen quality; Male genital anomalies; Breast cancer in young women; critical infant neurodevelopment, etc. have been estimated (Van Larebeke 2002; Farhang 2005; De Jager 2006; Aneck-Hahn 2007; Bhatia 2005; Cohn 2007; Eskenazi 2006; Torres-Sánchez 2007). It has been established that direct discharge of untreated municipality wastewater, manufacturing effluents and indiscriminate dumping of unused medicines remain the principal sources of

pharmaceuticals in the environment (Magureanu *et al.*, 2010; Rozas *et al.*, 2010). The most common classes of pharmaceuticals found in the environment include non-steroidal anti-inflammatory drugs (NSAIDs), antihypertensive, anticonvulsants, hormones, lipid regulators and antidepressants (Magureanu, Mandache and Parvulescu, 2015). Based on the impacts of pharmaceuticals on humans and aquatic species, different methods have been applied for their removal from water sources.

2.2 Advanced oxidation processes

Several conventional separation methods such as sedimentation, flocculation, filtration, electrocoagulation, etc. have been employed for the removal of organic contaminants from water and wastewater (Emile S.Massima Mouele *et al.*, 2015). Despite their effectiveness in water treatment, these methods produce a large amount of toxic sludge that needs extensive treatment since biological digestion processes have been found ineffective for this purpose. A few decades ago, new chemical oxidation processes such as chlorination and ozonation have emerged as alternative water remediation techniques. However, they have been found unsuccessful in the removal of total organic carbon (TOC) (Saracino et al. 2015). Recently, advanced oxidation processes (AOPs) have been established to decompose organic contaminants from water and wastewater converting them into harmless inorganic and organic substrates without needing any separation and post-treatment methods. The common AOPs documented in the literature include UV disinfection (photolysis) and various photolytic combinations among which UV/H_2O_2, UV/O_3, UV/H_2O_2/O_3 photocatalysis, electron-beam, plasma technologies, supercritical water oxidation, wet air oxidation, water sonolysis and ultrasound cavitation, electrochemical advanced oxidation processes (EAOPs), microwave, plasma-based AOPs, etc (Mouele *et al.*, 2015; Saracino et al. 2015). Although these procedures use different systems they all converge towards the production of powerful but short-lived non-toxic and non-selective hydroxyls radical (·OH) that mineralise water contaminants into simpler compounds. Wardman, (1989) showed that the production of OH· depends on the pH, and its oxidation potential of about E_o = 2.8 V makes it the most powerful benign oxidant. The use of AOPs technologies in water treatment facilities has been well documented to eliminate bio recalcitrant substances and hence prevent their escape to the environment during discharge processes (Ghatak, 2014). Furthermore, literature showed that most AOPs do not only produce OH·, likewise other oxidative and reducing species such as hydrogen atoms (H·), atomic oxygen

($O^{\cdot}$) and/or solvated electrons are also generated. These supplementary radicals induce a chemical process often referred to as advanced redox or remediation processes.

The removal of recalcitrant organic pollutants such as dyes, pharmaceuticals, and personal care products in industrial wastewater effluents has been the subject of research in recent years (Altinbas et al. 1995; Olcay and Isik, 1996; Ledakowicz et al. 2001; Al-Kdasi *et al.*, 2004; Abdelmelek *et al.*, 2011; Capobianco *et al.*, 2013; Slang et al. 2017). In this regard, various treatment methods such as adsorption on activated carbon, ozonation, and reverse osmosis, ion exchange on synthetic adsorbent resins, flocculation, and decantation have been developed (Altinbas, Dökmeci and Baristiran, 1995; Guivarch *et al.*, 2003; Li Puma, Bono and Collin, 2008; Rajeshwar *et al.*, 2008). However, most of these methods have high operating costs and/or are inefficient due to the complexity of the aromatic structures of pollutants (Rajeshwar *et al.*, 2008). Therefore, advanced oxidation processes (AOPs) have recently been considered as robust techniques capable of destroying organic pollutants in water and wastewater, converting them into harmless substances without any post-treatment processes needed (Arslan-Alaton and Dogruel, 2004b; Ghatak, 2014; Saracino *et al.*, 2016).

2.2.1 Plasma based AOPs

Often referred to as the fourth state of matter, plasma is a combination of various species, mainly electrons, free radicals, ions and neutral species that are usually produced in various electrical discharges. Depending on temperature effects, plasma technologies are subdivided into two groups: thermal and non-thermal plasmas. Thermal plasmas require high energy used for the production of the free radicals and related species and hence attain thermal equilibrium (Mouele *et al.*, 2015). On the other hand, non-thermal plasma demand less power and largely produce energetic electrons at ambient conditions (Jiang *et al.*, 2014). In addition to this, the generated energetic electrons may activate and dissociate the feed gas leading to various subsequent reactions that in turn produce numerous oxidising and reducing agents such as $O^{\cdot}$, $OH^{\cdot}$, HO_2, etc. that efficiently destroy water pollutants. For the last decade, liquid electrical discharges (EDs) mainly dielectric barrier discharges (DBDs) have become part of the most studied plasma systems for the removal of pollutants in water and wastewater. Their physical and chemical properties should be studied for their efficacy in water treatment.

2.2.1.1 Description of dielectric barrier discharge

Dielectric barrier discharge (DBD) has been characterised as a silent AC electrical discharge that offers thermodynamic properties and produces reasonable non-equilibrium atmospheric plasma. Valinčius et al. (2012) reported that based on DBD plasma properties and the various electrode configurations, various terms such as barrier discharge, silent discharge, arc-discharge, normal pressure glow discharge, ozonizer discharge, and display discharge are used to describe DBD. Most DBD configurations reviewed in the literature consist of the anode and cathode electrodes. Likewise, one of the two electrodes mainly the anode is usually surrounded by one or more dielectric layers such as pyrex, quartz or ceramic which present a high insulation constant. The aforementioned dielectric materials are often used to separate the anode from the gas layer (single dielectric) or usually placed between electrodes to separate two gas layers (double dielectric). The principal goal of atmospheric non-thermal DBD plasma is to ensure the continuous production of ozone gas that is directly circulated in the effluent being treated (Valinčius et al. 2012). Based on these findings, Nehra et al. (2008) differentiated traditional discharges from novel DBD configurations by the fact that in conventional DBD electrode arrangements, both cathode and anode are directly in contact with the feed gas and plasma. This often results in electrode etching and precipitated corrosion during the plasma discharge process. Conversely, in DBD systems, the existence of one or more insulating layers eliminates the risk of electrode etching and corrosion also intensifying the electric and magnetic fields, thus ensuring the even distribution of highly energised electrons around the dielectric materials. Moreover, research indicated that the air gap (distance between electrodes) could range from a few to several centimeters (Lopez, 2008; Valinčius et al. 2012). In addition to this, the aforementioned authors clarified that the dielectric materials in DBD geometries distribute the charges transported by a single micro discharge (micro plasma) over the entire surface of the anode rod. Furthermore, non-thermal plasma operation conditions are simple compared to those of electron beam, low-pressure discharges and pulsed high-pressure corona discharges (Konelschatz, 1997). The most common DBD electrode configurations involve either single or double planar or cylindrical dielectric-barrier discharges. These have earlier been reviewed by Kogelschatz, (2000, 2003) and their electrode geometries are presented in Figure 2-2.

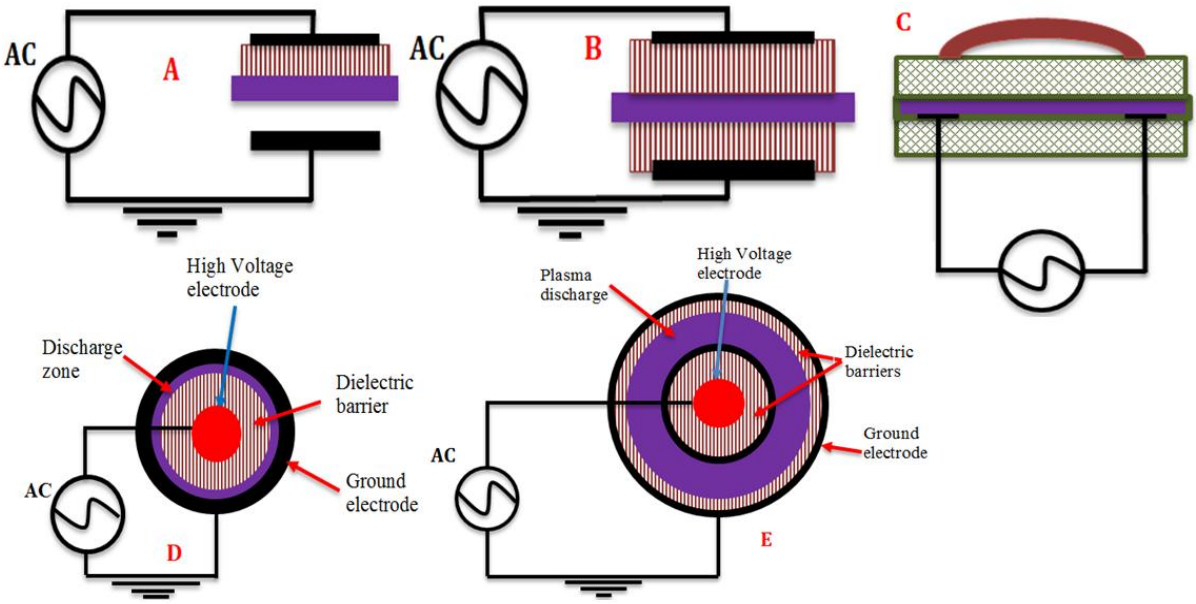

Figure 2-2 Common dielectric barrier discharge electrode configurations used in water and wastewater treatment; A = single planar DBD, B&C = Double planar DBD; D&E = single and double cylindrical DBD (Kogelschatz, 2000, 2003).

Based on the DBD benefits previously described, DBD configurations shown in Figure 2-2 have recently been used as effective water and wastewater treatment technologies even though the upscaling of these configurations has always been challenging. Despite the rising utilisation of DBD configurations in recent years, the electrode geometric presented in Figure 1 E, termed double cylindrical dielectric barrier discharge (DBD) has restrictively been used in the literature for the removal of pharmaceuticals. Therefore, this study focuses on the use of DBD for the removal of selected dyes and pharmaceuticals at ambient conditions. But beforehand, a full description of DBD reactor configuration is detailed in the following paragraphs.

2.2.1.1.1 Description of double cylindrical dielectric barrier discharge system and discussion of the different zones and formation of the free active species

The choice of dielectric barrier electrohydraulic discharge (DBD) as one of the AOPs is based on its ability to decompose persistent organics and eliminate microbes. DBD offers advantages such as efficiency, energy saving, rapid processing, use of few or no chemicals, and non-destructive impact on the ecosystem. The system is also capable of generating ozone, hydrogen peroxide, singlet oxygen, superoxide radicals, hydroxyl radicals, and other active species. The combination of these reactive species has been reported to degrade biological and chemical pollutants rapidly and efficiently. In order to understand the prominence of DBD systems and

where the UV light and some of the highlighted species are formed, a schematic of a double cylindrical DBD plasma reactor is presented in Figures 3-2 and 3-3 and the different reaction zones are subsequently discussed.

2.2.1.2 Degradation of pharmaceuticals by DBDs

Advanced oxidation processes such as dielectric barrier discharges (DBD) involving the generation of non-selective hydroxyl radicals have been identified as promising for effective degradation and mineralisation of target pollutants in water and wastewater (Gauthier et al. 2013; Mouele *et al.*, 2018). Apart from the production of ·OH radicals, the DBD system also generates UV light, O_3, H_2O_2, O among other, and their combination in aqueous media allows water and wastewater treatment without the addition of chemicals. The decomposition of pharmaceuticals by non-thermal plasma, mainly dielectric barrier discharge, has been well reported (Magureanu *et al.*, 2010; Liu *et al.*, 2012; Rong, Sun and Zhao, 2014). Magureanu *et al.*, (2010) utilised dielectric barrier discharge (DBD) to decompose veterinary antibiotics such as lincomycin, ciprofloxacin, enrofloxacin, chlortetracycline, oxytetracycline, sulfathiazole, sulfamethoxazole, sulfamethazine and trimethoprim in aqueous solution. The influence of various parameters such as the type of gas used (air, O_2) and gas flow rates, the initial concentration of contaminants and the discharge power on the decomposition of the targeted antibiotics were assessed. The results of their study showed that different antibiotics decomposed differently and their degradability depended on the amount of energy provided and hence followed an exponential decay with respect to the energy delivered in the DBD system. The effect of the parameters evaluated showed that at an optimum antibiotic concentration of 5 mg/L, 90% degradation was achieved.

Some pharmaceuticals have been proved non-degradable by AOPs as well as in conventional treatment methods. A typical example focuses on both ionic and nonionic ICM-iopromide that have been claimed to be recalcitrant to ozone and traditional wastewater treatment plants (Liu *et al.*, 2012). Consequently, in 2012, Liu and co-workers investigated the removal of one kind of ICM-iopromide (IOPr) using dielectric barrier discharge (DBD). Their experimental results showed that about 98% removal of IOPr was achieved at the applied conditions. Unfortunately, the authors did not observe any decrease in total organic carbon (TOC). Likewise, by using FT-IR spectra, Liu and colleagues (2012) proved that the degradation of IOPr molecule was mainly induced by hydroxylation, carbonylation and deiodination processes. In addition, the authors used biological oxygen demand (BOD) and chemical oxygen demand (COD)

measurements to show that the biodegradability of IOPr increased significantly during DBD treatment and the removal of IOPr from the solution followed first-order kinetics. Furthermore, the authors reported that the resulting by-products of IOPr after DBD treatment were easily absorbed and biodegraded by activated sludge. Based on their results, the authors claimed that DBD can be used to increase the biodegradability of recalcitrant pollutants. Moreover, Magureanu et al. (2015) used dielectric barrier discharge to decompose enalapril and its metabolite, enalaprilat in aqueous solution. The authors reported that the discharge was initiated at the interface between the gas and the solution which flowed as a film on the surface of the inner electrode of the plasma reactor. The outcomes of their research showed that six degradation intermediates were identified using liquid chromatography coupled to mass spectrometry (LC-MS) analysis. Their study confirmed that the degradation by-products were decomposed to small molecules and their mineralisation (40 %) was determined by TOC and COD measurements. Most of these investigations have been concisely summarised by Magureanu et al. (2015). From the various studies highlighted in the literature, it could be observed that different degradation and mineralisation efficiencies of pharmaceutical compounds were achieved due to various various designs and various oxidative species produced in the corresponding configurations. Likewise, most pharmaceuticals in previous studies have been decomposed at optimised experimental conditions which included pollutant concentration, pH, UV radiation intensity, etc. This means that when dealing with the removal of pharmaceuticals from effluents, it is necessary to optimise the aforementioned parameters in order to achieve the maximum desired removal of the pollutant in each case. Other AOPs such as heterogeneous photocatalysis involving the application of semiconductor photocatalysts have also been used for the oxidation of pharmaceuticals in water effluents (Klavarioti et al. 2009). Among the heterogeneous photocatalysis, titanium dioxide (TiO_2) has been considered due its high efficiency, stability and low cost (Sirés and Brillas, 2012; Tong *et al.*, 2012; Duan *et al.*, 2015).

2.3 Semi-conductor photocatalysis

In comparison to other AOPs reported in the literature in the last two decades, photocatalysis has been the subject of many research studies. Though being applied for multiple purposes such as hydrogen production, self-cleaning coatings etc., the photocatalysis process has gained particular attention in drinking and wastewater treatment (Gilmour and Ray, 2012). Gilmour, (2012) emphasised that even if photocatalysis has been restrictively used at an industrial level

compared to ozonation and UV/H_2O_2, its application at the academic level has led to numerous publications in the last three decades using P25 TiO_2 as an inexpensive and non-toxic, powder form photocatalyst. The main advantage of this technology is the production of hydroxyl radicals, the highly non-selective oxidative species that ideally mineralise pollutants into CO_2, H_2O and harmless organic and inorganic end products.

The photo-catalysis process involves the use of ultraviolet or visible light as the source of energy that promotes electrons from the valence band of the TiO_2 photo catalyst to the conduction band leaving electronic vacancies or positive holes in the valence band (Al-Kdasi *et al.*, 2004). The positively charged holes are highly oxidative and can rapidly react with organic molecules adsorbed on the photo catalyst surface leading to their degradation, or may oxidise aqueous hydroxyl anions leading to the formation of OH radicals which in turn effectively degrade contaminants. In addition, excited electrons react with adsorbed water molecules and also cause the reduction of dissolved O_2, respectively, producing •OH and O_2^{2-} species that degrade nearby organic molecules (Nakata and Fujishima, 2012; Khan et al. 2015). Consequently, various classes of water pollutants including azo dyes have been treated using TiO_2 based photocatalysis (Konstantinou and Albanis, 2004; Rajeshwar *et al.*, 2008; Madhu *et al.*, 2009; Kuang et al. 2011).

Among various AOPs highlighted in the literature, heterogeneous photocatalysis has been identified as a robust process that slowly but totally decomposes and mineralise most contaminants (Rizzo *et al.*, 2009; Addis *et al.*, 2011). The degradation process is induced by UV-light illumination of powder TiO_2 in the aqueous medium that often results in slow kinetics (Rizzo *et al.*, 2009). Indeed, TiO_2 is considered as a suitable semiconductor often acting as dye-sensitizer inducing light redox-processes because of its electronic arrangement of metal atoms combined with other elements (Park *et al.*, 2011; Lewkowicz *et al.*, 2014; Y. T. Lin *et al.*, 2014). Besides, TiO_2 has been found efficient, nontoxic, highly photoactive, biologically and chemically inert, inexpensive, resistant to photo-corrosion and chemical corrosion, recyclable and has suitable band gap (Eg = 3.2 eV) in which oxidation and reduction processes occur (Cheng *et al.*, 2012; Lazar *et al.* 2012; Jiang *et al.*, 2014; Rajendran *et al.* 2014; Klaysri *et al.*, 2017). These characteristics have rendered TiO_2 a popular heterogeneous semiconductor catalyst for diverse environmental applications (Lin *et al.*, 2014; Klaysri *et al.*, 2017).

2.3.1 Photocatalytic mechanism

Based on its physical and chemical properties, Huisman and Reller, (2004) and Gilmour, (2012) reported that titanium dioxide (TiO_2) exists in either the anatase or rutile phase and has a band-gap of 3.2 or 3.0 eV. Any photons with a particular energy surpassing this gap ($\lambda < 388$ nm) causes excitation of electrons which are promoted to the conducting band, creating a positive hole in the valence band usually referred to as the electron-hole pair ($e^- - h^+$), where C_b and V_b indicates conduction band and valance band correspondingly as shown in Figure 2-3. Depending on their excitation wavelengths, Gilmour, (2012) sustained that the promoted particles likely fall back and recombine with the positively charged holes to generate heat or become trapped or migrate to the surface to contribute in a sequence of redox reactions as shown in Equations (2.1-2.4), where e_{tr}^- represents the trapped charge. The schematic description of this process suggested by Chen *et al.* (2000) is shown in Figure 2-3

$$TiO_2 + hv \rightarrow e^-_{cb} + h^+_{vb} \quad (2.1)$$

$$e^-_{cb} + h^+_{vb} \rightarrow \text{heat} \quad (2.2)$$

$$E_{cb} \rightarrow e^-_{tr} \quad (2.3)$$

$$h^+_{vb} \rightarrow h^+_{tr} \quad (2.4)$$

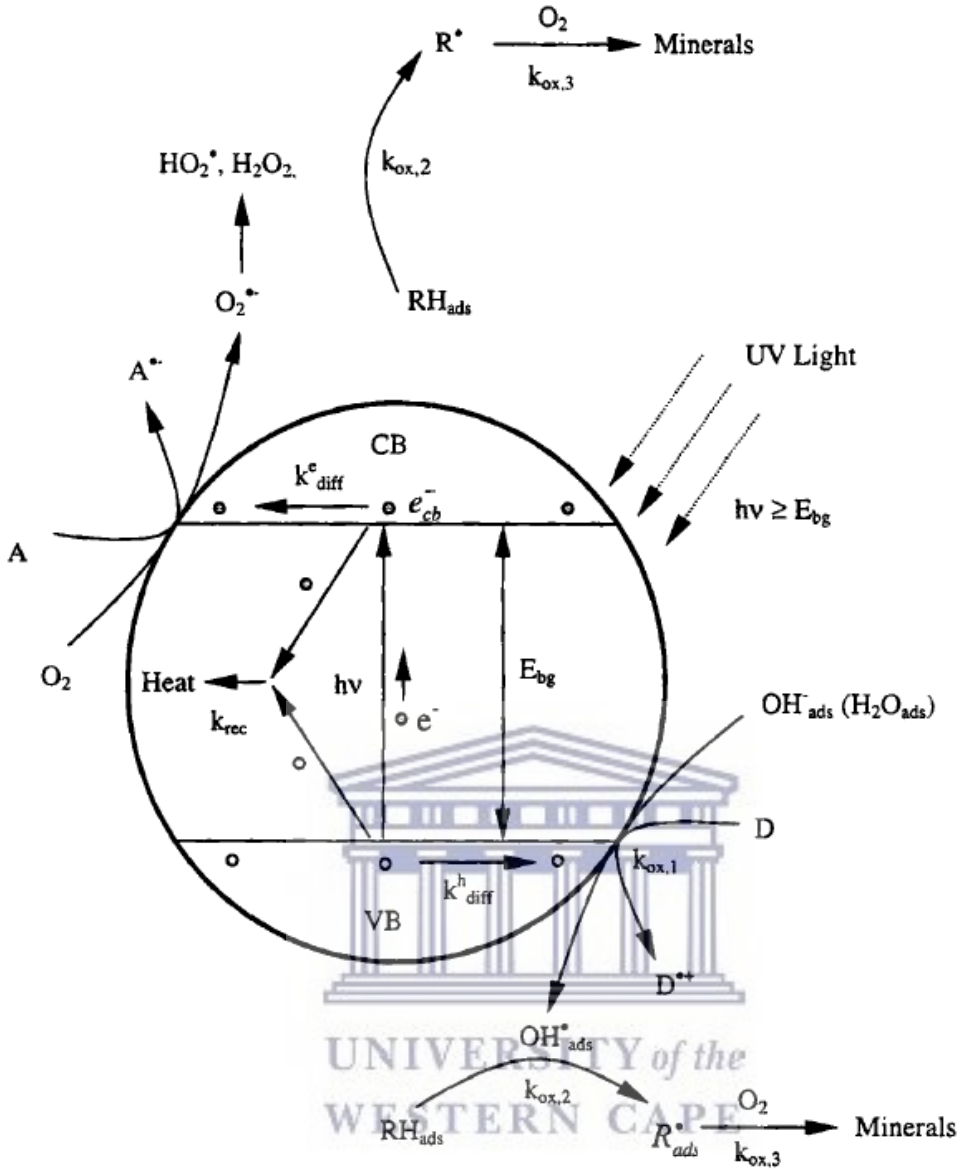

Figure 2-3 Photo-induced formation of electron–hole pair and corresponding reactions pathways in a spherical TiO_2 particle (Chen *et al*., 2000).

Moreover, Lafi and Al-Qodah, (2006) and Gilmour, (2012) stated that in an aqueous solution subjected to irradiation, the catalyst often becomes electrostatically stable. So in that steady-state, the number of electrons and positive holes moving to the surface becomes equal. Consequently, the mineralisation of the aqueous pollutants occurs either by an oxidation reaction with the surface trapped holes or by oxidation with hydroxyl radicals (·OH) or with surface adsorbed molecular water and hydroxide ions that in turn contribute to the production of ·OH as shown in Equations (2.5 - 2.12), where ads are the adsorbed species.

$D_{ads} + h^{+}_{tr} \rightarrow D + ads$ (2.5)

$H_2O_{ads} + h+tr \rightarrow OH^{\bullet}_{ads} + H^{+}$ (2.6)

$OH_{ads} + h+ tr \rightarrow OH^{\bullet}_{ads}$ (2.7)

$(O_2)_{ads} + e- \rightarrow O_2^{\bullet-}$ (2.8)

$H+ + O_2^{\bullet-} \rightarrow HO_2^{\bullet}$ (2.9)

$2HO_2^{\bullet} \rightarrow H_2O_2 + O_2$ (2.10)

$H_2O_2 + O_2^{\bullet-} \rightarrow OH^{\bullet} + O_2 + OH-$ (2.11)

$H_2O_2 + e- \rightarrow OH^{\bullet} + OH^{-}$ (2.12)

Furthermore, Gilmour, (2012) emphasised that since the surface holes participate in oxidation reactions the charge equilibrium in the aqueous system should be maintained. Therefore, oxygen is usually used as electron scavenger in such a way that the dissolved oxygen is adsorbed onto the catalyst surface and reduced by the surface trapped electrons. This then leads to various reactions producing numerous molecular and ionic species among which H_2O_2 that largely contributes to the production of ·OH, the major non-selective oxidant that mineralises the targeted toxins. The diversity of oxidants produced during photocatalysis has been widely employed for the degradation and mineralisation of pharmaceutical compounds in aqueous media.

2.3.1.1 Photo catalytic decomposition of pharmaceutical compounds

Photocatalytic degradation has been considered as a typical advanced oxidation technology (AOP) employed as efficient water treatment method that focuses on the production of powerful oxidants such as O_3, H_2O_2, O_2·, O·, O_2·· whose combination contributes to efficient degradation and mineralisation of organic pollutants in water and wastewater (Loures *et al.*, 2013; Kanakaraju *et al.*, 2014; Tijani *et al.*, 2014; Mouele *et al.*, 2015). AOPs can be categorised into homogeneous and heterogeneous or photochemical and non-photochemical processes. The homogeneous AOPs include: O_3/UV; H_2O_2/UV; H_2O_2/O_3; O_3/UV/ H_2O_2 while heterogeneous processes are: O_3/UV/TiO_2; $H_2O_2/O_3/TiO_2$; H_2O_2/UV/TiO_2, O_3/UV/ H_2O_2/TiO_2 (Madhu *et al.*, 2009; Iqbal, Bhatti and Ahmad, 2013; Babić *et al.*, 2015b). In order to improve the degradation and mineralisation efficiency of pharmaceuticals in water and wastewater, several studies on photolytic and photocatalytic decomposition of pharmaceuticals compounds have been conducted (P. Nyamukamba *et al.*, 2017; Pardon Nyamukamba *et al.*, 2017). In most of those studies, the following parameters: pollutant concentration, solution pH, catalyst

loading, the energy required in the degradation process as well as the pollutant degradation intermediates have been considered. (Kanakaraju *et al*., (2014) investigated the powder titanium dioxide/zeolite integrated photocatalytic adsorbents for the degradation of amoxicillin (AMX). The results of their study showed that AMX was successfully degraded and the efficiency of the synthesised TiO_2/zeolite material represented an economical means of decomposing pharmaceuticals from water effluents. Apart from antibiotics, anti-inflammatory drugs are also commonly used by communities for different purposes and their presence in the environment has become problematic, hence their removal in the aquatic media is required. Nadim *et al.,* (2015) studied the photocatalytic degradation of meloxicam in the presence of powder form TiO_2 nanoparticles (TiO_2NP). In their study, the authors examined the effects of pH, irradiation time, UV light intensity, TiO_2 NP loading, and initial meloxicam concentration on the degradation efficiency of the process. The results of their study showed that light intensity, irradiation time and pollutant concentration, respectively were the most important parameters in the decomposition process of the meloxicam drug. At optimum conditions and after 8 h, approximately 77% of meloxicam removal was achieved at concentration of 64.57 µg/mL with UV light (1012 $\mu W/cm^2$) in the presence of 0.4 mg/mL TiO_2NP at pH 9.0. Based on these results, the authors concluded that the treatment of a reasonable volume of collected wastewater with an optimised photocatalytic process using TiO_2 nanoparticles as catalysts could result in maximum removal efficiency of the targeted pharmaceutical compound. Diclofenac (DCF) is another anti-inflammatory pharmaceutical drug whose presence in trace amounts in wastewater induces serious environmental pollution. Das *et al.*, (2015) studied the photodegradation of DCF in the presence of ultraviolet irradiation at room temperature using powder form titania and titania-zirconia nanocomposite catalysts in a batch reactor. The experiment was conducted as a function of initial concentration of DCF, pH of DCF experimental solution and catalyst loading on the degradation of DCF. The results of their study showed that the catalytic activity (in UV light) of titania-zirconia nanocomposites was higher than that of the powder anatase form of titania without zirconia. However, the post-filtration of the powder form TiO_2 based catalysts such as TiO_2/zeolite and TiO_2NP in the treated water in a single or combined reactor system; and its recovery could be costly; and hence limit its photocatalytic application at large scale. In addition, the antibiotic oxacillin (OXA) that is often used to fight bacteria in the body is another pharmaceutical that is designed to fulfill a biological function in living organisms. Giraldo-Aguirre *et al.*, (2015) studied the photocatalytic degradation of OXA using powder form TiO_2 catalyst. In their investigation, the following parameters, pH, powder form catalyst loading and UV light intensity were

considered. The results of their studies showed that the optimum conditions to achieve greater degradation efficiency of OXA were: pH 6, 2.0 g L^{-1} of TiO_2 and 150 W of UV applied power. The removal of both the antibiotic and antimicrobial activity of OXA was achieved within 120 min however 100% mineralisation was slow and only obtained after 480 min reaction time. Furthermore, the decomposition of OXA resulted in five different degradation by-products and the degradation pathways were also proposed. In this regards, it is important to emphasise that, although the total degradation and mineralisation of the targeted pollutants are often difficult to achieve at the same time, these two parameters signify different concepts and may vary from study to another.

Literature supported that the synthesised powder TiO_2 based catalysts provide a large surface area and a high surface area to volume ratio. However, the suspension of powder catalysts during water treatment as reviewed above results in various disadvantages including the difficulty to remove suspended powder catalysts that is often costly. Small catalyst particles stay suspended in water and further impede the filtrations systems, clog filter membranes and penetrate filter materials. The agglomeration of particles during powder TiO_2 synthesis can reduce its dispersion in the solution and further prevent light penetration which consequently limits the catalyst activity (Mills and Le Hunte, 1997; Gilmour *et al.*, 2013)

Various authors sustained that the limitations countered with powder TiO_2 based catalysts could be overcome by immobilisation of the catalysts on adequate supports (Alzamani *et al.*, 2013; Lewkowicz *et al.*, 2014; Blanco et al. 2015). This may result in more cheaper, feasible and practical films that could be used to boost the photo catalytic efficiency for the removal of water pollutants. For instance, Babić *et al.*, (2015) investigated the photocatalytic degradation of sulfonamide antibiotic sulfamethazine (SMT) dissolved in Milli-Q water or in synthetic wastewater. In their study, the authors examined not only the direct photolysis process of the contaminant but also various advanced oxidation combinations including UV/H_2O_2, UV/TiO_2, and UV/TiO_2/H_2O_2 using UV-A and UV-C radiation for the decomposition of SMT. Of all the above-mentioned oxidation combinations, UV/TiO_2/H_2O_2 was found the most effective and complete degradation of SMT was achieved within 10 minutes and the experimental data fitted pseudo-first-order kinetics. Moreover, Babić *et al.*, (2015) reported that UV-A solar radiation was used in their study not only for practical purposes but for lowering the cost of the overall treatment process.

However, UV-A based process required more treatment time (120 min) and hence 2.7 times more electrical energy was consumed in the STM mineralisation process. Moreover, Babić and

co-workers in 2015 identified five degradation intermediates of SMT using tandem mass spectrometry (MS/MS) and NMR analysis and the structural formulae and degradation pathways of these intermediates are presented in Figure 2-4.

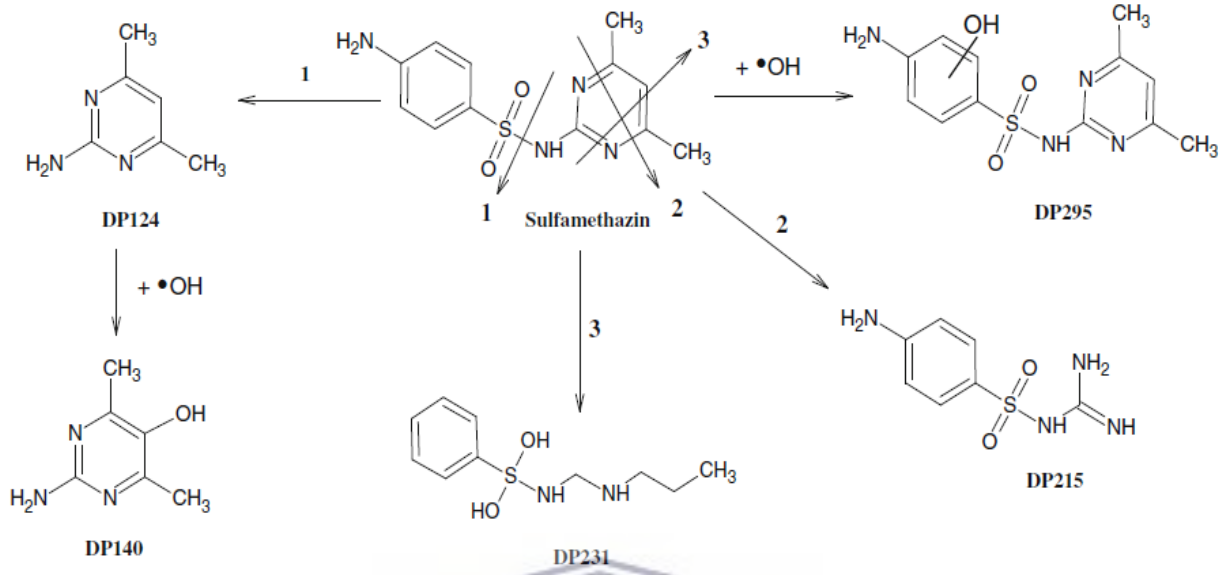

Figure 2-4: Proposed transformation pathways for sulfamethazine photocatalytic degradationSource: (Babić *et al.*, 2015a).

In addition, omeprazole (OMP) inhibitor prescribed to reduce gastric acids is one of the most consumed drugs and its decomposition by photolysis and photo electrocatalytic was investigated by Tantis *et al.*, (2015). Tantis and colleagues (2015) employed nanocrystalline titania films in alkaline media under UV light to degrade omeprazole. The results of their study showed that about 1.4 mg of omeprazole per gram of the photocatalyst per liter of solution per hour could be photo catalytically degraded at a rate of 6.7×10^{-4} min^{-1} under low-intensity UVA irradiation of 1.5 $mWcm^{-2}$ in the presence of a nanoparticulate titania film. The photocatalytic decomposition of OMP led to four degradation intermediates whose degradation pathways are presented in Figure 2-5.

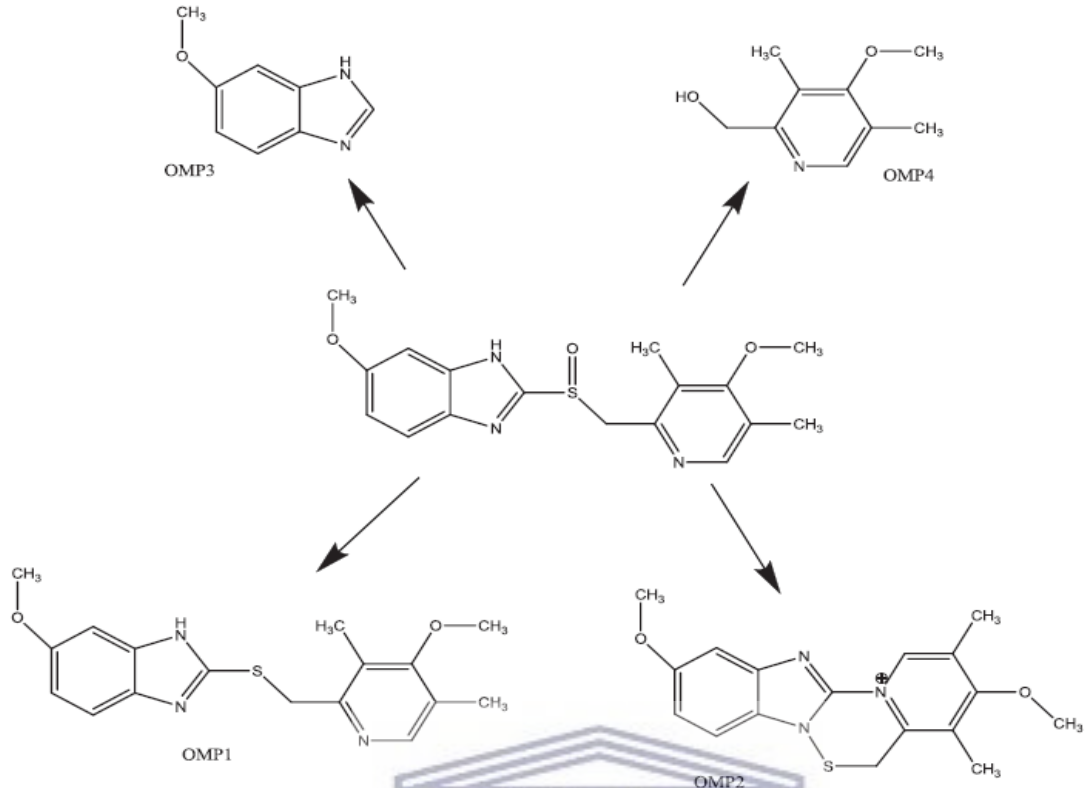

Figure 2-5: Proposed structures for omeprazole transformation products after photocatalytic degradation (Tantis *et al.*, 2015).

From the photocatalytic studies reviewed above, it could be noticed that either in most cases it took about 30 to 120 mins to reach complete decomposition of pharmaceuticals pollutants; or the targeted compounds were not fully degradation into harmless inorganics entities and hence might have required prolonged time to reach completion. This therefore showed that photo catalysis using both powder and supported catalyst form is a slow process due to limitations such as insufficient light penetration that is often prevented by the agglomerated catalyst particles in the solution that further decrease the catalyst activity. On the other hand, the reduced surface area to volume ratio and increased mass transfer limitations of the films might also slow down the photocatalytic decomposition processes of the model pharmaceuticals.

The main purpose of AOPs is the generation of a large amount of non-selective OH radicals that can directly oxidise contaminants to harmless end-products (Lafi and Al-Qodah, 2006; Stasinakis, 2008; Tijani *et al.*, 2014). In AOPs, heterogeneous photocatalysts such as TiO_2 have been used to accelerate the production of free radicals by both oxidation and reduction processes (Al-Kdasi *et al.*, 2004). TiO_2 has been used as a convenient photocatalyst due to its low cost and non-toxicity, high stability and exceptional photocatalytic effectiveness (Kuang

et al., 2011). However, the large band gap of TiO_2 could decelerate the production of ROS in aqueous systems and hence limit the decontamination of polluted water.

Therefore, numerous authors claimed that this limitation could be overcome by incorporation of various metals and non-metals into TiO_2 lattice.

The UV light generated in the DBD reactor could be used in combination with TiO_2 based catalysts discussed above to evaluate the efficiency of the system upon the degradation of pharmaceuticals. But due to the large band gap of TiO_2, its doping non-metal elements for example could be beneficial not only in band gap shifting but to stop charge recombination process (Hintsho *et al.*, 2014). This in return may improve the activity of the UV light produced in the DBD reactor.

2.4 Doping of TiO_2

Among various semiconductor materials, titanium dioxide (TiO_2) with a band gap varying between (3.0 – 3.2 eV) has been extensively utilised as a photocatalyst material for various applications including water and wastewater treatment (Khan *et al.*, 2017). The growing use of TiO_2 in literature is probably due to its non-toxicity, reduced cost and photo stability (Alemany *et al.*, 2000; Khan *et al.*, 2017). The exposure of TiO_2 under UV or visible light induces the generation of various free radicals ($^{\cdot}OH$, $O_2^{\cdot-}$, etc.) in aqueous systems (Asahi *et al.*, 2001; Palanivelu *et al.*, 2007). However, the formation of the maximum amount of these active species may be limited due to the large TiO_2 band gap that further requires high energy for the excitation of an electron from the valence band to the conduction band. Hence, doping TiO_2 with chemical elements such as transition metal and non-metal is believed to reduce TiO_2 band gap and accelerate the free radical formation process in the presence of UV or visible light (Chen *et al.*, 2007; Kanade *et al.*, 2007; Zhang and Song, 2009; Wang *et al.*, 2011; Cheng *et al.*, 2016; J O Tijani *et al.*, 2017). However, the accumulation or exceeding dosages of powder catalysts in the solution being treated could shadow the radiation and further limit the production of oxidants and hence decrease the degradation efficincies of the targeted pollutants. In addition, the substitution of Ti and O in TiO_2 lattice by transition metals (TMs) and non-metals have evolved as a worldwide method to improving TiO_2 optical and electronic properties, especially the shifting of its absorption to the visible region (Sakthivel and Kisch, 2003). This, in turn, may favour the utilisation of sunlight and UV light to induce photo chemically and photocatalysis processes that appear cost-effective and environmentally benign

(Di Valentin *et al*., 2005). However, literature claimed that the incorporation of TMs in TiO_2 frame often results in the formation of catalysts with reduced photostability (Sakthivel and Kisch, 2003). That is, the use of non-metals such as carbon (C), nitrogen (N) etc. has been considered as adequate alternatives to alleviate this drawback (Dvoranová *et al.*, 2002; Ruan *et al.*, 2005). In this regard, the incorporation of non-metals such as C and N in TiO_2 chemical structure has gained great attention in the past decades.

To begin with N, its loading into TiO_2 framework during synthesis of N doped TiO_2 (N-TiO_2) nanocatalysts has extensively been reported in the literature (Asahi *et al.*, 2001; Irie *et al*., 2003; Sakthivel *et al*., 2004). Of interest, the photochemical and photocatalytic properties of the fabricated N-TiO_2 have also been examined in these studies. One of the most investigated characteristics of the N-TiO_2 nanocomposites being the absorption spectra that have successfully been expanded into the visible region. The shifting of N-TiO_2 band gap into the visible domain is due to nitrogen impurities introduced in the TiO_2 lattice resulting in localized electronic states that various authors claimed to lye above the O 2p valence band (Irie *et al*., 2003; Lindgren *et al*., 2003; Sakthivel *et al*., 2004; Valentin *et al*., 2004; Demirev and Nenov, 2005). From these benefits, numerous studies focusing on the doping of TiO_2 with N have been conducted.

Mekprasart and Pecharapa, (2011) prepared N-TiO_2 nanocomposites by homogenisation and mechanically stirred technique in a deionised (DI) water system. The obtained nanopowders were annealed at 100 ºC at different holding time of 30, 60 and 120 min. Their outcomes showed that the introduction of N into the TiO_2 matrix shifted the absorption spectrum of the as-synthesised N-TiO_2 to the visible range. This consequently favourably enhanced the degradation of Rhodamine B upon exposure to visible light. On the other hand, Chainarong *et al.*, (2011) engineered a nitrogen-doped TiO_2 (N-TiO_2) nanocatalyst by a hydrothermal technique. Upon variation of the nitrogen sources and their concentrations, the results of Chainarong and colleagues, (2011) highlighted that the improved photocatalytic decomposition of methylene blue was achieved with N-TiO_2 deriving from the sample 0.5M guanidine carbonate that was used as the nitrogen precursor. Cheng *et al.*, (2012) synthesised an N-TiO_2 by the addition of water. The authors reported that the doping of TiO_2 with N impeded the phase transformation of the nanocatalyst from anatase to brookite. Their results further showed that the small synthesised N-TiO_2 nanocatalyst had high crystallinity, narrowband gap and absorbed light in the visible region. Based on these attributes, the as-prepared nanocatalyst exhibited high photocatalytic removal of phenol compared to P25 TiO_2 Degussa. Similar studies on the synthesis of N-TiO_2 using different methods were also conducted by various

authors (Asahi *et al.*, 2001; Sakthivel *et al*. 2004; Jang *et al.*, 2006; Junwei *et al.*, 2007). The studies reviewed above show that the doping of nitrogen into powder form TiO_2 framework exhibited numerous benefits among which the reduction of band gap, reduction of the recombination rate of electron hole pairs and the improvement of photocatalytic activity of the prepared powder form N-TiO_2 nanocatalysts towards the removal of organic pollutants from water and wastewater. Likewise, the doping of carbon into TiO_2 lattice has also received similar attention although, after an investigation of the degradation of 4-chlorophenol under visible light ($\lambda \approx 455$ nm), Sakthivel and Kisch, (2003) and Valentin, and Selloni, (2005) claimed that carbon-doped TiO_2 was five times more active than N-TiO_2, even though the degradation mechanistic pathways of the targeted contaminants were not defined in their studies. The identification of degradation by-products is crucial to understand the decomposition routes of the model pollutants and to determine wether their total degradation to simpler inorganics is achieved or not.

Nevertheless, various studies on the doping of carbon in TiO_2 matrix resulting in the shifted absorption spectrum in the visible range have been reported in the literature.

For instance, Sambandam *et al.*, (2015) prepared a dominant anatase phase C-TiO_2 by a microwave-assisted technique using the mixture of titaniumoxyacetylacetonate (TOAA), ammonium fluoride (NH_4F) and glucose and H_2O_2 for the degradation of carbamazepine persistent pollutants from water. The results of their study showed that the morphology of the prepared nanocrystal varied from spherical, distorted spherical, rice grain to hexagonal morphologies as revealed by SEM analysis. The particle size range of the synthesised C-TiO_2 nanocatalysts was between 50 and 70 nm. The authors reported that the carbon loaded into TiO_2 surface as graphitic carbon resulted in the shifting of C-TiO_2 nanocomposite band gap to visible light. Furthermore, their report sustains that the complete photocatalytic degradation of carbamazepine was highly achieved within 85 min with the rice grain shaped C-TiO_2 having a large surface area of 229 m^2/g. These findings are in line with the study conducted by Park *et al.*, (2009) who investigated the synthesis of carbon-doped TiO_2 (C-TiO_2) by the sol-gel method without using external carbon precursors. In their protocol, the titanium alkoxide incorporated in the TiO_2 framework was considered a source of carbon that created microstates in TiO_2 band gap that was tuned by variation of calcination temperature. The trace of carbon dopant considerably depended on the calcination temperature and was evidenced by UV–visible diffuse reflectance spectroscopy and X-ray photoelectron spectroscopy (XPS). The outcomes of their research showed that the maximum carbon doping was achieved at a calcination temperature range of 200–250 ^oC and increased at elevated temperature. In addition

to this, the higher photocatalytic degradation of 4-chlorophenol and iodide were achieved in the aforementioned temperature range. The authors hence claimed that the carbon doping could be performed involuntarily during the sol-gel synthesis process. Likewise, Tijani *et al.*, (2017) synthesised C-TiO_2 catalysts by sol-gel technique. Except that, in their synthesis procedure, 8% polyacrylonitrile (PAN) was used as carbon source that was dissolved in dimethylformamide (DMF) solvent followed by addition of titanium tetrachloride ($TiCl_4$), according to their experimental report. The presence of carbon in the TiO_2 matrix and the substitution of TiO_2 by carbon were well evidenced by energy dispersive spectroscopy (EDS) and XPS. The doping of carbon into TiO_2 framework has already been conducted by various authors (Chu *et al.*, 2005; Neumann *et al.*, 2005; Lin *et al.*, 2013; Saharudin et al., 2014) using different carbon precursors and diverse synthesis protocols. In these studies, high photocatalytic activities were reported and the photocatalytic performances of the synthesised nanomaterial depended on various factors such as the shape of the catalysts, dopant concentration, type of precursor, calcination time, etc. The variation of these parameters was found to positively impact upon the physical and electronic properties of the C-TiO_2 catalysts. From the studies reviewed above, it could be observed that the doping of TiO_2 with both nitrogen and carbon resulted in improved benefits of electronic and physical properties of the as-synthesised C-TiO_2 or N-TiO_2 nanocatalysts among which the shifting of the absorption spectra to the visible region, preventing charge recombination and hence the enhancement of the photocatalytic activities. In that regard, the doping of TiO_2 with both non-metals carbon and nitrogen could be more beneficial. A few studies in the literature have reported on the synthesis of C-N-TiO_2 nanocomposites using different methods. For example, (Yu and Yu, 2009) developed a practical technique for direct doping of carbon and nitrogen into the TiO_2 frame by annealing titanium carbonitride in air. The outcomes of their research indicated that the prepared C-N-TiO_2 annealed at 400 ^oC for 8 hours was photo-catalytically active under visible light which additionally reduced the recombination rate of electron-hole pairs. The authors stated that parameters such as calcination temperatures and treatment time played a significant role in the structure and activity of the co-doped nanocomposites. A similar study was conducted by Li *et al.*, (2017) who adopted a one-step micro wave (MW) irradiation technique for the doping of carbon and nitrogen residues into TiO_2 lattice and the synthesised C-N-TiO_2 catalyst was instantaneously deposited onto common brick ((C, N)-TiO_2/ brick). The results pointed out that the porous surface of (C, N)-TiO_2/brick noticeably enhanced the surface area of the sample that resulted into a longer lifetime for photo-produced electron-hole pairs, and subsequently boosted the photocatalytic properties of the catalysts. The synthesis of C-N-

TiO_2 nanocomposites was also conducted by various authors using different methods (Chen *et al.*, 2007; Yin *et al.*, 2007; Abdullah *et al.*, 2016; Ao *et al.*, 2018; Mohamed *et al.*, 2018). Apart from the fact that the investigations reviewed above sustain that the methods for engineering of C-N-TiO_2 catalysts were cost-effective, efficient, and environmental safety, this review has shown that C, N doped TiO_2 is a promising catalyst that can be used as a potential source of free radical production during water and wastewater treatment. The doping of C and N into TiO_2 matrix beneficially impacts on the physical-chemical properties of the prepared C, N, doped TiO_2. Hence its combination with the DBD system could be a promising advanced oxidation process for the removal of persistent organic pollutants such as dyes and pharmaceutical residues from wastewater. This could, therefore, be a preliminary answer to the research question in section 1.5 of chapter 1 stated as follows: can the process be intensified by catalysis or photo catalysis?

Though DBDs configurations are claimed to be an adequate system for the generation of UV light and various free active species that all contribute to the detoxification of polluted water, the incorporation of catalyst in DBDs is believed to improve the removal efficiency of the targeted pollutant in a reduced treatment time.

However, considering the upscaling of DBD configurations at industrial level catalyst, post-separation could be costly and hence a prominent limitation to the use of these technologies. Therefore, the immobilisation of the catalyst on appropriate supports could be promising for light penetration and catalyst incorporation in DBD configurations.

2.5 Immobilisation of TiO_2 on various supports

Literature claims that semiconductor photo catalysts in their single or co-doped form can also be deposited on particular supports (Samsudin & Hamid 2017; Yadav & Jaiswar 2017). Even though some studies claimed that the coating process may decrease its specific surface area (Fu *et al.*, 1996; Sopyan, 2007), coating of various material supports such as SS (Lichtin et al. 1994; Matsubara et al. 1995; Vohra et al. 2006; Tijani et al. 2017b), glass (Srikanth *et al.*, 2017; P. Nyamukamba *et al.*, 2017; Pardon Nyamukamba *et al.*, 2017) has been conducted. The prepared films in the aforementioned studies were mostly employed in photo catalytic removal of organic pollutants from water and wastewater. However, among the diverse deposition methods reported in the literature, sol-gel coupled with dip coating and spin coating have become more popular in the last decades. This is certainly due to the fact that the immobilisation of catalyst on inert supports using dip or spin coating is usually accomplished

at low temperatures that do not thermally affect the support. But the anatase form might not be achieved without a thermal annealing step.

2.5.1 Supporting TiO_2 on stainless steel mesh

In most photocatalytic applications, TiO_2 powder is dispersed in the aqueous solution to induce the photocatalysis process (Schäffer, 2012). However, the suspension of TiO_2 powder in aqueous media may result in (problems with light penetration into the bulk solution and incur) a high cost for filtration process used to remove suspended TiO_2 particles (Lindstrom and Wootton, 2007). This, in turn, represents a processing limitation from an industrial perspective. The immobilisation of TiO_2 on diverse supports has been suggested as a palliative solution to overcome this limitation (Schäffer, 2012). From this point of view, TiO_2 has been immobilised on various catalytic supports including glass, glass beads, quartz, silica, activated carbon, cellulose, Ti mesh, reactor walls, fiberglass cloth, zeolites, stainless steel, ceramics, clothes, monolith, and polymer and membranes (Shan et al. 2010). Though the decrease of TiO_2 surface area has been identified as the principal disadvantage during its deposition on the aforementioned supports (Brinker and Scherer, 1990; Mechiakh *et al.*, 2010); several methods including chemical vapour deposition, electron beam evaporation, reactive magnetron sputtering, spray pyrolysis, electrophoresis, cathodic arc evaporation (CAE), reactive thermal deposition, static-dynamic films compressed, sol-gel, dip coating, spin and spread coating methods have been used for immobilisation of TiO_2 on substrates (Avci *et al.*, 2009; Lewkowicz *et al.*, 2012; Calderon-Moreno *et al.*, 2014). From most of the catalysis deposition techniques mentioned above, the sol gel method has been widely applied to ensure perfect adherence of the catalyst to the support due to the oxygen bridges that are formed during the heating of the precursor (Lewkowicz *et al.*, 2012).

Likewise, Shang, Li and Zhu, (2003) developed a 50 – 360 nm photocatalytic active TiO_2 film coated on stainless steel (SS) webnet using the sol-gel technique. The prepared films were calcined at 400 °C for 10 min at a ramping rate of at 5 °C min^{-1} in an air flow oven. The XRD results showed that the synthesised TiO_2 with a thickness close to 10 nm were uniformly present in the anatase phase. The photocatalytic activity of the as-prepared catalysts upon the oxidation of formaldehyde (gaseous) was evaluated as a function of its thickness and crystallisation. That is, the best photocatalytic performance was achieved with thicker nanocatalyst films showing better crystallisation behaviour. However, the authors claimed that the photocatalytic activity of the catalyst became constant with films of thickness higher than

250 nm. They concluded that only films with thickness below 250 nm were photo-catalytically active. However, these authors did not highlight the stability of the films in the oxidising environment. On the other hand, Zhang *et al.*, (2003) synthesised mesoporous TiO_2 films immobilised on SS by sol-gel dip coating route. The coated films were annealed at 400 °C at a ramping rate varied between 3 and 4 °C/min for 60 mins. During the synthesis process, the authors used Ti (OC_4H_9) ethylene glycol as a precursor and as a structure directing-agent, respectively. Li Zhang and co-authors, (2003) confirmed that the mesoporous TiO_2 films were photo catalytically effective for the decomposition of Rhodamine blue (RB) under UV light at 365 nm compared to conventional TiO_2 photocatalyst. Moreover, Zhang *et al.*, (2003) affirmed that the mesoporous TiO_2 films showed an effective photo degradation rate of formaldehyde that was six times effective than that of the traditional TiO_2 photocatalyst films. Similar studies on supporting TiO_2 on SS mesh were already performed by various authors (Bamoulid *et al.*, 2006; Chen and Dionysiou, 2007) who used sol-gel methods coupled with dip coating to fabricate thick TiO_2 films (annealed at various temperatures, ramping rates and times) that were found photo-catalytically active for the removal of 4- chloro benzoic acid (4-CBA).

Beside the immobilisation of TiO_2 on SS by the sol-gel method, other techniques have been established. For instance, Murgolo *et al.*, (2017) used a metal organic chemical vapour deposition (MOCVD) method for the immobilisation of nanostructured TiO_2 films (nano-TiO_2) on SS mesh. Their outcomes showed that at the applied conditions, the newly prepared nano TiO_2- SS exhibited better photocatalytic activity upon the degradation of compounds of emerging concern compared to the powder commercial TiO_2 Degussa applied in the same dosage. That is, the authors confirmed that the removal rates of warfarin and trimethoprim achieved with 55 mg of nano TiO_2-SS within 60 mins was twice faster than that of TiO_2 Degussa. Similar photocatalytic performance of 55 mg nano TiO_2–SS at the same time was observed during decomposition of metoprolol, carbamazepine, and gemfibrozil by these authors.

A comparative study on the engineering of TiO_2 films supported on porous SS membrane was also carried out by Adán *et al.*, (2017). In their research, a new integrated photocatalytic/microfiltration configuration focusing on the utilisation of powdered TiO_2 supported by filtration on a porous SS substrate under UV/ordinary light was developed. The newly fabricated films showed interesting effectiveness in the photocatalytic removal/ inactivation of bacteria during the water disinfection process. The authors reported that the enhanced bacteria inactivation was related to the membrane pore size and catalyst (TiO_2) loading. Besides, Adán *et al.*, (2017) conveyed that apart from the effective bacteria

inactivation, the photocatalytic activity of the membrane was also beneficial in the removal (oxidation) of pollutants that were present in the polluted water. Next to these studies, the immobilisation of TiO_2 nanomaterials on SS supports has been widely reported in the literature (Sonawane et al., 2003; Guo *et al.*, 2010, 2018; Merajin *et al.*, 2013; Singh et al., 2013; Souzanchi *et al.*, 2013; Srikanth *et al.*, 2017).

These investigations have shown that supporting TiO_2 on SS supports is advantageous in achieving effective oxidation efficiencies not only for organic pollutants but for microorganisms and bacteria as well from contaminated water. However, none of these studies discussed about corrosion and the stability of SS supports in harsh oxidative environments.

So the incorporation of TiO_2 supported on SS in a DBD system that generates UV light insitu could perhaps promote the decomposition of persistence organic pollutants (POPs) such as dyes and pharmaceuticals model pollutants reviewed above. This could enhance the removal of POPs from water and wastewater. However, Shan *et al*. (2010) contended that, even tough, the immobilisation of catalyst might be a cost-effective route compared to suspension of the catalyst, the films obtained present some disadvantages such as low surface area to volume ratio, increased mass transfer limitations, uneven light penetration to the thickness of catalyst which further reduce of the rate of removal of the pollutants. Perhaps the choice of suitable support for catalyst immobilisation is of great importance.

In case the incorporation of TiO_2 suspended on SS in DBD reactor is challenging, the TiO_2 catalyst could directly be coated on the glass on the inner tube of the DBD reactor. This could be another route to introducing the catalyst in the DBD reactor to boost the removal efficiencies of pollutants. In this regard, Fernández *et al.*, (1995) established the comparison of the photocatalytic activity as a function of the nature of the support (fused silica, glass, and SS) as follows: TiO_2/quartz> TiO_2/steel ≈ TiO_2/glass > photolysis.

2.5.2 Spin coating immobilisation of sol-gel catalyst on glass and application for photocatalytic removal of organic pollutants

The sol-gel procedure has been considered as a suitable support coating technique because it offers benefits such as composition controllability and use of equipment at lower cost, Preparation of films over a large area and maintaining high photocatalytic activity, good adhesion and reproducibility of the process are challenges that must be overcome to engineer excellent homogenous nano-thin films of desired layers (Khan *et al.*, 2009; Mechiakh *et al.*, 2011; Aksoy and Caglar, 2014; Kumar *et al.*, 2015). During preparation of thin films, the sol-

gel method is often associated with other techniques such as dip coating (Alzamani *et al.*, 2013; Gilmour *et al.*, 2013; Blanco, González-Leal and Ramírez-del Solar, 2015), spin-coating (Chen and Dionysiou, 2008), etc., which are techniques used to spread even thin films on flat supports. For instance, in the spin coating process, an excess quantity of precursor solution is placed on the surface of the support. Thereafter, the support is rotated at a fixed speed to spread the gel by centrifugal force and create a wet thin layer. However, a few factors mainly the rotation speed, the sol-gel to solvent volume ratio and the evaporation rate to some extent may affect the thickness of the obtained films (Bamoulid *et al.*, 2006; Chen and Dionysiou, 2006). The developed films are often used for various applications such as photocatalysis (Chen et al. 2008; Stathatos et al., 2012) and solar cell energy storage (semiconductors) (Justin Schäffer, 2012). For instance, Wu *et al.*, (2013) used the sol-gel method coupled with the spin coating process to develop nanocrystalline thin films. The films were fabricated by mixing titanium tetraisopropoxide (TTIP) with the precursor at pH 3.5. After coatin, the films were calcined at 450 ^{o}C for 3 hours and characterised by various techniques including atomic force microscopy (AFM), XRD, XPS, etc. The results showed that the nano TiO_2 films exhibited greater aggregation, good optical transparency, consistent thickness, and hydrophilicity. The photocatalytic activity of the anatase films as a function of thickness was tested upon the degradation of acid yellow 17. The outcomes show that the best photocatalytic activity was achieved with films coated by 0.1 M TTIP with the thickness of 93 nm compared to those prepared by 0.3 M TTIP.

Lin *et al.*, (2014) prepared various iron ions doped TiO_2 (Fe^{3+}-TiO_2) by the sol-gel spin coating process. In their study, the effect of doping on the optical properties and photocatalytic activity of the films calcined at 550^{o}C were investigated. The SEM analysis showed that the surface of the films was smooth with granular microcrystalline anatase particles that XRD demonstrated to be one single crystalline anatase phase. Moreover, the increased of Fe^{3+} doping resulted in an increase in the crystallinity anatase and crystal size. In addition, the increase Fe^{3+} - doping resulted in a decrease of Fe^{3+}- TiO_2 band gap as dictated by the UV-vis analysis. Consequently, the increase of Fe^{3+}- doping content from 0 to 25 % led to an increase in the rate of MB degradation from 0.018 to 0.038h^{-1}. Extensive investigations on the sol-gel spin coating of doped TiO_2 films on glass have been reported in the literature (Lewkowicz *et al.*, 2014; Kumar *et al.*, 2015; Bsiri *et al.*, 2016).

The review on photo catalysis showed that, the powder photo catalysts exhibit some benefits such as great specific surface area and good surface area to volume ratio. However, the use of powder photo catalyst is associated with various disadvantages including the high cost of post-

treatment separation, the challenging filtration of small particles diffused in the treated water, the agglomeration of the slurry that impede light penetration and hence decreasing the catalyst activity, the high cost of the catalyst regeneration at large scale, etc. Gilmour *et al.*, (2013) highlighted that these limitations have prevented the use of suspension photo catalysis at large scale due to the fact that the filtration of small size powder catalysts in water is difficult and costly. The accumulation and agglomeration of suspended catalysts may prevent a uniform light penetration and hence decelerate the rate of removal of targeted pollutants. Furthermore, the regeneration of the suspended powder catalyst could also be a major limitation. In order to overcome these drawbacks, literature suggests that the catalysts could be immobilised on solid supports such as meshes, ceramics, glass, polymers, etc. using different techniques including sol gel dip coating, spread and spin coatings, etc. The desired properties of the obtained thin films are often good adherence of the catalyst to the support, thickness, porosity and the durability of the catalyst or the catalyst life spam. Despites these expected characteristics, a few authors believed that the prepared films often have a low surface area to volume ratio and an increased of mass transfer limitations which further reduce the activity of the films and hence decreasing the removal rate of contaminants. Besides, the corrosion of the catalyst support in harsh environments may also limit the photo catalytic removal of pollutants. Therefore, the immobilisation of catalyst on transparent supports such as glass has been identified as an alternative cost-effective route of catalyst coating. A few authors endorsed that a controllable affinity between catalyst and glass supports has been observed (Wu *et al.*, 2013; H. J. Lin *et al.*, 2014; Lewkowicz *et al.*, 2014; Kumar *et al.*, 2015; Bsiri *et al.*, 2016). This is often achieved by various methods such as spin and spread coating, etc. So far, the limitations of catalysts coated on glass are still under investigation. All in all, the review on photo catalysis showed that the catalyst can be used either in powder form for small scale reactor configurations or as films when immobilised on solid supports such as meshes, etc.in batch or semi-continuous systems. The disadvantages encountered in both cases could be overcome by coating the catalyst on glass supports. Consequently, to avoid the various photo catalysis problematic highlighted in this review, the catalyst could directly be coated on glass walls of a particular rector for effective pollutant decomposition in water. However, this later idea is still an on-going investigation or task in water and wastewater treatment technologies.

2.6 Corrosion review: why is corrosion a problem?

The most well-known alloys include steel that consists of iron (Fe) and carbon (C) which often corrodes fast due to the oxidation of Fe to Fe_2O_3 when exposed to water, air, and moisture. Conversely, stainless steel is carbon steel containing at least 10.5% chromium and has widely been recognised as a corrosion resistant alloy and explored in diverse research fields (Hauert and Patscheider, 2000; Kutschej *et al.*, 2005; Liney *et al.*, 2006; He, Ahn and Sippel, 2011) Indeed, when chromium contained in stainless steel reacts with water, chromium oxide (Cr_2O_3) is formed and is often referred to as the passive layer that protects metallic Cr and has the ability to self-repair (Riffard *et al.*, 2002). Therefore, corrosion of stainless steel may occur mostly when the Cr_2O_3 passive layer is scratched (Zhang and Wang, 2014). In addition to this, the main causes of metal corrosion include the medium and design, material and time. In these types of corrosions, the rusting of metals usually occur in a milieu where the pH is less than the critical pH value which further leads to the instability of the protective passive layer that spontaneously decays. This is often characterised by the loss of thickness and weight compared to localised corrosions previously summarised (Licausi et al., 2013; Fadlallah *et al.*, 2014; Fattah-Alhosseini and Vafaeian, 2016). The more acidic the medium, the quicker the erosion of the metal. Zhang & Wang (2014) reported that prolonged exposure of stainless steel in oxidising or acidic environments may result in its corrosion mostly when the Cr_2O_3 passive layer is scratched and may cause metal rusting, loss of thickness and weight. This can lead to contamination of water effluents being treated. Hence the corrosion of SS in the oxidizing environment of the DBD system need to be overcome in order to achieve the desired removal of the pollutant and avoid undesired water toxicity. Therefore, it would be imperative to understand the corrosion occurrence in an oxidising acidic environment and certainly the adequate alternatives that have been established to be overcome this challenge by using uncoated and coated SS mesh coated with anticorrosion layers.

2.6.1 Corrosion of stainless steel

In order to minimise the corrosion risk, literature advises the careful choice of the grade of SS to be used and a less acidic medium (Mackey and Seacord, 2017). Alternatively, the choice of a grade with a high content of Cr, Ni, Mo, and Cu may be preferable to limit the propagation of corrosion when the passive layer is cracked. Moreover, the temperature of the medium should be lowered and the contact time should be reduced (Mackey and Seacord, 2017).

Furthermore, stagnant areas on the material should be avoided and the concentration of halogens present in an oxidative environment should be reduced. Apart from these precautions, the use of a low carbon grade known as « L » (Low C % < 0.03%) is also recommended (He *et al.*, 2011; Mackey and Seacord, 2017). Finally, it would be preferable to use a material with an enlarged confined zone between the passive layer and the metal to escape all sort of impurity agglomerations that may further accelerate the rusting of stainless steel (He *et al*., 2011). Even though the literature claims that stainless steel may be the best, non-corrosive alloy, its exposure to harsh environments may still accelerate its erosion. Consequently, the effects of previously mentioned parameters on corrosion have been investigated (He *et al*., 2011).

In previous investigations on the application of catalyst immobilised on SS in DBD system for the degradation of micro pollutants (J O Tijani *et al.*, 2017, 2017), it was noticed that reactivity of reactive oxygen species (ROS) was not only limited to attacking the targeted pollutant but also the stainless steel catalyst support was corroding. This consequently led to corrosion of the photo catalycally coated SS suport which had to be overcome so as to achieve the principal goal that aimed at the total decomposition of pollutants in DBD advanced technologies. So coating of the SS support with corrosion protective layers and investigation of the coating corrosion resistance in AOP systems before catalyst immobilisation could be an alternative practice to preventing and avoiding corrosion occurrence during water and wastewater treatment process.

2.6.2 Transition metal coatings as anticorrosion layers

Transition metals (TMs), mostly those in the first and second rows of the d-block in the periodic table exhibit various analogous behaviours due to their chemical and electronic properties (Sayres *et al.*, 2011). Some d-block TMs are electron deficient and may reach their stability in combined forms with non-metal elements forming diatomic or polyatomic compounds such as metal oxides. Alternatively, electron rich TM elements would prefer to be in their single elemental states (Rao, 1989). The variation of factors such as concentration, pH, oxidising power, temperature, pressure, and the viscosity may disrupt TM stability and hence lead to undesired reactions (Roy *et al.*, 2011). For instance, corrosion of TMs appears as an electrochemical reaction that occurs at the interface between metals and their surrounding environments (He *et al*., 2011). The mixture of various TMs referred to as alloys, have been developed and considered as effective chemical prototypes to overcome corrosion phenomena

(Hauert and Patscheider, 2000; Endrino and Derflinger, 2005; Kutschej *et al.*, 2005; Liney *et al.*, 2006; Volovitch *et al.*, 2011).

Transition metal-based – alloys have been widely applied in the biomedical sector for various purposes (Licausi *et al*. 2013; Alvarez-Pampliega *et al.*, 2014; Fadlallah *et al.*, 2014). During materials coating, the behaviour of the coated films in various harsh media has been the most important parameter that affects the structure, morphology, and corrosion resistance of the deposited layers (Licausi *et al*. 2013; Lazar *et al.*, 2014). Transition metal-based coating alloys have multiple applications in various fields (Hauert and Patscheider, 2000; Kutschej *et al.*, 2005; Volovitch *et al.*, 2011). In material science, the principal goal of making strong and stable stainless steel coatings is to ensure their long term durability and advanced performance in different environments (He et al., 2011; Wood *et al.*, 2013). However, these ideal properties may often be influenced by factors such as temperature or corrosive media (Lister *et al.*, 2008; He *et al*., 2011; Möhring *et al.*, 2015).

In order to alleviate this dilemma, various coating materials have been studied for surface modeling. To begin with, nitride-based compounds such as TiN, ZrN, CrN and TiAlN have been suggested as hard coating for surface modification/implementation (Zhang and Zhu, 1993; Deng *et al.*, 2008; Sresomroeng *et al.*, 2011; Birol, 2013; Atar *et al.*, 2014). Various multilayer coatings have been developed to improve the mechanical properties, thermal stability and corrosion resistance of metals (Vladescu *et al.*, 2014; Braic, Vladescu, *et al.*, 2015; Dinu *et al.*, 2015, 2016). The biocompatibility of coating materials should also be investigated in order to understand the coalition of the coating elements. Recently, Parau *et al.*, (2016) investigated in vitro biocompatibility of Si alloyed multi-principal element carbide coatings. Anticorrosive and high-performance coatings that can resist corrosion in the desired way are still a topic of investigation (Vladescu *et al.*, 2016). For the past decades, nitrogen doped coatings such as TiN, ZrN, NbN have been used in forming binary or multilayer thin films. This has been achieved by physical vapour deposition (PVD) method, mainly by a cathodic arc evaporation method (CAE) (Braic, A. C. C. Parau, *et al.*, 2014; Constantin *et al.*, 2016; Parau *et al.*, 2016). Unlike the pulse high-intensity laser deposition (PHILD) technique CAE is often preferred for coating in order to achieve uniformity, colour control and, most importantly, to achieve great binding adhesion between the support and the deposited materials (Coman *et al.*, 2017). However, the limitations of CAE include the formation of micro-defects and macro-particles referred to as droplets within the coated films (Islam *et al.*, 2015). In the design of anticorrosion layers, the manufacturing of microstructures free from internal defects is one of the main goals in the coating process (Wood *et al.*, 2013). These defects in CAE techniques

can be reduced by prudently controlling the parameters during the deposition process (Balaceanu *et al.*, 2015; Braic *et al.*, 2017b; Dinu *et al.*, 2017a).The prepared coatings are often attacked in acidic or corrosive environments leading to their destruction (Vitelaru *et al.*, 2014; Braic, Vladescu, *et al.*, 2015).

2.6.3 Measurement corrosion

In order to follow the deterioration of coated layers or electrochemical processes occurring at material-electrolyte interfaces, electrochemical impedance spectroscopy (EIS) has widely been employed as a suitable method for corrosion analysis (Breugelmans *et al.*, 2012). Indeed, in common EIS technique, only one agitation signal is processed by the system in a particular frequency range. In turn, each frequency is solely quantified (Van Ingelgem *et al.*, 2009). The drawback of this method is the fact that the signal obtained from the system may often be nonlinear and non-stationary with respect to the practical signal (Breugelmans *et al.*, 2012). Alternatively, odd random phase multisine electrochemical impedance spectroscopy (ORP-EIS) has been employed to record supplementary information related to noise and non-linear alterations hence to determine the best setting parameters (Breugelmans *et al.*, 2012; Dinu *et al.*, 2017a). Nevertheless, the affordability of ORP-EIS equipment often limits its application. Hence, the corrosion behaviour of the bare and coated SS in acidic solution is often assessed by potentiodynamic polarisation technique. The corrosion performance of the coatings could be examined with respect to the coatings features, such as elemental and phase composition, surface morphology, hardness, reduced elastic modulus, and adhesion to SS substrate. Beforehand, a general descriptive review of potentiodynamic polarisation principal and corrosion study are presented below.

Metallic corrosion is an electrochemical process whereby metal atoms are converted to ions by losing their valence electrons; the released electrons in turn agglomerate on the metal surface and are available to reduce the electrochemically active species (EAS) present in the electrolyte (Fix et al. 2004; Lister et al. 2008; He et al. 2011).

The rate of metal depletion is often measured by plotting a polarisation curve of increasing potential vs. intensity using sophisticated electrochemical equipment (Balaceanu *et al.*, 2015; Braic *et al.*, 2017a). In this case, the current peak value reading permits the determination of corrosion resistance of diverse categories of stainless steel materials. Consequently, the higher the current, the faster the dissolution of the material occurs, and the less corrosion resistant the grade (De Tiedra et al., 2016).

A schematic diagram summarising this process was suggested by Tait (1994) and is presented in Figure 2-6.

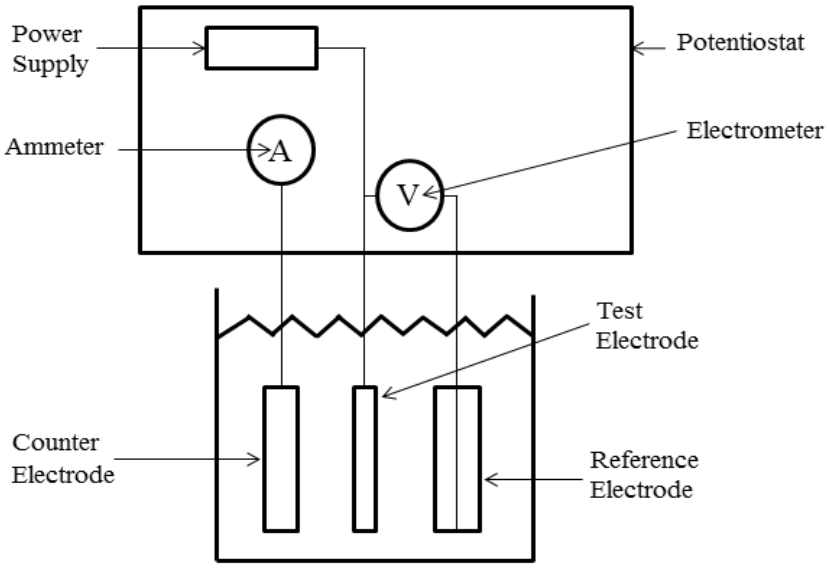

Figure 2-6: Three electrode test cell schematic (Tait, 1994).

The anode (test metal electrode) and the cathode are visibly separated by a certain distance to allow free circulation of cations and anions towards the anode and cathode, correspondingly. The initiation of both cathodic and anodic reactions may induce the corrosion process (Mackey and Seacord, 2017).

Like any chemical reaction, electrochemical corrosion is expressed by both oxidation and reduction reaction equations. For instance, according to Tait (1994) the anodic electrochemical equation for iron corrosion is given in Equation (2.16) as follows:

$$Fe^{\circ} \rightarrow Fe^{2+} + 2e^{-} \text{ (anodic)} \quad (2.16)$$

While the cathodic reduction of hydrogen, is shown in Equation (2.17).

$$2H^{+} + 2e^{-} \rightarrow 3\,H_2 \text{ (cathodic)} \quad (2.17)$$

Therefore, the overall corrosion reaction may be written as described in Equation (2.18):

$$Fe^{\circ} + 2H^{+} \rightarrow Fe^{+2} + H_2 \text{ (overall)} \quad (2.18)$$

Consequently, the electrochemical corrosion process is often studied in an electrochemical cell (set) consisting of the working electrode (anode metal test), a counter electrode (e.g. platinum) and a reference electrode (Ag/AgCl electrode) as shown in Figure 2-6.

The electron transfer involved during oxidation of metal atoms and reduction of EAS allows not only the electronic measurements but the study of metallic corrosion as well. The oxidation half-reaction of the metal is known as the anodic reaction and the metal area where corrosion occurs is called the anode. On the other hand, the reduction of EAS brought by the electrolyte

is referred to as the cathodic reduction half-reaction and that occurs at the cathode (electrolyte). The reduction of electrochemically active species is referred to as the cathodic reaction and the areas where reduction occurs are referred to as cathodes (He et al. 2011).

From the overall corrosion reaction preventing in Equation 2.18 it was hypothesised that corrosion could be avoided by either preventing the oxidation or the reduction half-reaction to occur, or by removing EAS such as CO_2, H_2S, HCI and O_2 from the electrolyte which is challenging (He et al. 2011; Wood et al. 2013). In the electrochemical experimental set up presented in Figure 2-6, a metal immersed in an electrolyte is known as the electrode or test electrode. In this case, there is no external applied voltage; the electrolyte and the metal together are electrically neutral due to the fact that there is no external current flowing to or from the electrode. The integration of a power supply in the electrochemical testing system supplies a range of voltages that may create potential differences between the anodic and cathodic spots and hence balancing the system to reach charge neutrality. Corrosion of metals is an electrochemical process during which metal atoms lose their valence electrons to become ions (Mastanaiah *et al*., 2013; Mackey and Seacord, 2017). In turn, the electrochemically active species such as hydrogen and oxygen are reduced by the free electrons giving rise to corrosion of the metal anode. The metal and electrolyte have different compositions, and the metal-electrolyte interface known as an electrical double layer (EDL) has its own properties based on charge distribution, capacitance, resistance, and voltage. Indeed, the application of voltage in metal-electrolyte electrochemical systems causes a flow of current from the anode to the cathode. Tait (1994) sustained that the application of voltage on an electrode or changing the structure of the electrolyte might also modify the EDL composition. So varying the EDL composition without applying any voltage might also change its corresponding open circuit potential (OCP).

2.6.4 Types of corrosion that can be electrochemically measured

Tait (1994) highlighted that corrosion can be categorised into two groups, namely general corrosion and localised corrosion. While general corrosion uniformly invades the entire metal surface, localised corrosion occurs at small and discrete metal surface areas at a scale of about microns to several centimeters. This erosion often occurs faster and deeper on the metal surface. Furthermore, the author clarified that potentiodynamic scanning (PDS) curves, linear polarization, Tafel plots, and electrochemical impedance spectroscopy could be used to measure general corrosion and its rates. On the other hand, electrochemical methods such as

cyclic polarisation could be employed to measure and characterise pitting and crevice localised erosions.

2.6.5 Electrochemical corrosion measurement

From the studies reviewed in this text, numerous corrosion resistant coatings have been developed mostly to prevent erosion of stainless steel meshes in oxidising media. Therefore, understanding corrosion behaviour of coated materials is an important step to achieving maximum protection of coatings and hence to improve their stability and durability in hash aqueous systems (Vladescu *et al.*, 2014, 2016). For this purpose, potentiodynamic polarization and electrochemical impedance spectroscopy (PP-EIS) have widely been employed as adequate techniques to study corrosion phenomena in oxidising environments (Breugelmans *et al.*, 2012; Licausi *et al.*, 2013; De Tiedra *et al*. 2016). Likewise, during electrochemical corrosion testing by PP-EIS, the open circuit potential E_{oc} (mV), linear polarization factor R_q (kΩ), corrosion current I_{corr} ($\mu A/cm^2$), porosity and the protection efficiency P_e (%) have been considered as the main factors whose examination and interpretation allow identification of the most corrosion resistant coatings (Azem *et al.*, 2014; Vitelaru *et al.*, 2014). The aforementioned corrosion factors have been reviewed by (Tait, 1994) and are subsequently presented in the following paragraphs.

2.6.5.1 Open circuit potential (OCP) behaviour with time

An open circuit potential (OCP) is a potential difference between two electrodes (reference and metal test electrodes) in the absence of an electrical current. Alternatively, the flow of current between the electrodes may shift the OCP to an electrode potential and hence induces the polarisation process (Licausi *et al*., 2013). The relationship between the chemical composition of the EDL and the measured or applied potential given by the Nernst equation (2.19) shows that the magnitude of potential, E depends on EDL metal ion concentration and metal ion activity coefficient y ± n. Therefore, the variation of one or these two factors might modify the extent of the measured potential (Dinu *et al.*, 2016).

$$E = E^{\circ} (RT/nF) 110+n [Me+11]\} \quad (2.19)$$

Since the conversion of the air-formed oxide film on a metal surface into an EDL takes longer, the OCP values might fluctuate when the metal is initially exposed to an electrolyte. So the variations of potential are characteristics of EDL chemistry adjustment when accommodating

electrolyte chemistry. Consequently, an increasing OCP would indicate that a passive layer protecting the metal from persistent corrosion is being formed on the metal surface. On the contrary, a decrease of OCP would indicate the formation of a porous hydroxide layer that is claimed to only decelerate the corrosion rate and does not protect the metal from corroding. Regardless of the metal type, the increase and decline of OCP values might reach steady stages where no change in OCP values is observed (Dinu *et al.*, 2017b). However, the fluctuation time taken for OCP values to reach a steady state might depend on the type of metal. For instance, Tait, (1994) showed that OCP values for type 1100 aluminum in water reach steady state faster than type 1018 mild steel in an emulsion. In addition, this author stated that the electrolyte chemical composition may impact on the extent of metal ion activity and coefficients (Mackey and Seacord, 2017). So the change in electrolyte composition may cause the EDL to readjust and hence resulting in different OCP values. Furthermore, the author conveyed that electrolyte pH and temperature might also affect the magnitude of metal ion activity coefficients. In total, the OCP can be examined as a function of time to define when the metal electrode tested is at steady state. Accordingly, OCP is considered the simplest, non-destructive corrosion measurement that can be employed in corrosion studies (Azem *et al.*, 2014). In total, the OCP can be examined as a function of time to define when the metal electrode tested is at steady state. For any metal, corrosion resistance corresponds to its capability to resist erosion/corrosion (Licausi *et al.*, 2013).This is also known as the resistance of any metal to losing its valence electrons that often reduce electrochemically active species in aqueous systems. Likewise, polarisation resistance is another terminology of corrosion resistance that refers to charge transfer resistance, expressed in ohms.cm^2 (Volovitch *et al.*, 2011). So from most direct current (DC) corrosion test approaches, the linear polarisation method that uses the smallest potential spectrum has been employed as a non-destructive technique to estimate corrosion resistance. Linear polarisation test starts around -20 mV from the OCP and finishes nearby +20 mV. Thus the -20 mV to +20 mV potential range is plotted against current logarithm (Dinu *et al.*, 2016, 2017a). Compared to other DC corrosion measurement techniques, linear polarisation is graphically plotted and the plotted data follow a linear trend. Unlike linear polarisation previously discussed, the Tafel plot occurring in the -250 mV to +250 mV from the OCP is an expression of potential versus log values of current density (Dinu *et al.*, 2017b). In addition to this, the Tafel plot consists of two branches, mainly the anodic branch and cathodic branch corresponding to oxidation and reduction corrosion half reactions, respectively (De Tiedra *et al.*, 2016). Furthermore, the potentiodynamic scanning method is another corrosion technique that relates potential to current logarithm and occurs in the range

of +250 mV to +1000 mV from the OCP (Licausi *et al*., 2013; Constantin *et al.*, 2016; De Tiedra *et al*., 2016). However, the anodic branch of the potentiodynamic scan is non-linear and often appears in an S-shape.

2.6.5.2 Linear polarisation

As previously mentioned in this text, linear polarisation is a non-destructive test whose small potential spectrum represents a principal advantage over other DC corrosion test techniques. Subsequently, the same test electrode can be utilised for repetitive linear polarisation measurements which further may indicate corrosion rate steady state (De Tiedra, Martín and San-Juan, 2016; Dinu *et al.*, 2017b). So, the slope of the straight line that is the change in Y-values (potential in mV) divided by the change in X values (current density in nA/cm^2) corresponds to the polarisation resistance, R_p and has been mathematically represented in Equation (2.20).

$$\text{Slope} = \Delta E/\Delta I \qquad (2.20)$$

Where, ΔE is the change in potential and ΔI the change in current density.

The R_p calculated in Equation 4.1 is expressed in ohms x cm^2 as shown in Figure 2-7.

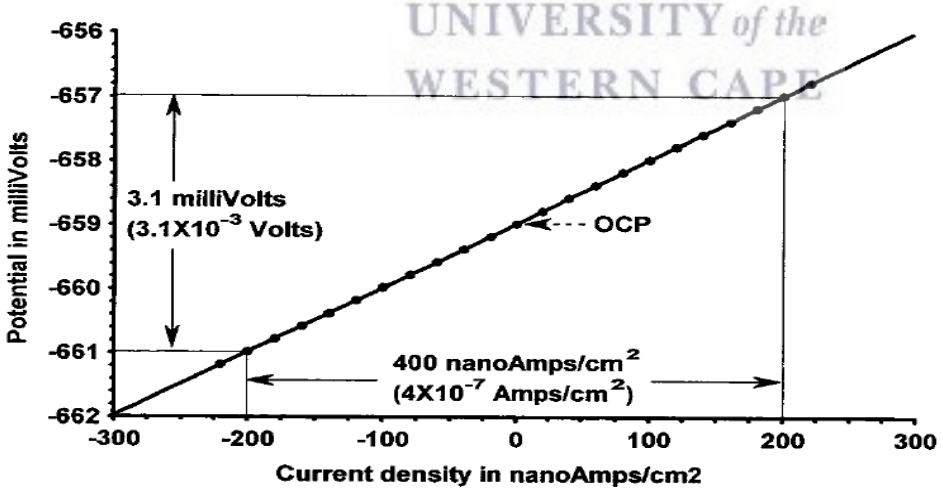

Figure 2-7:Graphical estimation of polarisation resistance (Tait, 1994).

Though linear polarisation allows determination of the polarisation/corrosion resistance R_p, it does not provide other parameters such as corrosion current and rate. Alternatively, corrosion measurement methods such as the Tafel plot can be used to estimate corrosion current and rate (Constantin *et al.*, 2016; Dinu *et al.*, 2016).

2.6.5.3 Tafel plot structure

Unlike linear polarisation previously discussed, the Tafel plot occurring in the range -250 mV to +250 mV from the OCP is an expression of potential versus log values of current density (Constantin *et al.*, 2016). In addition to this, the Tafel plot consists of two branches mainly the anodic branch and cathodic branch corresponding to oxidation and reduction corrosion half reactions, respectively (Vladescu *et al.*, 2013; Pruncu *et al.*, 2017). In addition, a broader DC potential spectrum (400 to 500 mV) is often used during Tafel plot corrosion measurement to obtain more corrosion information. The Tafel plot is often categorised either as activation or diffusion controlled. In activation controlled Tafel plots, the corrosion rate is determined by how quickly a metal is capable of losing its electrons that further reduce electrolyte reactive species (Braic, Balaceanu, *et al.*, 2015).

During this process, the current density magnitudes increase with an increase of potential for both branches. In that case, both branches become linear at approximately 50 mV from OCP as shown in Figure 2-8.

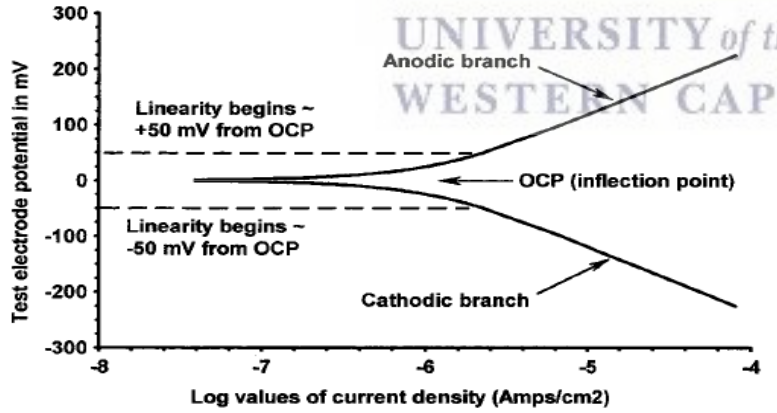

Figure 2 8:Tafel plot for activation controlled corrosion rates (Tait, 1994).

On the contrary, in diffusion controlled Tafel plots the corrosion rate is deduced by electrolyte active species diffusion rate (Mackey and Seacord, 2017). In this method, the diffusion of electrolyte active species (EAS) is restricted. Consequently, the diffusion of EAS on the surface of the electrode is extremely slow. For instance, the hydrogen gas bubbles produced from the reduction of hydrogen ions may limit hydrogen ions access to an electrode surface.

Furthermore, corrosion products such as thick metal-hydroxides layers might prevent the diffusion of EAS on the electrode surface. Diffusion control triggers the cathodic current to reach its steady state of about -50 mV from OCP as shown in Figure 2-9. Based on these limitations, it is important to prevent diffusion control during generation of the Tafel plot.

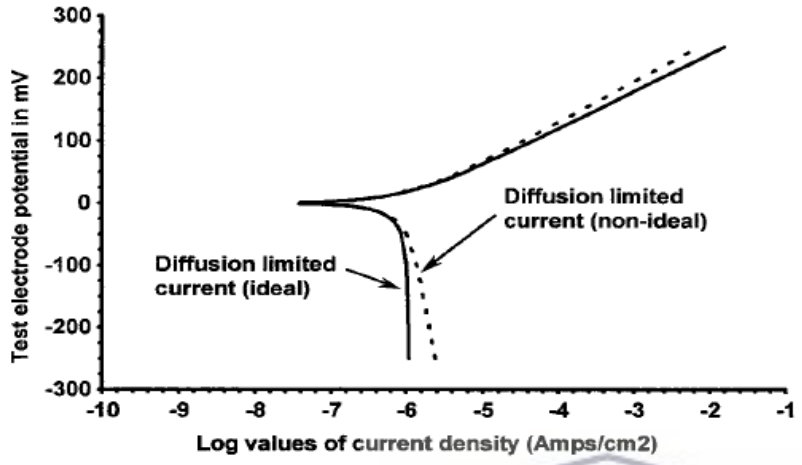

Figure 2-9:Tafel plot for diffusion controlled corrosion rates (Tait, 1994)

2.6.5.4 Determining Tafel slopes and corrosion rate

The Tafel plot is a current-potential curve that consists of anodic and cathodic branches which further correspond to the metal electrode transfer and the reduction of EAS. The anodic branch pointing upwards and the cathodic portion oriented downwards meet their linearity when the cathodic current reaches its steady state (Licausi, Igual Muñoz and Amigó Borrás, 2013; Constantin *et al.*, 2016). The slopes of both anodic and cathodic branches are determined by the ratio of change in test electrode potential (mV or V) over the logarithm of current density-decade where a decade is one order of magnitude current density for example from 0.10 amp/cm^2 to 1.0 amp/cm^2 as demonstrated in Figure 2-10.

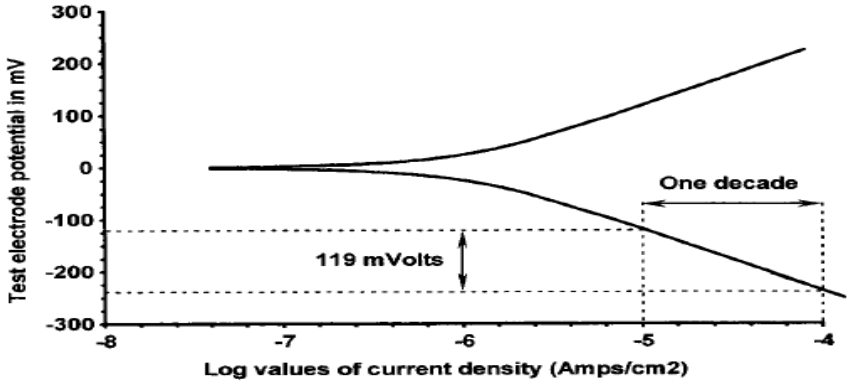

Figure 2-10: Determining Tafel slope from Tafel Plots (Tait, 1994).

Once the Tafel slopes values are determined, the mathematical relationship between corrosion resistance and corrosion current for linear polarisation data developed by Stern and Geary can be used to determine corrosion current density (nA/cm^2) given in Equation (2.21).

$$i_{corr} = [1/(2.303R_p][(\beta a \bullet \beta c)/1(\beta a+\beta c] \quad (2.21)$$

Where, i_{corr} is the corrosion current density in Amps/cm^2, R is the corrosion resistance in ohms•cm^2, βa is the anodic Tafel slope in Volts/decade or mV/decade (1000 mV = 1 Volt) of current density.

βc is the cathodic Tafel slope in Volts/decade or mV/decade of current density. While the quantity (βa.βc)/(βa+βc) is referred to as the Tafel constant.

Moreover, the corrosion current density (I_{corr}) can practically be read from a Tafel plot without Tafel slope values (Farzaneh *et al.*, 2011; Azem *et al.*, 2014). For instance corrosion current for an activation and diffusion control Tafel plots is the intersection of the anodic and cathodic linear extrapolations at OCP as shown in Figure 2-11 & 2-12.

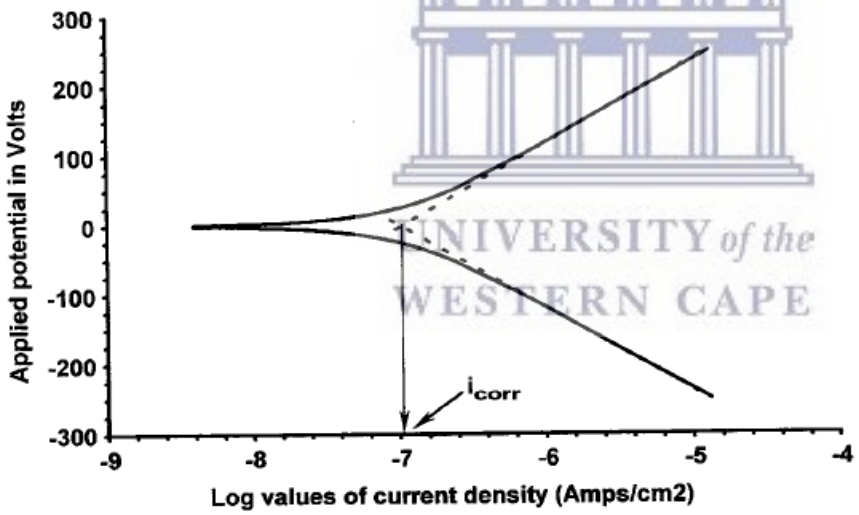

Figure 2-11: Corrosion current from activation controlled Tafel plots (Tait, 1994).

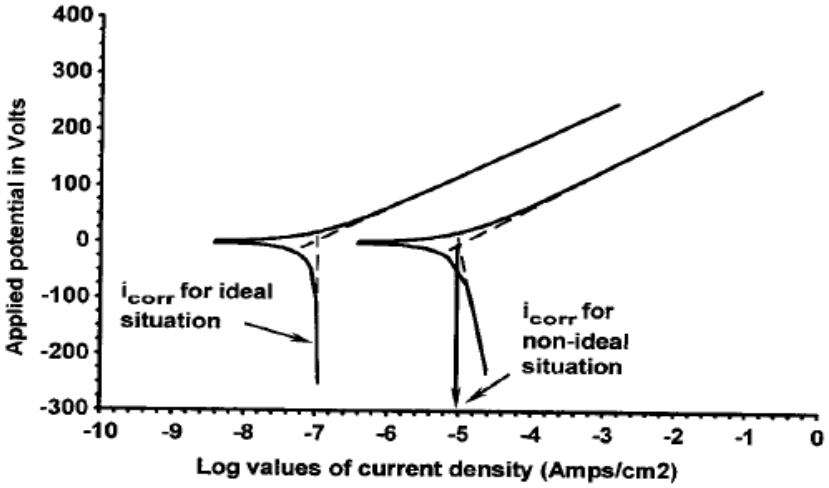

Figure 2-12: Corrosion currents from diffusion controlled Tafel plots (Tait, 1994).

Furthermore, corrosion current can be converted to a corrosion rate, in mils/year (mpy), using Equation (2.22) (Braic, Balaceanu, *et al.*, 2015).

$$MPY = i_{corr} (\Lambda) (1/\rho) (Ɛ) \quad (2.22)$$

Where Λ is a combination of several conversion terms and is 1.2866 x 105 [equivalents•sec-mils]/[Coulombs•cm•years]

i_{corr} is the corrosion current density in Amps/cm^2 (1 Amp = 1 Coulomb/sec) • p is metal density in grams/cc

Ɛ is equivalent weight (equivalent) in grams/equivalent. Equivalent weight is a metal's gram molecular weight divided by the number of electrons in a metal's anodic half-reaction.

2.6.6 Characterisation of coatings before and after corrosion

The roughness and thickness of coatings are among various coating parameters that need to be determined before and after corrosion. While roughness indicates whether the protecting layer has uniformly/evenly deposited on the substrate surface, the thickness may indicate an average size of the protecting layer. So the behaviour of these two factors measured before and after corrosion using typical equipment such as surface profilometry may define which material corroded most (Braic, A. C. Parau, *et al.*, 2014; Zoita *et al.*, 2014; Dinu *et al.*, 2017b). Similar techniques were adopted in this study to assess the thickness and roughness of Ti and Cr, Zr and ZrSi coating before and after corrosion. SEM and XRD analysis have also been employed

to determine the morphology of coatings and the presence of protective phases of coatings before and after corrosion (Braic, A. C. Parau, *et al.*, 2014).

In the current study, Cr, Ti, Zr, and ZrSi based nitride and oxynitride coatings were prepared by CAE. The electrochemical behaviour of the thin films was assessed by potentiodynamic polarisation technique described above. The obtained anticorrosion coatings were used as solid photocatalytic supports.

From most aspects reviewed in this chapter, it could be noticed that the impact of AOPs and particularly DBDs on removal efficiency of pollutants is measured by numerous analytical and characterisation techniques such as UV-vis, FT-IR, HPLC, LC-MS, TOC, COD, etc. whose principles and procedures are key to achieving the goals and objectives of the current studies.

The corrosion phenomena reviewed above is often caused by reactive oxidising species present in acidic environments. Hence their detection and quantification in AOPs are crucial to control and determine the efficiency of the system.

2.7 Detection and quantification of reactive oxygen species in advanced oxidation processes and electrical discharges during water treatment

The various quantification methods for the determination of reactive oxyen species (ROS) species in AOPs and other aqueous media reviewed in this text and summarised by (Mouele *et al.*, (2018) showed that indigo, titanyl sulphate and terephthalic acid methods coupled with UV-vis and fluorescent spectroscopy were the most convenient, feasible, applicable and affordable measurement techniques for determination of O_3, H_2O_2 and OH radicals in AOPs applied aqueous systems. It is noteworthy to mention that attempts using chemical spin traps alone or in some cases, coupled with other advanced techniques to quantify atomic oxygen and superoxide anions in aqueous media were unsuccessful (Finkelstein, 1980; Buettner, 1987; Wu *et al.*, 2012; Liao *et al.*, 2013). Studies confirmed by Wu *et al.*, (2012) documents that, though produced in plasma technologies, it could be possible that these short-lived radicals are totally transformed into ·OH via Haber – Weiss reactions when catalysed by Cu^+ as shown in Equations (2.23- 2.15). The highlighted disadvantages limit the quantitative analysis of solutions subjected to non-thermal plasma generation.

$$2\,{\cdot}O_2^- + 2H^+ \rightarrow H_2O_2 + O_2 \text{ (Self dismutation)} \quad (2.23)$$

$$H_2O_2 + Cu^+ \rightarrow {\cdot}OH + OH^- + Cu^{2+} \text{ (Fenton reaction)} \quad (2.24)$$

$Cu^{2+} + \cdot O_2 \rightarrow Cu^{+} + O_2$ (Oxidation and reduction) (2.25)

$\cdot O_2^{-} + H_2O_2 \rightarrow \cdot OH + OH^{-} + {}^1O_2$ (Haber –water reaction) (2.26)

The detection and accurate measurement of atomic oxygen and superoxide also attempted mostly in biomedicine media during treatment of water and wastewater effluents contaminated by organic pollutants disclose little information (Sawyer and Valentine, 1981; Sonntag, 1987; Sies and Menck, 1992; Calderon and Roberfroid, 1995; Rehman *et al.*, 2013). The complexities presented by the use of chemicals as well as the cost and unavailability of sophisticated equipment could limit effective measurements in systems other than biomedicine media. Furthermore, based on detection and trapping processes previously elaborated, it could be inferred that short-lived species such as $^1O_2$ and $\cdot O_2^{-}$ are mostly produced in medicinal and biomedicine systems where they have been proved to be more active in processes such as lipid peroxidation of bacteria (Joshi *et al.*, 1995, 2015) In contrast, trapping of these short-lived species in the treated contaminated water samples is challenging where they have been proved to contribute mostly to production of more long-lived species such as ozone and hydrogen peroxide (Ullmann, 1991; Kirk and Othmer, 1996). Furthermore, the quantification of these species in the proposed DBD configuration is crucial to gain insight, not only about the radical production cycle but to also understand their reactivity towards contaminants.

An extensive literature review has shown that reactive oxygen species have been widely quantified in various applications using different methods. Among them, indigo blue, titanyl sulphate, and terephthalic acid methods have been found the most feasible, affordable and applicable in the quantification of O_3, H_2O_2, and OH radicals.

2.7.1 Ozone quantification by Indigo method

The trapping of dissolved ozone underwater streamer discharge by Indigo method was described by Bader and Hoigni, (1981). The authors reported that Indigo absorbs light at 600 nm ($\varepsilon = 20000$ L $mol^{-1}cm^{-1}$) and one molecule of ozone decolourises one molecule of the indigo dye. The decolourised products barely use up supplementary ozone. The concentration of ozone scavenged can be estimated from the decolourisation of the reagent measured at 600 nm. Bader and colleagues (1981) further sustained that in plasma systems generating various oxygen species, the presence of H_2O_2 and $OH\cdot$ does not interfere with O_3 measurement.

2.7.2 Detection of hydrogen peroxide by Eisenberg method

The detection of H_2O_2 in aqueous plasma processes has been performed by using Eisenberg method that focuses on the photometric analysis of the strong yellow-orange colour resulting from the reaction of H_2O_2 and titanyl sulphate added in the plasma reactor (Eisenberg, 1943). The yellow colour product referred to as peroxotitanylsulfonic acid is formed according to Equation 2.27.

$$TiOSO_4 + H_2O_2 + H_2SO_4 \rightarrow TiO_2(SO_4)_2^{2-} + H_2O + 2H^+ \quad (2.27)$$

The concentration of the yellow-coloured peroxotitanyl complex could be assessed by UV absorption spectroscopy at 410 nm ($\varepsilon = 730\ M^{-1}\ cm^{-1}$) as suggested by Uher *et al*.,(1991) who claimed that the absorbance at this wavelength is directly proportional to the initial concentration of hydrogen peroxide.

2.7.3 Quantification of OH radicals using chemical probe Terephthalic acid

A few years ago, Sahni and Locke, (2006) revealed that chemical probes such as terephthalic acid (TA) could be used to detect and measure hydroxyl radicals in electro hydraulic discharge reactors.

In fact, the reaction of $OH^{\cdot}$ with non fluorescent TA results in the formation of fluorescent compound hydroxyterephthalic acid (HTA) as shown in the reaction in Equation (2.27). reported by various authors (Qu *et al.*, 2000; Didenko and Suslick, 2002).

Terephthalic acid (Non Fluorescent) + $OH^{\cdot}$ → 2-hydroxyterephthalic acid (Fluorescent) + further products (2.27)

Gupta, (2007) mentioned that the number of hydroxy terephthalic acid molecules formed is proportional to the fluorescence yield and this latter is directly proportional to the available $OH^{\cdot}$ radicals concentration. Terephthalic acid was found to be the best OH scavenger and widely applied due to its specificity and the availability the analytical instrument (Montesinos *et al.*, 2015; Badmus *et al.*, 2016; Massima Mouele *et al.*, 2018a).

However, literature presents little information on subsequent measurement of ROS in non-thermal plasma based on double cylindrical dielectric barrier discharge. In this way, this review shows that O_3, H_2O_2, and $OH^{\cdot}$ radicals have been widely quantified in AOPs during decomposition of organic pollutants while $^1O_2$ and $O_2^{\cdot -}$ have been measured mostly in biological systems during inactivation of bacteria. Mouele *et al.*, (2015) proposed that double cylindrical dielectric barrier discharge reactor configuration could efficiently decompose

organic pollutants and micro-organisms from water and wastewater, As a result, therefore, the measurement techniques mentioned could be used to successively quantify ROS such as O_3, H_2O_2, ·OH, O·, $O_2^{\cdot-}$ formed by the double cylindrical DBD system. The quantification of these species in the proposed configuration is crucial to gain insight, not only about the production cycle but to also understand their reactivity towards contaminants.

2.8 Reactivity of oxygen species with organic pollutants in advanced oxidation processes

In AOPs, the combination of UV light and other reactive oxygen species (ROS) such as O_3, H_2O_2 contribute towards the production of ·OH. The most common AOPs mainly O_3/UV, H_2O_2/UV, O_3/UV/H_2O_2 and their combination with the catalyst may be effective in the removal of organic pollutants and killing of bacteria (Pan and Schuchmann 1993; Bratsch1989). However, the utilisation of these techniques by themselves may be time-consuming and may involve a lot of wet chemistry. Conversely, AOPs based on non-thermal plasma processes like dielectric barrier discharges (DBDs) generate all ROS previously mentioned at once with few or no chemical additives. Apart from this, UV light is also produced in DBD systems and the benefit of producing O_3, H_2O_2, O·, $O_2^{\cdot-}$, OH·, etc. render DBD systems robust advanced oxidation technologies. O_3, H_2O_2, O·, and $O_2^{\cdot}$ are selective towards organic pollutants while OH· is non-selective (Malik et al. 2001). So it is certain that contaminants not decomposed by O_3, H_2O_2, O·, $O_2^{\cdot}$ in DBDs could be further oxidised and mineralised by ·OH following various reaction steps. Therefore, it is necessary to identify which type of free radical species such as O_3, H_2O_2, O., $O_2^{\cdot}$ are generated within DBDs and properly elucidate the reaction steps/mechanism that could be crucial to predicting what type of by-products could be formed during their reactions. This, in turn, may clarify what reagents researchers should use as additives in DBD reactors for the removal of toxins. This is important because sometimes, the newly formed intermediate by-products might be more toxic than the parent compounds. Hence assimilating the type of reagents and their interaction steps with ROS could be a way to avoid the formation of carcinogenic by-products in AOPs and thus in DBDs. Based on the benefits of ROS in DBDs, numerous DBD configurations have been employed for the degradation of organic pollutants (Mouele *et al.*, 2015). Though OH radicals are non-toxic oxidants that represent the general target of all AOPs, the complete mineralisation of organic pollutants into CO_2, H_2O, and simple organics is still an idea that has not been fully achieved in water

remediation. This can be observed from various studies reported in the literature which mostly show the restructuring of the carbon skeleton of initial/parent pollutants into intermediates (Rajeshwar *et al.*, 2008; Tijani *et al.*, 2017;Zhang *et al.*, 2018). Because of the fact that few authors showed/ suggested full mineralisation of the targeted compounds (Wang *et al.*, 2008; He *et al.*, 2014), further research still needs to be conducted. Since organic contaminants of several classes are found in water and wastewater treatment plants (WWTPs) effluents, pharmaceuticals have become the most considered due to their increasing abundance in water sources and because of their detrimental effects on the environment and on living organisms (Tijani *et al.*, 2014; Magureanu *et al*., 2015). These may further be related to the booming world population that uses these compounds for various purposes such as health and beauty, etc., (Emile S Massima Mouele *et al.*, 2015). Of several researchers who attempted the degradation of pharmaceuticals using AOPs, only a few showed their total conversion into CO_2, H_2O and harmless entities (Huang *et al.*, 2012; He *et al.*, 2014; Kim, Kam and Mok, 2015). For instance, verapamil, a common drug generally used to rectify cardiovascular disorders has become one of the most identified pharmaceutical contaminants in water matrixes. It was exposed to advanced oxidation processes induced in DBD plasma by (Krishna *et al*., 2016). TOC was used as a type indicator to follow the mineralisation of verapamil. Syam Krishna and colleagues (2016) showed that 98 % of mineralisation was achieved. The authors reported that the decomposition of verapamil was mainly governed by O_3 and $OH^{\cdot}$ via direct attack and resulted in various degradation intermediate by-products which further were converted to dissolved CO_2 as claimed by the authors. Similarly, Liu *et al.*, (2012) investigated the degradation of carbamazepine (CBZ) using ex-situ and in situ dielectric barrier discharge. The results showed that after 60 min 81% removal of CBZ was achieved with the in situ discharge compared to 100 % CBZ removal that was reached with the ex-situ after 3 min. The study further proved that the CBZ compound was broken down into various degradation intermediates; however, their mineralisation into CO_2 and inoffensive substances was not mentioned. Similar observations could also be made in studies conducted by Krugly *et al.*, (2015); Magureanu et al. (2015) and Marković *et al.*, (2015). Likewise, the toxicity of the degradation by-products in the aforementioned studies was not highlighted, showing that these studies omitted two criteria that are important in water and wastewater decontamination. To recall, the general issue claimed by most WWTPs is the production of sludge and the appearance of emerging micro pollutants in treated effluents which further limit their reusability for industrial purposes, distribution to recipients in need and their discharge into the environment. Therefore, complete removal of pharmaceuticals in/from final treated water is

mandatory in this regard. Perhaps OH· production systems need to be run for a prolonged time to allow a series of chemical reactions to occur till total degradation of the pollutants is achieved (Magureanu *et al.*, 2010; He *et al.*, 2014). In case of co-reactions between the degradation by-products, selected heterogeneous catalysts could be added to the treatment system to boost the generation of selective and non-selective oxidizers (Bubnov *et al*., 2007; Qu *et al*., 2009; Reddy and Subrahmanyam, 2012; Ghezzar *et al., 2013).* According to this point of view, Douglas *et al*., (2012) drew the mechanisms for the degradation of 1H-benzotri-azole during the ozonation process which was later reviewed by Hubner and von Gunten, (2015). The mechanisms pathway presented in Figure 2-13 shows that 1H-benzotri-azole was converted to a heterocyclic aldehyde that needed further oxidation or mineralisation to simpler molecules.

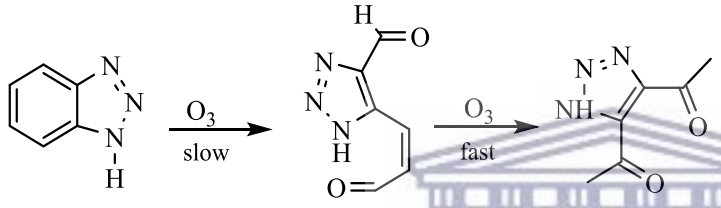

Figure 2-13: Ozonation decomposition pathway of 1H-benzotri-azole (Vanderford 2012; von Gunten 2015).

Similar investigations were conducted by Magureanu *et al.*, (2010); Liu *et al.*, (2013) and Marković *et al.*, (2015) where the parent compounds were not fully mineralised. On the other hand, Kim *et al.*, (2013); He *et al.*, (2014) and Kim *et al.*, (2015) investigated the removal of veterinary antibiotics, aqueous tetracycline and sulfonamide antibiotics by dielectric barrier discharge system respectively. The results showed that the OH radical was the main species that contributed to the destruction and mineralisation of the target pollutants into dissolved CO_2, H_2O, and simpler inorganics, etc. This was also reviewed by Sirés and Brillas, (2012) and (Feng *et al.*, 2016).

These findings show that by combining both incomplete and complete degradation processes, good mineralisation results could be achieved. This further inferred that effective AOPs aiming at producing high amounts of OH radicals should be employed for the decontamination of effluents in WWTPs. Therefore, radicals induced by DBD appear as potent species in AOP technologies that can be used as integrative stages to treat final effluents from WWTPs before being discharged into the environment. DBD configurations present numerous benefits as they produce UV, O_3, H_2O_2, O, $O_2^{\cdot-}$, $^{\cdot}OH$, etc. and the combination of these species could be a promising mixture that can be used to fully remove organic pollutants such as dyes and

pharmaceuticals from final effluents. However, understanding the degradation mechanisms of each oxidant towards specific pollutants is crucial either in DBD or in other treatment systems. Most studies reviewed above indicated that O_3 and $OH^{\cdot}$ are the principal reactive species that largely contribute to the decomposition of pharmaceuticals in DBD configurations followed by NOx and H_2O_2 that act as major precursors of OH radicals. All these excellent treatment methods developed in the literature show great removal efficiencies/percentages but only a few of them stipulate how the by-products formed or traced their behaviour in aqueous media. Based on these remarks, a few questions need to be asked: do these high removal percentages meant that complete oxidation of organic pollutants from water was achieved? If yes, why are the world's communities still facing a global water reclamation/scarcity while potent treatment methods have already been developed? These interrogations demonstrate that despite the fact that considerable numbers of treatment methods have been established; critical behaviour of pharmaceuticals in wastewater treatment plants (WWTPs) is still pertinent and hence needs to be addressed. During water and wastewater treatment, it is often believed that the following aspects might occur: 1) the operational/running cost of these advanced treatments is often beyond the allocated budget of various treatment facilities and hence limits their applicability at industrial level *(Andrew et al.* 2014). 2) the use of excessive chemicals often leads to toxic sludge and undesired by-products in the treated effluents (Boonnorat *et al.*, 2018). 3) the generated by-products often react together to form complex chains which in turn may be more harmful than parent molecules (Jimoh O. Tijani *et al.*, 2017). In this way, the treated effluents can neither be reused, distributed nor discharged into the environment without being properly treated. At this point, advanced treatment techniques need to be established to meet the global demand for clean water. Such technologies should incorporate both oxidation and mineralisation of target pollutant from water matrices. In addition to that, the technology should be applicable with reasonable costs to achieve global utilisation. Based on the DBD advantages highlighted in this text, their configurations are certainly capable to meet the aforementioned requirements. This review notes that studies in this field have not considered the toxicity of intermediate by-products generated in water treatment facilities. Therefore, it is important to emphasise that scientists involved in water and wastewater treatment should investigate and understand the properties of oxidants such as O_3, $\cdot OH$, etc. in aqueous media, considering not only their generation routes in the applied systems but also their reaction mechanisms towards targeted pollutants. The toxicity of the by-products formed should be carefully investigated and reported to assess the effectiveness of the treatment method used. Knowing the limitations of

the treatment options could assist scientists to develop suitable systems that achieve total oxidation of water contaminants. This may further relieve the global water crisis and make possible the provision of fresh, clean and water free from toxins. Among all oxidants reviewed in this manuscript, O_3 has numerous properties which justify its wide use for water and wastewater decontamination (William H Glaze, 1986; Lopez, 2008; Emile S Massima Mouele *et al.*, 2015). Moreover, O_3 as the precursor of various ROS in AOPs induced by DBDs presents numerous reaction possibilities with organic pollutants. The treatment time is another parameter that needs to be considered in water treatment (Magureanu *et al.*, 2010; He *et al.*, 2014). Its adjustment may vary relative to the treatment technology. On the other hand, toxic by-products might be obtained due to prolonged treatment times and could be avoided when running the system for a shorter period of time or vice versa. Apart from the deactivation of unsaturated olefins via epoxidation, ozone has other multiple selective reactions with a pollutant that needs to be controlled in water treatment systems. The hydroxyl radical ($OH^{\cdot}$) on the other hand is the main targeted product of AOPs. $OH^{\cdot}$ undoubtfully mineralises all types of contaminants, including bacteria and virus (Alkhimov et al. 1970; Lopez, 2008). Therefore, the efficiency of the particular system may depend on the density of $OH^{\cdot}$ produced. But based on its non-selective property, $OH^{\cdot}$ often reacts with its precursors or other scavengers that usually reduce its concentration in the treatment process (Lu *et al.*, 2003; Sahni and Locke, 2006a). This hence impacts upon the mineralisation of contaminants and their by-products and may further lead to unexpected outcomes. Parent molecules may react between themselves to form large carbon chain compounds. The generated by-products may react between themselves giving rise to new amalgams or parent molecules may combine with their by-products resulting in new complexes that are difficult to detect or to remove from the treated effluent. To some extent generated by-products may not necessarily be toxic; they could just be too complex to be removed from the treated water. Likewise, their consumption by water receivers could have long term effects which are still under investigation. One may also think that only larger molecules could be toxic. But tiny by-products such as amides may also be harmful (Nakada *et al.*, 2007). Hence the study of the product water's toxicity is beneficial. Based on the descriptive effects of ROS on toxic pollutants in DBD configurations, it could be inferred that DBD technologies can decompose many types of organic residues into CO_2, H_2O, and the simplest organics and inorganics. In that case, literature and further research offer the possibility to choose which chemical reagent to use, assist to predict what could be the degradation intermediate by-products formed, and hence clarify the toxicity of the by-products

formed after the reaction. Furthermore, the DBD technique reviewed in this text is cheap, feasible and environmentally benign. 1eV is enough as input energy to induce the plasma discharge. Although some studies may claim that the scalability of DBD systems is challenging, DBD configurations present various advantages over other electrical discharges and hence need to be considered as a feasible means for the direct removal of water pollutants. Many methods that meet the requirements for low cost, accessible treatment often lack good efficiency for complete removal of toxins from water. This is the case with various traditional techniques that have been used in water purification processes (Swartz et al., 2017). Certainly, they can treat water and wastewater but not all contaminants are removed. So, further integrative and competitive methods are needed to oxidise contaminants that escape water recovery plants or wastewater treatment plants (WWTPs). In this case, DBD configurations could be considered as a potent, efficient route for AOPs that may degrade and mineralise recalcitrant toxins. The reaction mechanisms of the species produced in DBD may favour the choice of reagents to be used but a better comprehension of non-thermal plasma properties and its application for water and wastewater treatment is needed. This may further give a better understanding of the types of by-products formed and hence predict necessary monitoring systems.

2.9 Model pollutants

Up to date, a large number of organic pollutants causing problems in the environment and threatening human lives are synthetically prepared in laboratories for various purposes such as material colouring, medicament, etc. Chemicals such as dyes are often synthesised in textile industries to achieve maximum colouration of desired materials. However, the release of wastewater from these facilities into the environment has significantly impacted on aquatic species (Panorel 2013). For instance, the absorption and scattering of sunlight by dyes may prevent the growth of algae. The intense colours of these substances in the environment persist and sometimes initiate secondary pollution when brought in contact with air. On the other hand, pharmaceutical compounds have recently been identified as emerging organic contaminants (EOCs) due to their resistance to conventional water and wastewater treatment techniques. The presence of these toxins in the environment is due to their large consumption while their recalcitrant behaviour in water and wastewater treatment plants (WWTPs) might be due to their high stability lipophilic characteristic and impeccable mobility. Since pharmaceutical contaminants are often identified in minute concentrations, they escape WWTPs where they

resist biological treatment and end up in surface and drinking water (Panorel 2013). Sulfamethoxazole (SMX) is a typical example of a pain killer (antibiotic) and is an analgesic drug that has been largely consumed worldwide. The occurrence in water and wastewater of such compounds has attracted global attention even though their long term effects on humans and the environment are still ununderstood. So based upon this review, orange II sodium salt dye and SMX pharmaceutical have been selected as targeted model pollutants for this study. A brief review of these two classes of contaminants is presented in the following paragraphs.

2.9.1 Model organic dyes in wastewater and their removal by AOPs

The presence of dyes in wastewater generates visual complications as their persistent colours may limit the utilisation of water and also decrease the effectiveness of biological treatment procedures. Apart from this, literature showed that dye degradation metabolites can be carcinogenic, mutagenic, or teratogenic and cause lasting health impact. Of main concern are dyes containing the azo group the –N = N- functional azo group which is often known as the chromophoric group responsible for the colouring phenomena in dye substances. Environmental research studies claimed that these azo compounds are widely used for many purposes and are largely released in the aquatic environment as wastes and hence impact upon humans health and the ecosystems (Supaka et al. 2004; Li et al. 2016). Indeed, dyes are often manufactured to achieve qualitative and quantitative desired aspects of materials such as clothes, food, etc. Therefore, these compounds have been designed to chemically and photochemically resist fading when exposed to water, detergent and light (Sahni & Locke 2006; Şahin et al. 2007; Li et al. 2016). Even though conventional biological processes have been employed in this regard, chromophoric organic dyes have shown incomplete removal in water and wastewater treatment facilities (Guimarães et al. 2012). Some of the common dyes found in wastewater effluents include methylene blue, orange II sodium salt dye, methyl orange and rhodamine blue whose abundance in aquatic bodies has attracted particular attention. The removal of these pollutants from water streams in treatment plants before being discharged into the environment is highly urgent. For these reasons, the implementation of traditional water treatment methods has become a priority research topic in the past few decades. Recently, advanced oxidation processes such as ozonation, Fenton reactions, TiO_2-mediated photodegradation, non-thermal plasma technologies, and various transition metal homogenous and heterogeneous catalysts in combination with oxidants such as ozone focusing on the production of nontoxic and nonselective hydroxyl radicals (.OH), have been established as

alternative remediation methods (Hsueh et al. 2007; Tizaoui and Grima 2011; Mozia et al. 2007; Pérez-Moya et al. 2011; Neyens & Baeyens 2003). This regards, the degradation of numerous organic dyes in aqueous solution using AOPs has been investigated. For instance, Sayed & El-Ashtoukhy (2013) investigated the removal of indigo carmine dye from synthetic wastewater by electrochemical oxidation in a new cell with horizontally oriented electrodes. In the study conducted by Sayed & El-Ashtoukhy (2013), the effect of current density, initial dye concentration, NaCl concentration, pH and solution flow rate on dye decolouration efficiency and COD were examined. The authors found that total colour removal and 88.2 % of COD removal content were subsequently achieved at the applied conditions. Similarly, a few studies on the degradation of orange II sodium salt dye using different AOPs have been conducted. For instance, Li et al. (2016) used zero valent iron (ZVI) and hydrogen peroxide (H_2O_2) for the degradation of Orange II dye solution. The outcomes of their study showed that the coupling of UV irradiation with ZVI/H_2O_2 (UV/ ZVI/H_2O_2) improved the decolouration of orange II dye. Moreover, the effect of pH, ZVI loading and H_2O_2 concentration on orange II decolouration efficiency were also assessed. In addition to this, about 68, 3% of COD removal was achieved and the biodegradability of orange dye was confirmed by the ratio of biological oxygen demand over chemical oxygen demand (BOD/COD) that increased from 0.019 to 0.41. In addition to this, Djaneye-Boundjou et al. (2012) studied the degradation of Orange II dye using two advanced oxidation processes TiO_2/UV and Fe^{2+}/H_2O_2. Both systems showed that the degradation of orange II increased with a decrease in pH. Apart from this, the authors also proved that orange II photodegradation efficiency increased when TiO_2 was varied from 0.0 g/L to 1.0 g/L. Since atmospheric non-thermal plasma processes produce UV light, shock waves and various free radicals, such as O_3, H_2O_2, $O^{\cdot}$,OH, etc. various electrical discharges or plasma configurations have been used to decompose wastewater dyes (Mok et al. 2008; Olszewski et al. 2014; Hoeben 2000). Hence in this study, double cylindrical dielectric barrier discharge (DBD) system that generates most of the aforementioned oxidants was used to degrade the orange II sodium salt which is presented in Figure 2-14 and was used as a model dye.

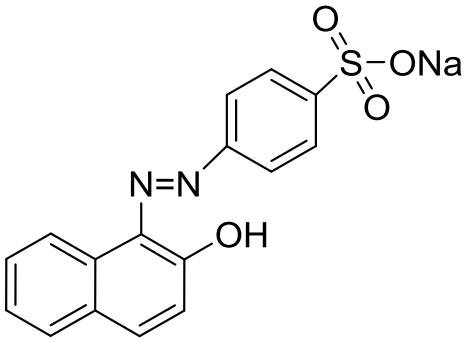

Figure 2-14: Chemical structure of azo-dye Orange II (M.F $C_{16}H_{11}N_2NaO_4S$ MW = 350.03 g/mol)

2.9.2 Pharmaceutical model pollutants

Recently, the occurrence of pharmaceutical residues, often referred to as compounds of emerging concern (CECs) in aquatic milieu has raised concern in the past few decades. Among these, literature claimed that antibiotics and nonsteroidal anti-inflammatory drugs (NSAID) are the two principal groups that have recurrently been identified (Lindqvist et al. 2005; Zhao et al. 2009; Nakada et al. 2006; Lishman et al. 2006).

Even though the long term effects and risks of pharmaceutical residues have not been established yet, their presence in the aquatic environment may be harmful to human beings and ecosystems (Murray et al. 2010). Therefore, the remediation of pharmaceuticals from the environment has become one of the most studied research fields in recent years (Hu et al. 2007; De Witte et al. 2010; Vasconcelos et al. 2009; Méndez-Arriaga et al. 2009; Klamerth et al. 2010). These authors highlighted that even if the concentration of pharmaceuticals in wastewater effluents has been estimated in the range of nanograms per liter (ng/L) to micrograms per liter (µg/L), the initial amount of pharmaceuticals in water bodies could reach up to 100 µg/l (Klamerth et al 2010). In this study, sulfamethoxazole (SMX) an antibiotic was selected as model water and wastewater pharmaceutical pollutant.

2.9.2.1 Sulfamethoxazole

Sulfonamides, as well as penicillins, are two widely known antibiotics groups that have been used in veterinary and human medicine. Likewise, sulfamethoxazole (SMX) known as an N-substituted pharmaceutical drug derives from sulfacetamide. Its chemical function aims at preventing the enzymatic production of dihydrofolic acid through competition with p-aminobenzoic acid (Injac and Kočevar 2009). This process consequently reduces the formation

of nucleic acids (Bogialli et al. 2003). SMX has extensively been used either for prevention and treatment of diseases or as a stabiliser to stimulate the growth process in animal nurturing techniques (Pereira 2005). According to Becker and Zittlau (2003), the number of sulfanomides and their derivatives used as additives could reach up to 100 mg/kg. Even though the use of these chemicals as additives in animal feeding processes was prohibited by the European Union in 1999, non-European countries still use these antibiotics for this purpose (Injac and Kočevar 2009). Therefore, the remains and incomplete digested additives of this compound often end up in water and wastewater streams which become directly or indirectly harmful to humans and their environments due to issues such as antibiotic resistance. Sulfamethoxazole with a molecular formula of $C_{10}H_{11}N_3O_3S$ and molecular weight of 253.3 g/mol is N1-(5-methylisoxazole-3-il) sulphanilamide is shown in Figure 2-15.

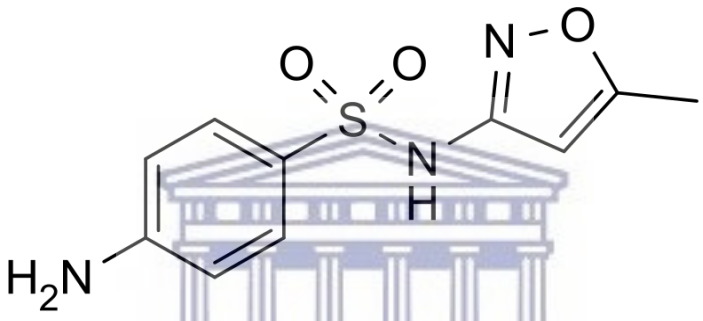

Figure 2-15: Chemical structure of sulfamethoxazole (M.F. $C_{10}H_{11}N_3O_3S$, M.W=253,279 g/mol, (Lazar 2014)

2.9.2.1.1 Degradation of sulfamethoxazole by advanced oxidation processes

Sulfamethoxazole as previously described is a worldwide used anti-infective sulfonamide antibiotic for prevention of enzymatic synthesis in bacteria. Its presence in the aquatic environment constitutes a threat to aquatic microorganisms. Hence its removal from water bodies is necessary. Various researchers have studied the removal of SMX by using different oxidative systems referred to as advanced oxidation processes (AOPs). For instance, Beltrán et al. (2008) used ozone and photocatalytic processes for the removal of the antibiotic sulfamethoxazole from water. In their study, several advanced oxidation processes including radiation, ozonation (O_3), catalytic ozonation (O_3/TiO_2), ozone photolysis (O_3/UVA), photocatalytic oxidation (O_2/TiO_2/UVA) and photocatalytic ozonation (O_3/UVA/TiO_2) were comparatively employed for the oxidation of SMX. The results of their study showed that higher removal of SMX was achieved by photocatalytic oxidation at low pH in less than 5 min. Likewise, about 93% of mineralisation (TOC removal) was achieved at pH 4. Moreover,

González et al. (2007) investigated the abatement of sulfamethoxazole by the photo-Fenton process. In their investigation, the biodegradability of the SMX was assessed by using the ratio of biochemical oxygen demand at five days/chemical oxygen demand (BOD5/COD). Microtox® equipment was used for toxicity and inhibition tests. The results on biodegradability (BOD5/COD) increased from zero to values higher than 0.3. The toxicity and inhibition tests showed no toxic effects on pure bacteria and no inhibition on activated sludge activity was reported.

Another removal of SMX was conducted by Mouamfon et al. (2011). In their study, the effectiveness of VUV-based methods mainly UV, VUV, UV/H_2O_2, and VUV/H_2O_2 on the removal of SMX in Milli-Q water and sewage treatment plant (STP) effluent was studied. During their investigation, the following parameters; initial pH, inorganic anions such as NO^{3-} or HCO^{3-}, and humic acid (HA) were considered. The outcomes of their research showed that at two pH values of 5.5 and 7.0, the best degradation of SMX was achieved with VUV/H_2O_2 followed by VUV, UV/H_2O_2, and UV, respectively. In addition to the studies described above, the degradation of sulfamethoxazole was also investigated by several authors using different AOPs systems (Sági et al. 2014; Ahmed et al. 2014; Dantas et al. 2008). Furthermore a number of authors have reviewed most AOPs used for the degradation of antibiotics mainly sulfamethoxazole (Ikehata et al. 2016; Ali 2014; Oller et al. 2011; Klavarioti et al. 2009), however, there is little or no information on the removal of SMX by AOPs induced by dielectric barrier discharges. This, therefore, justifies the choice of SMX as a model pollutant in the current study.

2.10 Review of most common analytical techniques used for water sample analysis

The decomposition of persistent organic pollutants (POPs) by DBD configurations, has been followed by several characterisation techniques among which UV/vis, and Fluorescence spectroscopy, high liquid chromatography (HPLC)/high liquid chromatography coupled to mass spectrometry(LC/MS), COD, TOC, and nitrate analysis have commonly been explored (Massima, 2014).When introducing photocatalysis process in DBD configurations, the following characterisation techniques: X-ray diffraction, High-resolution transmission electron microscopy, scanning electron microscopy, selected area electron diffraction, energy dispersion spectroscopy/ x-ray energy-dispersive spectroscopy need to be considered to determine the catalyst phase, partile sise, catalyst morphology, crystallinity, etc. Therefore in this section, a summarised chronological review of these techniques is presented.

2.10.1 Ultraviolet and Visible Spectroscopy (UV/VIS)

Ultraviolet and Visible Spectroscopy (UV/VIS) is frequently applied to detect unsaturated aromatic compounds Peuravuori et al. (2002). The excitation of periphery electrons of atoms in these molecules requires a specific amount of energy, hence the absorption of light (Pons et al. 2004). In this context, Peuravuori et al. (2002) sustained that both visible (VIS) and ultraviolet (UV) light are often absorbed by chromophoric functional groups present in dissolved organic carbon (DOC) and humic bodies of water samples. Moreover, literature showed that aqueous organic compounds with chromophore groups such as C=C and C=O, C≡C, or N=O double bonds absorb UV light at a wavelength range of 200 to 400 nm (Peuravuori et al. 2002; Abbt-Braun et al. 2004). In addition to this, the high absorption of UV light by organic compounds renders UV absorbance more usable than the visible (VIS) absorption. The UV absorption spectra resulting from UV analysis are often broad and difficult to distinguish and interpret. (Peuravuori et al. 2002) stated that the obtained peaks are usually ascribed to aqueous DOC chromophoric functional groups. Hence various authors (Croue et al. 2000; Chen, et al. 2003; Chouparova et al. 2004; Allpike et al. 2005) indicated that the concrete amount of unsaturated residues in water samples is generally specified in the UV spectrum at a wavelength of 54 nm. The specific UV absorbance (SUVA) which represents the ratio between UV absorbance and DOC mass concentration was reported (Thompson et al. 2003). According to Thompson and colleagues, SUVA was used to describe the hydrophobicity of aromatic substances in DOC. Hence, a high SUVA indicated bigger molecular size hydrophobic aromatic elements. Apart from this, SUVA was also perceived as typical of disinfection by-products (DBPs) (Krasner and Amy, 1995). Moreover, the ratio of UV absorbance at 253 and 203 nm (UV253/UV203) was found suitable to explain the DOC content between the phenolic and carboxylic fractions (Kim and Yu, 2005). Kim and co-worker reported that the higher UV253/UV203 ratio suggested a large content of phenolic substances which could possibly be due to DBP formation. A few years ago, the decolouration of typical simulated wastewater was considered as an initial degradation assessment of classic persistent organic pollutants during wastewater remediation (Tichonovas *et al.*, 2013). In this context, the authors used a UV/VIS spectrophotometer (Genesys™ 8, Thermo Scientific, UK) equipped with a 1 cm quartz cell to estimate the degradation concentration of dyes. While the first step dealt with scanning colorant samples in a specific UV/VIS range, the maximum absorbance was determined at a maximum wavelength. Afterward, the absorbance of standard concentrations was measured and a calibration curve of absorbance versus concentration was

plotted and used to determine the unknown concentrations of samples withdrawn during treatment. Accordingly, the UV-vis technique has broadly been utilised to study the degradation of organic contaminants. Likewise, additional techniques such as Fourier Transform Infrared Spectroscopy (FT-IR) are needed for identification and determination of functional groups in untreated and treated effluents.

2.10.2 Fluorescence spectroscopy

Fluorescence spectroscopy often referred to as fluorometry or spectrofluorometry, is a precise analytical technique used to measure the fluorescence of a particular sample. The instrument employed in this analysis is known as a fluorometer or fluorimeter. Indeed, fluorescence analysis involves the molecular absorption of light energy at a fixed wavelength; the absorbed light promptly excites the electrons in molecules of some composites and when returning to their ground state, the excited electrons emit light whose wavelength is constantly longer than that of the absorbed energy (Wang and Ku, 2003). Literature also sustained that some molecules may incandesce naturally while other complexes become luminous after they have been modified. Usually, fluorescent amalgams have two distinctive spectra: an excitation spectrum which is often obtained when the wavelength passing through the emission filter or monochromator is kept constant and the excitation monochromator is scanned. In this case, the excitation spectrum is often similar to the absorption spectrum as the fluorescence intensity is relative to the absorption. On the other hand, an emission spectrum wavelength is proportional to the amount of the light absorbed. The two types of spectra previously mentioned are usually referred to as fluorescence signatures or fingerprints. Consequently, the specificity of spectrofluorometry relies on the fact that it is for two fluorescent compounds to have the same fingerprint. Furthermore, the fluorometer dictates the wavelength of light needed to stimulate the analyte being studied and selectively diffuses the wavelength of the transmitted light and measures its intensity. Hence, the light given off is proportional to the maximum concentration of the analyte being measured. Literature highlighted that hydroxyl radicals react with various non-fluorescent molecules giving rise to fluorescent compounds whose fluorescence intensities could be approximated using fluorometry analysis (Sahni and Locke, 2006a; Badmus *et al.*, 2016). These luminescent molecules are often called OH scavengers among which Coumarin fluorescent scavenger, 5, 5-dimethyl-1-pyrroline-1-oxide (DMPO), the disodium salt of terephthalic acid are some typical chemical probes used for to trap OH radicals in aqueous solutions (Sahni and Locke, 2006a; Ji *et al.,* 2013).

2.10.3 Liquid chromatography

Chromatography is an analytical technique widely used for separation of chemical mixtures to their single constituents. The components are often separated according to their molecular structure and composition (Lukeš, 2001). The separation process implicates a stationary phase which could be a liquid supported on a solid and a mobile phase that is often a liquid or a gas (chromatographic packing material). Yet, the mobile phase transports the sample mixture/analyte when running through the stationary phase. So the analyte modules showing great interactions with the stationary phase will be eluted through the column more slowly than constituents having weak interactions. Moreover, the difference in elution rate results in separation of numerous molecular species. Therefore, separation by means of the chromatography technique can be achieved using different stationary phases among which immobilised silica on glass plates known as thin-layer chromatography, volatile gases referred to as gas chromatography, paper and liquids usually identified as paper and liquid chromatography, respectively (Mok *et al.*, 2008; Yan *et al.*, 2008; Zhang and Li, 2013).

2.10.3.1 High performance liquid chromatography - Mass spectroscopy

From previous descriptions on chromatography, high-performance liquid chromatography (HPLC) could be defined as a type of column chromatography that forces the analyte in a mobile phase at high pressure through a column packed with a stationary phase. Therefore, HPLC is an enhanced column liquid chromatography technique that has successfully been used for separation purposes. The difference between column chromatography and high-pressure liquid chromatography is that in column chromatography the mobile phase is allowed to flow through the column under gravity while in liquid chromatography the solvent is forced to drip through the column with high pressures of about 400 atmospheres. This, therefore, speeds up the elution process so as to minimise the separation time that is often prolonged by the interactions between the mobile and the stationary phases during separation of the sample into single components (Meyer, 2010). This principle is therefore applied in all chromatographic separation techniques together with HPLC. Besides the high-pressure aspect considered in HPLC analysis, the hydrophobicity nature (nonpolar) of the stationary phase also plays an important role in the reduction of separation time. Indeed, the solvent mixtures such as water and methanol or acetonitrile used as mobile phases are usually polar liquids; likewise, the column packing material is often nonpolar. So the elution process is also based on the principle

of hydrophobic interactions between the mobile phase and the stationary phase. Consequently, the more nonpolar the stationary phase is, the longer the eluent will be retained. After the different components of the sample have been separated, the obtained constituents are detected and their data are directly recorded on a computer screen based on their molecular structures and retention time. Since knowing the molecular weight of the eluted constituents in the sample is a crucial step in the chromatographic analysis, the mass spectrophotometer is usually coupled to HPLC (HP-LC) for the determination of eluent molecular weights.

2.10.4 Ecological parameters: chemical oxygen demand and total organic carbon

In chemical/photochemical oxidation of pollutants, UV-vis spectroscopy and/or chromatographic methods like high-performance liquid chromatography (HPLC) are often used to monitor the concentration of contaminants and identify their degradation intermediates. Likewise, other ecological parameters such as total organic carbon (TOC) and chemical oxygen demand (COD) can be used to control the overall organic pollution (Farouk, 2011). In 2004, Vijevic and colleagues reported that the measurement of TOC and COD of wastewater before and after treatment may indicate the reusability of the purified wastewater as process water. So both TOC and COD indicators have been widely used to evaluate the mineralisation of persistent compounds and their toxicity in contaminated water. Even though several studies (Sharma *et al.*, 1993; Vujevic *et al.*, 2004; Reddy *et al.*, 2014; Rong *et al.*, 2014) sustained the importance of TOC and COD as major ecological factors, their analytical procedures and their calculations have not been clarified in the literature. Consequently, a few authors namely Soresa, (2011), suggested comprehensive procedures for determination TOC and COD content during water treatment in electrical discharge using Fenton reagent. The analytical procedures proposed by Soresa, (2011) for TOC and COD determination have been successively reviewed and have been explored in this study to assess not only the toxicity of simulated orange II sodium salt dye, ibuprofen and sulfamethoxazole pharmaceuticals treated by DBD plasma reactor but also to determine their mineralisation extent.

2.10.4.1 Total organic carbon

The total organic carbon (TOC) is often assimilated as the number of carbon residues in an aqueous medium. Conversely, depending on the cost, the type of instrument suitable for such analysis may vary. For example, during the degradation of organic compounds from water by

adsorption and photocatalytic oxidation conducted by Farouk, (2011) a TOC-meter (TC Multi Analyser 2100 N/C) in which the organic molecules were completely oxidized at 850 °C in the presence of a platinum catalyst was used for TOC analysis. Alternatively, when Reddy *et al*., (2014) investigated the decomposition of endosulfan in an aqueous medium using a catalytic non-thermal plasma reactor, the TOC content was analysed by a standard method (5310 A combustion and detection method) using TOCVCPH total carbon analyser (Shimadzu, Japan). Furthermore, Reddy *et al*., (2014) used a Shimadzu 5000A TOC analyser to determine the mineralization of diclofenac during dielectric barrier discharge induced degradation. Although TOC instrumentation differs from one study to another, the analytical principle used for determination of TOC content in water samples is generally the same.

i) Total organic carbon analysis: Principle

The standard methods for the examination of water and wastewater, high-temperature combustion method 5310 B (APHA, AWWA, 1998) were used to determine TOC content. The TOC analytical principle includes the insertion of a homogenised sample in the micro portion into a heated reaction chamber packed with an oxidative catalyst such as barium chromate, cobalt oxide or platinum group metals. During water evaporation, the organic carbon is oxidized to CO_2 and H_2O. Furthermore, Soresa, (2011) highlighted that CO_2 formed is transported in the carrier-gas streams and measured by colorimetric titration or by a non-dispersive infrared analyser.

ii) TOC content

Reddy *et al*., (2014) specified that the difference between total carbon content (TC) and total inorganic carbon content (TIC) (referring to the sum of inorganic carbonspecies in a solution including carbon dioxide, carbonic acid, bicarbonate anion, and carbonate) can be used to estimate TOC content. In this case, the first step involving acidification of the sample is crucial for the removal of inorganic carbon (IC) for organic carbon (OC) examination. In addition to this, the TC was determined by catalytic oxidation of the samples at 680 ^{o}C while an infrared detector was used to determine the CO_2. Next, a calibration with potassium hydrogen phthalate standards was used to approximate TOC content. Regarding the acidification process, Farouk, (2011) and Reddy *et al*., (2014) emphasised that the addition of a few drops of concentrated phosphoric acid (84 %) to the sample may neutralise the inorganic carbon present in the

solution as carbonate (CO_3^{2-}), mono hydrogen carbonate (HCO_3^-) and dihydrogen carbonate (H_2CO_3). The CO_2 generated can be degassed by nitrogen flow into the system (Urbansky 2001; Reddy et al. 2014).

2.10.4.2 Principle of Chemical oxygen demand

Unlike TOC, chemical oxygen demand (COD) is defined (Hyunook Kim, 2007; Bustillo-Lecompte, Mehrvar and Quiñones-Bolaños, 2013) as the amount of oxygen necessary for the complete chemical oxidation of organic compounds and substances to inorganic by-products. This method is often used to determine the total amount of organic contaminants of wastes in municipal and industrial laboratories. In this process, potassium dichromate ($K_2Cr_2O_7$) known as a strong chemical oxidising agent is used in excess. Therefore, COD often expressed in milligrams of oxygen per liter is an important measure of water quality (Ai *et al.*, 2004; Zhao *et al.*, 2004; Zhang, Jiang and Zhao, 2006). It remains an inevitable and rapidly quantifiable factor for water samples analysis. Even if most research has mentioned using COD as a toxicity measurement technique, however details on the experimental procedure of this toxicity indicator present little information in the literature. Apart from TOC, Soresa, (2011) also proposed a logical COD measurement procedure which complies with that endorsed by standard methods for the examination of water and wastewater, high-temperature combustion method 5310 B (APHA, AWWA, 1998).

In the methodology suggested by Soresa, (2011) for the determination of COD, the following chemicals $K_2Cr_2O_7$, H_2SO_4, Ag_2SO_4, $FeSO_4{\cdot}7H_2O$, and ferrous ammonium sulphate titrant (FAS) [Fe $(NH_4)_2(SO_4)_2{\cdot}\ 6H_2O$] were used to prepare standard solutions.

Consequently, the amount of COD (mg/L) was calculated using the formula shown in Equation (2.28) as follows:

$$\text{COD (mg/L)} = [(\text{FASs} - \text{FASp}) * \text{N} * \text{f}] / \text{Vs} \qquad (2.28)$$

Whereby FASs expressed in mg/L represents the ferrous ammonium sulphate concentration used for the sample, FASp is the ferrous ammonium sulphate concentration (mg/L) used for pure water, f is the dilution factor (8000), while N and Vs are the normality of FAS and the sample volume (mL), correspondingly. This COD principle was explored in this study to approximate the COD quantity in raw and treated orange II sodium salt, ibuprofen and sulfamethoxazole drugs selected as model pollutants.

2.11 Material characterisation

In most photocatalytic studies, the following characterisation techniques, FT-IR, XRD, TEM, SEM, SAED, EDS, have been used subsequently in order to achieve a full understanding of the material properties (Guo *et al.*, 2015; Hassani *et al.*, 2015).

2.11.1 X-ray diffraction

X-ray diffraction (XRD) is a powerful analytical technique used for phase identification of crystalline powder materials. This technique further offers information about the unit cell dimensions. The operational principle of this method requires that samples to be analysed should be first ground, homogenised and their bulk composition could be determined. The determination of sample crystallinity and the identification of phase are often achieved by using different XRD instruments such as Rigaku – MiniFlex II (Japan) powder diffractometer with CuKα (λ for Kα = 1.54059 Å) over the desired 2θ range with a step width of 0.05°used for this study.

In this context, an example of XRD results of particular catalysts has been published by Hu *et al.*, (2011) during hydrothermal growth of freestanding TiO_2 nanowire membranes for photocatalytic degradation of pharmaceuticals. The XRD spectra of their study are presented in Figure 2-16.

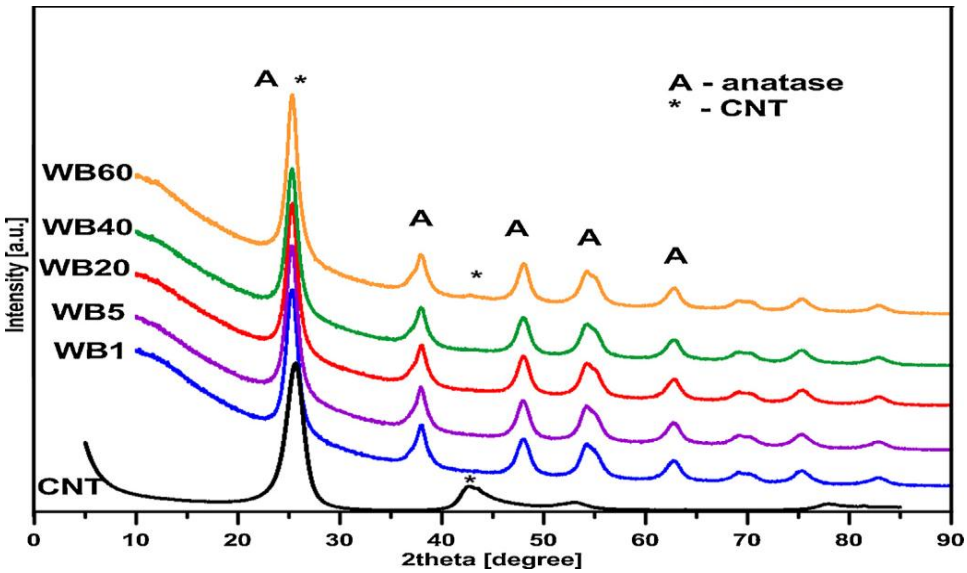

Figure 2-16: The XRD spectra of studied photocatalysts: A – anatase peaks, of carbon nano tubes (CNT) char-acteristic peaks (Hu *et al.*, 2011b).

To recall, literature showed that in numerous catalytic and photocatalysis studies, the XRD analysis exhibits different XRD plots and a typical example is presented in Figure 2-18 (Choina *et al.*, 2015; Das *et al.*, 2015). Moreover, XRD is often used to determine the crystallinity and catalytic phase. It has widely been employed as primary characterization method. For instance, Czech *et al.*, (2015) prepared CNT–TiO_2/SiO_2 nanocomposites by application of TiO_2 and SiO_2 co-precipitated in the presence of CNT. The XRD results cinfirmed the crystallinity of TiO_2/SiO_2 particles. In addition to this, He *et al.*, (2016) investigated the degradation of pharmaceutically active compounds namely propranolol, diclofenac and carbamazepine in wastewater using photocatalyst TiO_2 immobilised on 200–500 mm sand by a sol-gel method which was compared to solar irradiation. In their study, the authors used the XRD technique to determine crystallinity and identify the phase of the synthesized photocatalysis. In the same context, Guo *et al.*, (2015) prepared a magnetically separable graphene–TiO_2 (MG–TiO_2) hybrid photocatalyst by a one-step method for the photocatalytic degradation of tetrabromobisphenol A. The crystalline structure of the hybrid photocatalyst was dictated by XRD analysis. On the other hand, Lin *et al.*, (2015) synthesised a sensing graphene/TiO_2 (G/TiO_2) by sol-gel method with 1 wt%, 5 wt%, 10 wt%, and 20 wt% of graphene. The structure of the prepared materials was investigated by XRD analysis. Furthermore, Monteiro *et al.*, (2015) assessed the photocatalytic activity of N-modified TiO_2 on the degradation of diphenhydramine and on inactivation of *Escherichia coli* in aqueous solutions. The crystalline phases of TiO_2 were successfully defined by XRD analysis.

2.11.2 Microscopy

This subsection highlights the various microscopy techniques such as High resolution transmission electron microscopy (HRTEM), Scanning electron microscopy (SEM), Selected area electron diffraction (SAED), Energy dispersion spectroscopy (EDS), Fourier Transform Infrared (FTIR) Spectroscopy, that have been reported in the literature for the characterisation of the synthesised materials.

2.11.2.1 High resolution transmission electron microscopy

High resolution transmission electron microscopy often referred to as HREM or HRTEM is an imaging microscopic technique whereby a stream of electrons is passed through an ultra-thin

specimen, inducing the interaction between the supplied electrons and the atoms of the specimen. This results in the formation of an image that is further magnified and focused either onto a fluorescent screen or a photographic film layer or could be detected using specific sensors such as a conductively coupled device (CCD) camera (Ma *et al.*, 2006). The diverse applications of TEM include determination of the morphology, shape, size and the arrangement of particles on the scale of atomic diameters (Ma *et al.*, 2006). In addition to this, literature also proved that TEM analysis may provide crystallographic information from the diffracted electrons that is is often referred to as selected area electron diffraction (SAED). The arrangement, as well as the order of atoms and the detection of atomic-scale defects, could be obtained. Furthermore, TEM study may also indicate the chemical composition of particular substances know as enegy dispersion spectroscopy (EDS/EDX). One of the greatest benefits of TEM is the ability to detect both microscopic images and diffraction patterns of the same selected area by adjusting the electron lenses as the two parameters may provide information in real and reciprocal space, respectively. Moreover, Bendersky and Gayle, (2001) showed that the insertion of a selected area aperture and the use of a parallel incident beam illumination may give information in reciprocal space from a specific region as small as 100 nm in diameter for the same area.

Since most research studies in Physics, Chemistry, Biology, etc. require a morphological image of the object or subject being analised, a large number of studies based on TEM analysis have been conducted (Choina *et al.*, 2015; Guo *et al.*, 2015). Hassani *et al.*, (2015) examined the photocatalytic degradation of ciprofloxacin by synthesised TiO_2 nanoparticles on montmorillonite. The morphology of the catalyst was determined using TEM analysis. During a similar study, Murgolo *et al.*, (2015) analysed the UV and solar-based photocatalytic degradation of organic pollutants by nano-sized TiO_2 grown on carbon nanotubes. The morphology of the synthesized nanocatalysts was determined by TEM analysis. The use of TEM technique for imaging the morphology of specimens during catalytic studies has been extensively employed (Czech *et al.*, 2015; Das *et al.*, 2015; Guo *et al.*, 2015).

2.11.2.2 Scanning electron microscopy

Scanning electron microscope usually called SEM is another powerful microscopic technique used for characterisation and observation of heterogeneous organic and inorganic materials on an nm to μm scale. It has the capability to produce high-resolution images of a sample surface and may be valuable for elemental analysis (Ma *et al.*, 2006). During the SEM process, the

sample region to be analysed is often illuminated with a well-focused electron beam which might be picked up in the raster across the specimen surface leading to image formation or could be stagnant and hence facilitate analysis at one location. Literature sustains that SEM images often appear in three-dimensions and are convenient in showing the surface of the targeted material. Furthermore, Ma and colleagues, (2006) emphasised that secondary electrons, backscattered electrons, characteristic x-rays, and other photons of various energies are the different kinds of signals resulting from the interaction of the electron beam with the sample.

In summary, transmission electron microscopy (TEM) and scanning electron microscopy (SEM) have been extensively employed in material science. While TEM is an imaging technique whereby a stream of electrons are transmitted through a specimen leading to the formation of images that can be observed on a fluorescent screen or photographic film layer. SEM is an electron microscopic method that produces high-resolution images of a sample surface (Ma *et al.*, 2006; Zinin, 2009). Scanning electron microscopy (SEM) producing high-resolution images of specimens have also been broadly used in research studies. For example, Morales-Torres *et al.*, (2013) synthesized graphene oxide-P25 photocatalysts for the degradation of diphenhydramine pharmaceutical and methyl orange dye. A parallel study of this was carried out by Morales-Torres *et al.*, (2013). SEM analysis was used to determine the morphological images of the as-prepared catalysts. In addition to this, (Sarkar *et al*., (2015) studied the photocatalytic degradation of pharmaceutical wastes by alginate supported TiO_2 nanoparticles in a packed bed photoreactor (PBPR). In their research, scanning electron microscopy coupled with energy dispersive X-ray spectroscopy (SEM/EDS) was used to characterise the alginate supported catalyst beads. Furthermore, (Rioja *et al*., 2014) conducted a competitive removal of pharmaceuticals from environmental waters by adsorption and photocatalytic degradation. The images of activated carbons and TiO_2 photocatalysis were obtained by SEM analysis. Apart from these enumerated studies, the utilisation of SEM in the determination of catalyst and photocatalysis images were carried out by numerous other authors (e.g. Czech *et al*., 2015; Hassani *et al*., 2015; Monteiro *et al.*, 2015; Murgolo *et al*., 2015; Qi *et al.*, 2015; He *et al.*, 2016).

2.11.2.3 Selected area electron diffraction

The selected-area electron diffraction (SAED) is a microscopic technique possible during SEM/ TEM analysis. During the SAED process, the sample image originating from the objective lens is focussed and magnified on a diaphragm.

Moreover, during the SAED method, charge carriers (electrons) are transferred over the aperture if only they fit within its diameter D, which matches the diameter of D/M at the sample plane. Consequently, sample diffracted information could be achieved from the specimen area whose area is smaller than 0.2 µm. Therefore, the SAED technique offers important diffraction information of the specimen with upright angular and three-dimensional resolution which is achieved by using one or two condenser lenses mounted in parallel. This technique shows important information about a specific area of the specimen is often included during characterisation of catalytic solid materials. In addition; the SEAD technique gives an insight about the polycrystalinity of the prepared materials. In this regard, Weirich et al. (2002) and Li (2010) reported that the best polycrystalline material observed by SEAD should present a proliferation of indiscriminately oriented crystallites. On the other hand the authors stated that compared to distinct bulky crystals, a polycrystalline with scattered vectors, generates a group of concentric trigonometric circles (radius = 1) rather than isolated nodules. These circles are amended by the joined Ewald circle of elevated voltage electron deflection leading to different ring patterns often observed.

2.11.2.4 Energy dispersion spectroscopy

The energy-dispersive spectroscopy (EDS) during SEM analysis is a spectroscopic technique that uses a dispersive semiconductor diode often made from either silicon or germanium and slightly comparable to BSE sensor used in an SEM instrument. Each peak in the EDS spectrum characterises a specific element existing in a known area of the sample, well-defined by the fixed probe. EDS is a spectroscopic technique performed during SEM/TEM analysis that offers qualitative information about the chemical composition of the specimen being investigated. Determination of the chemical composition of the analyte is a crucial step in catalytic studies (Monteiro *et al.*, 2015). Various investigations based on EDS analysis have been conducted. Hassani *et al*. (2015) studied the photocatalytic degradation of ciprofloxacin by synthesised TiO_2 nanoparticles on montmorillonite. Among the various characterisation techniques used in their investigation, the EDS technique was used to determine the elemental microanalysis of

TiO_2/MMT samples. In addition to this, a large number of studies involving the elemental analysis of synthesised catalysts have been conducted (Pastrana-Martínez *et al.*, 2012; Monteiro *et al.*, 2015; Sarkar *et al.*, 2015). The aforementioned characterisation techniques have been used by various other authors (Choina *et al.*, 2015; Czech *et al.*, 2015; Monteiro *et al.*, 2015; Murgolo *et al.*, 2015; Qi *et al.*, 2015; He *et al.*, 2016) to determine morphology (SEM & TEM), chemical bonds (FT-IR) and mineral phases (EDS, XRD) of the prepared catalytic materials. Furthermore, numerous studies have been employed in a similar sequence of these techniques to attain the full characteristics of materials being investigated (Pastrana-Martínez *et al.*, 2012; Morales-Torres *et al.*, 2013; Fathinia and Khataee, 2015; Lin *et al.*, 2015; Sarkar, Chakraborty and Bhattacharjee, 2015).

2.11.2.5 Fourier Transform Infrared Spectroscopy

Besides UV-Vis spectroscopy previously illustrated in section 2.10.1, Fourier transform infrared spectroscopy (FTIR) is a complementary method to UV-vis that is recurrently employed for the determination of functional groups in liquid or solid materials (Bruice, 2004). This is due to its sensitivity and short time for analysis. Moreover, the author also accentuated that in conventional IR spectroscopy, an infrared spectrum derives from only one scan. Likewise, the integration of an interferometer in the FTIR method favours various scans and the transformation of the interferogram into an infrared spectrum. Based on these claims, various studies with reference to IR spectroscopy utilise the FTIR procedure. As a result, FTIR with different procedures has been used to determine DOC of purified or untreated water matrices (Kim and Yu, 2005). For example, Tichonovas *et al.*, (2013) studied the decomposition of several dyes as model contaminants subjected to DBD plasma treatment. In their research, FTIR analysis was used to identify dye degradation by-products. The FTIR results of their work indicated that amides, amines, carboxylic acids, and nitrates, were formed as by-products in the treated wastewater. A similar study was conducted by (Croue et al., 2000) during which the structure of organic pollutants producing haloacetic acids (HAAs), specifically ketones, aromatics, carboxylic acids, amides, and amino acids was examined. Their FTIR results showed that HAAs principally originated from HPOB and HPIB elements. Years ago, (Lin, 2000; Drewes *et al.*, 2006) and (Drewes *et al.*, 2006) emphasised that the wavenumber resolution of conventional FTIR falls in the range of 2 to 4 cm^{-1}. Only later, (Jones et al., 2006). Jones et al., (2006) applied a synchrotron light to attain a wavenumber resolution of 1/14 μm^{-1}. This was later supported by Peuravuori et al., (2002) who claimed that the high

sensitivity of FTIR spectroscopy with synchrotron light is a powerful tool to reveal the nature of diverse organic molecules. Based on these facts, several investigations focusing on water analysis (from harbour sediments and refinery effluents for petroleum organic compounds) using FTIR and synchrotron light have been reported (Song *et al*., 2001; Chouparova et al., 2004; Jones et al., 2006; Wang *et al.*, 2010; Tichonovas *et al.*, 2013). Apart from FTIR spectroscopy being used to follow the degradation of organic substances and for the identification of the functional groups of their end-product respectively, the understanding of the sample stability is crucial to identify temperature range in which the as –synthesised catalyst decomposes. In this case, it is crucial that additional characterisation such as thermal gravimetric (TGA) analysis should be considered to investigate the stability of the catalyst.

2.11.2.6 Thermal gravimetric analysis

Thermal gravimetric analysis (TGA) is a widely used characterisation technique that is employed to evaluate the thermal stability of the synthesised catalysts (Mohamed *et al.*, 2005; T.-H. Zhang *et al.*, 2012; Lee *et al.*, 2014). This descriptive method is often used as a complement with most of the characterisation systems reviewed above (Breugelmans *et al.*, 2012). For instance, Pang and Abdullah, (2012) synthesised powder and nanotube TiO_2 catalysts for the removal of various dyes including Methylene Blue, Reactive Blue 4, Methyl Orange, Rhodamine B, and Congo Red. Next to other characterisation methods such as FT-IR, TEM, etc., the authors used TGA to determine the thermal decomposition of TiO_2 and nanotube catalysts. Their results revealed that the weight loss percentages (0.1 wt. % and 0.74 wt. %) observed in the following temperature ranges 200-500 ^oC and 500 -700 ^oC were on the one hand due to the formation of anatase phase and disintegration of organic constituents contained in the TiO_2 gel and on the other hand to the oxidation of remaining carbon and disappearance of water that was chemisorbed on the catalyst framework. A similar investigation was carried out by Hasan *et al.*, (2015) who synthesised HCl-doped Au@polyaniline (Pani) nanocomposite fibers via the in situ oxidative polymerisation of aniline in the presence of gold nanoparticles. The thermal stability of the nanocomposites was evaluated by TGA and the results showed that both Pani and Au@Pani nanocomposite fibers thermally decomposed through three different weight loss stages. For temperature below 150 ^oC, the decomposition of both nanocomposites was related to the vaporisation of moisture and volatile matters that were adsorbed and retained in the composite matrices. Moreover, the decomposition of nanocomposites between 200 - 425°C, and above 425°C was attributed to

the elimination of higher oligomers of Pani and to the thermooxidative decay of Pani that yielded several degradation metabolites such as methane, aniline, acetylene, ammonia, etc., respectively. According to Hasan *et al.*, (2015), the larger thermal stability of Au@Pani nanocomposite fibers observed at higher temperatures above 800 ^{o}C could be due to gold nanoparticles that were successfully incorporated in the composite system. The authors further confirmed that the enhanced thermal stability of the Au@Pani nanomaterials could be ascribed to the minimal agility of the polymer restraints that impede the transfer of free radicals through interchain reactions, hence causing the alteration of the onset temperature of thermal decomposition to elevated temperatures. In addition, Yan *et al.*, (2016) synthesised gas sensing TiO_2 nanomaterials namely C-doped and N-doped reduced graphene oxide/TiO_2 composites by the hydrothermal process using HF as the morphology-controlling agent at 180 oC for 12 h. The authors used a Shimadzu TGA-50H analyser in air (10 $^{\circ}$C min^{-1}, from room temperature to 1000 $^{\circ}$C to examine the thermal gravimetric analysis of the prepared nanomaterials. Extended thermal stability variations were reported by Chandni Bhatt *et al.*, (2016) who used TGA to assess the thermal stability of polymer nanocomposite (PNC) films based on PEO/PAN + NaPF6 with different concentration (wt./wt.) filler of nano-sized (TiO_2) that were synthesised by a standard solution cast technique. The use of TGA towards the examination of the thermal stability of nanocatalysts synthesised has widely been explored (Abdullah *et al.*, 2016; Liu *et al.*, 2016; J O Tijani *et al.*, 2017). All these investigations demonstrate that TGA is a useful tool that is employed to define the temperature range in which the synthesised materials could be stable or decompose to various undesired products. Its utilisation in conjunction with other characterisation techniques such as FT-IR, SEM, EDS, XRD, etc. is crucial in assimilating the catalyst chemical behaviour during synthesis and pyrolysis processes.

2.12 Summary of the degradation of pharmaceutical compounds by DBDs or by photo catalysts

The double cylindrical dielectric barrier discharge and photocatalysis, separately described in this text, show that both systems converge towards the mineralisation of targeted pharmaceutical pollutants. On the one hand, the double cylindrical DBD configuration alone produces not only UV light and shockwaves, but this system is also a source of various oxygen based species such as O_3, H_2O_2, $O_2^{\cdot -}$, $O^{\cdot}$, etc. (as shown in Figure 2-3) that all participate directly or indirectly in the oxidation of pharmaceutical toxins and mostly contribute to the generation

of $OH^{\cdot}$, the non-selective, powerful oxidant that degrades and mineralises organic micropollutants into CO_2, H_2O and harmless by-products. The possible methods for the quantification of the free radical species, mainly ozone, H_2O_2 and OH radicals in aqueous systems and in DBD configurations have been reviewed and published. On the other hand, this review showed that photocatalysis processes (as shown in Figure 2-4) generate charged species including positive holes, and energised electrons which may contribute to degradation of pharmaceutical compounds by adsorption or, in contact with oxygen, produce other oxygen-based species such as superoxide anions that are major precursors of the powerful non-selective $^{\cdot}OH$ that completely mineralises the targeted contaminants. Likewise, this review highlighted that to overcome post separation process after treatment with a powder photocatalyst, the photocatalyst can be immobilised on various supports including solid SS based meshes and glass. However, it can be noticed that in most photocatalytic studies reviewed in section 2.4, SS used as a support has not been covered with corrosion protective layers before deposition of (gel) catalysts. This might raise doubts about the longevity of the coated films in acidic environments that could cause corrosion of the coated films. This consequently shows that supports such as SS should be first protected with anticorrosive layers before immobilisation of the catalysts. In addition, despite the fact that pharmaceutical compounds have been decomposed using either DBD or photocatalysis systems separately, literature presents very limited reports on the combination of these two processes towards the degradation of these toxins in aquatic media. The few studies conducted on this topic showed that incorporation of catalysts into the DBD systems would improve the concentrations of free reactive species in the combined systems (Okolongo, 2011). The UV generated in the DBD system could be sufficiently used to induce the photocatalysis process. It was demonstrated by Okolongo, (2011) that the increase in the yield of OH radicals by the combined systems could improve the degradation efficiency and reduced overall treatment cost and time. Since non-thermal plasma efficiency depends directly on reactor configuration (Nehra *et al*., 2008; Valinčius *et al*., 2012; Mouele *et al.*, 2015), the combination of double cylindrical DBD reactor configuration with photocatalysts could be a favorable process to enhance degradation efficiency of persistent organic pollutants such as pharmaceutical compounds. After the review of all studies presented in this text, it can be noticed that the pollutant concentration, pH, catalyst loading, kinetics and energy required in the process are very important parameters that influenced the removal of these compounds. Nevertheless, most of these parameters in studies on the decomposition of pharmaceuticals from water and wastewater were not fully examined.

Therefore, a complete investigation of these factors is required in order to establish the best degradation conditions for complete decomposition of these contaminants. The contaminant concentration is a very crucial parameter because many researchers have shown that the decomposition of pharmaceuticals decreases with an increase of pollutant concentration (Magureanu *et al*., 2015). This is probably due to the chemical stability of their molecular structures that are designed to resist particular types of oxidants. Apart from pollutant concentration, literature also showed that pharmaceuticals have been decomposed at different pH values. Some have been well removed in acidic, neutral or basic media (Magureanu *et al.*, 2010). Additionally, the stability of these compounds may also slow down the rate of their degradation which usually leads to pseudo-first-order kinetics (Reddy *et al.*, 2013). Reddy *et al.*, (2013) estimated the energy yield (Y) of MB decolouration in a DBD reactor. Likewise, the analysis of the studies reviewed in this text shows that the use of UV and ozone generators requires a certain amount of energy to induce oxidation processes. However, most papers reviewed in this text did not investigate the energy consumption which is an essential parameter. Therefore, with lower energy consumption, double cylindrical DBD could also be used not only as an efficient energy saving method that produces UV, O_3, H_2O_2, ·OH, etc. but also as a promising technology for the oxidation of pharmaceutical compounds from water effluents (Emile S Massima Mouele *et al.*, 2015). In addition to that, the limited use of chemicals in the double cylindrical DBD configuration is beneficial to avoid more toxicity of the effluent being treated. This therefore assited in refraiming the questions stated in chapter 1. Various studies (Rong *et al*., 2014; Babić *et al.*, 2015; Giraldo-Aguirre *et al.*, 2015; Tantis *et al.*, 2015) have demonstrated that degradation metabolites are sometimes more toxic than the parent pollutants. The combinations of various homogeneous AOPs such as UV/O_3, O_3/H_2O_2, UV/ H_2O_2, and UV/O_3/H_2O_2 have been proved to largely generate powerful non-selective hydroxyl radicals (Hoeben, 2000; Mededovic, 2007). This hence assisted in structuring the research question inquiring what active species are generated in DBD. Though various (planar) DBDs reactor configurations have been used to decompose organic pollutants from water and wastewater (Nehra *et al*., 2008; Valinčius *et al*., 2012), the degradation intermediates and mechanistic pathways have not been mentioned and should be detected and established. In fact, the challenge of completely removing pharmaceuticals from water has become a recurrent phenomenon because the degradation intermediates of most persistent organic pollutants are usually unknown. Therefore, it could be recommended that these decomposition intermediates should be detected and quantified in order to predict their degradation mechanistic pathways

and hence to facilitate their complete removal to achieve a total water treatment process. Besides, the toxicity test of the identified intermediates and the quantification of free active species generated during the oxidation process also demands adequate research attention. Furthermore, double cylindrical DBD has not been widely used in the decomposition of dyes and pharmaceuticals in effluents. To recall, in the single DBD reactor configuration, the high voltage electrode is protected by one dielectric barrier and usually exposed to a feed gas. So exposure of the high voltage electrode to a circulating gas could result in its corrosion (Okolongo, 2011; Tijani *et al.*, 2014; Mouele *et al.*, 2015). Likewise in double cylindrical DBD configuration, the high voltage electrode is protected by two dielectric barriers and separated from feeding gas. This, in turn, avoids corrosion and facilitates long term experimental runs (Okolongo, 2011; Mouele *et al.*, 2015). Therefore, this review helped to frame the research questions presented in chapter1. The region between the two dielectrics represents the plasma zone in which various oxidative species such as O_3, H_2O_2, $O_2^{\cdot-}$, etc. are produced and directly circulated into the polluted solution. This is advantageous in protecting the high voltage electrode from corroding in aqueous systems compared to other con-thermal plasma geometries in which the anode is directly submerged in the solution being treated and hence exposed to erosion after a number of experimental runs. So this review emphasises that through double cylindrical DBD and photocatalysis systems have been used separately for water and wastewater treatment, their combination could be a robust technology for the degradation of targeted pharmaceuticals.

CHAPTER THREE: EXPERIMENTAL AND ANALYTICAL METHODOLOGIES

3 INTRODUCTION

This chapter describes the chemical and physical materials, experimental procedures and analytical methods used for optimisation of the double cylindrical dielectric barrier discharge (DBD) system. In addition to these, experimental procedures on quantification of free radicals, corrosion and photocatalytic studies are subsequently discussed. Furthermore, the dip coating and spin coating procedures used to immobilise the sol-gel synthesised C-N-TiO_2 nano composites on SS, pure Ti and anticorrosion meshes and glass supports are also discussed in this chapter.

3.1 Materials and chemicals

The principal materials and chemicals used for optimisation of DBD system and quantification of free radicals, corrosion and photocatalytic study are summarised in Tables 3.1 & 3.2.

Table 3.1: Electrical apparatuses and physical tools used in this project.

Equipment	Suppliers
High voltage electrode [silver (1.5 mm)]	C.J.LABS
Quartz tubes reactors	Glass Chem./Stellenbosch, Glass tech / Johannesburg, RSA
GW INSTEK programmable power supply PSP- 405 with (Set volt. 10 kV, Set trip cur. 40A, Set P. 200 W, Set Fre. 2000Hz. Set modes: LF-P(Low-P)& HF-P(Med-P)	E, E & Eng./ Stellenbosch RSA
Electro-magnetic air compressor. Model: Acq-009. Set vol: 220 – 240 V, Fre:50 Hz; Power:185W, output: 60L/min	Boyu Industrie co. LTD, RSA
Air flow meter: Rotameter MFG.CO.LTD., made in England / tube number R868119/H.D. Free liter/minute Nitrogen 25 ºC 20 p.s.i.g.(Maximum flow rate 160 L/min)	Kimix, SA
Copper wire (Various sizes)	Kimix, SA
Cr based oxide and oxynitride coatings	NIOE, Romania
Zr based oxide and oxynitride coatings	NIOE, Romania

ZrSi bades oxide and oxynitride coatings (2.5 cm diameter, 0.4 cm thickness, 12 cm x 2 cm)	NIOE, Romania
Stainless steel meshes grade 304 (2.5 cm diameter, 0.4 cm thickness, 12 cm x 2 cm)	NIOE, Romania
Commercial pure Titanium meshes (12 cm x 2 cm, 2.5 cm diameter, 0.4 cm thickness)	Good fellow, England
Stainless steel disc grade 304 (2.5 cm diameter, 0.4 cm thickness, 12 cm x 2 cm)	NIOE, Romania

Table 3.2: Chemicals used for optimisation of DBD system and for detection and quantification of free radicals during DBD experiment. Chemicals used for synthesis of C-N-TiO_2 co-doped Nano composites.

Chemicals	Purity/ identifier	Suppliers
Sulphuric acid	20%	Kimix, RSA
Di sodium hydrogen orthophosphate, CP	99%	Kimix, RSA
Phosphoric acid	85%	Kimix, RSA
Sodium carbonate, CP	99%	Kimix, RSA
Terephtalic Acid (TA)	98%	Sigma Aldrich, RSA
2-hydroxyterphtalic acid (2-HTA)	95%	Sigma Aldrich, RSA
Sodium hydroxide flakes CP	97%	Kimix, RSA
Di potassium hydrogen orthophosphate, CP	98%	Kimix, RSA
Orange II sodium salt (O.II)	>85 %	Sigma Aldrich, RSA
Sulfamethoxazole (AS) [SMX]	Lot#BCBP8794V PCODE:101739693	Sigma Aldrich, RSA
Absolute Ethanol	99.9 %	Kimix, RSA
Hydrogen Peroxide CP	30 %	Kimix, RSA
Titanium (IV) oxysulfate	≥ 29%	Sigma Aldrich, RSA
Titanium tetrachloride purum, Titanium (IV) oxide (powder)	≥ 98.0 % 99.5%7.87 g/mol	Sigma Aldrich Sigma Aldrich
Polyacrylonitrile (PAN) powder	99.5%	Good fellow
Ammonium nitrate, ACS	95%	Industrial Analytical (Pty)
N,N dimethyl formamide	99%	Industrial Analytical (Pty)
Potassium indigo trisulfonate	Pubchem substance ID: 24854018 Reilstein Registry number: 4932187 MDL number: MFCD0013160	Sigma Aldrich, RSA

3.2 Experimental flow diagram of the present study

Since a number of aspects were covered in this study, a descriptive flow diagram summarising all experimental steps is presented in Figure 3-1. Chapter 3 is subdivided into four sections which include: Firstly optimisation of DBD system using orange II sodium salt dye and sulfamethoxazole drug as model pollutants followed by detection and quantification of free reactive species. The second section deals with anticorrosion coating by cathodic arc evaporation (CAE) and corrosion study while the third part focuses on the synthesis, characterisation of C-N-TiO_2 co-doped nano composite and its photocatalytic application for the removal of O.II dye at the applied conditions. The last section includes the immobilisation of the C-N-TiO_2 on SS, anticorrosion meshes and on glass substrates by dip and spin coating, respectively. The prepared films were photo catalytically tested for the removal of O.II dye at the applied conditions.

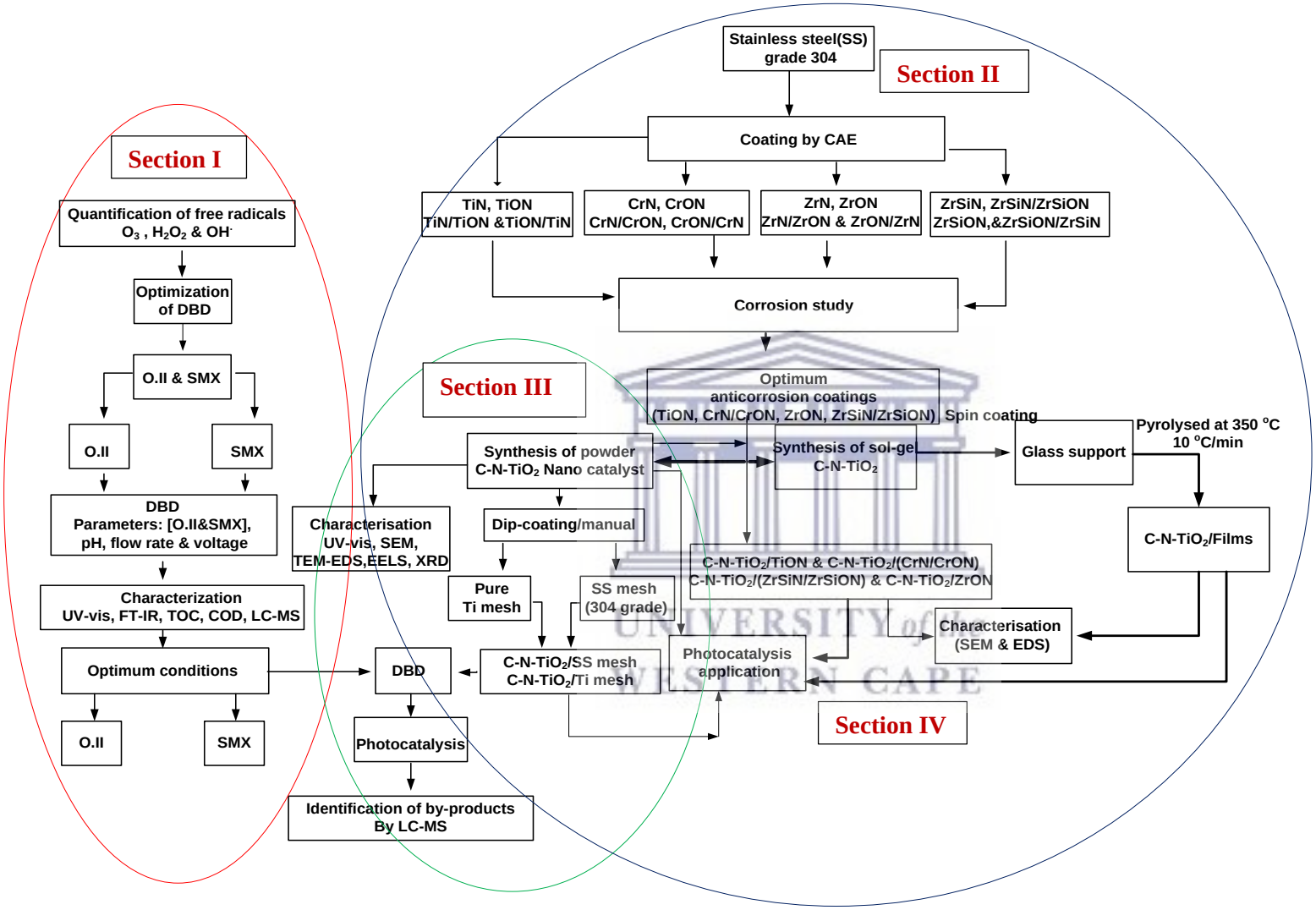

Figure 3.1: Experimental flow diagram of the study

3.3 Equipment and testing protocols

This section summarises all equipment including DBD reactors/configurations, experimental setups, and analytical instrument used in this study.

3.3.1 Reconfiguration of the DBD reactor to a new closed configuration

An open cylindrical double DBD system was optimised by Massima (2014) for water and wastewater treatment purposes using methylene blue (MB) as a model compound and also used by Mouele et al. (2015) for the degradation of BPA and 2-NP. After the optimisation process, the following optimum conditions: applied voltage 25 V, peak voltage 6.8 kV, [MB] = 5 mg/L, pH 2.5, pollutant volume 1 500 mL, air flow rate 3 L/min, 1.5 mm silver electrode, 50 g/L NaCl electrolyte, air gap 2 mm for a running time of 60 minutes were obtained. Likewise, during those electrohydraulic discharge experiments, it was noticed that most ozone escaped from the reactor which involved the use of an open beaker. This was mostly evidenced by the toxic smell of ozone. This was assumed to reduce the degradation efficacy of the reactor. Therefore, a reconfiguration process had to be considered in order to trap more ozone in the system and hence achieve the desired mineralisation of the pollutant. In this case, electrical parameters (electrode type and size and voltage) and reactor configuration mainly air gap as explored by Massima (2014) were considered and hence used to reconfigure a new closed DBD reactor presented in Figure 3-2 and was used in the current study. The rest of chemical, physical, and electrical parameters might depend upon the targeted pollutant. The reconfigured configuration was tested and used for further degradation of other persistent organic pollutants including O.II dye and SMX drug at corresponding conditions.

Hence the DBD configuration in Figure 3-2 (R1) was optimised and employed in the photochemical and photocatalytic decolouration of O.II dye as well as for the degradation of SMX at the applied conditions. Since one of the aims of this study was examine if the incorporation of a photo catalyst in the DBD reactor could improve the decolouration and degradation of the targeted pollutant POPs O.II and SMX, respectively, a new flanged DBD configuration/reactor (R2) was designed in the same dimensions as configuration (R_1) and is presented in Figure 3-3. The DBD experimental set up with R1 and R2 is presented in Figure 3-4 (A &B), respectively.

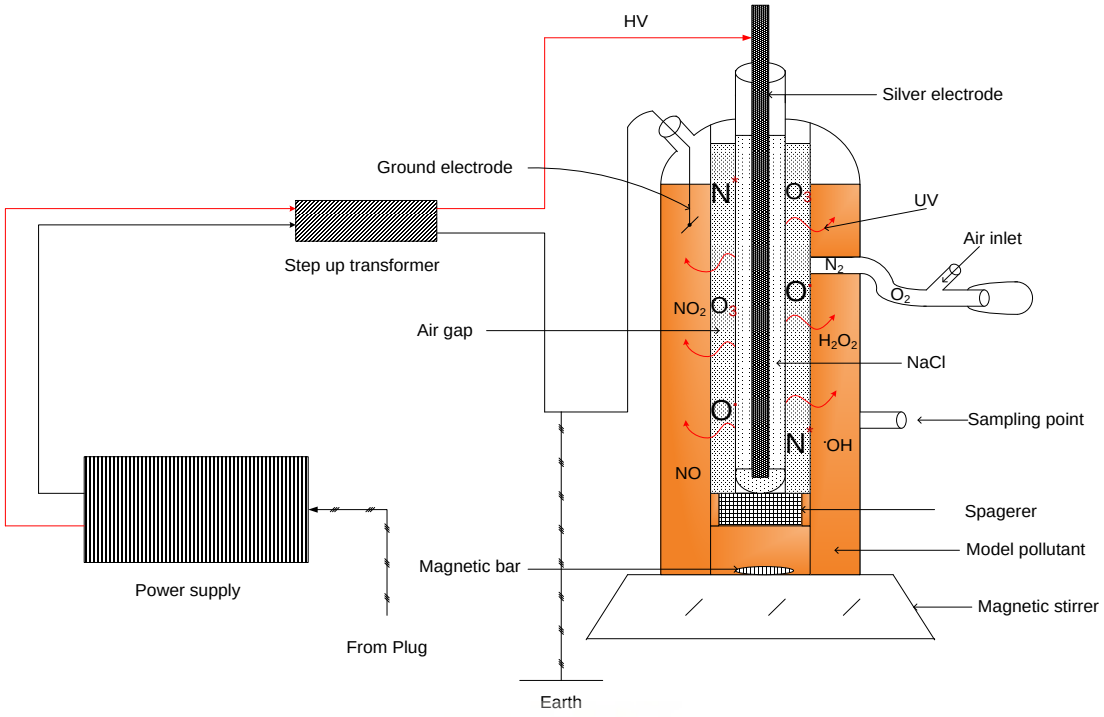

Figure 3.2: Reconfigured closed DBD reactor (R1) used in this study for the photochemical decolouration of O.II dye and degradation of SMX drug.

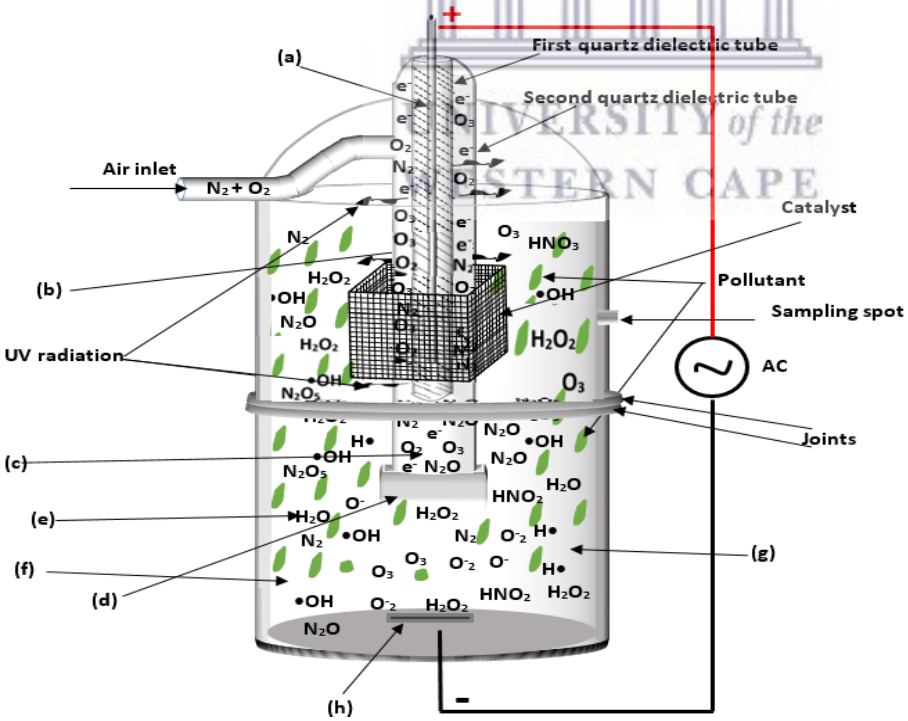

Figure 3.3: Reconfigured semi-batch closed and fringed DBD reactor (R2) + supported C-N-TiO_2 photo catalyst used for the decolouration of O.II and degradation of SMX.

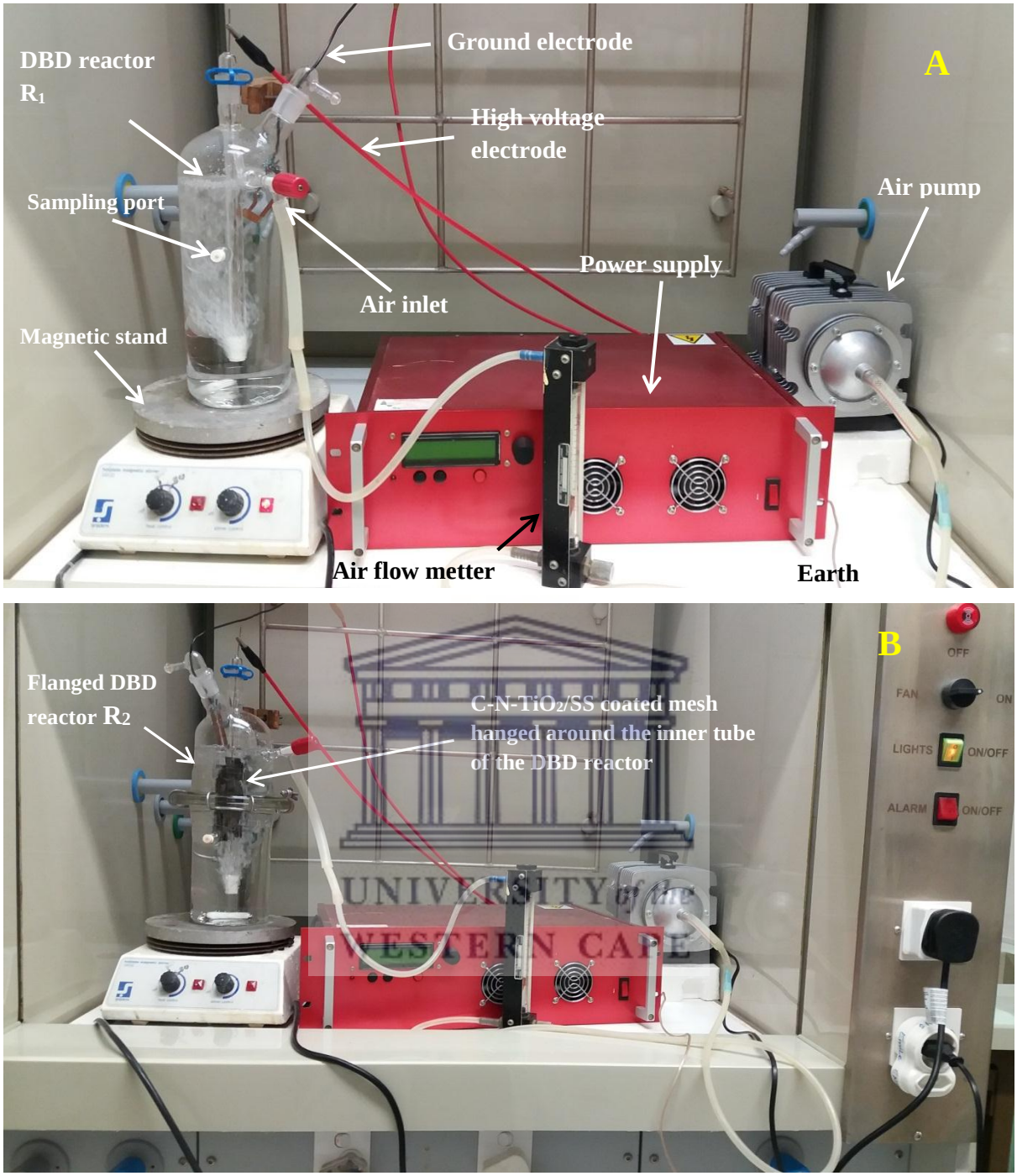

Figure 3.4: DBD experimental set up using reactors R1(A) and R2 (B), respectively.

The DBD reactor (R_2) in Figure 3-3 was used for the photocatalytic decolouration and degradation of O.II and SMX, respectively at the corresponding conditions with C-N-TiO_2 immobilised by dip coating on SS and pure Ti supports. So the C-N-TiO_2 coated SS (SS/C-N-TiO_2) and Ti (Ti/C-N-TiO_2) meshes were successfully arranged around the inner tube of the DBD reactor R_2, in such a way that the UV light generated by the DBD system can be used to induce the photo catalysis process.

Before immobilisation of C-N-TiO_2 on the various supports, the photo catalytic activity of the ground powder C-N-TiO_2 was tested for the decolouration of O.II dye using an open experimental set up as presented in Figure 3-5.

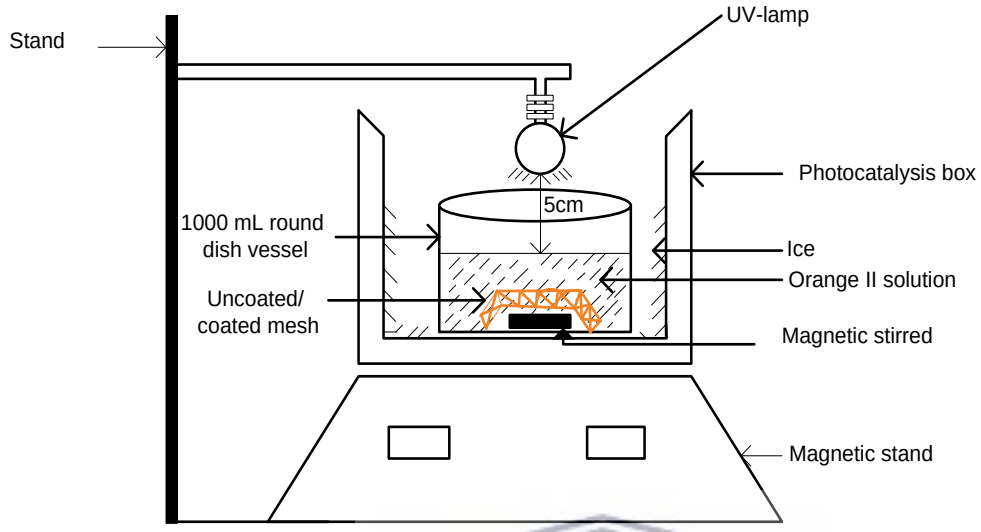

Figure 3.5: Photo catalysis set up for the photo catalytic decolouration of orange II dye at the following fixed parameters: [O.II] 5 mg/L, volume 500 mL, solution pH 2.5, a UV lamp (Mega-Ray 160 W/240 V MR160 SPL11/14 from Kimix).

Apart from powder C-N-TiO_2, the experimental set up in Figure 3-4 was also used to evaluate the photo catalytic activities of the uncoated and coated anticorrosion meshes (SS/TiON, SS/CrN/CrON, SS/ZrON and SS/ZrSiN/ZrSiON), SS and glass coated with C-N-TiO_2 upon the decolouration of O.II at the applied conditions. The photo catalytic protocols for the decolouration of O.II with each coated support are described in the following sections.

In addition to these reactors and experimental set up, the UV-vis instrument used to measure the decolouration of O.II in the two DBD reactors (Figures 3-2 & 3-3) and in the open experimental set up (Figure 3-4) is described and presented in Figure 3-5.

3.3.2 Instrumental set up for UV Vis spectroscopy analysis

During UV-vis analysis, Hellma precision cells made of quartz Suprasil of the following characteristics: cuvettes 2, Type No. 110-QS, light path nm: 10 nm and match.c: 284, as shown in Figure 3-5 (A) were used in GBC UV/VIS 920 spectrometer exhibited in Figure 3-5 (B) to analyse O.II solution sampled during the DBD experiments and other photo catalysis investigations.

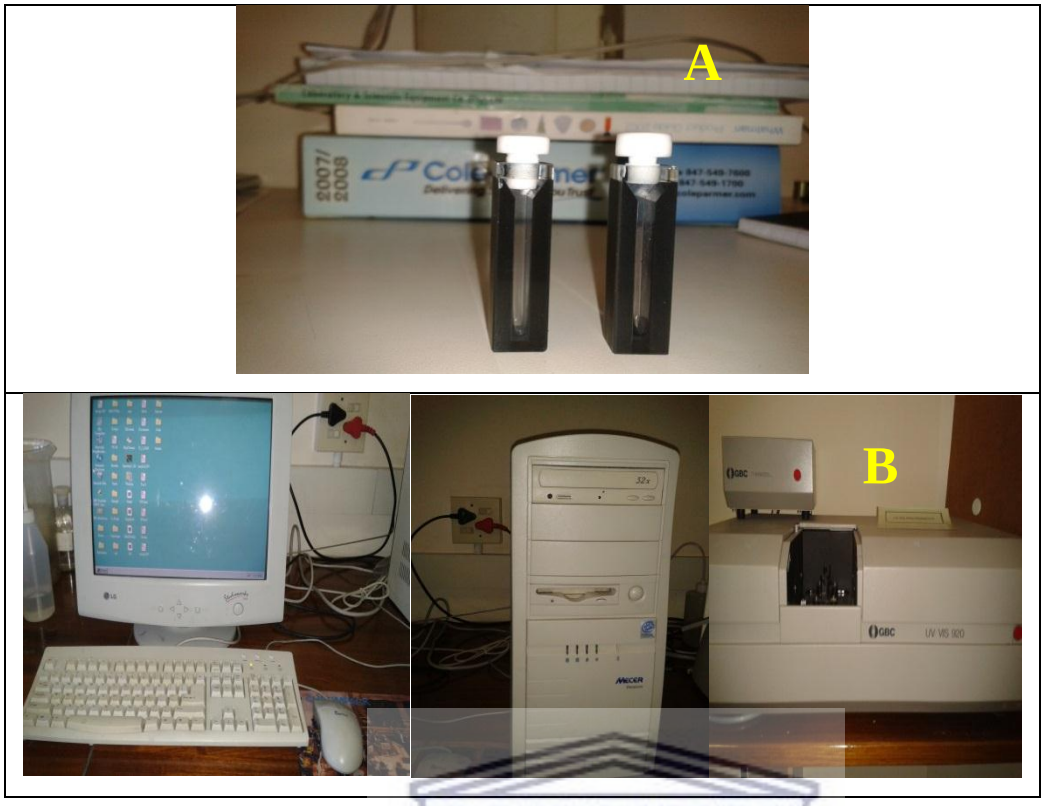

Figure 3.6: GBC UV/VIS 920 spectrometer used for analysis of O.II dye samples.

It is important to mention that the UV-vis analysis was used only for the analysis of O.II samples and could not be used for the colourless SMX model pollutant that was rather monitored by HPLC /MS analysis.

3.4 Solutions preparation

This subsection shows the procedures for the preparation of various solutions that were used to accomplish all experiments carried out in this study. These solutions include those used for the quantification of free radicals in the DBD reactor (Figure 3-2), for the degradation of O.II and SMX and those used for the synthesis of C-N-TiO_2 nano catalyst.

3.4.1 Solutions used for the determination of dissolved ozone in DBD reactor

Ozone, being one of the active species produced during DBD process, was detected and determined using the indigo method as described by Barder & Hoigne (1982). Indigo has a strong absorbance at 600 nm (ε = 20000 $L.mol^{-1}.cm^{-1}$). One molecule of ozone could

decolourise one molecule of the indigo dye. The decolourised products hardly react with ozone. The amount of ozone scavenged could be determined from the decolouration of the reagent measured at 600 nm. During measurement; no interference with OH radicals was expected after pulsing of the reactor. This was earlier demonstrated by Barder & Hoigne (1982) that the presence of hydrogen peroxide does not interfere with the measurement of OH radicals. The indigo reagent was prepared as follows:

Solution A: About 0.5 mL of phosphoric acid was mixed with 310 mg of Indigo trisulfanate in a volumetric flask and filled up to 500 mL with Millipore water.

Solution B: 14 g of sodium hydrogen phosphate was mixed with 17.5 g of H_3PO_4 together in a volumetric flask and filled up with Millipore water. The ozone measurement method is described in section 3.6.1.1.

3.4.2 Solution used for the determination of hydrogen peroxide in DBD configuration

In the determination of H_2O_2 concentration, the concentration of the yellow-coloured peroxotitanyl complex was determined by UV absorption spectroscopy at 410 nm (Uher and Hoefer, 1991). The absorbance at this wavelength was directly proportional to the initial hydrogen peroxide concentration according to the reaction given in Equation (3.1):

$$TiOSO_4 + H_2O_2 + H_2SO_4 \rightarrow TiO_2(SO_4)_2^{2-} + H_2O + 2H^+ \quad 3.1$$

So, approximately 2.4 g of titanyl sulphate (hydrate) was weighed and mixed with 100 mL (20%) H_2SO_4 in a 500 mL volumetric flask. The remaining volume of the flask was filled up to the mark with distilled water. The procedure for hudrogen peroxide determination is detailed in section 3.6.1.2.

3.4.3 Solutions used for the quantification of ·OH radicals in DBD reactor

In this section, OH radicals were quenched using Terephtallic acid (TA) probe. The effect of TA concentration on OH quenching was evaluated at the applied conditions. In addition to this, the impact of solution pH and scavengers' types, mainly Na_2CO_3 and NaCl, and their concentration on OH production was also assessed.

3.4.3.1 Preparation of standard solutions of 2-hydroxyterephthlic acid

About 5 distinctive standard solutions of hydroxyterephthalic acid (HTA) of 2, 4, 6, 8 and 10 ppm were prepared by dissolving 2, 4, 6, 8 and 10 mg of HTA powder each in 1000 mL volumetric flasks that were filled to the mark with distilled water. A Varian Cary Eclipse spectrophotometer using an excitation slit of 5 µm and an emission slit of 2.5 µm (excitation wavelength λex = 315 nm; emission wavelength λem = 425 nm) was used to analyse the prepared standard solutions. A linear increase of fluorescence yield versus concentrations was plotted and presented in Figure 3-6. This was later used as a calibration curve (Figure 3.7) to estimate OH radical concentration in the DBD reactor.

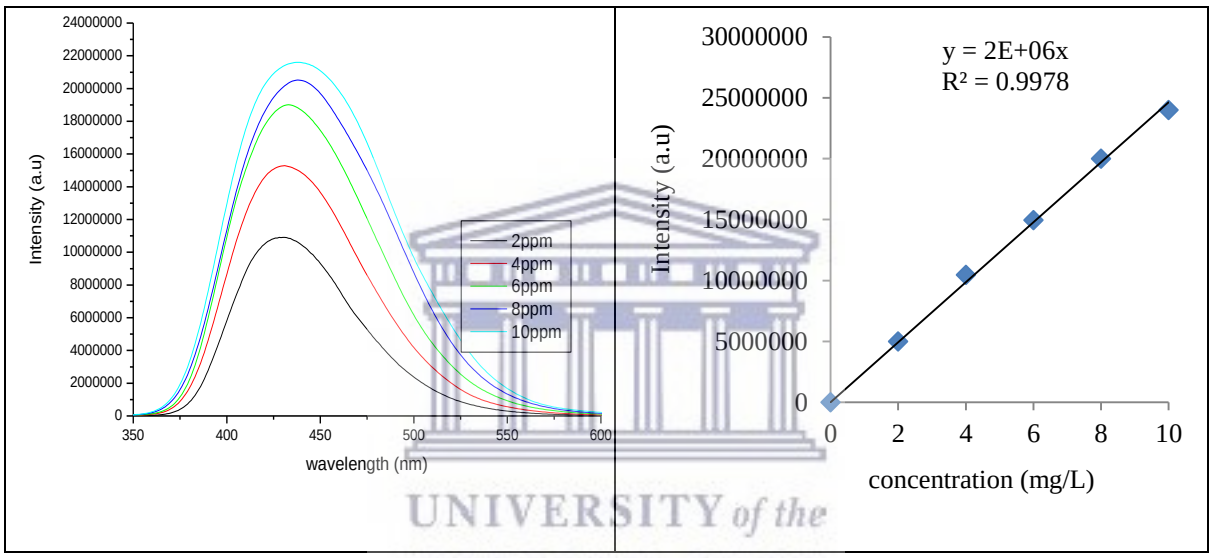

Figure 3.7: Linear trends/calibration curve of standard 2-hydroxy terphthallic acid

3.4.3.2 Preparation of Buffer solution

A buffer solution (pH 7.39) was prepared by mixing 0.588 g of KH_2PO_4 with 0.982 g of Na_2HPO_4 in a 1000 mL volumetric flask and then filled to the mark with distilled water. The obtained buffer solution (pH 7.39) was stored in a cool place for further use.

3.4.3.3 Preparation of 5 mM sodium hydroxide solution

A 5 mM NaOH solution was prepared by dissolving 0.02 g NaOH pellets in a 100 mL volumetric flask which was then filled up to the mark with distilled water.

3.4.3.4 Preparation of 2 mM terephthalic acid solution

About 0.75 g of therephthalic acid (TA) was dissolved in in 50 mL of 5 mM NaOH solution to obtain a 2 mM TA solution.

3.4.3.5 Preparation of 0.01M, 0.02M and 0.04M sodium carbonate solution

The mass of sodium carbonate (Na_2CO_3) to be dissolved in a volume of 1.5 L was calculated as set out in Appendix 3.1.

The mass corresponding to 0.02 M and 0.04 M were obtained as set out in Appendix 3.1 following the same procedure. Hence 3.18 g and 6.36 g were calculated to prepare 0.01 M and 0.04M of Na_2CO_3, respectively and were then dissolved in 1.5 L of 2 mM TA solution.

3.4.3.6 Preparation of 0.01M, 0.02M and 0.04M sodium chloride solution

The mass of sodium chloride (NaCl) corresponding to 0.01 M, 0.02 M and 0.04 M were calculated according to the procedure elaborated for Na_2CO_3 in previous section. The calculations in this regards are shown in Appendix 3.2.

In the same way, the mass corresponding to 0.02 M and 0.04M of NaCl was determined as set out in Appendix 3.2. In total three masses, 0.87, 1.74 and 3.48 g of NaCl powder were calculated. So each estimated mass of NaCl was dissolved in the 2 mM TA solution which was later exposed to the DBD experiment at the applied conditions.

3.4.4 Solutions used for the optimisation of the DBD system

This subsection shows the methods employed in the preparation of O.II and SMX solutions used for the optimisation of the DBD systems early shown in Figures (3-2 & 3-3).

3.4.4.1 Preparation of stock and standard solutions of orange II dye

The initial model solutions of 1000 mg/L O.II were prepared as follows: About 0.2 g of powdered O.II was weighed and quantitatively transferred into a 2 000 mL volumetric flask and made up to the mark with distilled water. Various solutions of concentrations between 10 20, 30, 40 up to 60 mg/L were prepared by serial dilution. Each of these solutions was separately used to perform the degradation of O.II in the DBD system shown in Figure 3-3.

Following this procedure, the absorbance of standard solutions (from 5 to 60 mg/L) of orange II was obtained using the UV-vis spectrometer and is recorded in Table 3.3. The absorbance of standard dye solutions recorded was used to plot a calibration curve as shown in Figure 3-8.

Table 3.3: O.II standard concentrations vs Absorbance

Standard concentrations (mg/L)	Absorbance
0	0
5	0.31
10	0.62
20	1.14
30	1.68
40	2.19
50	2.64
60	2.97

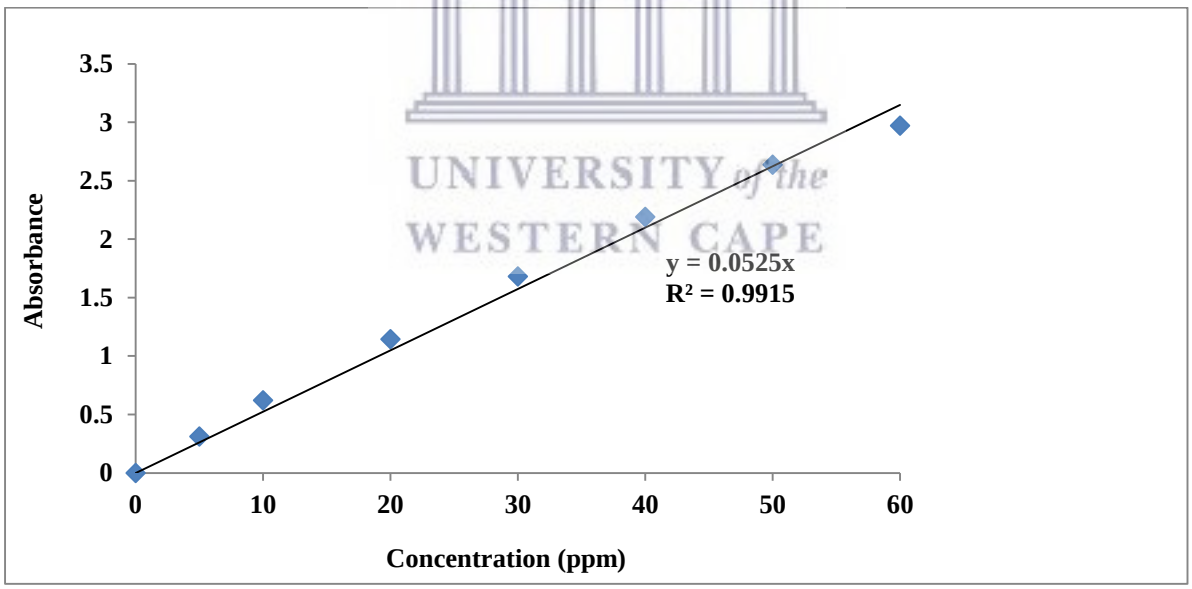

Figure 3.8: Calibration curve of absorbance vs. concentrations of orange II at t = 0 minutes for samples treated in the DBD systems (R1 & R2).

The data in Table 3-2 show that the absorbance of samples increased linearly with an increase of dye concentration.

3.4.4.2 Preparation of SMX stock and standard solutions

In this subsection, an SMX stock solution was prepared by dissolution of a specific amount of colourless SMX powder in ethanol and the standard SMX solutions were obtained by successive dilutions of the stock solution as described below.

3.4.4.2.1 Preparation of 600 mg/L SMX stock solution

An amount of 60 mg of SMX was weighed accurately and quantitatively transferred into a 100 mL volumetric flask and filled up to the mark with 99.9% absolute ethanol. This procedure was repeated three times. The three 600 mg/L SMX solutions obtained were stored in a fridge for further experiments.

3.4.4.2.2 Preparation of 60 mg/L SMX solution

Since the volume of the DBD reactor used in this study is 1500 mL, approximately 150 mL of 600 mg/L SMX was withdrawn from the stock solutions and diluted with 1350 mL of distilled water in a 2L volumetric flask. The prepared 60 ppm SMX solution was then used for DBD experiments. Other SMX concentrations of 20, 40, 60 to 100 mg/L were prepared by serial dilutions following the same procedure.

3.4.4.2.3 Preparation of SMX standard solutions

From the stock SMX solution prepared according to the procedure set out in section 3.3.4.3, standard solutions 10, 20, 40, 60, 80, and 100 mg/L of SMX were prepared by serial dillutions. These were later subjected to HPLC analysis. The peak area of each standard solution was recorded and a calibration curve of peak area versus concentration was plotted. The calibration curve obtained and presented in Figure 3-8 was used to estimate the concentration of SMX at different sampling times 0, 10, 20, 30, 40, 50 and 60 min during the DBD experiments.

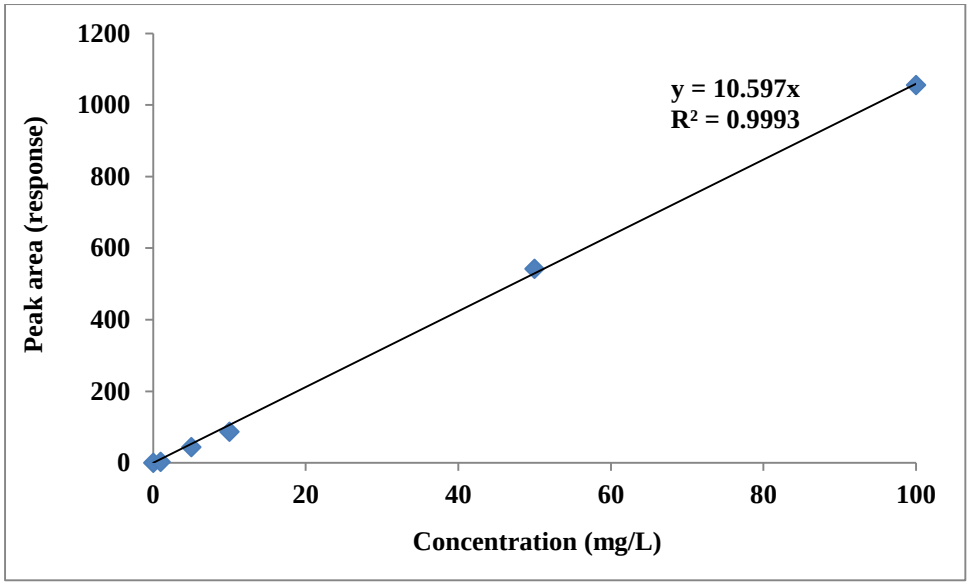

Figure 3.9: HPLC calibration curve for SMX standard solutions used to estimate the unknown concentrations of SMX samples withdrawn in DBD reactor.

3.4.4.3 Solutions used to test the photo catalytic activity of powder C-N-TiO_2 in the open experimental system

But beforehand, standard solutions of O.II with concentrations that varied between 1 and 10 mg/L were prepared by serial dilutions of a 20 mg/L O.II standard solution and their UV-vis absorbance was recorded and plotted against concentration and the linear trend of O.II concentrations (below 10 mg/L) obtained is shown in Figure 3-9. The unknown concentrations of orange II solution were determined using the calibration curve shown in Figure 3-9, which was further used to calculate the degradation efficiency of orange II dye using Equation 3.1.

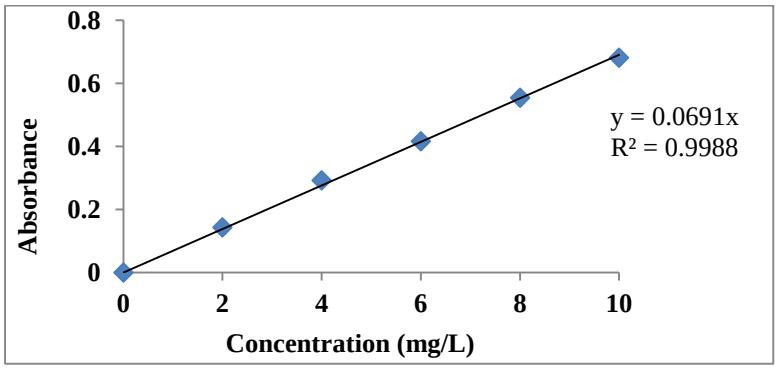

Figure 3.10: Calibration curve of absorbance vs concentration of O.II dye for samples tested in the open system (Figure 3-4).

To recall, the calibration curve in Figure 3-9 was only used for photo catalysis experiments carried out in the open experimental system for the degradation of O.II (taken at low concentration below 10 mg/L) with SS, anticorrosion meshes and glass coated C-N-TiO_2 catalyst.

3.4.4.4 Preparation of 5% ammonium nitrate solution used for the Sol-gel synthesis of C-N-TiO_2 co-doped nano catalyst

About 5 g of 95% granular NH_4NO_3 was weighed and dissolved in a 100 mL volumetric flask and made up to the mark with distilled water. The prepared 5% NH_4NO_3 was stored for further experiments.

3.5 Synthesis and coating

Summarises the experimental procedures for the synthesis of the carbon-nitrogen co-doped titanium oxide (C-N-TiO_2) nano catalyst; its characterisation and photocatalytic application are presented in sections 3.8.5 and 3.6.6.1 for the removal of the targeted pollutant O.II dye and SMX at specific conditions. In addition, the experimental protocols for the deposition of C-N-TiO_2 gel on SS and pure Ti mesh (Section 3.5.3) and the insertion of the prepared films in DBD configuration for the degradation of the model pollutants O.II and SMX (Section 3.6.6.2) are also highlighted. Furthermore, the techniques used for C-N-TiO_2 immobilisation on other supports (anticorrosive coatings and glass) are also defined (Sections 3.5.3.1 and 3.6.6.3).

3.5.1 Preparation of C-N-TiO_2 sol gel and pyrolysis protocol

8 g polyacrylonitrile (PAN) was weighed and mixed with 100 mL of 99% DMF in a 200 mL capped borosilicate glass bottle and stirred for 24 hrs at room temperature. Approximately 1.5 mL to 3 mL of 98% concentrated $TiCl_4$ was added dropwise into the prepared 8 % PAN/DMF mixture and stirred in a fume hood until the white HCl fumes disappeared from the resultant sol gel. Moreover, 1.5 to 3 mL of 5% NH_4NO_3 was added dropwise into the C-TiO_2 sol gel obtained and stirred for 15 to 30 min until the colour of the mixture slightly changed from brownish to yellow-brownish. Ceramic sample holders cleaned with acetone and ethanol, followed by distilled water, were dried in an oven at 25^oC for 15 min. Thereafter, 5 to 10 mL of the prepared C-N-TiO_2 gel was introduced into the washed sample holders and heated in a

furnace using a ramping rate of 50 °C/min under a nitrogen gas flow of 20 mL/min and annealed for different holding times of 1h 45 min (105 min), 2 hrs (120 min) or 2h 15 min (135 min) at 350 °C, respectively. The C-N-TiO_2 nano composites obtained at different calcination times were ground into powder and kept in 10 mL sample vials for characterisation purposes and photo catalytic test using the powder form catalyst.

3.5.2 Immobilisation of C-N-TiO_2 on SS and pure Ti supports

This subsection summarises the deposition of C-N-TiO_2 nano catalyst on stainless steel and pure Titanium meshes by dip coating, characterisation and its application in the DBD system for the photocatalytic removal of O.II dye. Beforehand, stainless steel (SS) and pure titanium (Ti) meshes were carefully cleaned with acetone, ethanol and water and dried in an oven at 60 °C for 30 min prior to use to remove impurities. Thereafter, the prepared C-N-TiO_2 sol gel was dip coated on the clean dried meshes. The coated meshes were placed on clean and dried crucibles which were calcined at 350 ºC using a heating rate of 50 °C /min in a furnace for a holding time of 105 min with nitrogen gas at a flow rate of 20 mL/min. The prepared TiO_2 layers were characterised by HR-SEM and EDS as described in section 3.8.3.

3.5.3 Immobilisation of the C-N-TiO_2 nano catalyst on anticorrosion coatings and glass, application for photocatalytic removal of O.II dye

In this subsection, three types of supports including SS, anticorrosion meshes and glass were used as catalytic substrates and were coated with C-N-TiO_2 nano catalyst either by dip or spin coating at the corresponding conditions. The coated films were further exposed to UV light for the removal of O.II dye at the convenient conditions.

3.5.3.1 Dip coating of stainless steel pure Ti and anticorrosion meshes with the prepared C-N-TiO_2 sol gel and calcination at 350 ºC

Beforehand, (2 cm x 6 cm) stainless steel (SS) or Ti meshes as well as the anticorrosion supports (described in section 3.5.1) mainly TiON, CrN/CrON, ZrON and ZrSiN/ZrSiON were carefully cleaned with acetone, ethanol and water and dried in an oven at 60 °C for 30 min prior to use to remove impurities. Thereafter, the prepared C-N-TiO_2 sol gel in section 3.5.1 was manually coated on the clean and dried meshes following the same procedure described in

section 3.2.5. The sol gel coated meshes were placed on clean and dried ceramic crucibles and were then calcined at 350 ºC in a furnace for 105 min using a heating rate of 50 °C /min with nitrogen gas at a flow rate of 20 mL/min. The prepared films were characterised by high resolution scanning electron microscopy and (HR-SEM) and energy dispersive spectroscopy (EDS) (See section 3.8.3). The photocatalytic effects of the supported photocatalytic layers were further investigated during irradiative degradation of orange II dye at the applied conditions.

3.5.3.2 Preparation of C-N-TiO_2 thin films by spin coating

The C-N-TiO_2 films on glass substrates were obtained through a spin coating method from a solution using a G3P-8 SPINCOAT. The films were achieved under dynamic (spin drop) method as compared to static (drop spin) method due to film uniformity achieved under this condition compared to the static spin coating conditions which resulted in non-uniform films. Firstly, the glass substrates were cut into 2 cm by 2 cm pieces, cleaned thoroughly in acetone then isopropanol in an ultrasonic bath for 10 minutes each, and thereafter repeatedly rinsed in deionised water and left to dry naturally. The films were obtained using optimised spinning speed (2000 – 2900 rounds per minutes) and solution viscosity was varied by adding 3, 4 or 5 mL of solgel per 5 mL of DMF solvent and spun for 90 seconds to allow the film to dry while spinning. Whitish films were realised immediately after spin coating, confirming a successful deposition of C-N-TiO_2 films. These films were crystallised on the glass through annealing using a horizontal 3-zone ceramic-tube furnace (Brother XD 1600MT manufactured by Zhengzhou Brother Furnace Co., LTD). The samples were placed at the centre of the zone which achieves a desired temperature of 350 °C and heated with a ramping rate of 10 °C /min. These films were left at a temperature of 350 ºC for 105 min under a continuous flow of dry N_2 afterwards to avoid any further oxidation of the films while annealing. The system was allowed to cool down and the annealed films were dark in colour. The film thickness was measured with a thickness profiler (Veeco DekTak 6M, stylus profiler) with a low force of the stylus to avoid scratching the films.

3.6 Measurement protocols

This section highlights the experimental methodologies used for the quantification of ROS in DBD (R_1); photochemical decolouration and degradation of O.II and SMX in DBD (optimisation of reactor R_1) and the photo catalytic decolouration and degradation of O.II and SMX in DBD (R_2), respectively at the applied conditions. The procedures for the photo catalytic decolouration of O.II by various supports (SS, anticorrosion meshes and glass) coated with C-N-TiO_2 catalyst are also presented. In addition, the protocols used for corrosion investigations are also discussed.

3.6.1 Experimental procedures for detection and quantification of active species in double cylindrical dielectric barrier discharge system

This subsection deals with the chemical methods used to detect and quantify hydrogen peroxide (H_2O_2), ozone (O_3) and OH radicals produced in DBD system. The protocols for ozone and hydrogen peroxide explored in this section were done accordin to (Massima, 2014). The sample preparation, the detection and measurement mode of each oxidant are presented in detail.

3.6.1.1 Procedure for determination of dissolved ozone in DBD reactor

About 2 mL of each solution A and B prepared as set out in Section 3.4.1were mixed together in a 25 mL volumetric flask and filled up to 25 mL with distilled water. The absorbance of the mixture was measured and recorded as a reference (blank).To determine the concentration of dissolved ozone in the water, again 2 mL volumes of each solution A and B was mixed together in 25 mL volumetric flask and the rest of the volume filled up with treated water. Then the absorbance of the solution was measured and recorded as the absorbance, as shown in Figure 3-10. This procedure was performed for each solution pH that was varied from 2.5, 6.5, and 8.5 to 10.5 at the following DBD fixed conditions: Peak voltage 6.8 kV, air flow rate 3 L/min, solution volume 1500 mL, 1.5 mm silver electrode, 50 g/L NaCl electrolyte, treatment time 60 minutes, sampling every 5 min.

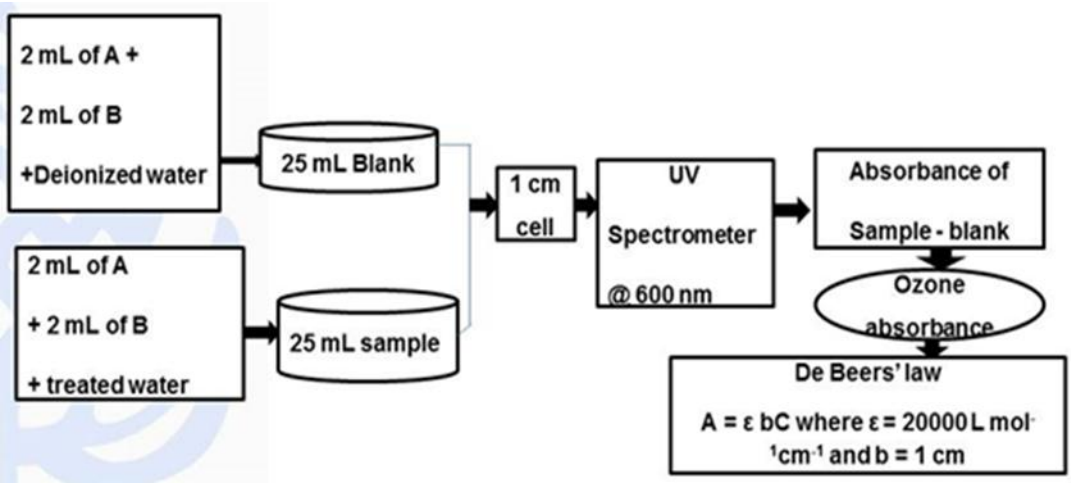

Figure 3.11: Summary of ozone quantification by Indigo technique in DBD configuration.

3.6.1.2 Procedure for determination of hydrogen peroxide in DBD reactor

During the DBD experimental run, 3 mL of the water sample was drawn from the reactor every 5 minutes and mixed with 0.3 mL of the prepared titanylsulphate solution in a cuvette (section 3.4.2). This method was summarised and is exhibited in Figure 3-12. From the absorbance measured with a UV-vs spectrophotometer at 405 nm (ε = 750 $M^{-1}cm^{-1}$), the H_2O_2 concentration generated by the DBD system was derived. This protocol was repeated for each solution pH that was altered from 2.5, 6.5, 8.5 to 10.5 at the following fixed parameters: Peak voltage 6.8 kV, air flow rate 3 L/min, distilled water solution volume 1500 mL, 1.5 mm silver electrode, 50 g/L NaCl electrolyte, treatment time 60 minutes sampling every 5 min.

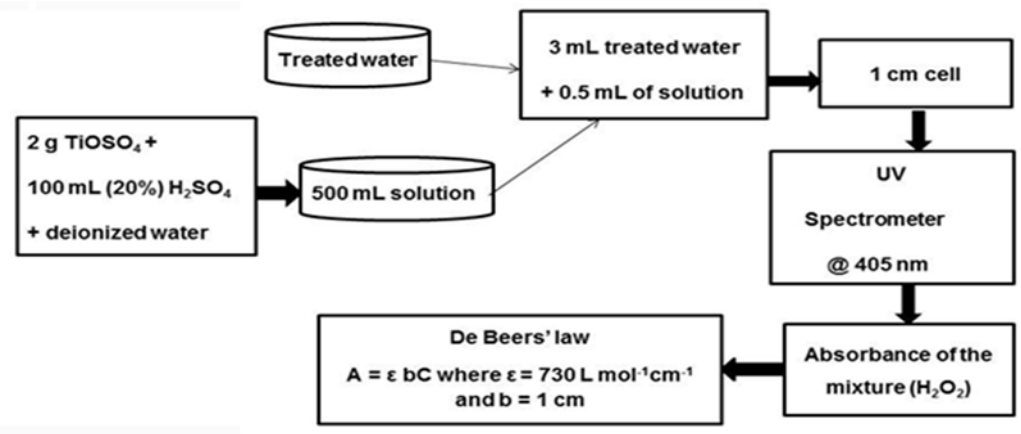

Figure 3.12: Determination of hydrogen peroxide by Titanyl Sulfate method in DBD reactor geometry.

3.6.1.3 Procedure for determination of OH radicals in DBD reactor

The prepared 2 mM TA solution (5 mL) was added to 1250 mL of distilled water solution in a 2L beaker. Thereafter, approximately 245 mL of the buffer solution (KH_2PO_4 + Na_2HPO_4, pH =7.39) was added to the mixture until the conductivity of the mixed solution reached 380 µS/cm. The obtained solution was then subjected to the DBD experiment for 60 minutes and sampled every 5 minutes. The HTA fluorescence yields from samples drawn from each run was detected with a Varian Cary Eclipse spectrophotometer using an excitation slit of 5 µm and an emission slit of 2.5 µm (excitation wavelength λex = 315 nm; emission wavelength λem = 425 nm) as previously described. From the calibration curve of fluorescent intensity versus concentration of HTA previously obtained in Figure 3.6 (section 3.4.3.1) the unknown concentrations of OH radicals were determined. This technique is summarised and presented in Figure 3-12.

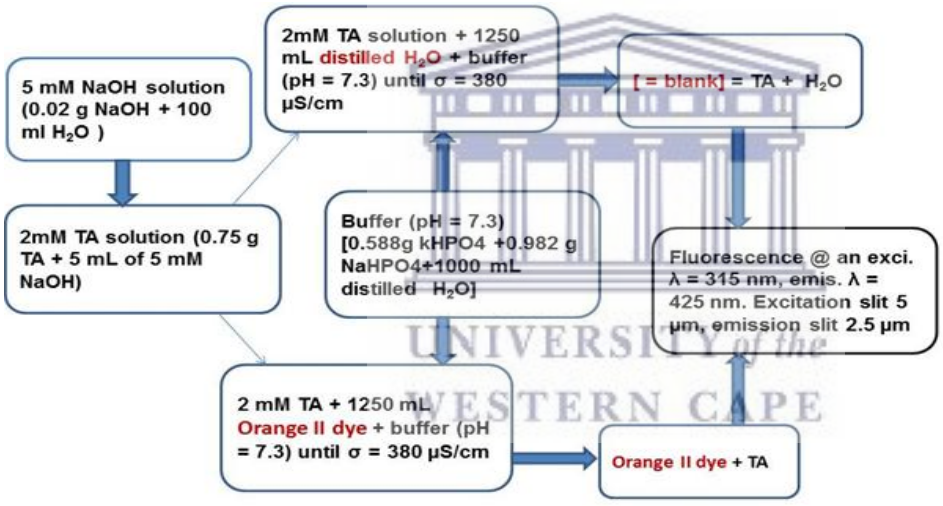

Figure 3.13: Summary of quantification of OH radicals in DBD reactor by Terephtalic acid.

3.6.1.3.1 Effect of pH on production of OH radicals in the DBD reactor

In order to verify the effect of pH on the production of OH radicals in the DBD configuration, the pH of the 2 mM TA solution was varied from 2.5, 6.5, and 8.5 to 10.5 using NaOH and H_2SO_4 solutions. Thereafter, TA solution at each pH value was subjected to the DBD experiment at the applied conditions: Peak voltage 6.8 kV, 1.5 mm silver electrode, 50 g/L NaCl electrolyte, TA concentration 2 mM, in distilled water used as a solvent, for 60 minutes. Similarly, pH behaviour during the DBD experiment was also assessed at the applied conditions. In this case, the DBD experiment was carried out in the presence and absence of

$KHPO_4$ buffer, respectively.These experiments are blank control runs during which distilled water was used as a model solution in the DBD reactor.

3.6.1.3.2 Effect of scavengers on the production of OH radicals in DBD reactor

In this subsection, sodium carbonate (Na_2CO_3) and sodium chloride (NaCl) were selected as two distinctive scavengers for the quenching of OH radicals in DBD system at the following conditions: Peak voltage 6.8 kV, 1.5 mm silver electrode, 50 g/L NaCl electrolyte, solution pH 5.49, distilled water used as a solvent, for 60 minutes. Since the volume of the DBD vessel used in this study was 1500 mL (1.5 L) the corresponding mass of Na_2CO_3 and NaCl that needed to be dissolved in 2 mM TA solution were calculated as shown in Appendices 1 and 2, respectively. These experiments were blank control runs conducted in the DBD system using distilled water as a model solution.

Procedure

In order to investigate the impact of *sodium carbonate* (Na_2CO_3) on the production of OH radicals in DBD, the Na_2CO_3 concentration was varied from 0.01 M, 0.02M to 0.04 M and added to the 2 mM TA solution probe which was in turn exposed to DBD experiment at the applied conditions. A similar method was used to investigate the scavenging effect of NaCl on ·OH in DBD system.

3.6.1.3.3 Effect of Terephtallic acid probe concentration on the quenching of OH radicals produced in the DBD reactor

To achieve the measurement of OH concentration in the DBD reactor, three specific TA masses corresponding to 0.01, 0.02 and 0.04 M were calculated. Then after, each calculated TA mass was dissolved in dissolved water to obtain 0.01, 0.02 and 0.04 M of TA solution, respectively. Next, TA at these concentrations was exposed to DBD experiment at the following experimental conditions: voltage 6.8 kV, 1.5 mm silver electrode, 50 g/L NaCl electrolyte, solution volume 1500 mL, solution pH 4.58-5.49 (varied according to TA concentration) and a treatment time of 60 minutes.

The mass of terephtalic acid to be dissolve in a volume of 1.5L and corresponding to concentrations highlighted above was calculated as set out in Appendix 3.

Again, the mass of TA corresponding to 0.02 M and 0.04 M were calculated as set out in Appendix 1. Therefore, 4.98 g and 9.64 g of TA were weighed and dissolved in 2 mM solution of TA probe which was further subjected to DBD experiment for 60 minutes at the applied conditions.

3.6.2 Optimisation of DBD system

In this subsection, O.II dye and SXM were used as model water contaminants for the optimisation of DBD reactor (Figure 3-2) at the applied conditions. This was performed by assessing the effect of electro-physicochemical parameters up on the degradation efficiencies of O.II and SMX.

This subsection describes the DBD system shown in Figure 3-2 and clarifies the methodology and experimental procedure used in DBD experimentation. At the end of each DBD investigation, the absorbance of untreated and treated O.II dye was measured using UV-vis spectroscopy to further determine the DBD induced degradation percentage of the dye. In contrast, high liquid performance chromatography (HPLC) was utilised to monitor the concentration of treated or untreated SMX after the DBD experiment whose values were used to estimate SMX degradation percentage. The HPLC-MS protocol used for the identification of the degradation intermediate by-products of the two pollutants is summarised in sections 3.7.2.1 and 3.7.2.2. Moreover, the spectroscopic techniques employed for the detection of the free radicals in the DBD reactor at optimum conditions are also presented.

3.6.3 Description of the DBD system

The closed DBD reactor (Figure 3-2) consisted of the inner and outer quartz dielectric barriers/tubes and the region between the two tubes is often referred to as the air gap or discharge zone. The two tubes were sealed at the top to the outer part of the reactor. At the bottom, the second barrier was sealed to a porous sparging outlet. The inner tube diameter was around 1 mm and that of the outer tube was 7 mm. The DBD reactor was 23 cm long with an inlet and outlet for air circulation (Massima, 2014). The air gap was about 2 mm. The simulated wastewater placed in the reactor was considered as ground electrode and earthed to complete the circuit. The air gas fed from the inlet freely circulates through the plasma zone and is uniformly spread as bubbles into the simulated wastewater via the porous sparging material to achieve maximum oxidation of the pollutant. The air compressor had a maximum output flow

rate of 60 L/min that was controlled with the aid of a flow meter as detailed in the experimental section 3.6.5. The set voltage, air flow, dye volume and other factors were either varied or kept constant as specified in optimisation procedures. In this study, the double cylindrical DBD electrode geometry was employed as an AOP for treatment of simulated wastewater at ambient conditions of temperature and pressure. Orange II sodium salt dye (O.II) and sulfamethoxazole (SMX) drug were used as model persistent organic pollutants in synthetic wastewater. The graphical representation of DBD reactor used in this study including its annotation is presented in Figure 3.3. That is, a power supply set at 8 kV and 60 mA delivering a set current of 60 mA was directly connected to a 1.5 mm silver electrode that was immersed in a 50 g/L sodium chloride electrolyte placed in the inner tube of the reactor. The interaction between the highly energised electrons around the inner tube and air gas (N_2 and O_2) induced the formation of UV light and various excited unstable species such as N*, $O^{\cdot}$, O_3, etc. in the plasma zone. The generated species in the air gap follow an avalanche of chemical reactions and are directly circulated into the polluted water.

3.6.4 Experimental procedure in DBD system

A high voltage electrode from a 200 W AC power supply was connected to a 1.5 mm silver electrode that was directly immersed in a 50 g/L sodium chloride electrolyte in the inner tube of DBD reactor. The 23 cm long DBD reactor has a total volume capacity of 2 mL however; 1500 mL of O.II/SMX was selected as the optimum solution volume to avoid overflow of the solution and short circuits during DBD experiments. An air compressor with an output of 60 L/min was connected to an air flow meter that was attached to the DBD reactor as source of air/oxygen. Simulated orange II dye and SMX solutions at the indicated concentrations were treated in DBD system for 60 min and sampled every 10 min. Orange II solution withdrawn at these sampling times was analysed by UV-vis spectroscopy in the range of 200 to 1000 nm. The absorbance values of O.II measured at 384 nm were noted down and used in the calibration curve presented in Figure 3-5 to estimate unknown concentrations of O.II samples. From the initial and calculated concentrations, the degradation percentage of O.II was determined. Following this procedure, the influence of some parameters such as dye initial concentration, applied voltage and air flow rate on O.II degradation were investigated at the applied conditions. The degradation of SMX in the DBD reactor was performed following this method except that SMX samples were analysed using HPLC (see section 7.3.2). Likewise, O.II and

SMX degradation metabolites were identified and determined by LC-MS analysis (see sections 3.7.2.1 & 3.7.2.2).

3.6.4.1 Optimisation of physico-chemical parameters of the DBD reactor

The following: solution pH, air flow rate and O.II/SMX initial concentrations were the main Physico-chemical parameters assessed during the optimisation of DBD system in Figure in 3-2. The experimental procedures for the optimisation of these factors at the applied conditions are given in the following subsections.

3.6.4.1.1 Optimisation of chemical parameters

In this subsection, the initial concentration of both O.II and SMX was the main chemical parameter investigated. The alteration of O.II and SMX concentrations were denoted O2C and SMXC, separately and are shown in Table 3-4.

Table 3.4: Optimisation of chemical parameters of DBD reactor

Unique number	Varied parameters	Fixed parameters
O2C	O.II concentration (mg/L)	Set voltage 7.8 kV, O.II volume 1 500 mL, pH (5.04 – 6.03), solution, air flow rate 3 L/min, 50 g/L NaCl, 1.5 mm silver electrode, air gap 2 mm and treatment time of 60 min.
Range	10 - 60	
SMXC	SMX concentration (g/L)	Applied voltage 7.8 kV, SMX volume 1500 mL, pH (4.04 -5.06), air flow rate 3 L/min, 50 g/L NaCl, 1.5 mm silver electrode, air gap 2 mm and treatment time of 60 min.
SMXC1	20	
SMXC2	40	
SMXC3	60	
SMXC4	100	

i) Effect of O.II initial concentration on its degradation (Unique number: O2C)

In this section, different solutions of 10, 20, and 30 up to 60 mg/L with O.II increments of 10 mg/L were prepared by serial dilution of a 1000 mg/L initial solution of O.II dye as described in section 3.4.1. This was performed to determine the optimum concentration at which model O.II dye pollutant could degrade fast, that is the O.II concentration at which the current DBD reactor would operate effectively. The O.II solutions of concentrations in the range of (10 - 60) mg/L were separately run in the DBD system while the following parameters: applied voltage 7.8 kV, O.II volume 1500 mL, pH (in between 5.04 and 6.03), air flow rate 3 L/min, 50 g/L NaCl, 1.5 mm silver electrode, air gap 2 mm and contact time of 60 minutes were kept constant. Also O.II solution pH and conductivity behaviour during DBD experiments was documented particularly at 60 mg/L O.II.

ii) The effect of SMX initial concentration on its degradation percentage (Unique number: SMXC)

The influence of initial concentration on SMX degradation percentage was evaluated by varying its concentration values from 20, 40, 60 to 100 mg/L as shown in Table 3.3. But beforehand, the following steps for the preparation of SMX solution were achieved.

3.6.4.1.2 Optimisation of physical parameters

Solution pH and air flow rate were the two principal physical parameters optimised during the degradation of both O.II and SMX in DBD system described in Figure 3-2. Their variations were denoted by SPHO & AFRO for O.II dye and SMXPH & AFRS for SMX, correspondingly. The experimental steps employed to achieve this task are summarised in Table 3-5. The experimental procedures used for their optimisation are discussed in the following paragraphs.

Table 3.5: Experimental procedures for the optimisation of physical parameters

Unique number	Varied parameters	Fixed parameters
SPHO	Solution initial pH of O.II dye	Applied voltage 7.8 kV, O.II concentration 60 mg/L, O.II volume 1500 mL, air flow rate 3 L/min, 50 g/L NaCl, air gap 2 mm, 1.5 mm silver electrode and contact time of 60 min
SPHO1	2.5	
SPHO2	4.5	
SPHO3	6.5	
SPHO4	8.5	
SPHO5	10.5	
SMXPH	Solution initial pH of SMX drug	
SMXPH1	20	Applied voltage 7.8 kV, O.II concentration 40 mg/L, solution volume 1500 mL, air flow rate 3 L/min, 50 g/L NaCl, air gap 2 mm, 1.5 mm silver electrode and contact time of 60 min
SMXPH2	40	
SMXPH3	60	
SMXPH4	100	
AFRO	Air flow rate (L/min) for O.II dye	
AFRO1	3	Applied voltage 7.8 kV, O.II concentration 60 mg/L, O.II volume 1500 mL, air flow rate 3 L/min, 50 g/L NaCl, air gap 2 mm, 1.5 mm silver electrode and contact time of 60 min
AFRO2	6	
AFRO3	9	
AFRS	Air flow rate (L/min) for SMX drug	
AFRS1	3	Applied voltage 7.8 kV, SMX concentration 40 mg/L, solution volume 1500 mL, air flow rate 3 L/min, 50 g/L NaCl, air gap 2 mm, 1.5 mm silver electrode and contact time of 60 min
AFRS2	6	
AFRS3	9	

Effect of solution pH on degradation percentage of orange II dye and sulfamethoxaole

In this subsection, the solution pH for degrading O.II and SMX marked as (SPHO) and SMXPH, correspondingly summarised in Table 3-4 was optimised as follows:

A few drops of concentrated H_2SO_4 or NaOH were carefully diluted in separate beakers containing approximately 400 mL of deionised water. About 1500 mL of 60 mg/L O.II or 40 mg/L SMX solutions was placed in a 2000 mL beaker in which a pH/conductivity probe was submerged. The pH of O.II or SMX solution was varied from 2.5 to 10.5 and was adjusted to the desired value by adding a reasonable amount of diluted H_2SO_4 and NaOH drop wise using a 5 mL pipette. During this process the solution was continuously swirled with pH/conductivity meter probe to get the pH value needed. The monitored solution was further used in the DBD

experiment at the following experimental conditions: applied voltage 7.8 kV, air flow rate 3 L/min, air gap 2 mm, 1.5 mm silver electrode and 50 g/L of NaCl for 60 minutes.

Effect of air flow rate on O.II/SMX degradation efficiency

Using the DBD system (Figure 3-2), most parameters were kept constant (applied voltage 7.8 kV, pollutants concentration 60 mg/L for O.II and 40 mg/L SMX, solution pH (in between 6.04 and 6.64), 50 g/L NaCl electrolyte and solution volume 1500 mL, air gap 2 mm) while the air flow rate coded as AFRO and AFRS in Table 3-4 was altered from 3, 6 to 9 L/min, respectively. In total 3 experiments were performed for each pollutant in the same way during a period of 60 minutes whilst sampling every 10 minutes. The sampled solutions were analysed using a UV-vis spectrophotometer (See section 3.3.2 & Figure 3-5). Absorbance of these samples was used to determine unknown concentrations. These later were used to calculate the decolouration efficiency of O.II and SMX.

3.6.4.1.3 Optimisation of electrical parameter

The electrical parameter evaluated in the DBD system (Figure 3-2) was the applied voltage. Its variation was termed APV and the experimental procedures for its optimisation are presented in Table 3-6 and detailed in the following paragraphs.

Table 3.6: Summary of electrical parameters optimisation

Unique number	Varied parameters	Fixed parameters
APVO	Applied voltage (V) with O.II	[O.II] 60 mg/L, solution volume 1500 mL, pH (6.04 – 6.64), air flow rate 3 L/min, 50 g/L NaCl, air gap 2 mm,1.5 mm silver electrode and contact time of 60 min.
APVO1	6.8	
APVO2	8	
APVO3	10.5	
APVS	Applied voltage (V) with SMX	[SMX] 40 mg/L, solution volume 1500 mL, pH (4.04 - 5.06), air flow rate 3 L/min, 50 g/L NaCl, air gap 2 mm,1.5 mm silver electrode and contact time of 60 min.
APVS1	6.8	
APVS2	8	
APVS3	10.5	

3.6.5 Effect of peak voltage on degradation percentage of orange II and SMX

In this section the applied voltage was altered from 6.8 kV, 8 kV and 10.5 kV, accordingly. The following parameters were kept constant: [O.II] concentration 60 mg/L, [SMX] 40 mg/L, solution pH (between 6.04 and 6.64), air flow rate 3L/min, air gap 2 mm, 50 g/L NaCl electrolyte and dye volume 1500 mL and 1.5 mm silver electrode. Altogether three DBD experiments were performed by varing the applied voltage between 6.8 kV and 10.5 kV as indicated above. The DBD experiments were performed over 60 minutes and polluted water was sampled every 10 minutes.

3.6.6 DBD experiment performed at optimal conditions

In order to assess the efficiency of the DBD reactor two DBD experiments at optimum conditions were carried out with each pollutant. The following: Peak voltage 7.8 kV, [O.II] 60 mg/L, [SMX] 40 mg/L, pH 2.5 for O.II and 6.5 for SMX, solution volume 1500 mL, air flow rate 3L/min, 1.5 mm silver electrode, 50 g/L NaCl electrolyte, air gap 2 mm and running time of 60 min were used as the optimum conditions for both O.II and SMX pollutants.

3.6.7 Photo catalytic activity testing

This subsection deals with the photo catalytic activities of the following systems: C-N-TiO_2 powder, [(SS/C-N-TiO_2 and Ti/C-N-TiO_2) + DBD], C-N-TiO_2 immobilised on anticorrosion meshes and on glass at their corresponding conditions.

3.6.7.1 Photo catalytic activity of powder C-N-TiO_2 upon the removal of O.II in the open photocatalytic system

In order to measure the photocatalytic activity of the C-N-TiO_2 powder approximately, 500 mL of 5 mg/L orange II solution at pH 2.5 was introduced in a 1000 mL round vessel (d = 21cm width & 10 cm height) in which 0.02, 0.08 or 0.14 g of ground powder catalyst was added. The pH of 2.5 was chosen based on previous research outcomes supporting that azo dyes degrade well in acidic medium (Kuang, Zhao and Liu, 2011; Sayed and El-Ashtoukhy, 2013). The vessel was placed in a light proof photocatalytic box around which ice was packed to cool down the vessel as shown in Figure 3-4. This later was positioned on a magnetic stirrer. While

stirring, orange II dye solution was irradiated for 2 hours with a UV lamp (Mega-Ray 160 W/240 V MR160 SPL11/14) placed at 5 cm above the solution in the vessel as shown in Figure 3-4. The solution was sampled every 30 min and was taken for UV-vis analysis. For control experiments, the 500 mL of 5 mg/L O.II mixed with 0.08g of powder TiO_2 was stired in the 1000 mL round vessel without UV light. The second control experiment involved the stiring of the 500 mL of 5 mg/L O.II in the 1000 mL round vessel in the absence on UV light at the same experimental conditions.

3.6.7.1.1 Effect of photo catalyst pyrolysis time on the degradation of orange II dye in the open photo catalytic system

The activity of the three photo catalysts pyrolysed at 350^{o}C for 105, 120 or 135 min was evaluated using the photo catalysis procedure described in section 3.6.6.1. About 0.8 g of each powder catalyst was weighed and added into 500 mL orange II solution which was further exposed to UV light as previously described and shown in Figure 3-4. Samples were taken each 30 minutes and the unknown concentrations of orange II were calculated using the linear trend in Figure 3-9 and used to determine the percentage degradation of orange II irradiated in the presence of each catalyst over time.

3.6.7.1.2 Effect of photo catalysts dosage on the degradation of orange II dye in the open photo catalytic system

The catalyst prepared at different pyrolysis time (Section 3.5.1) that gave the highest degradation of orange II was selected as the best photo catalyst. So in this section, three different amounts (0.02, 0.08 and 0.14 g) of the best photo catalyst (105 min C-N-TiO_2) were weighed and used for photo catalysis decomposition of orange II dye using the same procedure previously described in section 3.2.4 at the same experimental conditions.

3.6.7.2 Photocatalytic test of O.II by C-N-TiO_2 immobilised on SS and pure Ti mesh

The photo catalytic activity of the SS or pure Ti meshes coated with C-N-TiO_2 upon the degradation of O.II dye and SMX was performed as follows:

The coated C-N-TiO_2/SS or C-N-TiO_2/Ti meshes (2 cm x 6 cm mesh) were configured in a rectangular fashion and were arranged around the inner tube of the DBD reactor as shown in

Figure 3-3 for the degradation of orange II dye and SMX drug at the applied optimum conditions following the DBD procedure described in section 3.6.4. The degradation intermediate by-products of the two pollutants were identified by HPLC-MS described in sections 3.7.2.1 and 3.7.2.2.

3.6.7.3 Photocatalytic degradation of O.II by C-N-TiO_2 immobilised on SS and anticorrosion meshes

The photocatalytic activity of the C-N-TiO_2 coated SS and anticorrosion meshes were assessed during degradation of orange II sodium salt at temperature below 20 °C in the open photo catalytic system (Figure 3.4). In the photo catalysis procedure, uncoated and anticorrosion coated meshes were coated with C-N-TiO_2 (2 cm x 6 cm mesh) and were individually and horizontally immersed in 5 mg/L orange II solution in a 1000 mL round vessel and irradiated with UV light at the following conditions: [O.II] 5 mg/L; solution pH 2.5; solution volume 500 mL, and irradiation time of 120 min (shown in Figure 3-4). The sampled solution was taken for UV-vis analysis (See section 3.6.6.1). The unknown concentrations of orange II solution after UV irradiation were determined using a calibration curve $y = 0.0691x$, $R^2 = 0.9988$ given in Figure 3-9. The concentrations were further used to calculate the degradation efficiency of orange II dye at each sampling time according to Equation (3.1).

3.6.7.4 Effect of spin coating speed and catalyst dilution on the thickness of TiO_2 thin films on quartz and application for the photocatalytic removal of O.II dye

The impact of spin coating rotation speed on the thickness of thin films was investigated by varying the speed from 2000, 2300, 2600 to 2900 rounds per minute (rpm) following the spin coating process described in Section 3.5.3.2 while the catalyst-solvent volume ratio (3: 5) and the spinning time of 90 s were kept constant. Conversely, the viscosity of the catalyst-solvent volume ratio (v: v) was examined by altering C-N-TiO_2 Nano catalyst gel volume from 3, 4 to 5 mL while that of DMF solvent (5mL) was kept constant. So three solutions of catalyst to solvent ratio 3:5; 4:5 and 5:5 were prepared and stirred for 24 hours at room temperature and each coated at a speed of 2600 rpm for 90 s following the same coating procedure. The thickness of the films in all cases was assessed by profilometry analysis. The morphological distribution /deposition of the nano catalyst on the glass were investigated by scanning electron microscopy (SEM) while the composition of the coated films was investigated by energy

dispersive spectroscopy (EDS). Furthermore, in both speed and viscosity studies, the activity of the of the resulting annealed films was assessed by the photocatalytic degradation of orange II dye at the applied conditions using the same experimental set up presented in Figure 3-4.

3.6.8 Cathodic arc evaporation procedure

The coating of SS with Cr-based anticorrosion layers was performed according to the method detailed by Dinu *et al.*, (2018). Nitride and oxinitride Cr-based coatings were developed on 304 stainless steel (SS) discs (Θ = 20 mm) and Si pieces (20 x 20) mm^2 by reactive cathodic arc evaporation (CAE) using a Cr cathode (99.5% purity, Cathay Advanced Materials Ltd., Guangdong, China). The chemical composition of the SS used as coating support was already highlighted by Dinu *et al.*, (2018).

Procedure

Each 304 SS substrate was sanded using a SiC abrasive paper (grit 800), polished (Ra = 60 nm), ultrasonically washed in isopropyl alcohol and water for 10 min, then dried at 120 ^oC for 1 h.
To control the coating uniformity, the samples were placed on a rotating sample holder. Moreover, before deposition, the substrates were sputter etched with Ar + for 5 min to remove any contaminant layer at a residual pressure of 2 x 10^{-3} Pa that was lower than the total pressure (8 x10^{-2} Pa) of the deposition system. Nitrogen gas was fed in the chamber at a flow rate of 60 sccm for nitride coatings. On the other hand, the same value of the nitrogen mass flow rate mixed with 17 sccm of the oxygen was used for the oxynitrides coatings. The arc current applied on the Cr cathode was 90 A, and the substrates were biased at -200 V. The selection of this value aiming at improving coatings' corrosion resistance was based on previous studies (Dinu *et al.*, 2017b) claiming that the coating properties related to their crystallinity and surface roughness could be tuned by an appropriate selection of the bias voltage. Similar parameters were used for the bilayer coatings. Furthermore, the deposition time of each layer was altered in order to achieve nearly the same thickness of approximately 1 µm for all coatings.

3.6.9 Electrochemical corrosion study

In this section, a few aspects are addressed, these included determination of the anticorrosion coating thickness/roughness before and after corrosion studies while the second aspect involved the determination of corrosion behaviour of the coatings in acidic media. The surface morphology analysis of the anticorrosive films using SEM and EDS techniques are described in section 3.8.2.1. The experimental protocols of the corrosion experiments are summarised in the following paragraphs.

3.6.9.1 Determination of the thickness and roughness of the anticorrosive coatings

The coating thickness and the surface roughness were investigated using a Dektak 150 surface profilometer (Veeco-Bruker). The roughness of each sample, before and after the corrosion measurements, was determined over a length of 10 mm, for 200 seconds, using a 2.5 µm diameter stylus. The roughness of the investigated specimens was evaluated based on arithmetic average deviation from the mean line (Ra) and the root mean square average of the profile heights over the evaluation length (Rq). Moreover, the asymmetry of the profile about the mean line was indicated by the skewness parameter (Sk). The presented values represent the average data obtained from 5 measurements performed on different areas of each specimen.

3.6.9.2 Corrosion measurement

Corrosion measurements were evaluated by potentiodynamic techniques in 0.1M NaCl+ 6% H_2O_2 (pH=4), at room temperature using a Versa Stat 3 Potentiostat/Galvanostat. A typical three-electrode cell described in Figure 2-9 was used, with a Pt counter electrode and a Ag/AgCl reference electrodes. The coated or uncoated (used as control) stainless steel was used as working electrode and it was placed in a Teflon holder with a working area of $1cm^2$. First, the open circuit potential (E_{OC}) was monitored over 15 h of immersion. To identify the polarisation resistance (R_p), the linear polarisation technique was used by applying a perturbation potential of −0.01 V to 0.01 V vs. E_{OC} at a scanning rate of 1 mV/s. R_p parameter was determined as the slope of the linear region of the ΔE-Δi curve at corrosion potential (E_{corr}) Furthermore, Tafel plots were recorded from -0.25 V to 0.25 V vs. E_{OC} at a scanning rate of 1 mV/s. The E_{corr} parameter, anodic (β_a) and cathodic (β_c) slopes, and corrosion current density (i_{corr}) were extracted from Tafel plots. Moreover, the porosity (P) of the coatings was estimated from Elsener's empirical equation (Equation 3.2) based on the polarisation resistance of the uncoated (Rps) and coated (Rpc) SS specimen, the difference between the corrosion potentials of the coated and uncoated SS specimen (ΔE_{corr}) and corresponding anodic slope (β_a).

$$P = \left(\frac{R_{ps}}{R_{pc}}\right) \cdot 10^{\frac{-|\Delta E_{corr}|}{\beta_a}} \quad (3.2)$$

The protective efficiency (P_e) was also calculated (Equation 3.3) based on the corrosion current densities of the coatings (i_{corr_c}) versus the SS specimen (i_{corr_s}).

$$P_e = \left(1 - \frac{i_{corr\_c}}{i_{corr\_s}}\right) \cdot 100 \quad (3.3)$$

3.7 Analytical methods

This section presents various analytical methods such as UV-vis spectroscopy, HPLC (LC-MS), TOC, COD, nitrates and sulphates tests that were used for the analysis of treated and untreated O.II and SMX samples. Among these, UV-vis was used to follow the decolouration of O.II while TOC, COD, nitrates and sulphates analysis were specifically used to examine the O.II polluted water quality. On the other hand, although HPLC was used to assess the degradation of SMX in the DBD systems, LC-MS was employed for the identification of the degradation intermediate by-products of both O.II and SMX decomposed in the DBD systems. The detailed protocols of these analyses have been summarised in the following paragraphs

3.7.1 UV-vis spectroscopy

Quick analysis of O.II dye was performed by UV-is spectroscopy whereby the recorded absorbance was directly substituted in the UV-Vis linear calibration curves shown in Figures (3-7 & 3-9) to estimate unknown concentration of O.II. However, UV-vis could not be used for colourless SMX analysis.

3.7.1.1 Procedure

First, the two quartz Suprasil cuvettes were washed and filled up with deionised water. Then the cuvettes were placed in the UV machine for baseline analysis and deionised water was used as reference solution. After the baseline run, one cuvette was removed from the instrument and the other was left as reference. The removed cuvette was washed with deionised water and filled up with the sample of interest and placed back into the instrument. All the samples were run at a fixed wavelength of 384 nm. Wavelength, absorbance and other parameters of these samples could be obtained from the UV-vis instrument.

Since the calibration curve was a straight line passing through the origin, it therefore obeyed the equation: y = mx, where y represents absorbance of O.II measured at 483 nm, the slope of the line and x the unknown concentration that needed to be determined. According to the calibration curve in Figure 3-7, the equation of the line was given by Equation (3.4).

$$Y = 0.0525x \quad (3.4)$$

Where m = 0.0525 and y any absorbance value on the y-axis.

Similarly absorbance of samples taken in the time scale of 60 minutes at various O.II concentrations was extrapolated on the calibration curve to find unknown concentrations of O.II samples. The absorbance of O.II solutions sampled between 0 and 60 minutes declined with the decrease of dye concentration during degradation experiments. This trend showed that O.II dye was being decolourised with increasing treatment time. Specifically, absorbance of the solution sampled after 10 minutes for instance was higher than that of the one withdrawn after 20 minutes and so on.

Therefore, unknown concentrations of O.II samples (represented by x in the Equation (3.5) withdrawn after 10, 20, 30, 40, 50 and 60 minutes were estimated using

$$X = Y/0.0525 \quad (3.5)$$

Alternatively, once the absorbance value was identified on the y-axis, the value can be extrapolated on the straight line to calculate the corresponding value of x, thus measuring the inferred concentration. This procedure was applied to all solutions of unknown concentrations of O.II dye. In the current study, the decolouration percentage of O.II in DBD system was calculated using the formula suggested by Reddy *et al.*, (2013) and presented in Equation (3.6):

$$\text{Decoluration percentage (D \%)} = [(C_o - C_t) / C_o] \times 100 \quad (3.6)$$

Where, C_o and C_t are the initial and the final concentrations of O.II solution, correspondingly.

3.7.2 Liquid chromatography/Mass spectroscopy analysis

High performance liquid chromatography coupled with mass spectroscopy (HPLC-MS/LC-MS) analysis was used to determine O.II and SMX degradation intermediate by-products achieved in the DBD systems (R_1 and R_2).

3.7.2.1 LC-MS determination of O.II degradation by-products

The identification of O.II degradation intermediate by-products of O.II at optimum conditions was performed using high liquid performance chromatography coupled with Mass spectroscopy (HPLC-MS) technique at the following conditions: A 250 mm x 4.6 mm Zorbax C_{18} (5 µ) analytical column operating at normal conditions of temperature and pressure. The mobile phase consisted of a mixture of phosphoric acid-acetonitrile-water with the ratio of 0.5:340: 600 v/v which was allowed to equilibrate, and was diluted to 1000 mL volume with distilled water. The injection sample volume of 20 µL was performed using an auto sampler. While the detection limit was set at 214 nm, the flow rate of the mobile phase was 2.0 mL/min.

This procedure was also used for the optimisation of the DBD system using SMX and for the identification of its degradation intermediate by-products. A calibration curve was prepared for quantification of SMX. The preparation of 600 mg/L sulphametoxazole stock solution was performed as set out in section 3.3.4.3

3.7.2.2 High performance liquid chromatography analysis of Sulfamethoxazole

The analysis of SMX samples obtained during the optimisation processes was performed using a high liquid performance chromatography (HPLC) technique at the following conditions, using a 250 mm x 4.6 mm Zorbax C_{18} (5 µL) analytical column operating at normal conditions of temperature and pressure. The mobile phase consisted of a mixture of phosphoric acid-acetonitrile-water with the ratio of 0.5:340: 600v/v which was allowed to equilibrate and was diluted to 1000 mL volume with distilled water. The injection sample volume of 20 µL was performed using an auto sampler. While the detection limit was set at 214 nm, the flow rate of the mobile phase was 2.0 mL/min. Following this HPLC procedure, and by using SMX standards solutions (10, 20, 40, 60, 80 and 100 mg/L) previously prepared from the stock solutions a calibration curve of peak area versus concentration was plotted for SMX compound (see Figure 3-8). Consequently, the unknown concentration of SMX, and the degradation percentages at each sampling time was determined using the obtained linear plot. This calibration curve was therefore used in the optimisation processes in order to determine the optimum degradation parameters of SMX compound. Furthermore, the same HPLC method was coupled to Mass spectroscopy (LC/MS) and used at the same conditions for the identification/ determination of degradation intermediates of both O.II dye and SMX at the optimum applied DBD conditions (see section 3.6.5).

3.7.3 Total organic carbon

The total organic carbon (TOC) is defined as all carbons covalently bonded in organic molecules and in surface and ground water as well as organic carbon which is not purgeable by acidification and gas stripping (Hoeben, 2000; Mohamed Elham Farouk, 2011). The TOC measurement as stated in section 2.10.4.1 was performed according to standard methods for the examination of water and wastewater, using a high temperature combustion method 5310 B (APHA, AWWA, 1998). Initially, a few µmL of the sample was acidified with 2 N HCl (pH 2) and a reasonable amount of the acidified sample was inserted into the analyser. The resulting

CO_2 was purged, removing any inorganic carbon present in the sample. Afterwards the remaining carbon from the sample prepared in this manner was determined via combustion. The digestion was performed in the multi N/C 3100 analyser by thermocatalytic high-temperature oxidation in the presence of a platinum catalyst. This enables the quantitative digestion even for very stable, complex carbon compounds. The sample aliquot was directly dosed into the hot zone of the filled reactor (combustion tube). Here the pyrolysis and oxidation of the sample in the carrier gas flow was performed with the aid of the catalyst (Equations (3.7) - (3.9). The carrier was also used as an oxidation agent.

$$R + O_2 \rightarrow CO_2 + H_2O \quad (3.7)$$

$$R - N + O_2 \rightarrow NO + CO_2 + H_2O \quad (3.8)$$

$$R - Cl + O_2 \rightarrow HCl + CO_2 + H_2O \quad (3.9)$$

Where R is a carbonic substance.

The measuring gas was cooled in the condensation coil and condensed water was separated from the measuring gas in the subsequent total inorganic carbon (TIC) condensate container. After further drying and removal of corrosive gases, the measuring gas CO_2 was added to the NDIR detector. The calculations of TOC in this study were achieved as described in section 2.10.4.1.

3.7.4 Chemical oxygen demand

As defined by Grabowski et al. (2007), chemical oxygen demand (COD) is a measure of water quality that is expressed in milligrams of oxygen per litre. It is the measure of the quantity of oxygen required to totally oxidise and mineralise organic substances to inorganic derivatives. The chemical oxygen demand (COD) for the degradation of O.II in the DBD system was evaluated using the methodology suggested by Pitwell, (983) and is described as follows:

A sample volume of 2 mL was oxidised in a Hach sample vial containing 4.17 mM of potassium dichromate in 5 mL of sulphuric acid and digested at 150^{o}C for 2 h. Samples were determined spectrophotometrically using a Hach DR/2010 spectrophotometer at an absorbance of 420 nm described by the manufacturer's instruction manual method 8000 (Hach, Colorado, USA)

(Pitwell, 983). The calculation of COD in this study was performed according to the comprehensive methodology suggested by Soresa (2011) and described in section 2.3.4.1.

3.7.5 Nitrate and nitrite analysis

The amount of nitrate and nitrite was determined according to Protection Agency, (1983). About 10 mL of filtered sample was injected into a LACHAT QuickChem® flow injection analyser (FIA) carrier stream with flow rate of 2.5 µL/cm. The sample was moved through a QuikChem® 10-107-04-1-A cadmium column for reagent preparation. The activated cadmium reduced the entire nitrate in the sample to nitrite. The nitrite was then determined by diazotising with 58.07 mM of sulphanilamide followed by coupling with 3.85 mM of N-(1-naphthyl) ethylenedaimine dihydrochloride (Merck, Germany). The absorbance of nitrites and the reduced nitrates were measured at 520 nm with a colorimeter detector. Nitrite alone was determined in the absence of the cadmium column. The data were exported from the Omnion software as an excel sheet. Correlation coefficient of > 0.999 was accepted. In house quality control samples as well as external proficiency testing (PT) samples were used for quality control.

3.7.6 Determination of the amount of sulphate

Filtered liquid samples were injected into the nebuliser of a cyclonic spray chamber of QuikChem® 10-107-04-1-A analyser and carried into plasma through an injector tube located at the torch. The sample aerosol was injected directly into the inductively coupled plasma (ICP, Thermo scientific, MA, USA), subjecting the constituent atoms to a temperature range of 6 000 to 8 000 K with a constant flowing stream of argon gas ionised by applied radio frequency field typically oscillating at 27.1 MHz. Ionisation of a high percentage of the atoms producing ionic emission spectra was then recorded. Ionic emission was detected and quantified by induced coupled plasma (ICP) detector. A correlation coefficient of > 0.999 was accepted. In house quality control samples as well as external proficiency testing (PT) samples were used for quality control.

Furthermore, photo luminescent fluorescence spectroscopy (PLS) used for the determination of ·OH radical concentration in the DBD system was carried out according to the section 2.10.2 of chapter II

3.8 Characterisation of catalyst and coatings

In this subsection, various techniques including XRD, FT-IR, SEM, TGA used for the characterisation of anticorrosive coatings, C-N-TiO_2 nano catalyst and the various C-N-TiO_2 coated supports have been outlined. Likewise, TEM/EELS, SAED, EDS, EELS procedures were performed according to sections 2.11.2.1, 2.11.2.2 and 2.11.2.3 of chapter II.

3.8.1 X-ray diffraction

The phase composition of the samples (C-N-TiO_2 powder and films) was investigated by X-ray diffraction (XRD) using a Smart Lab diffractometer (Rigaku), with a CuKα radiation (λ= 0.15405 nm). The XRD patterns were obtained in a 2θ range of 20° to 100°, at a step size of 0.02°. The XRD characterisation protocol was fully discussed in section 2.11.1 of chapter 2.

3.8.2 Fourier Transformer Infra-red spectroscopy

As much as UV-vis reveals information about absorption bands related to the extent of decolouration of O.II when exposed to plasma treatment, FT-IR was used to qualitatively analyse untreated and treated samples to determine intermediate degradation products. The main objective was to determine the types of degradation products remaining in the solution, hence showing the degree of O.II and SMX degradation during exposure to electrical discharge. FT-IR of O.II and SMX samples was performed on a Perkin Elmer spectrum 100 FT-IR spectrometer as described in the following procedure.

3.8.2.1 Procedure

Initially, 4 mL of dichloromethane was dropped on a towel paper to clean the attenuated total reflectance (ATR) sample holder of the Perkin Elmer spectrum 100 FT-IR spectrometer. About 0.5 mL of O.II or SMX sample was withdrawn from the sample container with a 5 mL dropper and was placed on the attenuated total reflectance (ATR) sample holder of the Perkin Elmer spectrum 100 FT-IR spectrometer. The sample was analysed in the range of 4 000 - 380 cm^{-1}. After the desired background was measured, the baseline was corrected and the spectra were smoothened. The spectra obtained showed various vibration bands of different functional groups suggesting the presence of several organic and inorganic compounds.

3.8.3 Scanning Electron Microscopy

The scanning electron microscopy (SEM) was used to investigate various aspects covered in this study. These include the morphologies of the powder C-N-TiO_2 and C-N-TiO_2 films as well as SS, pure Ti and anticorrosion meshes and glass substrates used as catalysis supports. Next to this, SEM was also coupled with energy dispersive spectroscopy for the determination of the elemental composition of the prepared nano composites and their derivative films. Therefore, powder C-N-TiO_2 or a small portion of its films were viewed by SEM for surface analysis. This was performed using Hitachi X 650 Scanning Electron Microscope at an applied voltage of 5.00 kV, a working distance of 3.5 nm and at various magnifications. The instrument resolution depended on the nature of the specimen and experiment. Nevertheless, the procedure used for SEM analysis is highlighted in the following paragraph.

3.8.3.1 Procedure

A small portion of about 1 cm of films or powder on mesh substrate was placed on a carbon tape which in turn was placed on top of a sample holder. After polishing samples with carbon, the holder was positioned in the SEM instrument. In order to get a clear area of the specimen, various scans were accomplished. The scans performed at different magnifications led to multiple sample images. However, only those showing clear images of the sample surface were selected and recorded for typical interpretation. Comparable procedures were used to analyse approximately 0.6 g of powder C-N-TiO_2 nano catalyst or mesh samples.

3.8.3.2 Scanning electron microscopic surface morphology analysis of anticorrosion coatings

A scanning electron microscope (SEM) (Hitachi TM3030 Plus) coupled with an energy dispersive X-ray spectrometer (EDS) (Bruker) was used for the surface morphology and elemental composition investigation following the procedure described above. Images of the surface morphology for each specimen were recorded at both 30x and 100x magnification. Moreover, for identification of corrosion products, mapping elemental images were also acquired in different areas of the coating surface.

3.8.4 Thermal gravimetric analysis

The thermal gravimetric analysis of C-N-TiO_2 nano catalysts was performed using a PerkinElmer Thermo gravimetric analyser TGA 4000.

3.8.4.1 Procedure

Initially, a small sample holder was exposed to a batch benzene flame until it became red, so as to clean up these sample holders and remove impurities. The sample holder was then cooled down to room temperature and inserted into the TGA instrument and zeroed to obtain the mass of the empty crucible sample holder. Thereafter, a reasonable amount of sample was introduced into the crucible and weighed. Finally the start/stop button on the instrument was pressed to start the analysis in the temperature range of 0 to 850 ^oC in N_2 gas. After 2 hours, the results obtained were collected from the PC and plotted using excel software. The graphs of weight (mg)/weight percentage versus temperature (^oC) were obtained.

3.8.5 General characterisation of the synthesised powdered C-N-TiO_2 photo catalyst

In this study, various characterisation techniques were used to analyse the powdered synthesised C-N-TiO_2 nano photo catalyst. UV-vis (Section 3.7.1.1) and FT-IR spectroscopy (Section 3.8.2) were used to investigate the absorption wavelength and the functional groups of the nano photo catalyst, respectively. Scanning electron microscopy (Section 3.8.3), scanning transmission electron microscopy (Section 2.11.2.1) and energy dispersion spectroscopy (Section 2.11.2.4) were all employed to determine the surface morphology, particles distribution and the elemental composition of the synthesised nano composites. Moreover, X-ray diffraction (Section 3.8.1) and transmission electron microscopy (TEM) techniques (Section 2.11.2.1) were used to determine the crystalline phases, crystal size and particle size distribution of the synthesised co-doped C-N-TiO_2 nano particles. Furthermore, electron energy loss spectroscopy (EELS) under TEM analysis was used to determine the bonding between C, N, and Ti in the TiO_2 framework. Furthermore, thermal gravimetric analysis descried in section 3.8.4 was used to evaluate the mass loss percentage of the synthesised C-N-TiO_2 catalysts and to further show the pyrolysis and degradation of the carbon source PAN. In this study Degussa TiO_2 powder was used as control and for comparison with the synthesised C-N-TiO_2 nano composites.

CHAPTER FOUR: QUANTIFICATION OF FREE RADICALS IN DBD REACTOR

4 Introduction

The effectiveness of the redesigned DBD configuration presented in Figure 3-2 was evaluated by quantification of the generated major molecular and radical reactive species, mainly ozone (O_3), hydrogen peroxide (H_2O_2) and hydroxyl radicals ($OH^{\cdot}$) using spectroscopy techniques at the applied conditions (see sections 3.6.1) using water as a control solution. In this chapter, the effects of pH and the amount of scavenger as well as the amount of chemical probe (TA) on the production of the free radicals were also investigated. The results of these assessments are discussed below.

4.1 Effect of pH on dissolved ozone concentration in DBD reactor

Ozone which is considered as one of the most abundant but unstable species produced in the DBD reactor is a powerful oxidant that reacts with various molecules leading to excited species that emit light when falling back to their ground states, often known as chemiluminescence (CL). Several colorimetric methods employed for the determination of O_3 in aqueous systems have already been reviewed by Mouele et al. (2018). Among them, the indigo method was identified as the most practical measurement technique that was employed in this study (see sections 3.4.1 and 3.6.1.1) to approximate the amount of O_3 produced in the current DBD reactor over time using distilled water only as a model solution. Most importantly the concentration of O_3 was followed with respect to the change in pH values at the applied conditions (Section 3.6.1.1). The outcomes of these experiments are presented in Figure 4-1.

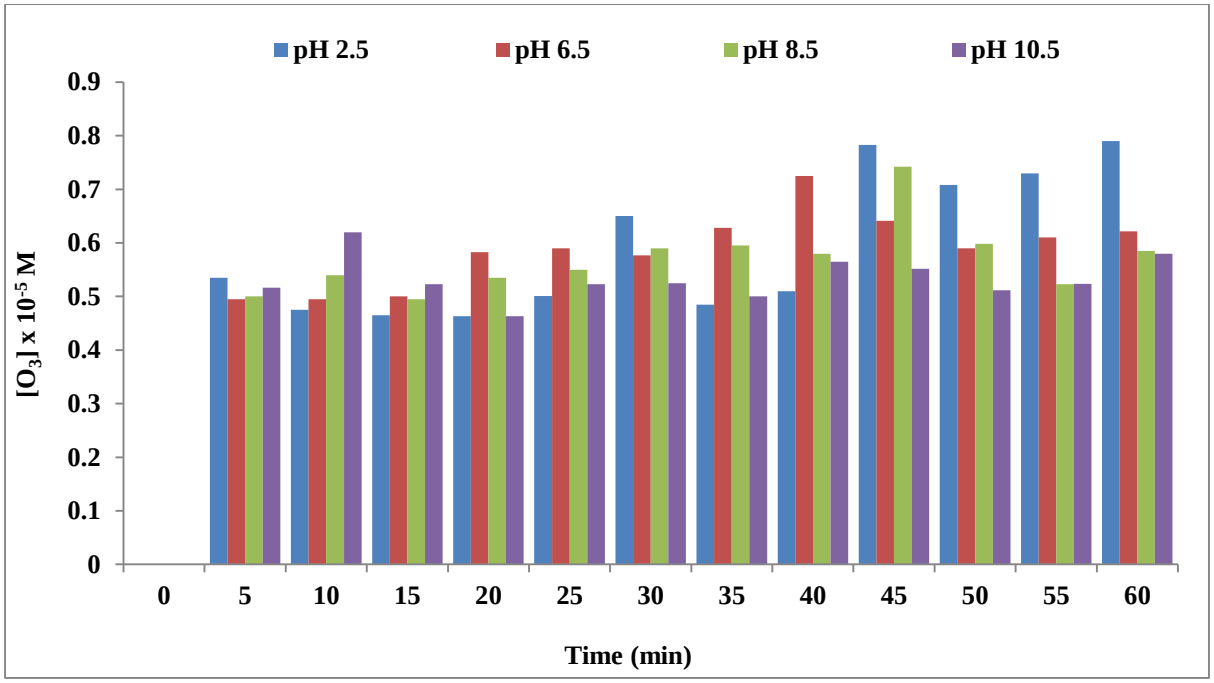

Figure 4.1: Effect of pH on ozone generation in DBD reactor at the following experimental conditions, varied parameter, distilled water (pH from 2.5, 6.5, and 8.5 to 10.5). Fixed parameters: applied voltage 6.8 kV, power 60 W, trip current 10 A, set current 60 mA, frequency 1000Hz, air flow rate 3 L/min, solution volume 1500 mL, 1.5 mm silver electrode, 50 g/L NaCl electrolyte, treatment time 60 minutes, sampling every 5 min.

Figure 4-1 displays the effect of pH on the concentration of ozone produced in the DBD reactor at the applied conditions as measured by the indigo method. The results in Figure 4-1 shows that a significant molar concentration of O_3 was present for the duration of 60 min operation time but the amount of ozone produced in the DBD fluctuated with time and did not follow a constant trend. However, the highest amount of ozone was generated in acidic pH 2.5 followed by pH 10.5, 8.5 and 6.5, correspondingly. For instance, at pH 2.5, the fluctuating ozone concentration quantified after 5 minutes increased from 0.535 mol/L to 0.783 and 0.79 mol/L after 45 and 60 min of DBD run, respectively. In contrast, the 0.516 M of O_3 depicted after 5 min at pH 10.5 increased to 0.62 M after 10 min and progressively fluctuated down to 0.58 M after 60 min. Moreover, at pH 8.5, the 0.5 M of O_3 recorded after 5 min increased to 0.742 M after 45 min and decreased to 0.585 M after 60 min. On the other hand, at pH 6.5, the 0.495 M of O_3 captured after 5 min increased to 0.725 M after 40 min and declined to 0.621 M after 60 min of DBD run. The fluctuation of O_3 observed at all pH values during the 60 min of DBD run meant that O_3 was being produced and scavenged/consumed in the DBD reactor following different routes. That is, the slight decrease within the 60 minutes of DBD signified that O_3

was certainly involved in various side chain reactions which at some point might have induced the slight reduction of its amounts.

Indeed, the UV light produced in the DBDs systems is diffused in the aqueous solution and irradiates the O_3 dissolved in the water. Atkinson (1985) showed that when exposed to UV light at $\lambda \leq 310$ nm, ozone decomposes to singlet oxygen atom and singlet oxygen molecules according to Equation (4.1). Moreover, the highly reactive singlet oxygen atom with a life time of 4.4 µS in aqueous media reacts with water to produce hydroxyl radicals as shown in Equations (4.2) (Haugland 1996). The generated OH radicals might also have recombined to form H_2O_2 as presented in Equation (4.3).

$$O_3 + hv \rightarrow O(^1D) + O_2(^1\Delta g)\ \lambda \leq 310\ nm \quad (4.1)$$

$$O(^1D) + H_2O(g) \rightarrow 2OH \quad (4.2)$$

$$O(^1D) + H_2O(l) \rightarrow H_2O_2 \quad (4.3)$$

Another property of ozone responsible for its decrease in DBD configuration is the fact that O_3 could have been converted into oxygen by hydroxyl radicals according to Equations (4.4) & (4.5).

$$O_3 + OH\cdot \rightarrow O_2 + HO_2\cdot \quad (4.4)$$

$$HO_2\cdot + O_3 \rightarrow OH\cdot + 2O_2 \quad (4.5)$$

In addition, among the indirect reactions of O_3 in DBD reactor, the initiation reaction of ozone as sustained by Foster, (2017) is a reaction step characterised by the decomposition/inhibition of ozone by the OH-molecule as presented in Equation (4.6).

$$O_3 + OH^- \rightarrow O_2^{\bullet-} + HO_2^{\bullet}\ (pKa = 4.8) \quad (4.6)$$

Whereby, the hydroxyl peroxide radical formed in Equation 4.6 has a pK_a value of 4.8 above which it formed a superoxide radical as shown in Equation (4.7).

$$HO_2^{\bullet} \rightarrow O_2^{\bullet-} + H^+\ (pK_a = 4.8) \quad (4.7)$$

Various studies (Ullmann 1991; Kirk and Othmer 1996) have shown that ozone with an oxidation potential of $E_0 = 2.08V$ is a strong oxidiser and its oxidation reaction yields hydrogen peroxide. Likewise, Lide (1999) showed that at normal conditions of temperature and pressure, ozone has a very low solubility. In that regard, Ullmann (1991), Kirk and Othmer (1996) and Lide, (1999) proved that at room temperature, ozone is able to oxidise water molecules to hydrogen peroxide. This was supported by Glaze (1986) and is presented in Equations 4.8 &4.9.

$$H_2O_2 \rightarrow H^+ + H_2O^- \quad (4.8)$$

$$O_3 + H_2O- \rightarrow {}^{\bullet}O_2^- + {}^{\bullet}OH + O_2 \quad (4.9)$$

Moreover, based on the O_3 decline in DBD system, Gurol and Vatistas (1987) reported that the chemical instability of ozone may lead to its decay through systematic reaction chains resulting in the production of OH radicals and related intermediates species. Consequently, the fluctuating production of ozone might be due to the recombination of those species as shown in chemical Equations (4.10 – 4.16) below suggested by Tarr, (2003).

$$2O_3 + H_2O_2 \rightarrow 2\ OH + 3O_2 \quad (4.10)$$

$$O_3 + h\nu + H_2O \rightarrow H_2O_2 + O_2 \quad (4.11)$$

$$H_2O_2 + h\nu \rightarrow 2\ OH \quad (4.12)$$

$$O_3 + OH^- \rightarrow O_2^{\cdot -} + HO_2 \quad (4.13)$$

$$O_3 + HO_2^- \rightarrow HO^{\cdot} + O_2^{\cdot -} + O_2 \quad (4.14)$$

$$O_3 + O_2^{\cdot -} \rightarrow O_3^{\cdot -} + O_2 \quad (4.15)$$

$$O_3 + HO^{\cdot} \rightarrow HO_4 \quad (4.17)$$

Furthermore, ozone generated by the discharge dissolves into the plasma treated water and under alkaline conditions decomposes via a series of chain reactions to produce secondary $OH^{\bullet}$ radicals in water (Equation 4.18). The presence of H_2O_2 may accelerate the decomposition of ozone and increases the $OH^{\bullet}$ radical concentration (Equation 4.19). This process occurs very slowly at low pH, but at pH values above 5, it is greatly accelerated. This therefore justifies the prominent amount of ozone quantified at pH 2.5 in the DBD reactor compared to its lower concentrations detected at higher pH values.

$$2\ O_3 + H_2O + OH^- \rightarrow OH^{\bullet} + HO_2^{\bullet} + 2\ O_2 + OH^- \quad (4.18)$$

$$O_3 + H_2O_2 + OH^- \rightarrow OH^{\bullet} + HO_2^{\bullet} + O_2 + OH^- \quad (4.19)$$

The various disintegrations of ozone highlighted in the equations above consequently diminished its concentration in aqueous DBD and facilitated the generation of other active species. Conversely, the fluctuating values suggested that $O_3$was not only produced via one route but via multiple reaction mechanism possibilities such as those presented in Equations (4.10 – 4.19). In other words, the recombination of other generated active species yielded O_3. This therefore, led to the slight increase of its concentration at 60 min. The two processes mainly the decomposition of O_3 to active species and the recombination of the unstable oxygen based metabolites induced the behaviour of O_3 during the 60 min of DBD experimental run. Likewise, the high concentration of O_3 observed at elevated pH 10.5 and 8.5, suggest that in basic conditions, the rate of recombination of secondary species in DBD reactor increased, favouring the back formation of ozone and hence induced its accumulation in the solution. Since DBD technology appears as a robust AOP, these observations also suggest that it is difficult to predict the exact routes via which O_3 and its derivatives can be produced or

consumed in DBD system. Nevertheless, the most probable chemical reaction chains in DBD configurations have already been proposed by Gupta (2007) and reviewed by Mouele *et al*. (2015). The reconfigured DBD system certainly functioned well compared to other systems. That is, the highest amount of O_3, 0.79 M measured in the current DBD reactor after 60 mins is higher than 0.09 M of O_3 quantified after 30 min by *Tichonovas et al*., (2013) and much higher than 0.0001M of O_3 achieved after 66 min by (Marotta *et al.*, 2011) using different DBD reactor configurations.

4.2 Effect of pH on hydrogen peroxide production in DBD reactor

Besides O_3, hydrogen peroxide (H_2O_2) is another molecular reactive oxygen species (ROS) that has been widely known as an active antimicrobial agent with various applications including destruction of bacterial spores and viruses, and has minor toxicity properties (Von Woedtke *et al.*, 2004). The various procedures for its detection in aqueous media have also been reviewed by Mouele et al. (2018). In this study, the Eisenberg method (Sections 3.4.2 and 3.6.1.2) suggested by Eisenberg, (1943) and reinforced by Uher & Hoefer (1991) was found the most applicable, affordable and feasible technique for the quantification of H_2O_2 in aqueous milieu. In this method, the initial concentration of H_2O_2 is proportional to the absorbance of the peroxotitanyl ($TiO_2(SO_4)_2^{2-}$) complex solution measured at 407 nm. Therefore, a simple UV-VIS measurement can be used to approximate hydrogen peroxide concentration. Consequently the Eisenberg technique was used in this study to measure the H_2O_2 concentration generated in the DBD system at various applied conditions. That is, the effect of solution pH of distilled water on the generation of H_2O_2 was evaluated (as set out in Section 3.6.1.2) and the outcomes of this analysis are exhibited in Figure 4-2.

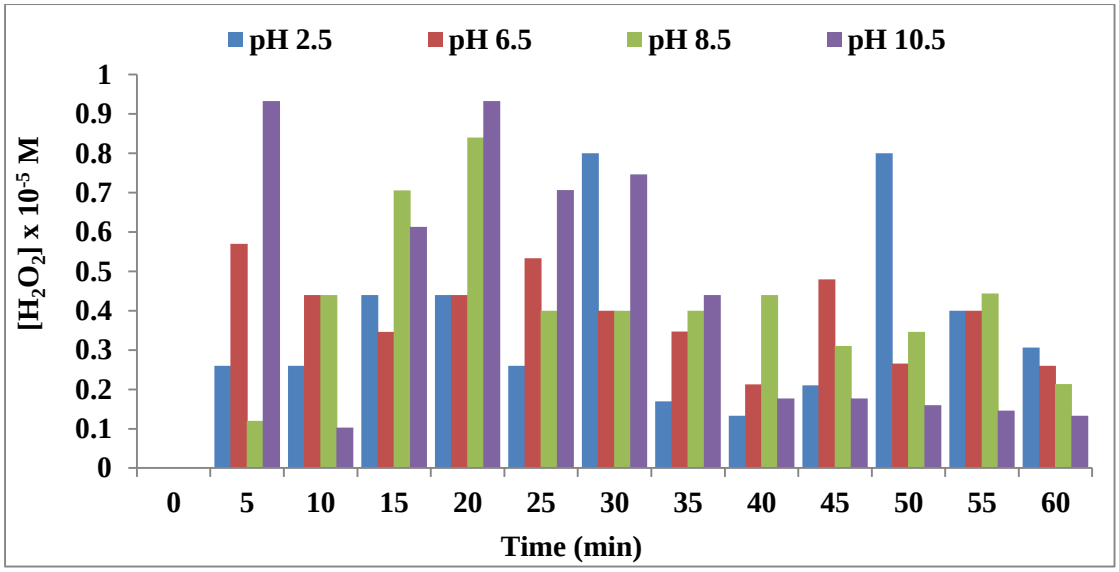

Figure 4.2: Effect of pH on hydrogen peroxide concentration over time in the DBD reactor. Experimental conditions, varied parameter: distilled water pH (from 2.5, 6.5, 8.5 to 10.5). Fixed parameters: applied voltage 6.8 kV, power 60 W, trip current 10 A, set current 60 mA, frequency 1000Hz, air flow rate 3 L/min, solution volume 1500 mL, 1.5 mm silver electrode, 50 g/L NaCl electrolyte, treatment time 60 minutes sampling every 5 min.

Figure 4-2 shows the impact of pH on the production of H_2O_2 from distilled H_2O at the applied conditions. The results in Figure 4-2 indicate that the amount of H_2O_2 at different pH values in the DBD reactor fluctuated with time and did not describe a continual trend. Nevertheless, the highest concentrations of H_2O_2 in DBD configuration was noticed at a basic pH of 10.5 and 8.5 respectively compared to acidic pH 2.5 and 6.5, separately. Consequently, at pH 10.5, the 0.933M of H_2O_2 detected after 5 min decreased to 0.613 M after 15 min and increased back to the initial value which progressively followed a sinusoidal decline to 0.133 M after 60 min. These results were similar to those achieved at pH 8.5 whereby, the 0.44 M of H_2O_2 measured after 10 min increased to 0.84 after 20 min and decayed to 0.213 M after 60 min. Alternatively, at pH 6.5, the 0.57 M of H_2O_2 decreasingly fluctuated down to 0.26 M after 60 min. The last variation of H_2O_2 concentration observed at pH 2.5 shows that 0.26 M H_2O_2 measured after 5 min increased up to 0.8 M after 30 min and fluctuated down to 0.306 M after 60 min. The fluctuating decrease of H_2O_2 concentration in both acidic and basic pH indicated that either H_2O_2 was being self decomposed, photo decomposed to H^+, H_2O^- and $OH^{\cdot}$ or was being used up to yield other oxygen based active/reactive species such as $O_2^{\cdot -}$, $O^{\cdot}$, O_2, etc. as shown in Equations (4.19 – 4.21) below.

$$H_2O_2 \rightarrow H^+ + H_2O^- \quad (4.20)$$

$H_2O_2 + h\nu \rightarrow 2\ OH^{\cdot}$ (4.21)

$O_3 + H_2O_2 + OH^- \rightarrow OH^{\bullet} + HO_2^{\bullet} + O_2 + OH^-$ (4.22)

Moreover, although the highly energised electrons around the inner tube (first dielectric) of the DBD configuration may have a short migration length, a reasonable density of these charge particles often escape to the plasma zone and diffuse into the bulk solution and become solvated according to Equation 4.23.

e^- (Plasma zone of DBD) + n $H_2O \rightarrow e^-_{aq}$ (solvated) (4.23)

Moreover, at the interface of the plasma channel and water, one of the most prominent reaction mechanistic pathways for the production of aqueous free radicals is the dissociation of water molecules through collisional excitation with aqueous energised electrons. This results in the formation of active hydroxyl and hydrogen radicals as given by Equation (4.24).

H_2O (DBD discharge) + $e^- \rightarrow {}^{\bullet}OH + H^{\bullet} + e^-$ (4.24)

Similarly, close to the plasma-water interface and in the bulk water, the aqueous energetic electrons react with H_2O_2 and yield hydroxyl radicals as from Equation (4.25).

$e_{aq}^- + H_2O_2 \rightarrow {}^{\bullet}OH + OH^-$ (4.25)

The H_2O_2 produced in the solution may also react with various aqueous species such as $OH^{\cdot}$, $H^{\cdot}$, O_2, $O^{\cdot}$, etc. forming diverse secondary species such as perhydoxyl radicals ($HO_2^{\cdot}$), H_2, $O_2^{\cdot -}$, H+, H_2O, etc. as described in the chain of Equations (4.26 - 4.33) below.

$H_2O_2 + OH^{\cdot} \rightarrow H_2O + HO_2$ (4.26)

$H_2O_2 + H^{\cdot} \rightarrow H_2O + OH^{\cdot}$ (4.27)

$H_2O_2 + H \rightarrow OH + H_2O$ (4.28)

$H_2O_2 + H \rightarrow HO_2 + H_2$ (4.29)

$H_2O_2 + O_2 \rightarrow 2HO_2$ (4.30)

$H_2O_2 + O^{\cdot} \rightarrow HO_2^{\cdot} \rightarrow OH^{\cdot}$ (4.31)

$H_2O_2 + O^{\cdot -} \rightarrow H_2O + O_2^{\cdot -}$ (4.32)

$H_2O_2 + OH^{\cdot} \rightarrow H_2O + H^+ + O_2^{\cdot -}$ (4.33)

Consequently, the disintegration processes of H_2O_2 showed in Equations (4.26 – 4.33) contributed to the decline of its concentration in the DBD reactor. Conversely, the abundance of H_2O_2 in basic pH media complements the high concentration of O_3 at basic pH values previously described. Indeed, in the previous section, it was shown that at a pH greater than 7 the rate of decomposition of O_3 increased, making O_3 highly unselective and hence interacting with any type of inorganic species, consequently boosting various chemical reactions such as that of O_3 and H_2O that mostly contributed to the production of H_2O_2 as shown in Equation (4.34).

$O_3 + h\nu + H_2O \rightarrow H_2O_2 + O_2$ (4.34)

Besides, the OH radicals resulting from the water molecule splitting by UV light generated in the DBD system and its dissociation by e^-_{aq} may recombine to form H_2O_2 as disclosed in Equations (4.35 – 4.36). Likewise, the perhydroxyl radicals early generated in Equations (4.29 & 4.31) may self react or interact with H_2 yielding H_2O_2 as indicated in Equations (4.37 - 4.38). Furthermore, due to the stirring effect, constant air flow/feeding into the system and the continuous UV light irradiation/glow in the bulk as sustained by Mededovic (2007), water molecules in the DBD reactor might have self collided resulting in the production of H_2O_2 as indicated in Equations (4.39 – 4.41).

$H_2O \rightarrow H + OH^{\cdot}$ (4.35)

$OH^{\cdot} + OH^{\cdot} \rightarrow H_2O_2$ (4.36)

$HO_2^{\cdot} + HO_2^{\cdot} \rightarrow H_2O_2 + O_2$ (4.37)

$HO_2 + H_2 \rightarrow H_2O_2 + H$ (4.38)

$2H_2O \rightarrow H_2 + H_2O_2$ (4.39)

$6H_2O \rightarrow 4H_2 + 2H_2O_2 + O_2$ (4.40)

$O\ (^1D) + H_2O\ (l) \rightarrow H_2O_2$ (4.41)

These chemical reactions believed to occur in DBD reactor would contribute to the fluctuating increase of H_2O_2 concentration in the system at low or elevated pH. In total, the fluctuating increase and decrease of H_2O_2 in the DBD configuration presented in Figure 3.3 demonstrated the numerous chains of chemical reactions occurring during the DBD experimental run. These were summarised by Gupta (2007) and presented in Figure 3-3. This was earlier sustained by Ullmann (1991) and Kirk and Othmer (1996). Even though H_2O_2 does not directly attack organic pollutant, on its own, it represents a potential source of secondary reactive oxygen species, mainly OH radicals that directly or indirectly degrade the target contaminants in water and wastewater.

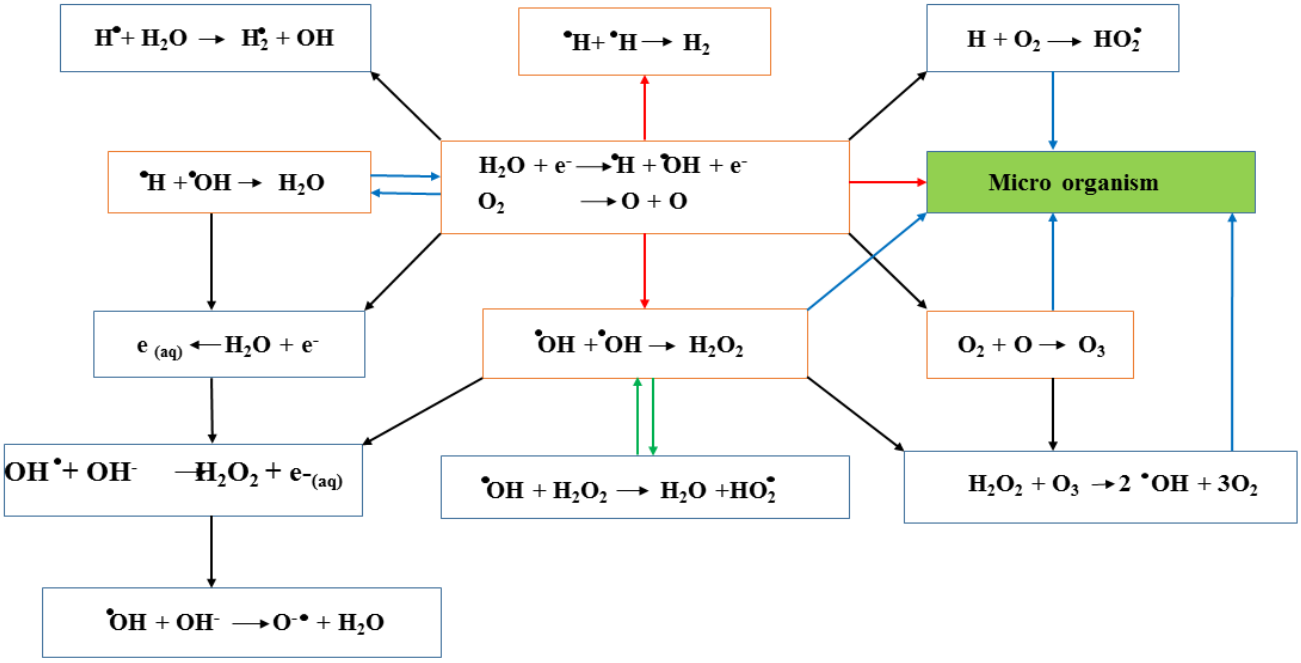

Figure 4.3: Principal mechanistic reaction pathways leading to the formation of free reactive species in double cylindrical dielectric barrier discharge/corona discharge configurations (whereby the blue dots denote reactions occurring in the bulk solution; the red dots indicate the interactions happening at the interface and inside the plasma channel) (Gupta, 2007b).

4.3 Quantification of OH radicals in DBD reactor for water and wastewater treatment using distilled water

Advanced oxidation processes (AOPs) commonly converge towards the production of non-toxic and highly non-selective hydroxyl radicals (OH·) that initiate oxidation processes (Lomoră, Drăghici and Eneşca, 2011). In the preceding sections, the DBD reactor was proved adequate in the production of various free reactive species that could be measured, among which OH radicals. The OH radicals with an oxidation potential of 2.8 eV mineralise any type of pollutant. Therefore, the efficiency of a particular AOP system such as the actual DBD may depend on the amount of OH generated. In this regard, Mouele et al. (2018) reviewed the different methods used for the quantification of OH radicals. From their study, the authors emphasised that the fluorescent technique using Terephtallic acid (TA) as the chemical probe was the ideal measurement procedure that is cost effective and fast and feasible. Therefore, the TA method was used in this research to approximate the amount of OH radicals generated in the DBD system at the applied conditions. This was achieved by investigating the impact of

pH on OH concentration in distilled water within 60 min of DBD run at corresponding conditions.

4.3.1 Effect of solution pH on the production of OH radicals

During the DBD experiment, air which used as a feeding gas is a source of various N and O acidic species such as nitrites and nitrates that form and often lower the pH of the solution. So as to prevent this situation, a buffer solution was employed to maintain the desired solution pH. Also, an opposite situation whereby no buffer was added to the solution was considered.

4.3.1.1 Effect of solution pH on OH production in the absence of buffer

The solution pH was adjusted using H_2SO_4 and NaOH to a desired value; however no buffered solution was added. Thereafter, the effect of solution pH on OH concentration was assessed by performing a DBD experiment at each pH value for 60 min at the corresponding conditions. The results of these experiments were plotted and are presented in Figure 4-4.

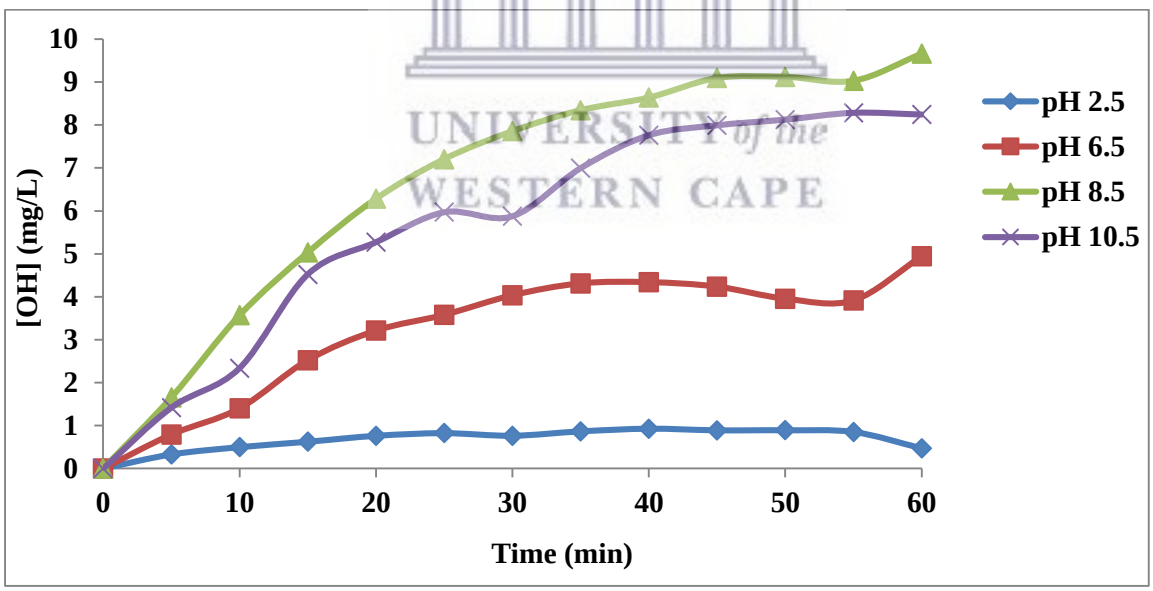

Figure 4.4: Impact of solution pH on OH· production in the DBD reactor without buffer at the following experimental conditions. Varied parameter: distilled water (pH from 2.5, 6.5, and 8.5 to 10.5). Fixed parameters: applied voltage 6.8 kV, power 60 W, trip current 10 A, set current 60 mA, frequency 1000 Hz, air flow rate 3 L/min, solution volume 1500 mL, 1.5 mm silver electrode, 50 g/L NaCl electrolyte, treatment time 60 minutes, sampling every 5 min.

The effect of pH on OH· concentration in the absence of buffer solution is presented in Figure 4-4. The results show that at pH 6.5, 8.5 and 10.5 the amount of OH· generated in the DBD reactor continuously increased with an increase of DBD run time. At pH 2.5 the OH· concentration was almost constant during the 60 min of the experimental run. Yet, for the 60 min of DBD experiment, the highest amount of OH· radicals was trapped at pH 10.5 followed by pH 8.5, 6.5 and 2.5, respectively. For instance after 60 min of DBD run time, 9.661 mg/L of OH· radical was achieved at pH10.5 compared to 8.24, 4.941 or 0.473 mg/L OH· reached at pH 8.5, 6.5 and 2.5, respectively. This trend was observed at each sampling time during the DBD experiment. This therefore implied that in the absence of buffer, high amounts of OH· radicals were generated from distilled water at basic pH. These results are in line with the results obtained in sections 4.3.1 and 4.3.2. In fact OH radicals remain the targeted non-toxic and non-selective species in most AOPs particularly in DBD technology. In the ozone section, the equation showing the disintegration of O_3 mainly resulted in the formation of OH·. In addition**,** the homolitic cleavage of H_2O_2 and its decomposition also yields OH· as shown in Figure 4-4. Therefore, it was evident that OH· concentration increased with an increase of treatment time and a high concentration of OH· (9.661 or 8.246 mg/L) was achieved in basic pH (10.5 or 8.5). These observations compliment the results obtained by (Kanazawa *et al.*, 2011) who also noticed an increase in time – integrated OH· concentration trapped with TA during pulsed discharge plasma process. Even if in acidic pH (6.5 and 2.5), the concentration of OH· radicals increased with treatment time, the amount of OH· at these pH values were less than those obtained in basic conditions as supported by Sahni & Locke (2006a). This means that DBD experiments conducted in acidic environment in the absence of buffer favours the production of O_3 and other active species (Mason *et al.*, 1994; Fang, Mark and von Sonntag, 1996; Sahni and Locke, 2006a). In other words, at pH below 7, O_3 and related oxygen intermediates other than H_2O_2 and OH· were majorly produced in the DBD configuration (Beltrán, Encinar and Alonso, 1998; Beltrán *et al.*, 2008). On the other hand, these results suggest that at acidic pH values, OH· radical scavengers such as nitrates + nitrites and sulphates,' etc. might have been present in the solution and consequently consumed the generated OH·, hence reducing its amount in the solution (Joshi *et al.*, 1995; Neppolian *et al.*, 2002). The results obtained in this study are in accordance the outcomes of Badmus et al. (2016) who successfully studied the behaviour of OH· radicals generated in a laboratory scale sonicator using therephthalic acid in the presence of phosphate buffer (1 M KH_2PO_4 and 1 M Na_2HPO_4). The authors showed that the amount of OH· radicals scavenged by TA in the sonicator for 60 minutes gradually increased with an increase of the treatment time and approximately 7.91 x

10^{-6} M of OH· was quantified after 60 minutes of sonication. This was probably linked to the fact that in the sonication system, OH· preferentially reacted with TA than with $H_2PO_4^-$ and HPO_4^- scavengers. Their study further confirmed that TA is an effective probe for the trapping of OH· radicals in aqueous systems.

4.3.1.2 Effect of solution pH on OH production in the presence of buffer

In this section, the impact of pH on OH concentration in the DBD reactor was also assessed but in the presence of 250 mL KH_2PO_4 buffer at the same conditions as described in section 3.6.1.4. The results of these experiments are shown in Figure 4-5.

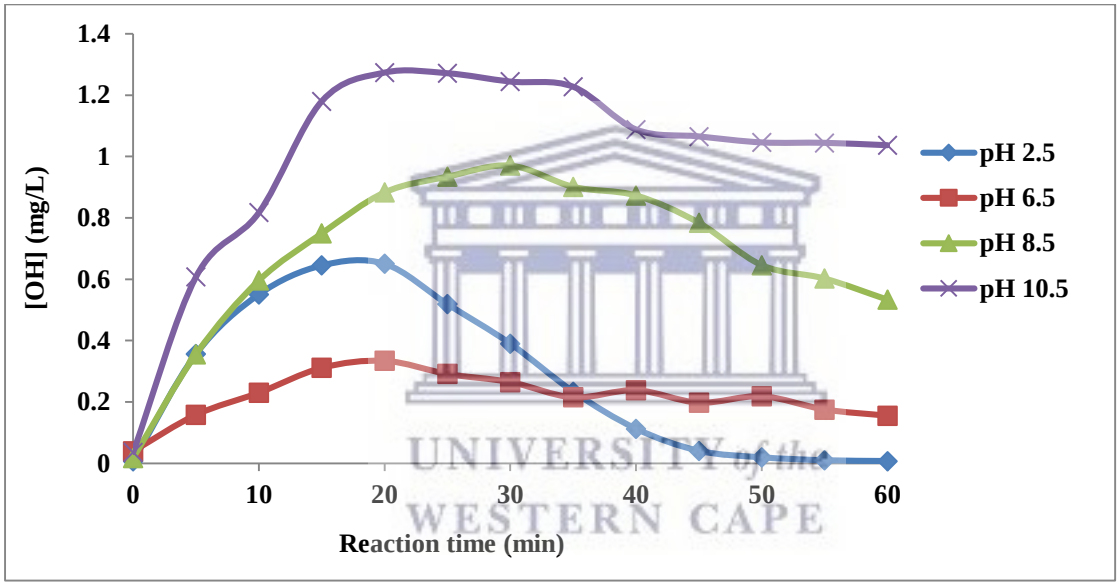

Figure 4.5: Impact of initial solution pH with phosphate buffer on the production of OH· in the DBD reactor. Varied parameter: distilled water pH from 2.5, 6.5, and 8.5 to 10.5. Fixed parameter: solution pH 5.49, applied voltage 6.8 kV, power 60 W, trip current 10 A, set current 60 mA, frequency 1000Hz, air flow rate 3 L/min, solution volume 1500 mL, 1.5 mm silver electrode, 50 g/L NaCl electrolyte, treatment time 60 minutes sampling every 5 min.

It was noticed that in the absence of buffer, the highest concentration of OH (9.66 mg/L) was achieved at pH 10.5 compared to (8.24 mg/L) reached at pH 8.5. In contrast when a small amount of buffer (Na_2HPO_4 and KH_2O_4) was introduced in the reactor only 1.27 mg/L of OH·, was reached at pH 10.5 after 20 min of DBD while 0.97 mg/L was attained at pH 8.5 after 30 min of DBD. These results suggest that in the presence of buffer in the solution, at pH 10.5 and

8.5, the phosphate anion scavengers, mainly $H_2PO_4^-$, HPO_4^- and PO_4^-, reacted slowly with OH radicals as demonstrated in Equations (4.42- 4.50)(Kochany and Lipczynska-Kochany, 1992).

$$^{\bullet}OH + H_2PO_4^- \rightarrow HPO_4^{-\bullet} + H_2O \quad (4.42)$$

$$^{\bullet}OH + H_2PO_4^- \rightarrow H_2PO_4^{\bullet} + HO^- \quad (4.43)$$

$$^{\bullet}OH + HPO_4^{2-} \rightarrow {}^{\bullet}HPO_4^- + OH^- \quad (4.44)$$

$$^{\bullet}OH + PO_4^{3-} \rightarrow PO_4^{2-\bullet} + HO^- \quad (4.45)$$

$$^{\bullet}H_2PO_4 + H_2O_2 \rightarrow H_2PO_4^- + {}^{\bullet}HO_2 + H^+ \quad (4.46)$$

$$^{\bullet}HPO_4^- + H_2O_2 \rightarrow HPO_4^{2-} + 2H^+ + {}^{\bullet}O_2^- \quad (4.47)$$

$$^{\bullet}H_2PO_4 + OH^- \rightleftarrows {}^{\bullet}HPO_4^- + H_2O \quad (4.48)$$

$$^{\bullet}H_2PO_4 + {}^{\bullet}H_2PO_4 \rightarrow H_2P_2O_8^{4-} + 2H^+ \quad (4.49)$$

$$^{\bullet}PO_4^{2-} + {}^{\bullet}PO_4^{2-} \rightarrow P_2O_8^{4-} \quad (4.50)$$

Hence scavenging led to the progressive decline of OH· amount in basic conditions as shown in Figure 4-5. This trend was also observed in acidic pH after the introduction of phosphate buffer in the solution at pH 6.5and 2.5. The amount of phosphate scavengers produced at pH 6.5 were probably higher than that obtained at pH 2.5 in the first 35 min. This consequently resulted in low concentrations (0.33 mg/L) of OH· at pH 6.5 after 20 min of DBD with phosphate buffer compared to 0.65 mg/L OH· achieved at pH 2.5 at the same sampling time. Beyond 35 min of DBD experiment, the abundance of phosphate scavengers at pH 2.5 was higher than that at pH 6.5. This therefore, resulted in a higher concentration of OH radicals (0.22 mg/L) at pH 6.5 after 50 min of DBD sampling compared to 0.02 mg/L of OH achieved at pH 2.5 at the same sampling time in the presence of the phosphate buffer. These side reactions show that during the formation of OH· radicals in DBD system, scavengers originating from the feeding gas (dry air) buffer such as phosphates might have reduced the amount of OH radical formed in the reactor.

The influence of pH on the amount of OH radicals in the DBD reactor in the presence of phosphate buffer, are presented in Figure 4-5. The trends observed in Figure 4-5 still show that during the 60 min of the DBD experimental run, the highest concentrations of OH radicals were achieved at basic starting pH 10.5 and 8.5 respectively. Specifically, after 25 min of the DBD experiment, 1.271 and 0.934 m/L OH were respectively reached at pH 10.5 and 8.5 compared to 0.518 and 0.291 mg/L obtained at pH 2.5 and 6.5. However, the amount of OH radicals in acidic initial pH showed unusual fluctuation in the first 35 min, where the concentration of OH· radicals at pH 2.5 was higher than that reached at pH 6.5. Beyond 35 min, the amount of OH· obtained at pH 6.5 became higher than that achieved at pH 2.5. For example after 20 min of DBD run, the 0.650 mg/L achieved at pH 2.5 was higher than 0.334

mg/L OH· reached at pH 6.5. At 35 min of DBD experiment, the same amount of OH· radicals 0.215 mg/L was reached at both pH 2.5 and 6.5. However, after 40 min the 0.238 mg/L OH· attained at pH 6.5 was higher than 0.112 mg/L OH· obtained at pH 2.5. Despite the presence of the phosphate buffer solution in the DBD reactor, high amounts of OH radicals were produced at basic pH as a result of the abundance of O_3 and H_2O_2 generated and their interaction certainly yielded OH radicals. Apart from this, extended side chain reactions such as the disintegration of H_2O_2 by UV light might have also contributed to improving the concentration of OH in DBD reactor at higher pH.

The main precursor of OH· radicals in the DBD might have been used up by interaction with various species to generate various oxygen based ionic and radical or molecular unstable intermediates as earlier shown in Equations (4.26 – 4.33). On the other hand, Kanazawa et al. (2011) sustained that the decay of OH· in non-thermal plasma is mainly caused by OH· diffusion from the discharge network and the termination reactions or recombination reaction during which the following Equations (4.51 – 4.56) take place (Joshi *et al.*, 1995; Mededovic, 2007).

$OH^{\cdot} + OH^{\cdot} + (M) \rightarrow H_2O_2 + (M)$ (4.51)

$OH^{\cdot} + OH^{\cdot} \rightarrow H_2O + O$ (4.52)

$OH^{\cdot} + O \rightarrow O_2 + H$ (4.53)

$OH^{\cdot} + H \rightarrow O + H_2$ (4.54)

$OH^{\cdot} + H + (M) \rightarrow H_2O + (M)$ (4.55)

$OH^{\cdot} + H \rightarrow H_2O$ (4.56)

These in turn reduced the amount of OH· radical either with or without buffer in the solution. Similar observations on OH· radicals' behaviour in open DBD system were reported by Tijani et al. (2017) who quantified the concentration of OH· radicals and secondary intermediates in DBD during degradation of 2-nitro phenol. These results consequently show that during treatment of specific water effluent by DBD non-thermal plasma technologies, one should pay attention to chemical additives or anions which instead of boosting the detoxification process, may impede the removal of the targeted pollutants due to competitive reactions of OH· radicals with scavengers leading to the formation of various reactive aqueous species.

4.3.1.3 pH trends during quantification of OH radicals in the DBD reactor

In this section, the pH trends during quantification of OH· radicals was evaluated in the absence of buffer. In this regards, the initial pH value was regulated using H_2SO_4 and NaOH, so its tendency over the 60 min of DBD experiment was followed at the applied conditions (Section 3.6.1.4). The results of these assessments are shown in Figure 4-6.

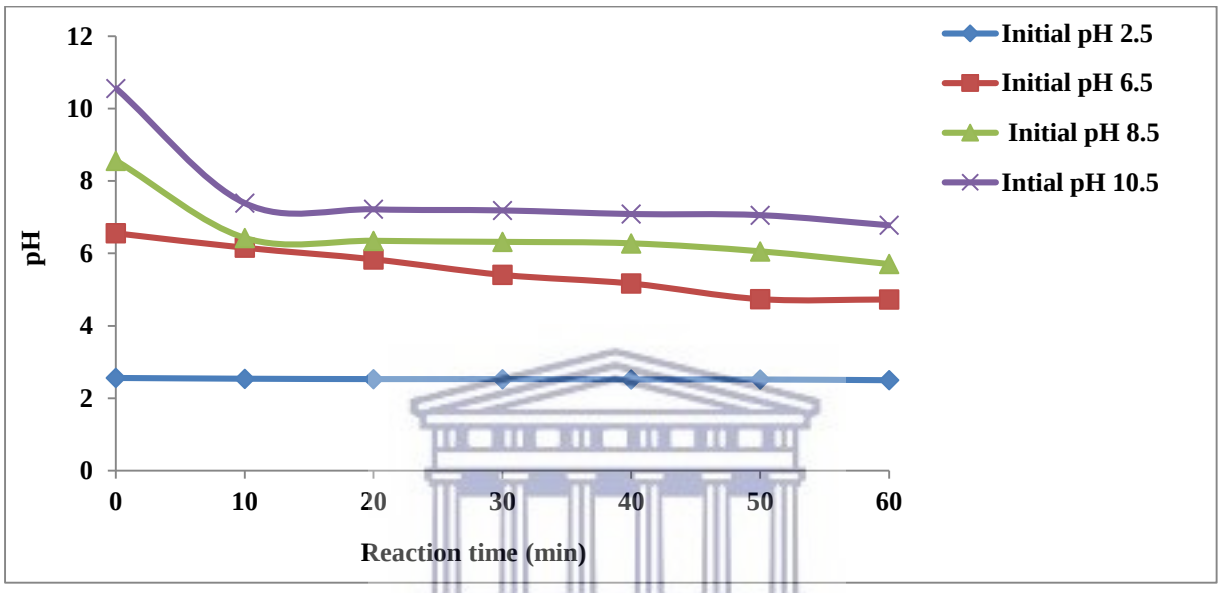

Figure 4.6: pH trends during the production of OH in the DBD reactor at the following experimental conditions.Varied parameter: distilled water pH (from 2.5, 6.5, 8.5 to 10.5). Fixed parameter: applied voltage 6.8 kV, power 60 W, trip current 10 A, set current 60 mA, frequency 1000Hz, air flow rate 3 L/min, solution volume 1500 mL, 1.5 mm silver electrode, 50 g/L NaCl electrolyte, treatment time 60 minutes sampling every 10 min.

The pH trends during quantification of OH· radicals in the DBD configuration is displayed in Figure 4-6. The outcomes of these assessments indicate that the basic pH values experienced a significant decrease in the first 10 min which slightly declined with time. That is, the initial pH 10.5 significantly declined to 7.9 after 10 min of DBD run and thereafter slightly decreased further to 6.78 after 60 min. Moreover, the initial pH 8.5 also significantly decreased to 6.43 in the first 10 min of DBD and then slightly dropped to 5.71 after 60 minutes of DBD run. Likewise, the initial pH 6.5 slightly and progressively decreased to 4.73 over the 60 min of DBD run. The experiment conducted at pH 2.5 did not experience any change, the initial pH 2.5 remained constant during the 60 min of DBD experiment. The decline of pH 10.5, 8.5, 6.5 to their lower values in the first 10 min of DBD run was certainly due to the formation of acidic

species in the solution. Indeed, the dry air circulated in the air gap of the DBD reactor contains N_2 and O_2 whose interaction with energised electrons lead to excited N_2^* and O_2^* metastable species which generate not only UV light when falling back to their energy ground states, but largely contribute to the production of oxygen and nitrogen based species such as O_2, $O^{\cdot}$, O_3, $N^{\cdot}$, N_2, NO, N_2O etc. either via ionisation, dissociation and recombination or other chemical reactions according to Equations (4.57 – 4.72) (Hoeben, 2000; Jo and Mok, 2009; Massima, 2014).

$O_2 + e^- \rightarrow 2O + e^-$ dissociation (4.57)

$O_2 + e^- \rightarrow O_2^+ + 2e^-$ ionisation (4.58)

$O_2 + e^- \rightarrow O_2^-$ attachment (4.59)

$O_2 + e^- \rightarrow O^- + O$ dissociative attachment (4.60)

$O_2 + O \rightarrow O_3$ association (4.61)

$N_2 + e^- \rightarrow 2N + e^-$ dissociation (4.62)

$N_2 + e\text{-} \rightarrow N_2^+ + 2e^-$ ionisation (4.63)

$N + O \rightarrow NO$ association (4.64)

$NO + O \rightarrow NO_2$ association (4.65)

$N_2^+ + O_2^- \rightarrow 2NO$ recombination (4.66)

$N_2 + O \rightarrow N_2O$ association (4.67)

$N2+O \rightarrow NO+N$ (4.68)

$N+O_2 \rightarrow NO+O$ (4.69)

$NO+ O_3 \rightarrow NO_2+O_2$ (4.70)

$NO_2 + O_3 \rightarrow NO_3 + O_2$ (4.71)

$NO_3 + NO_2 \rightarrow N_2O_5$ (4.72)

These active and unstable species formed in the plasma zone are diffused into the solution through the continuous air flow and become solvated. Their coexistence in DBD aqueous media lead to the formation of various acids including nitric and nitrous acid (HNO_2 and HNO_3) which consequently induced the decrease of the acidity in DBD reactor as shown in Equations (4.73 – 4.77) (Jo and Mok, 2009).

$2NO_2 + H_2O \rightarrow HNO_2 + HNO_3$ (4.73)

$HNO \rightarrow H^+ + NO^-$ (4.74)

$HNO \rightarrow H^+ + NO^-$ (4.75)

$OH^{\cdot} + OH^{\cdot} \rightarrow H_2O_2$ (4.76)

$2H2O + UV \rightarrow H_3O^+ + OH^-$ (4.77)

All these interactions of O_2 and N_2 derivatives in non-thermal plasma technologies have already been summarised by Lopez (2008). The decrease of pH in the first 10 minutes and its constant tendency from 10 to 60 min of DBD experiment could suggest that the amount of the generated acidic species was getting close to their threshold boundaries. After 10 minutes, some of the acidic species might have behaved as scavengers and consumed the OH radicals produced in the system and hence promoted the abundance of nitrogen and oxygen like species that reinforced the acidity in the solution. These observations were also reported by Magureanu et al. (2013) who claimed that during plasma discharge process the decrease in pH is often due to the formation of nitric and nitrous acids in such a way that the transferred gaseous nitrogen oxides (NO, NO_2) from the air gap into the bulk solution, are converted into nitrite (NO_2^-) and nitrate ions (NO_3^-) and further to nitric acid (HNO_3), nitrous acid (HNO_2) and peroxynitrous acid (ONOOH). In addition to these, the authors stated that the H_2O_2 produced in acidic conditions (Equations 4.36 – 4.41) and often considered as a weak acid, even at a lower amount might have slightly contributed to the decline of pH observed in Figure 4-6. Besides, the hydronium cations (H_3O^+) resulting from water splitting by UV light in DBD reactor might have participated in the pH decay to acidic values (Burlica *et al*., 2004; Zhang *et al*., 2007; Porter *et al*., 2009.; Dojčinović *et al*., 2011). These arguments were recently supported by Tijani *et al*., (2017). For the DBD experiment performed at pH 2.5, the undisturbed behaviour of pH 2.5 suggest that 2.5 was the operational pH value at which acidic species that were produced did not change the pH and hence the pH trend in the DBD reactor shows that adjusting initial pH is not an effective strategy as the default low pH over time confounds any pH adjustment.

4.3.2 Effect of sodium carbonate on the production of OH radicals in DBD system

It is demonstrated in previous sections of this chapter that OH· radicals, being the main reactive species generated by most AOPs, can interact in side reactions with solution impurities as well as with the targeted contaminants themselves. The solution by-products often referred to as scavengers, may preferentially react with OH· radicals and thus reduce OH· concentration in the solution. This consequently limits or slows the oxidation and mineralisation of the targeted pollutants. So scavengers such as carbonates (CO_3^{2-}), bicarbonate (HCO_3^{2-}), Cl^-, SO_4^{2-}, PO_4^{3-} etc., in AOP are believed to reduce the amount of OH· generated in the DBD system. Therefore the effect of carbonate scavengers on OH· radicals' concentration was investigated in this study. That is, the impact of scavenger on OH concentration in DBD system was evaluated by

introducing 250 mL of sodium carbonate (Na_2CO_3) in the DBD reactor at concentrations that varied from 0.01, 0.02 to 0.04 M in the presence of (Na_2HPO_4 and KH_2O_4) buffer at the applied conditions as described in section 3.6.1.5. The results of these investigations are shown in Figure 4-7.

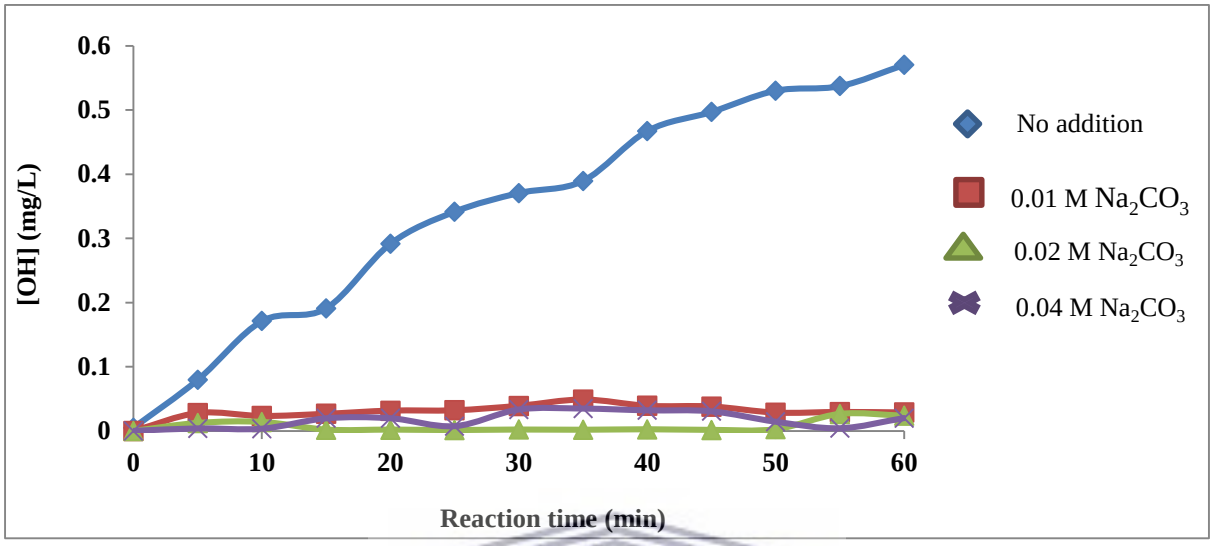

Figure 4.7: Impact of sodium carbonate (Na_2CO_3) scavenger concentration on the production of OH in DBD reactor in the absence of phosphate buffer at the following experimental conditions.Varied parameters: Na_2CO_3 mass 1.59, 3.18 g and 6.36 g were calculated according to Appendix 1 respectively and were dissolved in 1.5 L of 2 mM TA solution; Fixed parameter: solution initial pH, 5.49, peak voltage 6.8 kV, power 60 W, trip current 10 A, set current 60 mA, Frequency 1000 Hz, air flow rate 3 L/min, solution volume 1500 mL, 1.5 mm silver electrode, 50 g/L NaCl electrolyte, treatment time 60 minutes sampling every 5 min.

The influence of bicarbonate/carbonate anions on OH· radical concentration in the DBD reactor at the applied conditions is presented in Figure 4-7. The outcomes of these experiments point out that in the absence of phosphate buffer and Na_2CO_3 scavenger, the amount of OH· radicals in the DBD reactor progressively increased with an increase of DBD reaction time. This trend is in accordance with the results previously obtained in Figure 4-4 in the absence of phosphate buffer in the solution. In contrast the concentration of OH· radicals significantly decreased with addition of Na_2CO_3 in the DBD system. Specifically, after 35 min of the DBD experiment, the amount of OH· radicals generated in the absence of scavenger was found to be about 0.389 mg/L which considerably decreased to 0.034, 0.032 and 0.001 mg/L upon addition of 1.59, 3.18 g and 6.36 g of Na_2CO_3 in 1.5 L of 2 mM TA solution, respectively in the DBD reactor, hence corresponding to 0.01, 0.02 and 0.04 M of Na_2CO_3. This trend was visible at all sampling

times and for all three molarities of the scavenger during the DBD experiments. This observation shows that $NaCO_3$ significantly affected the amount of OH· radical generated in DBD reactor. This was certainly due to the scavenging interaction of carbonate/bicarbonate (CO_3^{2-}/HCO_3^-) with OH· radicals as shown in the series of Equations (4.78 -4.89) earlier described by Guy & Eng (1992).

$CO_3^{2-} + H_2O \rightarrow HCO_3^- + OH^-$ (4.78)

$^{\bullet}CO_3^- + H_2O_2 \rightarrow HCO_3^- + {}^{\bullet}HO_2$ (4.79)

$HCO_3^- + OH^- \rightarrow CO_3^{2-} + H_2O$ (4.80)

$HCO_3^- + OH^{\bullet} \rightarrow {}^{\bullet}CO_3^- + H_2O$ (4.81)

$HCO_3^- + {}^{\bullet}O_2^- \rightarrow {}^{\bullet}CO_3^- + HO_2^-$ (4.82)

$OH^{\bullet} + HCO_3^- \rightarrow CO_3^{-\bullet} + H_2O$ (4.83)

$CO_3^{2-} + {}^{\bullet}OH \rightarrow CO_3^{2-} + OH^-$ (4.84)

$^{\bullet}CO_3^- + O_3^- \rightarrow CO_3^- + O_3$ (4.85)

$CO_3^{2-} + O^- + H_2O \rightarrow CO_3^- + 2OH^-$ (4.86)

$^{\bullet}CO_3^- + {}^{\bullet}O_2^- \rightarrow CO_3^{2-} + O_2$ (4.87)

$^{\bullet}CO_3^- + {}^{\bullet}HO_2 \rightarrow CO_3^{2-} + {}^{\bullet}HO_2$ (4.88)

$OH^{\bullet} + CO_3^{2-} \rightarrow CO_3^{-\bullet} + OH$ (4.89)

Similar impact of carbonate and bicarbonate anions on OH· in solution was already claimed by Buxton et al. (1988) and Sahni & Locke (2006b). For decades, the oxidising CO_3^{2-}/HCO_3^- couple has been claimed to be effective scavengers of OH· radicals in aqueous media (Abdullah *et al*.,1990; Kochany *et al*., 1992). This negative effect of HCO_3^- and CO_3^{2-} anions deactivating the OH· radicals as shown in Equations 1 &2 has been investigated by Staehelin & Hoigné (1983); Hoigne (1988) and Tschirch et al. (2008), respectively. Recently, the scavenging effect of carbonate and bicarbonate anionic species on OH· radicals, was reported by Ann Liebert *et al*. (1999); Qifu *et al*. (2008); Wang *et al*. (2000); Neppolian *et al*. (2002). This further implies that, during degradation of organic pollutants in the DBD reactor, the presence of species such as CO_3^{2-}, HCO_2^-, SO_4^{2-} or NO_2^- may reduce the amount of OH· produced and hence slow down the mineralisation process of the targeted compounds. Even though high degradation percentages of pollutants such as dyes might be achieved, the amount of scavenger in the solution may thus significantly impact on the degree of mineralisation /decomposition of the targeted pollutant, hence these species should be controlled or removed to ensure an adequate amount of OH· radical is generated that majorly contributes to the destruction of targeted pollutants in the DBD reactor.

4.3.3 Effect of sodium chloride scavenger on the generation of OH radicals

Besides Na_2CO_3, NaCl that usually is considered in the form of chloride anion (Cl^-) was also considered as the second scavenger and its impact on OH· concentration in the DBD reactor was also investigated in the presence of (Na_2HPO_4 and KH_2O_4) buffer by varying its amount from 0.01, 0.02 to 0.04 M at the corresponding conditions as described in section 3.6.1.5. The results of these investigations are exhibited in Figure 4-8.

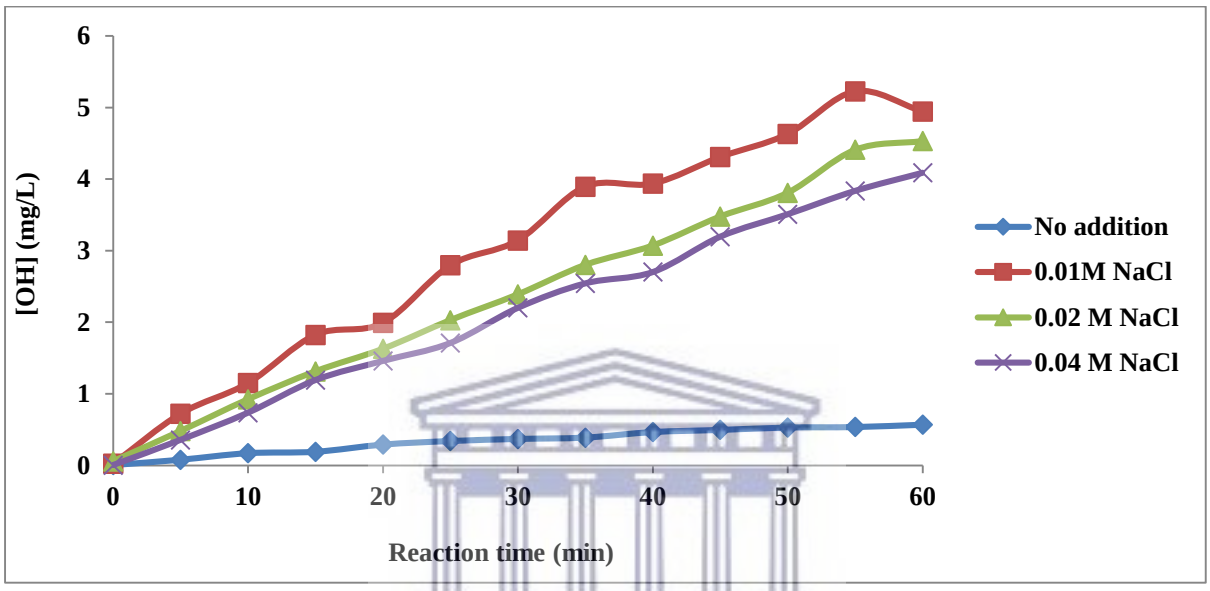

Figure 4.8: Impact of NaCl scavenger concentration on OH· production in the DBD reactor without sulphate buffer at the following experimental conditions. Varied parameter: NaCl concentration 0.01, 0.02, or 0.04 M. Fixed parameters: solution initial pH 5.49, applied voltage 6.8 kV, power 60 W, trip current 10 A, set current 60 mA, frequency 1000Hz, air flow rate 3 L/min, solution volume 1500 mL, 1.5 mm silver electrode, 50 g/L NaCl electrolyte, treatment time 60 minutes sampling every 5 min.

The effects of NaCl on OH· concentrations are presented in Figure 4-8. The results show that after addition of NaCl in DBD system, the concentration of OH· radical continuously increased with DBD run time and was well above 0.57 mg/L OH· earlier obtained in distilled water in the presence of the phosphate buffer as shown in Figure 4-5 but without the addition of Na_2CO_3. In fact it was expected that OH concentration would be below 0.57 mg/L upon the addition of NaCl. Unlike in the case of Na_2CO_3, the addition of NaCl in the DBD system boosted the production of OH radicals to a considerable extent. It can also be observed that the concentration of OH· increased with a decrease in the amount of NaCl. That is, high concentrations of OH· radicals were achieved with the addition of 1.59 g NaCl followed by

4.98 g and 9.64 g NaCl in 1.5 L of 2 mM TA in the DBD reactor and hence corresponding to 0.01, 0.02 and 0.04 M NaCl molarities, respectively. For instance after 25 min of DBD experiment, 2.796 mg/L OH· was obtained with 0.01 M NaCl, which was higher than 2.030 or 1.710 mg/L OH· obtained with 0.02, 0.04 M of NaCl in the presence of phosphate buffer, respectively. These results demonstrate that NaCl in the actual DBD configuration is not a scavenger but an OH· promoter. The concentrations of $OH^{\bullet}$ obtained in the presence of phosphate buffer (with the highest OH· amount of 5.22 mg/L at pH 5.49) in Figure 4-5 (Section 4.3.2) are below those achieved with NaCl in Figure 4-8 (4.94 mg/L at pH 6.5) in the absence of phosphate buffer. This clearly shows that NaCl slightly improved $OH^{\bullet}$ production in the DBD reactor. Indeed, during the dissociation of NaCl to Na^+ and Cl^- in the solution. The cation Na^+ readily reacts with dissociated water to yield sodium hydroxide (NaOH) whose further decomposition might have resulted in the formation of hydroxide anions (OH^-). Consequently, the reaction of OH^- with various aqueous species formed by addition of NaCl as shown in Equations (4.90 - 4.97) could amplify the generation of OH· radicals in the DBD system. Thus the presence of NaCl promoted the formation of OH· radicals.

$NaCl\ (s) \rightarrow Na^+\ (aq) + Cl^-\ (aq)$ (4.90)

$H_2O\ (l) + UV \rightarrow H^+ + OH^-$ (4.91)

$Na+\ (aq) + OH-\ (aq) \rightarrow NaOH\ (aq)$ (4.92)

$O_3 + OH^- \rightarrow {}^{\bullet}O_2^- + {}^{\bullet}HO_2$ (4.93)

$O_3 + {}^{\bullet}HO_2 \rightarrow 2O_2 + OH^{\bullet}$ (4.94)

${}^{\bullet}HO_3 \rightarrow O_2 + OH^{\bullet}$ (4.95)

$OH^- + H_2O_2 \rightarrow {}^{\bullet}HO_2 + H_2O$ (4.96)

${}^{\bullet}HO_2 + H_2O \rightarrow H_2O_2 + OH^{\bullet}$ (4.97)

Alternatively, the scavenging behaviour of NaCl observed in Figure 4-8 could be a factor as the amount of OH· radicals (mg/L) decreased with an increase of NaCl quantity yet OH· values were still high. In fact, various studies have demonstrated that NaCl is an OH· scavenger. This is in conformity with Liebert *et al.*, (1999) who reported that Cl^- could lessen the photocatalytic/ oxidation reaction rate by trapping the oxidising OH· radicals as shown in Equations (4.98 – 4.99),

$OH^{\bullet} + Cl^- \rightarrow Cl^{\bullet}$ (4.98)

$Cl^{\bullet} + Cl^- \rightarrow Cl^{\bullet -}$ (4.99)

This may consequently reduce the concentration of aqueous OH· radicals. This was also supported by Abdullah et al. (1990) who agreed that Cl^- and SO_4^{2-} compete with OH· as shown in the equations above to yield corresponding radicals that are often transitory aqueous species

during the oxidation process. Though the results obtained by the above authors claim that NaCl is a OH· scavenger, the experimental systems used in their studies and those employed in the current DBD reactor are far different and hence it is unlikely to lead to the same results. Furthermore, the extended effect of chloride ions on H_2O_2 was reported by Haarstrick *et al*., (1996) who stated that the chlorine radicals formed (Equation 4.98) can interact with H_2O_2 leading to the production of O_2 and Cl^- in aqueous systems. This consequently may impact on the rate of oxidation during the Cl^- scavenging scenario which diminished H_2O_2 concentration beyond a certain molar amount of NaCl when applied in the DBD reactor and hence resulted in the reduction of OH· radical concentration in the system, recalling that H_2O_2 is one of the principal precursors of OH· radicals in aqueous media. Despite the fact that, literature has supported these claims, the experimental conditions used in their studies were far different from those employed in the investigated DBD system in this study. This inferred that depending on the system and the NaCl concentration, NaCl could be considered as either OH· scavenger or promotor.

4.3.4 Effect of chemical probe concentration on the trapping of OH· radicals

Apart from scavengers, the concentration of chemical probe (TA) on the generation of OH· radicals in the DBD system was also inspected at the applied conditions as detailed in section 3.6.1.6. The results of these experiments are shown in Figure 4-9 and TA was varied from 0.01 to 0.04 M.

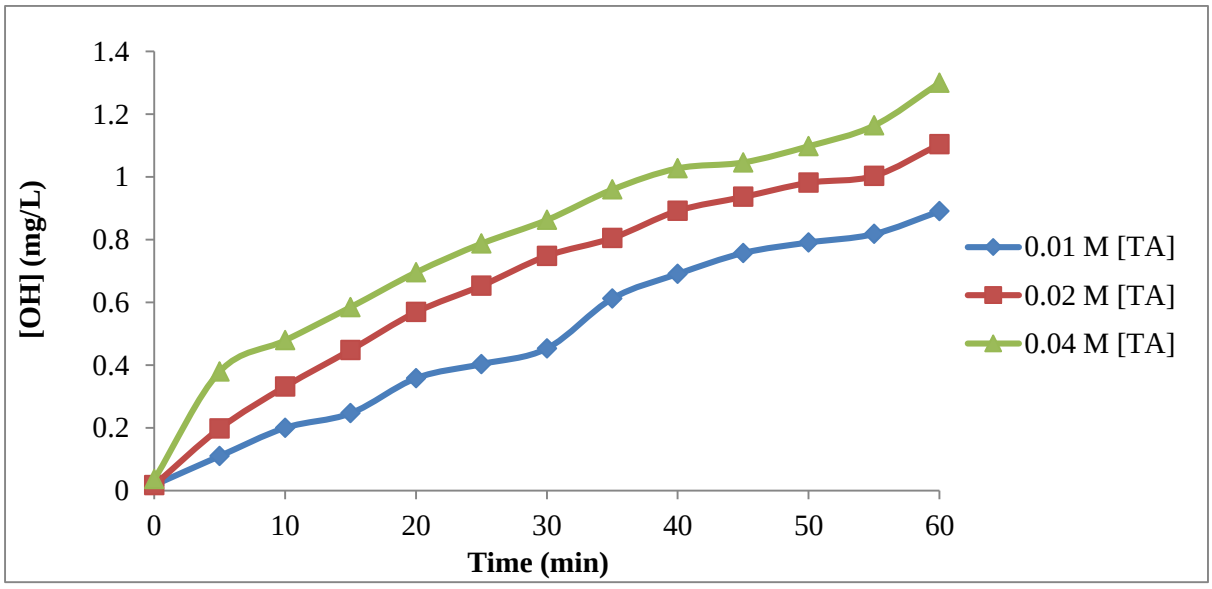

Figure 4.9: Impact of TA generation on OH. production in distilled water in the DBD reactor at the following experimental conditions. Varied parameter: TA mass 2.49, 4.98 g and 9.64 g each dissolved in 1.5 L of distilled water and corresponding to concentrations of 0.01, 0.02, to 0.04 M TA, respectively. Fixed parameters: solution initial pH, 5.49, peak voltage 6.8 kV, power 60 W, trip current 10 A, set current 60 mA, frequency 1000 Hz, air flow rate 3 L/min, solution volume 1500 mL, 1.5 mm silver electrode, 50 g/L NaCl electrolyte, treatment time 60 minutes, sampling every 5 min.

Figure 4-9 shows the effect of the concentration of chemical probe (TA) on the concentration of OH· radicals generated in the DBD configuration. The results show that for each dose of TA probe, the OH· concentration in DBD reactor continuously increased with an increase in DBD exposure time. This compliments the outcomes discussed in sections 4.3.3.4 & 4.3.3.5. These results confirm that DBD is a typical AOP configuration in which OH· radicals are uninterruptedly produced via several chemical mechanisms as shown in Equations (4.1- 4.97). Regardless of the fact that OH· was proved to interact with other species and hence could be consumed in side reactions, its increasing concentration at each concentration of TA probe suggests that the rate of formation of OH· predominates over its consumption by other chemical reactions taking place in the reactor. Likewise, the results also show that the use of too little amount of TA in the DBD reactor may not capture all the OH radicals produced in the reactor. Similar observations have been reported by Kanazawa et al. (2011) who measured OH· radicals in aqueous solution produced by atmospheric-pressure LF plasma jet. During their study, the authors used fluorescence spectroscopy to measure the yellow coloured hydroxyterephthalic acid (HTA) resulting from the reaction of TA with OH· radicals and hence detecting an approximate amount of OH· radicals formed in their discharge system. On the other hand, Kangle et al. (2010) investigated the effect of mineral phase structures on the formation rate of hydroxyl radicals on the surface of TiO_2 using different aqueous system. In their study, the authors noticed that the fluorescence intensity of OH· gradually increased with an increase in UV illumination time. These results are also in good agreement with Li et al. (2015) and Hayashi et al. (2016) who also quantified OH· radicals using the TA method in a pulsed discharge systems based on the same principle as DBD and demonstrated that OH· concentration increased with an increase of treatment time. This trend was extensively highlighted by various authors (Hirakawa *et al.*, 2007; Liu *et al.*, 2008; Nakabayashi and Nosaka, 2015). Besides, the results in Figure 4-9 also show that the amount of OH· radicals

increased with an increase of the amount of TA used. For instance, after 5 min of DBD run time 0.479 mg/L OH· was generated with 0.04 M of TA which was higher than 0.198 and 0.110 mg/L OH· generated with 0.02 and 0.01M of TA correspondingly. This trend was also observed at each sampling time in the 60 min of DBD run. This indicates that a higher amount of TA probe in the solution may assist to capture all produced OH· generated in DBD reactor for example. These results demonstrated that TA is a suitable probe for the quantification of OH· in DBD aqueous system. The interaction of TA and OH· yielding the yellow coloured 2-hydroxy terephtallic acid is thus capable of trapping the maximum of the OH· radicals produced in the DBD reactor, similar results were already obtained by Bianco *et al*. (2015); Gonzalez *et al*. (2018); Lallement *et al*. (2018) who investigated the quantification of OH· using TA probe in aqueous systems other than DBD. Even though different experimental systems have been utilised for the determination of OH· radicals, the results obtained in this study sustain that TA is a suitable chemical probe for the detection and quantification of OH· in aqueous media.

4.4 Summary of chapter 4

The results discussed in this chapter have clearly demonstrated that the DBD design is an effective advanced oxidation technology that produces significant amount of free active species among which O_3, H_2O_2 and OH· radicals that were successfully measured using spectroscopic techniques. Moreover, the results showed that O_3 is highly generated in acidic media (pH 2.5) with a fluctuating concentration. The variation of O_3 concentration within 60 min not only signified that O_3 originated from several reactions but also disclosed a scavenging behaviour that led to the fluctuating reduction of its concentration with time as shown in Equations (Equations 4-1 – 4-19). Instead, at elevated pH values (pH > 7), the minimal values of O_3 concentration were probably related to its disintegration indicating that O_3 was involved in side reactions that certainly contributed to the production of species such as OH·, O_2, $O_2^{\cdot-}$ etc. whose interactions with parent species led to the chain of chemical reactions exhibited in Figure 4-3. Following these outcomes, it can be inferred that the pH of the solution had an influence in the production of O_3 in the current DBD system and should therefore be carefully monitored during treatment of water and wastewater effluents. The H_2O_2 considered as the primary source of OH· radicals, was highly produced in basic conditions (pH> 7) indicating that its formation evolved from different reactions as shown in Equations (4-36 - 41). In contrast, the fluctuating decrease of H_2O_2 concentration in both acidic and basic media implied that H_2O_2 participated in parallel aqueous interactions yielding secondary species as disclosed in Equations (4-26 -4-

33) whose further interactions contributed to the production of OH radicals. Finally, the concentration of OH· radicals quantified in either the absence or presence of buffer solution showed opposing results. In the absence of buffer, the concentration of OH· radicals continuously increased with an increase of DBD running time and a high amount of OH· radicals was achieved in basic pH values as shown in Figures 4-4 and 4-5. However, after the addition of buffer, OH· radicals were still highly generated in basic pH values. Likewise at pH > 7 and after 30 min, the amount of OH· decreased with an increase of treatment time showing that either OH· was involved in side chain reactions as shown Equations 4-51 – 4-56 or OH· was scavenged by phosphate based species as detailed in Equations 4-42 to 4-50. In addition, the introduction of scavenger Na_2CO_3 in the DBD reactor significantly reduced the amount of OH· radical over the treatment time due to the reactivity of CO_3^{2-} with OH·. On the other hand, the addition of NaCl increased OH· concentration but depending on the concentration of NaCl either scavenging or OH· promotor was noticed. Consequently, the results demonstrated that solution pH significantly affected the formation of OH· radicals in the DBD reactor and that the presence of scavengers such as phosphates, bicarbonates and carbonates in the solution diminished the amount of OH· in the system and hence could impact on the detoxification of targeted pollutants during water and wastewater treatment. In addition, the production of acidic species over time confounded pH trends, reducing to acidic solution after 10 mins. Furthermore, this chapter proved that the variation of the amount of O_3, H_2O_2 contributes to the generation of OH· radicals in the DBD design and hence show it to be an adequate advanced oxidation technology for water and wastewater treatment. Having demonstrated that the DBD design generates sufficient active species that could be used as a chemical cocktail to induce decontamination of water pollutants, its optimisation is mandatory before any application.

CHAPTER FIVE: OPTIMISATION OF THE DOUBLE CYLINDRICAL DBD SYSTEM

5 INTRODUCTION

Following the reconfiguration procedure described in section 3.3.1, a double cylindrical dielectric barrier discharge (DBD) reactor was designed and constructed and is presented in Figure 3-3. The DBD reactor conditions were further optimised using two model pollutants, orange II (O.II) sodium salt dye and sulfamethoxazole (SMX) drug at the applied conditions. In this regard, the effect of physico-chemical and electrical parameters on O.II and SMX degradation efficiencies were investigated at the respective applied conditions. Various analytical techniques including UV-vis, FT-IR, LC-MS, TOC, etc. were employed to follow the degradation and mineralisation of the two targeted pollutants. The results of these experiments are subsequently presented and discussed in the following sections.

5.1 Optimization of the DBD reactor using orange II dye as a model pollutant

In this section, the reconfigured DBD reactor presented in Figure 3-2 was optimised following DBD experimental procedure described in section 3.6.3 to degrade O.II dye whose molecular structure is shown in Figure 5-1 as a model pollutant, using air as the feeding gas. During the optimisation process, the effects of the following physico-chemical parameters: orange II concentration, solution initial pH, peak voltage and air flow rate on orange II degradation efficiency were assessed subsequently at the applied conditions as shown in Tables 3-3, 3-4 and 3-5. UV-vis spectroscopy analysis and other analytical techniques were used to analyse orange II samples. Initially, the absorbance of orange II standard solutions was recorded to plot a calibration curve shown in Figure 3-7. This was further used to estimate the concentration of treated and untreated orange II samples.

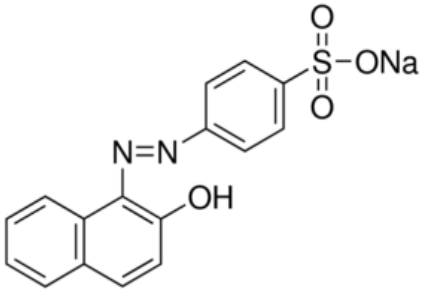

Figure 5.1: Structure of orange II sodium salt (Molar mass = 350.52 g/mol)

5.1.1 Effect of initial concentration on decolouration of orange II sodium salt

In this subsection the impact of initial concentration of orange II on its degradation efficiency was evaluated to assess the performance of the DBD reactor. The principal objective of this subsection was to determine the optimum concentration which the DBD would work efficiently and which orange II degradation by-products could be detected and identified as described in sections 3.6.4.1.1 and 3.6.1.3. The absorbance of orange II samples with treatment time as well as the change in colour of orange II dye was considered. Hence, the concentration giving rapid decolouration in a short period of time would be considered as the optimum value. Therefore, the impact of initial concentration on decolouration efficiency was assessed by plotting the decolouration percentage of orange II dye versus its concentration as measured by UV-vis. The concentration of orange II dye was varied from 10, 20, 30, 40, 50 and 60 mg/L during DBD experiments while the other parameters (Peak voltage 6.8 kV, air flow rate 3L/min, pH (in between 6.09 – 6.68), solution volume 1500 mL, 1.5 mm silver electrode, air gap 2 mm and treatment time of 60 minutes) were kept constant. The absorbance of orange II solution was sampled over a period of 60 minutes. The effect of initial concentration on orange II decolouration efficiency are presented in Appendices (4 a - c), plotted from UV-vis results and presented in Figure 5-2.

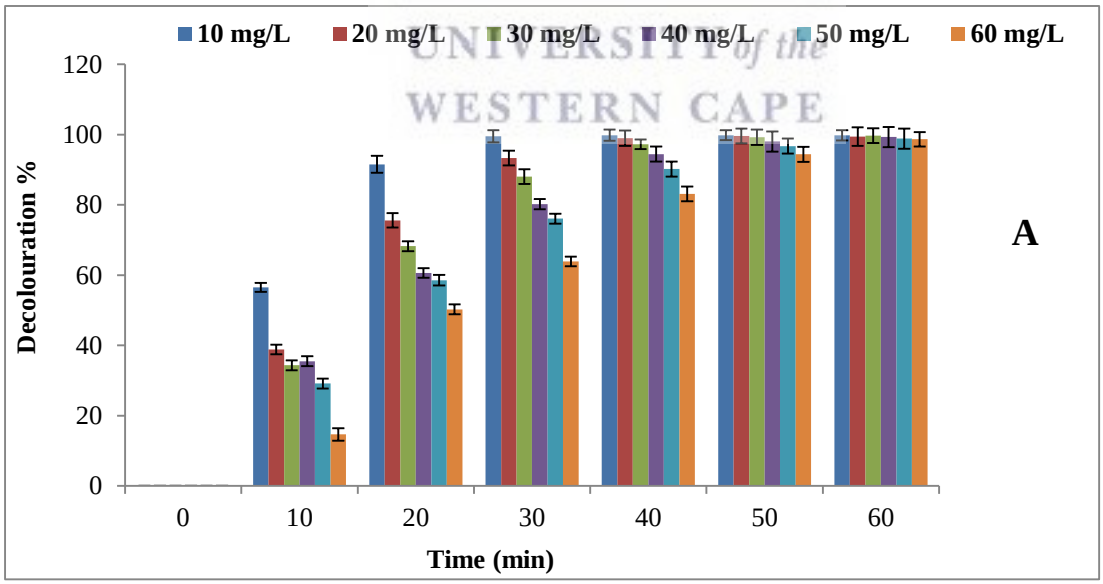

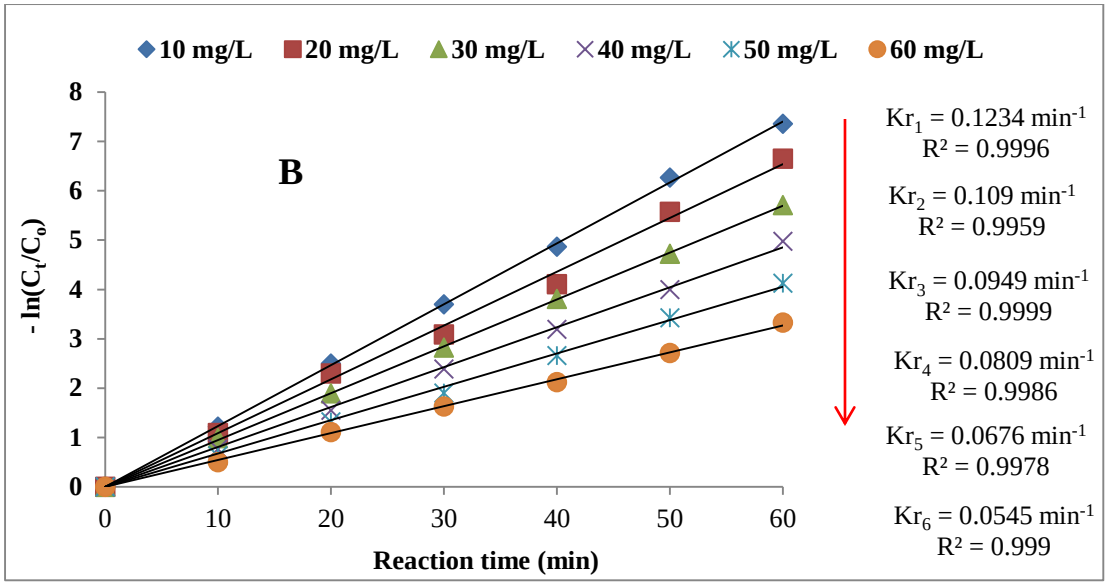

Figure 5.2: Effect of concentration on orange II decolouration efficiency. Experimental conditions: Peak voltage 6.8 kV, air flow rate 3L/min, pH (in between 6.09 – 6. 68), Solution volume 1500 mL, 1.5 mm silver electrode, air gap 2 mm and treatment time up to 60 minutes, (n=2).

Figure 5-2 presents the decolouration rate of orange II dye at different concentrations sampled at 10 minute intervals at the applied conditions within 1 hour of treatment time. The results plotted in Figure 4-3 showed that the decolouration of orange II solution decreased with an increase in initial concentration at treatment time between 10 to 50 minutes. From that trend, it could be inferred that in terms of colour change and hence decolouration concept, 10 mg/L as shown in Figure 5-2 is the optimum concentration. At a concentration of 10 mg/L Kr_1 = 0.1234 min^{-1} decolouration rate constant of orange II was achieved within 60 min of experiment compared to Kr_2 = 0.109 min^{-1} that was obtained within 60 min at an O.II concentration of 20 mg/L. This inferred that the complete decolouration of dye at higher concentrations occurred slowly and required longer time. Hence enough radicals are generated after 50 minutes to achieve total decolouration of O.II at higher concentrations. However, when low concentration such as 10 mg/L are used, intermediate by-products might be difficult to detect and identify by techniques such as high performance liquid chromatography (HPLC) due to the low sensitivity of such instruments. Therefore, a higher O.II concentration of 60 mg/L was chosen as the most practical concentration and was used for the rest of DBD experiments performed in this study. The increase of orange II decolouration rate with an increase in the initial concentration observed during optimisation of this parameter might also be due to the fact that the intensity of the UV-light generated in the DBD reactor might be weak and therefore could not penetrate

the entire bulk solution as the dye concentration was gradually increased. That is, the polluted water surrounding the second dielectric barrier would have been irradiated first by the plasma generated UV light and consequently got decolourised whereas the bulk of the solution required substantial and continued irradiation over a longer period to achieve maximum decolouration. Moreover, the amount of ozone produced during the first 30 minutes in the DBD reactor might have been insufficient to achieve effective decolouration of orange II dye when its concentration was higher than 60 mg/L. Or perhaps the ozone generated in the air gap of the DBD system was enough for the decolouration of orange II dye but might initially have been consumed by side reactions with other aqueous species yielding powerful OH· radical oxidants that were then dispersed in the solution after 30 minutes and non-selectively mineralised orange II dye pollutant. From this point of view, the quantity of ozone produced in the DBD reactor might have decreased over time and hence slowed down the decolouration of orange II dye. Indeed, literature presents no information on the degradation of orange II using double cylindrical dielectric barrier reactor. Nevertheless a number of researchers have performed similar investigations on degradation of dyes using other kinds of electrical discharge systems. For instance, Ozone et al. (2011) and Zhang et al. (2012) showed that the decolouration efficiency of dye diminishes with an increase of its initial concentration. This was also confirmed by Reddy & Subrahmanyam (2012) who during degradation and mineralisation of aqueous organic pollutants by plasma discharges conveyed that various dyes could be removed at low concentration. This was justified by the fact that the performance of the reactor used might lessen with an increase of initial dye concentration, due to insufficient radical production. Comparatively, it could be noted that trends highlighted in the literature are similar to the one observed in Figure 5-3. Therefore, it could be inferred that the decolouration of a typical dye depends on the amount of active radicals species generated over time as well as the concentration of the pollutant. Indeed, it was earlier demonstrated in sections 4-1, 4.2 and 4.3 of chapter 4 that at pH 2.5, the concentration of O_3 generated in produced in the DBD reactor ranged between 0.535 to 0.783 M after 45min of reaction time and slightly increased to 0.79 M after 60 min. Similarly, at pH 2.5 and the same conditions, the amount of H_2O_2 reached 0.8 M after 30 minutes and decreased to 0.306 M after 60 min of DBD run and further resulted in a lower amount of OH radicals (0.32 – 0.47 mg/L) at pH 2.5 after 60 min. These fluctuating amounts of radicals produced in the DBD reactor within 30 and 60 minutes reaction times represent the rate limiting steps of DBD efficiency and might be used up completely if there is an excess of dye. In conclusion of this section, although 10 mg/L was the best concentration at which orange II was efficiently decolourised, 60mg/L was used because otherwise degradation

intermediate by-products are difficult to detectly HPLC at such small concentrations. The 60 mg/L was thus used in all DBD experiments performed in this study. Figure 5-2 (A) descriptively shows that the decolouration of orange II dye diminishes with an increase of its initial concentration, due to consumption of produced free radicals which are limited by the system and applied conditions. Thus the concentration of pollutant may be chosen according to a particular interest or goal being aimed at. Furthermore, apart from pollutant concentration, various authors sustained that solution initial pH is also an important factor that needs to be investigated during water and wastewater treatment. The investigation of the effect of solution initial pH is DBD treatment system is crucial due to the impacts of the nitrates produced during the DBD experiment that consequently reduced the initial pH to acidic solutions.

5.1.2 Effect of pH on O.II dye decolouration efficiency

In this subsection, the initial pH of the orange II solution was varied from 2.5 to 10.5 and was adjusted to the desired value using diluted H_2SO_4 and NaOH solutions (as described in section 3.6.4.1.2). The monitored solutions were exposed to DBD plasma experiments at the following experimental conditions: voltage 6.8 kV, air flow rate 3 L/min, air gap 2 mm, 0.5 mm silver electrode and 50 g/L of NaCl electrolyte and a volume of 1500 mL 60 mg/L orange II for 60 minutes. To evaluate the effect of pH on decolouration efficiency of orange II dye, the absorbance, concentrations and orange II decolouration efficiency are presented in Appendices (5a - c). The results obtained are plotted and shown in Figure 5-3.

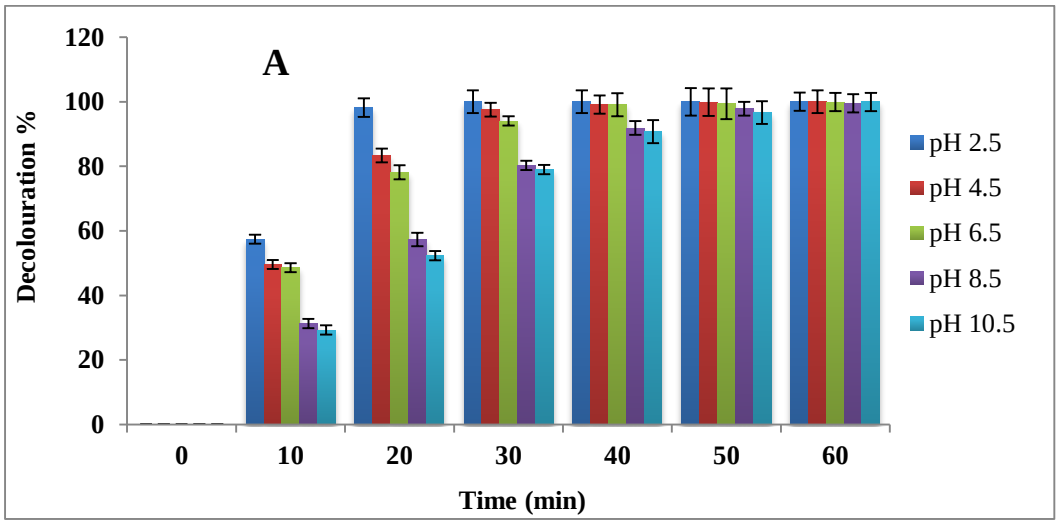

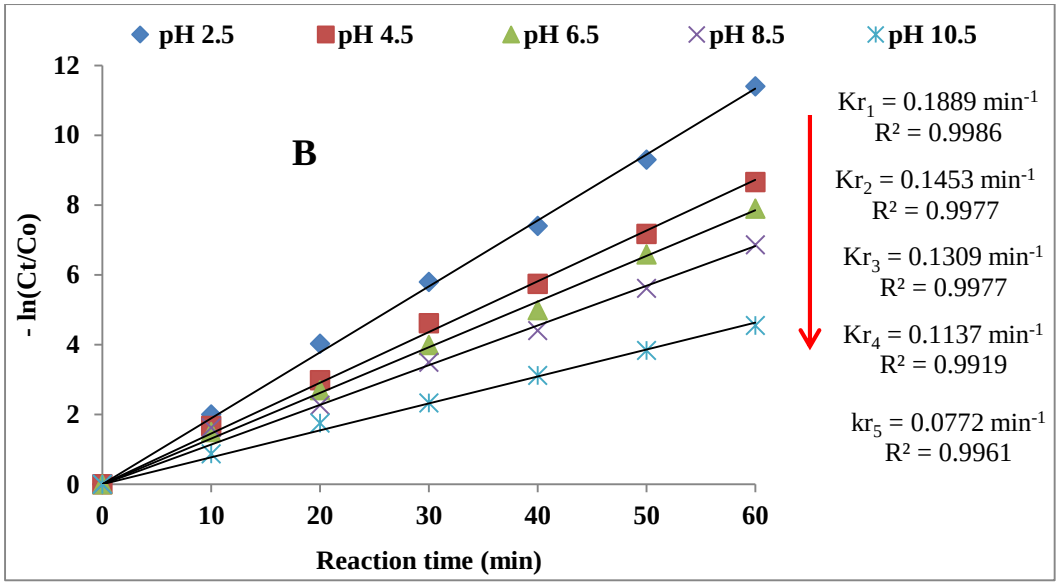

Figure 5.3: Effect of pH on orange II decolouration efficiency. Experimental conditions: Orange II concentration 60 mg/L, Peak voltage 6.8 kV, air flow rate 3L/min, Solution volume 1500 mL, 1.5 mm silver electrode, air gap 2 mm, 50 g/L NaCl electrolyte, and treatment time up to 60 minutes,(n = 2).

Figure 5-3 presents the results calculated from UV data based on the impact of initial pH on orange II decolouration efficiency at the applied conditions. The results illustrated in Figure 5-3(A) show that, at 10 minutes under the applied conditions, the % decolouration of orange II increased with decrease in pH from 8.5, 4.5 to 2.5. That is, about 57.4%, 48.5% and 31.27% decolouration were achieved at pH 2.5, 4.5 and 8.5. Hence the dye decoloured most effectively at an acidic pH. This pH effect could be seen up to 30 minutes. This trend was also observed after 20 and 30 minutes of the DBD experiment. So 100%, 94.5 and 97.05 % decolouration were consecutively obtained at pH 2.5, 4.5 and 8.5 within 30 minutes. Complete decolouration of orange II was achieved within 20-30 minutes at pH 2.5. That is 57.4%, 98.2% and 99.9% decolouration of orange II were reached after 10, 20 and 30 minutes respectively at pH 2.5. Likewise, in Figure 5-3 (B), higher rate constants for O.II decolouration were achieved at low pH. That is, the rate constant increased with a decrease in solution pH. For instance, about 0.1889 min^{-1}, 0.1453 min^{-1} and 0.1309 min^{-1} rate constants for the decolouration of O.II were obtained at pH 2.5, 4.5 and 6.5 within 60 minutes. This meant that the rate of orange II decolouration lowered when increasing solution pH initially but later confounded by pH decrease due to nitrate and sulphate formation in the DBD system. In other words, the decolouration efficiency of orange II increased with a decrease in pH and was highest in acidic

media after 30 minutes. The experimental performed at pH value 8.5 gave lower decolouration. This was probably due to the abundance of scavenging nitrate residues evolving either from the decomposition of air or from that of orange II dye by reactive oxygen species. The presence of so called acidic inorganic components was confirmed by nitrate and sulphate tests performed on the untreated and treated orange II samples as detailed in sections 3.7.5 and 3.7.6. In addition to this, extensive acidic organic substrates mainly aliphatic carboxylic acids, carbonate scavengers, etc., might likely have originated from the degradation of orange II dye in DBD reactor. This was evidenced by the decline in TOC content of the contaminant and further supported by the FT-IR analysis (see sections 3.7.3, 3.8.2 and Table 5.2 of Section 5.2.2, respectively). From the aforementioned aspects, it could be inferred that decolouration of orange II dye in a double cylindrical DBD is a pH dependent process initially but later confounded by decrease due to nitrates, etc. Even though the decomposition of orange II by DBD system might have been conducted by a few authors, different configurations may have been used and, the effect of pH on orange II degradation efficiency was not fully investigated. For instance, the effective removal of orange II dye by electrical discharge has been attempted by various authors. For instance, Sugiarto et al. (2003) used pulsed plasma discharge in water to degrade various types of acidic dyes. The authors observed that the decolouration of acidic dyes was favoured in acidic media. The favourable decolouration of dyes at lower pH values was already reported by Ince & Tezcanh (1999). This is probably due to the unselective reaction of hydroxyl radicals with scavengers such as carbonate ions resulting from the breakdown of the organic substances during the oxidation processes at pH higher than 7. This may therefore diminish the oxidation efficiency substantially. In addition to this, the nucleophilic and electrophilic disintegration reactions of $O^{\cdot}$ and $OH^{\cdot}$, respectively may lead to various co-produced intermediates which may follow diverse reaction pathways (Jiang *et al.*, 2013; Joshi and Thagard, 2013). This consequently limits the degradation of the target pollutant at higher pH values. From the aspects discussed above, it follows that solution pH is an important feature during the treatment of dyes by non-thermal plasma technologies. This information was further reinforced by Thagard et al. (2009) who showed that the amount of hydrogen peroxide for example produced in gas or liquid phase largely depends on solution pH. Apart from this Thagard and colleagues mentioned that acid base equilibrium processes between plasma generated entities are pH-dependent too and may have a considerable impact on the removal of aqueous pollutants. The pH trend discussed in previous research investigations showing that efficient degradation of numerous dye stuffs is best achieved in acidic conditions corroborates with the pH behaviour observed in this actual study whereby the initial solution pH becomes

acidic over time despite starting pH. This was due to the formation of nitrates and nitrites by-products during DBD experiment as discussed in Section 5.2.3. Nevertheless, the optimal pH in this regards may depend on plasma configurations utilised. For example Sugiarto et al. (2003) demonstrated that the degradation rate of dyes at pH 3.5 was at last three times faster than that at pH 10.5. Based on these findings, Sugiarto and co-workers selected 3.5 as the optimum pH in their system. In summary, the pH behaviour previously documented and that observed in the current investigation emphasise that the pH of dyes pollutant is a crucial parameter in wastewater treatment. Therefore, the decomposition of selected dye such as orange II sodium salt is a pH dependent process regardless of the reactor geometry employed, and pH should be monitored and adjusted accordingly.

5.1.2.1 Behaviour of solution pH during DBD experiments (pH trends during DBD experiments)

After optimisation of initial pH during decolouration of orange II dye by DBD system, the behaviour of the pH trend during DBD experiment was studied to confirm the optimum pH value obtained in this section. This was compared to the DBD experiment performed at optimum pH. So, two DBD experiments were run with equivalent conditions in this subsection (see section 3.6.4.1.2). The first one was performed without pH adjustment at orange II initial pH that fluctuated between (6.34- 6.74) and the other experiment was run at the optimum pH value of 2.5. The UV results (absorbance, concentrations and degradation efficiency) of these experiments were tabulated in Appendices 5 (a – c) and were plotted and are presented in Figure 5-4. The results in Figure 5-4 show that the pH of orange II solution decreased with time during the DBD treatment process to below pH 3 when no pH adjustment is made. That is, Figure 5-4 shows that at a concentration of 60 mg/L and an initial pH of 6.57 and after 60 minutes of DBD experiment, the initial pH of orange II solution progressively declined from 6.57 to about 2.59. This trend was noticed in all DBD experiments which further confirmed that the optimum degradation of orange II solution was achieved at pH below 2.5. While at the same conditions, orange II solution whose initial pH was adjusted initially to the optimum value 2.5 did not show remarkable pH changes during DBD experiment. In this case the solution pH set at 2.5 remained almost constant during the 60 minutes of treatment. This was perhaps due to the fact that the numerous acidic species formed in the bulk solution during treatment process reached their steady state. These acidic substances might have resulted either from the decoloured orange II dye or likely from gaseous air that was used as feed gas in the DBD reactor. In this

regard, the interaction of electrical discharge with air consisting of nitrogen and oxygen might have been the principal source of formation of the acidic species in the system. These findings were previously reported by Zhang *et al.*, 2007) and (Dojčinović *et al.*, 2011). In addition to this, Brisset *et al*. (2011) sustained that the impact of electrical discharge on air may result in the formation of various nitrogen species (NOx) that often dissolve in the solution and producing various species such as nitrite (NO_2^-) and nitrate ions (NO_3^-) which further may result in the formation of nitric acid (HNO_3), nitrous acid (HNO_2) and peroxynitrous acid (ONOOH) in the bulk solution. This documentation is in line with the results obtained in the current study. For instance, the results discussed in section 5.1.1.7.3 of this chapter show that the quantity of nitrogen including (nitrate + nitrites) reached 8.2 mg/L in the treated samples of orange II dye. Therefore the formation of these inorganic nitrogen species might have caused the steady pH decrease observed during DBD plasma treatment of orange II dye when the initial pH is not adjusted. In summary, during dielectric barrier discharge treatment of orange II dye, the pH of the solution decreased below 2.6. This was confirmed by the experimental runs at optimum values which did not show any change during the course of the DBD experiment. The continuous decline of pH during treatment of orange II solution can thus be ascribed to the formation of aqueous nitrogen species such as nitrite (NO_2^-), nitrate ions (NO_3^-), nitric acid (HNO_3), nitrous acid (HNO_2) and peroxynitrous acid (ONOOH) over time in the solution during plasma degradation of orange II dye as indicated in Table 5.3 of Section 5.2.3.

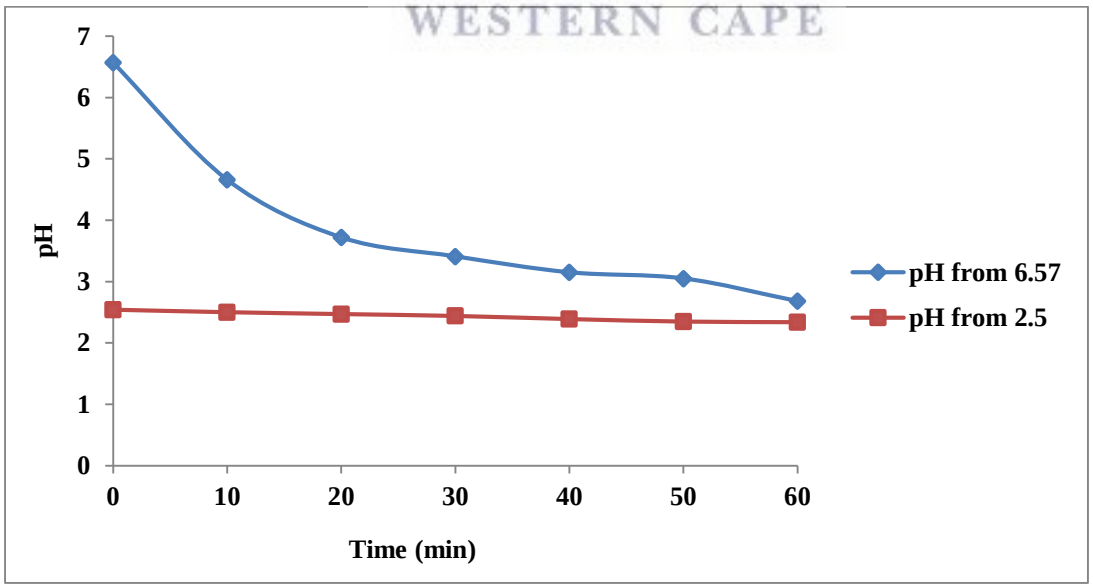

Figure 5.4: Fluctuation of pH during DBD experiment. Experimental conditions: Peak voltage 6.8 kV, O.II concentration 60 mg/L, , pH 6.57 and 2.5, solution volume 1500 mL, 1.5 mm silver electrode, air gap 2 mm, 50 g/L NaCl electrolyte, and treatment time of 60 minutes.

5.1.3 Effect of voltage on orange II decolouration efficiency

In this subsection, the impact of voltage on orange II decolouration efficiency was evaluated by altering the peak voltage from 4.8, 6.8 to 10 kV at the applied conditions as described in the experimental procedure (Section 3.3.4.5). The UV-vis data based on absorbance, % concentration and decolouration efficiencies of orange II dye at the applied conditions were respectively tabulated in Appendices (10-12) and plotted and are presented in Figure 5-5.

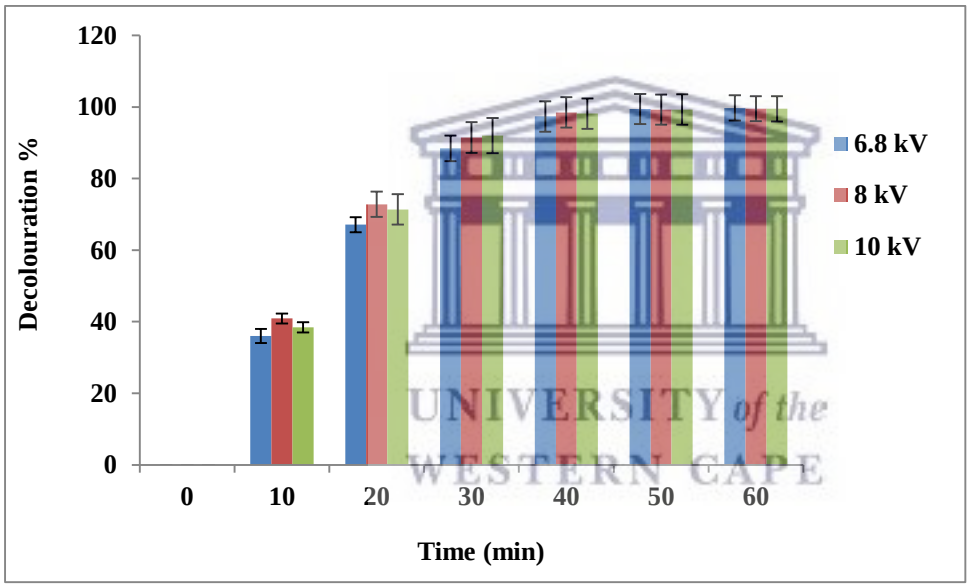

Figure 5.5: Effect of voltage on orange II decolouration efficiency. Varied parameter: Peak voltage from 6.8, 8 to 10 kV. Fixed conditions: Orange II concentration 60 mg/L, air flow rate 3L/min, solution pH 2.5, solution volume 1500 mL, 1.5 mm silver electrode, air gap 2 mm, 50 g/L NaCl electrolyte, and treatment time of 60 minutes,(n=2).

The % decolouration derived from UV-vis data shown in Figure 5-5 show the effect of peak voltage on the degradation efficiency of orange II dye at the corresponding conditions. Even though the results obtained at voltages 8 and 10 kV are close, the results shown in Figure 5-5 prove that the most efficient decolouration of orange II dye was achieved with a voltage of 8 kV at the indicated conditions. Even if the decolouration efficiencies of orange II tabulated in

Appendices 7(a –c) that were plotted and exhibited in Figure 5-5 reached 100 % after 60 minutes of DBD experiments, some fluctuating trends were observed during the 60 minutes of treatment. That is, in the first 20 minutes the decolouration of orange II at voltage 8 kV was higher than at 10 kV and 6.8 kV, respectively. Likewise, after 30 minutes orange II degradation percentage at 10 kV was only slightly higher than at 8 kV and 6.8 kV, correspondingly. Beyond 30 minutes orange II decolouration efficiencies obtained at both 8 and 10 kV were greater than that at 6.8 kV but overall voltage did not impact the efficiency as much as dye concentration or solution pH. These changes in decolouration efficiency of orange II in the DBD system were probably related to the production of free radicals in the reactor. In the case in which orange II is more reactive with ozone than with hydroxyl radicals, the amount of O_3 generated in the first 50 minutes was not enough to fully decolourise orange II dye. This might be due to the fact that various reaction mechanisms responsible for the production of ozone in the DBD reactor could have occurred and hence required a prolonged time to yield a reasonable amount of ozone that selectively degraded ozone. In previous studies (Massima, 2014), it was proven that increasing the applied/peak voltage of the power supply may increase the number and the length of the micro discharges and hence intensifying the UV-vis light in the DBD reactor. This in turn may boost the amount of free radicals produced in the applied reactor. This supports the high O.II decolouration efficiencies obtained at voltages 8 and 10 kV during DBD experiment. Based on the operating stability of the DBD reactor at ambient conditions and looking at the best results obtained at 8 kV in the first 20 minutes, 8 kV was chosen as the optimum voltage for this DBD system and was used in further DBD experiments. Despite the fact that the effect of peak voltage on decolouration of efficiency of orange II in DBD reactor is not well documented in the literature; a few authors like Gupta (2007) investigated the impact of voltage on degradation of different dyes using corona discharge systems. Gupta (2007) indicated that increasing voltage in corona reactors results in an increase of the number and length of streamers which in return increased the quantity of free reactive species in the corona reactor. This trend is similar to that observed in this study even though different reactor configurations and dyes were used. Hence the influence of voltage on the decolouration of O.II may be by the production of a greater quantity of free radicals. Although the trend between voltage and decolouration efficiency of orange II in this study was only slight, the voltage increase still impacted on orange II decolouration. This is mainly ascribed to the increase in the number and length of the micro discharges and streamers around the inner tube of the DBD system that irradiate the polluted water and hence likely generating a significant amount of free

reactive species that decompose the target contaminant. Overall, 8 kV was chosen as the optimum voltage for the current study.

5.1.4 Effect of air flow rate on orange II decolouration rate

As air was being used in the DBD system as a feeding gas it is a source of oxygen and ozone being generated in the DBD reactor. Therefore, it was necessary to assess the effect of its amount (flow rate) utilised in the DBD system for the decolouration of orange II dye as described in Table 3-4 and in Section 3.6.4.1.2. The UV-vis results of the effect of air flow rate on the decolouration efficiency of orange II were tabulated in Appendices 6 (a - c) and plotted in Figure 5-6.

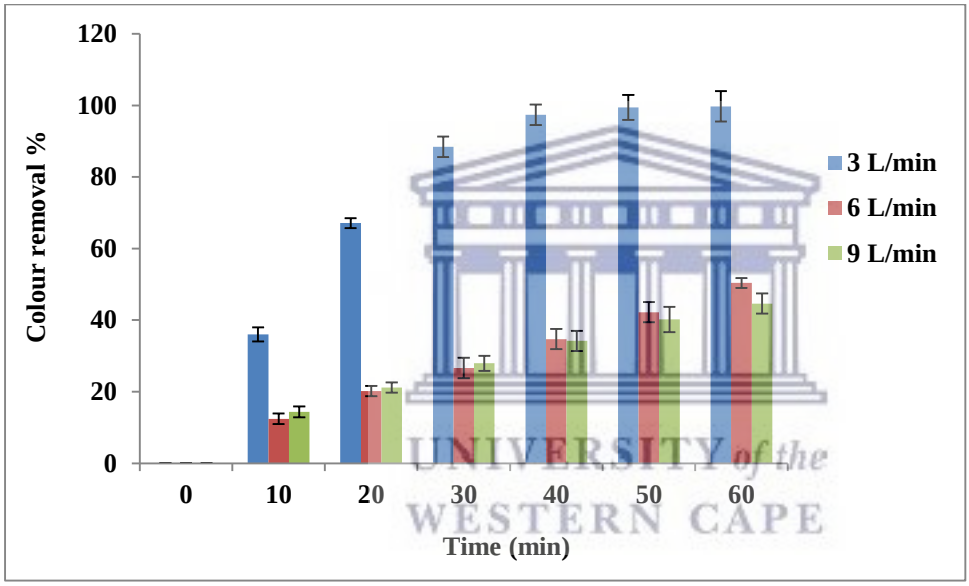

Figure 5.6: Effect of air flow rate on orange II decolouration efficiency of orange II. Experimental conditions: Peak voltage 8 kV, O.II concentration 60 mg/L, pH 2.5, solution volume 1500 mL, 1.5 mm silver electrode, air gap 2 mm, 50 g/L NaCl electrolyte, and treatment time of 60 minutes,(n=2).

Figure 5-6 presents the decolouration trends based on the UV-vis showing the effect of air flow rate on decolouration efficiency of orange II dye at the applied conditions. The highest decolouration of orange II dye was achieved at an air flow rate of 3 L/min and complete decolouration was reached within 50 min. This probably means that the amount of reactive oxygen species produced at an air flow rate of 3 L/min was adequate to decolourise orange II after 50 min. This is probably because 60 mg/L O.II was slightly higher than the optimum

concentration and hence O.II required a reasonably long time to totally decolourise. This was earlier discussed in Section 5.1.1.1, where the trend between concentration and decolouration efficiency of orange II dye showed that the removal of dye pollutants decreased with an increase in concentration. In this case, the decolouration of orange II might have occurred in a shorter period of time if a lower concentration than 60 mg/L were used. Nevertheless, the results presented in Figure 5-6 show that after 30 minutes the decomposition of orange II at an air flow rate of 3 L/min was higher than that at 9 L/min followed by that at 6 L/min. However, from 40 min to the end of the experiment orange II decomposition was higher at an air flow rate of 3 L/min than that at 6 L/min followed by 9 L/min. Indeed at sea level as reported by Naz et al. (2012), air consists of about 20.95% of oxygen (O_2) and 78.08% of nitrogen (N_2) and small traces of other gases. In addition to this, the author also supports that despite the diversity of properties oxygen may show; this diatomic molecule is also a potent oxidiser. Hence flowing more oxygen in the DBD reactor for 60 minutes implied increasing the amount of ozone produced in the DBD system as well as other free radicals such as hydrogen peroxide, atomic oxygen, hydroxyl radicals, etc. that all contributed directly or indirectly to the decolouration of orange II dye. This therefore justifies the high decolouration rate/efficiencies of orange II dye obtained within 60 minutes at the applied conditions and at an air flow rate of 3 L/min. In fact, according to explanations previously mentioned in this section it was expected that increasing the amount of air in the DBD system might result in an increase of free radicals and hence might induce higher decolouration of orange II dye at higher air flow rates. Conversely, the opposite of this trend was observed as the highest removal efficiencies were achieved at the lowest air flow rate of 3 L/min. This indicated that the non-selective ·OH and other free radicals species that decoloured orange II dye might had been produced by various reaction sequences. This in turn might have favoured the production of ozone and other free radicals. In this regard, higher air flow rates may have disturbed the steady production of reactive oxygen and hence have limited the decolouration of orange II at higher air flow rates. Apart from the aforementioned reasons, nitrogen in the air flow especially at higher flow rates was probably favouring the generation of oxygen scavenging nitrogen species such as NO, NO_2 N_2O_5, etc., (as stated in Section 5.1.1.7.3 and in Table 5-3 of this chapter) instead of ozone being produced in the plasma zone of the reactor. Based on the highest decolouration efficiencies of orange II obtained at 3 L/min air flow rate, this value was then chosen as an optimum air flow rate in the DBD operational parameters and was used in all further DBD experiments performed in this study. From the results obtained and discussions of this section, it could be inferred that DBD air flow rate is an important parameter in the degradation of

organic pollutants. Its optimum value in non-thermal studies may depend on the reactor configuration employed. In summary, the optimisation results of DBD system discussed in this section showed that the following parameters, dye initial concentration (varied from 10, 20, 30,40, 50 to 60 mg/L), solution pH (varied from 2.5, 4.5, 6.5, 8.5 to 10.5) and air flow rate (varied from 3, 6 to 9 L/min) significantly impacted the decolouration efficiency of O.II. That is, O.II % decolouration decreased with an increase of dye initial concentration though 60 mg/L was considered as the optimum O.II concentration. On the other hand, the decolouration efficiency of O.II decreased with an increase of starting solution pH, consequently the best O.II removals were achieved at low pH 2.5 that was recorded as the optimum pH. As for air flow rate, the % decolouration of O.II decreased with an increase of air flow rate in the DBD system and best O.II removal % was achieved with an air flow rate of 3 L/min. In contrast, the peak voltage did not really impact on O.II decolouration efficiency although slight increase of O.II % decolouration was observed as peak voltage was increased from 6.8, 8 to 10 kV.

5.1.5 Degradation of orange II dye at optimum conditions

To assess the effectiveness of the actual DBD reactor after optimisation of parameters initial O.II concentration, peak voltage solution and pH, air flow rate, a DBD experiment of orange II degradation was accomplished at optimum conditions presented in Table 5-1 below.

Table 5.1: Optimum operational conditions during optimisation of the DBD system for all decolouration

Parameters	Optimum
Orange II concentration (mg/L)	60
Solution pH	2.5
Inlet air flow rate (L/min)	3
Peak voltage (kV)	8

The UV-vis absorbance, concentrations and the degradation percentages of orange II dye obtained at these optimum conditions are presented in Appendix 8. These results were plotted versus treatment time and are presented in Figure 5-7.

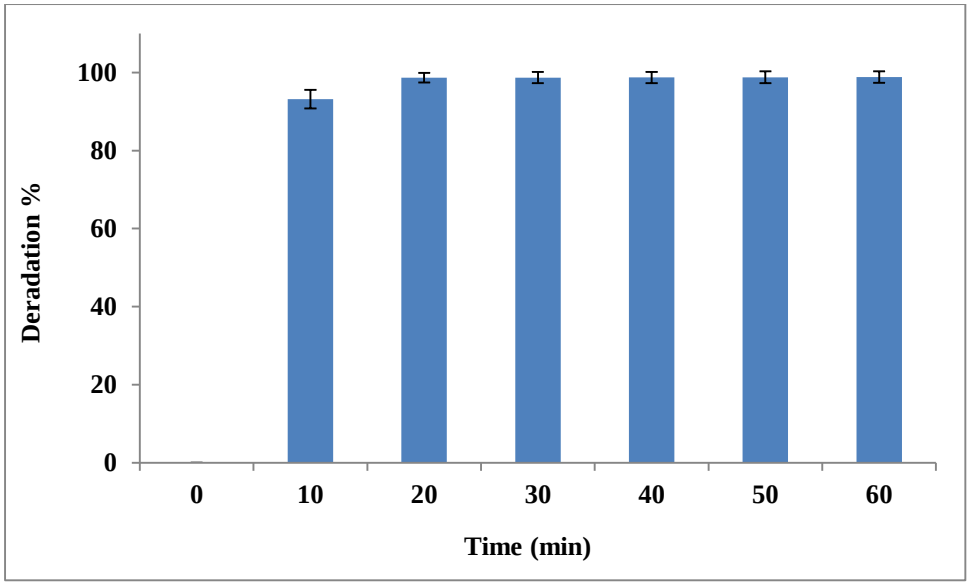

Figure 5.7: Decolouration of O.II within 60 minutes at the following optimum conditions: Peak voltage 8 kV, [O.II] = 60 mg/L, V= 1500 mL, air flow rate 3 L/min, 1.5 mm silver electrode, 50 g/L NaCl inner electrode electrolyte, air gap 2 mm, (n=2).

Figure 5-7 shows the plot of orange II decolouration efficiency at the optimum conditions. The results presented in Table 5-1 and Figure 5-7 show that at the optimum conditions, orange II dye decolourised rapidly within 10 minutes and complete decolouration was almost achieved within 10 minutes. Orange II dye contains an azo group that is responsible for its intense orange colour (Peralta-Hernández *et al.*, 2008). Therefore the continuous decolouration of orange II observed during these experiments could be due to the destruction of the azo group by free reactive species such as O_3, H_2O_2, etc. generated during DBD plasma treatment (Mok and Whitehead, 2008). The reduction in treatment time to 10 minutes at which complete orange II decolouration was attained confirms the high performance of the optimised DBD system for removing recalcitrant dyes. In order to identify and quantify the remaining contaminants, further characterisation of the treated solution was investigated.

5.2 Characterisation of untreated and treated orange II samples

This subsection deals with analysis of orange II samples withdrawn within 60 minutes of DBD experiments performed at the optimum conditions. The following analytical techniques: UV-vis, FT-IR, TOC, COD, sulphate and nitrate analysis were employed to characterise orange II

untreated and treated samples, and determine whether decolouration was equivalent to degradation.

5.2.1 UV-vis spectroscopy analysis of orange II samples at optimum conditions

The UV-vis spectra showing the degree of degradation of orange II dye at optimum conditions are presented in Figures 5-8 and 5-9.

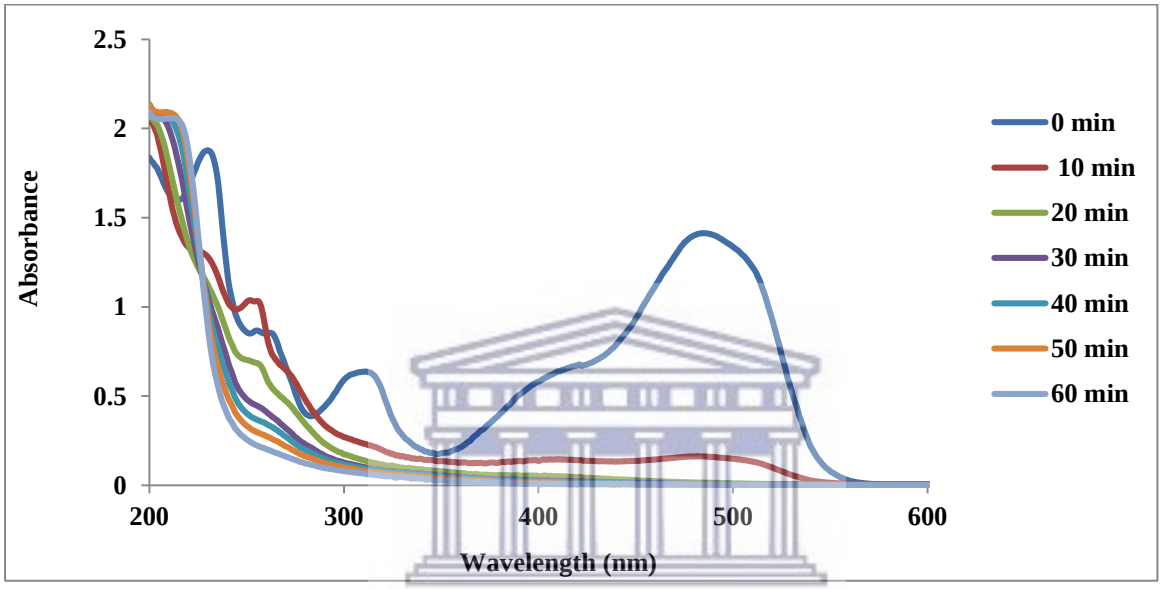

Figure 5.8: Ultra violet- Visible Spectra of orange II dye samples analysed during 60 minutes of DBD experiment at the following conditions: Peak voltage 8 kV, O.II concentration 60 mg/L, pH 2.5, air gap 2 mm, air flow rate, 3 L/min, O.II volume 1500 mL, 50 g/L NaCl electrolyte, 1.5 mm silver electrode and contact time of 60 minutes.

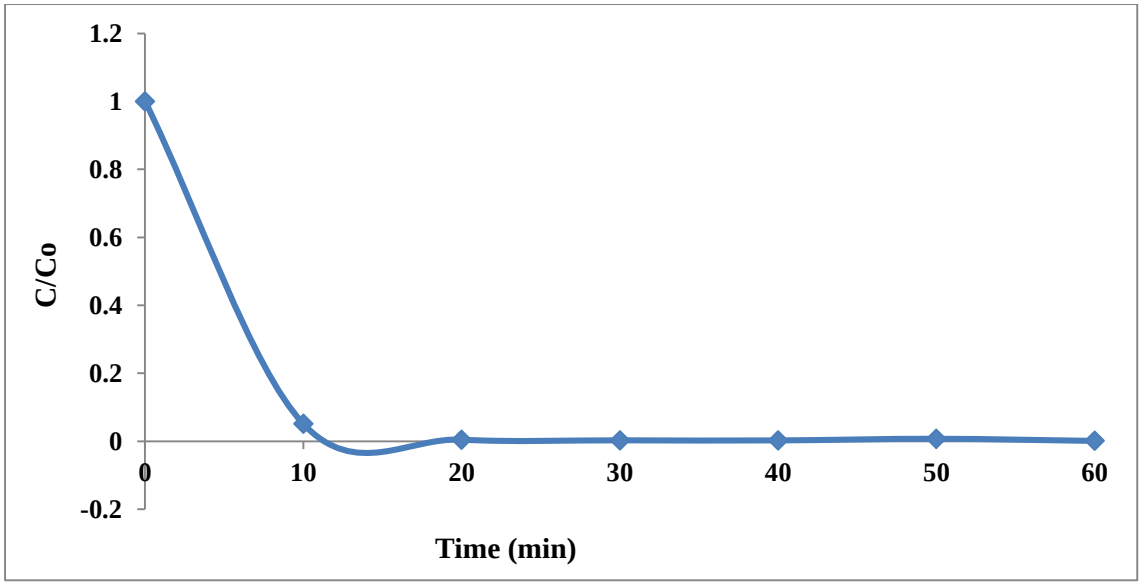

Figure 5.9: Intensity Vs time of O.II degradation showing progressive decolouration of O.II (using UV-vis data) between 350 and 550 nm at the following conditions: Peak voltage 8 kV, O.II concentration 60 mg/L, pH 2.5, air gap 2 mm, air flow rate, 3 L/min, O.II volume 1500 mL, 50 g/L NaCl electrolyte, 1.5 mm silver electrode and contact time of 60 minutes.

The plot in Figures 5-8 and 5-9 shows the continuous decolouration of orange II dye with time performed at optimum conditions. The results shown in Figure 5-8 show two absorption bands that occurred in two distinct regions. The higher energy absorption band occurred between 350 and 550 cm^{-1} while the lower energy absorption band appeared in 280 cm^{-1} - 340 cm^{-1} region. The spectra in Figure 5-8 showed a decrease in absorption band intensity (between 350 and 550) with time, indicating a significant decrease of orange II concentration. Therefore, considerable decolouration efficiencies of orange II was achieved with an increase of treatment time. The spectra plotted in Figure 5-8 show that complete decolouration of orange II was achieved within 10 minutes of DBD experiment because the absorption bands in the two regions previously introduced overlap. To recall, most organic molecules absorb electromagnetic radiations in the UV-visible range with a wavelength ranging from 190 to 800 nm. The absorbance bands presented in Figure 5-8 result from electron transitions when the orange II molecule absorbs energy from the highest occupied molecular orbital (HOMO) to the lowest unoccupied molecular orbital (LUMO) of higher energy. Indeed, organic dyes such as orange II comprises chromophoric groups that are responsible for their intense colours that further give rise to the UV-vis or visible spectra for instance, the azo group –N=N- in orange II molecular structure was already discussed in section 2.9.1. The sulphonate group (SO_3^- Na^+)

that is at the same time a nucleophilic and electrophilic centre may be vulnerable to free reactive oxygen attacked by species such as O_3 and ·OH generated in the DBD reactor. This may consequently induce the degradation of orange II dye when exposed to DBD plasma treatment. So the two energy absorption bands observed in the 280 - 450 cm^{-1} and 460 – 580 cm^{-1} might be due to the azo and sulfonate groups present in orange II molecular structure. In addition to this, the broadness of the absorption band observed around 460 – 580 cm^{-1} region in the UV-vis spectra is probably due to overlapping of aromatic rings governed by their conjugated pi electron system that are detectable in this range. In this regard, the possible destruction of the azo (–N=N-) and sulfonate (SO_3^-) groups in orange II structure might have been the principal causes for colour fading when orange II was subjected to plasma treatment. In total the drastic reduction of the UV-vis absorption bands shown in Figure 5-8 indicates the decrease in orange II dye concentration. Likewise these visible observations need to be confirmed by using qualitative or quantitative extended analytical techniques. For instance, FT-IR spectroscopy could be used for qualitative examination and determination of the ionic and molecular species present in untreated and treated orange II samples.

5.2.2 FT-IR spectroscopy of orange II treated by DBD at optimum conditions

This subsection aimed at comparing the current stretching vibration functional groups present in the untreated and treated orange II samples. Therefore, investigating the possible formation of orange II by-products when O.II is exposed to the DBD plasma process, the FT-IR spectra of deionised water and orange II samples taken over 60 minutes at optimum DBD conditions are presented in Figure 5-10.

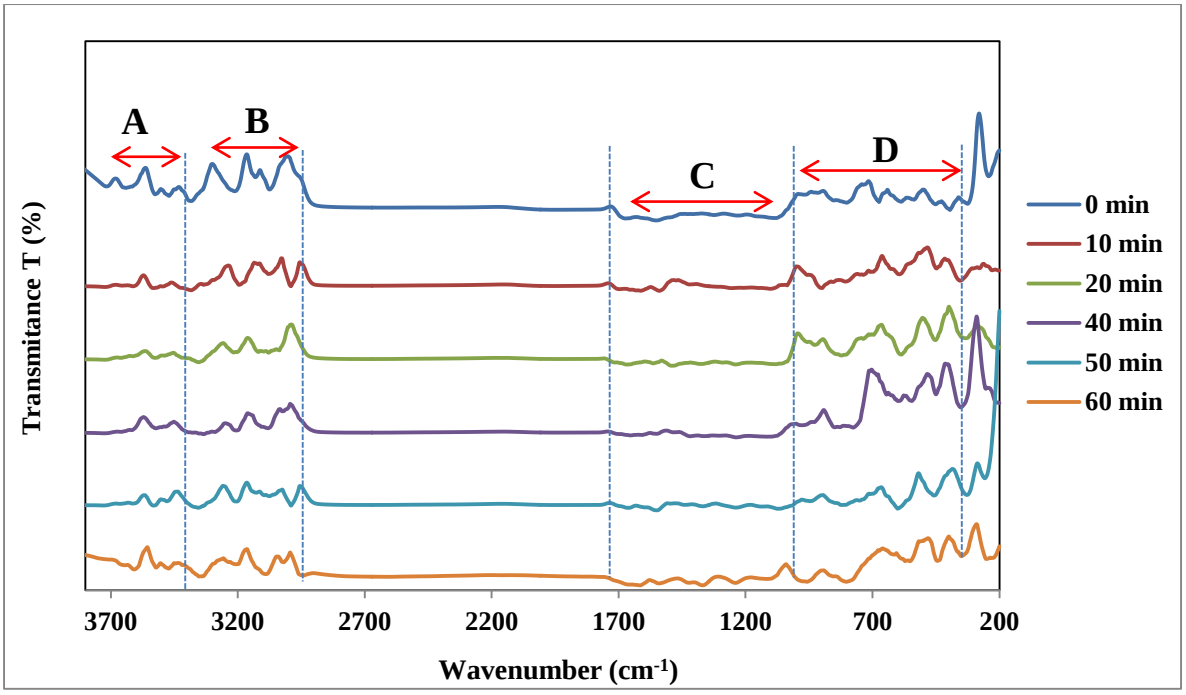

Figure 5.10: FT-IR of Orange II dye subjected to DBD experiment at the following experimental conditions: Peak voltage 8 kV, O.II concentration 60 mg/L, , pH 2.5, air gap 2 mm, air flow rate, 3 L/min, O.II volume 1500 mL, 50 g/L NaCl electrolyte, 1.5 mm silver electrode and contact time of 60 minutes.

The FT-IR plots presented in Figure 5-10 were divided into four distinct regions A, B, C and A such as A (3700 -3500 cm^{-1}), B (3400 - 3000 cm^{-1}), C (1850 - 1100 cm^{-1}), D (1000 - 200 cm^{-1}) as described in Table 5-2.

Table 5.2: FT-IR results of O.II solution treated at optimum conditions: Peak voltage 8 kV, O.II concentration 60 mg/L, , pH 2.5, air gap 2 mm, air flow rate, 3 L/min, O.II volume 1500 mL, 50 g/L NaCl electrolyte, 1.5 mm silver electrode and contact time of 60 minutes.

	Wavenumber (cm^{-1})	Functional group	Vibration	Susceptible compounds
Region A	3400 – 3550	N-H	weak	Diluted solution (1° amine, 2 bands)
	3300 - 3400	N-H	weak	Diluted solution weak N-H 2° amines
	3580 - 3650	O - H	Var. (free)	Usually sharp
	3200 - 3550	O - H	Stretching	H-bonded, usually broad

Region B	3020 - 3100	= C - H	Stretching	Alkene
	3030 - 3310	C - H	Stretching	unsaturated aromatics
Region C	1450 - 1600	C = O	var. Assym	Carbonyl compounds
	1600 - 1680	C = C	Var.	unsaturated olefins
	1630 - 1575	-N = N-	Str.	Azo group
Region D	1000 – 1200	C - N	med	Shift on H-bonding
	1000 -1320	O - C	Med/vibrations	Carboxylic acids
	965 - 960	CH = CH	Stretching	Olefins
	1030 - 1345	S = O	Stretching	sulfoxide
	1490 – 1410/880-860	CO_3^{2-}	Stretching	Carbonate ion
	1130 – 1080/680 - 610	SO_4^{2-}	Stretching	Sulfate ion
	1380- 1350/840 – 815	NO_3^-	Stretching	Nitrate ion
	1365- 1340/1200 - 1100	$-SO_3$	Stretching	Sulfonates aliphatic compounds

Even though the stretching vibrations of functional groups in these regions look similar, the intensity of vibrational stretches in untreated orange II is higher than those in the DBD treated samples. This meant that some chemical reactions such as oxidation or reduction of orange II dye might have occurred during the plasma treatment process. For instance in region A (3700 -3500 cm^{-1}), the sharp stretches in raw orange II spectra can be ascribed the O-H free vibration of the ortho-hydroxyl group the on orange II structure. However, the presence of these weak vibrations in reduced intensities in treated samples spectra probably characterises the existence of aqueous 1^o and 2^{nd} amines. In region B (3400 - 1900 cm^{-1}) two types of functional groups mainly = C-H (3020-3100 cm^{-1}) and C-H (3030 - 3310 cm^{-1}) stretching that are characteristic of unsaturated aromatics such as alkenes have been identified. These vibrational stretching correspond to the = C-H in orange II aromatic system and aliphatic group probably obtained during degradation of orange II dye. Moreover, about three functional groups were identified in region B. That is the C= C (1600-1680 cm^{-1}) of the azo group (-N=N-) stretching (1630-1575 cm^{-1}) in olefin O.II carbon form work have been identified in region B. In addition, the asymmetric vibration of C=O (1450 -1600 cm^{-1}) characterising carbonyl compounds formed during irradiation of O.II were also detected in region B. Finally in region D (1000 - 200 cm^{-1})

most functional groups in O.II and its plasma generated by-products have been assigned in this region. For instance, the stretching vibration of CH=CH group (965-960 cm^{-1}) characteristic of the olefin group orange II and the medium vibration of C-N (1000 – 1200 cm^{-1}) due to H-bond shifting and the stretch vibration of S=O bond, characteristic of sulfonic/sulfoxide (1030 – 1345 cm^{-1}) group in O.II were also identified. Apart from these, a medium vibration of the O-C group between 1000 and 1200 cm^{-1} shows the presence of carboxylic acid in the plasma treated solution. In addition to this, sulfonate aliphatic compounds might possibly be present in the treated solution. This was evidenced by the stretching vibration of $–SO_3$ group in the 1365 – 1340/1200 – 1100 cm^{-1} region. Furthermore, the region also showed the stretching vibration of the carbonate ion (CO_3^{2-}: 880- 860 cm^{-1}); sulphate ion (SO_4^{2-} (1130 – 1080/ 680 – 610). Nitrate ion (1380 1350/840 – 815 cm^{-1}). Therefore, region D shows the presence of various inorganic by-products of O.II when exposed to DBD plasma process. From the FT-IR analysis discussed in this section, it can be concluded that orange II was degraded into various organic and inorganic by-products. Even though most vibrations and stretching of functional groups identified in the spectrum of the untreated O.II were still present in the treated solutions, the new functional groups identified in the treated samples showed that orange II dye was decomposed to various by- products that need to be identified. These might have been further mineralised into dissolved CO_2 and H_2O over time. This qualitative FT/IR analysis of treated O.II samples shows the presence of various degradation by-products of orange II dye. Quantitative determination of the amount and identification of these intermediates is crucial to confirm their existence in DBD plasma treated samples.

5.2.3 Quantitative analysis of orange II dye: Determination of the water quality parameters

The mineralisation of orange II dye by DBD plasma treated was quantitatively assessed by determining the following parameters: total organic carbon (TOC), chemical oxygen demand (COD), sulphate content and nitrogen (as nitrate + nitrite) contents as previously described in chapter three (as described in Sections 3.7.3, 3.7.4, 3.7.5 and 3.7.6). The outcomes of these evaluations are presented in Table 5-3.

Table 5.3: Water quality parameters of the untreated and treated Orange II sodium salt at optimum conditions:Peak voltage 8 kV, O.II concentration 60 mg/L, pH 2.5, air gap 2 mm, air flow rate, 3 L/min, O.II volume 1500 mL, 50 g/L NaCl electrolyte, 1.5 mm silver electrode and contact time of 60 minutes.

		Raw O.II	Treated O.II					
Analysis	Unit	A0	A10	A20	A30	A40	A50	A60
Sulphate as SO_4 Dissolved	mg/l	88	88	88	85	87	87	87
Nitrate + Nitrite as N *	mg/l	<0.1	0.3	1.1	2.4	4.4	5.9	8.2
Total Organic Carbon	mg/l	26	24	24	24	23	23	22
Chemical Oxygen Demand *	mg/l	70	60	60	56	43	43	27
Total Organic Carbon	%	0	7.692308	7.692308	7.692308	11.53846	11.53846	15.38462
Chemical Oxygen Demand	%	0	14.3	14.3	20	38.57	38.57	61.43

The quantitative results presented in Table 5-3 shows that the high amount of sulfate slightly decreased from 88 mg/L at 0 min to 85 mg/L after 30 minutes under the applied conditions. This sulfate content somewhat increased to 87 mg/L and stayed constant for the last 30 minutes of the DBD experiment. The higher amount of SO_4 in this series of samples was certainly due to the addition of sulfuric acid that was used to regulate the pH of orange II solution. Likewise its slight decrease over time demonstrated that the sulfonate/ sulfoxide group of the orange II structure was broken down to aqueous SOx such as sulphate (SO_4^{2-}) anions. These ionic by-products might have further reacted with free reactive oxygen species such as O_3, $O^{\cdot}$, etc., produced during DBD experiment and led to the formation of various sulfate containing species. This was evidenced by the increase of SO_4 content in the last 30 minutes of DBD plasma treatment. Apart from this, nitrogen (Nitrate + Nitrite as N*) content that was less than

0.1 mg/L before the experiment gradually increased up to 8.2 mg/L after 60 minutes of treatment time. This was probably due to the nitrogen content in air that was used as a feed gas and continuously flowed into the DBD plasma system. Air largely consists of nitrogen and a small amount of oxygen. This was earlier mentioned by Magureanu, Bradu, et al. (2013) who argued that nitrogen based compounds that were detected in plasma treated MB sample mainly derived from air and not from MB degradation. Or some nitrogen content might have derived from the degradation of the azo group the during the decomposition of orange II dye in the DBD system. On the other hand, the total organic carbon (TOC) content that was 26 mg/L before plasma exposure slightly decreased to 22 mg/L after 60 minutes of treatment time as disclosed in Table 5-3 and Figure 5-11. This represented only 15.38 % of orange II mineralisation. This clearly shows that orange II was only slowly converted to smaller organic entities that were being further degraded into CO_2 and perhaps other smaller molecules. In addition to TOC, chemical oxygen demand (COD) of orange II was also measured before and after the experiment. Results in Table 5-3 show that 70 mg/L of COD estimated before treatment decreased to 27 mg/L after 60 minutes of treatment time. This corresponded to about 61.43% of toxicity reduction as shown in Table 5.3 and Figure 5-11. The trends of TOC mineralisation and COD reduction percentages over time were plotted and presented in Figure 5-12.

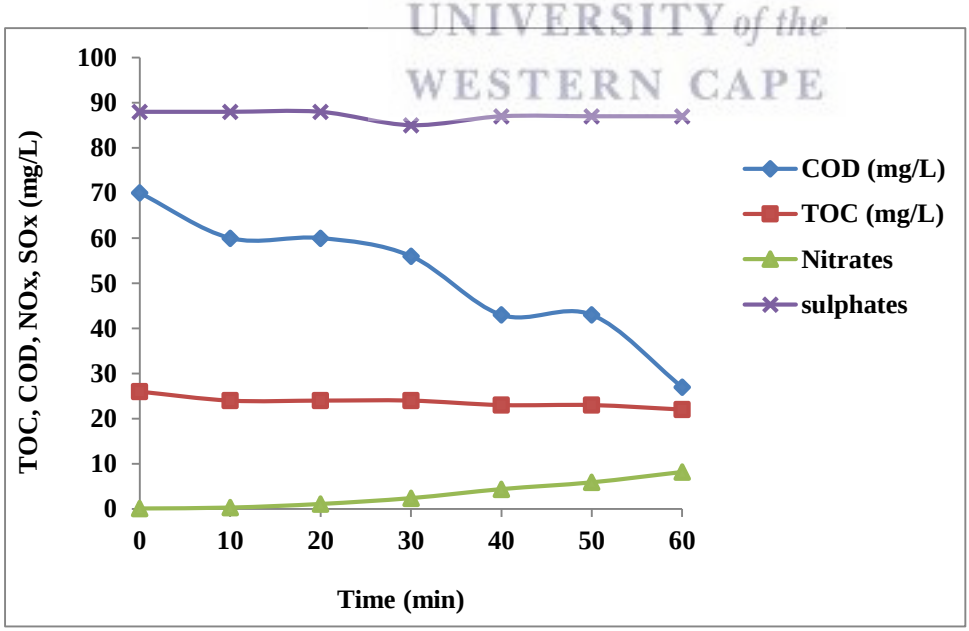

Figure 5.11: Evolution of ecological parameters of orange II sodium salt samples treated in DBD reactor at optimum conditions: Peak voltage 8 kV, O. II concentration 60 mg/L, , pH 2.5,

air gap 2 mm, air flow rate, 3 L/min, O.II volume 1500 mL, 50 g/L NaCl electrolyte, 1.5 mm silver electrode and contact time of 60 minutes.

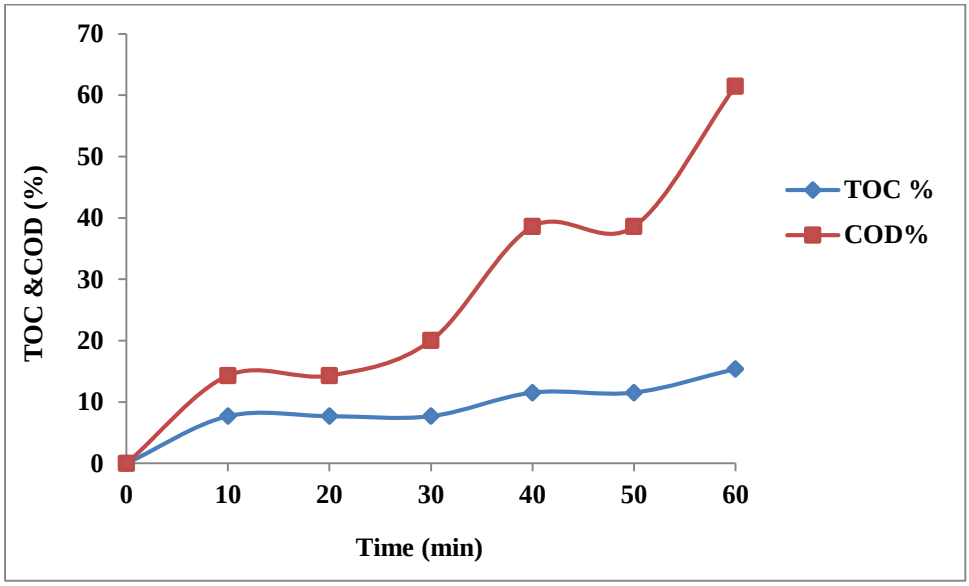

Figure 5.12: Mineralisation (TOC %) and toxicity reduction (COD %) of O.II dye during DBD experiment at optimum conditions: Peak voltage 8 kV, O.II concentration 60 mg/L, pH 2.5, air gap 2 mm, air flow rate, 3 L/min, O.II volume 1500 mL, 50 g/L NaCl electrolyte, 1.5 mm silver electrode and contact time of 60 minutes.

In case the final TOC and COD contents in treated solutions obtained after 60 minutes of DBD plasma treatment do not fall into the permissible limits recommended by the World Health Organisation (WHO) regulations, the DBD treatment time can still be prolonged in order to reach the desirable limits.

A few years ago, Reddy et al. (2014) suggested a convenient formula for determination of the TOC mineralisation efficiency. This was given as follows:

TOC removal percentage % = $[(TOC_o - TOC_t)/TOC_o] \times 100$ (5-1)

Therefore, in the present study, TOC removal efficiency was calculated as follows:

TOC removal percentage % = $[(26 - 22)/26] \times 100 = 15.38$ %

Similarly, the chemical oxygen demand (COD) reduction percentage was calculated as follows:

COD removal percentage % = $[(COD_o - COD_t)/COD_o] \times 100$ (5-2)

Hence in the actual study, the COD percentage removal was estimated as shown below:

COD removal percentage % = $[(70 - 27)/70] \times 100 = 61.43$ %

The results on degradation of orange II dye by the DBD system at optimum conditions show that even though 100% decolouration was achieved after 10 minutes of DBD experiment when measured by UV-vis, only 7.69 and 15.38 % of carbon content removal were obtained after 10

minutes and 60 minutes of plasma exposure, respectively. The TOC mineralisation percentage obtained in this study is far different from 98% and 48 % reported by Reddy & Subrahmanyam (2012) and Vujevic et al. (2004), respectively. This discrepancy may be due to the fact that experimental conditions and apparatus used in this study were different from those applied in literature. In addition to optimising experimental conditions, the presence of high quantities of scavenging ions produced during DBD experiments might significantly impact on the mineralisation of the dye. Indeed, Soares et al. (2006) reported that the formation of salts in wastewater being treated can considerably affect the TOC removal of a particular dye. The production and reduction of salt by-products in the treated water may lead to reduction of pH and hence induce the formation of acidic substances such as HNO_3, HOON, H_2SO_4, etc. which ultimately may decreased solution pH. In addition to this, Still, Salome and co-workers in 2006 accentuated that during the ozonation process, organic compounds may be hydrolysable when the solution pH is near 7. Likewise their hydrolysis at lower pH than 3.9 is uncertain. These claims were also highlighted by Magureanu et al. (2013) and clearly observed in the current study. For instance, the high amount amounts of sulfate (88-87 mg/L) and nitrates (0.1-8.3 mg/L) recorded in Table 5-3 would significantly reduce the pH of the solution during DBD plasma treatment. This trend was earlier discussed and plotted in Figure 5-4. Since the findings obtained in this study corroborate observations made by Soares et al. (2006) and Magureanu et al., (2013) as well as Magureanu et al., (2013), therefore it can be inferred that the formation of high contents of salts such as sulphates and nitrates + nitrites in the DBD system prevented TOC removal and favoured the degradation/decolouration of orange II dye. Alternatively, the resulting intermediate by-products such as carboxylic acids, aldehydes, amines, amides, etc. obtained during degradation of orange II were not mineralised into CO_2 and H_2O but perhaps remained in the solution. This statement was also supported by Shen et al., (2008) who confirmed that during removal of dye substances from water and wastewater by non-thermal plasma (NTP) systems both factors (TOC content and degradation efficiency) cannot be effectively attained at the same time. Hence extensive TOC removal in the current DBD reactor is inevitably needed to overcome this limitation.

5.2.4 High liquid performance chromatography analysis of orange II dye samples at optimum conditions

In addition to the UV-vis technique used in this study to investigate the % decolouration of orange II dye, high performance liquid chromatography (HPLC) was also used to prove the decomposition of orange II by DBD plasma reactor, which is needed to elucidate the difference between decolouration and degradation efficiency which does not mean the same thing. The high pressure liquid chromatography (HPLC) chromatograms showing the continuous decomposition of orange II are shown in Figure 5-13.

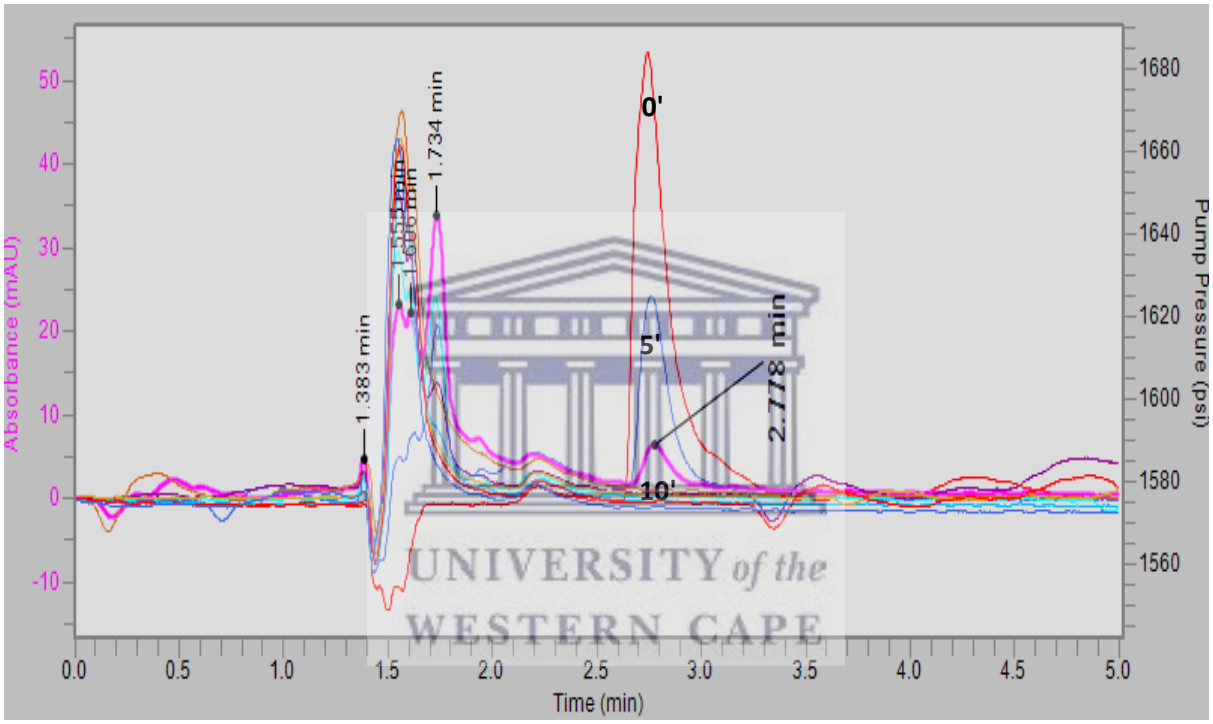

Figure 5.13: HPLC results of orange II dye solutions sampled at different times during DBD treatment optimum conditions: Peak voltage 8 kV, O.II concentration 60 mg/L, , pH 2.5, air gap 2 mm, air flow rate, 3 L/min, O.II volume 1500 mL, 50 g/L NaCl electrolyte, 1.5 mm silver electrode and contact time of 60 minutes.

The results presented in Figure 5-13 demonstrate that the degradation of the O.II molecules reached completion within 15 minutes of DBD treatment. That is, the chromatograms in Figure 5-13 show that from 0 to 15 minutes of sampling time, the intensity of the characteristic orange II dye peak decreased and disappeared after 15 minutes of DBD experiment. This was ascribed to the interaction of O_3, ·OH and other active radical species with the O.II molecule. Figure 5-13 also shows that the progressive diminishing of the orange II peak was related to the

concomitant formation of various degradation by-products that were identified by high performance liquid chromatography coupled to mass spectroscopy (HPLC/MS). The detected intermediates are listed in Table 5-4 and the proposed degradation pathways are shown in Figure 5-14.

Table 5.4: LC-MS identified degradation by-products of orange II (O.II) dye during DBD treatment after 20 min reaction time at the following conditions: Peak voltage 8 kV, O.II concentration 60 mg/L, solution volume 1500 mL, solution pH 2.5, air flow rate 3 L/min, 1.5 mm silver electrode, 50 g/L NaCl inner electrode electrolyte, air gap 2 mm and an experimental time of 60 min.

Compound	Molecular formula	Structure	Retention time (min)	Molecular ion $[M-H]^+$
Orange II sodium Salt (I)	$C_{16}H_{11}N_2NaO_4S$	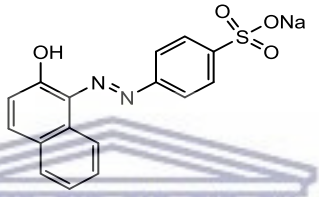	3.52	350.03
4-methyl-5-vinyl-3H-benzo[d][1,2,3]dioxazole (II)	$C_9H_9NO_2$	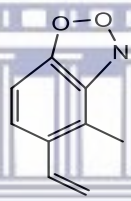	2.52	163.06
2,3-dimethylaniline (III)	$C_8H_{11}N$		2.71	121.09
2-methyl-1-nitroso-3-vinylbenzene (IV)	C_9H_9NO	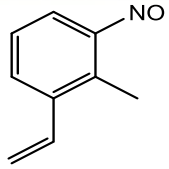	3.37	147.07
6-hydroperoxy-2-methyl-3-vinylaniline (V)	$C_9H_{11}NO_2$	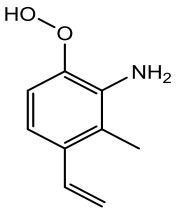	2.71	165.08
Sodium 4-(2l2-diazenyl)benzenesulfonate (VI)	$C_6H_4N_2NaO_3S$	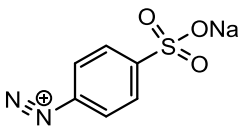	2.52	207.16
N-phenylmethanimine (VII)	C_7H_7N	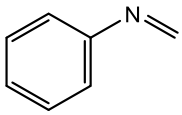	2.14	105.06

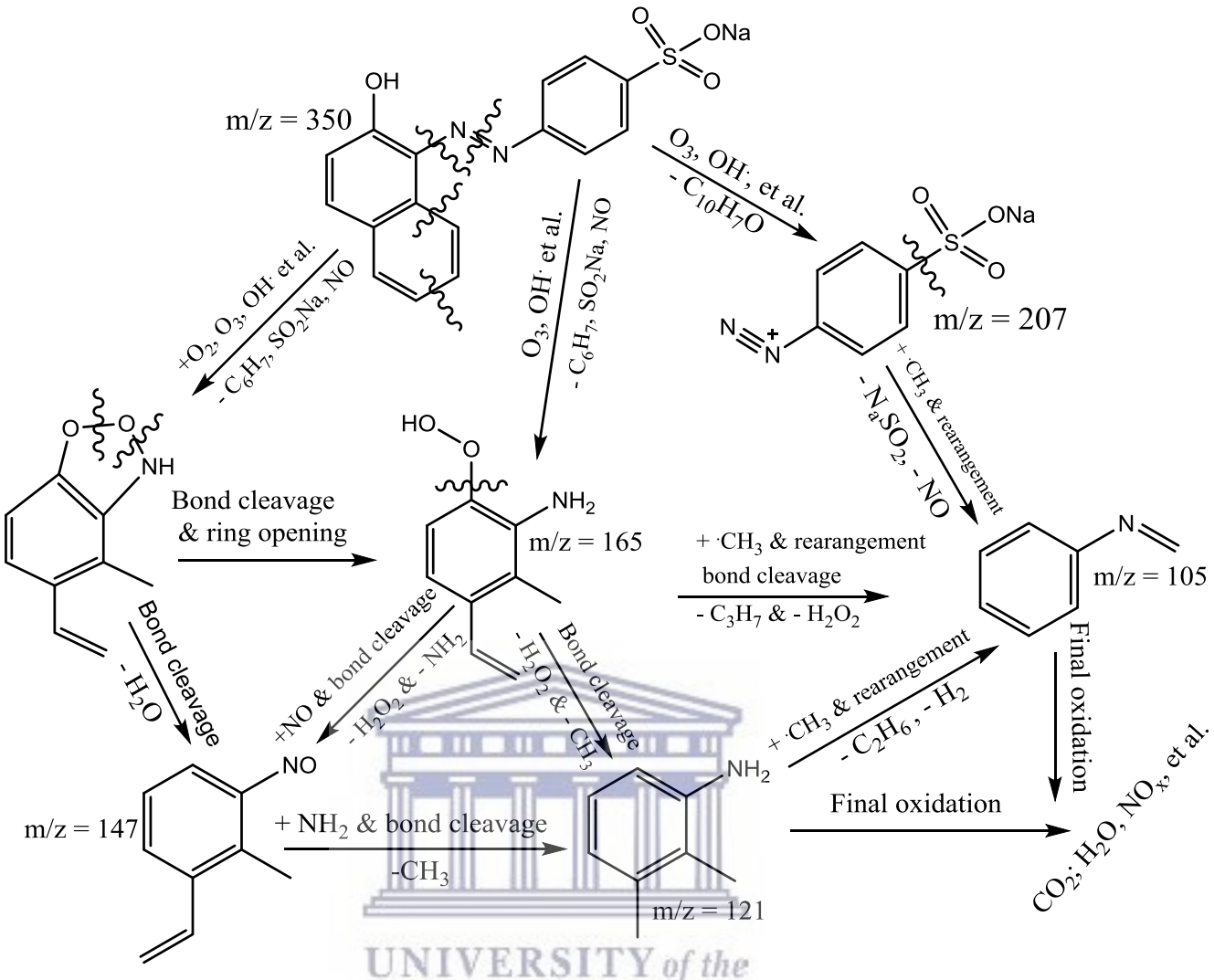

Figure 5.14: Suggested degradation pathways of O.II decomposed by DBD reactor (R_1) at optimum conditions: Peak voltage 8 kV, O.II concentration 60 mg/L, solution volume 1500 mL, solution pH 2.5, air flow rate 3 L/min, 1.5 mm silver electrode, 50 g/L NaCl inner electrode electrolyte, air gap 2 mm and an experimental time of 60 min.

Table 5-4 discloses the degradation intermediate by-products of O.II identified by LC-MS at the applied conditions while their suggested degradation mechanistic pathways are presented in Figure 5-14. The outcomes disclosed in Table 5-4 indicate that the O.II dye pollutants ($C_{16}H_{11}N_2NaO_4S$, m/z = 350.03) was decomposed into six degradation metabolites m/z = 105.06, 121.09, 147.07, 165.08, 207.16, 163.06 that eluted after 2.14, 2.71, 3.37, 2.71, 2.52 and 2.52 min, respectively. The results recorded in Table 5-4 show that the mineralisation of O.II was mainly activated by bond cleavage and ring opening of the azo group and the aromatic ring, correspondingly. Figure 5-14 shows that the degradation of O.II followed three principal

degradation mechanistic pathways. The first O.II degradation route involves the electrophilic attack of O_3 and OH radicals on O.II with elimination of – $C_7H_{10}O$ resulting in the formation of m/z = 207 whose methylation and rearrangement was followed by elimination of – N_aSO_2 and – NO which led to the formation of the intermediate m/z = 105 that was further mineralised into CO_2, H_2O and dissolved inorganics. The second pathway includes the electrophilic attack of O_3 and ·OH on O.II accompanied by elimination of - C_6H_7, - N_aSO_2 and - NO fragments yielding the intermediate m/z = 165 which by bond cleavage and elimination of – H_2O_2 and – CH_3 resulted in the formation of m/z = 121 that was totally converted into CO_2, H_2O and simpler inorganics. The third degradation pathway of O.II involves the subsequent attack of O.II by O_2, O_3 and ·OH followed by bond cleavage and elimination of - C_6H_7, - N_aSO_2 and – NO remains forming m/z = 165 whose dehydration and bond cleavage led to the formation of m/z = 147 intermediate. The addition of amine group (-NH_2) and bond cleavage followed by elimination of – CH_3 yielded the metabolite m/z = 121 that was fully oxidised and mineralised into simpler aqueous entities. For comparison purposes, the degradation of O.II by DBD is scarce in the literature, however, Mok et al. (2008) attempted the removal of O.II dye in a single cylindrical dielectric barrier discharge alone and in combination with powder TiO_2 catalyst at the following condition, O.II concentration 25 and 500 mg/L, solution pH 5.3, air flow rate 6 L/min, copper electrode for 60 min.

The results obtained by Mok et al. (2008) showed that the single cylindrical DBD was effective in removing the chromaticity and cleaving the benzene and naphthalene rings of O.II contaminant at the applied conditions. Likewise, the authors complained that from the 9% TOC removal after 60 min and LC-MS results, the O.II degradation by-products were recalcitrant to further oxidation and hence in good agreement with the observation encountered in the current study. Even if the authors did not report any degradation by-product obtained, their refractory behaviour implied that, perhaps the authors needed to reassess or optimise their single cylindrical DBD reactor before using it or probably they did not apprehend the mitigation between TOC and degradation efficiency that often cannot be achieved at the same time due to the high salinity induced by inorganic end products/salts as conveyed by Soares et al.(2006). In the actual study however, it can be suggested that the treatment time should be extended to a few hours to ensure full oxidation of the fragments or remains. Otherwise, sophisticated techniques for TOC amendment need to be developed. On the contrary, the degradation of O.II was also conducted by Peralta-Hernández et al. (2008) during experimental test of three distinct AOPs including direct photolysis, electro-Fenton and photoelectron-Fenton processes at the following condition: O.II concentration 50 mg/L, pH 3 for 60 min running time at room

temperature. The outcomes showed that all three systems completely decolourised O.II dye in less than 5 min. However, the photoelectron-Fenton system at lower iron content was the best. Unfortunately, the authors did not inform about O.II degradation by-products and their degradation mechanistic pathways. Parallel results on the degradation and mineralisation pathways of O.II dye to those obtained in this study were also reported by Yan *et al*. (2008) but instead of DBD configuration, the authors used a gas–liquid gliding arc discharge system at the following conditions: Peak voltage 10 kV, O.II concentration 500 mg/l, O_2 flow rate 0.4m^3/h, solution pH 6.20 and a treatment time of 20 min. Li *et al*. (2013) on the other hand investigated the removal of O.II using various AOPs different from DBD and the degradation metabolites and degradation pathways were successfully proposed. The degradation of O.II dye by systems other than DBD has been conducted by a number of authors (Mu *et al.*, 2004b; Silva *et al.*, 2009; Li *et al.*, 2013; Siuleiman *et al.*, 2014) whose studies did not highlight any degradation intermediates or decompositions mechanism pathways. The outcomes of the current study confirm that the current optimised DBD system is a potent advanced oxidation process that can be used for complete removal of dye pollutants from water and wastewater. However, these results can also be compared with DBD combined with a photo catalyst to study the decomposition behaviour of dye pollutants in this system. Besides dyes abundantly present in textile wastewater, pharmaceutical contaminants found in urban, municipalities and hospital wastewater that cause serious threats to human and their ecosystems have attracted global attention. Hence the current DBD could also be an adequate advanced technology for the detoxification of pharmaceuticals from water and wastewater.

5.3 Degradation of sulfamethoxazole: optimisation of working parameters (electrophysicochemmical parameters)

Following the same procedure as the one used for the optimisation of DBD reactor using O.II as the model pollutant, section 5.2, deals with the optimisation of the DBD reactor conditions for degrading the sulfamethoxazole (SMX) drug whose chemical structure is shown in Figure 5-15 as a model water and wastewater pharmaceutical contaminant. The effects of various parameters including initial concentration, solution pH, air flow rate and the applied voltage on the degradation percentage of SMX derived from high performance liquid chromatography coupled to mass spectroscopy (HPLC-MS) analysis were investigated at the applied conditions (see sections 3.6.4.1 and 3.6.4.1.3). High performance liquid chromatography (HPLC) coupled to mass spectroscopy (LC-MS) was used to follow the decay of SMX concentration in DBD

reactor, and hence the determination of SMX degradation efficiency within 60 minutes reaction time as described in Section 3.7.2.2. The degradation mechanistic pathways of SMX are proposed herewith, but the quatitative analysis for the determination of TOC, sulphates, nitrates and nitrites was not achieved due to the high analytical cost. The experimental results are subsequently presented in the following sections.

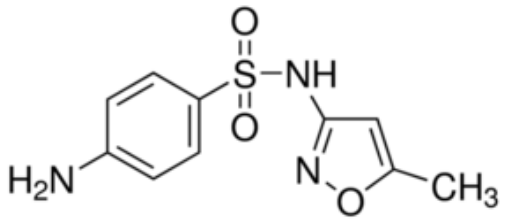

Figure 5.15: Chemical structure of sulfamethoxazole (SMX)(Molar mass 253,279 g/mol)

5.3.1 Effect of initial concentration on degradation efficiency of sulfamethioxazole

The impact of initial concentration on SMX degradation percentage was assessed by varying the SMX concentration from 20, 40, 60 to 100 mg/L while other parameters including pH 5.634, solution volume 1500 mL, voltage 6.8 kV, air flow rate 3L/min, 1.5 mm silver electrode, 50 g/L NaCl electrolyte were kept constant (see Section 3.6.4.1.1). In this section, high performance liquid chromatography coupled to mass spectroscopy (HPLC-MS) analysis was used at the applied conditions (Section 3.7.2.2) to follow the concentration of SMX with time during DBD treatment. The resulting concentrations obtained by HPLC and their corresponding degradation efficiencies are tabulated in Appendices 9 (a & b) and the plots of these experiments are shown in Figure 5-16.

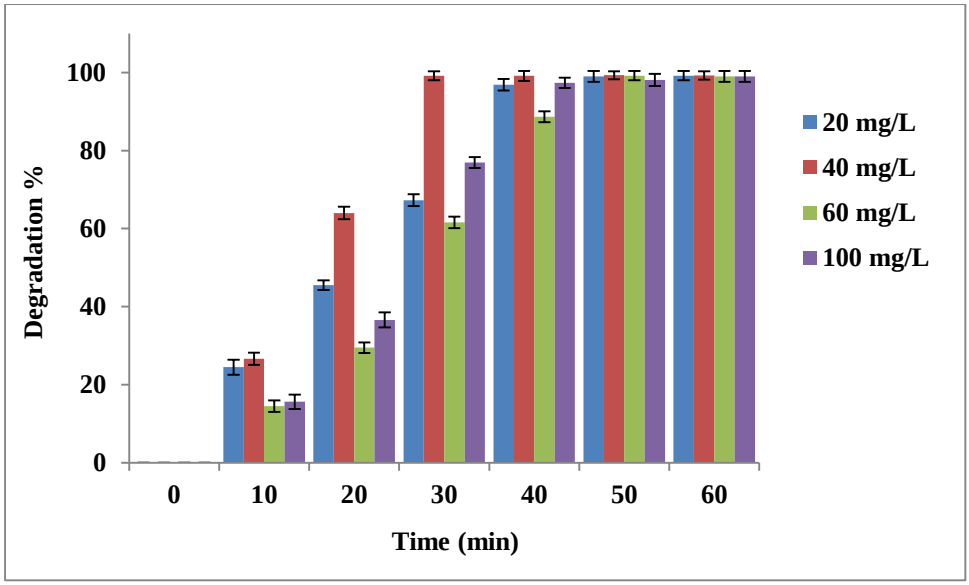

Figure 5.16: Effect of initial concentration on degradation of sulfamethoxazole (SMX). Experimental conditions: varied parameter: initial SMX concentration from 20, 40, 60 to 100 mg/L. Fixed conditions: pH 5.6, solution volume 1500 mL, Peak voltage 6.8 kV, air flow rate 3 L/min, 1.5 mm silver electrode, 50 g/L NaCl electrolyte and 60 minutes of treatment time (n = 2).

Figure 5-16 discloses the impact of initial concentration on SMX degradation percentage in the DBD configuration surveyed by varying SMX concentration from 20, 40, 60 to 100 mg/L at the applied conditions. The outcomes in Figure 5-16 show that the removal percentage of SMX increased with an increase of treatment time. That is, complete degradation of the drug was achieved after 30 minutes with 40 mg/L followed by 76.94, 67.26 and 61.60% removals that were attained with 100, 20 and 60 mg/L, respectively. A similar trend was observed after 10 and 20 min while different behaviour was detected after 30 min of DBD exposure. These results showed that the DBD reactor has an excellent performance for the decontamination of SMX at different doses. The change in oxidative percentages of SMX at different concentrations observed in Figure 5-16 could principally be attributed not only to the productive proportionality of reactive oxygen species but to their reactivity with SMX as well (Wang *et al*., 2011). Indeed it was shown in section 4.3.1 that O_3 is abundantly produced at acid pH (< 7) and readily reacts with olefinic compounds (Gogate and Pandit, 2004; Munter 2001; Kim et al. 2013). In contrast, the non-selective ·OH which is not really active in acidic media is produced in small amounts (Staehelin and Hoigne, 1985). Therefore, it is reasonable to argue that O_3 dominantly interacted with SMX and its by-products inducing faster oxidation compared to OH whose interactions might have required a prolonged time to reach completion.

The degradation by-products of SMX obtained at each concentration in the DBD reactor are different in the sense that those vulnerable to O_3 or species other than OH· radicals degraded and this resulted in improved oxidation percentages such as 99.99, 92. 84 and 86.85% obtained with 40, 100, and 20 mg/L SMX dose after 40 min of treatment time at the applied conditions. On the other hand, the complete oxidation of by-products such as amides and amines are often recalcitrant to O_3 in DBD acidic media (Glaze, 1986; He *et al.*, 2014; Kuo *et al*., 2015) but vulnerable to attack by OH radicals (Gao, 2012; Qi et al. 2014). SMX degradation took a long time to reach completion and hence resulting in reduced % degradation of 68.79% attained with 60 mg/L after 40 min. There is little or no information in the literature of the effect of the initial concentration on SMX degradation efficiency in the DBD reactor. However, similar behaviour of the initial concentration on SMX removal percentage has been noticed by various researchers using different oxidation aqueous systems (Beltrán *et al.*, 2008; Wang *et al*., 2011; Dimitrakopoulou *et al.*, 2012). Hence the high/complete SMX degradation percentage (99.99%) achieved with 40 mg/L after 40 min of DBD exposure suggests that the degradation intermediate by-products obtained at this concentration were likely degraded by O_3 and co-species. Since this trend was observed across all sampling times, 40 mg/L was considered as the optimum concentration that was used throughout the following DBD optimisation. It can be inferred that the pollutant initial concentration significantly impacts on its removal percentage not only in the DBD reactor but in other aqueous systems and should be monitored during treatment as the treatment time may need adjustment.

5.3.2 Effect of solution pH on degradation efficiency of sulfamethioxazole

Next to initial concentration, the impact of solution pH on the degradation percentage of SMX was also examined by varying the initial pH values from 2.5, 6.5, 8.5 to 10 and keeping other factors constant as described in experimental Table 3-4. The resulting concentrations and their degradation efficiencies are disclosed in Appendices 10 (a & b) while the plots of these assessments are shown in Figure 5-17.

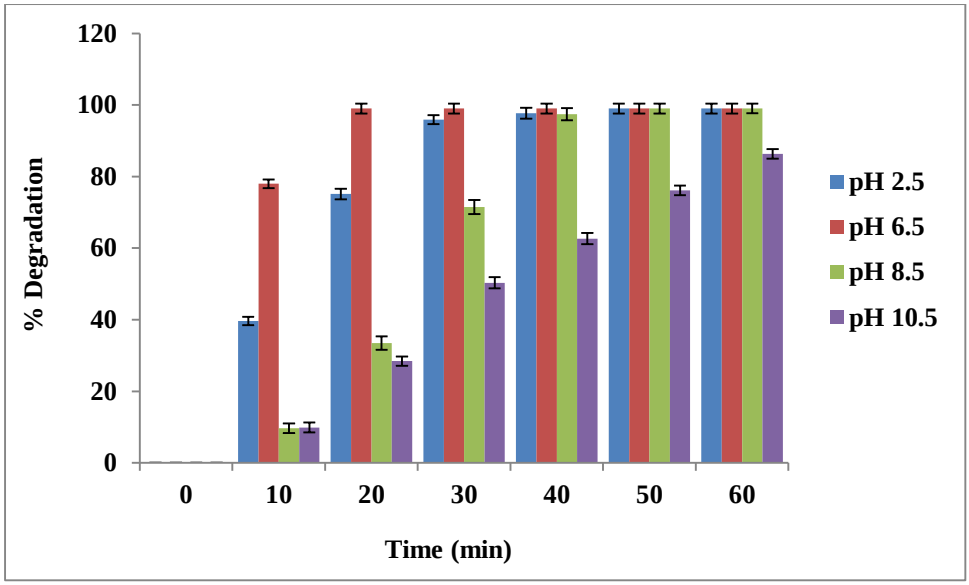

Figure 5.17: Effect of pH on degradation of sulfamethoxazole (SMX). Experimental conditions: varied parameter: solution pH from 2.5, 6.5, 8.5 to 10.5. Fixed conditions: [SMX] 40 mg/L, solution volume 1500 mL, peak voltage 6.8 kV, air flow rate 3L/min, 1.5 mm silver electrode, 50 g/L NaCl electrolyte and 60 minutes of treatment time, (n = 2).

Figure 5-17 indicates the influence of solution pH on the removal efficiency of SMX at the applied conditions. The results show that higher removal of SMX was achieved in slightly neutral (pH 6.5) solution and complete degradation of SMX at the same pH value was observed after 20 min of DBD exposure. Though, after 10 minutes, 75.18, 38.5 and 28.3% of SMX degradation were correspondingly achieved with pH 2.5, 8.5 and 10.5. The decomposition of ozone in acidic media occurs slowly (Garoma, Umamaheshwar and Mumper, 2010), hence the 99.99% SMX removal obtained with pH 6.5 after 20 min of DBD run was certainly due to its electrophilic interaction with aqueous ozone recalling that ozone is selective toward olefinic compounds and readily reacts with them via electrophilic attack (Dors, 2007; Rong *et al*., 2014; Chen *et al.*, 2015). The lower 38.5 and 28.3% SMX removals achieved at alkaline pH 8.5 and 10.5 after 10 min of treatment, respectively certainly implied that SMX degradation by-products obtained at that pH range were recalcitrant and hence required more time for complete mineralisation. This contradicts Munter, (2001) who reported that the disintegration of ozone increases with an increase in pH, hence leading to the formation of more OH radicals that could non-selectively attack the simulated contaminant. The results obtained in Figure 5-17 are in agreement with Lin et al. (2009) who investigated the ozonation of sulfonamide contaminants in ground and wastewater. They reported that the abatement of sulfonamides decreased with the rise in solution pH that was due to the decline of ozone concentration that majorly led to

the formation of OH radicals even though they did not specify the role/activity of OH radicals near neutral and alkaline pH.

In addition, from the chemical structure presented in Figure 5.16, it can be noticed that SMX consists of an amine group (–NH_2) that is basic and an acidic amide group (–NH–) often characterised by two pKa values pKa_1 = 1.85 and pKa_2 = 5.60 as shown in Figure 5-18 (Xekoukoulotakis et al. 2011). Therefore, under DBD conditions, the basic group protonates while the acidic SMX group deprotonates with the pKa_1representing the equilibrium dissociation constant between the positively charged (protonated amino group of SMX) and its neutral conjugate base, and pKa_2 stands for the equilibrium for the SMX proton loss yielding its negatively conjugate base. According to Xekoukoulotakis et al. (2011), at pH values less than pKa_1 and above pKa_2, SMX predominates in its positive and negative forms, respectively and exists in its neutral form for pH values between pK_1 and pKa_2. So from these SMX chemical properties and the outcomes plotted in Figure 5-17 it could be inferred that the solution pH significantly impacted up on SMX removal and the highest degradation efficiency of SMX was achieved at in its protonated form via electrophilic interaction with O_3 in near neutral media. This was earlier supported by Qiang & Adams (2004) and Qi et al. (2014). Since the highest removal of SMX was observed at pH 6.5 at all sampling times, 6.5 was considered as the optimum pH that was used throughout all further SMX experiments.

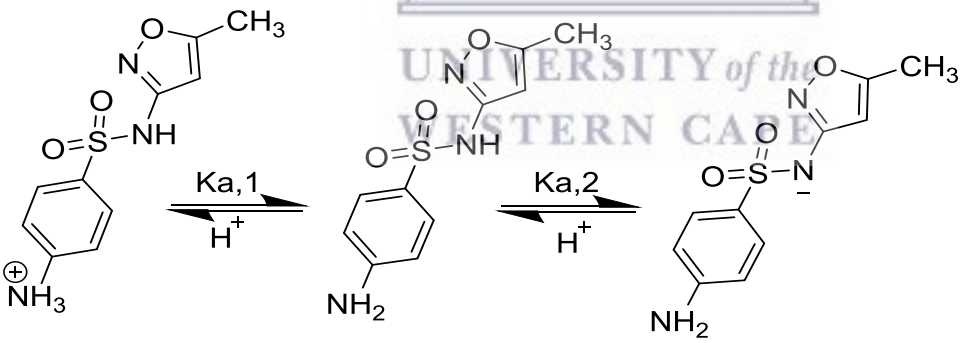

Figure 5.18: Acid - based dissociation equilibrium of sulfamethoxazole (Xekoukoulotakis et al. 2011).

5.3.3 Effect of air flow rate on degradation efficiency of sulfamethioxazole

Besides the initial concentration and solution pH of the pollutant, the effect of air flow rate on the degradation of SMX in the DBD reactor was also assessed by altering the flow rate values from 3, 6 to 9 L/min while the other parameters were kept constant. The resulting

concentrations and their related degradation percentages are exhibited in Appendices 11 (a & b) while the plots of these results are presented in Figure 5-19.

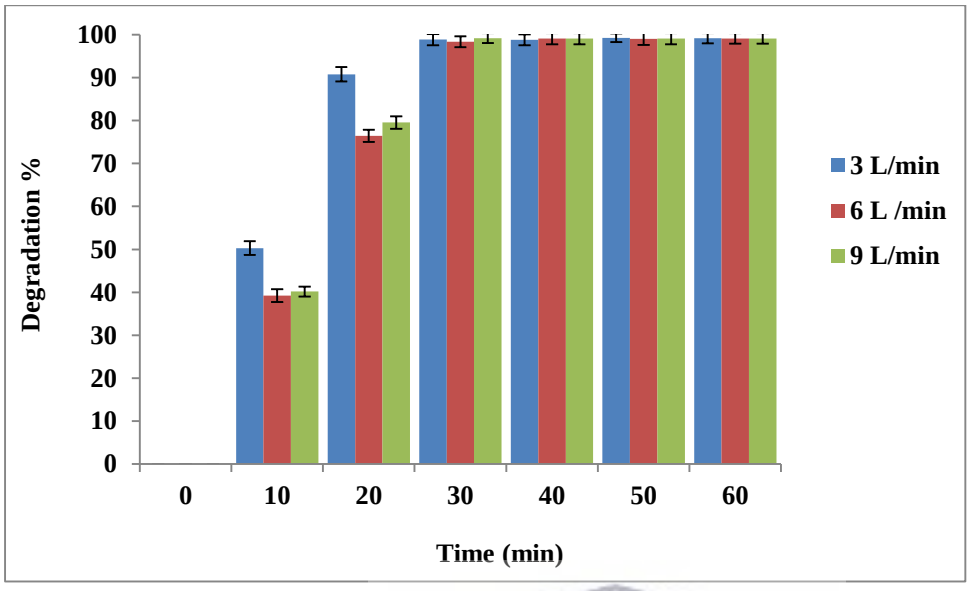

Figure 5.19: Effect of air flow rate (L/min) on degradation of sulfamethoxazole (SMX) determined by HPLC. Experimental conditions: varied parameters: air flow rate from 3, 6 to 9 L/min. Fixed conditions: [SMX] 40 mg/L, initial pH 6.5, solution volume 1500 mL, peak voltage 6.8 kV, 1.5 mm silver electrode, 50 g/L NaCl electrolyte and 60 minutes of treatment time, (n=2).

The influence of air flow rate on the percentage degradation of SMX shown in Figure 5-19 demonstrates that high removal efficiencies of SMX were achieved at lower air flow rate. For instance after 20 min of reaction time, 90.75 % removal of SMX was reached with an air flow of 3 L/min compared to 79.53 % and 76.42 % attained with 9 and 6 L/min, correspondingly. Analogous behaviour was observed after 10 and 30 min of experimental time. To recall, when air is exposed to electrical discharge, the highly energised electrons may dissociate nitrogen and oxygen molecules into unstable radicals, such as $N^{\cdot}$ and $O^{\cdot}$ whose reaction either between themselves or with parent molecules O_2 and N_2 results in various nitrogen and oxygen species including O_3, N_2, NO, NO_2, etc. that are circulated into the solution at a constant continuous flow (Jiang *et al.*, 2014). Thereafter, in the bulk, the bubbled species interact with aqueous entities and yield numerous oxidants among which $\cdot OH$, $O_2^{\cdot -}$, etc. that selectively or unselectively destroy and mineralise the contaminant into CO_2, H_2O and inorganics (Munter 2001). The active species formation starting in the plasma zone and then bubbled into the polluted water is enhanced by UV-light, hence increasing the number of oxidising species.

Therefore, increasing the air flow rate might limit the production of oxidants whose quantity in this case might not be sufficient to decompose the SMX and hence decreasing the percentage degradation of SMX over 10 or 20 min reaction time at higher flow as observed in Figure 5-19. These results are in contradiction with Shi et al. (2009) who investigated the degradation of *p*-chlorophenol (4-CP) in a pulsed high voltage discharge reactor and showed that the bubbling of gas in the discharge reactor had a great impact on the degradation of 4-CP. After 30 min of discharge, 64% of 4-cp removal was attained in the absence of gas bubbling while 64 % and 85 % removals were achieved with 1.3 L/min and 2 L/min of oxygen gas. A similar effect of air flow rate on the decomposition of phenols was also noticed by Sugiarto & Sato (2001) and Cheng et al. (2007). So the results presented here are different from those achieved in the literature because the air flow rate used seems higher than values used in the literature. For instance, the flow rate value 3, 6 and 9 L/min would correspond to 180 L/h, 360 and 540 L/h that are higher than 80 L/h and 120 L/h used by Wenjuan Bian and co-workers, (2009). Consequently, it is reasonable to believe that the trend observed in the literature (Sugiarto and Sato, 2001; Cheng *et al.*, 2007; Bian, Ying and Shi, 2009) could be well detected in the current DBD reactor at air flow rates lower than or equal to 3 L/min. Since 3 L/min was the lowest air flow rate used in this study, therefore it would be recommended that for future DBD applications/investigation a more practical flow rate instrument with lower values should be employed. Furthermore, it can be articulated that the results in Figure 5-20 are more effective than those obtained in the literature because after 20 min of DBD run 90.75% of SMX removal was attained while the 85 % of 4-CP obtained by Bian et al. (2009) was reached only after 30 min of pulsed electrical discharge. So, the difference between the results presented in Figure 5-19 and those extracted from the literature might be due to the type of electrical discharges and chemical structure of pollutant used as model compounds. From the results above, 3 L/min was chosen as the optimum air flow rate for the DBD reactor and was employed throughout the following experimental protocols.

5.3.4 Effect of voltage on degradation efficiency of sulfamethioxazole

In addition to the physico-chemical parameters discussed above, the peak voltage during the DBD experiment was also believed to have an impact on the percentage degradation of the targeted pollutant SMX. Hence peak voltage was altered from 6.8, 8 to 10 kV while other parameters were kept constant. The outcomes of these experiments are tabulated in Appendices 12 (a & b) and their plots are presented in Figure 5-20.

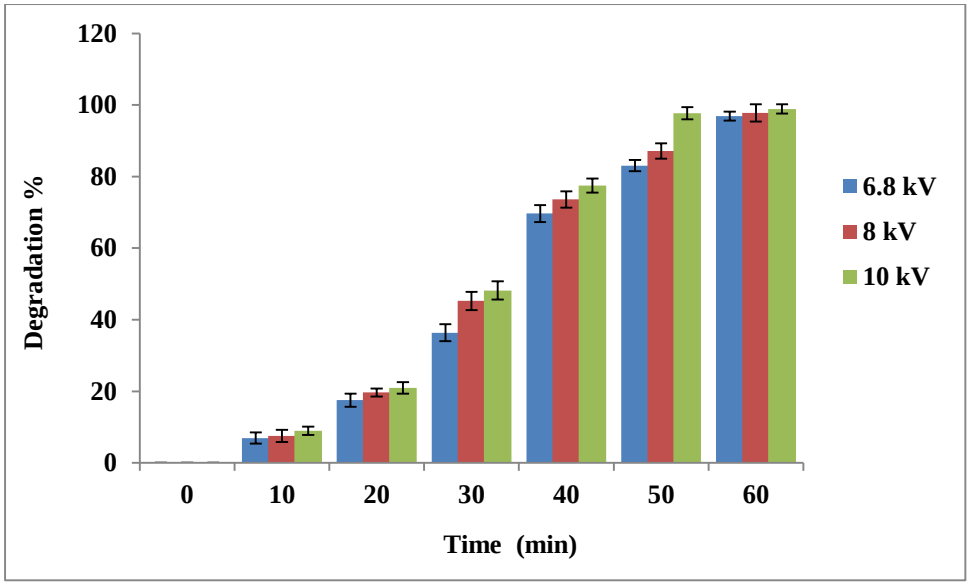

Figure 5.20: Effect of voltage (kV) on degradation efficiency of sulfamethoxazole (SMX). Experimental conditions: Varied parameter: Peak voltage from 6.8, 8 to 10 kV. Fixed conditions: [SMX] 40 mg/L, pH 6.5, solution volume 1500 mL, 1.5 mm silver electrode, 50 g/L NaCl electrolyte and 60 minutes of treatment time, (n =2).

Figure 5-20 shows the impact of changing the voltage on the percentage degradation of SMX at the applied conditions. The results in Figure 5-20 indicate that the removal percentage of SMX increased almost linearly with an increase of the applied voltage. That is, after 50 minutes of reaction time the highest percentage degradation of SMX (97.72) % was achieved with 10 kV followed by 97.75 and 96.86% reached with 8 and 6.8 kV respectively highlighting that this trend was constant at all sampling times. In fact, at elevated applied voltage, electrons are easily produced and form avalanches of charged particles around the second dielectric barrier (Nifuku *et al.*, 1997). Hence the electron energy at an elevated applied voltage was superior to the activation energy of the organic molecules whose chemical bonds were fragmented and transformed into diverse constituents as sustained by Cheng et al. (2007). Massima, (2014) demonstrated that the inner tube of the DBD reactor is governed by high energised electrons which are a direct consequence of the strong electric field intensity that in turn depends on the applied voltage. The energetic electrons fragment the feed gas air into various molecular or ionic, unstable species that are circulated in the solution, hence inducing the fragmentation of SMX contaminant. Therefore, increasing the peak voltage from 6.8 to 10 kV certainly enhanced the rate of formation of active species in the air gap and hence improved the amount of aqueous oxidants such as O_3, $^{\bullet}OH$, H_2O_2, $^{\bullet}O$, etc. that favoured the degradation of SMX in

the simulated wastewater to 83.06, 87.15 and 97.72 %, respectively at 50 min. Since it was already proven in section 4.3.1 that the current DBD produces a significant amount of O_3 and OH radicals, it is probable to assume that these two oxidants might have largely contributed to the decomposition of SMX by electrophilic attack resulting in bond/ring cleavage. This observation was also reported by Yan et al. (2006) and sustained by Cheng et al. (2007). Although, the impact of voltage on SMX degradation in DBD systems is scarce in the literature, the influence of the peak voltage on organic compounds/contaminants has already been investigated in different protocols. For example, Ruan et al. (2005) studied the decomposition of simulated odours in municipal wastewater treatment plants by a wire-plate pulse corona reactor. For their simulated wastewater, three organic model pollutants namely ethanethiol, trimethylamine and ammonia were considered. Their findings showed that the removal percentage of each contaminant increased with an increase of peak voltage that was altered from 40 to 80 kV. The authors reported that at high voltage the maximum removal efficiencies 100, 98 and 91% of ammonia, ethanethiol and tri-methyl amine were attained, respectively. These results seem higher than 89.85, 47.93 and 37.38% of SMX obtained after 50 min of DBD run when the peak voltage was raised up from 6.8, 8 to 10 kV, correspondingly. The results achieved in the current study seem different from those of Ruan et al. (2005) because the experimental conditions used in both studies are different. In addition, the corona discharge reactor they used is different from the DBD reactor though both are part of non-thermal plasma technologies. Furthermore, Ruan and colleagues, (2005) employed high voltage values (40 – 80 kV) which are four times higher than the maximum 10 kV employed in the actual DBD used to achieve the results presented here. Similar observations of the effect of peak voltage on phenol degradation efficiency was also claimed by Yan et al. (2006) who also confirmed that the decomposition of phenol increase with an increased voltage which is also in agreement with Chen et al. (2004) and Shi et al. (2009). Consequently, the removal of SMX in the current DBD reactor was strongly affected by electrical parameters such as peak voltage and indicates that SMX pollutant should be removed at a high voltage to perhaps minimise the energy consumption (Shi et al. 2009; Zhang et al. 2012). Even though the best SMX removal percentage was achieved with 10 kV, 6.8 kV was chosen as the optimum voltage value to avoid sparking in the DBD reactor and was used throughout the optimisation protocol.

5.3.5 Degradation of sulfamethoxazole by DBD at optimum conditions

After all optimum parameters were identified; a DBD reactor was tested at the optimum conditions for the removal of SMX. The conditions applied in of this experiment are shown in Table 5.5. The data tabulated in Appendix 13 were plotted and are shown in Figure 5-21.

Table 5.5: Optimum conditions applied after optimisation of the DBD system using SMX as model pollutant.

Parameters	Optimum
SMX concentration (mg/L)	40
Solution pH	6.5
Inlet air flow rate (L/min)	3
Peak voltage (kV)	6.8

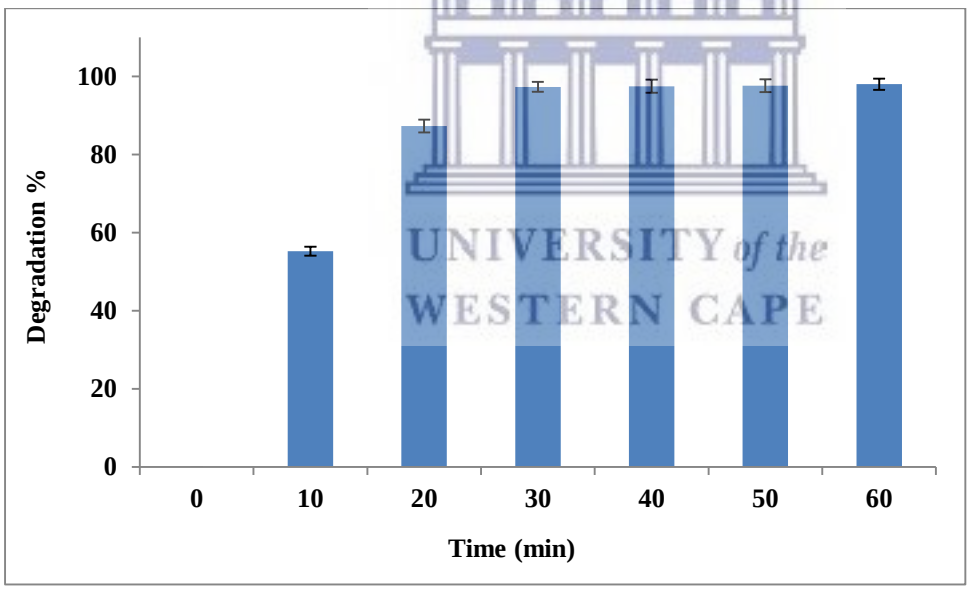

Figure 5.21: Degradation of SMX in DBD at optimum conditions: Peak voltage 6.8 kV, SMX concentration 40 mg/L, initial pH 6.5, solution volume 1500 mL, 1.5 mm silver electrode, 50 g/L NaCl electrolyte and 60 minutes of treatment time, (n = 2).

Table 5-5 tabulates the optimum applied parameters for the degradation of SMX and Figure 5-22 displays the decomposition percentages of SMX at the optimum conditions. The outcomes in Figure 5-21 show that at optimum SMX concentration 40 mg/L, initial pH 6.5, air flow rate 3 L/min and peak voltage 8 kV, the degradation of SMX continuously increased with an

increase in treatment time and total SMX removal was achieved within 30 minutes of reaction time. This demonstrates that SMX was highly vulnerable to O_3 and less prone to react with OH in acidic medium. Its destruction was certainly due to the electrophilic attack of ozone followed by hydroxyl radical attack. These results further inferred that the concentration of ozone in DBD was prominent and O_3 was very selective towards SMX compared to other active species. In other words, the two functional group reaction sites -NH_2 and –NH- in SMX carbon skeleton probably acted as bases and hence accelerated its decomposition within 30 min of DBD run. Due to the high cost for analysis extended characterisation of SMX at optimum conditions could not be performed, nevertheless, the degradation intermediate by-products of SMX obtained at the optimum conditions after 60 min reaction time were identified by LC-MS and are recorded in Table 5-6. The complete degradation of SMX that was reached after 30 minutes of reaction time also suggests an improved performance of the optimised reactor. The results demonstrated that the optimised DBD is an effective advance oxidation technology that can be used for contaminated water and wastewater remediation.

5.3.5.1 Breakdown by-products of SMX obtained in DBD experiment conducted at optimum conditions

After optimisation of the DBD reactor using SMX as model pollutant, its decomposition intermediate by-products at optimum conditions after 30 min were identified by liquid chromatography coupled with Mass spectroscopy (LC-MS) at the applied conditions and the detected metabolites are presented in Table 5-6 and their suggested degradation mechanism pathways are disclosed in Figure 5-22.

Table 5.6: LC-MS identified degradation by-products of sulfamethoxazole drug by DBD system after 30 min of reaction timeat the following conditions: Peak voltage 6.8 kV, SMX concentration 40 mg/L, solution volume 1500 mL, initial solution pH 6.5, air flow rate 3 L/min, 1.5 mm silver electrode, 50 g/L NaCl inner electrode electrolyte, air gap 2 mm and an experimental time of 60 min.

Compound	Molecular formula	Structure	Retention time (min)	Molecular ion $[M-H]^+$
4-amino-N-(5-methylisoxazol-3-yl)benzenesulfonamide (Sulfamethoxazole drug) I	$C_{10}H_{11}N_3O_3S$	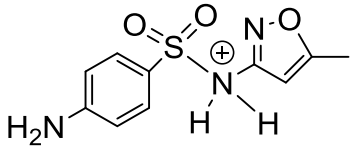	1.67	254.28
5-(4-hydroxyphenyl)-6-propyl-1,2,3,4,5l6,6-tetraoxathiazinan-6-ium 5-oxide (II)	$C_9H_{14}NO_6S^+$	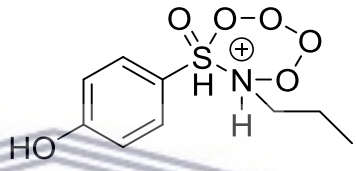	1.92	264.27
6-(1-hydroxyethyl)-5-(4-hydroxyphenyl)-1,2,3,4,5l6,6-tetraoxathiazinan-6-ium 5-oxide (III)	$C_8H_{12}NO_7S^+$	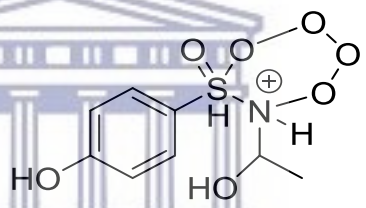	1.47	266.24
4-(hydroperoxydihydroxy-l4-sulfanyl)benzenaminium (IV)	$C_6H_{10}NO_4S^+$	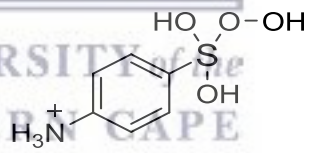	2.24	192.21
(E)-N-((4-aminophenyl)sulfonyl)-N'-hydroxyformimidamide (V)	$C_7H_9N_3O_3S$	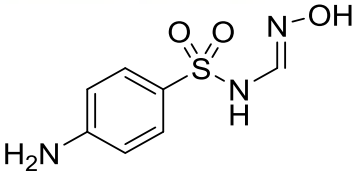	0.42	215.23
(4-(hydroperoxy-dihydroxysulfinyl)phenyl)azane (VI)	$C_6H_9NO_5S$	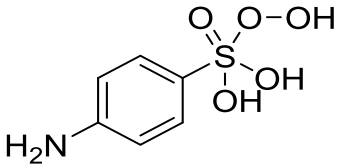	1.80	207.20
N-(5-methylisoxazol-3-yl)sulfonic amide (VI)	$C_4H_7N_2O_3S^+$	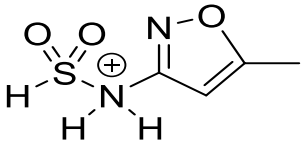	1.72	163.17

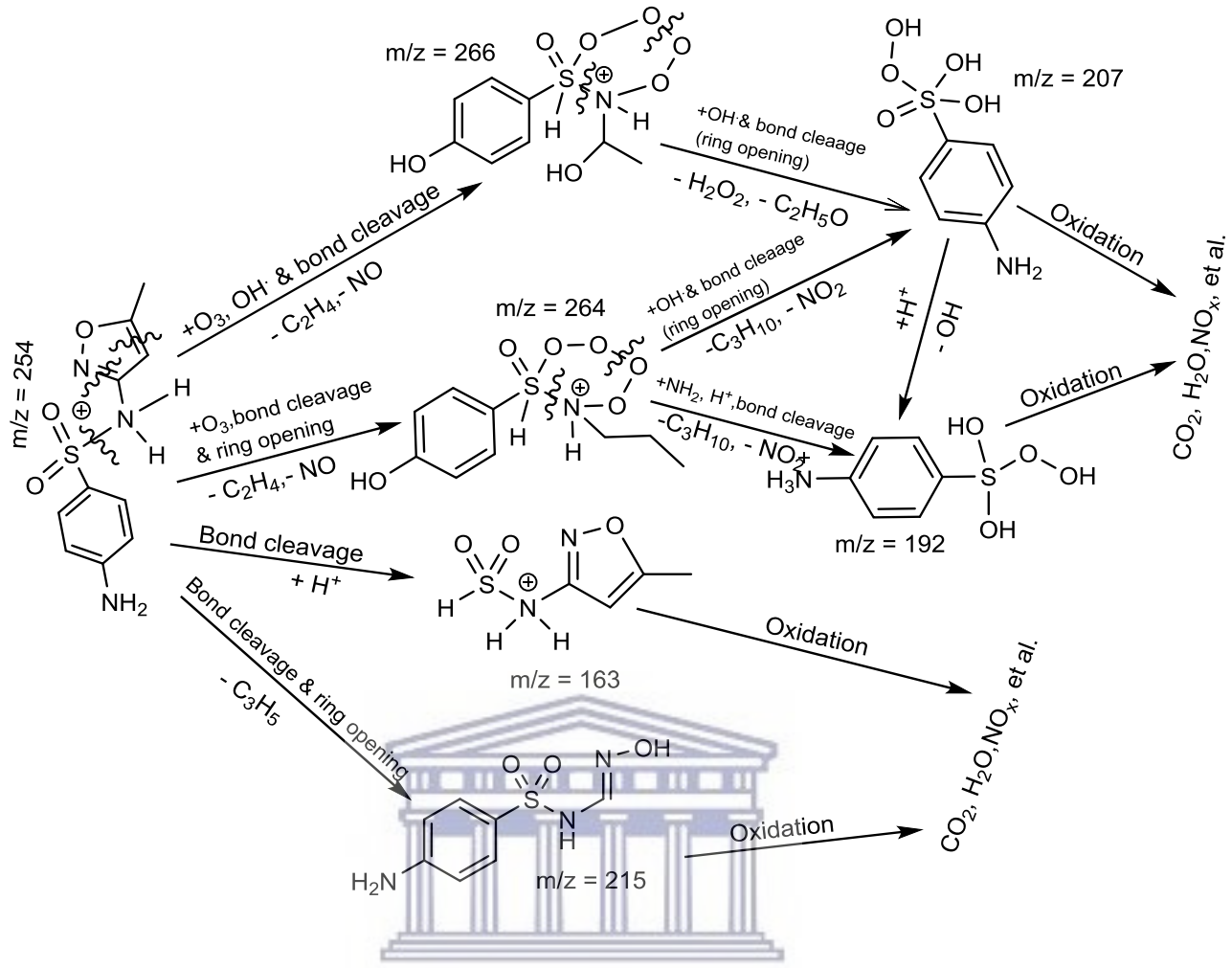

Figure 5.22: Suggested degradation mechanism pathways of SMX decomposed by DBD reactor at optimum conditions after 30 min reaction time: Peak voltage 6.8 kV, SMX concentration 40 mg/L, solution volume 1500 mL, solution pH 6.5, air flow rate 3 L/min, 1.5 mm silver electrode, 50 g/L NaCl inner electrode electrolyte, air gap 2 mm and an experimental time of 60 min.

Table 5-6 presents the degradation intermediate metabolites of SMX obtained with DBD reactor after 30 min of DBD run at the applied conditions while Figure 5-22 displays the suggested degradation mechanism pathways of the SMX metabolites detected by LC-MS analysis. The results in Table 5-6 show that about 6 degradation intermediates of SMX were identified after 30 min of reaction time. The decomposition of SMX contaminant ($C_{10}H_{12}N_3O_3S^+$, m/z = 254.3) that occurred within 30 minutes of DBD run at the applied conditions led to six metabolites mainly $C_9H_{14}NO_6S^+$, $C_8H_{12}NO_7S^+$, $C_6H_{10}NO_4S^+$, $C_7H_9N_3O_3S$, $C_6H_9NO_5S$ and $C_4H_7N_2O_3S^+$ corresponding to the following molecular mass of m/z = 264.27, 163.17, 192.21, 215.23, 207.20 and 266.24, that eluted from HPLC column after 1.92, 1.47,

2.24, 0.42, 1.80, 1.72 min, respectively. The chemical structures of SMX and its degradation intermediates recorded in Table 5-6 show that the mineralisation of SMX achieved beyond 30 minutes reaction time was mostly activated by bond and/or ring cleavage mechanisms on the protonated amide group and the heterocyclic five membered rings in SMX structure. This was followed by elimination process of – C_2H_4, -NO and – C_3H_5 that resulted in the formation of fragments m/z = 266, 264, 163 and 215, respectively as described in Figure 5-22. These intermediate by-products show that the mineralisation of SMX ($C_{10}H_{12}N_3O_3S^+$, m/z = 254) occurs via different pathways than claimed by Qi et al. (2014). The primary pathway involved the nucleophilic addition of ·OH, bond cleavage and ring opening followed by the elimination of -H_2O_2 and - C_2H_5O that induced the formation of m/z = 207 that was further oxidised and mineralised to dissolved CO_2, H_2O and inorganics. On the other hand, the addition of NH_2 group on m/z = 264 and its protonation followed by ring cleavage and elimination of - C_3H_{10} and - NO_2 resulted in the formation of the metabolite m/z = 192 that was further mineralised into CO_2, H_2O and other inorganic entities. The third and fourth pathways deal with the direct oxidation and mineralisation of the degradation metabolites m/z = 163 and m/z = 215 into CO_2, H_2O and aqueous inorganics. These results obtained are comparable to the findings of Kim et al. (2015) who defined the degradation pathways of sulfonamide antibiotics including SMX in a single cylindrical dielectric barrier discharge plasma system using air and oxygen as feed gases various conditions. Their outcomes showed that the absorption peak characteristic of SMX gradually decreased with an increase of pH, hence indicating that SMX was being decomposed and mineralised into various inorganic salts such as SO_4^{2-}, NH_4^+ and NO_3^- that were identified by TOC analysis. In addition the authors reported that degradation percentages of SMX and other antibiotics varied from 66.9 to 86.4% in both air and oxygen. Unlike the results obtained in this study, the increase of pH observed in their work signified that O_3 mostly disintegrated into OH radicals that induced the degradation of SMX and other pollutants as sustained by Gao et al. (2012). Consequently, about five SMX degradation intermediate by-products were identified by LC-MS and the degradation and mineralisation mechanism pathways were successfully proposed. So by comparison, it can be confirmed that the actual DBD reactor is more effective than the single cylindrical DBD used by Kim et al. (2015) due to the fact that in the current study, total degradation of SMX was achieved after 20 min while the 86.4 % obtained by Kim and colleagues, (2015) after 60 min required a prolonged time for total oxidation. Despite the fact that literature presents insufficient information on the degradation of SMX by DBD configurations, the removal of SMX by other single or combined AOPs such as ozonation, UV/visible light, ultrasound/ozone, etc. has been reported (Dantas *et*

al., 2008; Alam G. Trovó *et al.*, 2009; Guo *et al.*, 2015). Even though effective oxidation percentages along with degradation mechanism pathways of SMX have been reported in the aforementioned studies, the outcomes achieved in the actual work are more effective and hence validate that the DBD is an efficient advanced oxidation prototype that can be employed for the mineralisation of pharmaceutical pollutants and related toxins from water and wastewater effluents. However, the performance of this advanced technology alone on SMX should be compared with its combination with photo catalysts to evaluate the decontamination behaviour of the pollutant during treatment.

5.4 Summary of chapter five

In chapter five, a complete optimisation of the DBD reactor using two targeted pollutants orange II (O.II) dye and sulfamethoxazole (SMX) drug was accomplished. The optimised DBD system showed improved removals of both O.II and SMX at ambient conditions. The degradation of both pollutants was significantly influenced by the following parameters, initial solution concentration, solution pH and air flow rate. Hence the removal of O.II and SMX in the current DBD were dependent upon initial concentration, pH and air flow rate while, peak voltage did not show significant impact upon the degradation of both pollutants. The optimum conditions achieved for the decolouration of O.II in this study include: Peak voltage 8 kV, [O.II] 60 mg/L, pH 2.5 and air flow rate 3 L/min. At optimum parameters, complete decolouration of O.II was achieved within 20 min and the LC-MS analysis (shown in Table 5-4 and Figure 5-14 of Section 5.1.1.7.4) showed that O.II was broken down to six degradation intermediates m/z = 105.06, 121.09, 147.07, 165.08, 207.16 and 163.06 that eluted after 2.14, 2.71, 3.37, 2.71, 2.52 and 2.52 min from HPLC column, correspondingly. Moreover, beyond 20 minutes of DBD run, the LC-MS analysis did not detect any O.II intermediate by-products and the FT-IR, TOC, COD analysis showed that O_3 and OH were the principal active species that degraded and mineralised O.II into CO_2, H_2O and simpler inorganics (As shown in Table 5-3 and Figure 5-11 of Section 5.1.1.7.3). The deactivation of O.II was induced by homolytic or heterolytic cleavage of the azo group followed by epoxidation, elimination and rearrangement mechanisms. In opposition, total removal (99.99%) of SMX at optimum conditions was achieved after 30 min and its degradation resulted in six intermediate by-products m/z = 264.27,163.17, 192.21, 215.23, 207.20 and 266.24 that eluted from HPLC column after 1.92, 1.47, 2.24, 0.42, 1.80, 1.72 min, respectively. On the other hand, the optimum parameters achieved for the degradation of SMX included: [SMX] 40 mg/L, pH 6.5,

air flow rate 3 L/min, peak voltage 6.8 kV. The degradation of SMX within 30 min of DBD reaction time was initiated by epoxidation of the heterocyclic ring induced by the electrophilic attack of O_3 and OH followed by bond cleavage and elimination processes. Thereafter, beyond 30 min of DBD reaction time, SMX metabolites were mineralised into CO_2, H_2O and simpler inorganics as LC-MS analysis did not detect any intermediate peaks in SMX samples withdrawn beyond 30 min of DBD run. The comprehensive summary of chapter five showing the full optimisation of the DBD reactor configuration using O.II and SMX pollutants is presented in Appendix 14. Nevertheless, the optimum results obtained for both contaminants showed that SMX was the most resistant pollutant in the currently optimised DBD reactor. Perhaps the incorporation of the catalyst such as TiO_2 immobilised on supports could enhance the removal of these recalcitrant pollutants.

CHAPTER SIX: CARBON-NITROGEN CO - DOPED TIO_2 NANO CATALYSTS AND THEIR PHOTOCATALYTIC APPLICATION FOR THE REMOVAL OF ORANGE II DYE

6 INTRODUCTION

This chapter presents the results and discussion on the sol-gel manufactured powder form C-N-TiO_2 nano catalysts and their photo catalytic applications. It also presents the synthesis, characterisation of the engineered co – doped C-N-TiO_2 nano composites as well as the photocatalytic application of C-N-TiO_2 nano catalyst for the removal of orange II dye under UV light at the applied conditions. Thereafter, the chapter presents the incorporation of C-N-TiO_2 immobilised on SS (C-N-TiO_2/SS) and pure Ti mesh (C-N-TiO_2/Ti) into the DBD plasma reactor for the degradation of O.II dye and sulfamethoxazole drugs at the respective applied conditions.

6.1 Synthesis and characterisation of C-N-TiO_2 nano catalyst and its photocatalysis application for the removal of O.II dye

In this subsection, a co-doped C-N-TiO_2 nano catalyst in powder form presented in chapter 3, section 3.5 was synthesised by a simple sol gel method and the impact of annealing holding time on crystal structure, shape, size, and surface area of the prepared C-N-TiO_2 nano composites was investigated. The experimental details are presented in Section 3.5.1. The following characterisation techniques XRD, Ft-IR, EElS, TGA, SEM, TEM, TEM-EDS, and UV-vis spectroscopy were subsequently used to determine the aforementioned catalyst properties (See section 3.8 for characterisation procedures).

6.1.1 X-ray diffraction analysis of the as per synthesised catalysts

Since the main application of the C-N-TiO_2 nano materials synthesised in this study was for photocatalytic evaluation, the structure, morphology and size of particles as well as band gap of the nano catalysts were investigated. XRD analysis was used to determine the phase composition, particle size and the crystallinity of TiO_2 and C-N-TiO_2 co-doped nano particles and the results of this analysis are presented in Figure 6-1.

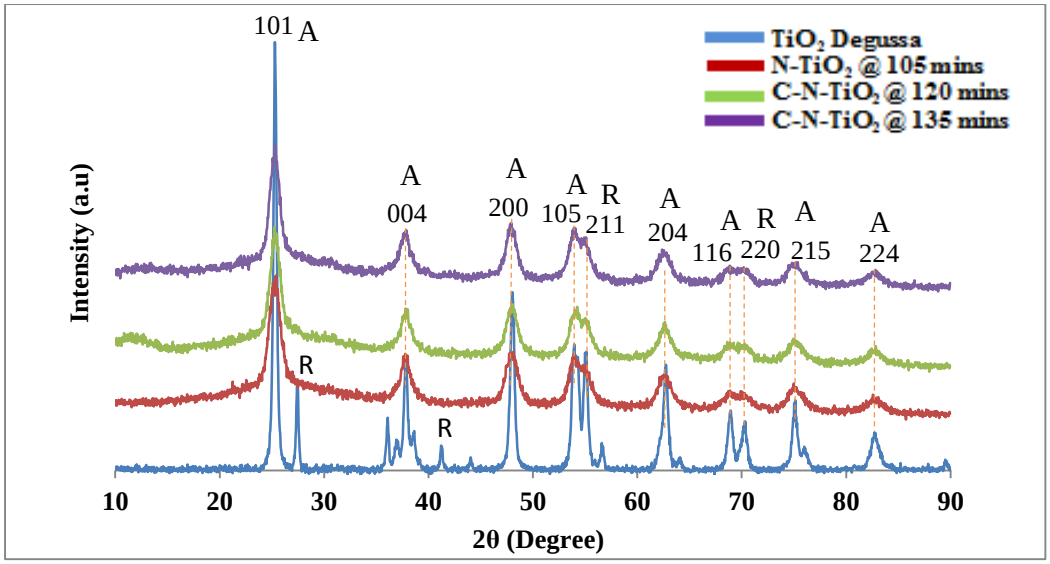

Figure 6-1: X-ray diffraction (XRD) analysis of TiO_2 Degussa and the synthesised C-N-TiO_2 nano catalysts pyrolysed at 350 ºC, (ramping rate of 50 ºC/min) for different holding times (105, 120 and 135 min) with A= anatase and R = rutile.

Figure 6-1 shows that pure Degussa TiO_2 consisted of both anatase (JCPDS, no 00-021-1272) and rutile phase (JCP, no 00-021-1276) with the anatase phase being predominant as indicated by its peak intensities (Lin *et al.*, 2015). The pure mineral anatase phase was characterised by the following diffraction peaks 2θ = 25.28º (101), 36.9 º (103), 37.8º (004), 48 º (200), 53.89 º (105), 55.06 º (211) and 62.69 º (204) which correspond to the body centred tetragonal lattice structure of the pure mineral anatase phase. The rutile phase was characterised by the presence of diffraction peaks at 2θ = 27.44 º, 36.08 º and 41.2 º as from (JCPS) no 00-021-1276 corresponding to the lattice tetragonal shape of the rutile phase. The synthesised C-N-TiO_2 nano catalysts had both anatase and rutile phases of TiO_2 with anatase being predominant. This meant that the synthesis procedure using the sol-gel protocol resulted mostly in the formation of the anatase phase which was deemed advantageous for photo catalytic applications (Cheng *et al.*, 2012a; Xie *et al.*, 2016). The size of TiO_2 Degussa and C-N-TiO_2 nano crystals were calculated using the Scherrer Equation (6.1) (Zhang, Gao and Guo, 2000) and the results are presented in Table 6-1**.**

$$d = K^*\lambda / B(2\theta)^*\cos\theta \qquad 6.1$$

Where d is the nano crystals size; K≈ 0.94 is a dimensionless shape factor; λ ≈ 0.15406 nm is the CuK_α diffraction wavelength; B (2θ**)** is the line broadening at half the maximum intensity (FWHM), expressed in radians (after subtracting the instrumental line broadening); and θ the Bragg angle in degrees.

Table 6-1: Summary of the particle sizes of TiO_2 Degussa and the synthesised C-N-TiO_2 photo catalysts pyrolysed for different times as estimated from XRD analysis.

Pyrolysed photo catalysts	Catalyst size (nm) XRD (Scherrer Equation)
TiO_2 Degussa	21.0
C-N-TiO_2 105 min	5.5
C-N-TiO_2 120 min	6.3
C-N-TiO_2 135 min	6.4

From the results presented in Table 6-1, it could be noticed that the size of the nano catalysts calculated by the Scherrer Equation decreased with particle sizes between 5.5 and 6.4 nm, being smaller than 21 nm of TiO_2 Degussa. The decrease in peak intensity of all modified C-N-TiO_2 nano composites compared to Degussa demonstrated the formation of small C-N-TiO_2 nano crystals supported by Figure 6-1. This signified that the crystalline structure of nano TiO_2 using sol-gel/pyrolysis procedure promoted the formation of small crystalline domains and that C and N impurities were probably located either in the interstitial or surface of the TiO_2 catalyst (Zhang *et al*., 2000; Cheng *et al.*, 2012a). The XRD patterns in Figure 6-1 also showed that diffraction peaks of C-N-TiO_2 pyrolysed for 105 min are slightly broader further confirming the smallest nano sized C-N-TiO_2 compared to those of C-N-TiO_2 calcined for 120 and 135 min for which the XRD peaks progressively became slightly more intense and narrower with an increase of pyrolysis time during preparation. This trend confirmed the slight increase of C-N-TiO_2 nano crystals' size from 5.5 nm to 6.3 and 6.4 nm when pyrolysis time was increased from 105, 120 to 135 min, respectively as shown in Table 6-1. The XRD results show no peaks characteristic of graphite indicating that carbon impurities are amorphous. Hence, from the XRD results obtained in this study, the catalyst mineral phases were successfully determined. Therefore, pyrolysis time had an effect not only on the composition and mineralogical phases of the nano materials but on their particle size as well, during the pyrolysis process.

6.1.2 Fourier transform spectroscopy of the catalysts

Fourier transform spectroscopy (FTIR) analysis was further used to elucidate the functional groups present in the synthesised C-N-TiO_2 nano catalyst pyrolised at 350 ^oC for different holding times (Figure 6-2). The functional groups formed between C, N, O and Ti and H, as indicated in Figure 6-2, appeared as three different absorption bands and are summarised and presented in Table 6-2. For instance, from 3400-3600 cm^{-1} the following OH/N-H stretching were identified (Shao, Zhang and Yuan, 2008; Geng *et al.*, 2009; Chainarong *et al.*, 2011),

relating to N-H; C-C, C-O, C-N and probably C=N, C=O, N=O, OH-stretch, etc. appearing in between 1000-1800 cm^{-1} and 1800 – 1200 cm^{-1} (Matsumoto *et al.*, 2007; Chu *et al.*, 2008; Xu *et al.*, 2008; Geng *et al.*, 2009). Finally, Ti-O, O-Ti-O, N-TiO_2, Ti–O–Ti, and N=O stretching are evident in the 1200 – 500 cm^{-1} range for all samples (Shao, Zhang and Yuan, 2008). The aforementioned functional groups demonstrate the presence of impurities C and N that were incorporated into the TiO_2 semiconductor or miht have resulted from the decomposition of PAN and NH_4NO_3.used as C and N sources, respectively during the sol-gel preparation. The unsaturated functional groups such as C=O, N=O resulted from random combinations of unstable C and N impurities in nano-TiO_2 during the pyrolysis process. The pyrolysis process might have further induced the formation of evaporated gases such as CO, NO, etc. that were evidenced by an unusual smell during the annealing process. Furtehrmore, during pyrolysis process, PAN was reported to decompose to various monomers and other species such as HCN, NH_3, H_2O and CO_2 (Balazs Szepcsik, Bela Pukanszky 2018) while NH_4NO_3, source of nitrogen likely decomposed to nitrous oxides (Joseph H. MacNeil et al. (1997;Stefania Cagnina et al. 2018) that were evident from FT-IR results. Furthermore, in Table 6-2, C-Ti bonds are not present at the longest holding time showing that C probably evaporated and caused band gap to revert to closer to TiO_2. However, the bonding between atomic pairs of the various gas highlighted above had to be confirmed by extended characterisation techniques such as electron energy loss spectroscopy.

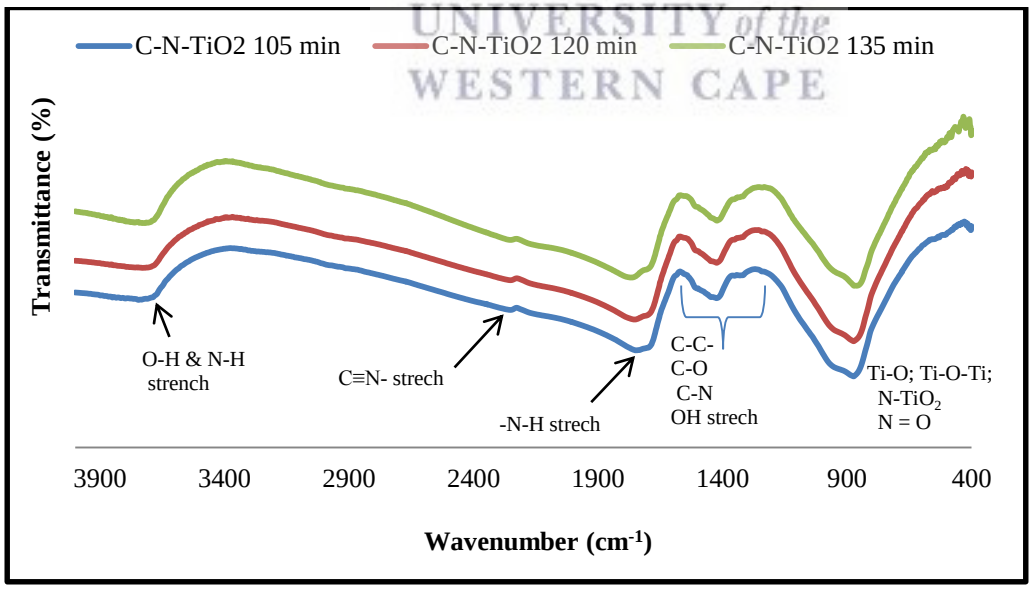

Figure 6-2: FTIR spectra of C-N-TiO_2 nano composites pyrolysed with nitrogen gas at 350^oC using a ramping rate of 50 ^oC/min and held at temperature for different times 105, 120 and 135 min.

Table 6-2: Functional groups of the synthesised C-N-TiO_2 nano catalysts, pyrolysed with nitrogen gas at 350 ^oC using a ramping rate of 50 ^oC /min and held at different times 105, 120 and 135 minutes.

Photo catalysts	Pyrolysis time (min)	Absorption bands (cm^{-1})	Functional groups/ Stretching/vibrations
C-N-TiO_2	105 min	3800 – 3600 1900 – 1800, 1800 - 1200 1200 - 700	OH/N-H Stretching, Ti-O, Ti-O-Ti, C-Ti-O, N-TiO_2, etc.
C-N-TiO_2	120 min		-N-H, -C-C-, C-O and C-N, C=N, C=O, N = O, Ti-O, Ti-O-Ti, N-TiO_2, etc.
C-N-TiO_2	135 min		Ti-O, Ti-O-Ti, N-TiO_2, N=O

6.1.3 Electron energy loss spectroscopy (EELS)

The presence of bonding between C, N, and Ti in the synthesised catalysts was investigated by electron energy loss spectroscopy (EELS) plotted in Figure 6-3.

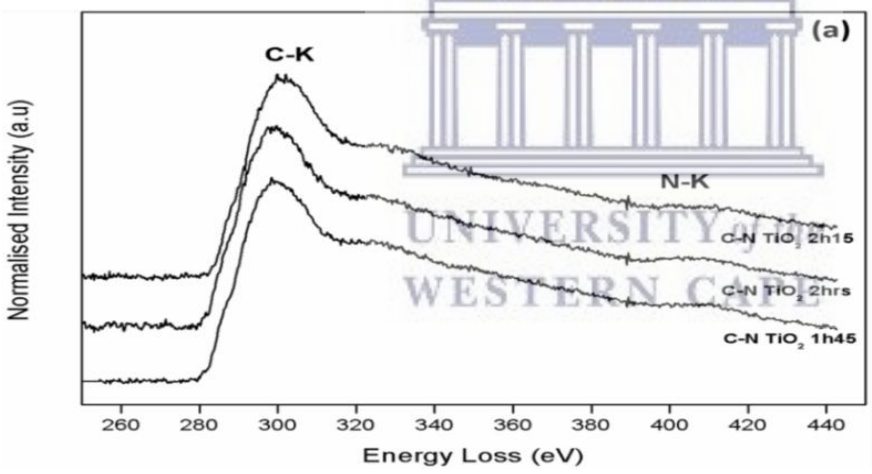

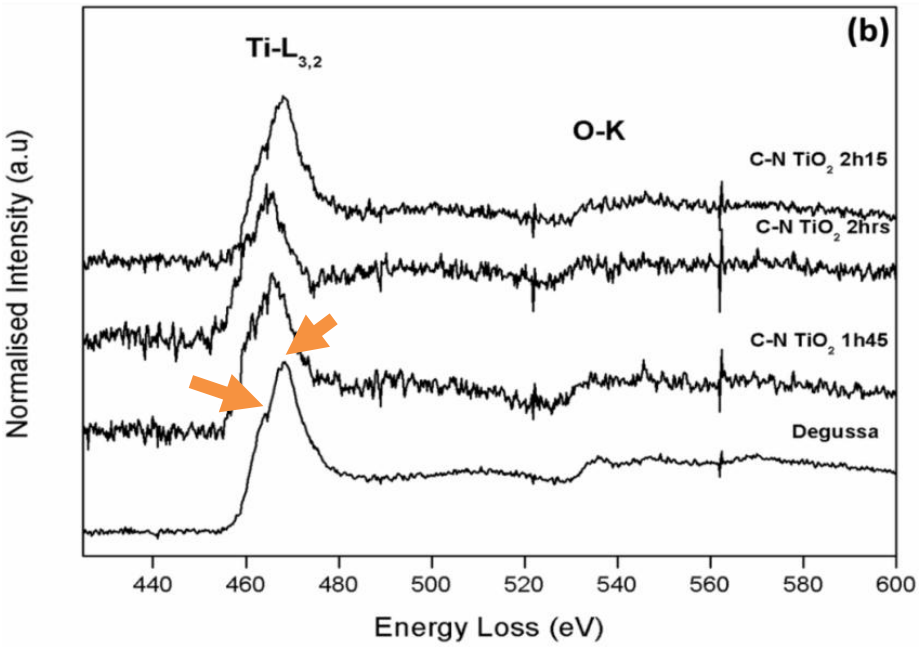

Figure 6.3: Electron energy loss spectra of (a) carbon K edge and nitrogen K edge line profiles and (b) Titanium L3,2 and Oxygen K edge line profiles of the different catalystspyrolysed in N_2 at 350 ^oC (50 ^oC/min ramping rate) for different holding times 1hr45 min (105 min), 2hrs (120 min) and 2hr15 min (135 min).

Figure 6-3 (a) confirms the presence of both carbon (K edge onset detected at 284 eV) and nitrogen (K edge at 404 eV) present in all three prepared specimens. Figure 6-3(b) shows the titanium $L_{3,2}$ line profile of the synthesised specimens against that of the undoped Degussa TiO_2. From the Degussa line profile, the common crystal field splitting from the predominantly rutile crystal structure is indicated by the arrows between 460 and 480 eV. The hump on the lower eV side is the L_3 peak, which originates from electron transitions from the inner $2p_{3/2}$ orbitals to empty 3d orbitals of the Ti metal. The L_2 edge, on the higher eV side, originates from $2p_{1/2} \rightarrow$ 3d electron transitions. In the case of Ti oxides, the near-edge structures found in the $L_{3,2}$ edges mainly reflect the covalent bonding states resulting from direct and/or indirect interactions between O and Ti atoms. As such, a study of this edge structure, i.e. its change in crystal field splitting and or shifting of peak position, can give an idea of the introduction of foreign atoms into the TiO_2 framework. From Figure 6-3(b), it can be seen that with an increase in synthesis time, there is a slight shift in the Ti $L_{3,2}$ lineshape position compared to that of the undoped Degussa TiO_2. This was further confirmed by the splitting of the $L_{3,2}$ peak located between 460 and 480 eV with TiO_2 Degussa into individual L_3 and L_2 humps at 462 eV in

Figure 6-3 (b) that were indiscernible in the case of the 105 min or 120 min samples, but well present at 470 eV in the 135 min sample.

6.1.4 Thermal gravimetric analysis of the synthesised catalysts

Thermal gravimetric analysis (TGA) was performed to assess the loss of catalyst mass or percentage loss and temperature ranges in which the aforementioned elements evaporated and hence to support the FT-IR and EELS results previously discussed. The TGA results presented in Figure 6-4 (A&B) showed the mass loss of C-N-TiO_2 nano catalysts over time during pyrolysis in N_2. The TGA results indicate that the loss of volatile components in the synthesised catalysts occurs between 100 and 130 ^oC.

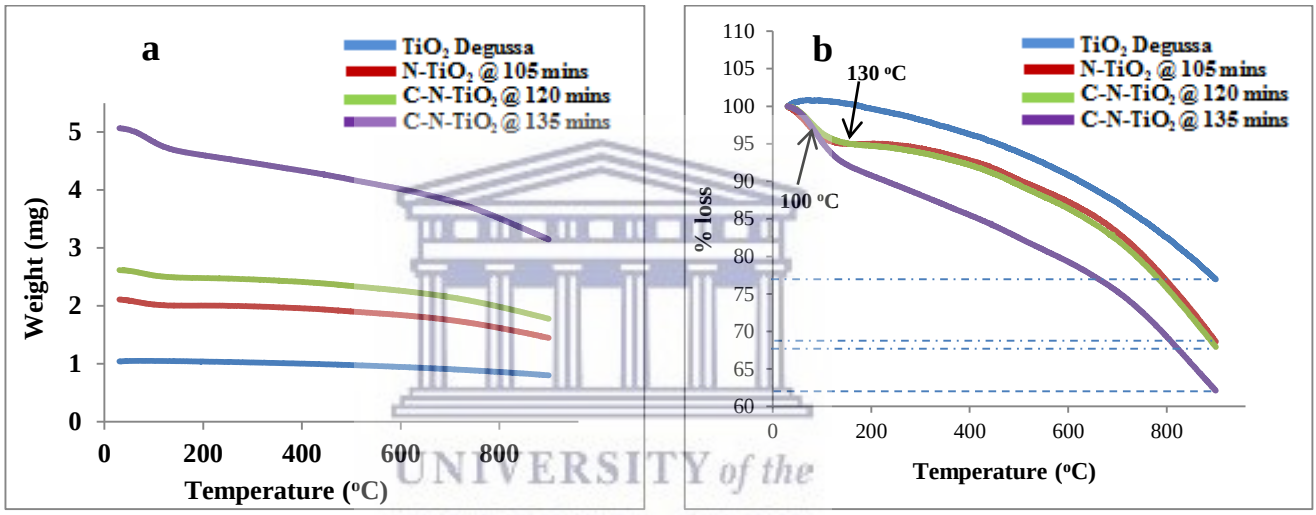

Figure 6.4: Thermal gravimetric analysis of the nano catalystspyrolysed at 350 ^oC with nitrogen gas for different times (ramping rate of 50 ^oC/min) showing the mass loss A) and the corresponding percentage loss B).

With reference to TiO_2 Degussa, about 8.7 % of the mass of the C-N-TiO_2 (105 min) was lost between 130 ^oC and 700 ^oC, compared to 10 % and 14.65 % mass loss recorded for C-N-TiO_2 (120 min) and C-N-TiO_2 (135 min). So increasing the pyrolysis time during the catalyst preparation resulted in an increase of catalyst mass loss due to carbon and nitrogen volatilisation during the temperature profile applied. These trends supplement the gas evaporation claimed in the FT-IR discussion. Alternatively, the catalyst mass loss experienced in this study was probably due to PAN decomposition that occurred between 130 and 700 ^oC. Indeed, the carbonisation of PAN in N_2 gas, certainly led to the cyclisation reaction whereby nitrile group appearing at 2261 cm^{-1} was converted to C=N bond that was evidenced by the

FT-IR along with C=C and C-N stretching between 1200 and 1800 cm^{-1} as supported by Sánchez-Soto et al. (2001), and Darányi Mária et al. (2011). Therefore, the detected C-N, C=N and C=C bonds resulted from chain conjugation whereby C=C bonds were formed during the tautomerisation of the cyclised product (Laffont *et al.*, 2004). Likewise, the C=O stretching from DMF solvent trapped in the polymer certainly evaporated during pyrolysis of C-N-TiO_2 at 350 ^oC recalling that the boiling point of DMF is estimated to be around 153 ^oC according to Darányi Mária et al. (2011), as a clear weight loss at below 130 ^oC was evident.

6.1.5 Scanning electron microscopy of C-N-TiO_2 pyrolysed at different holding times

Though FT-IR, EELS and TGA analysis demonstrated the impact of annealing holding time on chemical properties of the sol-gel synthesised nano catalysts, extended characterisation methods such as scanning electron microscopy (SEM) is of great importance to visualise the morphological changes of the nano materials during pyrolysis. Figure 6-5 presents SEM micrographs of pure TiO_2 compared with the co-doped C-N-TiO_2 nano composites synthesised by the sol gel method and pyrolysed in N_2 at 350 ^oC at 50 ^oC/min for 105, 120 or 135 min holding time.

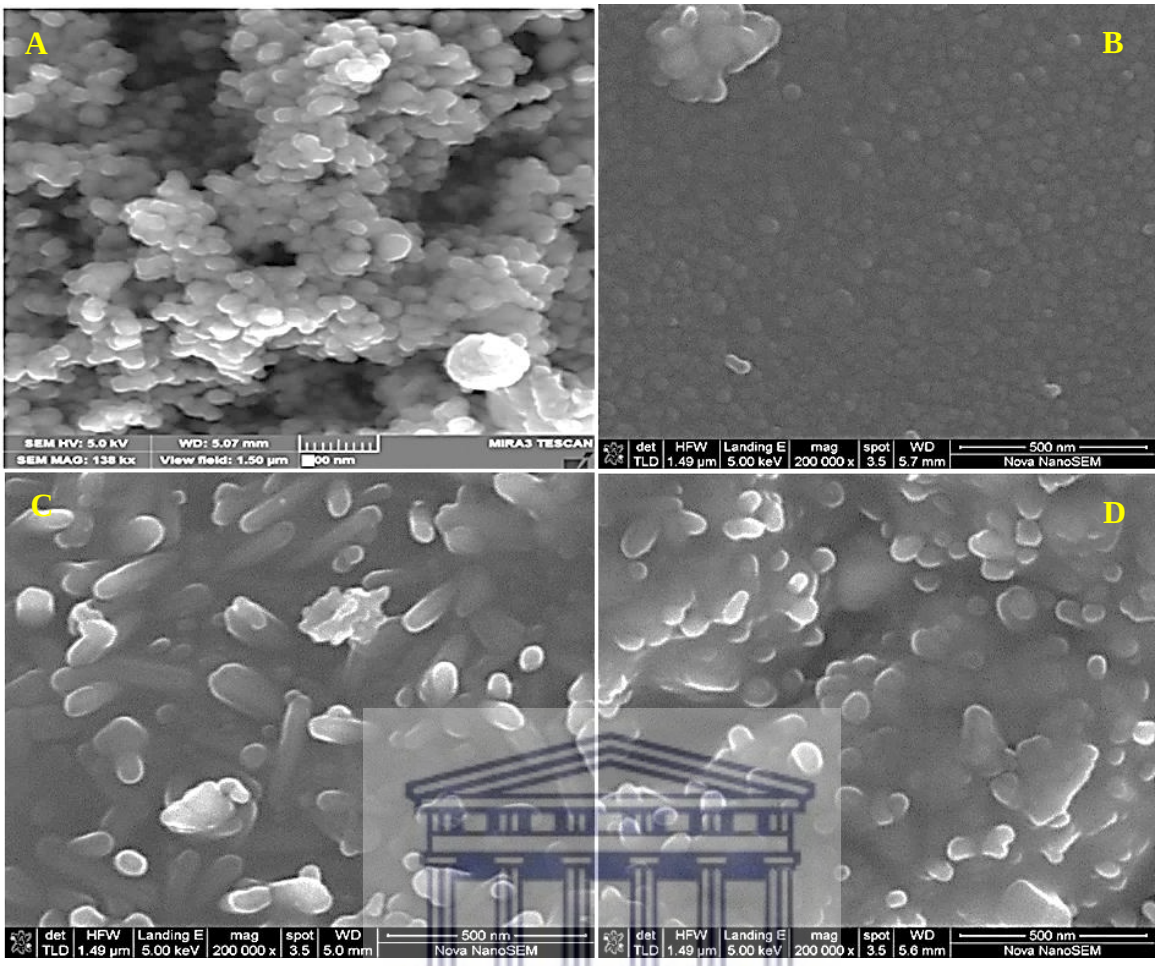

Figure 6.5: Scaning electron microcopy of C-N-TiO_2 pyrolysed at 350 ^oC using a ramping rate of 50 ^oC/min and hold at temperature for different different holding times: A) Pure Degussa, B) 105 min, C) 120 min and D) 135 min.

The SEM photograph in Figure 6-5 (A) is for Degussa P25 showing 10-21 nm spherical crystallites as confirmed by the Scherrer Equation. Figure 6-5 (B) shows the formation of small spherical and cubic granular- shaped C-N-TiO_2 nano crystallites when the sample was pyrolysed for 105 min, which were well distributed and had a size of 5.5 nm compared to the randomly dispersed longitudinal, spindle-and rod shaped crystals (6.3 nm) visible in Figure 6-5 (C) and condensed agglomerated forms (6.4 nm) in Figure 6-5 (D) when the pyrolysis time was increased to 120 and 135 min, respectively. Moreover, it can also noticed that SEM image of C-N-TiO_2 calcined for different holding times presents an agglomerated morphological aspect showing residual PAN whereas fine powder particles were observed for pure TiO_2 Degussa in Figure 6-5 (A). Similar morphological changes were noticed by Tijani et al. (2017) and Cheng et al. (2012) during the synthesis of C-TiO_2 and N-TiO_2 nano catalysts by different methods. These authors reported that isolated C and N impurities in their substitutional bonding

forms C-O-Ti-O and N-Ti-O in the forbidden band of TiO_2 lattice which became unstable when increasing the pyrolysis time. During pyrolysis in N_2 the PAN used as carbon source in this study degraded and its partially pyrolysed carbon residues are still evident as the matrix around each TiO_2 crystal in HRTEM as shown in section 6.1.8. At longer times, less of the carbon residue remained as was confirmed by TGA presented in Section 6.1.4. Thus when increasing pyrolysis holding time from 105 to 120 or 135 min, PAN decomposes into C and N in the TiO_2 matrix resulting in random recombination with O, giving off gases such as NO, NO_2, CO, CN, etc., during the pyrolysis process as earlier supported by FT-IR and EELS analysis. Longer pyrolysis times favoured the growth (in length and diameter) of C-N-TiO_2 nano particles. Thus increasing pyrolysis time reduced the amount of PAN residues due to the incorporation of C and N into the semiconductor matrix. Consequently an analysis of the relative concentrations of C, N and other elements in the catalysts had to be assessed to compliment the claims discussed in FT-IR, TGA, EELS and SEM analysis.

6.1.6 Energy dispersive spectroscopy spectrum and weight percentage of the synthesised C-N-TiO_2 Nano composites

Transmission electron microscopy coupled with energy dispersive spectroscopy (TEM-EDS) was used to determine the elemental composition of the prepared nano composites. Although the sensitivity of SEM-EDS was very low for N detection, the TEM-EDS results are presented in Table 6-3.

Table 6-3:TEM-Energy dispersive spectroscopy and weight percentage of synthesised nano catalystspyrolysed with nitrogen at 350 ^oC (50 ^oC/min ramping rate) and holding times of 105, 120 and 135 minutes.

Elements	Weight percentage (%)		
	105 min	120 min	135 min
C	72.32	64.00	40.00
N	7.10	Not detected	3.63
Ti	10.55	21.86	49.65
Cl	1.66	2.10	3.73
C to Ti ratio	7:1	3:1	1:1

The weight percentage of C (72.32 %), Ti (10.55 %), N (7.1 %) and O (8.26 %) in Table 6-3 after 105 minutes of holding time shows that all dopants C and N were successfully introduced into the TiO_2 matrix. While chlorine impurities (1.66 %) certainly derived from the Ti precursor ($TiCl_4$), Cu probably resulted from the copper grid used to support samples during TEM analysis. Moreover, the huge amount of carbon measured by TEM-EDS in Table 3 might not be doped into TiO_2 lattice but is residues of degraded PAN glueing the crystals together. In addition, it could be noticed that increasing the pyrolysis time resulted in a decrease of C content and the concomitant increase of Ti content as expected. This is proven by the EDS weight % results showing the decline of carbon content from 72.2% to, 40.60 % and then to 40.35 % after 105, 120 or 135 min of pyrolysis, while that of Ti content increased from 10.55, 21.86 to 49.65 % probably due to carbon loss as expected. Alternatively, it should mention that PAN has N in its structure, even though it was not measured before addition of NH_4NO_3. This could hae also contributed to the sliht increase of Ti content recorded in Table 6-3.

Furthermore, nitrogen content decreased from 7.1 to 3.63 % during the pyrolysis process. Therefore, pyrolysis time induced volatilisation of the impurities C and N introduced in TiO_2 matrix and led to different morphological changes of the synthesised nanoparticles as shown by SEM analysis in Figure 6-5.

6.1.7 Transmission electron microscopy/energy dispersive spectroscopy

To provide a visual aid of the distribution of the C and N atoms in the TiO_2 matrix at the above TEM-EDS percentages, scanning transmission electron microscopy (STEM) coupled with electron dispersive spectroscopy (EDS) (STEM-EDS) was performed and is shown in Figure 6-7. It must be noted that the samples did not endure well under the electron beam, when in spot (STEM) mode, and disintegrated after exposur e for more than about 10 seconds. As such, collecting the STEM-EDS spectral image maps proved very challenging. The data shown in Figure 6-6 is that of the best map collected. Figure 6-6 (a) and (b) show dark field TEM images collected using the HAADF solid-state detector. This allows for identification of a difference in atomic number in the images. From (a) and (b), the bright areas are the TiO_2 nanoparticles. The resultant SI maps are shown in Figure 6-6 (e) to (h).

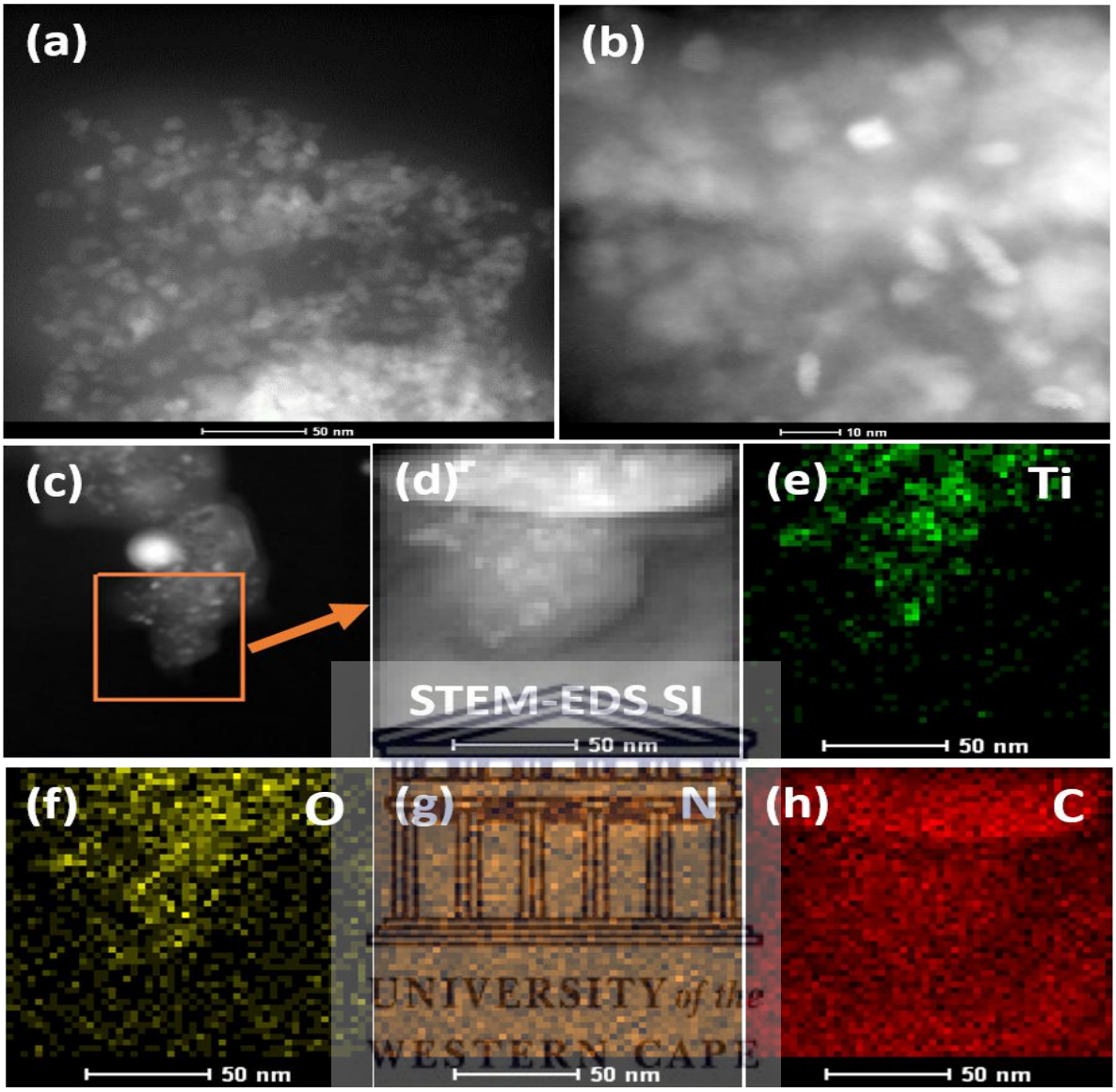

Figure 6.6: STEM-EDS spectral imaging (STEM-EDS SI): (a) and (b) HAADF dark field images of the C and N doped TiO_2 nanoparticles synthesised at 105 min; (c) 150 x 150 nm^2 square, divided into 50 x 50 pixels resulting in a pixel size of 9 nm^2, highlighting the area selected for spectral imaging (SI) collection; (d) the resultant STEM-EDS SI map (g) – (h) for respective elements.

The micrographs presented in Figure 6-6 (e, f, g & h) show that the elements C, N, Ti and oxygen were all present in the synthesised nano catalysts at percentages dictated by TEM-EDS analysis previous discussed. Nevertheless, other techniques such as selected area energy dispersive were explored to further investigate the intrinsic distribution of C and N in the TiO_2 framework of the prepared nano catalysts.

6.1.8 Scanning transmission electron microscopy coupled with selected area energy dispersive

The diffusion of the C and N atoms in the TiO_2 matrix of C-N-TiO_2 pyrolysed for different holding times was assessed by scanning transmission electron microscopy coupled with selected area energy dispersive/selected area energy dispersive (STEM-EDS/STEM-SAED) as shown in Figure 6-7. Figure 6-7 (c, f, I and l) presents the SAED patterns of TiO_2 Degussa (Figure 6-7- c) and those of C-N-TiO_2 Nano catalysts pyrolysed at 350 ^oC with nitrogen gas for 105 min (Figure 6.7 d-f), 120 min (Figure 6-7 ghi) and 135 min (Figure 6-7jkl). The STEM micrographs in Figure 6.7(a) show the Degussa P25 Ti crystals (bright crystals) and its SAED pattern (6-7C). While in Figure 6-7 (d, g and j), the STEM images showed that C & N impurities were well distributed throughout the TiO_2 matrix. These observations were also supported by crystals observed to be embedded in the carbon matrix surrounding the TiO_2 based catalysts as shown in Figure 6-7 (e, h and k). The bright polymorphic rings with small bright reflections observed in these images confirmed the polycrystalline nature of the TiO_2 nanoparticles. The bright reflections on the spherical lines with a d-spacing of 0.32 nm corresponded to the crystal plane (110) characteristic of distinctive C-N-TiO_2 nano crystals mostly in pure mineral anatase phase. However, the reflections of crystals are brighter in the Degussa sample (Figure 6-7 (c)) compared to those in Figure (6-7 f, j & l). This was probably due to small randomly oriented nanoscale TiO_2 domains and crystal size alterations also observed in HRTEM in Table 6.4 and also STEM- particle size distribution shown in the next section.

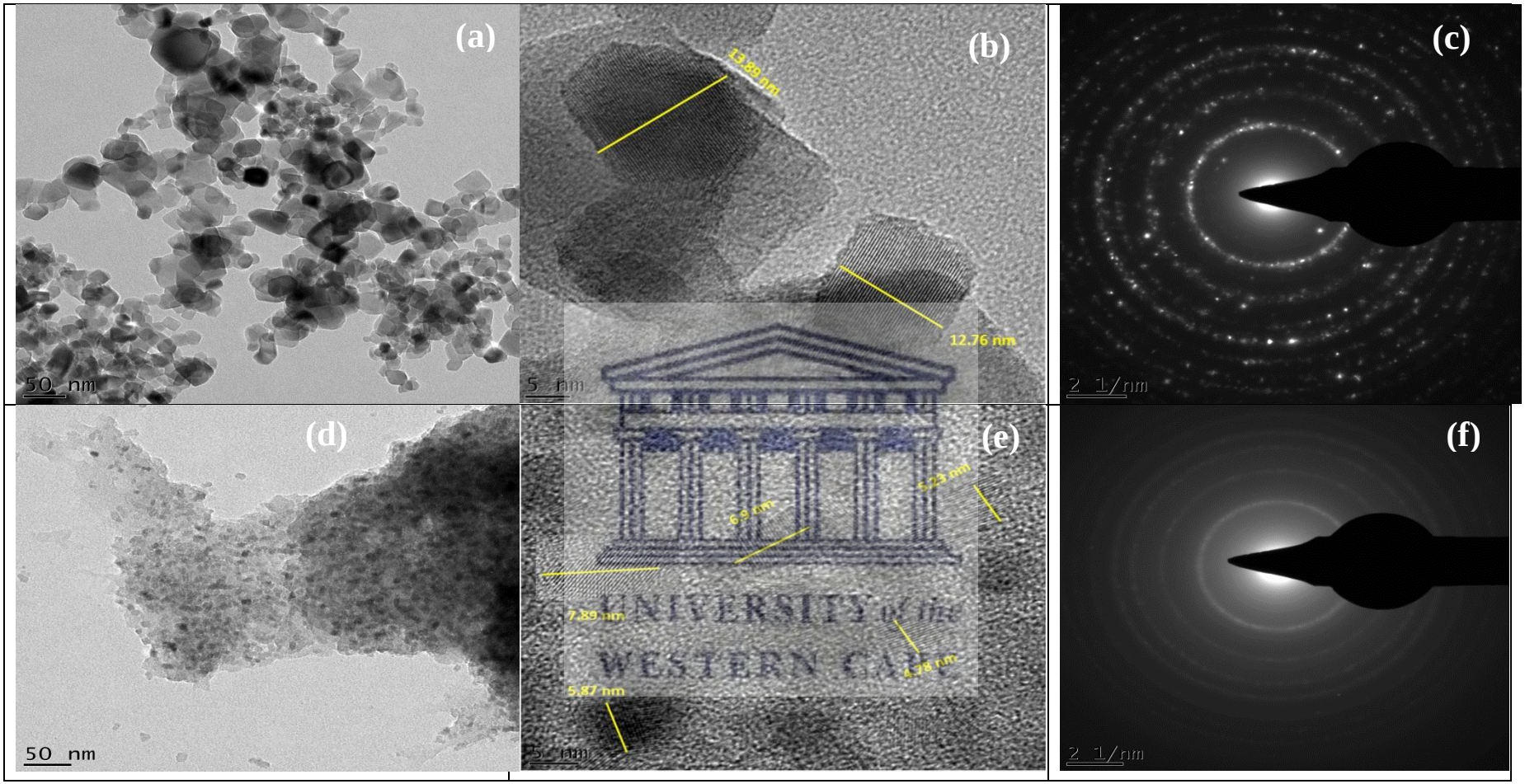

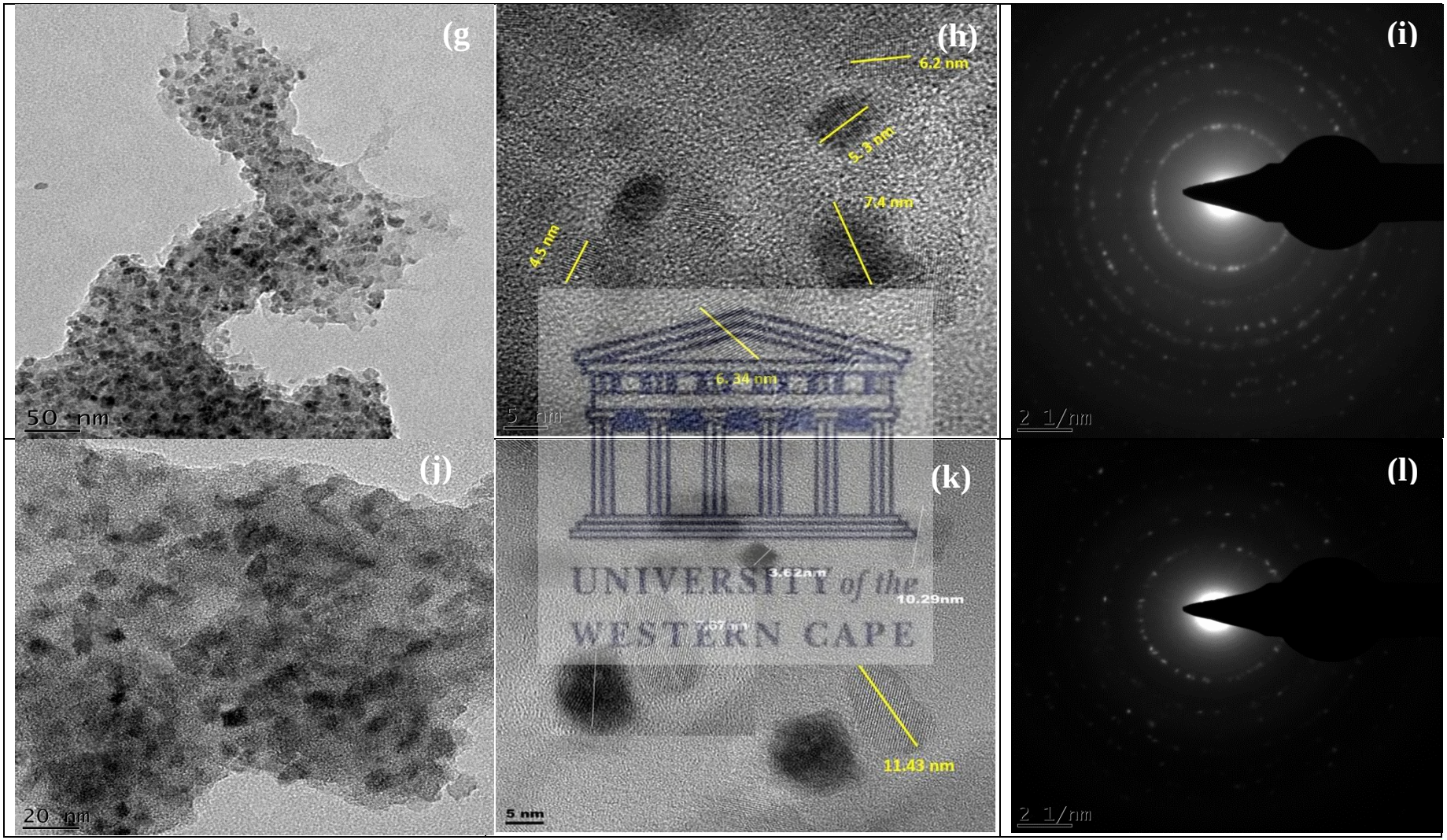

Figure 6.7: Bright-field micrographs and SAED patternsof (a) – (c) Degussa TiO_2; (d) – (f) 105 min C-N-TiO_2; (g) – (i) 120 min C-N-TiO_2; (j) – (l) 135 min C-N-TiO_2 pyrolysed at 350 ^oC at 50 ^oC/min ramping

Table 6.4: Calculated d-spacing for the first 5 diffraction rings from the SAED patterns of the commercial Degussa compared to the synthesised catalystsshown in Figure 6 -7.

Sample	Ring #	Diameters (nm^{-1})	Radius (nm^{-1})	d spacing = 1/Radius (nm)	Phase (hkl)
Degussa TiO_2	1	5,59	2,795	0,358	Anatase (101)
	2	8,24	4,12	0,243	Rutile (101)
	3	9,52	4,76	0,210	Rutile (210)
	4	11,68	5,84	0,171	Rutile (211)
	5	13,13	6,565	0,152	Rutile (002)
105 min C-N-TiO_2	1	5,55	2,775	0,359	Anatase (101)
	2	8,26	4,13	0,242	Rutile (101)
	3	11	5,5	0,181	Anatase(200)
	4	12,42	6,21	0,161	Rutile (220)
	5	13,25	6,64	0,151	Rutile (002)
120 min C-N-TiO_2	1	5,26	2,63	0,380	Anatase(101)
	2	7,81	3,90	0,256	Rutile (101)
	3	9,68	4,84	0,207	Rutile (111)
	4	10,84	5,42	0,184	Anatase (200)
	5	12,37	6,19	0,162	Rutile (220)
135 min C-N-TiO_2	1	5,56	2,78	0,360	Anatase (101)
	2	8,10	4,05	0,247	Rutile (101)
	3	10,09	5,05	0,198	Rutile (210)
	4	11,42	5,71	0,175	Rutile (211)
	5	13,17	6,58	0,152	Rutile (002)

The results presented in Table 6-4 show that both anatase and rutile phases were present in TiO_2 Degussa and in the prepared Nano catalysts and is in accordance with XRD findings early discussed in section 6.1.1. Rutile phase had the highest ring diameter range between 8.10 to 13.2 nm^{-1} with the radius ranging from 4.05 to 6.64 nm^{-1} and a d-spacing range of 0.15 to 0.247 nm. On the other hand the diameter of the anatase phase fluctuated between 5.26 and 11 nm^{-1} with a radius range of 2.63 to 5.42 nm^{-1} and a d- spacing between 0.181 -0.380 nm. It can also be observed that in all tabulated catalysts, rutile phase was predominant. This was probably due to impurities detected by the high sensitivity of the TEM instrument used for analysis as the XRD results demonstrated that the sol-gel prepared C-N-TiO_2 nano catalysts were mostly in anatase.

6.1.9 Scanning transmission electron microscopy coupled with particles size distribution

STEM analysis technique was further used to confirm the morphology of the catalysts and to determine the particle size distribution as shown in Figure 6-8. Figure 6-8 (A_1) presents the morphology of TiO_2 Degussa while the morphology of the synthesised C-N-TiO_2 Nano

catalysts are shown in Figure 6-8 (B_1, C_1 & D_1). These morphological images of TiO_2 Degussa and C-N-TiO_2 Nano particles taken at the same magnification (50 nm) were used to approximate their particle size distribution using ImagA software, correspondingly as shown in Figure 6-8 (A_2, B_2, C_2 and D_2). The TEM size distribution normalised results of the Degussa catalyst presented in Figure 6-8 (A_2) show that the particle size distribution of TiO_2 of Degussa P25 varies between 5 and 40 nm and the most abundant TiO_2 particle sizes were between 10 and 25 nm which is in conformity with XRD results. All synthesised C-N-TiO_2 specimens were in the nano scale and had smaller crystallite sizes than TiO_2 Degussa and their particle sizes varied from 3 to 13 nm which incorporates the 5.5- 6.4 nm range calculated by the Scherrer equation in XRD section. The size of the C-N-TiO_2 nano particles calcined for 105 min lies between 5 and 6 nm while that of C-N-TiO_2 pyrolysed for 120 or 135 min, ranged between 6 and 7 nm or between 7 and 8 nm respectively, as shown in Figure 6-8 (B_2, C_2 & D_2). Among the nano catalysts synthesised in this study, the granular C-N-TiO_2 calcined for 105 min had the smallest particle size range of 5 to 6 nm. Apart from being in nanotube shapes, and agglomerated forms, compared to C-N-TiO_2 obtained after 120 min or 135 min of pyrolysis as shown by SEM analysis, their most abundant particle size ranged consistently from 6 -7 nm to 7- 8 nm. These results show that the size of C-N-TiO_2 doped nano composites increased slightly with an increase in the calcination time.

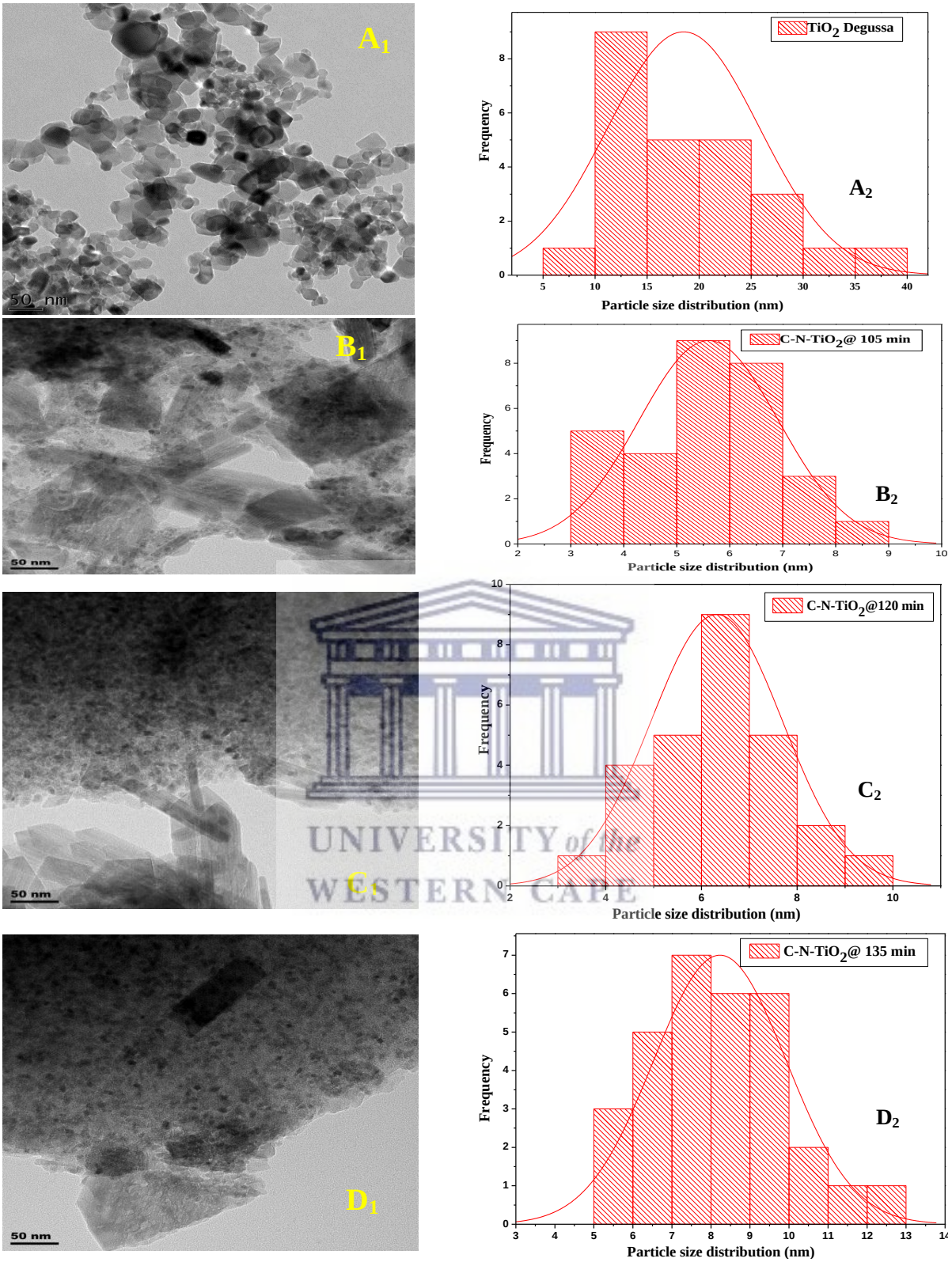

Figure 6.8: STEM micrographs and particle distribution of the Degussa TiO_2 (A) compared to the synthesised C-N-TiO_2 nano compositespyrolysed at 350 ^oC for 105 (B); 120 (C); 135 (D) minutes.

Besides the physical properties of the C-N-TiO_2 nano catalysts examined in this study, the electronic properties such as band gap and the photochemical properties of the prepared materials were also evaluated.

6.1.10 UV-vis spectroscopy analysis, determination of the nano catalyst band gap

Though literature claims that doping semiconductor photo catalysts with transition metals or non-metals may result in band gap shrinking (Akpan and Hameed, 2010; Riaz *et al.*, 2012; Khan *et al.*, 2014), the impact of pyrolysis holding time on band gap has not been well discussed in literature and hence was investigated in this study. The band gap of the catalysts was calculated using the Kubelka- Munk theory described in Equations (6.2 – 6.4) and the results are presented in Figure 6-9.

$$A = \log_{10}\left(\frac{1}{R}\right) \quad (6.2)$$

$$K = \frac{(1-R)2}{2R} \quad (6.3)$$

$$E\ (eV) = \frac{hV}{\lambda} \quad (6.4)$$

Where A is the absorbance of the sample converted to diffusion reflectance (R); K is the absorption coefficient, h = 6.626 x 10^{-34} m^3kg/s Planck's constant, C = 2.997 x 10^8 m/s the speed of light and λ (nm) the wavelength at the corresponding sample absorbance.

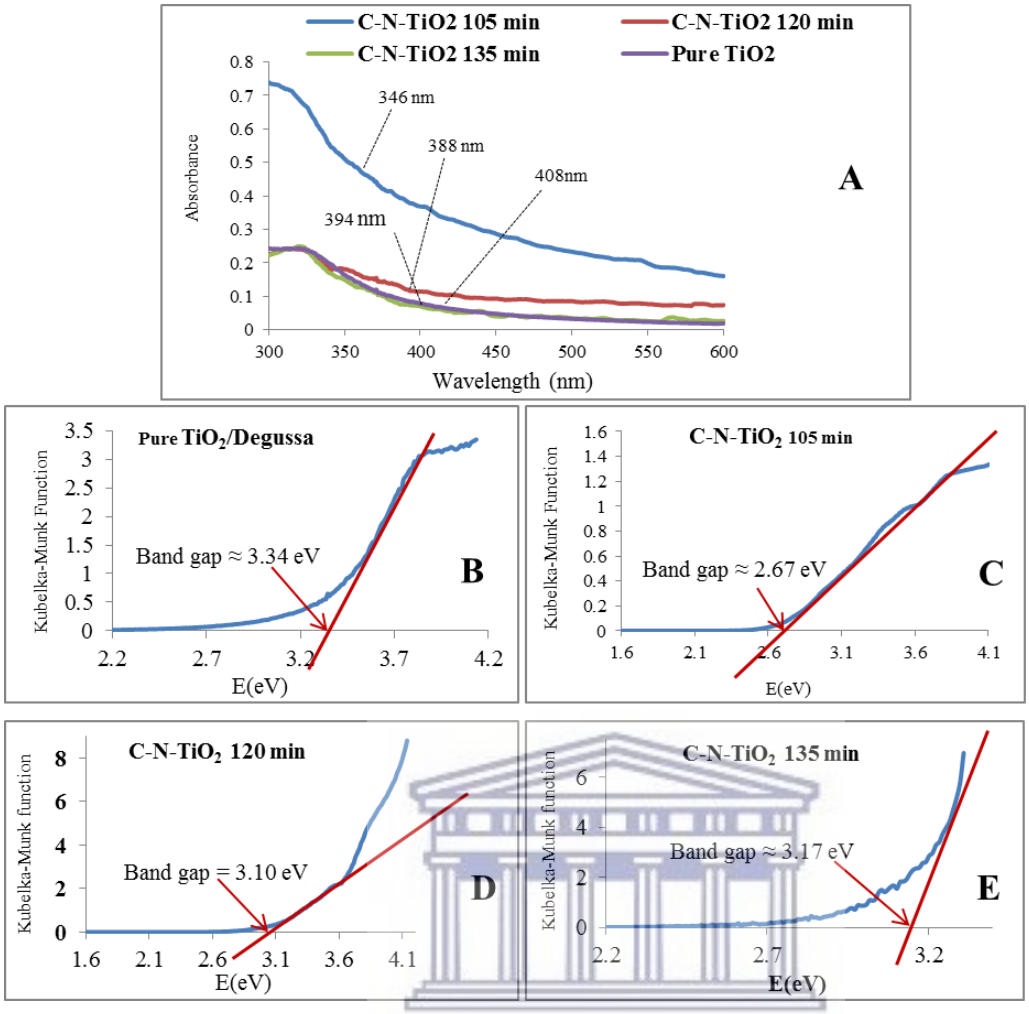

Figure 6.9: UV-vis Spectroscopy (A) and (BCDE) Kubelka- Munk graphs of the Degussa TiO_2 to carbon- nitrogen co-doped catalysts pyrolysed for different times with nitrogen gas at 350 ^oC at a ramping rate of 50^oC/min.

The outcomes of band gap calculations exhibited in Figure 6-9 (B, C, D & E) indicated that upon incorporation of C and N, the absorption band gap 3.34 eV of pure TiO_2 was narrowed to 2.67 eV, 3.0 and 3.17eV when pyrolysis time was altered from 105, 120 to 135 min, correspondingly showing how accurately the pyrolysis time allows band gap tailoring. The wavelengths and the approximated band gap recorded in this case are presented in Table 6-5.

Table 6-5: Effect of pyrolysis time on the band gap of the synthesised C-N-TiO_2 nano catalystspyrolysed with nitrogen gas at 350 ^oC and ramping rate of 50^o C/min.

Photo catalysts	Pyrolysis time (min)	UV-vis absorption wavelength (nm)	Band gap (eV)
Pure TiO_2 Degussa	NA	408	3.34
C-N-TiO_2	105	462	2.67
C-N-TiO_2	120	393	3.10
C-N-TiO_2	135	333	3.17

The results in Figure 6-9 (B, C, D & E) and those summarised in Table 6-5 showed that C-N-TiO_2 nano materials calcined at 350 ^oC for 105 min had a band gap of 2.67 eV, smaller than 3.10 and 3.17 eV obtained when pyrolysis time was increased to 120 min and 135 min, individually. The UV-vis data obtained in Figure 6-9 (A) showed that after doping C and N into the TiO_2 lattice, the C-N-TiO_2 nano sized materials pyrolysed for 105 min absorbed in the visible region while those pyrolysed for 120 and 135 min absorbed in the UV region. C-N-TiO_2 nano composites pyrolysed for 105 min had the highest estimated absorption wavelength of 460 nm followed by 393 and 335 nm of the same C-N-TiO_2 nano catalysts pyrolysed for 120 min and 135 min, respectively. The slight decrease of wavelength and small increase of band gap of the computed C-N-TiO_2 nano catalysts presented in Table 6.5 corresponded to the amount of C and N introduced during pyrolysis process as supported by FT-IR and TGA analysis. In comparison, the band gap of the prepared nano catalysts were all below that of TiO_2 Degussa (3.34 eV) estimated in Figure 6-9 (A) and highlighted by Carp et al. (2004); Li et al. (2015) and Gilmour & Ray (2012). This shows that C and N impurities were successfully integrated into the O-Ti-O network. Alternatively, the band gap of the designed C-N-TiO_2 nano composites slightly increased from 2.67 to 3.10 and 3.17 eV when the pyrolysis time was increased from 105, 120 to 135 min. The reduction of TiO_2 band gap from 3.34 in its usual state to 2.67 eV after 105 min of pyrolysis was probably due to oxygen vacancies that acted like electron-donors in the valence band of the nano photo catalyst support and hence accumulating more layers (microstates) with new electronic properties which further reduced its energy absorption gap. In this case, the modification of TiO_2 with C and N impurities occurred either by replacement of Ti or O leading to C−O−Ti−O and Ti−C−T−O, N-Ti-O and Ti-N-Ti-O lattice structures, distinctly as a consequence of altered Fermi states (Morikawa *et al.*, 2001; Sakthivel and Kisch, 2003; Di Valentin *et al*., 2005; Li *et al.*, 2005; Xu *et al.*, 2006). This supports the band gap narrowing observed in Figure 6-9. In this study, concentrations of

PAN and NH_4NO_3 precursors of C and N were kept constant during synthesis of C-N-TiO_2 co-doped nano catalyst. The increase of the band gap from 2.67 to 3.10 and 3.17 eV when systematically increasing pyrolysis time suggested that the stability of dopants C and N in TiO_2 structural lattice depended on the degree of volatilisation of these two substituents as previously shown by EELS and FT-IR. This inferred that the C and N content can be controlled accurately and thus engineered C-N-TiO_2 nano particles are stable at a specific pyrolysis holding time and an increase in holding time may lead to changes in their band gap, morphology, particle size and changes in other physical and chemical properties as shown by various characterisation techniques explored in this study. Therefore, to achieve maximum desired catalytic properties, it would be advisable that the holding time during pyrolysis should be optimised and controlled carefully when synthesising nano-TiO_2-based materials via the sol-gel pyrolysis protocol.

6.1.11 Summary of the synthesis and characterisation of C-N-TiO_2 Nano catalyst

Semiconductors such as TiO_2 are characterised by a valence band (VB) and a conductive band (CB). The VB is governed by positively charged holes while the CB is populated by negative charge carriers which are electrons. The space between VB and CB is referred to as the band gap. According to intrinsic and extrinsic Fermi-Dirac distribution in p-type semiconductors (Shriver and Atkins, 1994), introduction of impurities such as C and N into the Ti lattice led to the formation of new sub energy levels that consequently reduced the band gap from 3.34 to 2.67 eV. The incorporation of these foreign elements often results in the formation of holes and a narrow empty acceptor band that is above the full TiO_2 lower band as shown in Figure 6-9. At a temperature of 0^{o}C, the acceptor band is empty. So when increasing temperature the empty band can accept thermally excited electrons from the Ti valence band. This consequently creates holes in the later where the remaining electrons are mobile. From literature, the TiO_2 band gap is estimated to be about 3.2 eV which is closer to 3.34 eV obtained for Degussa in Figure 11(Carp, Huisman and Reller, 2004; Gilmour and Ray, 2012; Shuzhen Li *et al.*, 2015). So in this study, the incorporation of C and N into the TiO_2 framework and its calcination at 350 ^{o}C for 105 min narrowed C-N-TiO_2 nano particles band gap to 2.67 eV as shown in Figure 6-9. On the contrary, literature also claims that an increasing concentration of dopants may result in band gap increase (Shriver and Atkins, 1994; Mu et al. 2004) with high energy that may reduce the photocatalytic activity of the nano catalyst. In the current study, the TEM- EDS percentage abundance of C and N as shown in Table 6-3 decreased from 72 to 40 % and from 7.1 to 3.63%, respectively when increasing the pyrolysis time from 105, 120 to 135 min which

was probably due to the evaporation of C and N impurities as gases when PAN was systematically decomposed during the pyrolysis process (Darányi et al. 2011). This was further supported by the functional groups such as C=O, N=O, etc. depicted by FT-IR in Figure 6-2. The increasing pyrolysis time to some extent induced the morphological distortion/elongation of C-N-TiO_2 crystals in the nano composites. This was proven by SEM micrographs of the synthesised C-N-TiO_2 presented in Figure 6-5. The increase of Ti mass % was due to the loss of carbon as indicated by TEM-EDS in Table 6-3 and TGA results in Figure 6-4. Furthermore, from the SAED data it can be seen that the synthesised C-N-TiO_2 catalysts have both anatase and rutile phases present in the crystal structure. Therefore, during synthesis of C-N-TiO_2 nano catalysts by the sol-gel method, pyrolysis time affects the band gap, morphology (shape), and the dopant percentage, the particle size and the phase of the nano materials. Hence when employing the synthesis protocol using the sol-gel pyrolysis process, the pyrolysis time should be carefully optimised and controlled in order to achieve the desired impuritylevels and properties of the prepared photo catalysts.

6.2 Photo catalytic application of C-N-TiO_2 nano- catalyst for the degradation of O.II dye

In this subsection, the influence of catalyst parameters determined in Section 6.1 on the degradation of orange II dye under UV light at the applied conditions was assessed.

6.2.1 Effect of pyrolysis time of C-N-TiO_2 nano catalysts on photocatalytic degradation of orange II sodium salt

In order to confirm whether band gap, or dopant percentage or the shape and the size of nanomaterial made in this study had an impact on their photo catalytic activities, photocatalytic degradation of orange II (O.II) sodium salt dye was conducted using the as synthesised powder nano catalysts C-N-TiO_2 compared to Degussa TiO_2 at the following experimental conditions: mass of catalyst, 0.08 g, [O.II] concentration 5 mg/L; solution pH 2.5; solution volume 500 mL; and irradiation time of 120 min as shown in Figure 6-10 as described in Sections 3.6.6.1 and 3.6.6.1.1. The decrease of orange II concentration over time was followed using UV-vis technique as shown in Equation (6.5).

$$d\frac{[O.II]}{dt} = -kr[O.II] \quad (6.5)$$

Where [O.II] is the concentration of O.II dye and k_r the rate constant (per minutes).

So at t =0 min, the concentration of orange II was equivalent to $[O.II]_o$ and $[O.II]_t$ at any sampling time t. Therefore, integration of Equation (6.6) results in Equations 6.7 and 6.8 as follows:

$$\int_{[O.II]o}^{[O.II]t} \frac{d\,[O.II]}{[O.II]} = -kr \int_0^t dt \quad (6.6)$$

$$\ln([O.II]_o^t) = -krt \quad (6.7)$$

$$\text{Ln}\left(\frac{[O.II]t}{[O.II]o}\right) = -\,k_r t \quad (6.8)$$

In order to evaluate the removal percentage and performance of the rate constant for the decomposition of O.II with time, the decolouration percentage (Figure 6-10 A) and ln $\left(\frac{[O.II]t}{[O.II]o}\right)$ were plotted against time (t) for each case and the results are presented in Figures 6-10 (A & B). Equation (9) shows that the decolouration of orange II followed a first order reaction whose plots presented in Figure 6-10 (B) give straight lines with slopes corresponding to their rate constants k_r (min^{-1}).

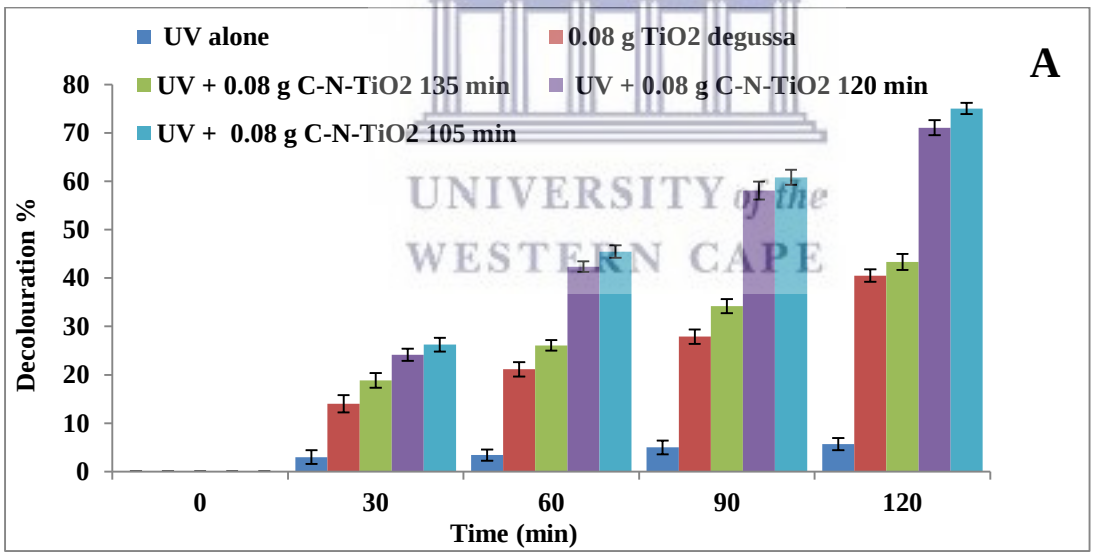

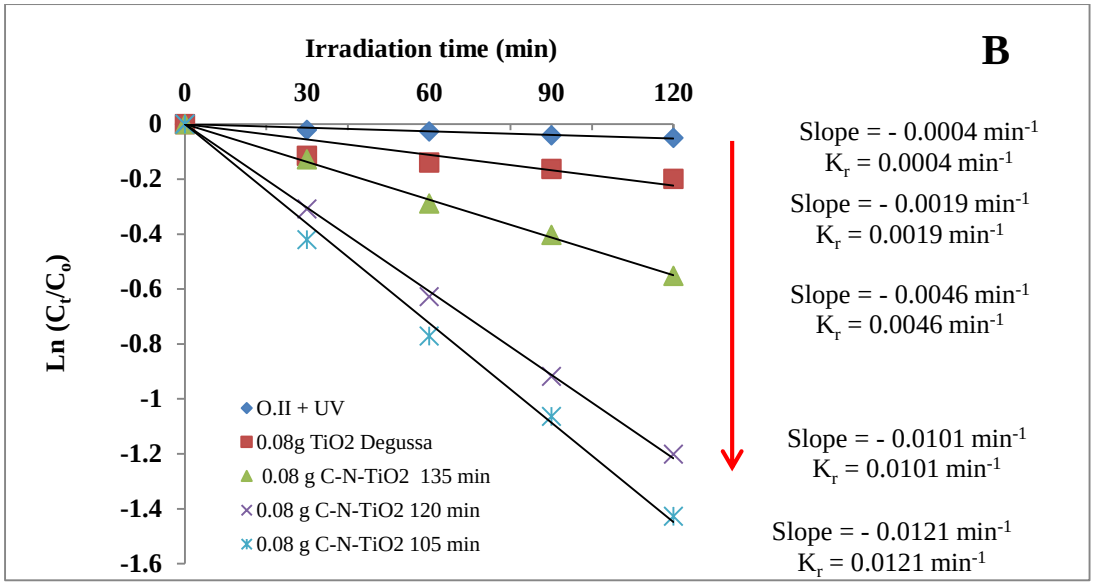

Figure 6.10: Photocatalytic decolouration of orange II by powder C-N-TiO2 Nano compositespyrolysed with N_2 gas at 350 ºC, (50 ºC/min ramping rate) at 3 different holding times (105, 120 and 35 min) and Kinetics studies. Experimental conditions [O.II] 5 mg/L, volume 500 mL, pH 2.5, catalyst dosage 0.08 g and UV irradiation time of 120 min (n = 2).

The photocatalysis results presented in Figure 6-10 (A) show that all C-N-TiO_2 nano catalysts are photo catalytically active. However, the best photocatalytic decolouration of O.II was achieved with C-N-TiO_2 calcined at 350 ºC for 105 min followed by C-N-TiO_2 for 120 and 135 min, respectively and the lowest activity was observed with pure TiO_2 Degussa, respectively. For instance after 120 min of irradiation time, 73.96 % of O.II decolouration was achieved with C-N-TiO_2 (105 min), compared to 69.9 %, 42.4% and 38.8% decolouration that were reached with C-N-TiO_2 pyrolysed for 120 and 135 min, and TiO_2 Degussa, correspondingly. These results showed that the catalysts with high band gap exhibited lower decolouration percentage of O.II. This is a consequence of poor promotion of excited electrons from the valence band (Vb) to the conductive band (Cb) of the semi-conductor which in return impeded the oxidation and reduction reactions that occur on Vb and Cb energy levels. Indeed, the oxidation of water molecules by the empty holes on the Vb and the reduction of oxygen molecules by highly energised electron on the Cb largely contributed to the production of non-selective hydroxyl radicals (OH·) that unselectively destroyed the pollutant. Therefore, higher band gap 3.2, 3.17 and 3.10 limited the production of ·OH and co-produced oxidants under UV light; and thus, low degradation percentage of O.II dye. The high catalytic activity was supported by the kinetics shown in Figure 6-10 (B) whereby C-N-TiO_2 calcined for 105 min

had the highest rate constant of $1.21x10^{-2}$ min^{-1} followed by $1.01x10^{-2}$ min^{-1}, $4.3 x10^{-3}$ min^{-1} and $1.9x10^{-3}$ min^{-1} achieved with C-N-TiO_2 calcined for 120 and 135 min, and pure TiO_2 Degussa, separately. These photocatalytic activities are in line with properties of the prepared C-N-TiO_2 previously discussed. The correlation of C-N-TiO_2 activity and other properties previously discussed shows that the C-N-TiO_2 nano composites with particle size between 5 and 6 nm and a band gap of 2.6 eV achieved 76 % removal of O.II dye in their mainly anatase phase. While lower percentage removals of O.II were reached with C-N-TiO_2 with higher particle sizes (6 – 25 nm) and band gap (3.1, 3.17 and 3.2 eV). Consequently, the band gap (Cernuto *et al.*, 2011; Khan *et al.*, 2014), crystal structure (Gnanasekaran, Hemamalini and Ravichandran, 2015), the shape (Wang *et al.*, 2008; Saravanan *et al.*, 2013), and the size of nanomaterial (Cernuto *et al.*, 2011; Han *et al.*, 2014; Khan, Adil and Al-Mayouf, 2015) have an impact on their photocatalytic activity.

6.2.2 Effect of catalyst dosage on photocatalytic decolouration of orange II sodium salt

Since the powder form C-N-TiO_2 nano catalyst annealed at 350 ºC for 105 min exhibited a higher decolouration percentage of O.II as shown in Figure 6-10, its dosage was varied from 0.02; 0.08 to 0.14 g at the applied photocatalytic conditions (see section 3.6.6.1.2) to assess the effect of catalyst dosage on decolouration of orange II dye and the results of these experiments are shown in Figure 6-11.

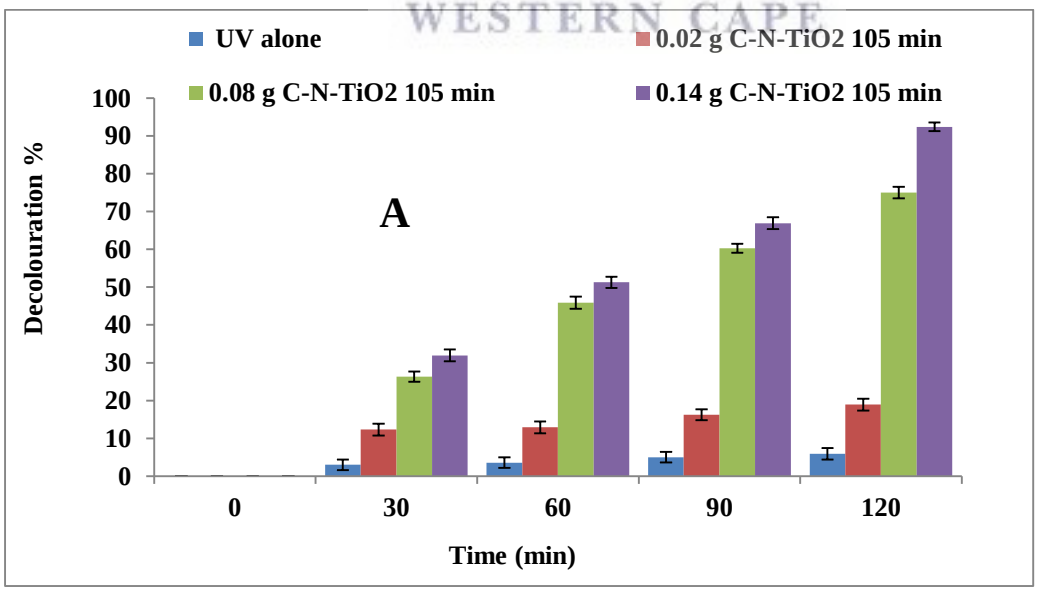

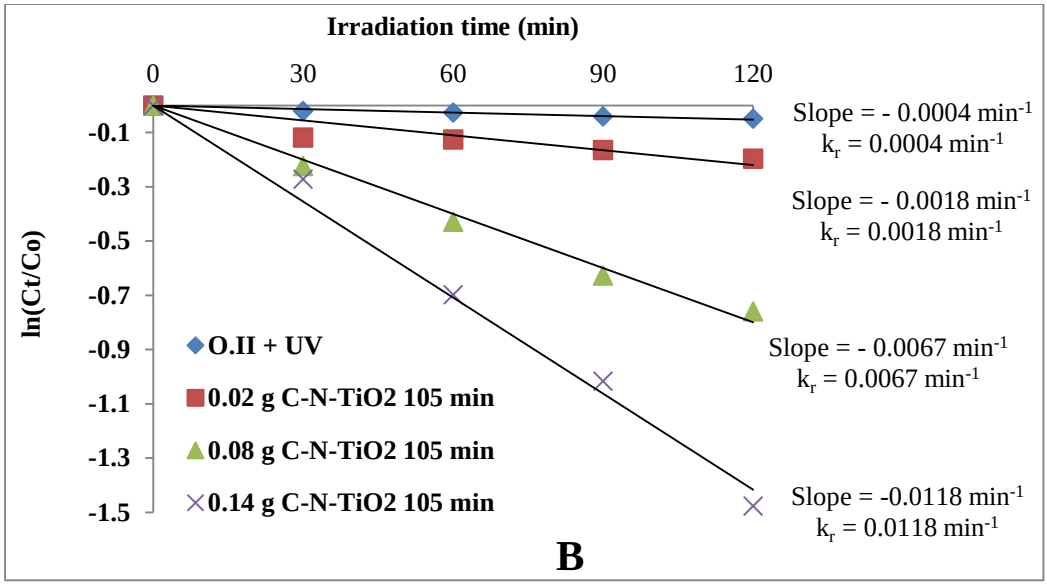

Figure 6.11: Effect of photo catalyst dosage on decolouration efficiency (A) and rate of decolouration (B) of orange II sodium salt by C-grounded powder N-TiO_2 nano composite pyrolysed with N_2 gas at 350 ^oC, (50 ^oC/min ramping rate) for 105 min at 3 different loadings. Experimental condition [O.II] 5 mg/L, volume 500 mL, pH 2.5 and irradiation time of 120 min (n = 2).

The outcomes of the photocatalysis experiments presented in Figure 6-11(A) show that the decolouration percentage of O.II dye increased with an increase of the amount of catalyst as expected. That is, after 120 min of photocatalytic irradiation, about 18.8 % of O.II removal was attained with 0.02 g of C-N-TiO_2 pyrolysed for 105 min. This increased to 53.2 and 91.6 % with 0.08 and 0.14 g of the same nano catalyst. This increasing catalytic trend was observed throughout at all sampling times of the three photo catalysis experiments, and the amount of catalyst had a positive effect on the removal of contaminants from polluted water. For dosage up to 0.14 g/500 mL, no light penetration problem relating to obscuring UV flux by particulates of photo catalyst was observed. A similar trend of dosage related removal was reported by (Djaneye-Boundjou (2012); Rajeshwar et al. (2008); Klamerth, (2010) and Khan et al. (2017). Kinetics investigations presented in Figure 6-11 (B) also support that the rate of decolouration of orange II linearly increased when increasing the applied catalyst dosage. Hence, the fastest removal of orange II occurred with 0.14 g C-N-TiO_2 at a rate of $1.18x10^{-2}$ min^{-1} followed by a rate of $6.7x10^{-3}$ min^{-1} achieved with 0.08 g of C-N-TiO_2 and $1.8x\ 10^{-3}$ min^{-1} obtained with 0.02 g C-N-TiO_2. The time constant r (tau) is a specific indication of the rate of first-order

decolouration of O.II dye. This indicator describes the decolouration rate of O.II concentration to 1/e of its initial value (Shriver and Atkins, 1994). So from Equation (6.9),

$\ln(\frac{[O.II]_t}{[O.II]_o}) = -krt \Leftrightarrow k_r\tau = -\ln(\frac{[O.II]_o/e}{[O.II]_o}) = -\ln(\frac{1}{e}) = 1$

$$\tau = \frac{1}{kr} \quad (6.9)$$

This is a reciprocal of the rate constant of a first-order reaction as described by Atkins, (2010). Hence the synergy between the rate constant k_r and the time constant τ of the first order decolouration of O.II discussed in Figures 6-10 and 6-11 was summarised and is presented in Tables (6-6 & 6-7).

Table 6-6: The effect of catalyst pyrolysis holding time upon the first order reaction kinetics parameters for the photocatalytic decolouration of orange II by powder form C-N-TiO_2 nano composite pyrolysed with N_2 gas at 350 ºC, (50 ºC/min ramping rate) at 3 different holding times (105, 120 and 135 min). Experimental condition [O.II] 5 mg/L, volume 500 mL, pH 2.5 and irradiation time of 120 min.

Decolouration process	Slope (min^{-1})	Kr (min^{-1})	Correlation coefficient (R^2)	Time constant τ (min)
UV	-0.0004	0.0004	0.9568	2500
UV + 0.08 g C-N-TiO_2 135 min	-0.0046	0.0046	0.9981	217
UV + 0.08 g C-N-TiO_2 120 min	-0.0101	0.0101	0.9993	99
UV + 0.08 g C-N-TiO_2 105 min	-0.0121	0.0121	0.9947	82

Table 6-7: First order reaction kinetic factors for the photo catalysis degradation of orange II dye with different dosages of C-N-TiO_2 pyrolysed at a holding time 105 min. Experimental condition [O.II] 5 mg/L, volume 500 mL, pH 2.5 and irradiation time of 120 min.

Catalyst dosage	Slope (min^{-1})	Kr (min^{-1})	Correlation coefficient (R^2)	Time constant τ in min
UV alone/Control	-0.0004	0.0004	0.9568	2500
0.02 g C-N-TiO_2 105 min	-0.0018	0.0018	0.7801	555
0.08 g C-N-TiO_2 105 min	-0.0067	0.0067	0.9899	149
0.14 g C-N-TiO_2 105 min	-0.0118	0.0118	0.9908	84

The synergic effect between the rate constant and the time constant r observed in Tables 6-6 & 6-7 shows that the increase of the rate constant results in the decrease of the time constant r. For instance, in Table 6-6 the increase of the rate constant from 4.6 $x10^{-3}$ min^{-1} to $1.01x10^{-2}$ min^{-1} and $1.21x10^{-2}$ min^{-1} with increased dosage of nano catalysts led to the decline of the time constant from 217, 99 to 83 min, respectively. A similar trend was observed in Table 6-7 whereby the increase of the rate constant from $1.8x10^{-3}$ min^{-1} to $6.7x10^{-3}$ min^{-1} and $1.18x10^{-2}$ min^{-1} corresponded to the time constant decreasing from 555, 149 to 85 min, individually with the same nanocatalyst depending on dosage. So the relationship between the rate constant kr and time constant r during first order decolouration of O.II described in Tables (6-6 & 6-7) demonstrates that the fastest decolouration of dye occurred in the shortest period of time with 0.14 g of catalyst. Furthermore, the poor correlation coefficients (R^2) in Tables (6-6 & 6-7) ranging between 0.7801 and 0.9908 resulted from low rate constants that were defined by the long times taken to decolour O.II dye using insufficient catalyst.

6.2.3 Summary of the synthesis, characterisation of the C-N-TiO_2 Nano catalyst and its photo catalytic application for the decolouration of O.II dye under UV light

The C-N-TiO_2 nano composite photo catalyst was successfully prepared by a sol-gel/pyrolysis method. The doped C-N-TiO_2 was pyrolysed at 350 ºC for different holding times of 105, 120 and 135 min. This study showed for the first time that pyrolysis holding time had an effect on the band gap, shape, and particle size and photocatalytic activity of the prepared nano photo catalysts. Carbon and nitrogen were well doped into the TiO_2 matrix. When increasing pyrolysis time beyond 120 minutes, the dopants C and N likely evaporated and their benefit was lost as photocatalytic activity decreased. This was further detected by the unusual smell during the pyrolysis process evidenced by the formation of gas such as CO, CN, etc. highlighted by FT-IR, EDS and EELS results. The C-N-TiO_2 band gap estimated at 2.67 eV after 105 min pyrolysis increased to 3.10 and 3.17 eV when pyrolysis time was increased to 120 and 135 min, respectively. The particle size range (5 – 6) nm obtained with C-N-TiO_2 pyrolysed for 105 minutes increased to (6-7) nm and (7-8) nm with an increase of the pyrolysis time to 120 and 135 min, respectively. This would affect the surface area of the prepared nano materials. The synthesised C-N-TiO_2 nano photo catalysts pyrolysed for 120 min showed excellent photocatalytic activity when UV irradiation was applied, C-N-TiO_2 pyrolysed for 105 min showed a high decolouration percentage of orange II dye (73.96 %) followed by 69.9 and 42.4 % obtained with 120 and 135 min C-N-TiO_2, correspondingly. The decolouration of O.II

in both cases followed a first order reaction whose kinetics plots exhibited linear trends with slopes corresponding to their rate constants. The highest rate constants were achieved at higher decolouration percentage that occurred in short period of time. Furthermore, the degradation percentage of O.II increased with an increase of the catalyst dosage as 18.8, 53.2 or 91.6% O.II decolouration were respectively achieved with a dosage of 0.02, 0.08 or 0.14 g of C-N-TiO_2 pyrolysed for 105 minutes.

6.3 Immobilisation of C-N-TiO_2 nano catalyst on SS and pure Ti meshes and incorporation of the coated films into DBD for the degradation of orange II dye and sulfamethoxazole drug

In this section, the C-N-TiO_2 sol-gel was deposited on SS and pure Ti meshes by dip coating which involved withdrawing the mesh from the gel as described in Section 3.5.3.1. The obtained composites immobilised C-N-TiO_2/SS and C-N-TiO_2/Ti coated meshes were arranged around the outer tube in the DBD plasma reactor for the degradation of O.II dye and sulfamethoxazole at the corresponding conditions as shown in Figure 3-12. The SEM and SEM-EDS characterisation results of the prepared films as well as their photo catalytic efficacies when combined with DBD on the decolouration of O.II and SMX are subsequently discussed in the following subsections.

6.3.1 Characterisation of C-N-TiO_2/SS and C-N-TiO_2/Ti films before DBD experiments

The principal goal of the SEM-EDS characterisation in this case was to first investigate the adherence of C-N-TiO_2 nano catalyst on SS and Ti meshes after the pyrolysis process conducted at 350^{o}C (heating rate of 50^{o}C/min) for 105 min. Hence, before running any DBD experiments for the decolouration of O.II and SMX in combination with composite C-N-TiO_2/SS and C-N-TiO_2/Ti coated meshes it was necessary to visualise the morphological behaviour of C-N-TiO_2 nano composites coated on the mesh grids of the two supports SS and pure Ti. In this regard, electron microscopy coupled with energy dispersive spectroscopy SEM-EDS was used to determine the morphology and elemental composition of the C-N-TiO_2/SS and C-N-TiO_2/Ti coatings. The SEM micrographs are presented in Figure 6-12 (A&B), and the EDS results are exhibited in Table 6-8 respectively.

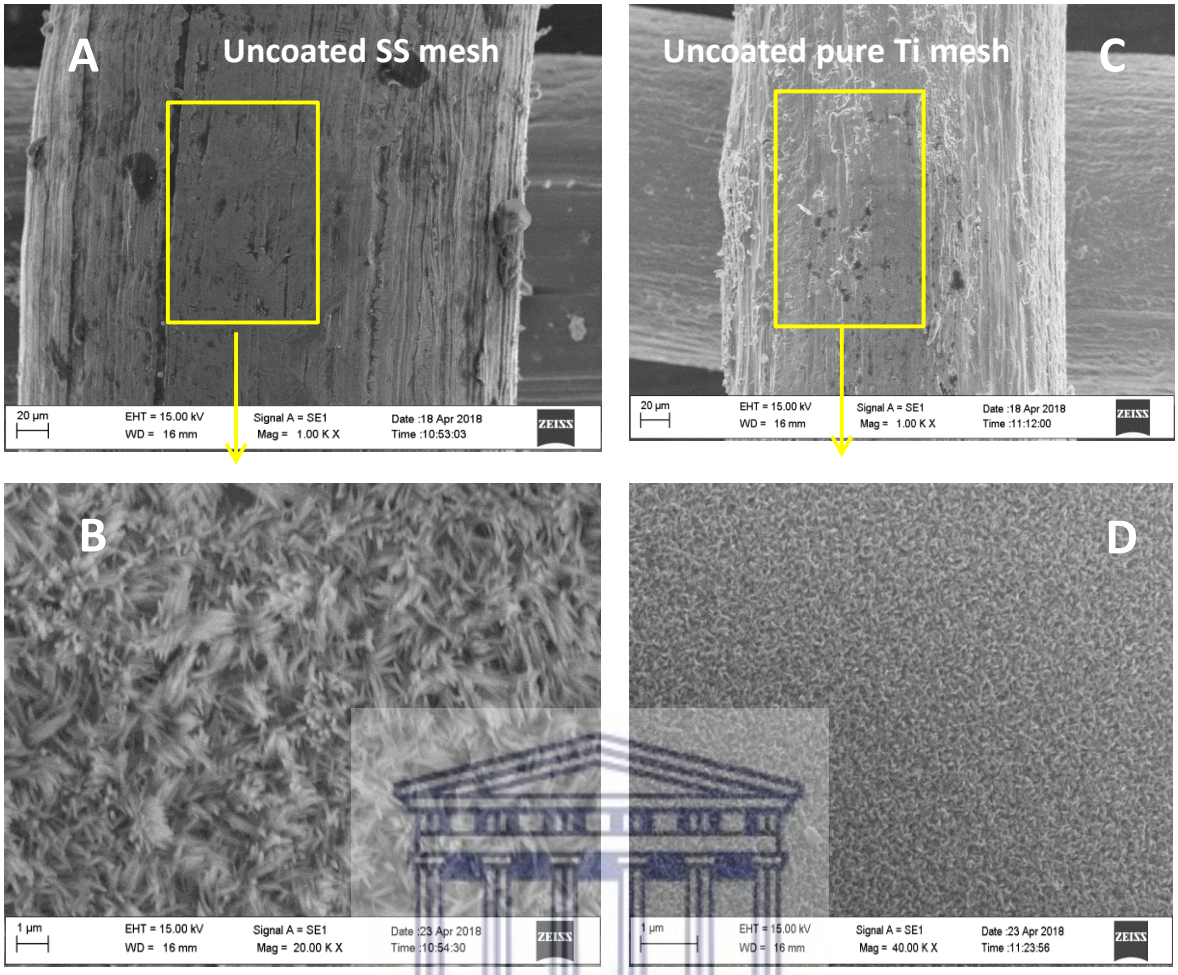

Figure 6.12: SEM images/micrographs of A = uncoated SS mesh, B = C-N-TiO_2/SS, C = uncoated Ti and D = C-N-TiO_2/Ti mesh.

The SEM micro graphs in Figure 6-12 show that C-N-TiO_2 nano catalyst was successfully coated on SS and pure Ti mesh. For instance, the uncoated SS in Figure 6-12 (A) was fully covered by the catalyst resulting in Figure 6-12 (B) showing good adherence behaviour between the catalyst and SS substrate.

The SEM of the coated mesh exhibited in Figure 6-12 (B) demonstrated that the C-N-TiO_2 nano composite were well dispersed on SS support. The selected section of Ti mesh at 1 µm magnification presented in Figure 6-12 (F) shows that the porous C-N-TiO_2 was present on the Ti mesh as tiny compact nano crystals that are in agreement with the findings of Çomakli et al. (2014). The morphologies of the C-N-TiO_2 coated of the two metal mesh supports SS and Ti meshes are shown in Figures 6-12(C) and 6-12 (F). These results show that C-N-TiO_2 successfully adhered on the two metal supports. It could be inferred that C-N-TiO_2 immobilised on different supports at the same conditions may adopt different morphologies and hence have

different behaviours. These perhaps may impact on their extended properties such as photocatalytic activity (Liao *et al.*, 2012; Çomakli, Yetim and Çelik, 2014; Çomakli *et al.*, 2016; Yetim, 2016; Zhang *et al.*, 2016). This is in line with the findings reported by (Zhang *et al.*, 2003; Merajin *et al.*, 2013; Souzanchi *et al.*, 2013; Kr´ysa *et al.*, 2014).

Table 6-8: Weight percentages of elements C, Ti and O measured by EDS in uncoated and meshes coated with C-N-TiO_2 calcined at 350^{o}C, at heating rate of 50^{o}C/min in N_2 gas at a flow rate of 20 ml/min for 105 min.

Sample	Elemental composition (W%) of uncoated and C-N-TiO_2 coated meshes							
	C	Ti	O	Si	Cr	Mn	Fe	Ni
Uncoated SS	1.56		30.1	0.46	12.96	1.12	48.07	4.16
C-N-TiO_2/SS	3.14	6.1	30.4	0.45	22.01	0.72	34.08	2.84
Uncoated Ti mesh	2.91	50.68	43.54					
C-N-TiO_2/Ti	4.07	53.2	44.94					

Table 6-8 discloses the elemental composition (W %) of uncoated and C-N-TiO_2 coated SS and Ti meshes by EDS. The results presented in Table 6-8 show that the amount of C in uncoated 304 SS was 1.56% that increased to 3.14 in the C-N-TiO_2 coated SS, while unidentified Ti content in the uncoated SS increased to 6.1% on the C-N-TiO_2 coated SS. The C trace detected in uncoated SS was probably due to the C stickers used to carbon coat the sample before SEM analysis. This could be justified by the study conducted by Mouele et al. (2018) during which the authors showed that the trace amount of C in 304 SS was about 0.004%. Therefore, the 1.56% C content depicted in uncoated SS of this study might have originated mostly from carbon stickers or from the environment during SEM analysis. In comparison with the 3.14% of C in C-N-TiO_2/SS, the EDS showed that an additional 1.58% of C was detected in the case of the co-doped C-N-TiO_2 demonstrating that C was present in the prepared nano composites. Likewise, the increase of Ti content from 0 in the case of the uncoated SS to 6.1% in the case of the C-N-TiO_2/SS, respectively shows that Ti was also present in the immobilised nano catalyst. On the other hand, the amount of C in uncoated Ti mesh (2.91%) increased to 4.07% in C-N-TiO_2/Ti after coating, showing that about 1.16 % of C content derived from C-N-TiO_2 nano catalyst and a similar trend was observed with Ti content that was 50.68% in the uncoated Ti mesh and which increased to 53.2% in C-N-TiO_2/Ti after coating showing that approximately 2.52% of Ti content originated from the manufactured C-N-TiO_2 nano composites. It could be noticed that 1.58 % C and 6.1% Ti contents were present in the C-N-TiO_2/SS composite which contents were both superior to that

of 1.16% C and 2.2% Ti content present in C-N-TiO_2/Ti composite. Therefore these results compliment the different morphological aspects observed in C-N-TiO_2/SS and C-N-TiO_2/Ti composites in the SEM micrographs shown in Figures 6-12 (D & F) which further could influence the photo catalytic activities in oxidative environments.

6.3.2 Photo catalytic performance of C-N-TiO_2/SS and C-N-TiO_2/Ti combined with DBD for the decolouration of O.II dye

In this subsection, the photo catalytic effectiveness of C-N-TiO_2/SS and C-N-TiO_2/Ti films combined with DBD plasma reactor on the degradation of O.II dye at the indicated optimum conditions was assessed. In order to achieve this, four pieces (8 cm long x 2 cm large) of each prepared composites were gathered in rectangular configurations and arranged around the outer tube of the DBD system to induce the photo catalytic decolouration of O.II at the applied conditions from the UV generated by the DBD system insitu.The results of these experiments are presented in Figure 6-13.

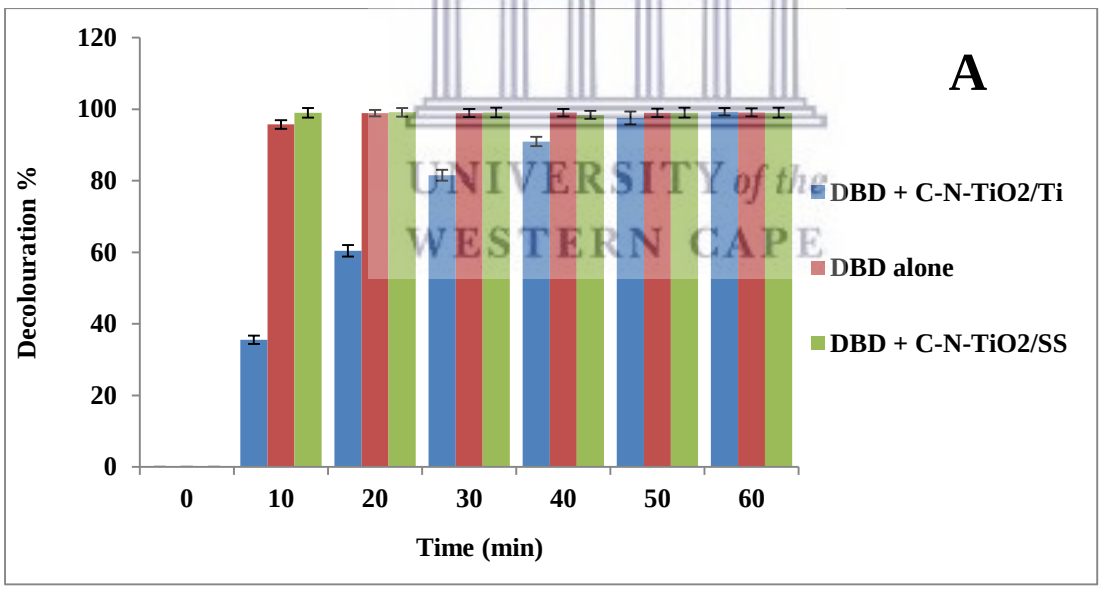

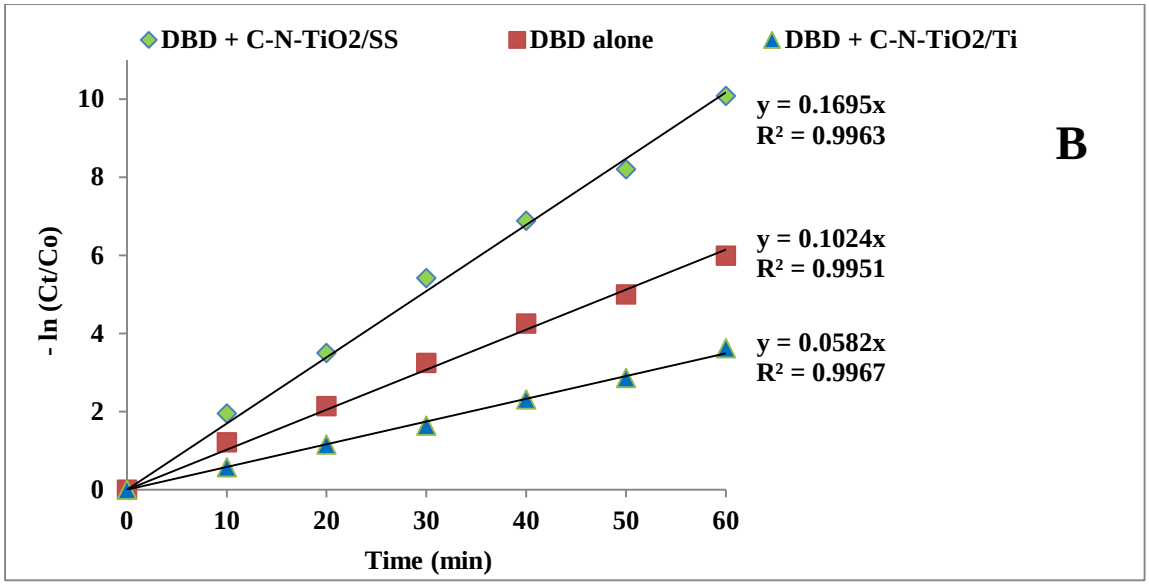

Figure 6.13: Decolouration efficiency (A) and rate of decolouration (B) of orange II sodium salt dye by combined DBD and C-N-TiO_2 immobilised on SS (C-N-TiO_2/SS) or Ti mesh (C-N-TiO_2/Ti) at the following optimum conditions: Peak voltage 8 kV, [O.II] 60 mg/L, solution volume 1500 mL, solution pH 2.5, 50 g/L NaCl inner electrode electrolyte, air gap 2 mm, 1.5 mm silver electrode, experimental time 60 min, (8 cm long x 2 cm large) x 4 uncoated or coated meshes enfolded around the outer tube of the DBD reactor.

Figure 6-13 displays the results for the decolouration of O.II dye by the optimised DBD system and DBD combined with C-N-TiO_2/SS or C-N-TiO_2/Ti composites at the applied conditions as described in Section 3.5.5 of Chapter 3. The results presented in Figure 6-13 (A) show that O.II dye was completely decolourised by DBD, DBD + C-N-TiO_2/SS and DBD + C-N-TiO_2/Ti systems within 60 min of treatment. Likewise, high removal of O.II was achieved with DBD + C-N-TiO_2/SS followed by DBD alone and DBD + C-N-TiO_2/Ti, respectively. That is, after 10 min of reaction time, 99.90 % of O.II decolouration was achieved with DBD + C-N-TiO_2/SS compared to 94.87% O.II decolouration percentage reached with DBD alone that were both higher than 34.73% of O.II decomposition obtained with DBD + C-N-TiO_2/Ti combined system. This trend was also observed after 20 min reaction time. However, from 30 to 50 min of experiment, complete removal of O.II dye reached with DBD + C-N-TiO_2/SS and DBD alone were higher than O.II decomposition obtained with DBD + C-N-TiO_2/Ti whose total decolouration of the dye was only attained after 60 min of treatment. These results correlate with high decolouration rates (1.695 $x10^{-1}$ $min^{-1}$and 1.024 $x10^{-1}$ min^{-1}) achieved with DBD + C-N-TiO_2/SS and DBD alone, correspondingly, compared to 5.82 $x10^{-2}$ min^{-1} obtained with DBD + C-N-TiO_2/Ti as shown in Figures 6-13 (B & C). The greatest decolouration percentage

of O.II corresponding to 1.695 $x10^{-1}$ min^{-1} achieved with DBD + C-N-TiO_2/SS demonstrated that the slightly improved dye decolouration was achieved though the optimised DBD itself was already effective for the degradation of O.II dye as discussed in Section 5.1.1.6 of Chapter 5. On the other hand, the low decolouration of O.II observed with DBD + C-N-TiO_2/Ti was likely due to the fact that C-N-TiO_2 sol-gel entirely covered the pores of the pure Ti mesh during the immobilisation process. This in return impeded not only the free circulation of the polluted water throughout the C-N-TiO_2/Ti composites mesh arranged around the DBD outer inner tube but also prevented the generated UV light from shining in the solution. Therefore, this might have obstructed the production of OH radicals by water splitting when exposed to UV light. This consequently led to slow decolouration rate of O.II dye that led to lower dye removal percentages within 50 min of treatment even though complete O.II decolouration was reached after 60 minute of DBD experiment. These results are closer to the outcomes of Liao et al. (2012) who investigated the photocatalytic degradation of Methyl orange using a TiO_2/Ti mesh electrode with 3D nanotube arrays. The results of their study showed that the higher photocatalytic activity ≈ 48% was achieved with TiO_2/Ti mesh photo electrode calcined at 550 °C as a result of the presence of mixed crystal phases of anatase and rutile in the film. The removal of O.II by C-N-TiO_2/Ti mesh incorporated in the DBD has not been reported in the literature. A few studies involving the immobilisation of various doped and co-doped catalysts such as TiO_2, N-F, Ag-TiO_2, N-S-C-tridoped TiO_2, iron (Fe), zinc (Zn)–doped tin oxide on Ti mesh have been reported (Liao *et al.*, 2012; Çomakli, Yetim and Çelik, 2014; Vignesh *et al.*, 2014; Çomakli *et al.*, 2016; Yetim, 2016; Zhang *et al.*, 2016) for the removal of various targeted pollutants using systems that differ from the DBD described in the current study. The aforementioned authors claimed that Ti mesh is an adequate photocatalyst support but presents poor tribiological functions related to its surface that requires proper treatment before coating. None of these authors outlined the intermediate metabolites of the targeted pollutants. Even if colour removal is an important parameter during treatment of dyes, the identification of the degradation intermediate by-products is also an important step to understand whether the targeted pollutant is broken down or not during treatment process. Therefore, in this case, it was crucial to identify the decomposition intermediates of O.II achieved with DBD + C-N-TiO_2/SS and DBD + C-N-TiO_2/Ti advanced systems The results of intermediates obtained with DBD alone were presented in Table 5-4 and their degradation mechanisms were established in Figure 5-14 of Chapter 5.

6.3.2.1 Identification of the degradation by-products of O.II dye and suggestion of the degradation mechanistic pathways achieved with C-N-TiO_2/SS film suspended in optimised DBD reactor

Though the results presented in Figure 6-13 of Section 6.3.2 showed that both C-N-TiO_2/SS and C-N-TiO_2/Ti combined with the optimised DBD reactor contributed to the degradation of O.II dye, it was necessary to identify the structure of O.II degradation intermediate metabolites achieved with each of these combinations in the DBD configuration. This was crucial to understand dye recalcitrance or vulnerability and hence its behaviour in this particular advanced oxidation process. Therefore O.II degradation end products after exposure to DBD combined with C-N-TiO_2/SS, were determined by LC-MS analysis and are presented in Table 6-9 while their suggested degradation mechanism pathways are exhibited in Figure 6-14.

Table 6-9: LC-MS identified degradation by-products of orange II sodium salt obtained at optimum conditions with C-N-TiO_2/SS in DBD system at the following conditions: Applied voltage 8 kV, [O.II] 60 mg/L, volume 1500 mL, solution pH 2.5, air flow rate 3 L/min, 1.5 mm silver electrode, 50 g/L NaCl inner electrode electrolyte, air gap 2 mm, (8 cm long x 2 cm wide each) x 4 coated meshes enfolded around the outer tube of the DBD reactor and an experimental time of 60 min.

Compound	Molecular formula	Structure	Retention time (min)	Molecular ion $[M-H]^+$
Sodium (E)-4-((2-hydroxynaphthalen-1-yl)diazenyl)benzenesulfonate or Orange II sodium Salt	$C_{16}H_{11}N_2NaO_4S$	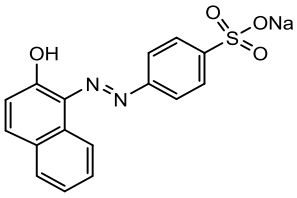	4.005	350.03
Sodium (E)-dihydroxy(7-((2-hydroxynaphthalen-1-yl)diazenyl)-3a,7a-dihydrobenzo[d][1,2,3]trioxol-4-yl)-l4-sulfanolate	$C_{16}H_{13}N_2NaO_7S$	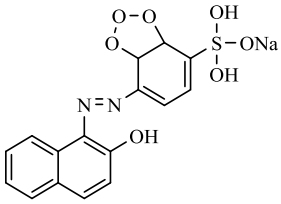	2.52	400.03

(E)-2-hydroxy-3-((2-hydroxynaphthalen-1-yl)diazenyl)butanoic acid	$C_{14}H_{14}N_2O_4$	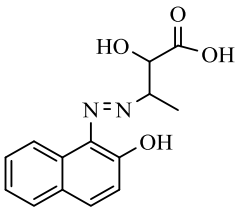	2.71	274.3
(E)-2-((E)-naphthalen-1-yldiazenyl)hex-2-en-5-ynoic acid	$C_{16}H_{12}N_2O_2$	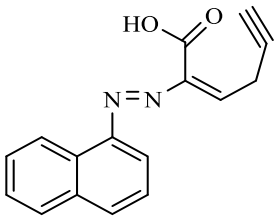	3.37	264.3
(E)-2-((2-hydroxynaphthalen-1-yl)diazenyl)propane-1,1-diol	$C_{13}H_{14}N_2O_3$	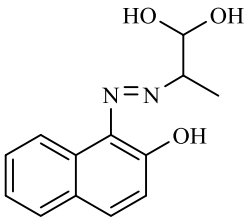	2.71	246.3

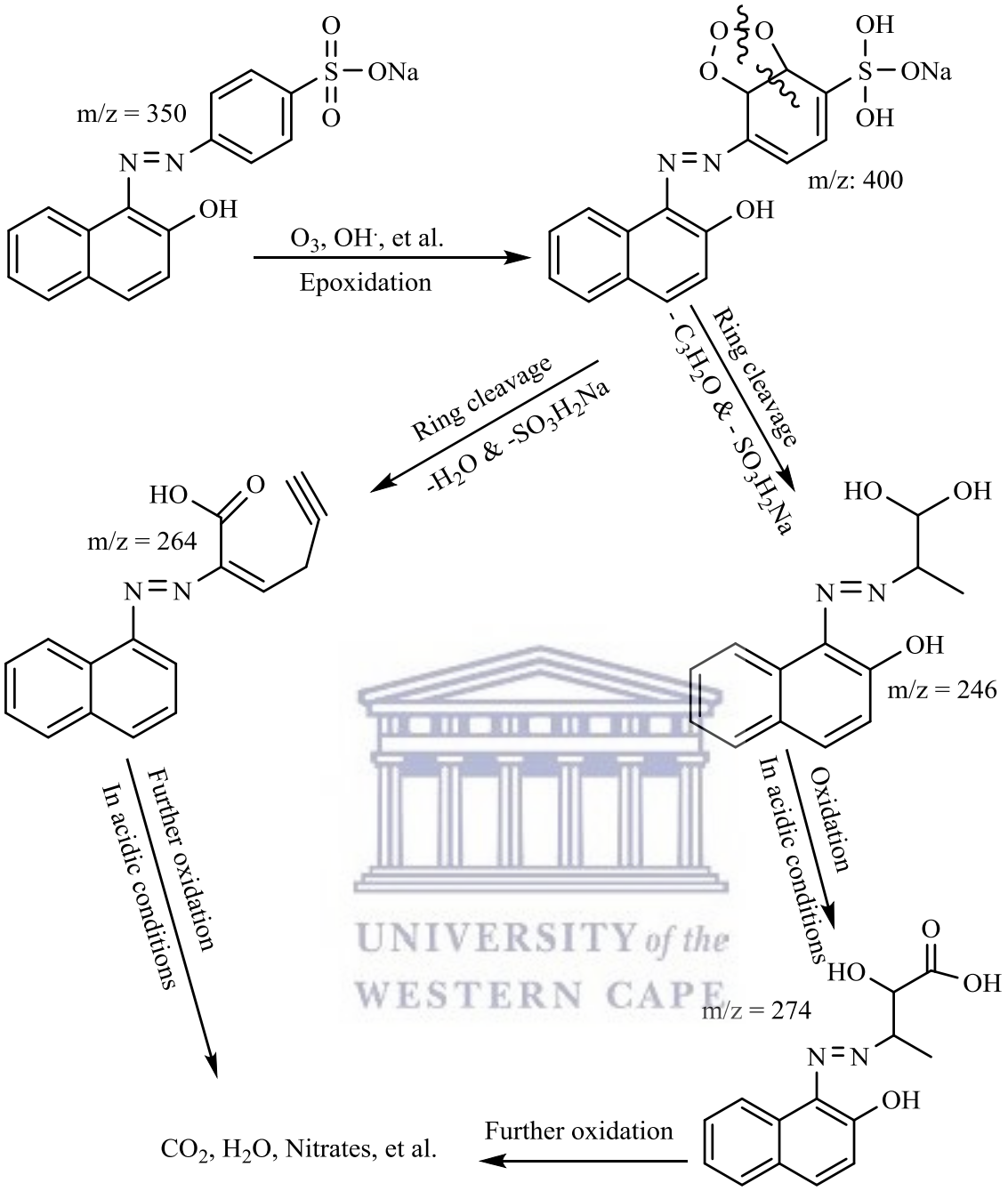

Figure 6.14: Suggested photo degradation mechanism pathways of orange II sodium dye obtained with C-N-TiO_2/SS mesh in DBD reactorat the following optimum conditions: Applied voltage 8 kV, [O.II] 60 mg/L, volume 1500 mL, solution pH 2.5, , air flow rate 3 L/min, 1.5 mm silver electrode, 50 g/L NaCl inner electrode electrolyte, air gap 2 mm, (8 cm long x 2 cm large each) x 4 uncoated and coated meshes enfolded around the outer tube of the DBD reactor and an experimental time of 60 min.

Table 6-9 presents the degradation intermediate by-products of O.II achieved with DBD/C-N-TiO_2/SS advanced oxidation system at the applied conditions. The results presented in Table

6-14 show that O.II was decomposed principally into four intermediates including $C_{16}H_{13}N_2NaO_7S$ (m/z = 300.1) and $C_{14}H_{14}N_2O_4$ (m/z = 274.3) that appeared after 2.52 and 2.71 min, while $C_{16}H_{12}N_2O_2$ (m/z = 264.3) and $C_{13}H_{14}N_2O_3$ (m/z = 246.3) eluted after 3.37 and 2.71 min. The chemical structures of the degradation intermediates presented in Table 5.9 demonstrate that the decomposition of O.II was mostly induced by epoxidation, oxidation and reduction reactions. Likewise, these chemical structures show that the azo group (-N=N-) in O.II and its degradation metabolites was still present, suggesting that the azo group is not the only parameter responsible for the intense colour of O.II dye but other chromophores such as the olefin or double bond groups in the chemical structure are also responsible for dye colour that faded when the unsaturation of the compound was destroyed by the free radicals generated in DBD/C-N-TiO_2/SS combined oxidation protocol. Alternatively, the degradation mechanistic pathway established in Figure 6.14 shows that the epoxidation of O.II derived from its interaction with O_3 and the hydroxyl radicals oxidise the sodium sulfonic group (-SO_3Na) in O.II carbon framework to sodium sulfonic acid system (-SO_3H_2Na) which resulted in the intermediate m/z = 400.1. This is in agreement with the findings of Silva et al. (2009) who studied the ozonation of azo dyes (Orange II and Acid Red 27) in saline media and pointed out that O_3 largely contributed to the decolouration even though the authors did not identify the degradation by-products of the targeted pollutants. Similar observations were also reported by Soares et al. (2006). The epoxide ring in m/z = 400.1 metabolite was disconnected by ring cleavage releasing water and -SO_3H_2Na group and yielding m/z = 264 and m/z = 274 degradation intermediates. On the one hand, the m/z = 264 by-product was further mineralised into dissolved CO_2, H_2O and inorganic salts. On the other hand, the m/z = 246 degradation intermediate was oxidised in DBD acidic environment to m/z = 274 which by further oxidation in harsh media was mineralised into CO_2, H_2O and simpler entities as suggested by Yan et al. (2008) who investigated the degradation of acid orange II using gas–liquid gliding arc discharge. Altogether, the results presented in Table 6.9 and the suggested degradation mechanistic pathways drawn in Figure 6.14 show that O_3 and OH radicals were the two most active species that contributed to the destruction of O.II by DBD/C-N-TiO_2/SS advanced oxidation process. Hence these outcomes confirm that the disappearance of O.II during treatment was complimented/ associated with the destruction of O.II chromophore groups as also sustained by Kuang et al. (2011). This consequently resulted in the complete oxidation and mineralisation of O.II dye in DBD combined with C-N-TiO_2 nano catalyst. Since the degradation intermediates of O.II achieved with DBD alone and DBD/C-N-TiO_2/SS were identified and discussed in sections 5.5.5 and 6.3.2.1, therefore, it was also important to detect

O.II decomposition intermediates obtained with DBD/C-N-TiO_2/Ti film for comparison purposes. The efficiency of the optimised DBD alone, DBD/C-N-TiO_2/SS and DBD/C-N-TiO_2/Ti systems for the degradation of orange II dye focusing on colour removal were already compared in this study as shown in Section 6.3.2.

6.3.2.2 Identification of the degradation by-products and suggestion of the degradation mechanistic pathways of O.II dye achieved with DBD/C-N-TiO_2/Ti advanced oxidation process

As introduced in Section 6.3.2.1, O.II dye was fully degraded by DBD combined with C-N-TiO_2/Ti (DBD/C-N-TiO_2/Ti) system and its degradation intermediate by-products are presented in Table 6-10 while their proposed degradation mechanism pathways are shown in Figure 6-15.

Table 6.10: LC-MS identified degradation by-products of orange II sodium salt obtained with C-N-TiO_2/Ti mesh in DBD reactor at the following conditions: peak voltage 6.8 kV, [O.II] 60 mg/L, volume 1500 mL, solution pH 2.5, air flow rate 3 L/min, 1.5 mm silver electrode, 50 g/L NaCl inner electrode electrolyte, air gap 2 mm, 4 Ti meshes (8 cm long x 2 cm large) coated with C-N-TiO_2 enfolded around the outer tube of the DBD reactor and an experimental time of 60 min.

Compound	Molecular formula	Structure	Retention time (min)	Molecular ion $[M-H]^+$
Orange II sodium Salt (I)	$C_{16}H_{11}N_2NaO_4S$	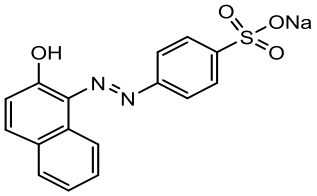	3.77	350.03
Sodium (E)-dihydroxy(7-((2-hydroxynaphthalen-1-yl)diazenyl)-3a,7a-dihydrobenzo[d][1,2,3]trioxol-4-yl)-l4-sulfanolate	$C_{16}H_{13}N_2NaO_7S$	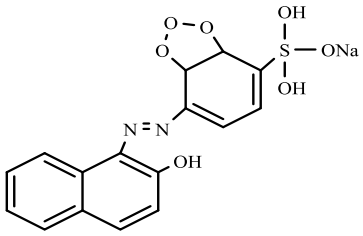	10.990	400
(E)-4,6-dihydroxy-2-((E)-(2-hydroxynaphthalen-1-yl)diazenyl)-5-(trihydroxy-l4-sulfanyl)hex-2-enoic acid	$C_{16}H_{18}N_2O_8S$	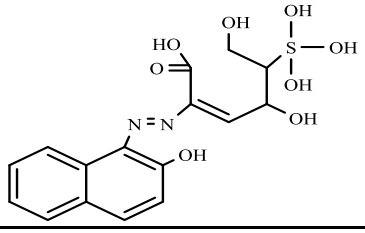	10.679	398

(E)-2-hydrosulfonyl-5-((E)-(2-hydroxynaphthalen-1-yl)diazenyl)pent-4-enal	$C_{15}H_{14}N_2O_4S$	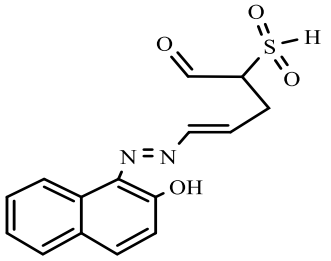	6.628	318
(2E,4E)-2-((E)-(2-hydroxynaphthalen-1-yl)diazenyl)-6-oxo-5-sulfamoylhexa-2,4-dienoic acid ion	$C_{16}H_{14}N_3O_6S^+$	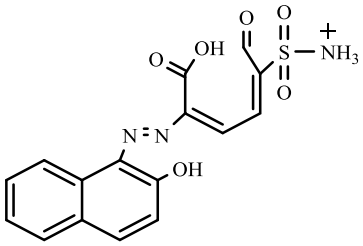	2.786	376
(2E,4E)-2-(((E)-(2-hydroxynaphthalen-1-yl)methylene)amino)-5-(nitrososulfonyl)-6-oxohexa-2,4-dienoic acid	$C_{17}H_{12}N_2O_7S$	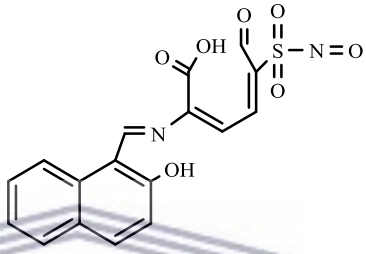	2.457	388
(2E,4Z)-2-((E)-(2-hydroxynaphthalen-1-yl)diazenyl)hexa-2,4-dienoic acid	$C_{16}H_{14}N_2O_3$	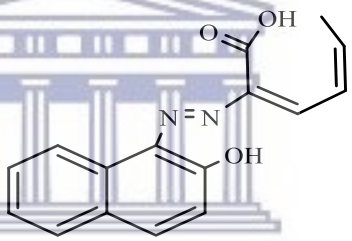	11.290	282
(E)-2-hydroxy-3-((2-hydroxynaphthalen-1-yl)diazenyl)butanoic acid	$C_{14}H_{14}N_2O_4$	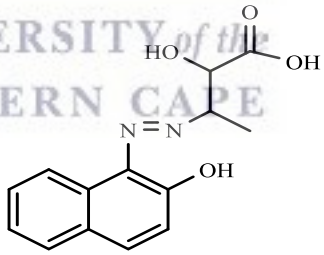	6.538	274
(E)-2-((2-hydroxynaphthalen-1-yl)diazenyl)propane-1,1-diol	$C_{13}H_{14}N_2O_3$	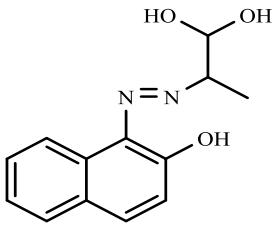	5.386	246
(E)-2-((E)-naphthalen-1-yldiazenyl)hex-2-en-5-ynoic acid	$C_{16}H_{12}N_2O_2$	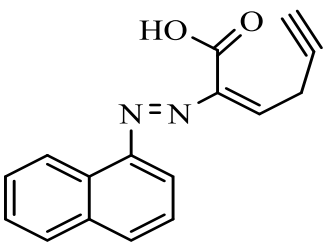	5.370	264

2-(2-hydroxyethyl)-1-(2-hydroxynaphthalen-1-yl)hydrazin-1-ium	$C_{12}H_{15}N_2O_2^+$	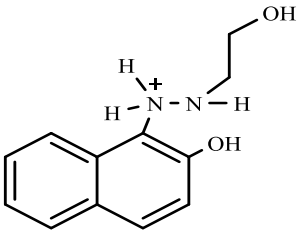	5.393	219

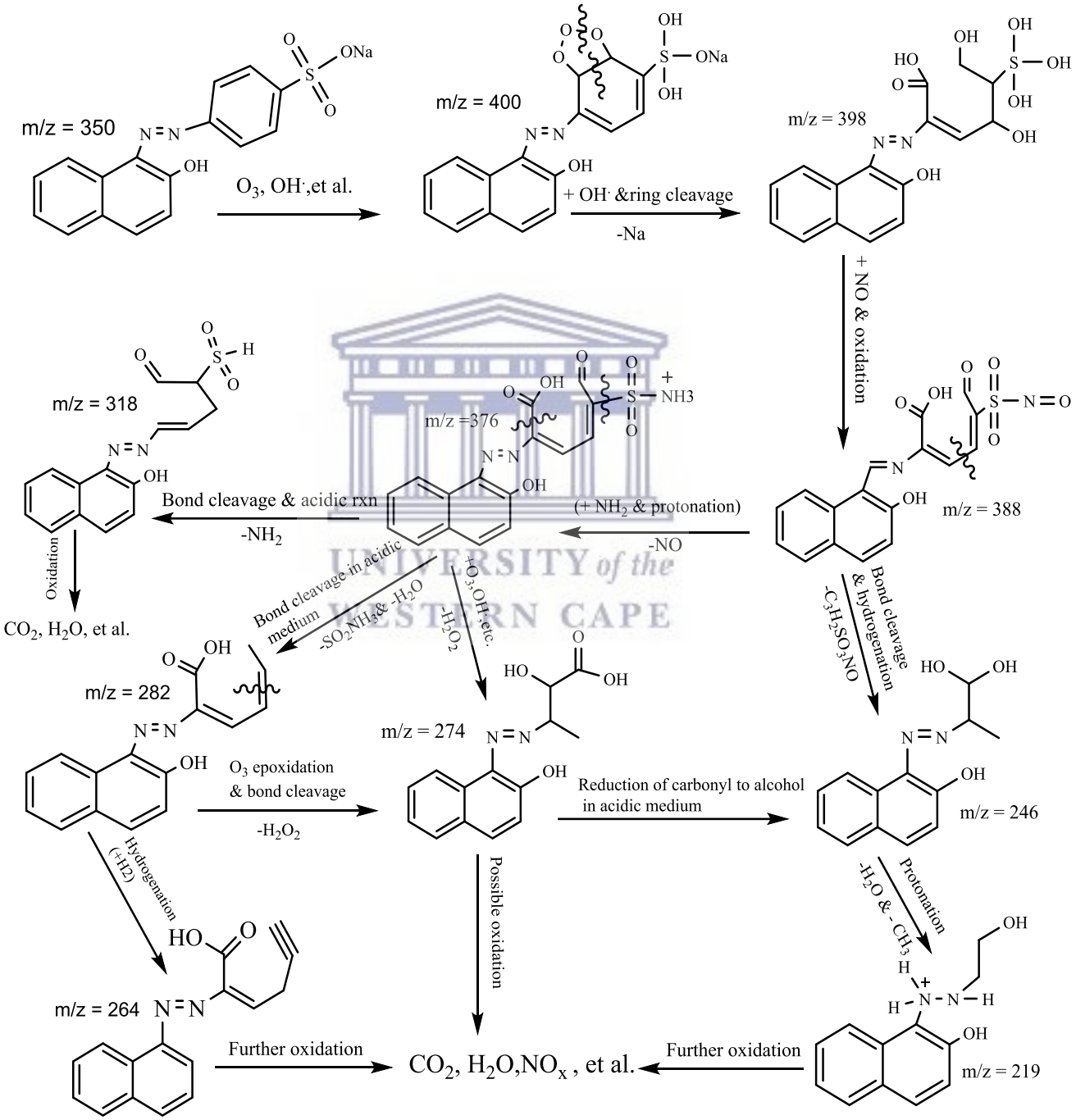

Figure 6.15: Suggested photo degradation mechanism pathways of orange II sodium dye obtained with C-N-TiO2/Ti mesh in DBD reactor at the following optimum conditions: Peak voltage 6.8 kV, [O.II] 60 mg/L, volume 1500 mL, solution pH 2.5, air flow rate 3 L/min, 1.5 mm silver electrode, 50 g/L NaCl inner electrode electrolyte, air gap 2 mm, 4 Ti meshes (8 cm long x 2 cm large) coated with C-N-TiO_2 enfolded around the outer tube of the DBD reactor and an experimental time of 60 min.

Table 6-10 presents the degradation intermediates by-products of O.II obtained with DBD/C-N-TiO_2/Ti advanced oxidation system at the applied conditions while Figure 6-15 shows the proposed decomposition mechanism pathways of these metabolites. The outcomes set out in Table 6-10 show that O.II was decomposed into various intermediates whereby the ten most abundant metabolites depicted by HPLC-MS (LC-MS) analysis include $C_{16}H_{13}N_2NaO_7S$, $C_{16}H_{18}N_2O_8S$, $C_{15}H_{14}N_2O_4S$, $C_{16}H_{14}N_3O_6S^+$, $C_{17}H_{12}N_2O_7S$, $C_{16}H_{14}N_2O_3$, $C_{14}H_{14}N_2O_4$, $C_{13}H_{14}N_2O_3$, $C_{16}H_{12}N_2O_2$ and $C_{12}H_{15}N_2O_2^+$ with corresponding molecular weights m/z of 219, 398, 318, 376, 388, 282, 274, 246, 264 and 400 that eluted at 10.990, 10.679, 6.628, 2.786, 2.457, 11.290, 6.538, 5.386, 5.370 and 5.393 min, respectively. The IUPAC names and chemical structures of these metabolites are also displayed in Table 6-10. These results are unique as the degradation of O.II by C-N-TiO_2/Ti in DBD configuration has never been reported in the literature. The few studies that have used Ti mesh as photocatalytic support for the removal of various water contaminants including O.II dye never mentioned the degradation by-products of the targeted pollutants (Liao *et al.*, 2012; Çomakli, Yetim and Çelik, 2014; Vignesh *et al.*, 2014; Çomakli *et al.*, 2016; Yetim, 2016; Zhang *et al.*, 2016). The metabolite structures in Table 6-10 show that the decomposition of O.II by DBD/C-N-TO_2/Ti system began with epoxidation evolving from the nucleophilic or electrophilic attack of O_3 on O.II framework. The ring cleavage of the generated epoxide led to the formation of several intermediates with different functional groups such as alcohols that were oxidised to aldehydes, ketones and mostly to carboxylic acids or vice versa. The chemical structure of the degradation intermediates by-products shown in Table 6.10 show that the hydroxylation of -SO_3Na group to –SO_3H_2Na was governed by ·OH radicals and led to the formation of m/z = 400 metabolite which by further attack of OH radicals and ring cleavage resulted in compound m/z = 398. This in returned was oxidised to m/z = 388 upon addition of nitrogen oxide (NO) deriving from the air that was bubbled through the DBD system. In addition, the m/z = 388 intermediate by-product experienced protonation upon reaction with amine group (-NH_2) that yielded m/z = 376 (amide/amine) that was converted to m/z = 318 by bond cleavage in DBD acidic milieu

and further mineralised to CO, H_2O and simpler inorganics (Feng *et al.*, 2003). Alternatively, following the bond cleavage scenario, the intermediate m/z = 376 could also be transformed to m/z = 282 whose hydrogenation resulted in m/z = 264 that was further oxidised to dissolved CO_2, H_2O, NOx, etc. Or it was also possible that the compound m/z = 376 could be attacked by O_3 and ·OH yielding m/z = 274 that was further mineralised to CO_2, H_2O and other harmless species. Then again, the bond cleavage and hydrogenation of m/z = 388 yielded m/z = 242 whose protonation led to m/z = 219 was oxidised and mineralised into dissolved CO_2, H_2O and various inoffensive inorganic bodies as described in Figure 6-15. These results showed that the removal of O.II by DBD/C-N-TiO_2/Ti system resulted in 10 degradation by-products whose mineralisation to CO_2, H_2O and other inorganics might have taken long (60 min). In other words, the presence of these multiple intermediates by-products might have slowed the conversion of O.II into H_2O, CO_2 and other dissolved species (Hastie *et al.*, 2006), compared to the degradation of O.II by DBD/C-N-TiO_2/SS that yielded four degradation metabolites and exhibited effective and quick conversion of O.II into CO_2, H_2O and extended aqueous entities (within 10 min). This is in conformity with results obtained in Figure 6-13 of section 6.3.2. Hence the abundance of by-products during water treatment process may impede the complete mineralisation of the targeted pollutant. In total, the incorporation of C-N-TiO_2/SS film in the optimised DBD system improved the degradation of O.II dye by 3 %, compared to the DBD system alone. However, the insertion of C-N-TiO_2/Ti film in the DBD system decelerated O.II degradation % by 26 %. This was probably due to the uneven UV light penetration on the C-N-TiO_2/Ti film or to the low surface area to volume ratio and further to an increase of mass transfer limitations as earlier discussed in section 2.5.1 of chapter 2.

6.3.3 Degradation of sulfamethoxazole by C-N-TiO_2/SS and C-N-TiO_2/Ti films suspended in the optimised DBD plasma configuration

Following the same procedure performed for the removal of O.II, the second selected model pharmaceutical drug SMX was also subjected to the optimised DBD system alone and to combined DBD with either C-N-TiO_2/SS or C-N-TiO_2/Ti composites. The outcomes of these experiments are presented in Figure 6-16.

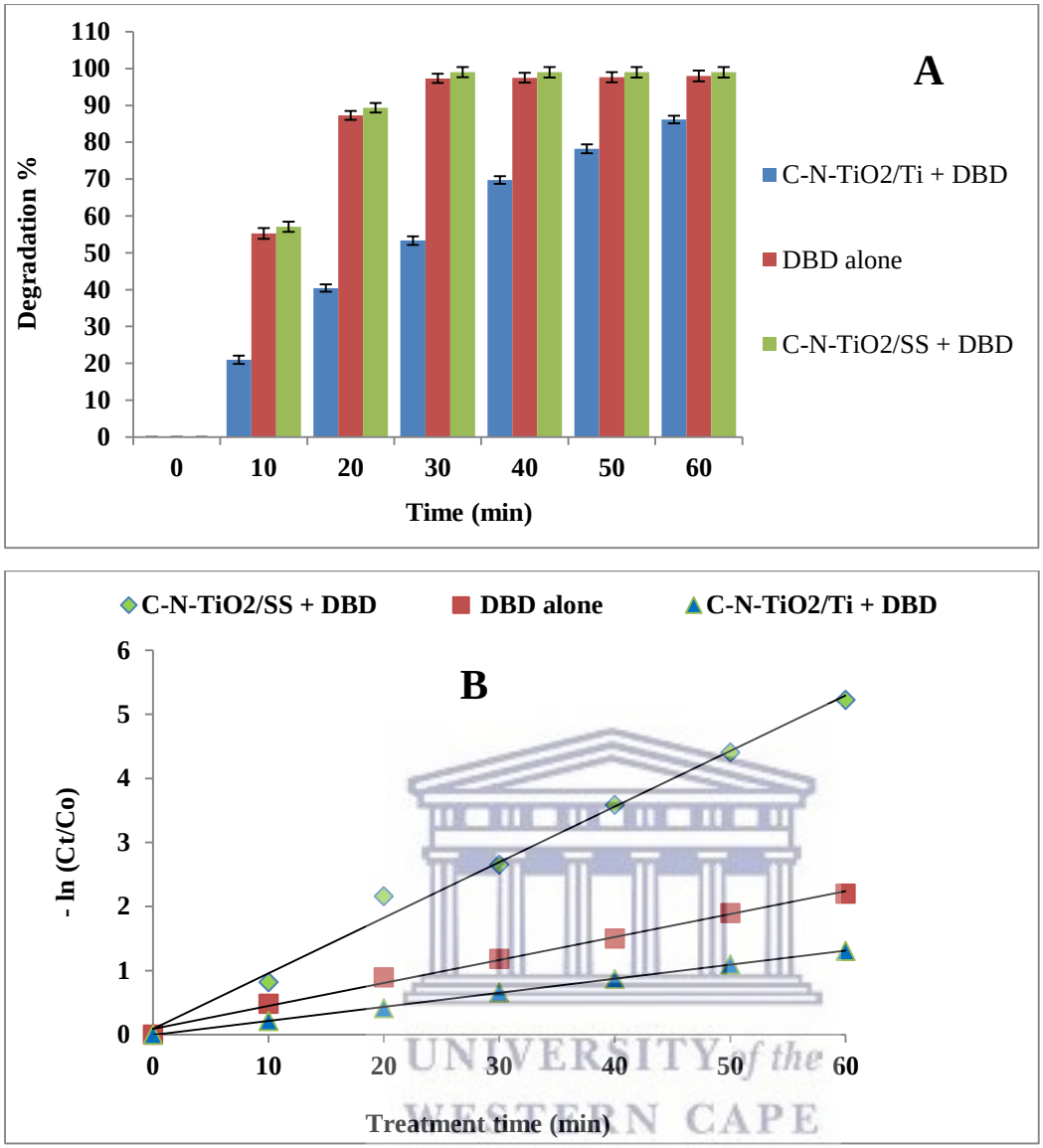

Figure 6.16: Degradation efficiency (A) and rate (B) of SMX by DBD C-N-TiO_2/SS an DBD C-N-TiO_2/Ti mesh compared to DBD alone at optimum conditions: Applied voltage 8 kV, SMX concentration 40 mg/L, solution volume 1500 mL, solution pH 6.5, air flow rate 3 L/min, 1.5 mm silver electrode, 50 g/L NaCl inner electrode electrolyte, air gap 2 mm, 4 coated meshes (8 cm long x 2 cm large) enfolded around the outer tube of the DBD reactor and an experimental time of 60 min.

Figure 6-16 presents the degradation of SMX drug by DBD alone compared with DBD combined with either C-N-TiO_2/SS or C-N-TiO_2/Ti films at the applied conditions. The results exhibited in Figure 6-15 (A) show that though 97% of SMX removal was attained after 30, 40 and 50 minutes of reaction time, full degradation of SMX was almost achieved after 60 min of reaction time with DBD alone at the applied conditions. On the other hand, complete removal

of SMX was achieved with DBD + C-N-TiO_2/SS after 30 min of DBD run at the applied conditions. The highest removal of SMX was achieved with DBD + C-N-TiO_2/SS followed by DBD alone then by DBD + C-N-TiO_2/Ti system. For instance after 10 min of treatment, 57.04% or 55.25 % of SMX removal was attained with DBD + C-N-TiO_2/SS or DBD alone compared to 20.95% obtained with DBD + C-N-TiO_2/Ti. This trend was also observed at each sampling time during treatment. The slight superiority of DBD + C-N-TiO_2/SS over DBD alone which were higher than DBD + C-N-TiO_2/Ti combination could be ascribed to the incorporation of C-N-TiO_2 nano photocatalyst coated on SS support in the DBD aqueous medium that probably accelerated the production of ·OH by both oxidation and reduction processes occurring on the valence and conducting bands of Ti semiconductor as reported by Hikmet Sayılkan et al. (2007); Xekoukoulotakis et al. (2011) and Qi Zhu et al. (2018). Moreover, the incorporation of C and N into TiO_2 lattice might have improved the electron hole recombination that further reduced the band gap and hence enhanced the free and rapid promotion of energised electrons on the conducting band (Abellan, et al. 2007). These later boosted the generation of superoxide anions whose interactions with water molecules and other species generated more OH radicals that selectively destroyed SMX carbon framework. Alternatively, the complete degradation of SMX reached within 60 min with DBD alone implied that SMX was recalcitrant in the optimised DBD reactor compared to O.II dye whose total decomposition was achieved within 20 minutes of reaction time. Nevertheless, the full removal of SMX achieved with DBD + C-N-TiO_2/SS and DBD alone led to superior degradation rates of 8.83 $x10^{-2}$ min^{-1} and 5.7 $x10^{-2}$ min^{-1}, respectively that were both higher than 2.18 x $10^{-2}min^{-1}$ observed with DBD + C-N-TiO_2/Ti system as shown in Figures 6.16 (B). Comparable results were also obtained by Ying Chen et al. (2015) who studied the degradation of 17β-estradiol (E2) by dielectric barrier discharge non-thermal plasma combined with Pt–TiO_2 powder. The result of their studies showed that successful removal of E2 was achieved under acidic conditions at a pH of 5.6. The removal efficiency was 72.0% with DBD alone and 98.9% using DBD combined with TiO_2 respectively. The results obtained by Chen and co-workers showed that the UV light formed in DBD experiment was used to strengthen the decomposition of E2 at ambient conditions and are in agreement with the outcomes obtained with DBD combined with C-N-TiO_2/SS mesh in this study. This hence sustains that the results obtained in the current study are more attractive compared to literature as the immobilisation of the C-N-TiO_2 on SS may be useful to overcome the cost involved in the post separation of the powder catalyst. By comparison with literature, the degradation of SMX by the DBD has never been investigated in the literature. Hence, the current work is unique and the results

achieved in this study showed that DBD offers a promising advanced oxidation technology that can be employed in the decontamination of water and wastewater. Furthermore, to overcome the limitation encountered with C-N-TiO_2/Ti film, it would be advisable to either carefully choose a suitable coating procedure or to use a more suitable support as catalytic support on which the C-N-TiO_2 can be immobilised. Even though SMX was colourless in solution, its total degradation achieved with DBD/C-N-TiO_2/SS and DBD alone suggested that SMX was decomposed to new chemical entities that had to be identified.

6.3.3.1 HPLC identified degradation intermediates by-products of SMX degraded by combined DBD/C-N-TiO_2/SS advanced oxidation system

The experimental results discussed in section 6.3.3 showed that SMX was well decomposed by DBD system combined with C-N-TiO_2/SS but not with C-N-TiO_2/Ti films. The degradation intermediates of SMX broken down by DBD/C-N-TiO_2/SS system were also identified by LC-MS at the indicated conditions. The detected molecular structures are shown in Table 6-11 and their anticipated disintegration pathways are presented in Figure 6-17.

Table 6.11: LC-MS identified degradation by-products of sulfamethoxazole drug by C-N-TiO2/SS in DBD system at the following conditions: Applied voltage 8 kV, SMX concentration 40 mg/L, solution volume 1500 mL, solution pH 2.5, air flow rate 3 L/min, 1.5 mm silver electrode, 50 g/L NaCl inner electrode electrolyte, air gap 2 mm, 4 coated meshes (8 cm long x 2 cm large) enfolded around the outer tube of the DCDBD reactor and an experimental time of 60 min.

Compound	Molecular formula	Structure	Retention time (min)	Molecular ion $[M-H]^+$
4-amino-N-(5-methylisoxazol-3-yl)benzenesulfonamide (I): Sulfamethoxazole	$C_{10}H_{12}N_3O_3S^+$	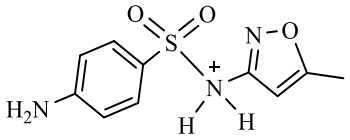	3.72	254.3
N-(6-(4-aminophenyl)-1,2,3,4,5,6l4-pentaoxathian-6-yl)-5-methyl-4-oxo-4,5-dihydroisoxazol-3-aminium (II)	$C_{10}H_{12}N_3O_7S^+$	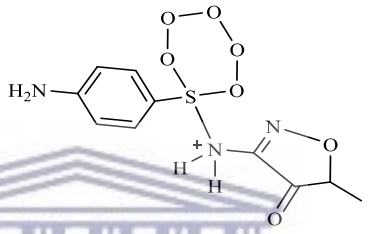	6.59	318.3
((5-hydroxy-5-methyl-2,5-dihydroisoxazol-3-yl)amino)(4-hydroxyphenyl)-l4-sulfanediol (III)	$C_{10}H_{14}N_2O_5S$	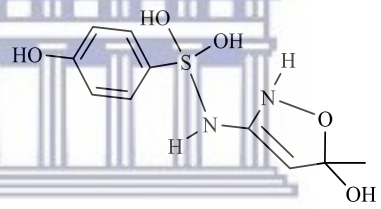	6.53	274.3
1-(5-amino-5-((6-(4-hydrazinylphenyl)-1,2,3,4,5,6l4-pentaoxathian-6-yl)(hydroxy)amino)-1,2,3-trioxolan-4-yl)ethane-1,1-diol (IV)	$C_{10}H_{16}N_4O_{11}S$	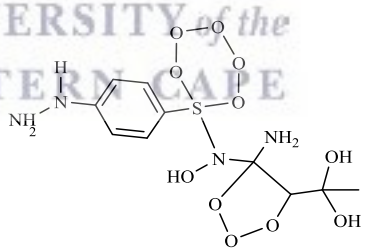	10.98	400.3
4-amino-4-((6-(4-hydrazinylphenyl)-1,2,3,4,5,6l4-pentaoxathian-6-yl)(hydroxy)amino)butan-2-ol (V)	$C_{10}H_{18}N_4O_7S$	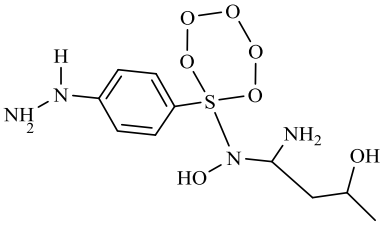	13.12	338.3

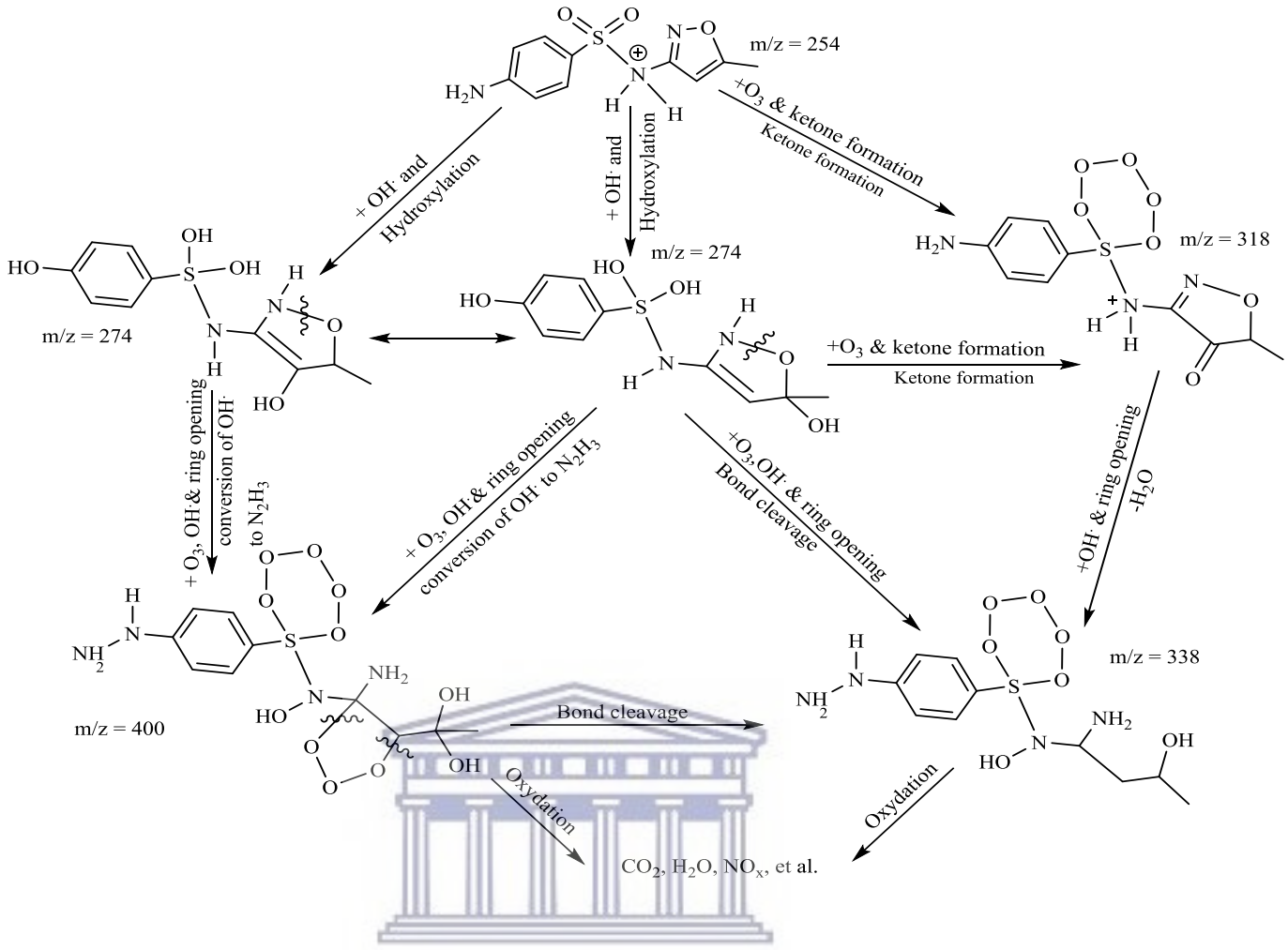

Figure 6.17: Suggested degradation mechanism pathways of SMX decomposed by C-N-TiO2/SS in DBD system at optimum conditions: Applied voltage 8 kV, SMX concentration 40 mg/L, solution volume 1500 mL, solution pH 2.5, air flow rate 3 L/min, 1.5 mm silver electrode, 50 g/L NaCl inner electrode electrolyte, air gap 2 mm, 4 coated meshes (8 cm long x 2 cm large) enfolded around the outer tube of the DBD reactor and an experimental time of 60 min.

Table 6-11 presents the degradation intermediates resulting from the decomposition of SMX drug by combined DBD/C-N-TiO_2/SS advanced oxidation system at the applied conditions while Figure 6-17 provides the suggested degradation pathways of these secondary metabolites identified by LC-MS analysis. The decomposition of SMX drug ($C_{10}H_{12}N_3O_3S^+$, m/z = 254.3) at the applied conditions resulted in four major intermediates, including $C_{10}H_{12}N_3O_7S^+$, $C_{10}H_{14}N_2O_5S$, $C_{10}H_{16}N_4O_{11}S$ and $C_{10}H_{18}N_4O_7S$ with corresponding molecular mass of m/z = 318.3, 274.3, 400.3 and 338.3 that eluted after 6.59, 6.53, 10.98 and 13.12 minutes, respectively**.** As stated earlier, this study reports for the first time the degradation of SMX by

combined DBD with SS supported C-N-TiO_2 nano catalyst, therefore literature presents no information complimenting these findings even though the oxidation of SMX by various photocatalytic systems has been conducted and different intermediate by-products have been identified (Beltrán *et al.*, 2008; Wang, Li and Estrada, 2011; Ghauch, Ayoub and Naim, 2013). The chemical structures of SMX and its degradation metabolites recorded in Table 6-11 show that the mineralisation of SMX was mostly initiated by epoxidation induced by the nucleophilic and electrophilic attacks of O_3 on the sulphonic group in SMX carbon framework. This was reinforced by ring opening, dehydration and substitution reactions as described in Figure 6-17. The decomposition mechanisms suggested in Figure 6-17 show that mineralisation of SMX ($C_{10}H_{12}N_3O_3S^+$, m/z = 254) followed different reaction routes than those highlighted in literature (Abellán *et al.*, 2007; Alam G Trovó *et al.*, 2009; Liu and Wang, 2013). The first pathway involved the hydroxylation of SMX to the metabolite m/z = 274 which by reaction with O_3 and the substitution of ·OH by ($-N_2H_3$) group led to the formation of the intermediate compound m/z = 400 that was further oxidised to CO_2, H_2O and other dissolved species. This slightly contradicts Wang et al. (2011) who showed that the degradation of SMX can primarily be initiated by OH radicals and supplemented by other species. This consequently may depend on the oxidation system used for the decontamination of SMX. The second pathway suggests that the m/z = 274 metabolite could be attacked by O_3, or ·OH, followed by ring opening and substitution of OH radicals by N_2H_3 resulting in to the formation of m/z = 400 that was directly mineralised as described above. Various mineralisation pathways of SMX leading to CO_2, H_2O and simpler inorganics in numerous photocatalytic systems have been proposed (Dirany et al. 2010; Wang et al. 2011; Kim et al. 2015). Or the m/z = 274 metabolite could have interacted with O_3 or OH· accompanied by ring opening to yield m/z = 338 that was directly converted to CO_2, H_2O and inorganic salts. Finally, the reaction of O_3 with SMX in acidic DBD conditions resulted in m/z = 318 whose interaction with ·OH followed by ring opening and dehydration led to m/z = 338 that was further mineralised to CO_2, H_2O and dissolved inorganics. Yet even if SMX was claimed to be fully mineralised in the DBD reactor within 30 minutes, it should be noted that the intermediate by-products of contaminants such as SMX often remain in the treated solution and exhibit refractory behaviour and hence may require prolonged time for complete conversion (Dirany *et al.*, 2010; Guo *et al.*, 2015). These results further showed that DBD/C-N-TiO_2/SS is an effective combined advanced oxidation process that can be used for the destruction of pharmaceutical contaminants and other related pollutants from water and wastewater. However, the performance of this advanced combination should be compared with

DBDC-N-TiO_2/Ti in order to assess the behaviour of the pollutant in DBD technology combined with different composites.

6.3.3.2 HPLC identified degradation intermediate by-products of SMX degraded by DBD + C-N-TiO_2/Ti in DBD at optimum conditions

Besides C-N-TiO_2/SS, the removal of SMX with DBD/C-N-TiO_2/Ti combined advanced oxidation system was also promising from the results obtained in Section 5.3.3. The decomposition metabolites of SMX after the DBD/C-N-TiO_2/Ti experiment were determined by LC-MS and the molecular and structural conformers of the detected by-products are shown in Table 6-12 and their suggested decay mechanisms are presented in Figure 6-18.

Table 6.12: LC-MS identified degradation by-products of sulfamethoxazole drug achieved with DBD/C-N-TiO2/Ti advanced systemat the following conditions: Applied voltage 8 kV, SMX concentration 40 mg/L, solution volume 1500 mL, solution pH 2.5, air flow rate 3 L/min, 1.5 mm silver electrode, 50 g/L NaCl inner electrode electrolyte, air gap 2 mm, 4 coated meshes (8 cm long x 2 cm large) enfolded around the outer tube of the DBD reactor and an experimental time of 60 min.

Compound	Molecular formula	Structure	Retention time (min)	Molecular ion $[M-H]^+$
4-amino-N-(5-methylisoxazol-3-yl)benzenesulfonamide (I): Sulfamethoxazole	$C_{10}H_{12}N_3O_3S^+$	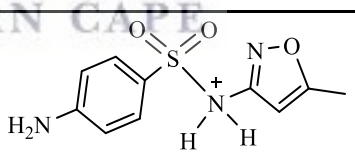	3.73	254.3
((5-hydroxy-5-methyl-2,5-dihydroisoxazol-3-yl)amino)(4-hydroxyphenyl)-l4-sulfanediol (II)	$C_{10}H_{14}N_2O_5S$	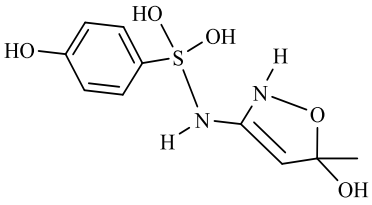	6.54	274.3
1-(5-amino-5-((6-(4-hydrazinylphenyl)-1,2,3,4,5,6l4-pentaoxathian-6-yl)(hydroxy)amino)-1,2,3-trioxolan-4-yl)ethane-1,1-diol (III)	$C_{10}H_{16}N_4O_{11}S$	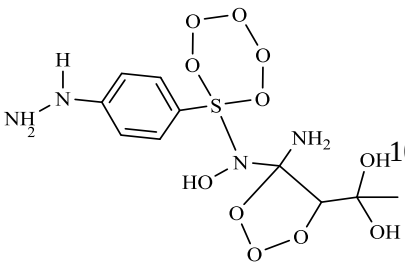	10.99	400.3

N-(6-(4-hydrazinylphenyl)-1,2,3,4,5,6l4-pentaoxathian-6-yl)-N-(hydroxymethyl)hydroxylammonium (IV)	$C_7H_{12}N_3O_7S^+$	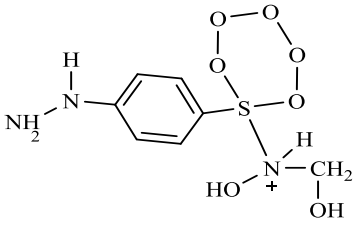	11.33	282.2
1-(5-amino-5-((6-(4-diazenylphenyl)-1,2,3,4,5,6l4-pentaoxathian-6-yl)(hydroxy)amino)-1,2,3-trioxolan-4-yl)ethane-1,1-diol (V)	$C_{10}H_{14}N_4O_{11}S$	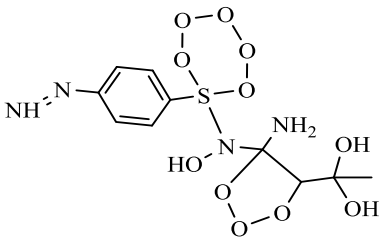	10.69	398.3
N-((4-(hydroxyamino)phenyl)(pentaoxidanyl)-l4-sulfanyl)hydroxylammonium (VI)	$C_6H_{11}N_2O_7S^+$	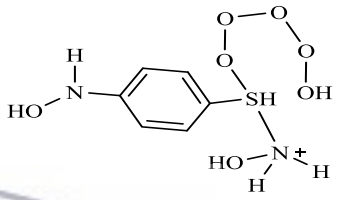	8.48	255.2
1-(5-(((4-hydrazinylphenyl)(hydroxy)-l4-sulfanyl)(hydroxy)amino)-1,2,3-trioxolan-4-yl)ethane-1,1-diol (VII)	$C_{10}H_{17}N_3O_7S$	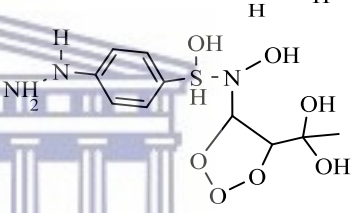	7.76	323.3
1-(6-(4-hydrazinylphenyl)-1,2,3,4,5,6l4-pentaoxathian-6-yl)-1-hydroxyurea (VIII)	$C_7H_{10}N_4O_7S$	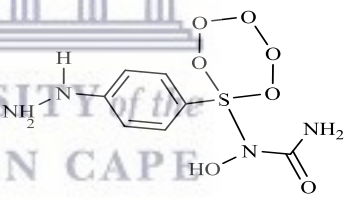	6.34	294.2

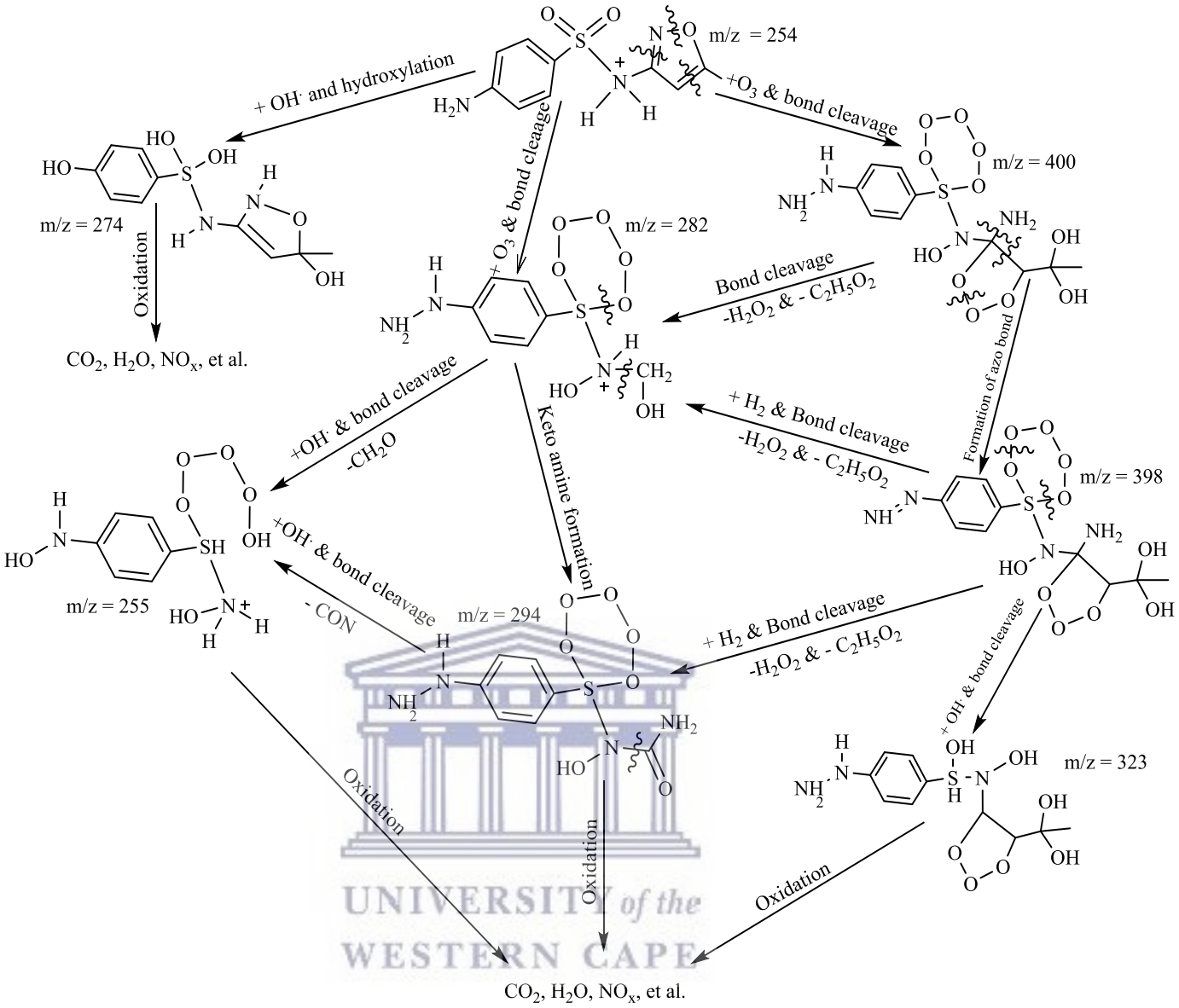

Figure 6.18: Suggested degradation mechanism pathways of SMX decomposed by C-N-TiO2/Ti mesh in DBD system at optimum conditions: Applied voltage 8 kV, SMX concentration 40 mg/L, solution volume 1500 mL, solution pH 2.5, air flow rate 3 L/min, 1.5 mm silver electrode, 50 g/L NaCl inner electrode electrolyte, air gap 2 mm, (8 cm long x 2 cm large) x 4 coated meshes enfolded around the outer tube of the DCDBD reactor and an experimental time of 60 min.

Table 6-12 and Figure 6-18 present the intermediate by-products of SMX achieved with the combined DBD/C-N-TiO_2/Ti advanced oxidation system at the applied conditions and their suggested decomposition pathways, respectively. The outcomes displayed in Table 6-12 show that SMX ($C_{10}H_{12}N_3O_3S^+$, m/z = 254.3) was decomposed into seven degradation metabolites $C_7H_{10}N_4O_7S$, $C_{10}H_{16}N_4O_{11}S$, $C_7H_{12}N_3O_7S^+$, $C_{10}H_{14}N_4O_{11}S$, $C_6H_{11}N_2O_7S^+$, $C_{10}H_{17}N_3O_7S$ and

$C_{10}H_{14}N_2O_5S$ with corresponding molecular weights of 294.2, 400.3, 282.2, 398.3, 255.2, 323.3, 274.3 that eluted after 6.54,10.99, 11.33, 10.69, 8.48, 7.76 and 6.34 min. These photocatalytic transformation products of SMX obtained with DCDBD combined with C-N-TiO_2/Ti mesh have not been outlined in the literature. The respective IUPAC names of these metabolites are also presented in Table 6-12. The degradation pathways exhibited in Figure 6.-18 show that the decay of SMX followed four different pathways. First, the hydroxylation of SMX resulted in m/z = 274 metabolite that was directly mineralised into dissolved CO_2, H_2O and simpler inorganics (Lam and Mabury, 2005; Alam G Trovó *et al.*, 2009). Secondly, the reaction of O_3 with SMX followed by bond cleavage resulted in the formation of m/z = 282 epoxide which on the one hand interacted with OH radicals followed by bond cleavage yielding m/z = 255 that was further transformed to CO_2, H_2O and simpler inorganics. On the other hand, bond cleavage of the m/z = 282 intermediate led to the formation of m/z = 294 keto amine that was directly mineralised into H_2O, dissolved CO_2 and related metabolites. The fourth pathway involved the reaction of SMX with the OH radical and bond cleavage that resulted in m/z = 400 which by substitution and rearrangement resulted in m/z = 398 intermediate. This later reacted with $OH^{\cdot}$ followed by bond cleavage and resulted in m/z = 323 that was further mineralised to CO_2, H_2O, NOx and other harmless end-products. In comparison with DBD/C-N-TiO_2/SS, the removal of SMX with DBD/C-N-TiO_2/Ti led to seven intermediate by-products whose slow oxidation probably denoted the recalcitrant behaviour of the transformation by-products that obstructed the total mineralisation of SMX by DBD/C-N-TiO_2/Ti system (Dirany *et al.*, 2010; Guo *et al.*, 2015). This could be justified by the low degradation efficiencies and slow removal rates of SMX achieved within 60 min with DBD/C-N-TiO_2/Ti in Figure 6-18 (Section 6.3.3). In contrast complete removal of SMX with DBD/C-N-TiO_2/SS at a higher degradation rate $8.83x10^{-2}$ min^{-1} was reached within 30 min and only four degradation intermediate metabolites were detected that were quickly mineralised. These results also confirm the trends observed during degradation of O.II by DBD/C-N-TiO_2/SS or DBD/C-N-TiO_2 (Section 6.3.2). The lower efficiency of the Ti supported catalyst could be attributed to the morphological defects of C-N-TiO_2/Ti film that occurred after dip coating of C-N-TiO_2 nano catalyst on pure Ti mesh substrate. Hence an elevated number of by-products in the effluent being treated by advanced oxidation processes can slow down complete mineralisation of the targeted pollutants. Therefore, the immobilisation technique of the catalyst on the substrate and the choice of the catalytic support are important aspects in synthesis processes that should be optimised with care to achieve photocatalytic films with the desired properties.

6.4 Summary of chapter 6

In this chapter, C-N-TiO_2 nano composite photo catalyst was prepared by a sol-gel/pyrolysis process. The doped C-N-TiO_2 was pyrolysed at 350 ^oC for 105, 120 or 135 minutes holding time. This study demonstrated that pyrolysis holding time had an effect on the band gap, shape, and particle size and photocatalytic activity of the synthesised nano catalysts. Likewise, the non-metals, carbon (C) and nitrogen (N), were well incorporated into the TiO_2 matrix using the temperature profile given above. When increasing calcination time beyond 120 minutes, the dopants C and N likely vaporised and their benefit was lost because photocatalytic activity declined. This was proved by the unusual smell during the pyrolysis process evidenced by the formation of gas such as CO, CN, etc. further highlighted by FT-IR, EDS and EELS results. Next, the C-N-TiO_2 band gap 2.67 eV calculated after 105 min calcination increased to 3.10 and 3.17 eV when pyrolysis time was increased to 120 and 135 min, respectively. On the other hand, the particle size range (5 – 6) nm obtained with C-N-TiO_2 calcined for 105 minutes increased to (6-7) nm and (7-8) nm with an increase of the pyrolysis time to 120 and 135 min, respectively. This might affect the surface area of the prepared nano materials. The sol-gel prepared C-N-TiO_2 nano photo catalysts at different holding times was mostly in its anatase phase as shown by the XRD results in Figure 6.1. likewise, the C-N-TiO_2 nano catalyst pyrolysed for 105 min showed superior photocatalytic activity when UV irradiation was applied, C-N-TiO_2 pyrolysed for 105 min showed a high degradation percentage of orange II dye (73.96 %) followed by 120 min C-N-TiO_2 (69.9%) and 135 min C-N-TiO_2 (42.4 %), respectively. The degradation of O.II in these cases followed a first order reaction whose kinetics plots exhibited linear trends with slopes corresponding to their rate constants. Furthermore, the degradation percentage of O.II increased with an increase of the catalyst dosage as 18.8, 53.2 or 91.6% O.II removals were respectively reached with 0.02, 0.08 or 0.14 g of C-N-TiO_2 pyrolysed for 105 minutes. These results showed that during sol-gel synthesis of catalysts, the pyrolysis holding time has an impact on the catalyst physical properties which further may improve its electronic and chemical properties. In this case, the powder C-N-TiO_2 nano catalyst was found effective for the removal of organic pollutants such as O.II dye. However, for industrial purposes it was believed that post separation of the catalyst from the treated effluent could be challenging, time consuming and costly. Therefore, supporting the catalyst on SS or pure Ti mesh could be an alternative to present C-N-TiO_2 nano catalyst in combination with the DBD system, hence forming a dual advanced oxidation process that can utilise the UV enerated by the DBD system. In that regard, the optimised DBD reactor in

chapter 4 was proven effective for the degradation of the targeted pollutant. The incorporation of the photo catalyst immobilised on the two different supports provides a route to combined advanced treatment technologies. However, the choice of the support is crucial due to the adherence of the catalyst there on. In this study, C-N-TiO_2 was successfully deposited on both SS (C-N-TiO_2/SS) and pure Ti mesh (C-N-TiO_2/T) by a sol-gel dip coating process. SEM analysis showed that C-N-TiO_2/SS and C-N-TiO_2/Ti films had different morphologies. That is, the porous C-N-TiO_2 was well dispersed on SS grids in fine needle like morphologies while C-N-TiO_2 nano crystals formed as fine particles on pure Ti mesh. These morphological differences resulted in different photo catalytic performances of the two films in the degradation of O.II dye at the same experimental conditions. For instance, complete removal of O.II was achieved within 10 min with the combined DBD/C-N-TiO_2/SS system at the applied conditions resulting in four degradation intermediate by-products that were quickly mineralised into H_2O, CO_2 and innocuous inorganics. Conversely, the total degradation of O.II with the DBD/C-N-TiO_2/Ti system was only attained within 60 min and resulted in the formation of 10 degradation intermediate metabolites whose slow oxidation decelerated O.II mineralisation to simpler entities. Similar trends were observed during the degradation of the second targeted pollutant sulfamethoxazole (SMX) drug whereby its total decomposition by the DBD/C-N-TiO_2/SS system was reached within 30 min. the mechanism of decomposition included 4 degradation metabolites that were rapidly oxidised to harmless inorganic by-products. However, the % removal (89.64%) of SMX that was achieved with DBD/C-N-TiO_2/Ti at the applied conditions within 60 min resulted in seven degradation intermediates that required prolonged reaction time to be fully mineralised into H_2O, CO_2 and other inorganic species. Overall, the sol-gel method is still a good practical coating method that can be used to immobilise the photo catalyst on a suitable support such as SS mesh. Yet during film preparation by the sol-gel method, the choice of catalytic support is a critical step that should be carefully considered, because any defect encountered in the film during the coating process might result in unexpected morphologies which in turn can impact upon the photo catalytic performance of the supported catalyst. However, SS likely corrodes when suspended in DBD configuration due to the oxidative attack initiated by the free radicals generated in the bulk solution whereas the Ti support would not corrode, under the DBD conditions. In the future, the Ti support could find applications. But in this study, it was believed that corrosion could be overcome by coating SS mesh with anticorrosion protective layers before immobilisation of the photocatalyst as SS mesh is much cheaper than Ti mesh. Coating SS for corrosion protection is thus the topic of the next chapter.

CHAPTER 7: CORROSION STUDY

7 INTRODUCTION

Chapter 6 focuse on the degradation of selected organic pollutants in simulated water using advanced oxidation processes induced by dielectric barrier discharge (DBD) system. It was found that high removal of model pollutants (dyes and pharmaceuticals) was achieved with DBD alone as well as when the DBD system was combined with photo catalysts immobilised on stainless steel mesh. However, after a long reaction time in the DBD photocatalytic experiment it was observed that stainless steel corroded in the DBD acidic oxidative environment Tijani *et al.*, (2017). Therefore, to overcome corrosion, it was believed that stainless steel mesh could be coated with corrosion resistant layers so that the desired degradation of contaminants in the DBD reactor could be achieved without any corrosion of the catalyst supports. Hence this section deals with the improvement of corrosion resistance of the 304 stainless steel (SS) meshes by Ti and Cr-based nitrides and oxynitrides coatings. Ti and Cr nitride and oxynitride coatings were prepared by cathodic arc evaporation (CAE) technique. The electrochemical behaviour of the as prepared films was investigated by potentiodynamic polarisation at selected parameters. Some key parameters such as thickness and roughness of coatings before and after corrosion were assessed by surface profilometry, while the surface morphology and grain size of the specimens were determined by SEM and XRD analysis. The results of these characterisations and corrosion measurement are presented in Sections 7.1 and 7.2.

7.1 Enhancement of the corrosion resistance of 304 stainless steel by Cr-N and Cr (N, O) coatings

In this subsection, 304 SS was coated with chromium nitride (Cr-N) and chromium oxinitride (Cr (N,O)) anticorrosion protective layers by CAE. The experimental protocols of this subsection are presented in Section 3.6.7 of Chapter 3. The surface morphology and structure of coatings before and after corrosion were determined by SEM and XRD analysis, respectively and the results of corrosion behaviour of Cr-N and Cr (N, O) coatings are discussed below.

7.1.1 Surface morphology and elemental composition of the coatings before corrosion measurements

The scanning electron microscopy (SEM) analysis was used to investigate the morholoical appearance of the coatings and their elemental composition before the corrosion study. The representative SEM micrographs of Cr-N and Cr (N,O) coatings are presented in Figure 7-1.

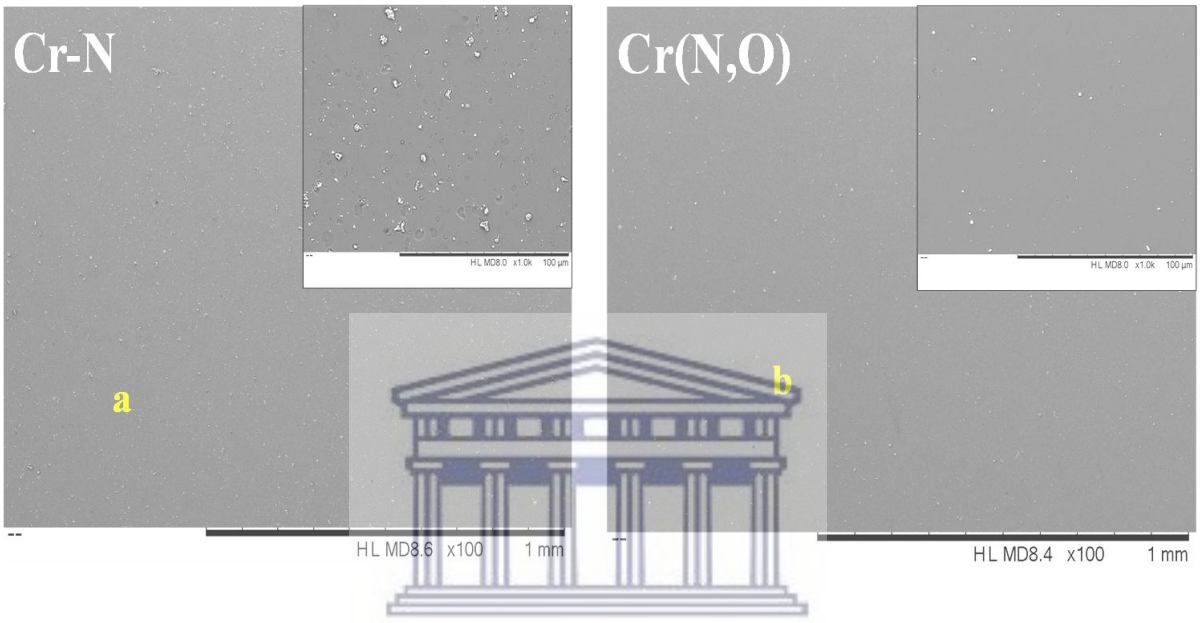

Figure 7.1: SEM micrographs of the investigated monolayers before the corrosion tests: (a) Cr-N; (b) Cr (N, O).

Figure 7-1 presents the SEM micrographs of Cr-N and Cr (N,O) anticorrosion films. As expected in CAE deposition, microdroplets can be noticed over the surface of all the investigated specimens, which was more evident in Cr-N coating, while Cr (N, O) coating presents a smoother surface, as seen on the magnified images. The observed differences in roughness may be explained by the difference between the T_m of Cr and its compounds: T_m^{Cr2N}(1923 K) < T_m^{CrN}(2043 K) < T_m^{Cr} (2143 K) < T_m^{Cr2O3}(2708 K), as documented by the binary phase diagrams of Cr–N and Cr–O (Massalski 1990). The process is related to the temporary formation on the cathode surface of small islands of the reactive compounds due to the dense plasma arc condition. The islands are melted by the steering arc, such that the resulting microdroplets are propelled to the substrate. In a nitrogen atmosphere the surface of the metallic Cr cathode is covered with Cr_2N and Cr-N, and mainly with Cr-N or even Cr_2O_3 if the deposition atmosphere consists of a mixture of oxygen and nitrogen, as a direct result of

the higher reactivity of oxygen compared to the nitrogen molecule. It is reasonable to believe that the observed difference in surface roughness of Cr-N and Cr (N,O) coatings is related to the different T_m of the reactive compounds formed on the cathode as a result of metal target poisoning in reactive CAE. Despite this peculiarity, the surface of both coatings was uniform, without major morphological defects such as pores, pinholes and voids, which may be as deleterious for corrosion protection of the steel substrate.

The elemental composition of the 304 SS, as given by the manufacturer, is: C=0.02 %; Mn=1.23%; Si=0.41%; P=0.036%; S=0.024%; Cr=18.09%; Ni=8.04%; Cu=0.47%; Mo=0.34%; Co=0.15%; N=0.07% and Fe=balance. The elemental compositions of the deposited coatings determined by EDS are presented in Table 7.1.

Table 7.1: The elemental composition of the monolayered coatings deposited on Si substrates.

Coating	Elemental composition (at. %)				O/N	O/Cr	(O+N)/Cr
	N	O	Cr	C			
Cr-N	30.5±1.2	2.6±0.2	63.4±2.5	3.5±0.2	0.085	0.041	0.522
Cr(N,O)	*35.6±1.7*	14.9±0.8	46.8±2.2	2.6±0.1	0.419	0.318	1.079

From Table 7-1, one can notice the presence of oxygen and nitrogen in the coatings, as well as a small amount of carbon, which is probably due to the external handling of samples. High oxygen content was measured on Cr (N, O) coatings. The low oxygen concentration found in the Cr-N coatings referred to as contamination, was also reported (Ehrlich *et al.*, 1995). Chromium oxynitride coating has a complex structure, its composition and properties being controlled by the deposition parameters, which should ensure the reproducibility of each deposition run. The deposition of chromium oxynitride coating, performed in a mixture of two reactive gases such as O_2 and N_2, is a complex process due to the different reactivity of the Cr with nitrogen and the more reactive oxygen atoms and ions. The observed increase of O/N ratio (about 5 times) demonstrates the successful deposition of chromium oxynitride coating. The observed significant increase can be ascribed to the higher affinity of Cr for oxygen compared to nitrogen (Minami *et al.*, 2014). Similar results were reported by Li Ming-sheng on the reactive CAE deposition of chromium in nitrogen and oxygen atmosphere (Massalski 1990). It was documented by Munz that a cathode material with low melting temperature (T_m) generates an increased number of droplets with larger size (Dinu *et al.*, 2017a).

7.2 Phase composition

The phase composition of Cr-N and Cr (N,O) coatings was determined by x-ray diffraction (XRD) and the results of this analysis are shown in Figure 7-2.

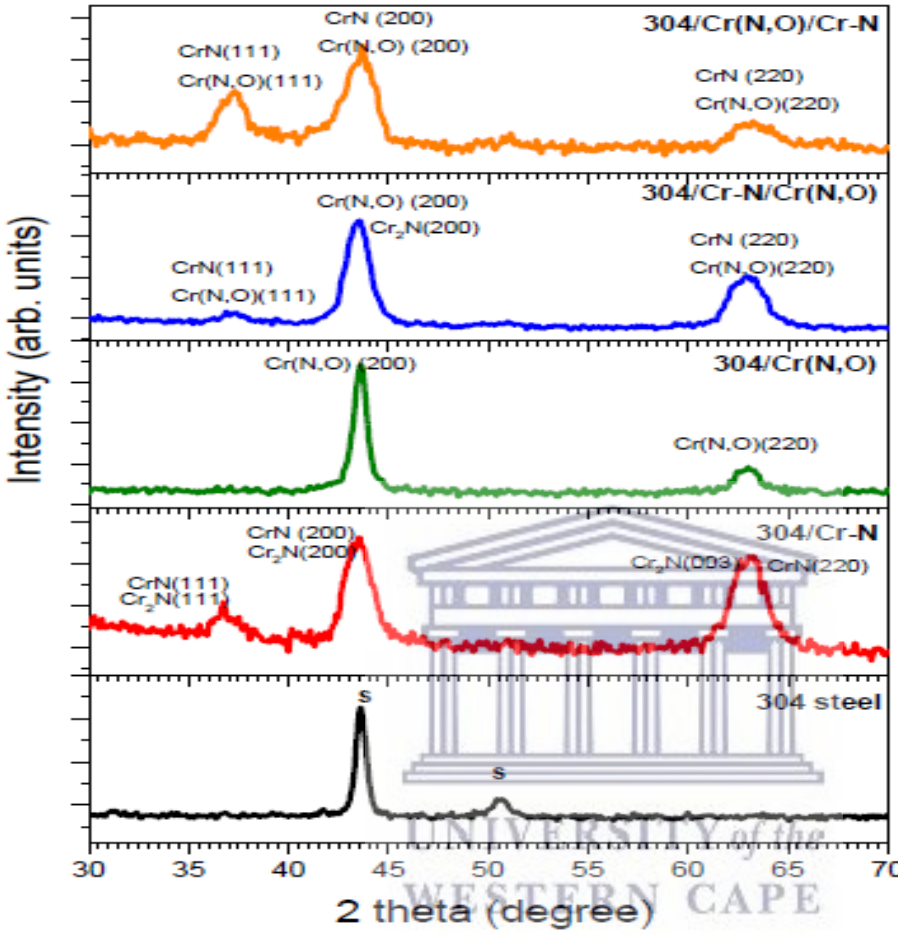

Figure 7.2: Grazing Incidence X-ray diffraction patterns of the Cr-N and Cr (N, O) coatings deposited on SS.

Figure 7-2 presents the XRD patterns of the coatings deposited on SS. The results disclosed in Figure 7.2 shows the significant overlapping of 304 SS peaks and those of the deposited coatings. The diffractogram of the Cr-N monolayer presents a shallow peak at 37.7^0 that corresponds to (111) cubic CrN phase (JCPDS 11-0065, at 37.57^0) or to the hexagonal (110) Cr_2N phase (JCPDS 35-0803, at 37.35^0). Also, a second small peak situated at 43.38^0 was attributed to (200) plane of hexagonal Cr_2N phase (JCPDS 35-0803, at 43.40^0), which is more likely than to (200) plane in B1 phase (JCPDS 11-0065, at 43.74^0). The high intensity peak observed at 67.6^0 was ascribed to the hexagonal Cr_2N phase (JCPDS 35-0803, at 67.3^0), suggesting that the deposition conditions favour the formation of a highly stressed Cr_2N

coating. These results are in good agreement with those reported by Rebholz et al. (2009) who showed that in chromium nitride with nitrogen content of about 30 at.% only the Cr_2N phase is present, similar to these result (30.5 at.% N). Also they showed that both Cr_2N and CrN phases coexist in coatings if the nitrogen content is raised to about 40 at.% (Rebholz *et al.*, 1999). This result is also consistent with the phase diagram of the Cr-N system (McHale 1994). In Cr(N,O) coating, three peaks were observed at 37.9^0 , 44.2^0 and 63.6^0, shifted to higher 2θ angles compared to the cubic CrN phase (JCPDS 11-0065, at 37.6^0, 43.7^0 and 63.6^0). The observed shift is due to oxygen incorporation, as also reported by Suzuki et al. (2013) for PLD grown Cr (N, O) with different oxygen contents. The observed decrease in the lattice constant and peak shift to higher angles suggests the formation of a solid solution which stabilises the single-phase cubic solid solution of Cr(N,O) (Suzuki et al. 2013). The conclusion is supported by the almost unity value of (N+O)/Cr ratio obtained by EDS. Considering the bilayer coatings, one may observe that the peak location is shifted in between the positions observed in Cr-N and Cr(N,O) monolayers, indicating the overlapping of the peaks specific for each monolayer. On the Cr-N/Cr (N, O) diffractogram, one can observe the (111) preferred orientation, as well as the presence of the (300) Cr_2N peak. As the Cr-N layer is located closest to the substrate the peak has a lower intensity, especially in the grazing incidence measurement set-up. As expected, in Cr (N,O)/Cr-N bilayer, the Cr_2N peak is more intense, but also a (111) significant orientation is present. Moreover, in this bilayer, two diffraction lines were found at 43.3° and 44.3°, ascribed to Cr_2N and Cr(N,O), respectively. Summarising, the crystalline structure of Si/Cr-N/Cr (N, O) coating is accurately depicting the two composing monolayers. However, the crystalline structure of Si/ Cr (N, O)/Cr-N is more complex, as the crystalline Cr (N, O) layer seems to promote the growth of crystallites in the Cr-N top layer.

7.3 Coating roughness

The surface roughness of the Cr-N and Cr (N, O) coatings was determined by a Dektak 150 surface profilometer (Veeco-Bruker) as described in Section 3.6.7.1. To achieve this goal, the following three parameters including the arithmetic average deviation from the mean line (Ra), the root mean square average of the profile heights over the evaluation length (R_q) and skewness parameter (S_k) were considered. The values of the roughness parameters, R_a and R_q and S_k, determined for the SS substrate and all deposited coatings, are presented in Figures 7-3a, 7-3b and 7-3c, respectively.

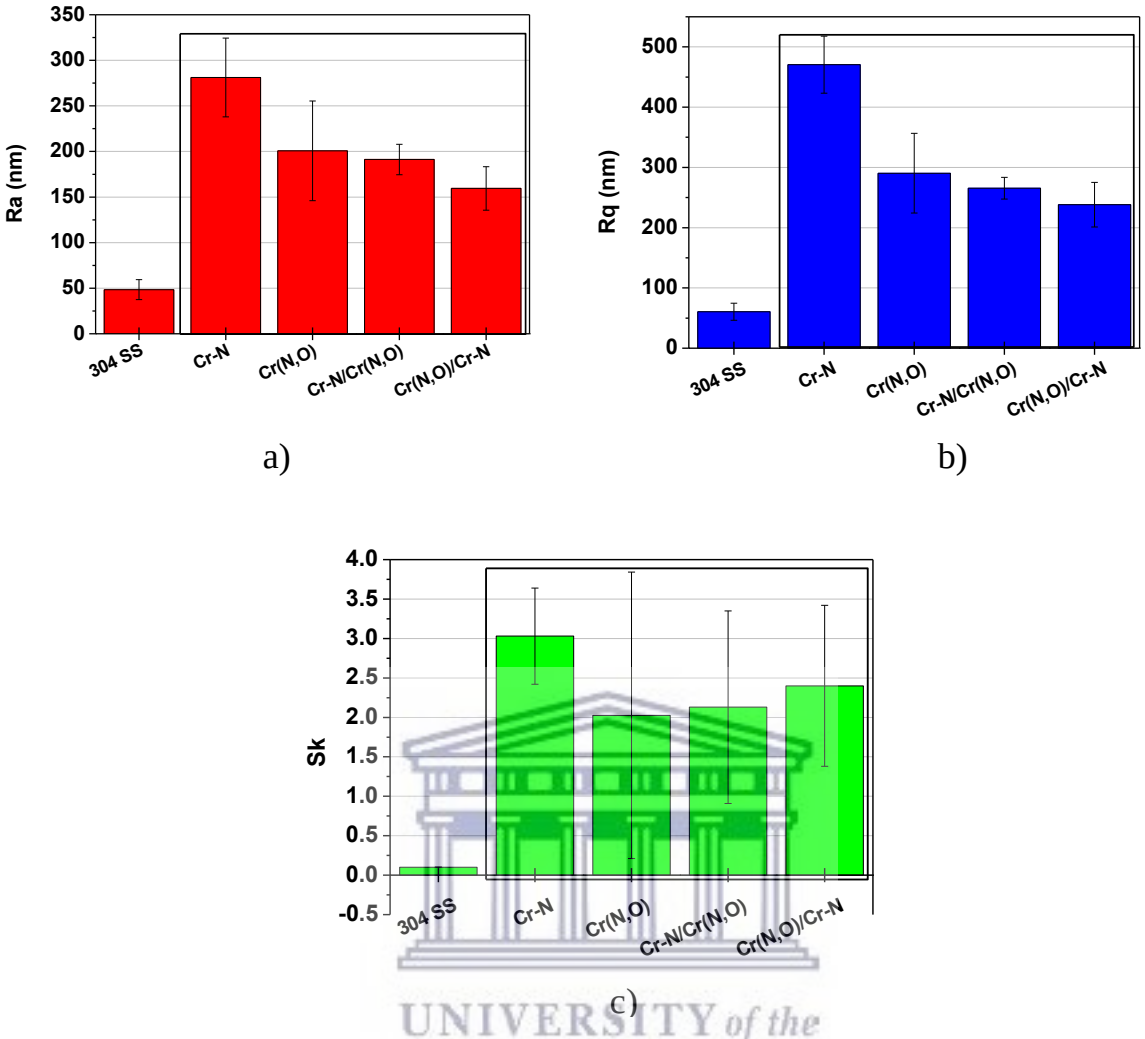

Figure 7.3: The roughness of Cr-based coatings before the corrosion test: (a) Ra parameter; (b) Rq parameter; (c) Sk parameter.

The outcomes in Figure 7-3 show a noticeable increase of coating roughness (by a factor of up to approximately 8.5) compared to the bare substrate (R_a= 48 nm, R_q= 60 nm). The highest values were obtained, in accordance with SEM images, for the Cr-N coating: R_a= 281.2 nm, R_q= 470.6 nm. This result is due to the observed microdroplets generated from the target material during the reactive cathodic arc deposition, determining the presence of the most numerous peaks. The oxygen addition in the deposition atmosphere slightly decreased the surface roughness, as observed in Cr (N, O) monolayers. In the case of bilayers, considering the errors, the surface roughness is in the same range as that of the oxynitride coating. The observed decrease of the roughness for both bilayers, as compared to the nitride coating, may be ascribed to the lower roughness of Cr (N, O) layer in the bilayer, and to the thinner dimensions of the composing individual layers in the bilayers, compared to the monolayer. The

trend evidenced for R_a parameter (Figure 7-3a) was also for R_q parameter (Figure 7-3b). Since R_a and R_q parameters are not enough to evaluate the surface quality, the skewness parameter (S_k) values are presented in Figure 7-3c. One may notice the value close to 0 for the SS substrate, indicating a relatively uniform distribution of the peaks and valleys on the surface. The S_k values corresponding to the coatings are in the 2 – 3 range, indicating the presence of high peaks, since a positive number relates to a higher percentage of profiles situated above the mean line. The presence of these peaks on the surface of coatings is the results of the droplets, as observed by SEM. As mentioned above, this is a characteristic topography of the coatings obtained by the CAE deposition method. It was also reported that other hard coatings (Cr-N (Sebastiani, Piccoli and Bemporad, 2013), TiN/Cr-N (Steyer *et al.*, 2008) deposited by CAE present structural defects on the surface in the form of overgrown droplets, leading to an increased surface roughness, which can affect the corrosion behaviour.

7.4 Coating adhesion

In this section, the coating adhesion of (showing the adherence of protective layers on SS suport) the coatings were examined by SEM analysis and the SEM micrographs of the scratch traces are illustrated in Figure 7-4.

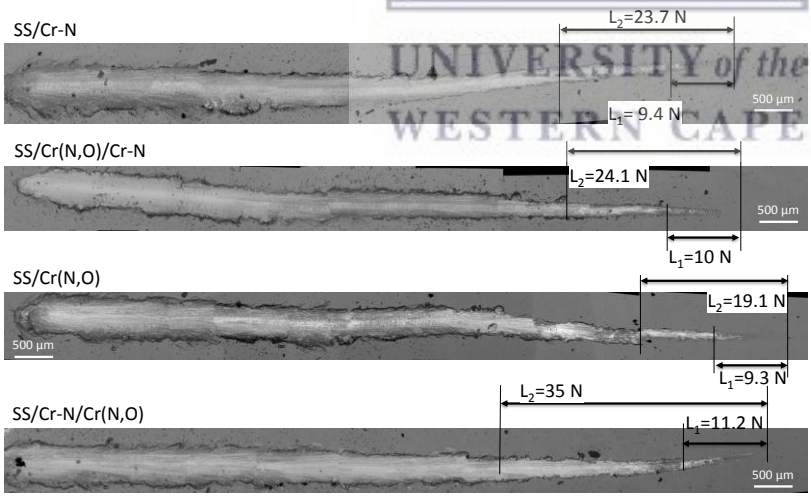

Figure 7.4: Scratch traces of Cr-based coatings deposited on 304 SS steel

In Figure 7-4, the first sign of coating delamination (L_1) was measured around 10 N loads on the coatings. The highest value, 11.2 N, was obtained for the Cr-N/ Cr(N,O) coating.

The Cr (N, O) monolayer was completely delaminated for a load L_2 higher than 19.1 N, while Cr-N coating withstood the gradual increasing loading force up to 23.7 N, denoting an excellent adhesion to the metallic substrate. Considering the two bilayered coatings, the one containing Cr(N,O) layer at the metal interface presented lower values for both loads (L_1 and L_2), but was notably higher than the ones corresponding to Cr(N,O) monolayer. As expected, the presence of Cr-N layer at the metal interface determined the highest values for both L_1 and L_2 (35 N). The best adhesion was measured for the coating Cr-N/ Cr (N, O), as a result of the good adhesion of the Cr-N monolayer to the substrate (L_2 = 23.7), in comparison with the one exhibited by the Cr (N, O) monolayer (L_2 = 19.1N). To sum up, both types of bilayers exceeded the delamination load values obtained for monolayers: $L_{1,2}$(Cr(N,O)) < $L_{1,2}$(Cr-N) < $L_{1,2}$(Cr(N,O)/Cr-N) < $L_{1,2}$(Cr-N/ Cr(N,O)). The higher adhesion of the two bilayers may be ascribed to the lower internal stress in the bi- and multi-layers, as a reduced intrinsic stress is commonly associated with an enhanced adhesion. Also, the presence of a supplementary interface between the two monolayers may hinder the crack propagation, determining a better adhesion of the coating to the substrate.

7.5 Corrosion measurements

In this section, the corrosion measurement was investigated by assessing the behaviour of various parameters such as open circuit potential (OCP) often abbreviated as (Eoc), linear polarisation also known as corrosion resistance (R_p), corrosion potential (E_{corr}) and corrosion current density (i_{corr}), porosity (P) and corrosion protection efficiency (P_e) with time for each coating. These factors were carefully examined to deduce the most corrosion protective layers of Cr based coatings as described in section 3.6.7.2.

7.5.1 Behaviour of open circuit potential with time

To recall, the open circuit potential is one of the most non-destructive corrosion tests that indicates when the metal electrode tested is at a stable state. Its increase may show the formation of a passive layer on the surface of the metal electrode while its decrease dictates that a porous hydroxyl layer is being formed which at some point may slow down the corrosion process but does not protect the metal from corroding. Hence the open circuit potential evolution during 15 h immersion in 0.1M NaCl+6% H_2O_2 of Cr based coatings made in this study is presented in Figure 7-5.

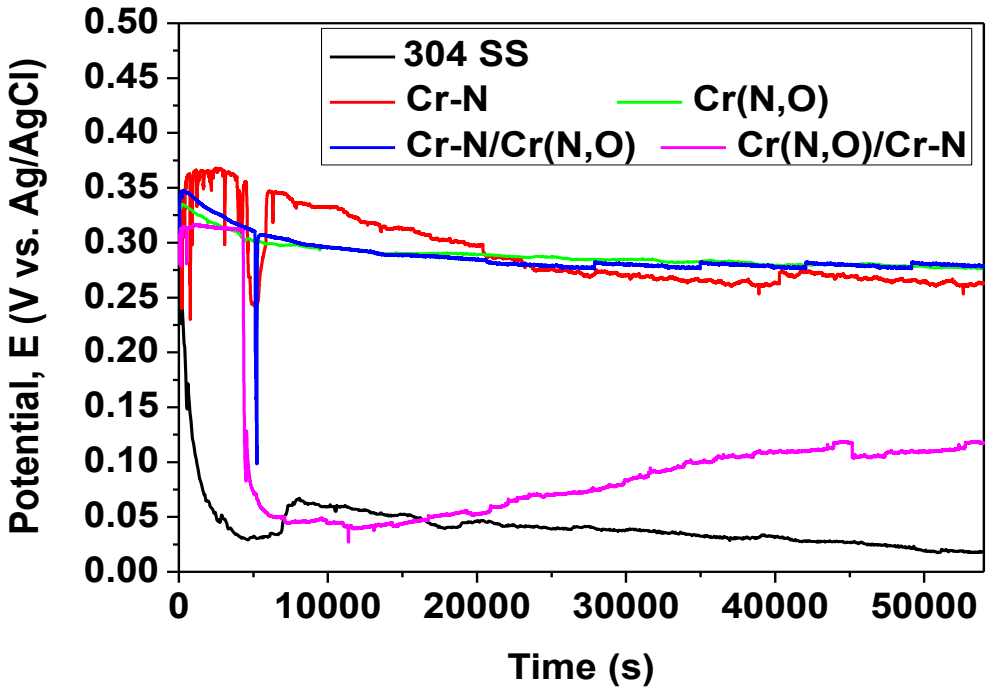

Figure 7.5: Open circuit potential evolution of Cr-based coatings deposited on 304 SS steel

Figure 7-5 presents the OCP behaviour with time for CrN and Cr(N,O) coatings. The results in Figure 7-5 show that in the first hours of immersion, a slight decrease of potential was observed for all analysed specimens, which was more pronounced for 304 SS. However, all the coated specimens reached a steady state, the corresponding E_{OC} being in the range 0.1 – 0.3 V. The stable E_{OC} of the coated specimens shows the formation at the surface of a stable passivation layer. The slow decrease of the potential corresponding to 304 SS indicates the instability of the passive layer. For the Cr (N, O)/Cr-N bilayer the initial rapid decrease of the E_{OC} value was followed by a steady increase, such that after 15 h of immersion the value exceeded the one obtained for 304 SS, displaying an increasing tendency up to 117 mV, proving the protective nature of this coating. The most passive layers were formed on the surfaces of the Cr-N/ Cr (N, O) and Cr (N, O) coatings, both presenting almost the same variation tendency for E_{OC}, leading to the conclusion that the presence of Cr (N, O) at the point of contact with the corrosive environment has a beneficial effect on the corrosion resistance. In contrast with the above result, the Cr-N monolayer exhibited a better passivation of its surface, compared to the Cr (N, O)/Cr-N bilayer, showing an E_{OC} value as low as 0.1 V. This result may be ascribed to the poorer adhesion measured for the Cr (N, O)/Cr-N bilayer. From these analysis, it was inferred that Cr (N, O) and Cr (N, O)/Cr-N were the most corrosion resistant coatings. However, this factor could not solely employed to conclude the corrosion

behaviour of Cr based coatings, therefore the corrosion effect extended parameters was required.

7.5.2 Linear polarisation/corrosion resistance

Next to OCP, linear polarisation is another corrosion indicator that allows the determination of polarisation resistance (Rp) also known as corrosion resistance which is the slope of the linear trend of potential (mV) versus current density (nA/cm^2) expressed in ohms-cm^2. The R_p hence indicates the corrosion rate steady state as described in section 2.6.5.2. Its increasing values demonstrate the resistant character of the specimen to corrosion while its decline may indicate the coating erosive vulnerability to harsh oxidative environments. Moreover, in the current study, the Rp values were directly read from the corrosion instrument. Its values and those of E_{OC} as well as corrosion potential (E_{corr}) were recorded and are presented in Table 7-2.

The R_p parameter, presented in Table 7-2 indicates the resistance of the investigated coatings when only a small perturbation was applied (±10 mV). When compared with the uncoated substrate, all the coatings have a higher R_p value (with a factor of 40 to 106). The bilayer Cr-N/Cr (N, O) exhibited higher polarisation resistance, followed by the Cr (N, O) monolayer. This result can be explained first by the double layer structure which acts as an enhanced barrier to the ingress of the electrolyte through the surface defects, and secondly, by the lower porosity of the Cr (N, O) layer, as indicated in Table 7-2, which further blocked the electrolyte ingress. According to Inoue et al., the oxygen atoms in the Cr(N,O) crystallites diffuse outwards, forming Cr_2O_3 layers which surround the crystallites and slow down the oxidation speed, such that the oxidation resistivity of Cr(N,O) is increased (Suzuki *et al.*, 2013). No significant differences were found between the Cr-N monolayer and Cr (N, O)/Cr-N bilayer. As early stated in section 2.6.5.2 linear polarisation is limited by the fact that it can only allow determination of the corrosion resistance R_p but does not provide any information on extended aspects mainly corrosion current and rate. Hence measurement techniques such as the Tafel plot can further be explored to determine corrosion current and rate, which are crucial in understanding the corrosion resistance of the coatings.

7.5.3 Tafel plots structure: determination of corrosion current density and corrosion rate

In contrast to linear polarisation previously discussed, the Tafel plot as defined in section 2.6.5.3 was used in this study to obtain more information about the corrosion behaviour of Cr-

N and Cr(N,O) coatings. In this regard, both oxidation and reduction branches corresponding to the anode and cathode respectively were extrapolated to determine the corrosion current and rate. Theoretically, the most anticorrosive layers are defined by their lower current densities and corrosion rates. The Tafel plots of Cr-N and Cr (N,O) specimens obtained in this study are presented in Figure 7-6 and the different parameters extracted from the Tafel plots were recorded in Table 7-2.

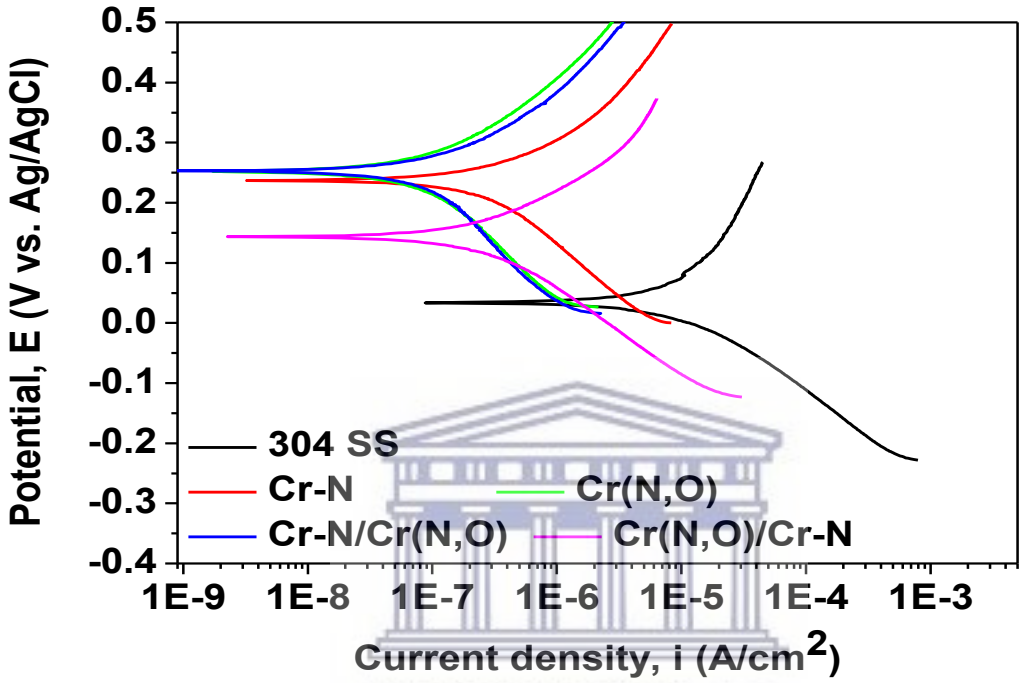

Figure 7.6: Tafel plots of Cr-based coatings deposited on 304 SS steel

Table 7.2: Corrosion parameters of Cr-based coatings.

Sample	E_{OC} (mV)	R_p (kΩ)	E_{corr} (mV)	i_{corr} (μA/cm^2)	P	P_e (%)
304 SS	18	2.109	34	14.689	-	-
Cr-N	263	86.136	236	0.492	0.016	96.7
Cr(N,O)	277	187.75	250	0.137	0.007	99.1
Cr(N,O)/Cr-N	117	85.599	143	0.336	0.020	97.7
Cr-N/ Cr(N,O)	276	223.047	250	0.168	0.006	98.9

Figure 7-6 presents the Tafel plots of Cr based coatings from which the corrosion potential (E_{corr}), corrosion current density (i_{corr}) and other factors were extracted and are presented in Table 7-2. From Figure 6.6, the current density parameter showed that the coated surfaces were

not enhanced and hence favoured the current flow. That is, the i_{corr} parameter was two orders of magnitude lower in value than the SS substrate as shown in the fourth column of Table 7-2. Considering this parameter, the Cr (N, O) monolayer showed the lowest i_{corr}, followed by Cr-N/Cr (N, O), Cr (O, N)/Cr-N and Cr-N coatings. The corrosion rate is proportionally related to the i_{corr} as explained in section 2.6.5.4. This demonstrated that the Cr (N, O) monolayer had the lowest corrosion rate and therefore was the most corrosion resistant followed by the Cr-N/Cr (N, O) bilayer coating. These results corroborate the findings obtained in Section 7.5.3. In addition, the porosity and protection efficiency of the investigated coatings were calculated based on Equations (3.2) and (3.3). By comparing the porosity values, it could be concluded that the addition of oxygen led to the porosity decrease in Cr- based coatings. As the Cr (N, O) layer is on top, this inferred that its porosity was lower as indicated by the results exhibited in Table 7-2. Alternatively, the Cr (N, O)/Cr-N system showed higher porosity than that of Cr-N/Cr (N, O) or Cr (N, O) coatings; its properties were thus more similar to that of Cr-N. Furthermore, these results complement those achieved with corrosion potential and corrosion current densities discussed above and all presented in Table 7-2.

Regarding the protection efficiency, the best value was found for the Cr (N, O) monolayer, indicating better corrosion resistance. This result is in good agreement with the above mentioned findings. Moreover, its presence on the top of a bilayer also produced high protection efficiency, superior to that observed in Cr (N, O)/Cr-N bilayer. This was probably due the beneficial effect of the oxide layers surrounding the crystallites, preventing further oxidation. In total, the corrosion study of Cr based coatings was successfully investigated. The corrosion behaviours of the factors considered showed that Cr(N,O) and CrN/Cr(O, N) were the most corrosion resistant coatings, respectively compared to Cr-N and Cr(N,O)/Cr-N layers that were defenceless to the oxidative environment. Nevertheless to support these findings, further characterisation of these coatings was required.

7.5.4 Characterisation of the coatings after the corrosion tests

After the corrosion investigation, the physical appearance based on the morphological aspects of the specimens and the elemental content had to be assessed in order to investigate the effect of the corrosive environment on the coatings. In this regard, a few factors mainly the roughness, surface morphology and the elemental composition of the samples were considered, after the corrosion tests.

7.5.4.1 Coating roughness

The roughness of the Cr based coatings after the corrosion tests was investigated using the procedure described in Section 3.6 and the results of this analysis are presented in Figure 7-7.

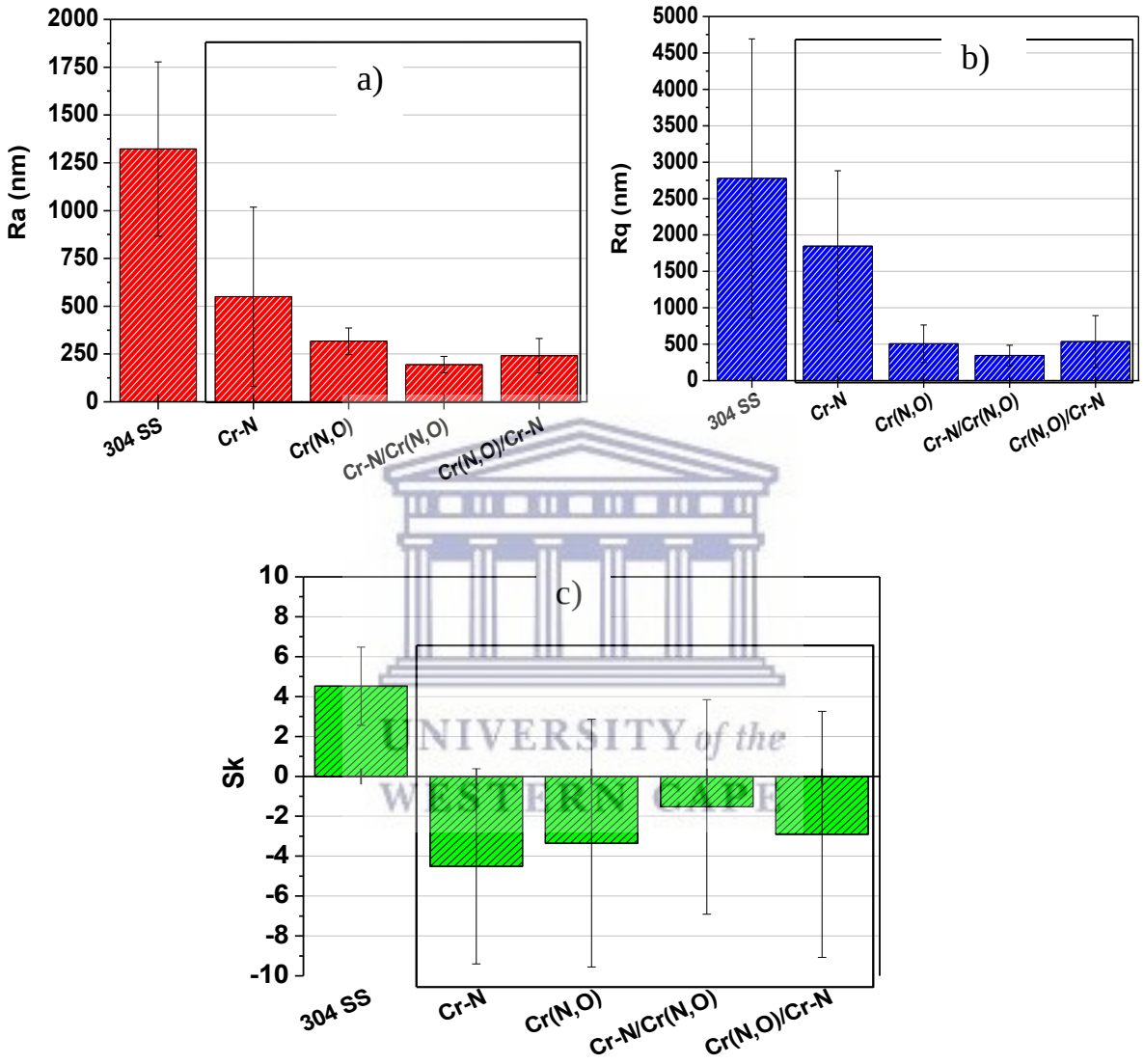

Figure 7.7: The roughness of Cr-based coatings after the corrosion test: (a) Ra parameter; (b) Rq parameter; (c) Sk parameter.

Figure 7-7 discloses the roughness of Cr base coatings after the corrosion study. The outcomes in Figure 7.7 show that the roughness of all investigated surfaces increased significantly due to corrosive attack, thus it could be concluded that all surfaces were affected by the corrosive environment to different extents, as detailed below. Indeed, the roughness parameter R_a of the 304 SS support increased from 50 µm before corrosive attack to about 1300 µm (Figure 7-7a),

demonstrating that a significant corrosion process affected the bare SS support. The Cr-N monolayer was also considerably affected by corrosion, the R_a increased from 281 nm (Figure 7-7a) before corrosion to 549 nm (Figure 7-7a). This outcome is in good agreement with the electrochemical results, as the R_a value after corrosion increased from 200 nm to 316 nm. On the contrary, the bilayer with Cr (N, O) on top exhibited an almost similar R_a value before and after the corrosive attack, indicating that the roughness was not the main factor influencing the corrosion behaviour. It should be emphasise that within the limit of experimental error, the protection efficiency P_e and the roughness parameters R_a and R_q exhibited the same trend. Moreover, the lower roughness measured on the bilayered coatings, compared to the monolayered ones, could be explained by the cracks and dislocation blocking at layer interfaces. After the corrosion tests, all of the coated surfaces showed negative values of S_k compared to the surfaces before corrosion (Figure 7-7c), pointing to the formation of more valleys on the corroded surfaces, as a consequence of significant corrosive processes taking place locally, where the electric field was more intense due to specific surface morphology. The Cr-N monolayer might well illustrate this conclusion; since, compared to all the other coatings, it showed the most negative S_k value and also had the lowest corrosion resistance, as presented in Table 7-2. Yet morphological visualisation was essential to confirm these intrinsic variations.

7.5.4.2 Surface morphology and elemental composition

In order to gain a deeper insight into the corrosion mechanism in relation to the alteration of the roughness parameters after the corrosion tests, the surface morphology of corroded surfaces was investigated and the SEM images of the Cr-based coatings after the corrosion test are presented in Figure 7-8.

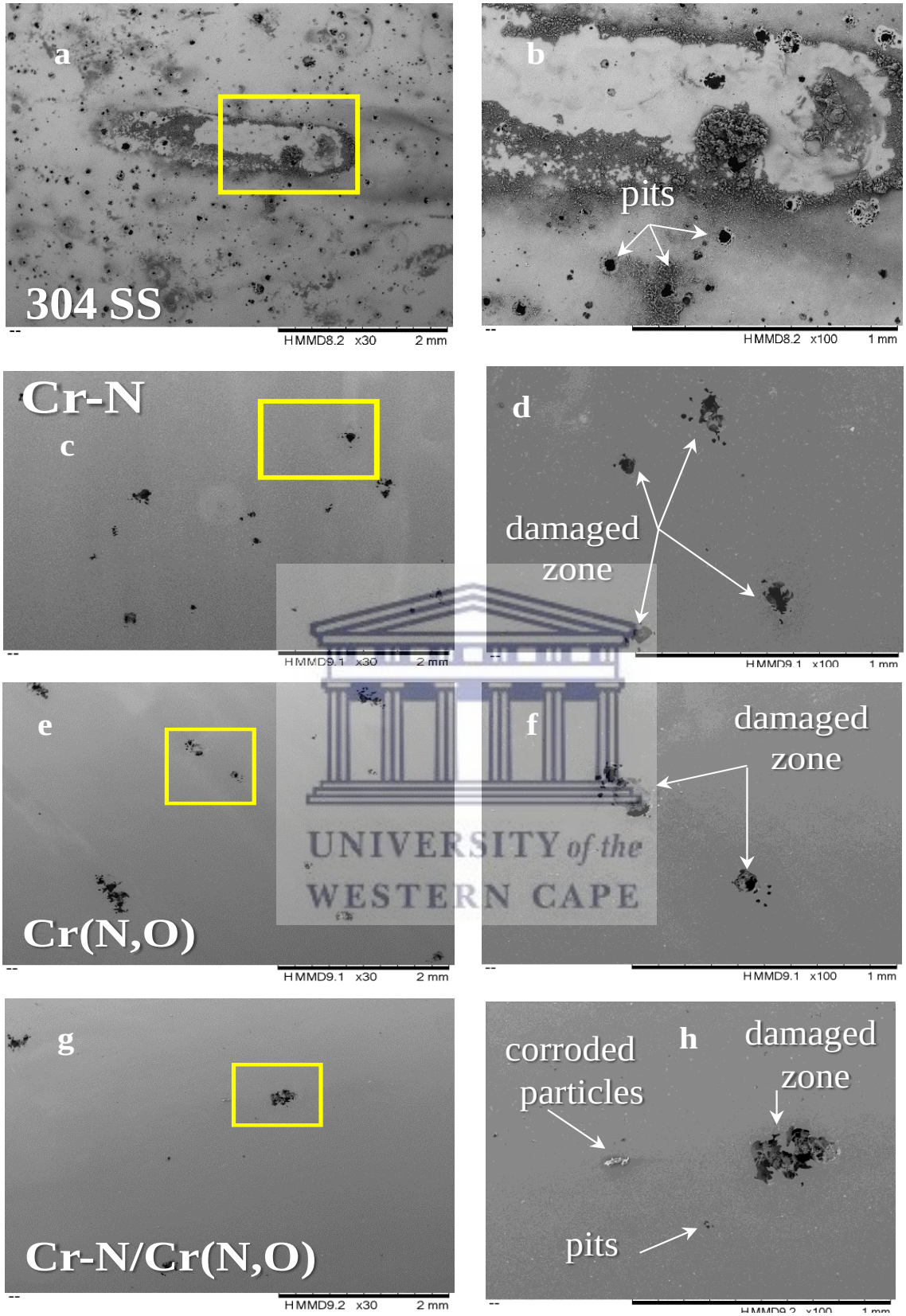

Figure 7.8: SEM micrographs of Cr-based coatings after the corrosion test: at x30 magnification and at x100 magnification, SS (a & b), Cr-N (c & d), (Cr(N,O)(e & f), Cr-N/Cr(N,O)(g & h), Cr(N,O)/Cr-N(I & j).

Figure 7-8 resents the SEM micrographs of Cr based coatings after the corrosion test. As can be seen from Figure 7-8, the 304 SS uncoated substrate was significantly affected by corrosion, this result was in agreement with the electrochemical tests. Also the surface of Cr-N monolayer was deteriorated by the corrosive attack, with numerous damaged zones being observed where the coating was cracked. Some corrosion products were also found on coated surfaces. The poor corrosion resistance of Cr-N monolayer was probably due to the high density of microdroplets and high porosity; this was confirmed by SEM images and electrochemical tests, and further facilitated chloride penetration and that reached the coating-substrate interface and hence accelerated the corrosion processes. Besides, the damaged zones of the investigated coatings were mapped by EDS and the micrographs are presented in Figure 7-9 while the elemental compositions of the coatings on SS supports, before and after the corrosion tests, are presented in Table 7-3.

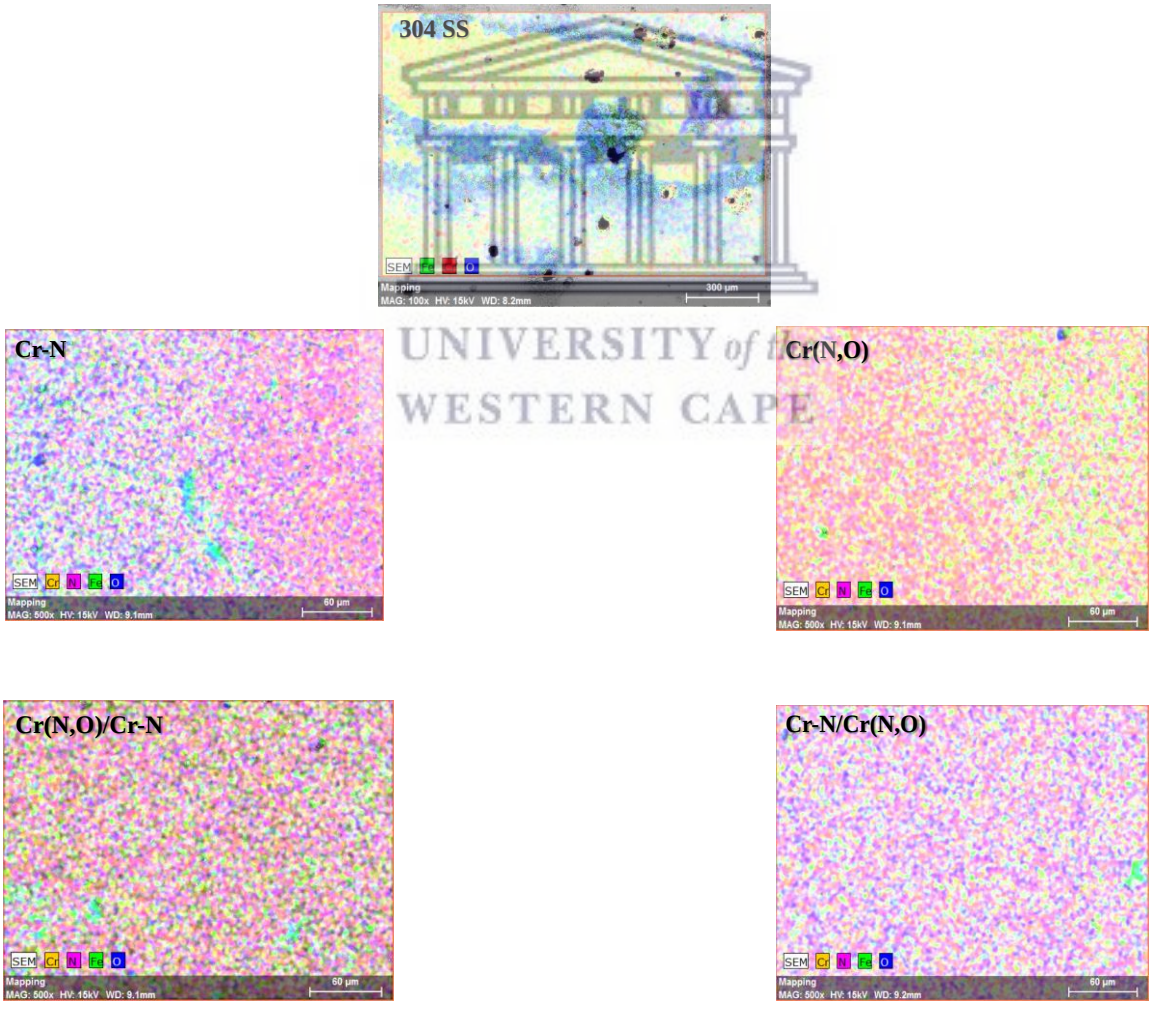

Figure 7.9: EDS mapping micrographs of the Cr-based coatings after the corrosion test

Table 7.3: The elemental composition of the investigated specimens before (B) and after (A) the corrosion testin the areas shown in Figure 7-9.

Substrate/Coating	Elemental composition (at. %)				
(image zone)	N	O	Cr	C	Fe
304 SS (A)	-	41.0±2.8	9.5±0.1	-	49.5±3.2
Cr-N (B)	30.5±1.2	2.6±0.2	63.4±2.5	3.5±0.2	-
Cr-N (A)	22.7±0.8	17.5±0.1	56.8±1.8	-	3.0±0.1
Cr(N,O) (B)	35.6±1.7	14.9±0.8	46.8±2.2	2.6±0.1	-
Cr(N,O) (A)	32.4±1.5	20.2±0.3	46.2±2.1	-	1.2±0.1
Cr-N/ Cr(N,O) (B)	36.9±1.7	13.5±0.7	49.3±2.2	2.2±0.1	-
Cr-N/ Cr(N,O) (A)	35.8±1.5	17.4±0.8	46.6±1.8	-	0.5±0.1
Cr(N,O)/Cr-N (B)	31.5±1.3	2.8±0.2	61.5±2.5	4.2±0.2	-
Cr(N,O)/Cr-N (A)	31.1±1.3	22.9±1.3	44.1±2.1	-	1.9±0.1

The results in Figure 7-9 and Table 7-3 show that a low content of the SS support's elemental composition was found in coatings with high corrosion resistance, such as Cr (N, O) monolayer and Cr-N/ Cr (N, O) bilayer. In contrast, a high amount of Fe originating from the SS support was detected on the Cr-N monolayer surface, confirming that this coating was significantly affected by the corrosion. In summary, the results obtained from SEM and EDS analyses carried out on corroded surfaces sustain the electrochemical/corrosion results earlier obtained in this section.

7.5.5 Summary of Cr-N and Cr (O, N) coatings

In summary, in this section Cr-based coatings in monolayered (Cr-N and Cr (N, O)) and bilayered structures (Cr-N/ Cr (N, O) and Cr (N, O)/Cr-N) were prepared by the cathodic arc evaporation (CAE) method described in Section 3.6.7. The presence of Cr_2N, Cr-N and Cr (N, O) and also mixtures of these phases in the coatings' composition was evidenced by XRD analysis. The oxynitride coatings were smooth, compact and homogenously deposited on 304 SS, with few microdroplets. The corrosion protection performance of the developed mono and bilayered Cr-based coatings was evaluated in 0.1M NaCl + 6% H_2O_2 and showed that Cr(N ,O) was the most corrosion resistant layer followed by Cr-N/Cr(N ,O) coating compared to Cr-

N and Cr(N ,O)/Cr-N coatings that showed minimal corrosion resistance, respectively. Apart from Cr derived protective layers, extended coatings designed with other transition metals mainly Ti were fabricated in the same fashion and their corrosion resistance was evaluated following the same procedure as described in Section 7.1 of this chapter.

7.6 Enhancement of the corrosion resistance of 304 stainless steel by Ti nitride and oxynitride coatings

In this section, Ti nitrides and oxinitrides coatings were also designed by CAE according to the procedure described in Section 3.6.7, their anticorrosion behaviours were also investigated by potentiodynamic polarisation as detailed in Section 3.6.7.2 of Chapter 3. The characterisation of coatings before and after corrosion was performed using the same techniques as in Section 7.1 of this chapter. In this section the characterisation involved the determination of elemental composition, phase composition and grain size, coating roughness and surface morphology of Ti based coatings before and after corrosion.

7.6.1 Elemental composition of Ti based coatings before corrosion test

The elemental compositions of the stainless steel support and Ti coatings before corrosion was performed using EDS as described in Section 3.6 and the results of this analysis are shown in Table 7-4.

Table 7.4: The elemental composition of the investigated Ti specimens before the corrosion test.

Substrate/Coating	Elemental composition (at. %)			(O+N)/Ti
	Ti	N	O	
SS /TiN	49.89	50.11	-	1.00
SS /TiON	49.66	43.05	7.29	0.98
SS /TiN/TiON	49.42	44.96	5.62	1.03
SS /TiON/TiN	49.84	50.09	0.6	1.01

Table 7-4 lists the elemental composition of Ti based coated samples before the corrosion test. From these results, it was noticed that the presence of Ti concentration was approximately 49 at. % in all coatings. On the other hand, in the oxynitride monolayer, O concentration was higher than in the bilayer where the monolayer was on top. On the bilayer with TiN on top, the concentration of oxygen was very low, as expected, due to the signal absorption in the ~ 500 nm thick TiN layer. Based on the calculated (O+N)/Ti ratio, the deposited coatings were nearly stoichiometric, as intended.

7.6.2 Phase composition and grain size of Ti coatings

The phase composition and grain size of the Ti based coatings before the corrosion test were determined by XRD analysis and the results of this analysis are exhibited in Figure 7.10 and the coatings grain sizes calculated by Scherrer principle earlier presented as Equation (6.1) are shown in Table 7-5.

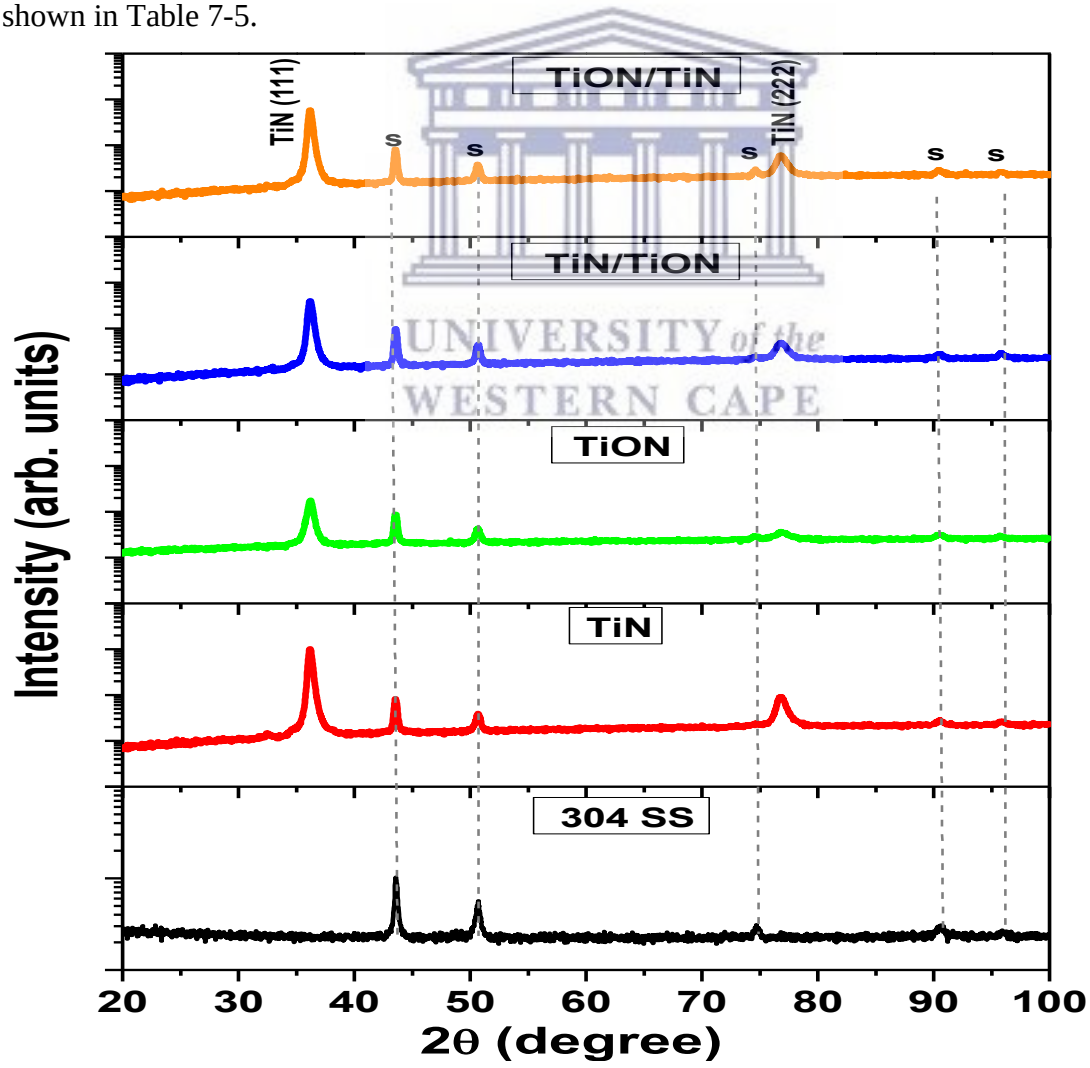

Figure 7.10: X-ray diffraction patterns of the Ti based coatings on SS support.

Table 7.5: Grain size (d) of the coatings

Coating	d (nm)
SS/TiN	23.8
SS/TiON	16.3
SS/TiN/TiON	19.9
SS/TiON/TiN	22.1

Figure 7-11presents the XRD patterns of Ti based specimen before corrosion. The results exhibited in Figure 7-11 showed only TiN phases with cubic structure with (111) and (222) preferred orientations (indexed according to JCPDS 04-017-6803). Moreover, the peaks corresponding to the SS support were also identified. The highest crystallinity was exhibited by the TiN coating, as indicated by the largest grain size in Table 6.4 (d=23.8 nm), followed by SS/TiON/TiN (d= 22.1 nm), SS/TiN/TiON (d=19.9 nm) and TiON (d=16.3 nm). No Ti oxides were observed, probably due to the low amount of oxygen, of only 5─7 at. %, as determined from the EDS analysis.

7.6.3 Coating roughness

The roughness of Ti based coatings before corrosion was performed by profilometry analysis and the results of the analysis are given in Figure 7-11.

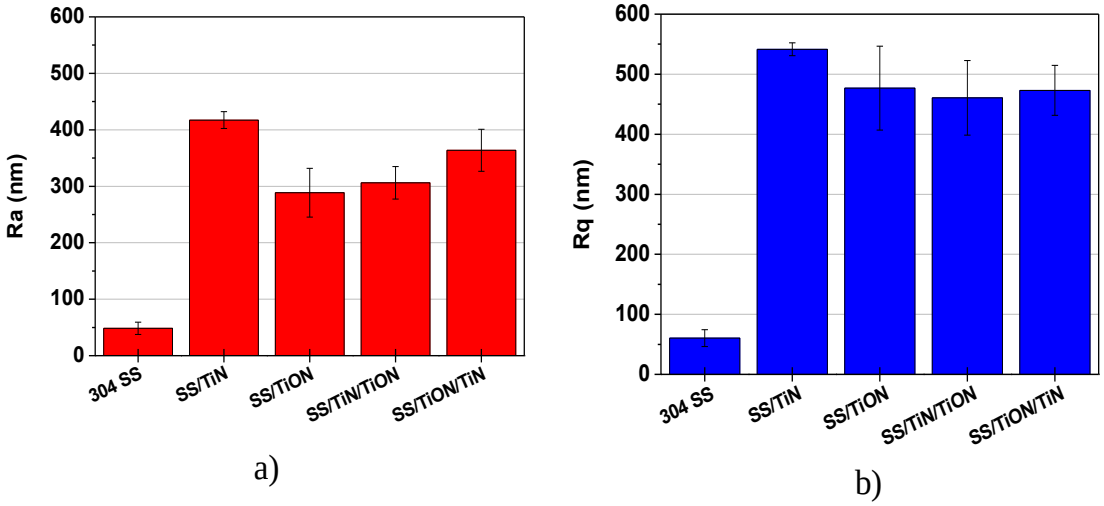

Figure 7.11: The roughness of coatings before the corrosion test

Figure 7-12 shows the roughness of Ti based coatings before the corrosion tests. The outcomes displayed in Figure 7-12 show that the coating roughness values increased with a factor spanning from 5.9 (SS/TiON) to 8.6 (SS/TiN), recalling that the uncoated substrate was polished up to R_a = 50 nm. The roughness of the two types of bilayer was in between those of the monolayers. The TiON monolayer exhibited the lowest R_a value, while that of TiN was the highest (R_a ~ 417 nm), indicating that the addition of oxygen generated a significant decreased in the surface roughness, due to coating amorphisation, as revealed by the decrease grain size values (Table 7-5). In the case of the bilayer, with TiON on top, the roughness was close to that of TiON monolayer. As expected, according to the grain size values, the bilayer with TiN on top presented a lower roughness than TiN and higher than TiON monolayers. Considering the R_q parameters, their values presented the same trend as those of R_a parameter.

7.6.4 Surface morphology of Ti coatings before corrosion test

The morphology of coated surfaces was evaluated by both SEM and AFM methods. The SEM and AFM images of Ti monolayers are presented in Figure 7-12a and Figure 7-12b, respectively.

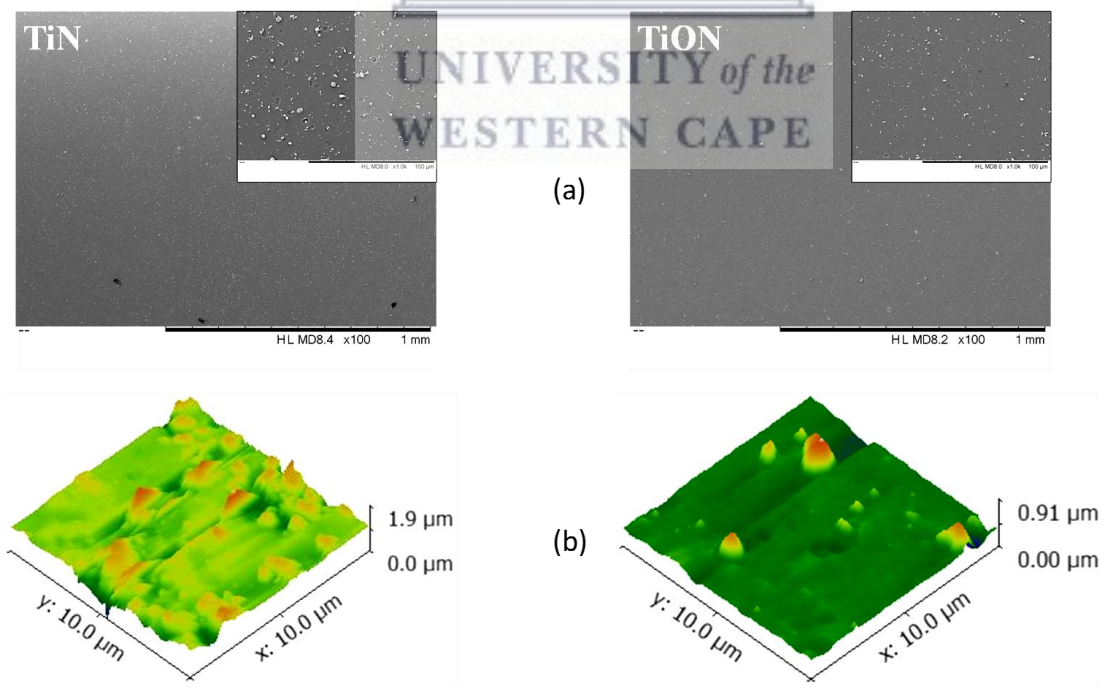

Figure 7.12: (a) SEM and (b) AFM images of the SS/TiN and SS/TiNO monolayers

Figure 7-13 presents SEM (a) and (AFM) images of Ti based specimen. The results in Figure 7-13 (a & b) show that the surfaces of both monolayers were covered by micro droplets of different diameters as expected. This finding is in line with the surface profilometry measurements displayed in Figure 7.12. Likewise, higher droplet densities with larger diameters were observed on the TiN surface, compared to TiNO. Despite the presence of droplets, both coatings were uniformly deposited, without any major defects such as pinholes, voids or cracks. On the TiN coated surface, an agglomeration of particles can be observed with high peaks. These peculiarities of CAE deposition, in which a dense plasma is formed due to the arc discharge, which locally melts the cathode surface, might be related to the different melting temperatures (T_m) of the reaction products formed on the cathode surface during the reactive deposition (TiN, TiO): T_m^{TiN}(2950°C) > T_m^{TiO}(1750°C) (Holleman, 2001). Even if the deposited monolayer coating consists mainly of TiN or TiON (in which oxygen entered the rock-salt cubic structure of TiN interstitially or as a substitute for N), due to the lower T_m^{TiO} value, the small TiO islands on the cathode surface are ejected as smaller microdroplets, compared to the TiN compound, which is more frequently ejected, forming large microdroplets on the coatings surface, as evidenced by AFM measurement shown in Figure 7-13b.

7.6.5 Corrosion tests

In this section, the corrosion study of Ti based coating was performed by evaluating the behaviour of two selected parameters including open circuit potential (OCP) and Tafel plots. That is, the OCP was considered as a quick non-destructive measurement to detect the formation of the passive layer on the surface of the SS support that was meant to protect the metal from erosive depletion in an acidic milieu. The Tafel plots on the other hand were used to extract more parameters such as corrosion current density (i_{corr}) and rate, the porosity (P) and the protection efficiency (P_e) which corrosion behaviour may define the most anticorrosive coatings.

7.6.5.1 Evolution of open circuit potential with time

The evolution of open circuit potential (E_{oc}) was measured during the 15 h immersion in 0.10 M NaCl+1.96 M H_2O_2 and the results of this evaluation are presented in Figure 7-13.

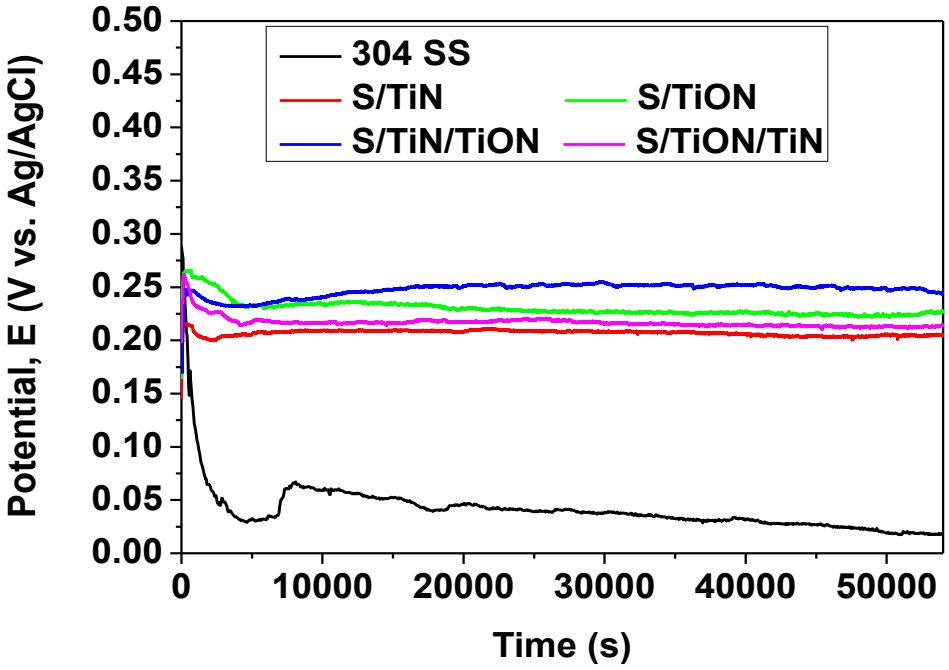

Figure 7.13: Open circuit potential evolution of Ti-based coatings

Figure 7-13 displays the evolution of the open circuit potential with time. The results in Figure 7-13 show that from the beginning, E_{oc} potential of the uncoated SS substrate started to decrease, and was stabilised after about 5 h of immersion. This result indicated that the oxide layer formed on its surface was instable, and was easily destroyed. All Ti coated samples reached a steady state after about 1.5 h of immersion around 0.2 V, indicating the formation of a stable passive layer at the surface. The most electropositive E_{oc} potential was found for the SS/TiN/TiON bilayer, which had a lower roughness compared to SS/TiON/TiN bilayer. Note that the TiON coatings, as monolayer or bilayer, exhibited the more electropositive E_{oc} potential, compared with the other coatings, with TiN layer facing the electrolyte. Though the E_{oc} discussed above demonstrated the formation of passive layers on the surface of SS substrate, more details were required to identify the most corrosion resistant coatings.

7.6.5.2 Tafel plots: determination of related corrosion parameters

In this subsection, the Tafel plots were drawn to determine extended corrosion parameters such as current density and rate, porosity, protection efficiency and polarisation resistance to some extent which values dictate their corrosion behaviour and hence illuminating the most corrosion

resistant Ti specimen. The Tafel plots obtained for Ti based coatings are presented in Figure 7-14 and the extracted corrosion parameters are shown in Table 7-6.

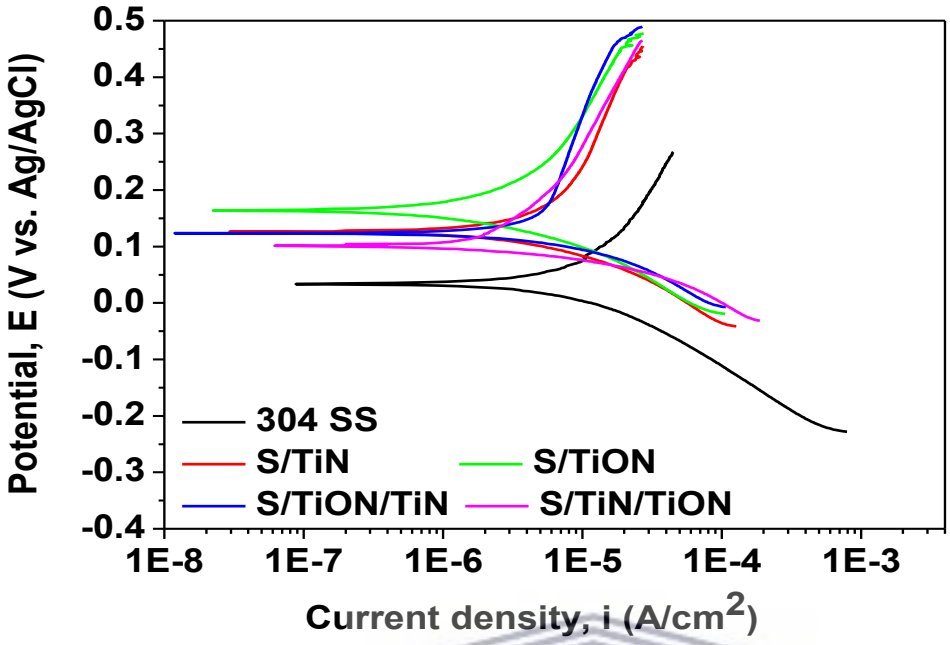

Figure 7.14: Tafel plots of Ti-based coatings

Table 7.6: Corrosion parameters of Ti and Cr-based coatings

	E_{oc} (mV)	E_{corr} (mV)	i_{corr} (µA/cm^2)	R_p (kΩ)	P	P_e (%)
SS	18	34	14.689	1.703	-	-
SS /TiN	205	126	7.734	6.450	0.001	47.3
SS /TiON	227	164	3.385	12.150	0.018	77.0
SS /TiN/TiON	214	101	3.723	7.170	0.040	74.7
SS /TiON/TiN	243	123	6.630	3.800	0.016	54.9

Figure 7-15 presents the Tafel curves of the coated and bare SS supports. Table 7.6 shows the corrosion potential (E_{corr}) and the corrosion current density (i_{corr}), extracted from Tafel plots. The results show that the most electropositive corrosion potential was displayed by the TiON monolayer, followed by TiN and SS/TiN/TiON. To recall, Pressouyre & Bernstein (1981) sustained that the grain boundary and voids can modify the kinetics of hydrogen evolution during the electrochemical process. Because hydrogen is a reversible trap at different points of dislocations, such as voids, this might be a reason for the measured shift to more positive values of the E_{corr} of coatings with smaller grain size values (Darken and Smith 1948). All the coated

surfaces showed decreased corrosion current density values together with a shift in the positive direction in the corrosion potential, indicating the decrease in the corrosion rate (Ahmad, 2006; Kirkland *et al.*, 2012) compared to the uncoated SS support. The R_p parameter, presented in Table 7-6, indicated the resistance of the investigated coatings when only a small perturbation was applied (±10 mV). In comparison with the uncoated SS support, all the Ti based coatings have a higher R_p value (with a factor of 2 to 4). SS/TiN/TiON bilayer had higher polarisation resistance, followed by TiON. This effect can be related to the double layer which acts as a greater barrier to the electrolyte penetration inside the defects found on the surface. Moreover, the lower porosity of the TiON layer (Table 7.5) could also be a reason for the high anticorrosion behaviour of this coating, which may be ascribed to O addition that blocked the electrolyte ingress. The combination SS/TiN/TiON had a higher protective efficiency (P_e) than that of SS/TiON/TiN, indicating that the TiON provided a good protection against corrosive attack when it is selected as the top layer or monolayer. The TiN monolayer exhibited the lowest protective efficiency. To summarise the Tafel results, one may observe that the TiON proved to have the best corrosion resistance in 0.1 M NaCl+6% H_2O_2, whatever the structure (as monolayer or top layer of bilayer).

Considering the monolayer structures, the high protective efficiency of TiON can be related to its chemical composition and low grain size as shown in Figure 7-15.

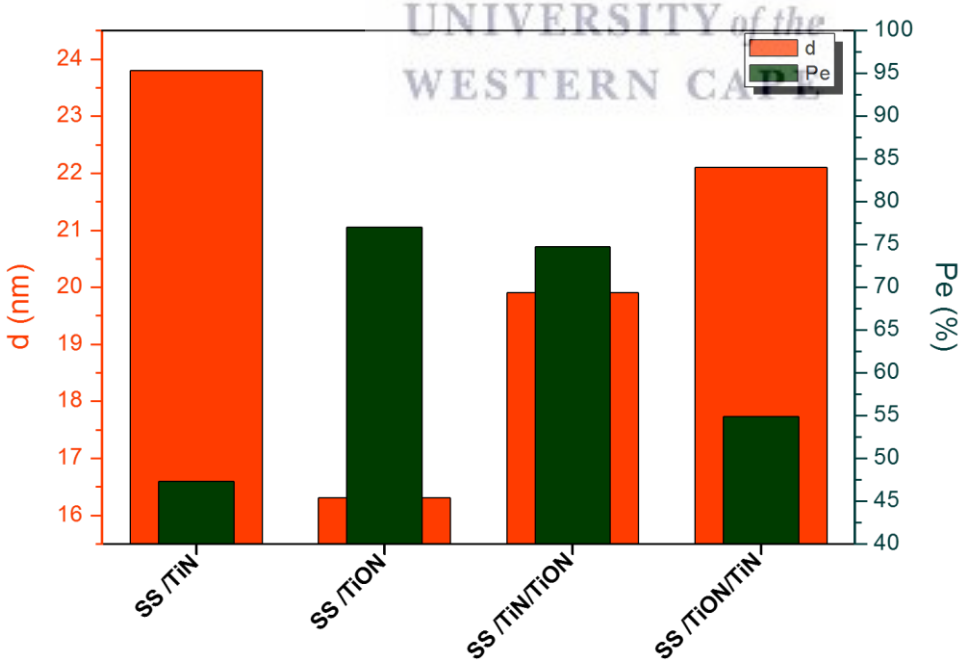

Figure 7.15: Protection efficiency (Pe) vs grain size (d) of investigated coatings

According to XRD measurements (Table 7-5), the oxygen addition in the TiN structure leads to decreased grain sizes values. The loss of a long range order in the oxynitride coating, compared to the nitride coating, was perhaps due to the competition between the growth of titanium nitride and oxide phases, taking place at the surface, since titanium presents a stronger affinity to oxygen than to nitrogen. The observed amorphisation of the oxynitride coatings are consistent with those reported by Bunjongpru et al. (2008) on aluminum oxynitrides, as the addition of small amounts of oxygen in the feed gas during deposition hindered the formation of a crystalline structure. In the literature many reports have tried to correlate the coating anticorrosive properties with respect to coating thickness (Rocha *et al.*, 2004; Patel *et al.*, 2010; Subramanian, Ananthakumar and Jayachandran, 2011), doping elements (Hassannejad *et al.*, 2010; Hua and Hou, 2012; Li and Fu, 2013; Cicek, 2014; Sedira *et al.*, 2014; Mansour, El-Dek and Ahmed, 2017) and grain size (QIN, LIAN and JIANG, 2010; Escobar, Caicedo and Aperador, 2014), but conclusive regular data are lacking. Therefore, it could be concluded that the grain size values represented just one cause of differences found in corrosion behaviour of Ti based coatings. The superior corrosion resistance of TiON as monolayer, which has the smaller grain size, could be explained by the fact that oxynitride can be easily passivated, especially in alkaline solution (Kinumoto *et al.*, 2015). The passivation process starts on the surface with smaller grain sizes, while the corrosion process is more active at the grain boundaries or along defects. The passive layer would prevent the Ti ions from migrating toward the surface and participating in the electrochemical reaction, or Cl^- minimise penetration inside the surface. Thus, it was accurate to conclude that the coating with smaller grain size exhibited a greater passive layer (Figure 7-14) which led to a low corrosion rate. Probably the poor corrosion resistance of the TiN coatings was related to its columnar growth, specific for the transition metal nitrides and stoichiometric carbides (Braic, A. C. C. Parau, *et al.*, 2014), with deeply separated columns, which accelerated corrosion due to micro electrochemical cells formed that led to an increase of the corrosion process. The same tendency was also observed in the case of HfN or VN coatings developed by Escobar et al. (2014). Next to these trends and complementarities observed in Ti based coatings, the determination of Ti coatings roughness and surface morphology after the corrosion test was also essential to depict intrinsic alterations and physical changes that occurred on SS protective coatings.

7.6.5.3 Roughness and surface morphology of Ti based coatings after corrosion measurement

Corrosion processes described in this chapter mostly occurred on the surfaces of the coated or uncoated electrodes. Consequently it was vital to investigate the coatings' roughness and surface morphology after the corrosion study to verify whether the trends discussed above compliment the physical changes observed on Ti coatings after the electrochemical corrosion process. In this regard, the roughness of Ti coatings was measured using the same method presented in Section 3.6.7.1 and the results are shown in Figure 7-16.

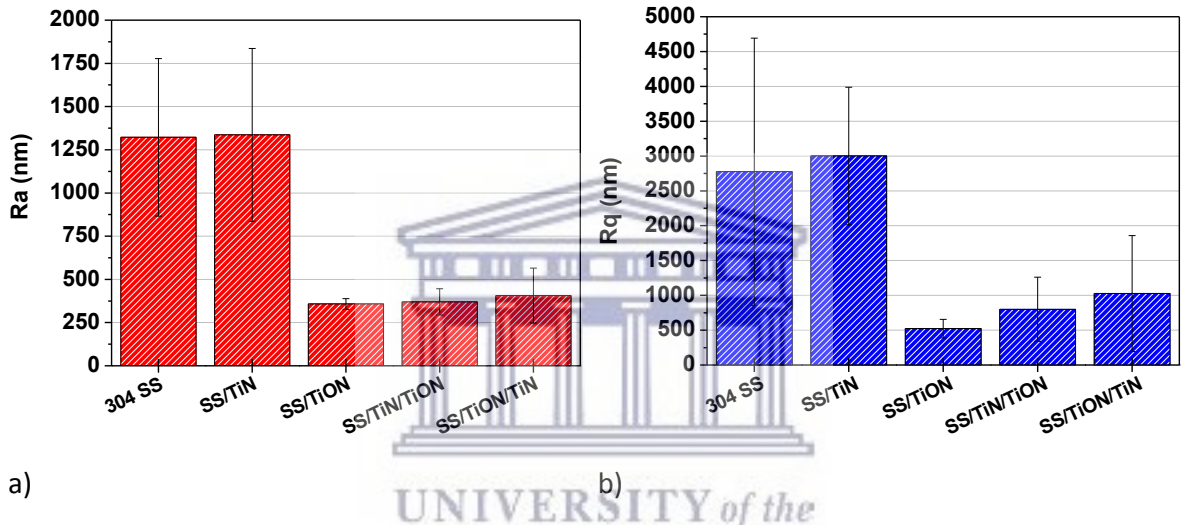

Figure 7.16: The roughness of Ti-based coatings after corrosion test

Figure 7-17 presents the R_a and R_q roughness parameters of the coating at the end of the corrosion tests. Usually, the initial roughness of a coating determines the increase of the electrochemical reactivity and the corrosion process (Cachet *et al.*, 2006; Park *et al.*, 2013; Gira, Tkacz and Hampton, 2016; Sivakumar, Pathak and Singh, 2017), as such an increase of the coating roughness is observed at the end of the corrosive attack. By comparing the results presented in Figure 7-17 and Figure 7-12, one may observe that the uncoated SS support was significantly affected by the corrosion process; so that R_a value increased after corrosion by a factor of 28%. An important difference in R_a values was also found for the TiN monolayer (~ 3.2%), indicating that its surface was also considerably affected by the corrosion process. The weak corrosion resistance of TiN could be ascribed to the presence of numerous microdroplets on its surface, which presented areas where the corrosion attack was more active.

For the bilayers, the differences in roughness before and after corrosion were not substantial, just a slight increase in R_a was observed after the corrosion tests, signifying that these surfaces were less affected by the corrosion process. Regarding the TiON monolayer, a small increase in roughness was found after the corrosion tests, indicating that the surface of this coating was just a bit polished by the corrosion process – probably the highest peaks were flattened. The low roughness of the TiON manolayer, providing a low surface for the contact with the electrolyte, hindered the abundant formation of micro electrochemical cells by limiting chlorine ions penetration inside valleys found on the surface, resulting in a superior corrosion resistance of the TiON monolayer.

Furthermore, the surface morphology of all coatings at the end of the corrosion tests was investigated by SEM analysis and the SEM images of Ti coatings are presented in Figure 7.18. The outcomes displayed in Figure 7.18 show that many corroded particles and some pits were detected on the TiN surface, while on the TiON surface only some corroded particles were found, indicating that the second coating exhibited a better corrosion resistance. Regarding the bilayers, pits were observed on both surfaces and corroded particles were more noticeable on the bilayer with TiN on top. The SEM images after the corrosion tests are in good agreement with the corrosion results and the roughness parameters values disclosed in Table 7-6 and Figures 7-12 and 7-16.

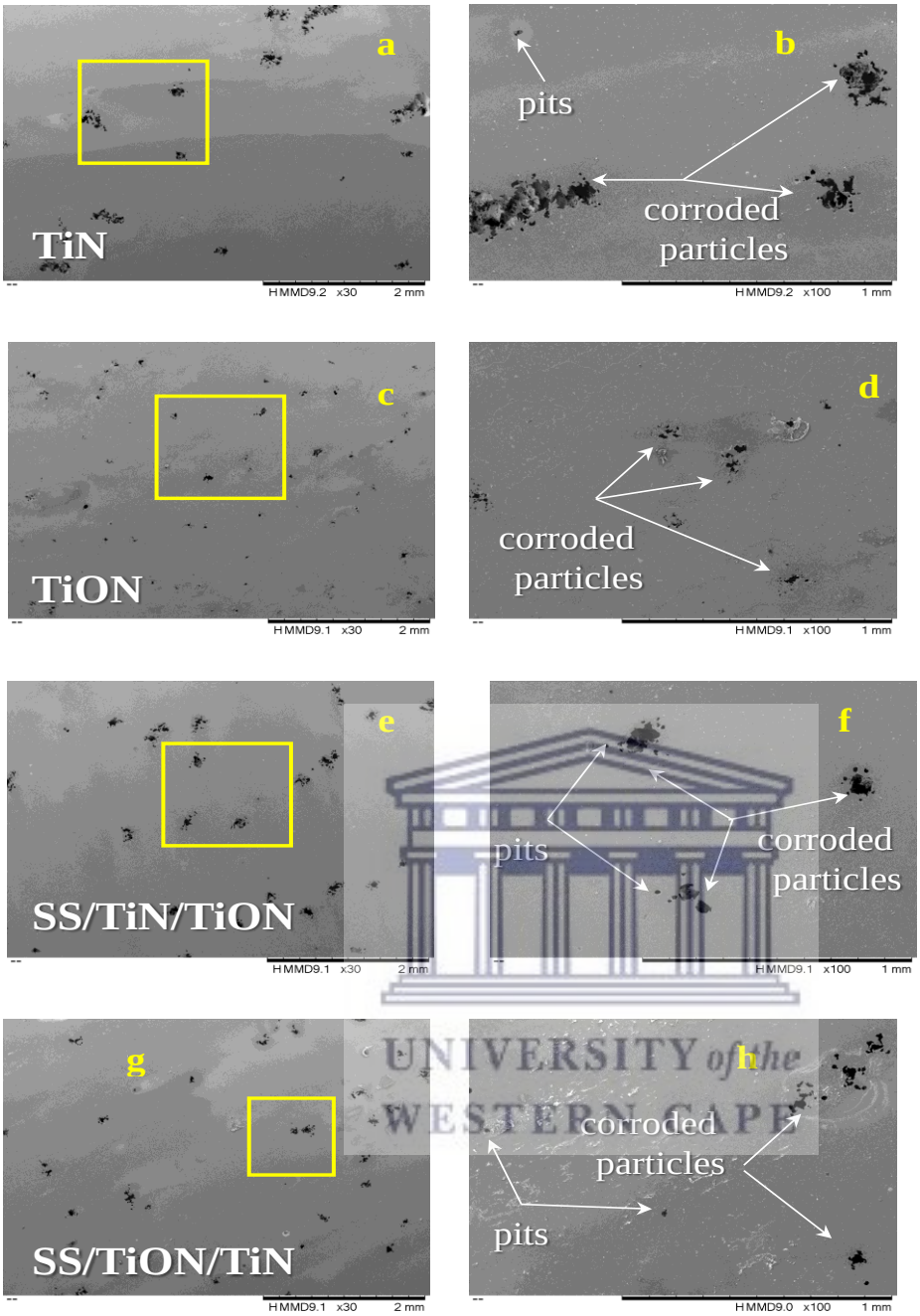

Figure 7.17: SEM micrographs of the Ti-based coatings after corrosion test (TiN (a & b), TiON(c & d), SS/TiN/TiON (e & f), SS/TiON/TiN (g & h).

In summary in section 7.2 on the corrosion study of Ti based coatings, the Ti coatings were successfully achieved by CAE, and their corrosion behaviour was evaluated in 0.1M NaCl + 6% H_2O_2 acidic environment. The roughness and surface of Ti coatings before and after corrosion were investigated by surface profilometry, SEM and AFM, correspondingly. The results from these analyses showed that most of the Ti films before corrosion had minimal roughness which increased in some cases after corrosion. On the other hand, the SEM analysis

showed that the surfaces of Ti coatings before the corrosion test were smooth and uniform; however some cracks and pits were detected on their surfaces after the corrosion test. Furthermore, the corrosion behaviour showed that SS/TiON and SS/TiON/TiN were respectively the most corrosion resistant layers followed by SS/TiN/TiON and TiN coatings, correspondingly.

7.7 Summary of chapter seven

In this chapter, two sets of Cr and Ti-based coatings were successfully prepared by the cathodic arc method in both mono and bilayered structures. The corrosion behaviour of these films was evaluated by potentiodynamic techniques in 0.1M NaCl+ 6% H_2O_2 (pH=4), at room temperature using a Versa Stat 3 Potentiostat/Galvanostat. The roughness and surface morphologies before and after corrosion tests in both cases were determined by surface profilometry, SEM and AFM analyses, correspondingly. In the case of Cr based coatings, the corrosion results showed that the Cr-N coating, as mono or bilayer, had high porosity and lower protective performance. The protective efficiency of Cr (N, O) coating (99.1%) and porosity (0.007) were excellent compared to that of 304 SS substrate and other coatings, because this Cr (N, O) coating was dense, less porous and more adherent to the substrate. Both bilayer coatings substantially improved the corrosion protection of 304 SS steel. The bilayer with Cr (N, O) on top possessed the best corrosion resistance behaviour having the lowest current density corrosion and consequently the highest protective efficiency and the lowest porosity. The corrosion resistance was ranked in the following order: Cr (N, O) > Cr-N/ Cr (N, O) > Cr (N, O)/Cr-N > Cr-N. In contrast, for the Ti- based films, the XRD diffraction patterns showed only TiN phases in rocksalt structure and (111) and (222) preferred orientations. Both mono and bilayer oxynitride coatings deposited on 304 SS substrate were smooth and homogeneous, having a low number of microdroplets. The oxygen addition in TiN structure led to a decrease in grain size, with higher density of nucleation sites for the passive film, which determined an enhanced formation of a passive layer, and thus a superior corrosion resistance. The SS/TiN/TiON bilayer had a higher protective efficiency than SS/TiON/TiN bilayer, indicating that TiON presented a better protection against corrosive attack when selected as top layer or monolayer. Consequently, the corrosion outcomes achieved in this chapter demonstrated that SS can be effectively coated with transition metal layers such as Cr and Ti-based coatings. In this regard, the most corrosion resistant coatings (SS/TiON, SS/Cr-N/Cr (O,N) and SS/Cr

(O,N) identified in this study could be utilised as adequate catalytic supports that could protect SS substrate from corrosion invasion in oxidative environments.

CHAPTER EIGHT: IMMOBILISATION OF C-N-TIO_2 NANO CATALYST ON SS AND ANTICORROSION MESHES AND ON GLASS SUPPORTS: APPLICATION FOR PHOTOCATALYTIC REMOVAL OF O.II DYE

After SS mesh was successfully coated with anticorrosion layers as discussed in chapter 7, it was believed that the SS coated with Cr, Ti-based nitrides and oxynitrides could be used as potent photocatalytic supports. This was necessary to overcome the corrosion dilemma highlighted in chapter 8 as well as to alleviate the cost of post separation processes when using powder catalysts. Therefore, this chapter deals with the deposition of the sol-gel synthesised nano catalyst on different substrates including SS and anticorrosion meshes and on glass by dip-coating and spin coating, respectively at the applied conditions. That is, chapter 8 has been divided into two sections 8.1 and 8.2 which correspondingly cover immobilisation on C-N-TiO_2 on SS and anticorrosion meshes, and spin coating of C-N-TiO_2 on glass as a control system.

8 Dip coating of stainless steel and anticorrosion meshes with carbon-nitrogen doped TiO_2 Nano catalyst: Assessment of photo catalytic activity of the films

In this subsection, about 24 mg of C-N-TiO_2 nano catalyst sol gel was coated on (8 cm long x 2 cm large) SS and TiON, CrN/CrON, ZrON and ZrSiN/ZrSiON anticorrosion meshes by dip-coating and then pyrolysed at 350 ^oC (heating rate of 50 ^oC/min) for 105 min. Scanning electron microscopy coupled with energy dispersive spectroscopy (SEM-EDS) were used to investigate the surface morphology and elemental composition of the C-N-TiO_2 coated anticorrosion meshes. Thereafter, the photocatalytic activity of the films was assessed upon the degradation of O.II dye at the applied conditions as described in Section 3.7.2.

8.1 Scanning electron microscopy/energy dispersive spectroscopy: characterisation of SS and anticorrosion meshes coated with C-N-TiO_2 Nano catalyst

In order to understand the adhesion between the Nano catalyst C-N-TiO_2 and the metal supports, SEM-EDS analysis of the coated supports (SS and TiON and Cr-N/CrON anticorrosion meshes) was conducted and the results of these analyses are presented in Figure 8-1 and the EDS results are exhibited in Table 8-1.

Before coating

After coating

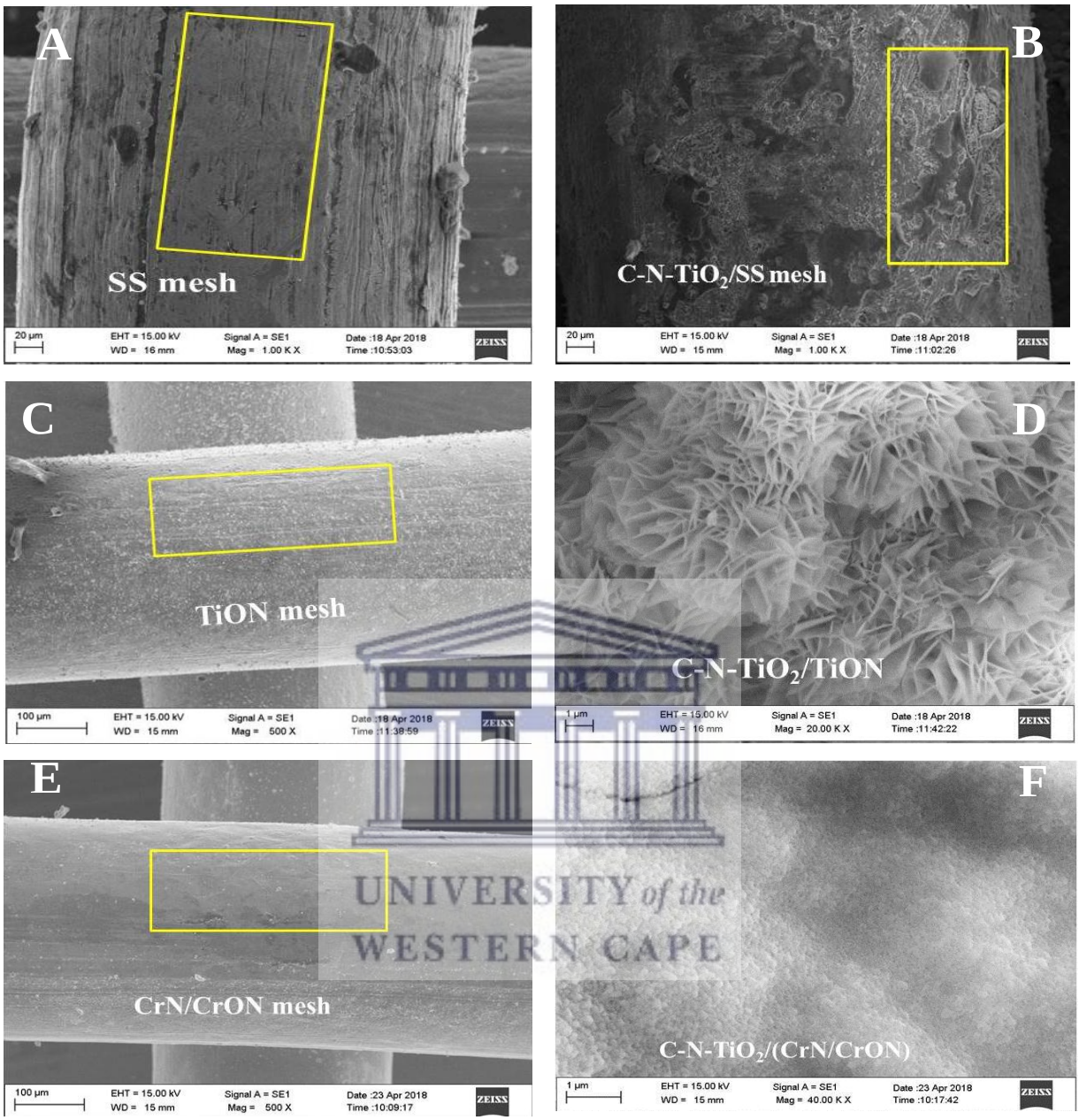

Figure 8.1: Scanning electron microscopy (SEM) and EDS micrographs of uncoated and C-N-TiO_2 coated stainless steel and anticorrosion meshes.

Table 8.1: Energy dispersive spectroscopy (EDS) of uncoated and C-N-TiO_2 coated stainless steel and anticorrosion meshes before photo catalysis.

Sample	C	Ti	O	Si	Cr	Mn	Fe	Ni	Zr	Cl
SS	1.52	-	30.16	12.96	22.01	48.07	34.08			
SS/C-N-TiO_2	3.14	6.10	30.40	0.45	1.12	0.72	4.16	2.84		1.34
SS/TiON	0.59	39.31	37.67	0.15	4.67	0.36	14.77	1.26		
SS/TiON/C-N-TiO_2	2.54	43.31	37.67	0.15	4.67	0.36	14.77	1.26		
SS/CrN/CrON	1.54	0.21	31.08	0.19	42.52	0.65	21.77	1.83		
SS/(CrN/CrON)/C-N-TiO_2	2.18	4.02	31.70	0.43	32.33	0.94	23.42	2.96		1.93

Figure 8-1 and Table 8.1 shows SEM micrographs and the qualitative elemental composition of the uncoated and C-N-TiO_2 coated SS and anticorrosion meshes. The SEM morphologies in Figure 8-1(B) show that, C-N-TiO_2 nano catalyst was successfully deposited on SS substrate. That is, the selected rough surface of uncoated SS in Figure 8-1 (A) changed to a region coated by C-N-TiO_2 nano composites in Figure 8-1(B). This was supported by the presence of Ti in SS/C-N-TiO_2 mesh shown by the elemental composition in Table 8-1. However, nitrogen (N) present in C-N-TiO_2 could not be detected by SEM-EDS, its content might have been smaller than the detection limit of the SEM-EDS instrument used for analysis. From SEM and EDS results obtained with SS/C-N-TiO_2, sol-gel was adhering on SS support. Besides SS, anticorrosion meshes mainly SS/TiON and SS/CrN/CrON were used as photocatalytic supports and coated with C-N-TiO_2 nano catalyst. The SEM-EDS analysis was carried out to investigate the adhesion of the nano photo catalyst layer on the selected supports. The SEM characterisation outcomes of SS/C-N-TiO_2/TiON and SS/(CrN/CrON)/C-N-$TiO_2$are presented in Figure 8-1(C-F). The EDS results of all C-N-TiO_2 coated anticorrosion meshes are provided in Table 8-1.

The micrographs in Figure 8-1 (C&D) shows that C-N-TiO_2 catalyst deposited on SS/TiON by dip coating appeared as well dispersed nano crystals and adhered to the SS/TiON support. This shows that C-N-TiO_2 catalyst was stable on SS/TiON. Similarly, the EDS results of C-N-TiO_2 deposited on various anticorrosion meshes show that C, O and Ti were present in the doped TiO_2 nano composites. As for SS/(CrN/CrON)/C-N-TiO_2, the SEM micrographs in Figure 8-1 (E&F) show that, C-N-TiO_2 adhered well to the anticorrosion supports. The C-N-TiO_2 nano crystals formed on SS/CrN/CrON support surface exhibited a condensed shape. The trace amount of Ti identified in SS/CrN/CrON by EDS in Table 8-1 slightly increased in the coated SS/(CrN/CrON)/C-N-TiO_2 hence qualitatively showing the presence of Ti resulting from C-N-TiO_2 nano catalyst. Otherwise, improving the deposition technique of the TiO_2 catalyst on the

anticorrosion mesh should receive further attention. Tijani et al. (2017) showed that a temperature range that varied from 300 to 400^{o}C had an impact on the physical and chemical properties of the synthesised C-TiO_2 nano composites. Similar trends were also observed by Pang et al. (2010) who showed that a temperature range from 300 to 900 ^{o}C had an influence on Nano tubes of TiO_2 morphologies. So the 350 ^{o}C pyrolysis temperature used in this study for 105 min fell within these ranges. In summary, during this characterisation process, the SEM images of the uncoated and coated substrates showed that C-N-TiO_2 photo catalyst was well deposited on the anticorrosion supports. However, the morphologies of the nano C-N-TiO_2 on these substrates differed from one another probably because of the internal elemental composition of each substrate or the pyrolysis temperature that should be further investigated. Furthermore, in all EDS results presented in Table 8-1 of this study, N could not be identified by SEM-EDS, but its presence in C-N-TiO_2 nano catalysts was proved in Section 6.1.3 of Chapter 6 by TEM-EDS and EELS analysis.

8.2 Photocatalytic performance of the uncoated and coated meshes on the degradation of O.II dye

The photocatalytic effect of uncoated and C-N-TiO_2 dip coated SS, SS/TiON and SS/CrN/CrON anticorrosion meshes on the decolouration of orange II dye was investigated at the applied conditions as given in section 3.6.6.3 and the results of these experiments are subsequently presented in Figures (8-2) for SS and SS/C-N-TiO_2; Figure (8-3) for uncoated SS/TiON and SS/CrN/CrON anticorrosion meshes and Figure 8-4 for C-N-TiO_2 coated SS/TiON and SS/CrN/CrON anticorrosion supports.

8.2.1 Photocatalytic performance of uncoated and C-N-TiO_2 coated SS mesh

In this section the photocatalytic effect dictated by UV-vis analysis of both uncoated SS and SS mesh coated with C-N-TiO_2 on the % decolouration of orange II dye at the applied conditions ([O.II] 5 mg/L, volume 500 mL, pH 2.5, Mega-Ray 160 W/240 V MR160 UV lamp, and irradiation time of 120 min (n = 2)) was assessed and the comparative results are presented in Figure 8-2.

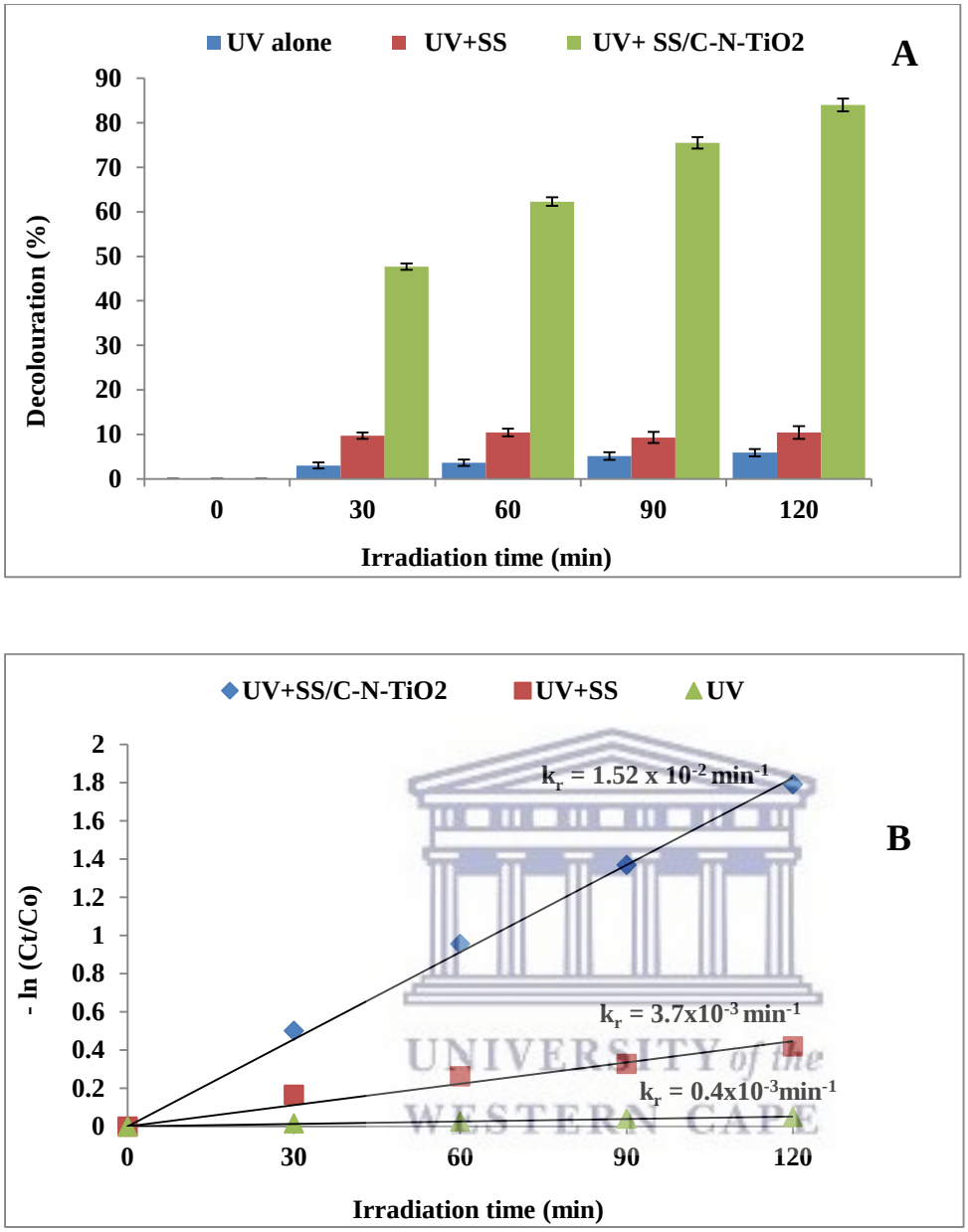

Figure 8.2: Photocatalytic activity of uncoated and C-N-TiO_2 coated stainless steel meshes for the decolouration of orange II (O.II) dye (A) and kinetics (B). Experimental conditions: [O.II] 5 mg/L, volume 500 mL, pH 2.5, Mega-Ray 160 W/240 V MR160 UV lamp, and irradiation time of 120 min (n = 2).

Figure 8-2 presents the photocatalytic decolouration efficiencies of uncoated and coated SS meshes (Figure 8-2A) and the rate constant during decolouration of orange II at the corresponding conditions (Figures 8-2 (B). The results in Figure 8-2 (A) show that high decolouration percentage of orange II dye (84 %) was achieved with C-N-TiO_2 dip coated and annealed on SS mesh (C-N-TiO_2/SS), compared with 9.4 % and 4.8% reached with SS + UV and UV alone, respectively. SS+UV was used as a control and these results showed that

coating SS with C-N-TiO_2 catalysts improved the removal of O.II about 17 times more compared to UV light alone, hence by a ratio of 17:1. SS has been proven unstable in acidic environments due to erosion of its passive layer that often leads to its corrosion (Tijani et al. 2017). In addition, it might be possible that the pre-treatment of SS mesh before catalyst deposition activated SS instability. So, the deposition of C-N-TiO_2 sol-gel on SS resulted in bonding adherence of TiO_2 coatings after pyrolysis at the applied conditions. This can be seen from SEM images shown in Figure 8-1(B) which exhibited catalyst delamination after pyrolysis of coating and hence before photo catalytic irradiation of O.II dye. The presence of transition metals (TMs) in uncoated and coated SS and anticorrosion supports highlighted by the elemental composition in Sections 7.1.1 and 7.5.4.2 of Chapter 7 in the solution might have accelerated the decolouration of O.II (Wu *et al.*, 1999; Ma *et al.*, 2006; Kinumoto *et al.*, 2015). Similar studies on sol gel deposition of TiO_2 doped or co-doped catalysts on SS have been conducted and high decolouration efficiencies were also achieved (Shin and Jeong, 2012; Ramasundaram *et al.*, 2013, 2016; Zhuo *et al.*, 2014). These results further confirm that the advanced oxidation using of UV+C-N-TiO_2/SS was effective as an oxidative route that can be used as treatment method for the decolouration of persistent organic dyes from wastewater before being discharged into the environment. The kinetic results presented in Figures 8-2 (B) showed that the photocatalytic decay of orange II dye over time followed a first order reaction as expressed in Equation 8.1.

$$d\frac{[\mathrm{O.II}]}{\mathrm{dt}} = -\mathrm{kr}[\mathrm{O.II}] \quad 8.1$$

Where [O.II] is the concentration of O.II and k_r the rate constant (per minutes).

So Equation 8.1 could be reorganised to Equation 8.2 as follow:

$$\mathrm{d}\frac{[O.II]}{[O.II]} = -krdt \quad 8.2$$

At t = 0 min, the concentration of orange II corresponded to $[O.II]_o$ and $[O.II]_t$ the concentration of orange II at time t. Therefore, the integration of Equation 8.2 results in the following:

$$\int_{[O.II]o}^{[O.II]t} \frac{d\,[O.II]}{[O.II]} = -kr\int_0^t dt \quad 8.3$$

$$\ln([O.II]_o^t) = -krt \quad 8.4$$

$$\Leftrightarrow \ln([O.II]_t - [O.II]_o) = -krt \quad 8.5$$

$$(\ln(\frac{[O.II]t}{[O.II]o}) = -\,k_r t \Leftrightarrow -(\ln(\frac{[O.II]t}{[O.II]o}) = k_r t \quad 8.6$$

So as to assess the kinetic behaviour for the decomposition of O.II over time, $-(\ln(\frac{[O.II]t}{[O.II]o})$ was plotted against time (t) for each photocatalytic system as presented in Figures 8-2- 8-5. Likewise, it could be observed that the plot of the first order reaction for the decolouration of

orange II presented in Figures 8.2 (B) gave a straight line whose slope corresponded to the rate constant (min^{-1}). In the case of uncoated and coated SS mesh, results exhibited in Figures 8.2 (B) show that the rate constant for the decolouration of O.II was slow with UV alone (0.4 $x10^{-3}$ min^{-1}) as well as UV + SS (7.3 $x10^{-3}$ min^{-1}) but increased to 1.52 $x10^{-2}$ min^{-1} with coated C-N-TiO_2/SS irradiated with UV. In comparison, the decoloration rate 1.52 $x10^{-2}$ min^{-1} of O.II achieved with C-N-TiO_2/SS film under UV light was higher than 1.21 $x10^{-2}$ min^{-1} O.II decoloration rate reached with powder 105 min C-N-TiO_2 catalyst under UV light at the same conditions shown in Section 6.2. This further proved that the immobilised C-N-TiO_2 on SS support improved the decolouration of O.II by 15 % and hence compliments the review of catalyst immobilisation earlier stated in Section 2.5 of chapter 2.

8.2.2 Photo catalysis of the uncoated anticorrosion coatings

The following mono and double layers coatings, SS/TiON and SS/CrN/CrON were identified as the most corrosion resistant coatings in acidic environments (Dinu et al. 2018.). Therefore, in the current study the photo catalytic effect of the SS supports without corrosion layers but without coating of C-N-TiO_2 nano catalyst was investigated for the decolouration of orange II dye and the outcomes of these experiments are presented in Figure 8.3.

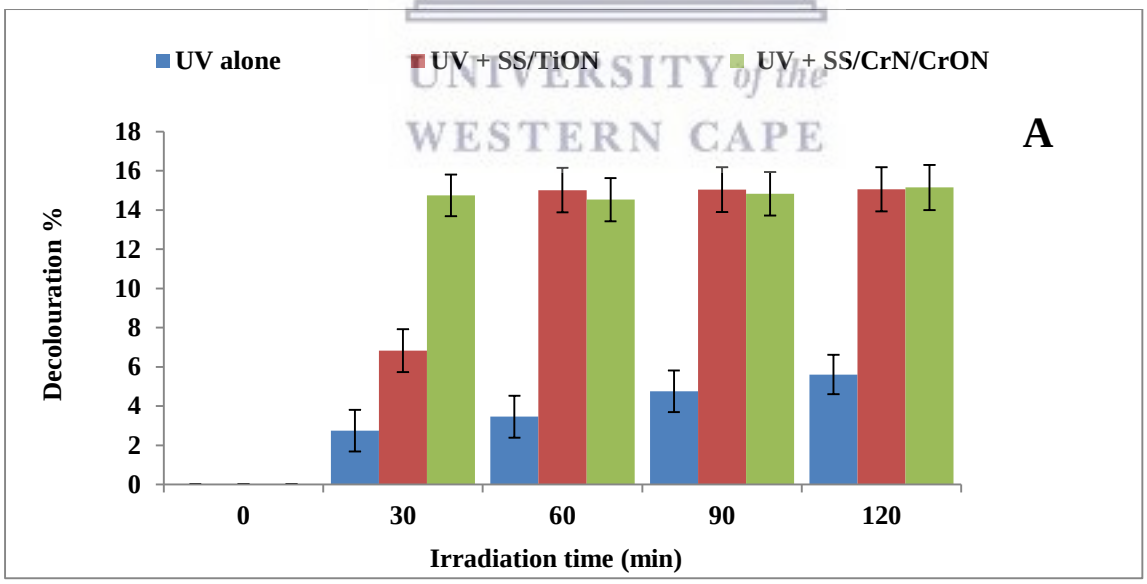

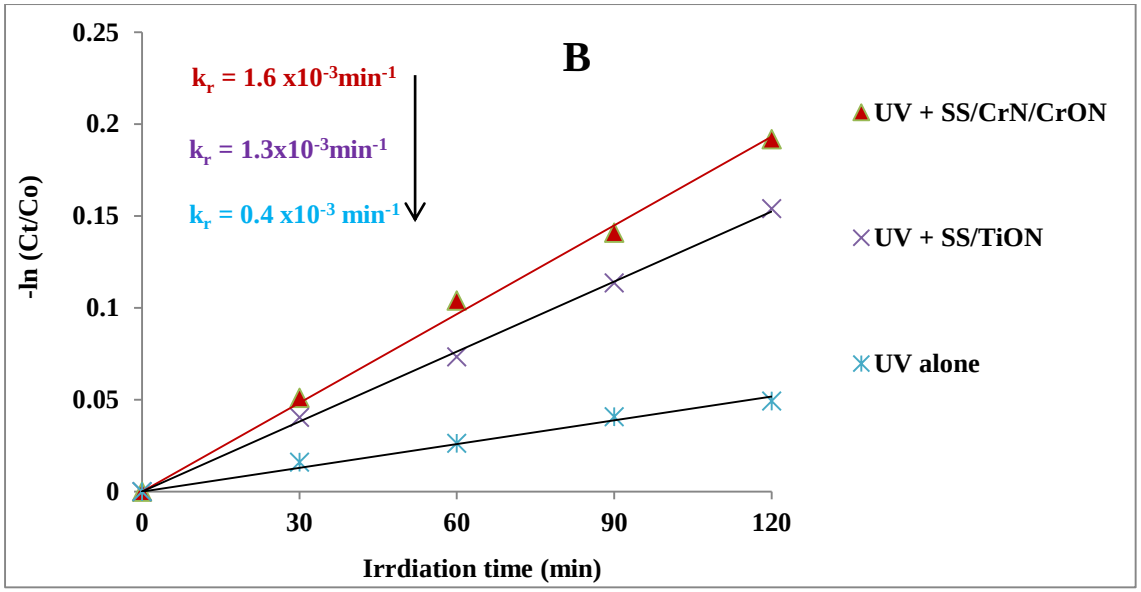

Figure 8.3: Photocatalytic activity/decolouration percentage (A) and kinetics (B) of anticorrosion coatings without a catalyst for the degradation of orange II (O.II) dye. Experimental conditions: [O.II] 5 mg/L, pH 2.5, volume 500 mL, Mega-Ray 160 W/240 V MR160 UV lamp and an irradiation time of 120 min (n =2).

Figure 8.3 shows the photo catalytic performance of the SS supports with various anticorrosion coatings for the decolouration of orange II dye (A) and the evolution of the decolouration rate constant of O.II achieved with each mesh during its exposure to UV light (B). Figure 8.3(A) shows that the anticorrosion coatings without the additional nano catalyst exhibited a low photocatalytic activity for the decolouration of O.II dye even though after 120 min of UV exposure, 15.06 % dye removal was reached with SS/CrN/CrON followed by 15.03 % achieved with SS/TiON coatings, respectively. In Figure 8.3(A), it could be observed that the decolouration of orange II reached about 5 % with UV alone. In comparison with uncoated SS supports, it can be estimated that anticorrosion coatings contributed to approximately 10.06 % of O.II removal reached with SS/CrN/CrON after 120 min of UV exposure followed by 10.3 % achieved with SS/TiON, respectively after the same time. This trend was supplemented by the kinetic results presented in Figure 8.3 (B) whereby a slightly elevated rate constant during irradiation of O.II dye was noticed with SS/CrN/CrON (1.6x10^{-3} min^{-1}), which was higher than 1.3 x10^{-3} min^{-1} obtained with SS/TiON, correspondingly. These results showed that uncoated anticorrosion coatings do have some photocatalytic activity which could be due to their redox behaviour in oxidative environment.

8.2.3 Photo catalysis of C-N-TiO_2 coated anticorrosion coatings

After proving that anticorrosion meshes without the nano catalyst were not highly photo catalytically active, the anticorrosion meshes were coated with C-N-TiO_2 as specified in Section 3.5.3.1 and their photocatalytic performance results were obtained as described in Section 3.6.6.3 and are plotted in Figure 8.4.

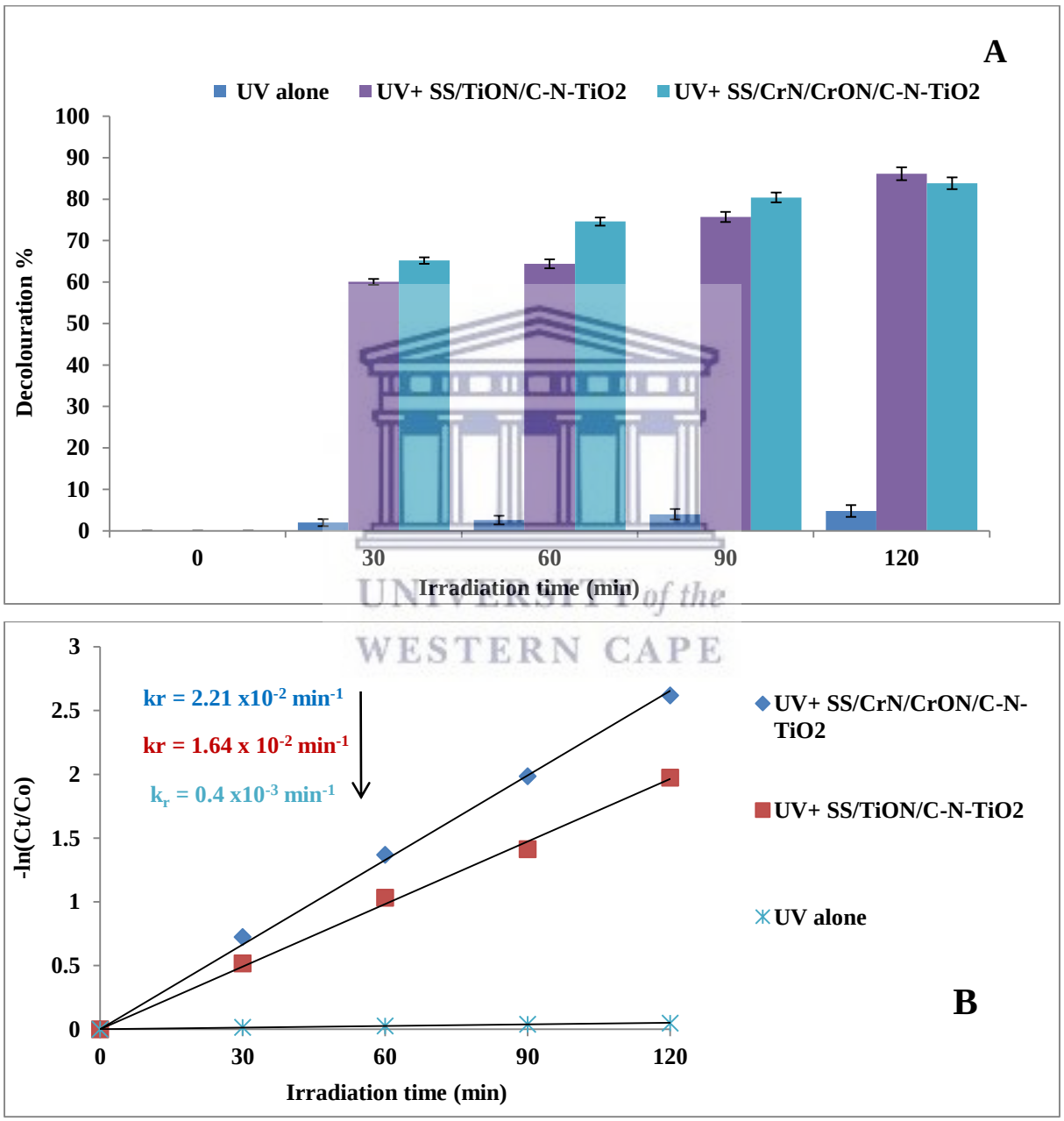

Figure 8.4: Photocatalytic activity/decolouration efficiency (A) and kinetics (B) of anticorrosion coatings coated with C-N-TiO_2 nano catalysts for the decolouration of orange II

(O.II) dye. Experimental conditions: [O.II] 5 mg/L, pH 2.5, volume 500 mL, Mega-Ray 160 W/240 V MR160 UV lamp and an irradiation time of 120 min (n = 2).

The decolouration of orange II in Figure 8.4 (A) shows that the best removal of orange II was achieved with SS/CrN/CrON coated with C-N-TiO_2 nano composite (SS/(CrN/CrON)/C-N-TiO_2) for sampling times below 120 min. For instance after 90 min of UV irradiation, 80.4% of O.II removal was obtained with SS/(CrN/CrON/C-N-TiO_2) compared to 75.7% dye decolouration attained with SS/TiON/C-N-TiO_2, respectively. These results were ascribed to the effectiveness of the C-N-TiO_2 coatings (Tijani et al. 2017) that achieved over 70 % removal of O.II as demonstrated in Section 6.2.2 of Chapter 6 of this study. These results confirm that C-N-TiO_2 is photo catalytically effective and the anticorrosion meshes can be utilised as excellent and durable supports. Similar trend was also observed after 30 and 60 min of UV exposure. After 120 min of photo catalysis, 83.6% and 86.12% decolouration of O.II was achieved with SS/(CrN/CrON)/C-N-TiO_2 and SS/TiON/ C-N-TiO_2, accordingly. These findings were complimented by kinetics presented in Figure 8 (B) which show that the fastest O.II removal was reached with SS/(CrN/CrON)/C-N-TiO_2 followed by SS/TiON/ C-N-TiO_2, corresponding to rate constants of 2.21 $x10^{-2}$ min^{-1} and 1.64$x10^{-2}$ min^{-1}, respectively. These further confirm that anticorrosion coatings can successfully be used as catalytic supports to achieved desired catalytic efficiencies. Indeed, the morphology of C-N-TiO_2 on SS and anticorrosion meshes varied from well dispersed crystals, condensed nano crystals, smoothed to nano road shapes which all probably absorbed the UV light differently. This consequently confirmed that the morphology of the catalyst can impact upon its properties such as photocatalytic activity. Subtle differences in morphology were induced by the underlying anticorrosion coating.

8.2.4 Kinetics study for the degradation of orange II

In addition to the rate constant discussed in Figures 8.4 (B), the half-life ($t_{1/2}$) was selected as supplementary indication of the first order chemical decomposition of O.II also presented in Figures 7. (2-4). This indicator denotes the time taken for the concentration of orange II to decrease to half its initial concentration during the photo catalysis process. Hence the time taken for the concentration of orange II to decline from $[O.II]_o$ to $1/2[O.II]_o$ in the first –order reaction of each catalyst system was mathematically expressed in Equation 8.7.

$K_r t_{1/2} = -\ln(\frac{1/2[O.II]_o}{[O.II]_o}) = -\ln(\frac{1}{2}) = \ln 2 = 0.693$

Therefore, $t_{1/2} = \frac{ln2}{Kr} = \frac{0.693}{Kr}$ 8.7

So from Equation (8), it could be noticed that from the first order decomposition of O.II, its half-life is independent of its initial concentration. Therefore, at t = 0 min, [O.II] = 5 mg/L has fallen to ½ $[O.II]_o$ after further integration of $ln2/k_r$. Consequently Equation (8.7) was used to approximate the half-life of orange II dye during UV irradiation in the presence of composite catalysts on various supports. Therefore, the rate constant (k_r), correlation coefficient (R^2) and calculated half-life of O.II dye decompositions of each oxidation process are presented in Table 8-2.

Table 8.2: Kinetics parameters for the degradation of orange II dye at the following conditions: [O.II] 5 mg/L, pH 2.5, solution volume 500 mL, Mega-Ray 160 W/240 V MR160 UV lamp and an irradiation time of 120 min.

Oxidation process	K_r/min	Correlation coefficient (R^2)	Half- life (min)
UV alone	$0.4x10^{-3}$	0.9869	1732.5
Uncoated and coated SS meshes			
UV + SS	$3.7x10^{-3}$	0.9474	187.3
UV + SS/C-N-TiO_2	$1.52x10^{-2}$	0.9974	45.59
Uncoated anticorrosion meshes			
UV+SS/TiON	$1.3x10^{-3}$	0.9989	533
UV+SS/(CrN/CrON)	$1.6x10^{-3}$	0.9965	433
Coated anticorrosion meshes			
UV + SS/TiON/C-N-TiO_2	$1.64\ x10^{-2}$	0.9971	42.256
UV+ SS/(CrN/CrON)/C-N-TiO_2	$2.21x10^{-2}$	0.9984	31.35

The results presented in Table 8-2 show that of all prepared composite samples, the highest rate constant for the photo catalytic degradation of O.II $2.21\ x10^{-2}\ min^{-1}$ was achieved with SS/(CrN/CrON)/C-N-TiO_2 followed by $1.64\ x10^{-2}\ min^{-1}$ and $1.52\ x10^{-2}\ min^{-1}$ obtained with SS/TiON/C-N-TiO_2 and SS/C-N-TiO_2, individually. These rate constants indicate how fast O.II dye was decoloured by each composite. So at such rates, the half-lives approximated in Table 8-2 describe how long it took for the O.II concentration to fall to half its initial value (½

$[O.II]_o$). That is, it took about 31 min for O.II concentration to decay to 5/2= 2.5 mg/L when O.II was irradiated in the presence of SS/(CrN/CrON)/C-N-TiO_2 coated catalyst. This was confirmed by the 65. 2% O.II decolouration achieved after 30 min of UV exposure as shown in Figure 8-4 (A). Alternatively, about 42.3 and 45.6 correspond to the time elapsed for O.II concentration to decline to 2.5 mg/L during UV irradiation with SS/TiON/C-N-TiO_2 and SS/C-N-TiO_2, distinctively. Furthermore, it would have taken longer (1732 min) for O.II concentration to go down to 2.5 mg/L during its irradiation with UV alone, independently. So the rate constants and half-lives recorded in Table 8-2 sustain that stainless steel supplemented with its anticorrosion layers could be used as convenient photocatalytic supports in AOPs, and their subsequent coating with doped heterogeneous nano photo catalysts can significantly improve the removal of persistent organic dye from wastewater, preferably before being discharged into the environment. These results sustain those achieved in section 5.3 of chapter 5 and proved that the sol-gel synthesised C-N-TiO_2 could be deposited on solid supports such as SS or SS protected with anticorrosion layers. However, the procedure used for the C-N-TiO_2 coatings and its incorporation in typical configuration such as DBD could be challenging at industrial scale and may require alternative types of supports and different catalyst deposition techniques. Therefore, in the next Section spin coating of the sol gel and glass as support was evaluated.

8.3 Spin coating immobilisation of C-N-TiO_2 gel on glass and application for photocatalytic removal of orange II sodium salt dye

In order to improve the sol gel coating procedure and avoid corrosion, the spin coating technique was developed and glass (as substitute for quartz) was used as support.

The most important parameters investigated in this section include the spinning rotating speed and the viscosity (sol gel precursor-solvent volume ratio) of the sol gel precursor to the catalyst at the applied conditions. To recall, C-N-TiO_2 nano catalyst was separately prepared by the sol-gel method involving the dissolution of PAN in DMF solvent stirred for 24 hours at room temperature, resulting in a gel in which $TiCl_4$ and NH_4NO_3 were subsequently added as sources of Ti and N, respectively. The obtained sol-gel was then spincoated on glass support and annealed at 350 ^oC at a ramping rate of 10^oC/min for a holding time of 105 mins. This was previously detailed in experimental sections 3.5.1 and 3.5.3.2 of chapter 3. Hence the experimental results of the effect of spin coating speed (for C-N-TiO_2/glass films) on the photocatalytic decolouration of O.II dye are subsequently presented in the paragraphs below.

8.3.1 Effect of spin coating speed on the thickness of C-N-TiO_2 thin films

The influence of coating speed on the thickness of thin films of the sol gel precursor was assessed by varying the speed from 2000, 2300; 2600 to 2900 rpm while the sol gel-solvent volume ratio 3 mL of sol gel diluted in 5 mL of DMF solvent and spinning time of 90 minutes were kept constant. The thickness of films after thermal annealing at 350 ^{o}Cwas determined by Dektak profilometry analysis (n = 2) and the results of this investigation are presented in Table 8-3 and plotted in Figure 8-5.

Table 8.3: Effect of spin coating speed on the thickness of the C-N-TiO_2 films: sol gel: solvent ratio (v: v) = 3 mL of sol gel diluted in 5 mL of DMF solvent (3:5), spin coating time 90 S. The samples were pyrolysed in N_2 at 350 ^{o}C (ramping rate of 10^{o}C/min) for 105 mins.

Coating speed (rpm)	Sol gel to DMF solvent volume ratio (v:v)	Annealed C-N-TiO_2 film thickness (nm) n = 1	Annealed C-N-TiO_2 film thickness (nm) n = 2	Average thickness (nm)	Standard deviation	Mass (g) of C-N-TiO_2 on films
2000	3:5	539.4	564	551.7	± 17.39483	0.23295
2300	3:5	459.6	432.1	445.85	± 19.44544	0.2198
2600	3:5	383.4	329.4	356.4	± 38.18377	0.2197
2900	3:5	329.1	157.1	243.1	± 121.6224	0.21695

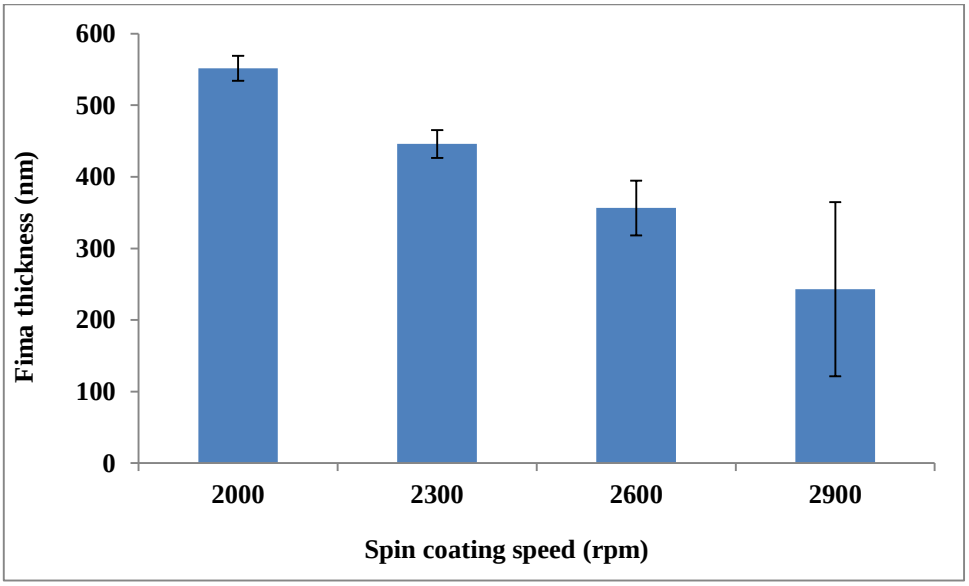

Figure 8.5: Effect of rotational coating speed on the annealed C-N-TiO_2 film thicknessobtained at the following conditions: sol gel to solvent volume ratio (v: v) 3:5, spinning time 90 min. The samples were pyrolysed in N_2 at 350 ^oC (ramping rate of 10^oC/min) for 105 mins where after the thickness of the annealed was determined by Dektak profilometry analysis (n = 2).

The results in Figure 8-5 show that the annealed C-N-TiO_2 film thickness correlated inversely with an increase of rotational speed. The thickest films of 551 nm were achieved at 2000 rpm followed by 445 nm at 2300 rpm at the applied conditions described in Figure 8-5. Likewise, the coatings of 356 nm and 243 nm were obtained at speeds of 2600 and 2900 rpm, respectively as shown in Table 8-4. Consequently, the thinnest film thickness was reached at 2900 nm. These results showed that 243 nm thin films could be obtained at high rotational speeds. A similar trend related to the spin coating showed that the mass of the C-N-TiO_2 catalyst deposited on the glass decreased with an increase of spin coating speed as shown in Table 8-4. This further inferred that, spin coating speed is a very crucial parameter in film engineering that needs to be considered. For optimisation purposes in this study, 2600 rpm was selected as the optimum rotation coating speed that was used throughout. Even though various studies on immobilisation of TiO_2 on glass have been conducted (Chen, Stathatos and Dionysiou, 2008; Pelentridou *et al.*, 2009; Pelaez *et al.*, 2010; Zhuang *et al.*, 2010; Han *et al.*, 2011; Han, Luque and Dionysiou, 2012; Stathatos *et al.*, 2012); only a few have studied the trend between sol gel spin coating speed and thickness of annealed film layers as described in this study.

Table 8.4: Mass (g) of C-N-TiO_2 deposited on films coated at different spinning speeds at the following conditions: sol gel-solvent volume ratio (v: v) 3:5, coating time 90 min. The samples were thereafter pyrolysed at 350 ^oC at a ramping rate of 10^oC/min for 105 mins (n = 2).

Spinning speed (rpm)	Average mass (g) of the C-N-TiO_2 film	Uncoated glass Average mass (g)	Mass (g) of C-N-TiO_2 used
2000	1.04465	0.8117	0.2329
2300	1.0315	0.8117	0.2198
2600	1.0314	0.8117	0.2197
2900	1.02865	0.8117	0.2169

8.3.1.1 Scanning electron microscopy and energy dispersive spectroscopy

The distribution the sol gel precursor had an influence upon the final annealed film of C-N-TiO_2 nano catalyst on the glass and the presences of C, Ti and O in the catalyst layers after the pyrolysis step were further evaluated by scanning electron microscopy coupled with energy dispersive spectroscopy (SEM-EDS) analysis. The SEM images of the obtained C-N-TiO_2 films at each rotation speed are presented in Figure 8-6. The composition of the each annealed film was measured by EDS and is presented in Table 8-4.

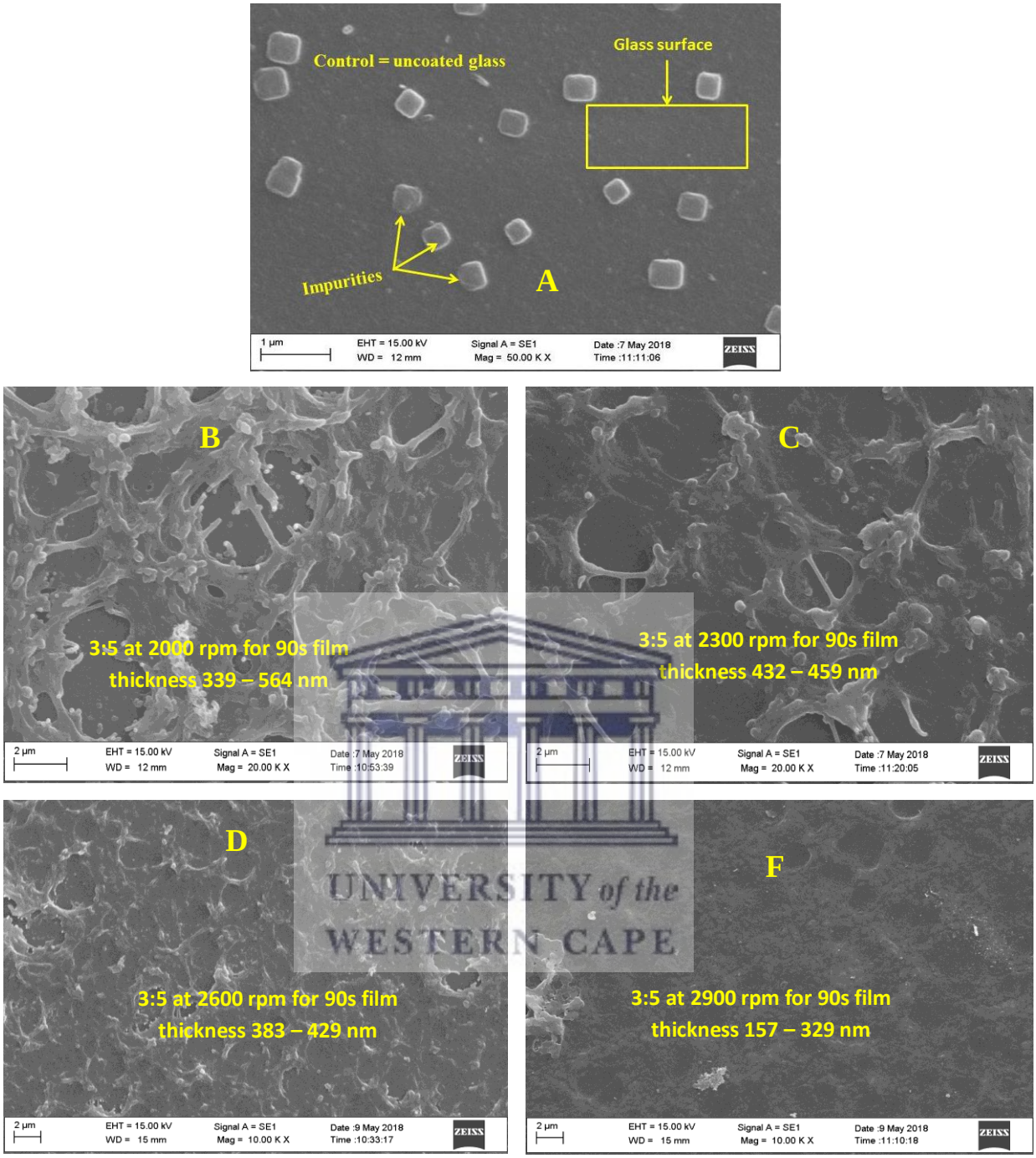

Figure 8.6: SEM morphology of annealed films of C-N-TiO_2 coated on glass at different rotating speed (2000, 2300, 2600 to 2900 rpm), and constant sol gel-solvent volume ratio of 3:5 for 90 seconds. The samples were annealed in N_2 at 350 ^oC (ramping rate of 10^oC/min) for 105 mins and the thickness of samples was determined by Dektak profilometry analysis.

The SEM images shown in Figures 8-6 present the morphologies of the annealed C-N-TiO_2 films that were prepared from the sol gel spun at rotational speeds from 2000, 2300, 2600 to 2900 rpm. Figure 8-6 shows that the highly porous network of C-N-TiO_2 nano catalyst was

well dispersed on the glass surface after annealing in N_2 at 350°C for 2 hrs. However, the morphology of the films changed with spin coating speed. For instance Figures 8-6 (B & C) taken of glass coated at 2000 and 2300 rpm show that a distinctive needle-like morphology formed upon the glass support, showing the nano composite was well dispersed on the glass surface and the layer thickness was 432 – 459 nm (Figure 8-7). The SEM images of C-N-TiO_2 film coated at 2600 rpm (Figure 8-6 D) that C-N-TiO_2 was also well distributed on the glass support. Moreover, the SEM images of the films coated at 2900 rpm presented in Figure 8-6(F) clearly showed that thin layers (157 nm) of C-N-TiO_2 nano composite were not really distinguishable from the glass surface due to catalyst homogeneity on the substrate. The compact and condensed morphology in SEM images in Figure 8-6 (F) suggested strong adherence between the nano catalyst and the substrate. Nevertheless, the SEM results further proved that the annealed nano catalyst adopted different morphologies on the glass support, depending upon coating at different rotation speeds. The EDS results presented in Table 8-4 show that C, Ti and O were present in the prepared thin films. The high amount of C in Table 8-4 shows that PAN related C residues were present after annealing. However, N was not detected due to the fact that its amount might have been lower than the detection limit/sensitivity of the EDS instrument.

Table 8.5: Normalised weight percentages of elements C, Ti and O in the films coated at different speeds and constant sol gel-solvent volume ratio (3:5) and coating time of 90 seconds, followed by annealing at 350°C, at a ramping rate of 10 °C/min for 105 mins.

Elemental composition (W%) of uncoated and C-N-TiO_2 coated films			
	C	O	Ti
Uncoated glass	19.3	80.7	
Glass coated at 2000 rpm	21.34	77.92	0.74
Glass coated at 2300 rpm	19.45	79.83	0.72
Glass coated at 2600 rpm	21.12	78.38	0.5
Glass coated at 2900 rpm	20.62	78.86	0.52

The results presented in this section showed that regardless of the coating speed, C-N-TiO_2 nano film adhered to the glass support after annealing as can be deduced from C and Ti content; therefore, the photocatalytic activity of the designed films was tested so as to assess the film stability/resistance in oxidative milieu.

8.3.2 Effect of spin coating speed on the degradation of orange II sodium salt dye

The photo catalytic activity of the prepared thin films was evaluated by degradation of O.II sodium salt dye at the applied conditions described in Section 3.6.6.4. Beforehand, O.II was exposed to UV light for 120 min and was considered as control (UV alone). The results of the duplicated activity are shown in Figure 8-7.

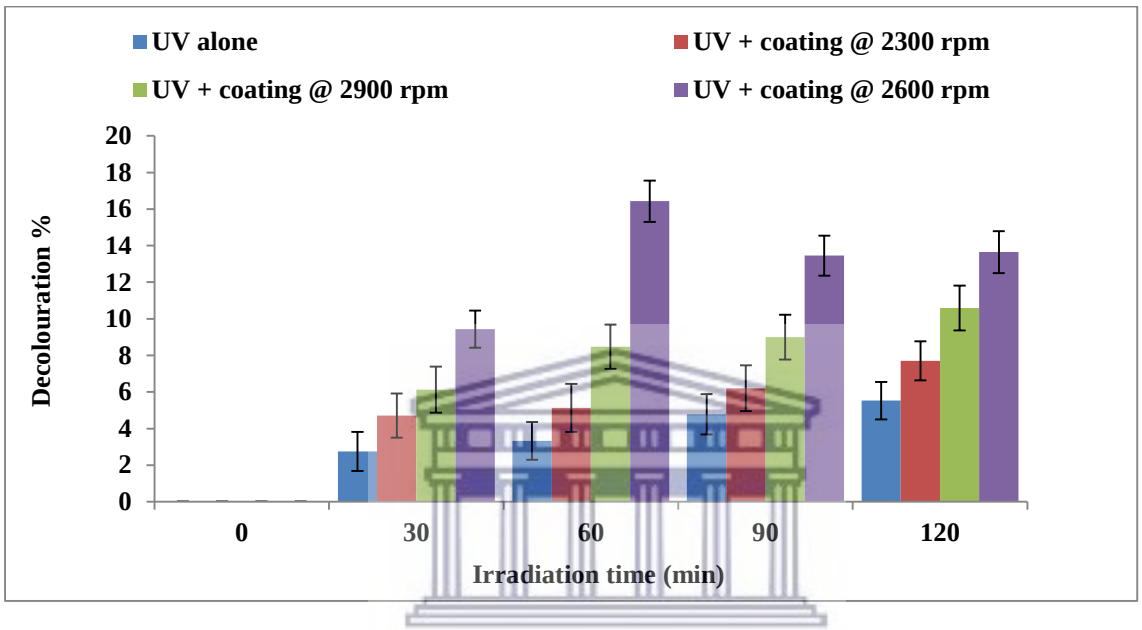

Figure 8.7: Photocatalytic activity of glass coated with C-N-TiO_2 nano composites at spin coating speed varied from 2300, 2600 to 2900 rpmat the following experimental conditions: [O.II] concentration 5 mg/L, volume 500 mL, of pH 2.5, Mega-Ray 160 W/240 V MR160 UV lamp, and sampled at 30 min intervals over an irradiation time of 120 min.

The UV-vis photo catalysis outcomes in Figure 8-7 show that O.II decolouration % increased with an increase of spin coating speed up to 2600 rpm. The photocatalytic activity films made at 2900 rpm were most consistent over time. The highest decolouration percentage of O.II was obtained with thin layers of C-N-TiO_2. For instance, after 60 minutes of UV-vis exposure, about 16.43 and 9.23 % removal of O.II were obtained with films coated at 2600 and 2900 rpm respectively, followed by 7.6 and 4.2 % of O.II removal achieved with films coated at 2300 and 2000 rpm, correspondingly. This inferred that thicker layers resisted light penetration which in turn induced low degradation of O.II. The results also show the film stability in acidic conditions. Indeed, during photo catalysis with thick layers, the majority of electrons and holes might have been created in the bulk of the doped nano semiconductor and hence could not

reach the surface of the film where the photo catalytic reaction took place. This consequently resulted in the lower photo catalytic degradation of O.II removal (Lazar, Varghese and Nair, 2012). This trend for the thicker films was also observed after 30, 90 and 120 minutes of UV irradiation. In the case of films coated at 2600 rpm, the 15.3 % O.II removal obtained after 60 minutes decreased to 12.67 and 12. 83 % after 90 and 120 minutes of treatment. This suggests that the films coated at 2600 rpm maximally absorbed the UV-light after 60 minutes of UV irradiation. Beyond this time, the thin layer of 353 nm films became less active in O.II acidic medium. The current study shows that the highest photocatalytic degradation percentages of O.II were achieved at lower film thicknesses. In other words, the degradation of O.II increased with a decrease of film thickness to about 350-250 nm. It can be inferred that high photocatalytic activities of composite films can be achieved with films of thickness ≤ 300 nm as the thinnest films obtained in this study fit within this range. Hence it could be inferred that the photocatalytic activity of sol-gel spin coated films is significant in a particular thickness range of ≤ 300 nm relative to the rotational spin coating speed. Conclusively, the thickness of the TiO_2 films has an impact on their photocatalytic activities and should therefore be controlled to reach the desired activity. The results obtained in this study demonstrated that during preparation of thin films by the spin coating process, the rotational speed is an important parameter that may influence the morphology of the films which further impacted on their photo catalytic activity. Hence spin coating speed should be optimised to achieve the desired layer thicknesses and improved photo catalytic performance of the prepared films. Even though the film obtained at 2900 rpm in this study and exhibited in Figure 8-7 (A & B) had the lowest layer thickness, its condensed, agglomerated morphology could be overcome by altering factors such as viscosity of the reaction mixture gel (Chen et al. 2010).

8.3.3 Effect of sol gel -solvent ratio on the thickness of thin films

The effect of sol gel viscosity on the thickness of the annealed film layers was assessed by varying the sol gel to DMF solvent volume ratio (v: v) from 3:5, 4:5 to 5:5, respectively at constant rotation speed 2600 rpm for 90 seconds as detailed in Section 3.6.6.4. The thickness of samples was determined by Dektak profilometry analysis and the outcomes of these evaluations are presented in Table 8.6 and plotted in Figure 8-8.

Table 8.6: Effect of sol gel to solvent volume ratio (v: v) on the film thickness. Experimental conditions: spin coating speed 2600 rpm, spinning time 90 min, pyrolysis temperature 350 ^{o}C in N_2 (ramping rate of 10^{o}C/min) for 105 min.

Sol gel to DMF solvent ratio (v:v)	Coating speed (rpm)	Film thickness (nm) n =1	Film thickness (nm) n = 2	Average Thickness (nm)	S. dev.	Film mass (g) n = 1	Film mass (g) n = 2	Average mass (g) of the film	Mass (g) of the uncoated glass	Mass of C-N-TiO_2 on films
3:5	2600	356.4	359.82	358.11	±2.418305	0.8579	0.8577	0.8578	0.8118	0.046
4:5	2600	420	423	421.5	±2.12132	0.8224	0.8222	0.8223	0.8118	0.0105
5:5	2600	453	456.63	454.815	±2.5667	1.0481	1.0486	1.0483	0.8118	0.2365

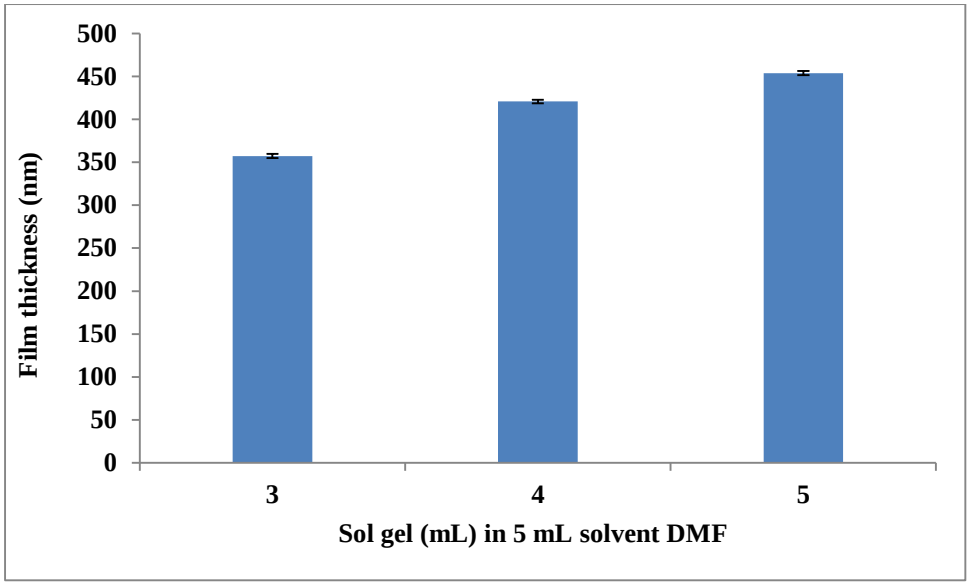

Figure 8.8: Effect of sol gel to solvent volume ratio on the thickness of films at the following conditions: Coating speed 2600 rpm, spinning time 90 min, pyrolysis temperature 350 ^{o}C (ramping rate of 10^{o}C/min) for 105 mins. The sol gel to solvent volume ratio (v: v) was varied from 3:5, 4:5 to 5:5 (n =2).

The results in Figure 8-8 show that the thickness of the films increased with an increase of sol gel to volume ratio. The thinnest catalytic layers (358 nm) were obtained at sol gel to solvent ratio of 3:5 while the thickest film layers (420 nm) and (453 nm) were achieved at 4:5 and 5:5 sol gel to solvent volume ratio. This implied that the ratio of 3:5 was the most suitable for spin coating performed in this study. Likewise the less diluted 5:5 sol gel-solvent ratio was more viscous and might have evaporated less during the spin coating process. This in turn resulted in thicker layers similar to those reported by (Lu et al. 2010; Kenanakis et al. 2015; Zabihi et al. 2015; Clausi et al. 2016). Based on these results and for optimisation purpose, 3:5 was identified as the optimum sol gel-solvent ratio in this study. Moreover, it was necessary to investigate the morphological behaviour of the films coated in this study to examine their distribution on glass supports.

8.3.3.1 Scanning electron microscopy and energy dispersive spectroscopy

The effect of sol gel to solvent ratio on the thin film morphology is often examined by various characterisation techniques among which scanning electron microscopy (SEM) (Zabihi *et al.*, 2015). In this study, SEM was used to visualise the deposition/distribution of the nano

composites on the glass supports. The energy dispersive spectroscopy (EDS) coupled to SEM was used to prove the presence of C, Ti and O though N could not be identified due to the low sensitivity of the SEM instrument toward the amount in the catalyst. The SEM images of films fabricated at each sol gel-solvent ratio (3:5, 4:5 and 5:5), are presented in Figure 8-9.

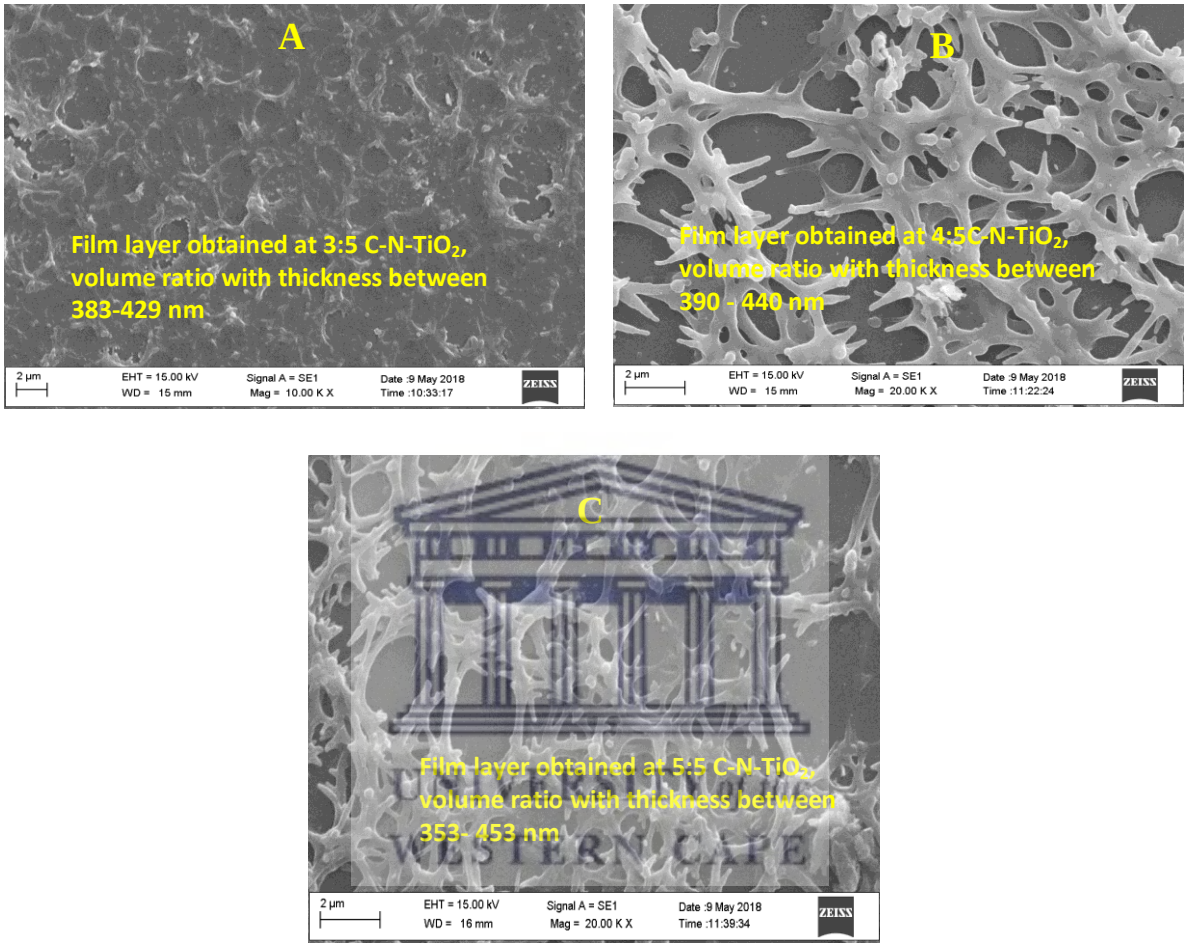

Figure 8.9: SEM morphologies of C-N-TiO_2 coated on glass at a sol gel-solvent ratio varied from 3:5, 4:5 to 5:5 and constant spinning speed of 2600 rpm for 90 secondsfollowed by pyrolysis at 350 ^oC in N_2 (ramping rate of 10^oC/min) for 105 min.

The SEM images recorded in Figure 8-9 show that the annealed C-N-TiO_2 coatings were well distributed on the glass surface. Despite increasing the sol gel-solvent ratio, the nano catalyst was well dispersed on the substrate. In Figure 8-9 (A), C-N-TiO_2 was well fused on the glass hence resulting in homogenous films with a thickness of 358 nm as previously described in Table 8-7. The fusion of C-N-TiO_2 upon the glass surface suggested that there was a strong adherence or bonding between the nano catalyst and glass support at low sol gel to solvent ratio. The low viscosity of the precursor sol gel to solvent in a ratio of 3:5 led to thin layer films

which were homogeneously fused to the support when spin coating at an optimised rotation speed of 3600 rpm. In contrast, SEM images in Figures 8-9 (B &C) show that a porous C-N-TiO_2 network at viscosities of 4:5 and 5:5 was produced on glass surface. Consequently, the elevated sol gel content led to nanocrystalline structured films with thicknesses of 420 to 453 nm when spin coated at a specific rotation speed of 2600 rpm and subsequently annealed. The EDS of the films obtained at varied ratios are shown in Table 8-7.

Table 8.7: Weight percentages of elements C, Ti and O in the films coated at different sol gel-solvent ratio (v: v)at a constant speed (2600 rpm) and coating time of 90 seconds followed by annealing at 350^{o}C, at a ramping rate of 10 ^{o}C/min for 105 mins.

Elemental composition (W%) of uncoated and C-N-TiO_2 coated films			
Sol gel to solvent ratio (v:v)	C	O	Ti
Uncoated glass	19.13	80.87	
3:5	21.12	78.38	0.5
4:5	22.96	76.52	0.52
5:5	22.873	76.33	0.797

Table 8-7 confirms that C, Ti and O were present in C-N-TiO_2 immobilised on the glass. Whereby, the elevated amount of carbon was probably due to C impurities resulting from the carbon in PAN which was part of the sol gel coating. Since the viscosity of the C-N-TiO_2 gel was also found to have an impact on the thickness of films, its influence on photo catalytic activity of the prepared film was also evaluated at the specified conditions.

8.3.4 Effect of sol gel -solvent ratio on the photocatalytic activity of the coated glass on orange II sodium salt dye removal

The photo catalytic test of the films fabricated at different viscosities on the removal of O.II sodium salt dye at the applied conditions as described in Section 3.6.6.4 are plotted in Figure 8 -10.

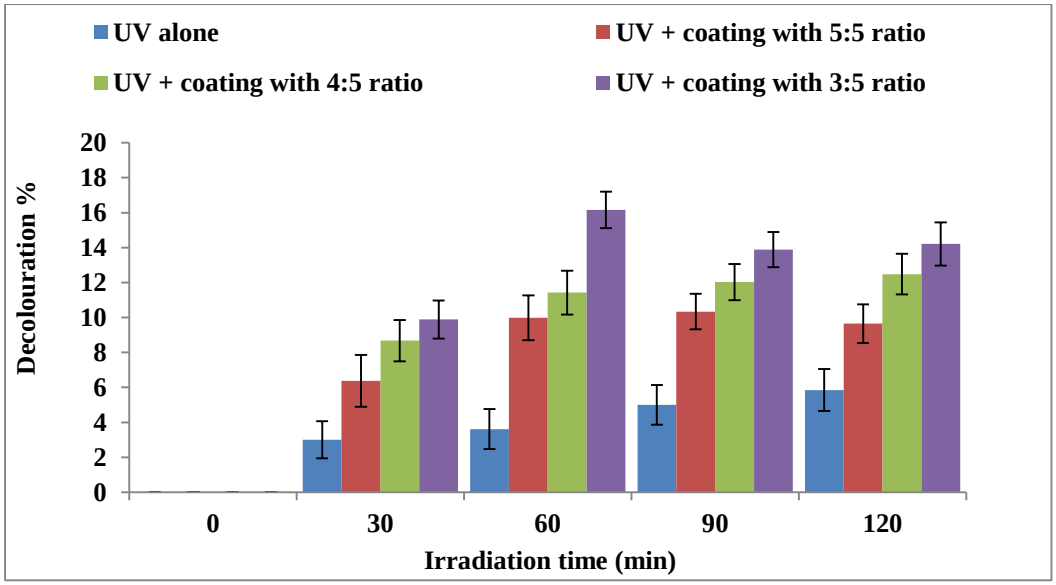

Figure 8.10: Photocatalytic activity of glass supported C-N-TiO_2 coatings formed at sol gel-solvent ratio from 3:5, 4:5 or 5:5 (Experimental conditions: O.II concentration 5 mg/L, volume 500 mL, pH 2.5, Mega-Ray 160 W/240 V MR160 UV lamp, and irradiation time of 120 min (n = 2).

The photo catalysis results presented in Figure 8-10 show that the decolouration % of orange II with UV light alone slightly increased up to 4.8% with an increase in treatment time. This might be due to the fact that the azo group (-N=N-) was progressively being destroyed as UV-vis light exposure time gradually increased. This was evidenced by a slight change of solution colour during the experiment. It was believed that a prolonged time beyond two hours might have given removal % above 4.8 % obtained with UV light alone and that was the lowest in all experiments. At each sampling time, the results in Figure 8.10 show that O.II decolouration correlated inversely to the sol gel to solvent ratio used. For instance after 30 minutes of UV-vis irradiation 5.3% degradation was obtained with the 5:5 ratio. This implied that the films with thick layers resulting from high viscosity had lower decolouration % of O.II. Conversely this shows that films with low thicknesses achieved at low sol gel to solvent ratio were more photo catalytically active than thicker ones and consequently led to improved decolouration % of O.II dye. In addition, the highest (15.42%) O.II decolouration was reached after 60 minutes of UV-vis exposure at 3:5 sol gel to solvent ratio. This then decreased to 12.67 and 12.83% and hence became constant. This indicated that at 60 minutes of reaction time, the supports coated with 3:5 sol gel to solvent ratio reached its maximum UV-light absorption and that induced photo catalysis and hence became stable in O.II acidic medium. Certainly, it should be

recalled that the concentration of gel/dopants and the viscosity of the gel are directly linked to one another. That is the more sol gel to solvent used, the more viscous the sol gel. Therefore, spin coating small amounts or low concentration of the gel on the substrates resulted in improved morphological properties of the prepared films. In this regard, films coated with low viscosity resulted in thin films of desired thickness and therefore improved photocatalytic activity. A similar variation was observed with the other two sol gel to solvent ratios 4:5 and 5:5 except that in these cases, O.II removals slightly increased from 10.39, 10.79 and 11.41 % after 60, 90 and 120 minutes of irradiation correspondingly with 4:5 ratio. As for the films coated with 5:5 ratio, the removal percentage of O.II slightly increased from 5.32 to 8.71, 9.11 and 8.50 % after 30, 60, 90 and 120 minutes of UV exposure. These results probably meant that the films with thicker layers in the range of 420 – 453 nm resisted UV-light penetration in aqueous acidic environment. Alternatively; the excited electrons did not reach the film surface where the reaction occurred and probably accelerated the electron-hole recombination process (Lazar, Varghese and Nair, 2012). This consequently resulted in reduced photocatalytic activity of the prepared nano films. This was also supported by Varshney et al. (2016) who highlighted that one of the few disadvantages of sol-gel spin coating process is the fact that, it is often difficult for thick layers of films to be attacked when exposed to photo oxidative environments which is in conformity with results obtained by Dijkstra et al. (2002). That is, film thickness related photo catalytic activities were assessed by Danish et al. (2015) upon the degradation of Methylene blue dye. The outcomes of their study showed that the removal percentage of MB decreased with a decrease of film thickness. Consequently the highest MB degradation percentage (95 %) was achieved with 160.3 nm film while the lowest MB removal percentage 73 % was reached with 112.8 nm thin films. This was also supported by Arabatzis et al. (2002) and Guillard et al. (2003). In addition, the study conducted by Kenanakis et al. (2015) showed that the photo catalytic removal of octadecanoic acid increased with increase of film thickness from 50 to 150 nm. This complements Varshney et al. (2016) who reported that high photocatalytic activity could be reached with films of low surface roughness. This was further reinforced by various authors (Gültekin *et al.*, 2013, 2014; Sobczyk-Guzenda *et al.*, 2013; Kumar and Rani, 2014). In total, from literature and results plotted in Figure 8-10, this study proved that spin coating is an adequate technique that can be used to immobilise catalysts on flat supports such as glass however; the speed spin coating and sol gel viscosity are two parameters among various that need to be cautiously tuned to obtain thin films of the desired thicknesses. Furthermore, the steadily increasing photo catalytic decolouration % of O.II obtained here (below 20% overall) demonstrates that the engineered films resist depletion or

delamination when exposed to harsh oxidative environments. This method can therefore be used to avoid post-separation/filtration of aqueous powder catalyst that is often a pertinent limitation in photo catalysis at industrial scale. Therefore spin coating the sol gel and so coating the outer quartz dielectric of the plasma zone in DBD system could be an alternative to boost photo catalytic degradation of the targeted pollutants during water and wastewater treatment. In comparison, the impact of viscosity on the photo catalytic activity of the films was also highlighted by Zabihi et al. (2015) and Pérez et al. (2017). This was earlier appealed by Hassan *et al.*, (2014) who stated that the presence of C or N in the TiO_2 lattice controls the photocatalytic sites and hence the photocatalytic activity. Altogether, these results further sustain that at an optimised sol gel to solvent ratio, with a support cleaned with a suitable solvent system; it is possible to engineer thin films of desired thicknesses (Jarka *et al.*, 2017). However, it was also noticed that the C-N-TiO_2 layers coated on glass were less photocatalytically active than C-N-TiO_2 immobilised on SS, Ti and anticorrosive supports. This showed that, it is possible to immobilise the catalyst on glass support. However, the direct deposition of C-N-TiO_2 on the outer walls of the second dielectric barrier of the DBD reactor may require a full optimisation of spin coating and annealing process including various parameters such as gel viscoscity, annealing temperature, etc.

8.4 Summary of chapter 8

In this chapter, the removal of O.II was achieved with C-N-TiO_2 nano catalyst synthesised by a sol-gel method at the applied conditions. In various types of catalyst supports, including SS mesh, various anticorrosion coated SS meshes and were well evaluated as supports. The anticorrosion substrates including SS/TiON and SS/CrN/CrON were effective supports after 120 min of photocatalytic irradiation. High removal efficiencies /degradation percentages (86.12%, 83%, 82%) after 120 min time on stream were achieved with SS/TiON/C-N-TiO_2, SS/(CrN/CrON)/C-N-TiO_2 and SS/C-N-TiO_2 respectively. The removal of O.II at these percentages followed a first order reaction and the degradation rate constants of these percentages obtained from linear kinetic fittings were: 1.6 $x10^{-2}$ min^{-1}, 2.21 $x10^{-2}$ min^{-1}, 1.52$x10^{-2}$ min^{-1}, 1.17 $x10^{-2}$ min^{-1} and 7.3$x10^{-3}$ min^{-1}, correspondingly. From these results, it was observed that SS/TiON/C-N-TiO_2 or SS/(CrN/CrON)/C-N-TiO_2 had removal efficiencies 86.12% or 83% and reaction rates of 1.64$x10^{-2}$ min^{-1} or 2.21$x10^{-3}$ min^{-1}. So C-N-TiO_2/TiON with high degradation efficiency had a lower degradation rate constant of 1.64 $x10^{-2}$ min^{-1}. While C-N-TiO_2/(CrN/CrON) with a removal percentage of 83% had the highest degradation

rate constant of 2.21 $x10^{-2}$ min^{-1}. This observation was ascribed to the morphologies of C-N-TiO_2 that appeared in condensed shape on SS/CrN/CrON substrate and well dispersed nano crystals on SS/TiON as shown by SEM micrographs in Figure 8-1 (D&F). These findings showed that coating SS mesh with transition metals and non-metals in mono and double protective layers contributed not only to its protection against corrosion of stainless steel in oxidative environment but also made good photocatalytic supports. The morphology of the catalyst being deposited may vary according to its adherence or upon the internal composition of the support which in turn could be influenced by interfacial issues or thermal properties that could be further investigated. The results discussed in chapter 8 also demonstrated that the synthesised sol-gel C-N-TiO_2 nano composites were successfully spin coated on glass. The spin coating rotation speed and gel viscosity were two important parameters that influenced the thickness of the films. In other words, during immobilisation of C-N-TiO_2 on glass support by the spin coating process, the thickness of the film was a very crucial parameter that further impacted up on the photocatalytic removal of O.II dye and hence needed to be controlled. In this investigation, the thickness of the film decreased with increase in spin rotation coating speed. The distribution of C-N-TiO_2 nano catalyst on glass support as examined by SEM analysis showed strong bonding adhesion between the nano composite and the substrate. The films with thin layers showed higher photocatalytic activity compared to thicker ones. On the other hand, the thickness of the films decreased with a decrease of the gel viscosity. In this regard, similar trends on the distribution of C-N-TiO_2 on glass support and photocatalytic activity for the removal of O.II were observed. The overall removals of O.II suggested that the prepared films were stable in O.II acidic milieu. These results signified that the thin photocatalytic layers on glass support absorbed UV-light to achieve the degradation of O.II up to about 15.43 % after 60 minutes of reaction time. The outcomes of this chapter further proved that different coating methods among which dip-coating and spin coating could be used for immobilisation of the nano catalyst on various substrates such as meshes and glasses. In the case where the insertion of the coated meshes into DBD advanced oxidation configuration are problematic, the nano composites could directly be coated on the surface of the dielectric quartz of DBD configuration so that the UV light produced in DBD reactor can effectively be used to induce the photocatalytic process and hence improve the degradation rate of the targeted pollutants. However, a critical optimisation of spincoating and anneling processes should be carefully optimised to achieve desired pollutant removals.

CHAPTER 9: CONCLUSIONS AND RECOMMENDATIONS

9 Introduction

Chapter nine presents the outcomes and conclusions of the overall study conducted on the optimisation of the DBD reactor and quantification of free active species generated in the system. The findings on support corrosion, catalyst synthesis, characterisation and immobilisation as well as photocatalytic applications for selected contaminants are also highlighted. The responses to research questions and aims/objectives accomplished in this work as well as endorsements for future work are also given.

9.1 Overview

The purpose of this study was to optimise the DBD reactor for decomposition of two selected pollutants O.II dye and SMX pharmaceutical and evaluate the continuous degradation efficiencies or kinetics of the selected O.II and SMX contaminants with time.

The influence of physicochemical and electrical parameters in the DBD system, namely initial concentration, solution pH, air flow rate and peak voltage, on the removal efficiencies of the selected pollutants was investigated followed by establishing their degradation mechanistic pathways. But beforehand, the pH dependence in the production of O_3, H_2O_2 and $OH^{\bullet}$ and their reaction mechanisms in the DBD reactor was investigated at the selected conditions. For O.II and SMX pollutants, the impact of initial concentration, solution pH, air flow rate and peak voltage was evaluated on the decomposition percentages, respectively. Thereafter, the DBD configuration was tested at optimum conditions with each pollutant and their degradation intermediates or end products were identified by LC-MS and the degradation mechanism pathways were suggested. After the DBD optimisation process, a C-N-TiO_2 nano catalyst was prepared by the sol gel protocol at convenient conditions. Once the best holding time (105 min) leading to the smallest TiO_2 band gap (2.7 eV) was identified, a fresh C-N-TiO_2 sol gel was prepared and dip coated on SS or on pure Ti meshes and then pyrolysed in N_2 at the optimum conditions. The obtained composites catalytic coated supports (SS/C-N-TiO_2 and Ti/C-N-TiO_2) were incorporated in the optimised DBD for the degradation of O.II and SMX which resulted in improved removal percentages of the pollutants. Next, the degradation intermediate by-products of O.II and SMX obtained with DBD + SS/C-N-TiO_2 and DBD + Ti/C-N-TiO_2

detected by LC-MS analysis and their disintegration pathways were well defined. SS corrodes in the oxidising acidic DBD environment; hence grade 304 SS mesh was coated with various Cr and Ti, Zr and Si nitride and oxynitride anticorrosion layers by cathodic arc evaporation (CAE). Their anticorrosion behaviour was evaluated by potentiodynamic techniques in 0.1M NaCl+ 6% H_2O_2 (pH=4), at room temperature using a Versa Stat 3 Potentiostat/Galvanostat. The most corrosion resistant coatings, including SS/TiON and SS/CrON/CrN, were coated with C-N-TiO_2 by dip coating and pyrolysed in N_2 at 350 ^oC, using a ramping rate 50 ^oC/min and held at temperature for 105 min. The photo activities of the support and the obtained C-N-TiO_2 coated films upon the anticorrosion supports were tested for the degradation of O.II at the applied conditions. Furthermore, the sol gel precursor of C-N-TiO_2 was immobilised on glass substrates and pyrolysed in N_2 at 350^oC using a ramping rate of 10 ^oC and held at temperature for 105 min. The adherence of the catalyst layer on glass support was visualised by SEM and further assessed for its photo catalytic removal of O.II in the presence of UV light. Finally, in all cases various analytical and characterisation techniques such as UV- spectroscopy, Fourier Transformer Infrared spectroscopy (FT-IR) and total organic carbon (TOC), XRD, SEM, EDS, TEM, etc. were used for analysis and characterisation purposes. The general conclusions of this study derive from the results achieved in this work and are subsequently outlined in the paragraphs below.

The literature reviewed in this study showed that dielectric barrier discharges (DBD) plasma systems are typical advanced oxidation technologies that are induced by the circulation of a small applied voltage of about 1 eV in contact with a feed gas (air, O_2, etc.) to generate plasma whose physical and chemical properties are known as a potent chemical mixture of various oxidants.

Various DBD configurations including, single and double planar DBDs and single and double cylindrical DBD have been reported. Double cylindrical DBD have been identified as the most robust geometries due to the fact that, the high voltage (HV) electrode is surrounded by two dielectric barriers that protect it against aqueous erosion and operate for longer times.

This configuration produces UV light and various reactive oxygen species such as O_3, H_2O_2, $OH^{\cdot}$, etc. Therefore the optimised double cylindrical DBD appeared as an effective plasma technology for water and wastewater decontamination.

9.2 Quantification of reactive species

The outcomes on quantification of the principal oxygen based species showed that the concentration of O_3 produced in the DBD system fluctuated with time at each pH value. This was due to its scavenging behaviour and various continuous chemical disintegration reactions leading to the formation of other aqueous species. The highest amount (0.79 mol/L) of O_3 was quantified in acidic pH 2.5 after 60 min of DBD run as a result of its stability in acidic conditions. On the other hand, the concentration of H_2O_2 at each pH value did not define a continuous trend but fluctuated with time due to its disintegrative contribution to the formation of related species such as OH radicals. Nevertheless, the highest amounts of H_2O_2 (0.613 and 0.933 mol/L) were produced at basic pH 8.5 and 10.5 after 10 and 5 min, respectively. At the same experimental conditions, and at pH above 2.5, the concentration of OH increased with an increase of treatment time. The highest amounts of OH radicals (8.24 and 9.66 mg/L) were reached after 60 min of DBD run at basic pH 10.5 and 8.5, respectively. Nevertheless, the investigation of pH trends during DBD experimentl run showed that all selected initial pH values above 2.5 progresively decreased to the lowest acidic values between pH 2.5 and 7. Thi was attributed to the formation of acidic species such as nitric and nitrous acid (HNO_2 and HNO_3) which accelerated the decline of the solution acidity in the DBD reactor. On the other hand, the presence of species such as phosphate anions and cations originating from buffer solution reduced the amount of OH radicals through scavenging processes. These results have never been reported elsewhere. Next, the presence of scavenging substances such as carbonates (CO_3^{2-}) in DBD reactor significantly reduced the concentration of OH radicals, while the introduction of NaCl in the DBD system only slightly reduced OH concentration. This is the first time, these mitigations/variations of the formation of free radicals in the double cylindrical have been observed.

All in all, this study showed that, DBDs configurations produce various oxidative species among which O_3, H_2O_2, $\cdot OH$, etc. that can successfully be quantified by colorimetric methods such as indigo, pertitanyl sulphate and terephtallic acid techniques, respectively.

However, it was found that O_3 was the species majorly generated in the first 30 min of DBD acidic environment, compared to H_2O_2 and $OH^{\cdot}$ that were mostly produced in basic conditions. However, for the first time this study showed that the self decomposition of H_2O_2, its peroxonation reaction with O_3 yielding various secondary reactive oxyen species contributed to the decrease of H_2O_2 concentration in the DBD system. Likewise, the decline of O_3

concentration in the DBD was due to various chemical side reactions such as the irradiation of O_3 UV light, O_3 onversion to O_2 by $OH^{\cdot}$, initiation reaction of $O_3$with hydroxide anions (OH^-), oxidation of water molecules as well as O_3 reaction with H_2O_2.

The study evidenced that the generation of all three species (O_3, H_2O_2 and $\cdot OH$) in DBD reactor is pH dependent. The self reaction of these species or their interaction resulted in continuous chains of chemical reactions that render DBD effective technology for water and wastewater treatment. The study further proved that the presence of scavengers in the DBD reactor can reduce the amount of free radical generated and consequently could diminish the removal efficiencies of the targeted contaminants. The amount of oxidants measured in the double cylindrical DBD reactor directly depended on the quantity of the chemical probe TA introduced.

This is the first time that the decrease of OH concentration in the double cylindrical DBD by scavenging species such as phosphate and carbonates anions originating from buffer solution used to equilibre the solution pH has been reported.

9.3 Optimisation of double cylindrical DBD configuration

The optimisation outcomes of the double cylindrical DBD reactor at the following conditions: Peak voltage 8 kV for O.II and 6.8 kV for SMX, [O.II] 60 mg/L and 40 mg/L [SMX], solution volume 1500 mL, solution pH 2.5 for O.II and pH 6.5, 50 g/L NaCl inner electrode electrolyte, air gap 2 mm, 1.5 mm silver electrode, experimental time 60 min showed that:

The degradation % of O.II decreased with an increase of initial concentration and the optimum initial concentration was 60 mg/L. On the other hand, the degradation % of SMX fluctuated with variation of its initial concentration; nevertheless, the optimum SMX concentration was 40 mg/L. Consequently, the initial concentration of pollutants is an important parameter that needs be carefully examined during water and wastewater treatment by DBD configuration.

In addition, the removal % of O.II increased with a decrease of solution pH and the best pH value 2.5. As for SMX, the optimum pH value obtained was 6.5. This demonstrated that the removal of both pollutants O.II and SMX in the DBD reactor was pH dependent. Moreover, the air flow rate also affected the degradation % of both pollutants and the optimum air flow rate obtained for the removal of both O.II and SMX was 3 L/min. Even though the peak voltage

was less significant during optimisation of the DBD system, the optimum peak voltage for O.II was 8 kV and 6.8 for SMX.

At the optimum conditions highlighted above, the total decolouration of O.II dye (98.6%) was achieved after 20 min of DBD reaction time and O.II degradation resulted into six degradation intermediate by-products m/z = 105.06, 121.09, 147.07, 165.08, 207.16 and 163.06 that were identified by LC-MS analysis. Alternatively, complete degradation of SMX (97.3%) was reached after 30 min of DBD reaction time and its decomposition resulted in six intermediate by-products. However, the degradation mechanisms pathways depended on the type of pollutant. Likewise the decomposition of both pollutants (O.II and SMX) was majorly initiated by O_3 followed by $^{\cdot}OH$ while H_2O_2 acted as a principal $^{\cdot}OH$ precursor. Their degradation mechanism pathways mostly followed ring opening by bond cleavage leading to small fragments that were totally oxidised into H_2O, CO_2, and simpler inorganics.

In brief, the outcomes of this optimisation process proved that an optimised DBD reactor configuration is an effective AOP that generates various selective and unselective free radicals that attack and convert POPs such as dyes and pharmaceuticals into H_2O, CO_2 and harmless aqueous species in a reduced treatment time.

9.4 Synthesis and characterisation of the C-N-TiO_2 and application for photocatalytic removal of O.II dye

The results for the C-N-TiO_2 nano catalyst synthesis showed that pyrolysis time in N_2 affected physical, chemical and electronic properties (morphology, shape and band gap) of the catalyst. The C-N-TiO_2 nano catalyst pyrolysed at 350 ^{o}C for 105 min had the smallest band gap 2.67 eV compared to 3.10 and 3.17 eV observed with C-N-TiO_2 calcined at 350^{o}C for 10 and 135 min, correspondingly. Therefore, the calcination time has an impact on catalyst band gap tuning. That is the band gap increased with an increase of calcination holding time. This was either due to the evaporation/volatilisation of the incotrporated elements (N, O) or decomposition of the PAN used as carbon precursor. In addition, the ground powder of the C-N-TiO_2 nano catalyst pyrolysed at 105 min exhibited the highest photo catalytic removal of O.II dye (75%) after 120 min under UV light compared to 71% and 43.3% removals obtained with C-N-TiO_2 pyrolysed for 120, 135 min and 40.51% for commercial TiO_2 Degussa catalyst, respectively.

In conclusion, the variation of band gap influenced the photo catalytic activity of the catalyst. That is, the photocatalytic activity of the C-N-TiO_2 catalyst increased with a decrease of the band gap that could be accurately tailored by pyrolysis time. This was due to the fact that the lower band gap facilitated the promotion of electrons from the valence band to the conduction band which accelerated the formation of free radicals and hence boosted the decolouration of O.II dye.

The immobilisation of C-N-TiO_2 on SS or Ti supports showed that the catalyst was adherent on both supports but adopted different morphologies and hence resulted in different photocatalytic behaviours. That is, the porous C-N-TiO_2 nano crystals were well dispersed on SS support but were compact and totally covering the Ti supports. This demonstrated that the catalyst adopted different morphologies on each support and hence resulted in different photocatalytic activities. The following conditions were applied in the combined DBD photo catalyst system: Peak voltage 8 kV, [O.II] 60 mg/L, solution volume 1500 mL, solution pH 2.5, 50 g/L NaCl inner electrode electrolyte, air gap 2 mm, 1.5 mm silver electrode, experimental time 60 min, 4 uncoated or coated meshes (8 cm long x 2 cm large) were enfolded around the outer tube of the DBD reactor. Total removal of O.II (99.9%) was achieved with C-N-TiO_2/SS; compared to 95.7% or 35.5% removals obtained with DBD alone or C-N-TiO_2/Ti + DBD, respectively after 10 min of reaction.

The removal of O.II with DBD + C-N-TiO_2/SS resulted in four degradation intermediate by-products m/z = 400.03, 274.3, 264.3, 246.3 that were subsequently mineralised by O_3 and $OH^{\cdot}$ to dissolved CO_2, H_2O and related aqueous species. Alternatively ten degradation intermediate by-products of O.II were achieved with C-N-TiO_2/Ti film + DBD at the same conditions. These were later transformed to H_2O, dissolved CO_2 and other entities by O_3 and $^{\cdot}OH$ via nucleophilic, electrophilic and epoxidation reactions.

In contrast, complete degradation 99.0% or 86.2 % of SMX were reached with DBD + C-N-TiO_2/SS or DBD +TiO_2/Ti films after 30 min or 50 min reaction time, respectively. In comparison with the removal of O.II and SMX by DBD alone, this signified that SMX was more resistant than O.II in the DBD system. Though, its total conversion to H_2O, CO_2, and other inorganics was achieved after prolonged reaction time of 60 min. The detoxification of SMX with C-N-TiO_2/SS + DBD resulted in four transformation by-products m/z = 318.3, 274.3, 400.3, 338.3 while seven conversion intermediate metabolites m/z = 318.3, 274.3, 400.3,

338.3 were obtained with DBD + C-N-TiO_2/Ti film system. All the aforementioned intermediates were further oxidised to H_2O, CO_2 and other simpler substances.

Consequently, the incorporation of C-N-TiO_2 in the DBD system enhanced the removal of O.II with the removal time being reduced from 20 (DBD alone) to 10 min (DBD + C-N-TiO_2/SS) while the combination of DBD and C-N-TiO_2/Ti was not effective for the degradation of O.II dye.

In the case of SMX, its degradation (97.3%) achieved with DBD alone after 30 min of reaction time and 99.0% or 86.2 % removal reached with DBD + C-N-TiO_2/SS or DBD +TiO_2/Ti after 30 min and 50 min, respectively demonstrated that SMX was more resistant to degradation than O.II in the DBD system. Though, its total conversion to H_2O, CO_2, and other inorganics was achieved after prolonged time of 60 min.

The study proved that POPs such as dye (O.II) can be easily removed from wastewater by DBD advanced technology. However, pharmaceutical residues such as SMX can be resistant /recalcitrant to typical treatment methods such as DBD and their total oxidation may require an extended reaction time.

The removal % of O.II and SMX obtained with DBD + C-N-TiO_2/Ti within the first 50 min of reaction time was lower than the percentage decomposition of both pollutants obtained with DBD alone. This was due to the fact that the pores of the Ti mesh supports were too small and were totally covered by the dip coated C-N-TiO_2 catalyst that blocked Ti support pores and did not only impede the free circulation of the solution between the mesh but also obstructed the propagation of the UV-light into the solution.

This consequently implied that during incorporation of catalyst into the DBD system, the catalyst support should carefully be chosen and the coating process should also be optimised to achieve maximum/ desired pollutant removals.

Since the degradation efficiencies of O.II and SMX achieved with DBD + powder C-N-TiO_2 nano catalyst and DBD + C-N-TiO_2 supported on SS and anticorrosion meshes were higher than those reached with DBD alone, this therefore demonstrated that the addition of the catalyst in the DBD system improved the degradation of the targeted pollutants.

9.5 Corrosion study

The results on cathodic arc evaporation coating of the SS support, followed anticorrosion tests demonstrated that SS was successfully coated with Cr and Ti nitride and oxynitride protective layers by CAE at the indicated conditions.

The corrosion test of Cr and Ti nitride and oxynitride coatings was measured in acidic mixture of 0.10M NaCl+1.96 M H_2O_2 for 15 hrs immersion. The most anticorrosive coating was found to have the lowest corrosion current (i_{corr}). So based on i_{corr} parameter among others the corrosion behaviour of Cr and Ti coatings showed that, the Cr (N, O) monolayer exhibited the lowest i_{corr}, followed by Cr-N/Cr (N, O), Cr (O, N)/Cr-N and Cr-N coatings. As for Ti coatings, following the same parameters coupled to the protection efficiency of coatings, the corrosion performance of Ti films TiNO was the most corrosion resistant coating followed by SS/TiN/TiON, SS/TiON/TiN and TiN, respectively. The deposition of C-N-TiO_2 nano catalyst on SS (C-N-TiO_2/SS) and on Cr and Ti anticorrosion coatings [C-N-TiO_2/SS/TiON and C-N-TiO_2/SS/(CrN/CrON) by dip coating pyrolysis showed that the catalyst successfully adhered on these supports in diverse morphologies and shapes and hence displayed different photocatalytic behaviours. So, at the following conditions: [O.II] 5 mg/L, pH 2.5, volume 500 mL, Mega-Ray 160 W/240 V MR160 UV lamp and an irradiation time of 120 min (n = 2), under UV light, the photo catalytic test of the most corrosion resistant SS/TiON and SS/CrN/CrON coatings and SS mesh showed that all supports were adequate inert catalytic supports. Upon their dip coating with C-N-TiO_2 nano catalyst (dip coating followed pyrolysis), the best O.II removals (84% or 80.4%) were reached with C-N-TiO_2/SS and C-N-TiO_2/SS/(CrN/CrON), respectively (after 120 min of treatment time); compared to 75.7% dye removal achieved with C-N-TiO_2/SS/TiON after 90 min under UV light exposure.

Conclusively, this research proved that the DBD acidic environment could be corrosive to a particular catalytic support; however, the corrosion scenario could be overcome by coating the supports with various transition metal layers such as Cr, Ti, etc. achieved in this study, before deposition of the desired catalyst. Thereafter, the anticorrosive supports coated with the catalyst could further be used in DBD system to achieve adequate photo catalytic activity. Nevertheless, the corrosion tests performed in this study showed that Cr and Ti nitride and oxinitride layers mainly SS/CrON, SS/CrN/CrON and SS/TiON were the most corrosion resistant coatings that could be used as adequate photo catalytic supports in harsh oxidative environments.

9.6 Conclusion on spin coating

Furthermore, the immobilisation of C-N-TiO_2 showed that the sol gel deposition depended on spin coating speed and on the sol gel to solvent ratio. That is at the following conditions: sol gel to solvent volume ratio (3: 5), coating time 90 s, pyrolysis temperature 350 ^oC, ramping rate of 10^oC/min for 2 hours, the thickness of films decreased with an increase of coating speed and the optimum speed was 2600 rpm corresponding to an average thickness 356.4 nm after pyrolysis. The thickness of samples was determined by Dektak profilometry analysis (n = 2)]. The impact of sol gel to solvent ratio showed that at varied sol gel to solvent volume ratios, speed 2600 rpm, coating time 90 s, annealing temperature 350 ^oC, ramping rate of 10^oC/min for 105 mins and n = 2, the thickness of the films increased with an increase of the amount of sol gel; however the optimum sol gel to solvent ratio was 3:5, exhibiting the smallest average film thickness of 358.11 nm. The influence of coating speed on photo catalytic removal of O.II at the following conditions ([O.II] concentration 5 mg/L, volume 500 mL, pH 2.5, Mega-Ray 160 W/240 V MR160 UV lamp, and sampled at 30 min intervals over an irradiation time of 120 min, n = 2) showed that the highest O.II percentage removals (15.43 and 9.23 %) were attained with films coated at 2600 and 2900 rpm respectively, compared to 7.6 and 4.2 % O.II removals achieved with films coated at 2300 and 2000 rpm, respectively after 60 minutes of UV exposure. The results further showed that films showing strong adhesion between CN-TiO_2 catalysts and glass support resulted in lowest removals of O.II dye. Likewise thinner films results in elevated O.II removal percentages while the thicker ones led to lower removals of the dye. These removal percentages of O.II with C-N-TiO_2 supported on glass were lower than those obtained with powder C-NTiO_2 photocatalyst at the same experimental conditions. This was certainly due to the fact that the UV light instead of being totally used in pthe the photo catalysis process, part of it was probably transparent absorded on the glass supports.

These outcomes further proved that dip-coating and spin coating followed by annealing could be used as suitable deposition techniques for the immobilisation of the nano catalyst on various supports such as meshes and glasses. In other words, in the DBD reactor optimised in this study, the catalyst can either be coated on anticorrosion meshes or directly on the outer tube of the DBD reactor using the dip or spin coating techniques to enhance the removal efficiencies of the targeted POPs.

From all results achieved in this study, the optimised reconfigured DBD reactor is a promising advanced oxidation technology that is able to significantly detoxify targeted POPs including dyes and pharmaceuticals from water and wastewater. The inclusion of the catalyst immobilised on various supports into the optimised DBD reactor induced total conversion of recalcitrant pollutants into dissolved CO_2, H_2O and various simpler inorganics in short treatment times.

9.7 Novelty of the study

This study proved that the optimised DBD configuration is an effective technology for the removal of POPs from water and wastewater. The DBD reactor produces various oxidants among which O_3 that is dominantly generated in acidic media, while H_2O_2 and $OH^{\cdot}$ are predominant in basic environment. The interaction of these three principal species led to chains of reaction mechanisms that directly or indirectly contributed to the deactivation of the model pollutants O.II and SMX. The degradation of O.II and SMX in the DBD reactor was mostly initiated by nucleophilic, electrophilic and epoxidation reactions of O_3 and $OH^{\cdot}$. These in turn induced the ring opening and bond cleavage of the epoxidised parent molecules leading to intermediate by-products that were further converted into H_2O, CO_2 and other inorganics. The degradation of O.II and SMX in the DBD reactor was pH confounded and their total decomposition also depended on the initial concentration and air flow rate. The integration of the supported nano catalyst into the DBD reactor enhanced the efficiency of the system.

This study proved that in order to improve the efficacy of the UV light generated in the DBD system, the nano atalyst C-N-TiO_2 could be either immobilised on mesh supports or directly on the walls of the DBD reactor. Likewise, the coordination of C-N-TiO_2 on glass support demonstrated that the catalyst can be directly coated on the outer side of the second dielectric barrier of the DBD reactor to improve the UV light efficiency and hence boost the degradation of the targeted pollutant.

The insufficient light penetration on the surface of the film may retard the photocatlysis process and result in various degradation intermediate by-products.

For both pollutants, various degradation by-products were obtained with DBD + C-N-TiO_2/Ti due to the fact that Ti mesh pores were totally covered by the catalyst and hence blocked not only the full propagation of the UV light into the solutions but the free circulation of the polluted water as well. This demonstrated that in DBD water treatment process, the choice of catalyst support and the coating procedure should be carefully performed. This study further

showed that coating SS support with anticorrosive layers could be an effective route to preventing corrosion of photocatalytic supports in oxidative environments. The degradation of the same targeted pollutant by a catalyst imoobilised on different supports in the DBD system leads to different degradation intermediate by-products.

Hence the DBD system optimised in this study can be utilised either as a single laboratory tested water treatment method or as an integrated step in water and wastewater treatment plants for complete removal of POPs.

9.8 Recommendations

It is recommended that the effect of temperature on ozone and H_2O_2 production during DBD experiment should be investigated.

Since it was proved that the buffer solution used to maintain the pH is a source of phosphate scavengers, the choice of suitable buffer is important.

Since SS mesh was successfully coated with anticorrosion layers, and their potential as adequate photo catalytic supports was evaluated separately under UV-light at the applied conditions, it would be recommended that the anticorrosion coatings should also be incorporated in the DBD system to follow the degradation of O.II dye and SMX targeted pollutants for comparison purposes.

Since this study proved that the precursor sol gel to solvent ratio had an impact on the thickness of pyrolysed C-N-TiO_2 films, it would be recommended that the viscosity of the C-N-TiO_2 sol gel should be well controlled/optimised to obtained photo catalysis of desired thickness range.

In order to minimise the formation of nitrates and nitrites derivatives that largely contribute to the acidification of the effluent being treated, it would be advised to appropriately (with proper equipment) use pure oxygen rather than air gas in the DBD.

As this study claimed the formation of CO_2 during mineralisation of contaminants, it would be recommended that the dissolved CO_2 should be quantified or monitored for extended purposes such as its conversion to hydrocarbons.

Though the measurement of UV light produced in the DBD reactor is challenging, an attempt to determination its wavelength and impact on the formation of free radicals would be suggested.

Since this study dealt with single model pollutants, it would be recommended that other recalcitrant compound or their mixture should be used to test the effectiveness of the optimised reconfigured DBD reactor.

REFERENCES

A. G. Bubnov, E. Yu. Burova, V. I. Grinevich V. V. Rybkin, J.-K. Kim, H.-S. C. (2007) 'Comparative Actions of NiO and TiO2 Catalysts on the destruction of phenol and its derivatives in a dielectric barrier discharge', *Plasma Chem Plasma Process*, 27, pp. 177–187. doi: 10.1007/s11090-007-9052-8.

A.E. McHale (1994) 'Borides Carbides and Nitrides', in *Phase Equilibria Diagrams*. The American Ceramic Society Westerville OH, p. 415.

Abbt-Braun G., Lankes, U., and Frimmel, F. H. (2004) 'Title: Structural Characterization of Aquatic Humic Substances - the Need for a Multiple Method Approach.', *Aquat. Sci.*, 66(2), pp. 151–170.

Abdelmelek, S. Ben *et al.* (2011) 'Removal of pharmaceutical and personal care products from reverse osmosis retentate using advanced oxidation processes', *Environmental Science and Technology*. doi: 10.1021/es104287n.

Abdullah, A. M. *et al.* (2016) 'Carbon/nitrogen-doped TiO2: New synthesis route, characterization and application for phenol degradation', *Arabian Journal of Chemistry*. doi: 10.1016/j.arabjc.2015.04.027.

Abdullah, M., Low, G. K. C. and Matthews, R. W. (1990) 'Effects of common inorganic anions on rates of photocatalytic oxidation of organic carbon over illuminated titanium dioxide', *The Journal of Physical Chemistry*. doi: 10.1021/j100380a051.

Abellán, M. N. *et al.* (2007) 'Photocatalytic degradation of sulfamethoxazole in aqueous suspension of TiO2', *Applied Catalysis B: Environmental*. doi: 10.1016/j.apcatb.2007.02.017.

Adán, C. *et al.* (2017) 'Bacterial inactivation and degradation of organic molecules by titanium dioxide supported on porous stainless steel photocatalytic membranes', *Chemical Engineering Journal*. doi: 10.1016/j.cej.2016.04.091.

Addis, A., Fenton, R. and By By By By Mekibib Soresa Mekibib Soresa Mekibib Soresa Mekibib Soresa, R. (2011) *School of graduate studies school of graduate studies school of graduate studies school of graduate studies department of chemical engineering department of chemical engineering department of chemical engineering department of chemical engineering*.

Ahmad, Z. (2006) 'Corrosion Kinetics', in *Principles of Corrosion Engineering and Corrosion Control*, pp. 57–119. doi: 10.1016/B978-0-7506-5924-6.50004-0.

Ai, S. *et al.* (2004) 'Study on photocatalytic oxidation for determination of chemical oxygen demand using a nano-TiO2–K2Cr2O7 system', *Analytica Chimica Acta*. Elsevier, 509(2), pp.

237–241. doi: 10.1016/J.ACA.2003.09.056.

Akpan, U. G. and Hameed, B. H. (2010) 'The advancements in sol-gel method of doped-TiO2 photocatalysts', *Applied Catalysis A: General*. doi: 10.1016/j.apcata.2009.12.023.

Aksoy, S. and Caglar, Y. (2014) 'Structural transformations of TiO2films with deposition temperature and electrical properties of nanostructure n-TiO2/p-Si heterojunction diode', *Journal of Alloys and Compounds*. doi: 10.1016/j.jallcom.2014.05.192.

Al-Kdasi, A. *et al.* (2004) *Treatment of textile wastewater by advanced oxidation processes-a review, Global Nest: the Int. J.*

Alemany, L. J. *et al.* (2000) *M orphological and Structural Characterization of a Titanium Dioxide System, MAterials characterization.*

Alkhimov A.P., Vorobyov V.V., Klimkin V.F., Ponomarenko A.G., S. R. I. (1970) 'Doklady AN SSSR', 194, pp. 1052–1054.

Allpike, B.P., Heitz, A., Joll, C.A., Kagi, R.I., Abbt-Braun, G., Frimmel, F. H., Brinkmann, T., Her, N., and Amy, G. (2005) 'Title: Size Exclusion Chromatography to Characterize DOC Removal in Drinking Water Treatment.', *Environmental Science and Technology.*, 39(7), pp. 2334–2342.

Altinbas, U., Dökmeci, S. and Baristiran, A. (1995) 'Treability study of wastewater from textile industry', *Environmental Technology (United Kingdom)*. doi: 10.1080/09593331608616280.

Alvarez-Pampliega, A. *et al.* (2014) 'Corrosion study on Al-rich metal-coated steel by odd random phase multisine electrochemical impedance spectroscopy', *Electrochimica Acta*. doi: 10.1016/j.electacta.2013.09.159.

Alzamani, M. *et al.* (2013) 'Influence of catalyst on structural and morphological properties of TiO2nanostructured films prepared by sol–gel on glass', *Progress in Natural Science: Materials International*. doi: 10.1016/j.pnsc.2013.01.012.

Andreas Haarstrick, Oemer M. Kut, E. H. (1996) 'TiO2-Assisted Degradation of Environmentally Relevant Organic Compounds in Wastewater Using a Novel Fluidized Bed Photoreactor', *Environ. Sci. Technol*, 30(3), pp. 817–824.

Andrew P. Hills, Najat Mokhtar, N. M. B. (2014) 'Assessment of physical activity and energy expenditure: an overview of objective measures: Review article', *Frontier in nutrition*, 1.

Ann Liebert, M. *et al.* (1999) *Photocatalytic Decolorization of Méthylène Blue in Aqueous Ti02 Suspension, Environmental engineering science*.

Ao, Z. *et al.* (2018) 'Photocatalytic Degradation of 4-Nitrophenol by C, N-TiO 2 :

Degradation Efficiency vs. Embryonic Toxicity of the Resulting Compounds', *Front. Chem*, 6, p. 192. doi: 10.3389/fchem.2018.00192.

APHA, AWWA, W. (1998) *Title: Standard methods for the examination of water and waste water*. 20th edn. Washington, DC: American Public Health Association.

Arabatzis, I. M. *et al.* (2002) *Preparation, characterization and photocatalytic activity of nanocrystalline thin film TiO 2 catalysts towards 3,5-dichlorophenol degradation, Journal of Photochemistry and Photobiology A: Chemistry*.

Arif Malik, M., Ghaffar, A. and Akbar Malik, S. (2001) *Water purification by electrical discharges, Plasma Sources Sci. Technol*. Available at: http://iopscience.iop.org/0963-0252/10/1/311.

Arslan-Alaton, I. and Dogruel, S. (2004a) 'Pre-treatment of penicillin formulation effluent by advanced oxidation processes', *Journal of Hazardous Materials*. doi: 10.1016/j.jhazmat.2004.04.009.

Arslan-Alaton, I. and Dogruel, S. (2004b) 'Pre-treatment of penicillin formulation effluent by advanced oxidation processes', *Journal of Hazardous Materials*, 112(1–2), pp. 105–113. doi: 10.1016/j.jhazmat.2004.04.009.

Asahi, R. *et al.* (2001) 'Visible-light photocatalysis in nitrogen-doped titanium oxides', *Science*. doi: 10.1126/science.1061051.

Atar, E. *et al.* (2014) 'Tribological properties of CrN coated H13 grade tool steel', *Journal of Iron and Steel Research International*. doi: 10.1016/S1006-706X(14)60037-6.

Atkins P., D. P. J. (2010) *Physical Chemistry*. ninth edition. Oxford University Press.

Atkinson, R. (1985) 'Kinetics and mechanisms of the gas-phase reactions of the hydroxyl radical with organic compounds under atmospheric conditions', *Chemical Reviews*, 85, pp. 69–201. doi: 10.1021/cr00071a004.

Auriol, M. *et al.* (2006) 'Endocrine disrupting compounds removal from wastewater, a new challenge', *Process Biochemistry*. doi: 10.1016/j.procbio.2005.09.017.

Avci, N. *et al.* (2009) 'Characterization of TiO2powders and thin films prepared by non-aqueous sol-gel techniques', *Journal of Sol-Gel Science and Technology*. doi: 10.1007/s10971-009-2028-9.

Azem, F. A. *et al.* (2014) 'The corrosion and bioactivity behavior of SiC doped hydroxyapatite for dental applications', *Ceramics International*. doi: 10.1016/j.ceramint.2014.07.116.

Babić, S. *et al.* (2015a) 'Photolytic and thin TiO<inf>2</inf> film assisted photocatalytic degradation of sulfamethazine in aqueous solution', *Environmental Science and Pollution*

Research, 22(15), pp. 11372–11386. doi: 10.1007/s11356-015-4338-5.

Babić, S. *et al.* (2015b) 'Photolytic and thin TiO2 film assisted photocatalytic degradation of sulfamethazine in aqueous solution', *Environmental Science and Pollution Research*. doi: 10.1007/s11356-015-4338-5.

Bader, H. and Hoigni~, J. (1981) *Determination of ozone in water by the indigo method*, *Water Research*.

Badmus, K. O. *et al.* (2016) *Quantification of Radicals Generated in a Sonicator*, *Iranian Chemical Society Anal. Bioanal. Chem. Res*.

Balaceanu, M. *et al.* (2015) 'Growth and characterization of arc evaporated TiSiC-Ni coatings', *Tribology Letters*. doi: 10.1007/s11249-015-0521-6.

Bamoulid, L. *et al.* (2006) 'Investigations on composition and morphology of electrochemical conversion layer/titanium dioxide deposit on stainless steel', *Surface and Coatings Technology*. doi: 10.1016/j.surfcoat.2006.05.037.

Barder, H. and Hoigne, J. (1982) 'Determination of ozone in water by the Indigo method. A submitted Standard', *Ozone: Science & Engineering*, 4, pp. 169–176.

Beltrán, F. J. *et al.* (2008) 'Ozone and photocatalytic processes to remove the antibiotic sulfamethoxazole from water', *Water Research*. doi: 10.1016/j.watres.2008.07.019.

Beltrán, F. J., Encinar, J. M. and Alonso, M. A. (1998) 'Nitroaromatic Hydrocarbon Ozonation in Water. 1. Single Ozonation', *Industrial and Engineering Chemistry Research*. doi: 10.1021/ie9704253.

Bendersky, L. A. and Gayle, W. (2001) 'Electron Diffraction Using Transmission Electron Microscopy', 106(6), pp. 997–1012.

Benotti, M. J. *et al.* (2009) 'Evaluation of a photocatalytic reactor membrane pilot system for the removal of pharmaceuticals and endocrine disrupting compounds from water', *Water Research*. doi: 10.1016/j.watres.2008.12.049.

Bian, W., Ying, X. and Shi, J. (2009) 'Enhanced degradation of p-chlorophenol in a novel pulsed high voltage discharge reactor', *Journal of Hazardous Materials*. doi: 10.23919/ChiCC.2017.8028875.

Bianco, A. *et al.* (2015) 'A better understanding of hydroxyl radical photochemical sources in cloud waters collected at the puy de Dôme station - Experimental versus modelled formation rates', *Atmospheric Chemistry and Physics*. doi: 10.5194/acp-15-9191-2015.

Birol, Y. (2013) 'Sliding wear of CrN, AlCrN and AlTiN coated AISI H13 hot work tool steels in aluminium extrusion', *Tribology International*. doi: 10.1016/j.triboint.2012.07.023.

Blanco, E., González-Leal, J. M. and Ramírez-del Solar, M. (2015) 'Photocatalytic TiO2sol-

gel thin films: Optical and morphological characterization', *Solar Energy*. doi: 10.1016/j.solener.2015.07.048.

Boonnorat, J. *et al.* (2018) 'Use of aged sludge bioaugmentation in two-stage activated sludge system to enhance the biodegradation of toxic organic compounds in high strength wastewater', *Chemosphere*. doi: 10.1016/j.chemosphere.2018.03.084.

Braic, M., Vladescu, A., *et al.* (2015) 'Corrosion behaviour of Ti-10Nb-10Zr-5Ta alloys in artificial saliva solution with fluoride content', *Materials and Corrosion*. doi: 10.1002/maco.201508382.

Braic, M., Balaceanu, M., *et al.* (2015) 'Investigation of multilayered TiSiC/NiC protective coatings', *Vacuum*. doi: 10.1016/j.vacuum.2015.06.019.

Braic, M. *et al.* (2017a) 'A comparative study of the structural, mechanical and tribological characteristics of TiSiC-Cr coatings prepared in CH4 and C2H2 reactive atmosphere by cathodic vacuum arc', *Applied Surface Science*. doi: 10.1016/j.apsusc.2016.12.160.

Braic, M. *et al.* (2017b) 'A comparative study of the structural, mechanical and tribological characteristics of TiSiC-Cr coatings prepared in CH4and C2H2reactive atmosphere by cathodic vacuum arc', *Applied Surface Science*. doi: 10.1016/j.apsusc.2016.12.160.

Braic, V., Parau, A. C. C., *et al.* (2014) 'Effects of substrate temperature and carbon content on the structure and properties of (CrCuNbTiY)C multicomponent coatings', *Surface and Coatings Technology*, 258, pp. 996–1005.

Braic, V., Parau, A. C., *et al.* (2014) 'Effects of substrate temperature and carbon content on the structure and properties of (CrCuNbTiY)C multicomponent coatings', *Surface and Coatings Technology*. doi: 10.1016/j.surfcoat.2014.07.044.

Bratsch, S.G, . (1989) 'Standard electrode potentials and temperature coefficients in water at 298.15 K', *J. Phys. Chem. Ref. Data*, 18(1), pp. 1–21.

Breugelmans, T. *et al.* (2012) 'Odd random phase multisine electrochemical impedance spectroscopy to quantify a non-stationary behaviour: Theory and validation by calculating an instantaneous impedance value', *Electrochimica Acta*. doi: 10.1016/j.electacta.2012.05.051.

Brinker, C.J. and Scherer, G. W. (1990) 'Solgel Science: The Physics and Chemistry of Solgel Processing.', *Academic Press Incorporation, San Diego*.

Brisset, J. L. *et al.* (2011) 'Acidity control of plasma-chemical oxidation: Applications to dye removal, urban waste abatement and microbial inactivation', *Plasma Sources Science and Technology*. doi: 10.1088/0963-0252/20/3/034021.

Bsiri, N. *et al.* (2016) 'Morphological, structural and ellipsometric investigations of Cr doped TiO2thin films prepared by sol-gel and spin coating', *Ceramics International*. doi:

10.1016/j.ceramint.2016.03.145.
Buettner, G. R. (1987) 'Spin Trapping - Electron-Spin-Resonance Parameters of Spin Adducts', *Free Radical Bio. Med.*, 3(4), pp. 259–303. doi: 10.1016/s0891-5849(87)80033-3.
Bunjongpru, W. *et al.* (2008) 'Oxygen Control on Nanocrystal-AlON Films by Reactive Gas-Timing Technique R.F. Magnetron Sputtering and Annealing Effect', *Advanced Materials Research*, 55–57(January 2016), pp. 573–576. doi: 10.4028/www.scientific.net/AMR.55-57.573.
Burlica, R. *et al.* (2004) 'Organic dye removal from aqueous solution by glidarc discharges', *Journal of Electrostatics*. Elsevier, 62(4), pp. 309–321. doi: 10.1016/J.ELSTAT.2004.05.007.
Bustillo-Lecompte, C. F., Mehrvar, M. and Quiñones-Bolaños, E. (2013) 'Combined anaerobic-aerobic and UV/H2O2 processes for the treatment of synthetic slaughterhouse wastewater', *Journal of Environmental Science and Health - Part A Toxic/Hazardous Substances and Environmental Engineering*. doi: 10.1080/10934529.2013.774662.
Buxton, G. V. *et al.* (1988) 'Critical Review of rate constants for reactions of hydrated electrons, hydrogen atoms and hydroxyl radicals (·OH/·O−in Aqueous Solution', *Journal of Physical and Chemical Reference Data*. doi: 10.1063/1.555805.
Cachet, H. *et al.* (2006) 'Correlation between electrochemical reactivity and surface chemistry of amorphous carbon nitride films', in *Surface and Interface Analysis*. doi: 10.1002/sia.2146.
Calderon-Moreno, J. M. *et al.* (2014) 'Effect of polyethylene glycol on porous transparent TiO2films prepared by sol-gel method', *Ceramics International*. doi: 10.1016/j.ceramint.2013.07.139.
Calderon, P. B. and Roberfroid, M. B. (1995) *Free radicals and oxidation phenomena in biological systems*. New York: CRC press.
Capobianco, M. *et al.* (2013) *Advanced Oxidation Processes for the remediation of water contaminated by emerging pollutants*.
Carp, O., Huisman, C. L. and Reller, A. (2004) 'Photoinduced reactivity of titanium dioxide', *Progress in Solid State Chemistry*. doi: 10.1016/j.progsolidstchem.2004.08.001.
Cernuto, G. *et al.* (2011) 'Size and Shape Dependence of the Photocatalytic Activity of TiO_2 Nanocrystals: A Total Scattering Debye Function Study.', *Journal of the American Chemical Society*. doi: 10.1021/ja110225n.
Chahbane, N. *et al.* (2007) 'FeIII-TAML-catalyzed green oxidative degradation of the azo dye Orange II by H2O2and organic peroxides: Products, toxicity, kinetics, and mechanisms', *Green Chemistry*. doi: 10.1039/b604990g.

Chainarong, S. *et al.* (2011) 'Synthesis and characterization of nitrogen-doped TiO2 nanomaterials for photocatalytic activities under visible light', in *Energy Procedia*. doi: 10.1016/j.egypro.2011.09.046.

Chandni Bhatt *et al.* (2016) 'Effect of Nano-Filler on the Properties of Polymer Nanocomposite Films of PEO/PAN Complexed with NaPF6', *Journal of Materials Science and Engineering B*. doi: 10.17265/2161-6221/2015.11-12.003.

Chen, W., Westerhoff, P., Leenheer, J. A., and Booksh, K. (2003) 'Title: Fluorescence excitation-emission matrix regional integration to quantify spectra for dissolved organic matter.', *Environmental Science and Technology.*, 37(24), pp. 5701–5710.

Chen, Z. J., G. L. Zhao, H. LI, J. J. Zhang, B. Song, G. R. H. (2010) 'Preparation of nanocrystalline TiO2 by sol - gel-method at room temperature. Journal of inorganic chemistry', *Journal of inorganic chemistry*, 26(5), pp. 860–866. doi: ISSN 1001-4861.

Chen, D. *et al.* (2007) 'Carbon and Nitrogen Co-doped TiO $_2$ with Enhanced Visible-Light Photocatalytic Activity', *Industrial & Engineering Chemistry Research*. doi: 10.1021/ie061491k.

Chen, D., Sivakumar, M. and Ray, A. K. (2000) 'Heterogeneous Photocatalysis in Environmental Remediation', *Asia-Pacific Journal of chemical Engineering*, 8(5–6), pp. 505–550. doi: 10.1017/CBO9781107415324.004.

Chen, Y. *et al.* (2015) 'Synergistic degradation performance and mechanism of 17β-estradiol by dielectric barrier discharge non-thermal plasma combined with Pt-TiO<inf>2</inf>', *Separation and Purification Technology*. doi: 10.1016/j.seppur.2015.07.061.

Chen, Y. and Dionysiou, D. D. (2006) 'Correlation of structural properties and film thickness to photocatalytic activity of thick TiO2 films coated on stainless steel', *Applied Catalysis B: Environmental*. doi: 10.1016/j.apcatb.2006.05.002.

Chen, Y. and Dionysiou, D. D. (2007) 'A comparative study on physicochemical properties and photocatalytic behavior of macroporous TiO2-P25 composite films and macroporous TiO2 films coated on stainless steel substrate', *Applied Catalysis A: General*. doi: 10.1016/j.apcata.2006.10.025.

Chen, Y. and Dionysiou, D. D. (2008) 'Bimodal mesoporous TiO2-P25 composite thick films with high photocatalytic activity and improved structural integrity', *Applied Catalysis B: Environmental*. doi: 10.1016/j.apcatb.2007.11.010.

Chen, Y. S. *et al.* (2004) 'Pulsed high-voltage discharge plasma for degradation of phenol in aqueous solution', *Separation and Purification Technology*. doi: 10.1016/S1383-5866(03)00169-2.

Chen, Y., Stathatos, E. and Dionysiou, D. D. (2008) 'Microstructure characterization and photocatalytic activity of mesoporous TiO2films with ultrafine anatase nanocrystallites', *Surface and Coatings Technology*. doi: 10.1016/j.surfcoat.2007.08.041.

Cheng, H.-H. *et al.* (2007) *NON-Thermal plasma technology for degradation of organic compounds in wastewater control: a critical review, J. Environ. Eng. Manage.*

Cheng, X. *et al.* (2012a) 'Energy Procedia Enhanced Photocatalytic Activity of Nitrogen Doped TiO2 Anatase Nano-Particle under Simulated Sunlight Irradiation peer-review under responsibility of RIUDS', *Energy Procedia*, 16, pp. 598–605. doi: 10.1016/j.egypro.2012.01.096.

Cheng, X. *et al.* (2012b) 'Enhanced Photocatalytic Activity of Nitrogen Doped TiO2 Anatase Nano-Particle under Simulated Sunlight Irradiation', in *Energy Procedia*. doi: 10.1016/j.egypro.2012.01.096.

Cheng, X. *et al.* (2016) 'Synthesis and characterization of N-doped TiO2and its enhanced visible-light photocatalytic activity', *Arabian Journal of Chemistry*. doi: 10.1016/j.arabjc.2012.04.052.

Choina, J. *et al.* (2015) 'The influence of the textural properties of ZnO nanoparticles on adsorption and photocatalytic remediation of water from pharmaceuticals', *Catalysis Today*. doi: 10.1016/j.cattod.2014.05.014.

Chouparova, E., Lanzirotti, A., Feng, H., Jones, K.W., Marinkovic, N., Whitson, C., and Philp, P., (2004). (2004) 'Title: Characterization of petroleum deposits formed in a producing well by synchrotron radiation-based microanalyses energy fuels.', 18(4), pp. 1199–1212.

Chu, D. *et al.* (2008) 'Efficient carbon-doped nanostructured TiO2 (anatase) film for photoelectrochemical solar cells', *Journal of Nanoparticle Research*. doi: 10.1007/s11051-007-9241-7.

Chu, S. Z. *et al.* (2005) 'Fabrication and photocatalytic characterizations of ordered nanoporous X-doped (X = N, C, S, Ru, Te, and Si) TiO2/Al2O3films on ITO/glass', *Langmuir*. doi: 10.1021/la050902j.

Cicek, V. (2014) *Corrosion Engineering, Corrosion Engineering*. doi: 10.1002/9781118720837.

Çomakli, O. *et al.* (2016) 'The effect of calcination temperatures on structural and electrochemical properties of TiO2film deposited on commercial pure titanium', *Surface and Coatings Technology*. doi: 10.1016/j.surfcoat.2015.11.055.

Çomakli, O., Yetim, T. and Çelik, A. (2014) 'The effect of calcination temperatures on wear properties of TiO2coated CP-Ti', *Surface and Coatings Technology*. doi:

10.1016/j.surfcoat.2014.02.059.
Coman, T. *et al.* (2017) 'Sequential PLD in oxygen/argon gas mixture of Al-doped ZnO thin films with improved electrical and optical properties', *Applied Surface Science*. doi: 10.1016/j.apsusc.2017.01.102.
Constantin, L. *et al.* (2016) 'Effects of Zr, Nb, or Si addition on the microstructural, mechanical, and corrosion resistance of TiCN hard coatings', *Materials and Corrosion*. doi: 10.1002/maco.201508737.
Croue, J.P., Korshin, G.V. and Benjamin, M. (2000) 'Title: Characterization of Natural Organic Matter in Drinking water.', *AWWA*.
Czech, B. *et al.* (2015) 'MWCNT-TiO2-SiO2nanocomposites possessing the photocatalytic activity in UVA and UVC', *Applied Catalysis B: Environmental*. doi: 10.1016/j.apcatb.2014.07.035.
Danish, M. *et al.* (2015) 'Optimization and comparative evaluation of optical and photocatalytic properties of TiO<inf>2</inf> thin films prepared via sol-gel method', *Journal of Saudi Chemical Society*. doi: 10.1016/j.jscs.2015.05.010.
Dantas, R. F. *et al.* (2008) 'Sulfamethoxazole abatement by means of ozonation', *Journal of Hazardous Materials*. doi: 10.1016/j.jhazmat.2007.05.034.
Darányi Mária, István Sarusi, András Sápi, Ákos Kukovecz, Zoltán Kónya, A. E. (2011) 'Characterization of carbon thin films prepared by the thermal decomposition of spin coated polyacrylonitrile layers containing metal acetates', *Thin Solid Films* , 520, pp. 57–63.
Das, L. *et al.* (2015) 'Aqueous degradation kinetics of pharmaceutical drug diclofenac by photocatalysis using nanostructured titania–zirconia composite catalyst', *International Journal of Environmental Science and Technology*. doi: 10.1007/s13762-013-0466-y.
Daughton, C.G., Ternes, T. A. (1999) 'Title: Pharmaceuticals and personal care products in the environment: agents of subtle change?', *Environ. Health Perspect.*, 107, pp. 907-938.
Demirev, A. and Nenov, V. (2005) 'Ozonation of two acidic azo dyes with different substituents', *Ozone: Science and Engineering*. doi: 10.1080/01919510500351834.
Deng, J. *et al.* (2008) 'Unlubricated friction and wear behaviors of ZrN coatings against hardened steel', *Materials and Design*. doi: 10.1016/j.matdes.2008.03.007.
Didenko, Y. T. and Suslick, K. S. (2002) *The energy efficiency of formation of photons, radicals and ions during single-bubble cavitation*. Available at: www.nature.com/nature.
Dijkstra, M.F.J., H.J. Panneman, J.G.M. Winkelman, J.J. Kelly, A. A. C. M. B. (2002) 'Modeling the photocatalytic degradation of formic acid in a reactor with immobilized catalyst', *Chemical Engineering Science*, 57(22–23), pp. 4895–4907. doi: ISSN 00092509.

Dimitrakopoulou, D. *et al.* (2012) 'Degradation, mineralization and antibiotic inactivation of amoxicillin by UV-A/TiO2photocatalysis', *Journal of Environmental Management*. doi: 10.1016/j.jenvman.2012.01.010.

Dinu, M. *et al.* (2015) 'Improvement of the tribological performance in corrosive environment of CoCr alloy by TiSiON coatings', *Applied Surface Science*. doi: 10.1016/j.apsusc.2015.01.221.

Dinu, M. *et al.* (2016) 'In vitro corrosion resistance of Si containing multi-principal element carbide coatings', *Materials and Corrosion*. doi: 10.1002/maco.201508788.

Dinu, M. *et al.* (2017a) 'Protective performance of Zr and Cr based silico-oxynitrides used for dental applications by means of potentiodynamic polarization and odd random phase multisine electrochemical impedance spectroscopy', *Corrosion Science*. doi: 10.1016/j.corsci.2016.11.018.

Dinu, M. *et al.* (2017b) 'Protective performance of Zr and Cr based silico-oxynitrides used for dental applications by means of potentiodynamic polarization and odd random phase multisine electrochemical impedance spectroscopy', *Corrosion Science*. doi: 10.1016/j.corsci.2016.11.018.

Dinu, M. *et al.* (no date) 'Enhancement of the Corrosion Resistance of 304 Stainless Steel by Cr-N and Cr(N,O) Coatings'. doi: 10.3390/coatings8040132.

Dirany, A. *et al.* (2010) 'Electrochemical abatement of the antibiotic sulfamethoxazole from water', *Chemosphere*. doi: 10.1016/j.chemosphere.2010.08.032.

Djaneye-Boundjou G., Etsri Amouzou, Tomkouani Kodom, I. T. and L. M. B. K. A. (2012) 'Photocatalytic degradation of orange II using mesoporous TiO2 (P25) and Fenton reactive (Fe2+/H2O2)', *International Journal of Environmental Science, Management and Engineering Research*, Vol. 1(No. 2), pp. 91–96.

Dojčinović, B. P. *et al.* (2011) 'Decolorization of reactive textile dyes using water falling film dielectric barrier discharge', *Journal of Hazardous Materials*. doi: 10.1016/j.jhazmat.2011.05.086.

Van Doorslaer, X., Dewulf, J., Van Langenhove, H., Demeestere, K. (2014) 'Title: Fluoroquinolone antibiotics: an emerging class of environmental Micropollutants.', *S. C. Total Environ.*, 500–501, pp. 250–269.

Dors M. (2007) 'Plasma for water treatment. Part-financed by the European Union. PlasTep. Centre for Plasma and Laser Engineering.', *The SzewalskiInstitute of Fluid-Flow Machinery Polish Academy of Sciences. Gdaosk, Poland.*

Douglas B. Mawhinney, Brett J. Vanderford, S. A. S. (2012) 'Transformation of 1H-

Benzotriazole by Ozone in Aqueous Solution', *Environ. Sci. Technol.*, 46, p. 7102−7111.

Drewes, J.E., Quanrud, D.M., Amy, G.L., and Westerhoff, P. K. (2006) 'Title: Character of Organic Matter in Soil-Aquifer Treatment Systems.', *J. Environ. Eng.*, 132(11), pp. 1447–1458.

Duan, F. *et al.* (2015) 'Activated carbon electrodes: Electrochemical oxidation coupled with desalination for wastewater treatment', *Chemosphere*. Elsevier Ltd, 125, pp. 205–211. doi: 10.1016/j.chemosphere.2014.12.065.

Dvoranová, D. *et al.* (2002) 'Investigations of metal-doped titanium dioxide photocatalysts', *Applied Catalysis B: Environmental*. Elsevier, 37(2), pp. 91–105. doi: 10.1016/S0926-3373(01)00335-6.

Ehrlich, A. *et al.* (1995) 'Complex characterisation of vacuum arc-deposited chromium nitride thin films', *Surface and Coatings Technology*. doi: 10.1016/0257-8972(95)02583-9.

Eisenberg, G. (1943) 'Colorimetric Determination of Hydrogen Peroxide.', *Industrial & Engineering Chemistry Analytical Edition*, 15(5), pp. 327–328. doi: doi:10.1021/i560117a011.

Endrino, J. L. and Derflinger, V. (2005) 'The influence of alloying elements on the phase stability and mechanical properties of AlCrN coatings', *Surface and Coatings Technology*. doi: 10.1016/j.surfcoat.2005.02.196.

Escobar, C. A., Caicedo, J. C. and Aperador, W. (2014) 'Corrosion resistant surface for vanadium nitride and hafnium nitride layers as function of grain size', *Journal of Physics and Chemistry of Solids*. doi: 10.1016/j.jpcs.2013.07.024.

Esplugas, S. *et al.* (2007) 'Ozonation and advanced oxidation technologies to remove endocrine disrupting chemicals (EDCs) and pharmaceuticals and personal care products (PPCPs) in water effluents', *Journal of Hazardous Materials*. doi: 10.1016/j.jhazmat.2007.07.073.

Evgenidou, E.N., Konstantinou, I.K., Lambropoulou, D. A. (2015) 'Title: Occurrence and A, removal of transformation products of PPCPs and illicit drugs in wastewaters':, *review. Sci. Total Environ.*, 505, pp. 905–926.

Fadlallah, S. A. *et al.* (2014) 'An overview of NiTi shape memory alloy: Corrosion resistance and antibacterial inhibition for dental application', *Journal of Alloys and Compounds*. doi: 10.1016/j.jallcom.2013.08.029.

Fang, X., Mark, G. and von Sonntag, C. (1996) 'OH radical formation by ultrasound in aqueous solutions Part I: the chemistry underlying the terephthalate dosimeter', *Ultrasonics Sonochemistry*. Elsevier, 3(1), pp. 57–63. doi: 10.1016/1350-4177(95)00032-1.

Farré, M. J. *et al.* (2005) 'Degradation of some biorecalcitrant pesticides by homogeneous and heterogeneous photocatalytic ozonation', *Chemosphere*. doi: 10.1016/j.chemosphere.2004.09.064.

Farzaneh, M. A. *et al.* (2011) 'Effects of Co and W alloying elements on the electrodeposition aspects and properties of nanocrystalline Ni alloy coatings', *Applied Surface Science*. doi: 10.1016/j.apsusc.2011.02.008.

Fathinia, M. and Khataee, A. (2015) 'Photocatalytic ozonation of phenazopyridine using TiO2nanoparticles coated on ceramic plates: Mechanistic studies, degradation intermediates and ecotoxicological assessments', *Applied Catalysis A: General*. doi: 10.1016/j.apcata.2014.10.049.

Fattah-Alhosseini, A. and Vafaeian, S. (2016) 'Influence of grain refinement on the electrochemical behavior of AISI 430 ferritic stainless steel in an alkaline solution', *Applied Surface Science*. doi: 10.1016/j.apsusc.2015.11.085.

Feng, J. *et al.* (2003) 'Degradation of azo-dye orange II by a photoassisted Fenton reaction using a novel composite of iron oxide and silicate nanoparticles as a catalyst', *Industrial and Engineering Chemistry Research*. doi: 10.1021/ie0207010.

Feng, J. *et al.* (2016) 'Dielectric barrier discharge plasma induced degradation of aqueous atrazine', *Environmental Science and Pollution Research*. doi: 10.1007/s11356-016-6148-9.

Fernández, A. *et al.* (1995) 'Preparation and characterization of TiO2photocatalysts supported on various rigid supports (glass, quartz and stainless steel). Comparative studies of photocatalytic activity in water purification', *Applied Catalysis B, Environmental*. doi: 10.1016/0926-3373(95)00026-7.

Finkelstein, E. (1980) 'Spin trapping. Kinetics of the reaction of superoxide and hydroxyl radicals with nitrones', *Journal of the American …*, (12), pp. 4994–4999. doi: 10.1021/ja00535a029.

Fix, D. V *et al.* (2004) *General and Localized Corrosion of Austenitic And Borated Stainless Steels in Simulated Concentrated Ground Waters*.

Fu, X. *et al.* (1996) *Effects of reaction temperature and water vapor content on the heterogeneous photocatalytic oxidation of ethylene, Journal of Photochemistry and Photobiology A: Chemistry*.

Galindo, C. and Kalt, A. (1998) *Pigments elsevier UV-H 2 02 oxidation ofmonoazo dyes in aqueous media: a kinetic study, Dyes and Pigments*.

Garoma, T., Umamaheshwar, S. K. and Mumper, A. (2010) 'Removal of sulfadiazine, sulfamethizole, sulfamethoxazole, and sulfathiazole from aqueous solution by ozonation',

Chemosphere. doi: 10.1016/j.chemosphere.2010.02.060.

Gauthier Nganda Okolongo, B. and Petrik Willem J Perold, L. F. (2013) *Advanced oxidative water treatment process using an electrohydraulic discharge reactor and tio 2 immobilised on nanofibres*.

Geng, J. *et al.* (2009) 'Nitrogen-doped TiO2nanotubes with enhanced photocatalytic activity synthesized by a facile wet chemistry method', *Materials Research Bulletin*. doi: 10.1016/j.materresbull.2008.03.010.

Ghatak, H. R. (2014) 'Advanced Oxidation Processes for the Treatment of Biorecalcitrant Organics in Wastewater', *Critical Reviews in Environmental Science and Technology*. Taylor & Francis, 44(11), pp. 1167–1219. doi: 10.1080/10643389.2013.763581.

Ghauch, A., Ayoub, G. and Naim, S. (2013) 'Degradation of sulfamethoxazole by persulfate assisted micrometric Fe0 in aqueous solution', *Chemical Engineering Journal*. doi: 10.1016/j.cej.2013.05.045.

Ghezzar M.R., S. Ognier, S. Cavadias, F. Abdelmalek, A. A. (2013) 'DBDplate-TiO2 treatment of Yellow Tartrazine azo dye solution in falling film', *Sep. Purif. Technol*, 104, pp. 250–255.

Gilmour, C. (2012) 'Water Treatment using Advanced Oxidation Processes : Application Perspectives', (September), pp. 1–111.

Gilmour, C. R. *et al.* (2013) 'Photocatalytic performance of titanium dioxide thin films from polymer-encapsulated titania', *Industrial and Engineering Chemistry Research*. doi: 10.1021/ie402096h.

Gilmour, C. R. and Ray, M. (2012) *Water Treatment Using Advanced Oxidation Processes: Application Perspectives*. Available at: https://ir.lib.uwo.ca/etdhttps://ir.lib.uwo.ca/etd/836.

Gira, M. J., Tkacz, K. P. and Hampton, J. R. (2016) 'Physical and electrochemical area determination of electrodeposited Ni, Co, and NiCo thin films', *Nano Convergence*, 3(1), p. 6. doi: 10.1186/s40580-016-0063-0.

Giraldo-Aguirre, A. L. *et al.* (2015) 'TiO<inf>2</inf> photocatalysis applied to the degradation and antimicrobial activity removal of oxacillin: Evaluation of matrix components, experimental parameters, degradation pathways and identification of organics by-products', *Journal of Photochemistry and Photobiology A: Chemistry*. doi: 10.1016/j.jphotochem.2015.06.021.

Glaze, W. H. (1986) 'Reaction products of ozone: A review', *Environmental Health Perspectives*. doi: 10.1289/ehp.8669151.

Glaze, William H (1986) *Reaction Products of Ozone: A Review*, *Environmental Health*

Perspectives.

Gnanasekaran, L., Hemamalini, R. and Ravichandran, K. (2015) 'Synthesis and characterization of TiO<inf>2</inf> quantum dots for photocatalytic application', *Journal of Saudi Chemical Society*. doi: 10.1016/j.jscs.2015.05.002.

Gogate, P. R. and Pandit, A. B. (2004a) 'A review of imperative technologies for wastewater treatment I: Oxidation technologies at ambient conditions', *Advances in Environmental Research*. doi: 10.1016/S1093-0191(03)00032-7.

Gogate, P. R. and Pandit, A. B. (2004b) 'A review of imperative technologies for wastewater treatment II: hybrid methods', *Advances in Environmental Research*. doi: 10.1016/S1093-0191(03)00031-5.

Gogate P.R. and Pandit A.B. (2004) 'A review of imperative technologies for wastewater treatment I: oxidation technologies at ambient conditions', *Adv. Environ. Res.* , 8, pp. 501–551.

Gonzalez, D. H. *et al.* (2018) 'Terephthalate Probe for Hydroxyl Radicals: Yield of 2-Hydroxyterephthalic Acid and Transition Metal Interference', *Analytical Letters*. doi: 10.1080/00032719.2018.1431246.

Gorga, M., Insa, S., Petrovic, M., Barcelo, D. (2015) 'Title: Occurrence and spatial distribution of EDCs and related compounds in waters and sediments of Iberian Rivers.', *Sci. Total Environ.*, 503–504, pp. 69–86.

Grabowski, L. R., Veldhuizen, van, E. M., Pemen, A. J. M., & Rutgers, W. R. (2007) 'Breakdown of methylene blue and methyl orange by pulsed corona discharge.', *Plasma Sources Science and Technology*, 16(2), pp. 226–232. doi: 10.1088/0963-0252/16/2/003.

Guang-Zhou Qu, Na Lu, Jie Li, Yan Wu, Guo-Feng Li, D. L. (2009) 'Simulataneous pentachlorophenol decomposition and granular activated carbon regeneration assisted by dielectric barrier discharge plasma.', *Journal of Hazardous Materials*, 172, pp. 472–478.

Guillard, C. *et al.* (2003) 'Influence of chemical structure of dyes, of pH and of inorganic salts on their photocatalytic degradation by TiO2comparison of the efficiency of powder and supported TiO2', *Journal of Photochemistry and Photobiology A: Chemistry*. doi: 10.1016/S1010-6030(03)00016-9.

Guivarch, E. *et al.* (2003) 'Degradation of azo dyes in water by Electro-Fenton process', *Environmental Chemistry Letters*. doi: 10.1007/s10311-002-0017-0.

Gültekin, A. *et al.* (2013) 'The influence of CdS quantum dots incorporation on the properties of CdO thin films', *The European Physical Journal Applied Physics*. doi: 10.1051/epjap/2013130418.

Gültekin, A. *et al.* (2014) 'Synthesis and characterisations of Au-nanoparticle-doped TiO2and CdO thin films', *Journal of Physics and Chemistry of Solids*. doi: 10.1016/j.jpcs.2014.01.011.

Guo, H. *et al.* (2010) 'Noble metal-modified TiO2 thin film photocatalyst on porous steel fiber support', *Applied Catalysis B: Environmental*. doi: 10.1016/j.apcatb.2010.01.014.

Guo, W. Q. *et al.* (2015) 'Sulfamethoxazole degradation by ultrasound/ozone oxidation process in water: Kinetics, mechanisms, and pathways', *Ultrasonics Sonochemistry*. doi: 10.1016/j.ultsonch.2014.07.008.

Guo, X. *et al.* (2018) 'Photocatalytic properties of P25-doped TiO2composite film synthesized via sol–gel method on cement substrate', *Journal of Environmental Sciences (China)*. doi: 10.1016/j.jes.2017.05.029.

Gupta, S. B. (2007a) *Investigation of a Physical Disinfection Process Based on Pulsed Underwater Corona Discharges*. doi: Forschungszentrum Karlsruhe in der Helmholtz-Gemeinschaft Wissenschaftliche Berichte FZKA 7336.

Gupta, S. B. (2007b) *Investigation of a Physical Disinfection Process Based on Pulsed Underwater Corona Discharges*.

Gurol M.D., V. R. (1987) 'Title: Oxidation of phenolic compounds by ozone and ozone and u.v. radiation: a comparative study', *Water Res.*, 21(8), pp. 895–900.

Guy, M. and Eng, Z. B. (1992) *The use of ozone for the treatment of logyard run-off*.

Han, C. *et al.* (2011) 'Innovative visible light-activated sulfur doped TiO2films for water treatment', *Applied Catalysis B: Environmental*. doi: 10.1016/j.apcatb.2011.06.039.

Han, C., Luque, R. and Dionysiou, D. D. (2012) 'Facile preparation of controllable size monodisperse anatase titania nanoparticles', *Chemical Communications*. doi: 10.1039/c1cc16050h.

Han, G. *et al.* (2014) 'Size-dependent optical properties and enhanced visible light photocatalytic activity of wurtzite CdSe hexagonal nanoflakes with dominant {0 0 1} facets', *Journal of Alloys and Compounds*. doi: 10.1016/j.jallcom.2014.04.164.

Hasan, M. *et al.* (2015) 'Electrical conductivity, optical property and ammonia sensing studies on HCl Doped Au@polyaniline nanocomposites', *Electronic Materials Letters*. doi: 10.1007/s13391-014-4200-9.

Hassan, M. E. *et al.* (2014) 'Synthesis and characterization of C-doped TiO2 thin films for visible-light-induced photocatalytic degradation of methyl orange', *Applied Surface Science*. doi: 10.1016/j.apsusc.2013.12.069.

Hassani, A., Khataee, A. and Karaca, S. (2015) 'Photocatalytic degradation of ciprofloxacin

by synthesized TiO<inf>2</inf> nanoparticles on montmorillonite: Effect of operation parameters and artificial neural network modeling', *Journal of Molecular Catalysis A: Chemical*. doi: 10.1016/j.molcata.2015.08.020.

Hassannejad, H. *et al.* (2010) 'Effect of cerium doping on corrosion resistance of amorphous silica-titanium sol-gel coating', *Current Applied Physics*. doi: 10.1016/j.cap.2009.12.033.

Hastie, J. *et al.* (2006) 'Electrochemical methods for degradation of Orange II (sodium 4-(2-hydroxy-l-naphthylazo)benzenesulfonate)', *Industrial and Engineering Chemistry Research*. doi: 10.1021/ie060310b.

Hauert, R. and Patscheider, J. (2000) 'From alloying to nanocomposites - Improved performance of hard coatings', *Advanced Engineering Materials*. doi: 10.1002/(SICI)1527-2648(200005)2:5<247::AID-ADEM247>3.0.CO;2-U.

Haugland R.P., H. R. P. (1996) *Title: Handbook of fluorescence probes*. 6th edn. Eugene (OR): Molecular Probes,.

Hayashi, H. *et al.* (2016) *Comparison of OH Radical Concentration Generated by Underwater Discharge Using Two Methods*.

He, D. *et al.* (2014) 'Aqueous tetracycline degradation by non-thermal plasma combined with nano-TiO2', *Chemical Engineering Journal*. doi: 10.1016/j.cej.2014.07.089.

He, X., Ahn, T. and Sippel, T. (2011) *Corrosion of borated stainless steel in water and humid air*.

He, Y. *et al.* (2016) 'Degradation of pharmaceuticals in wastewater using immobilized TiO2photocatalysis under simulated solar irradiation', *Applied Catalysis B: Environmental*. doi: 10.1016/j.apcatb.2015.09.015.

Heberer, T. (2002) *Occurrence, fate, and removal of pharmaceutical residues in the aquatic environment: a review of recent research data, Toxicology Letters*. Available at: www.elsevier.com/locate/toxlet.

Hintsho, N. *et al.* (2014) 'Photo-catalytic activity of titanium dioxide carbon nanotube nano-composites modified with silver and palladium nanoparticles', *Applied Catalysis B: Environmental*. doi: 10.1016/j.apcatb.2014.03.021.

Hirakawa, T., Yawata, K. and Nosaka, Y. (2007) 'Photocatalytic reactivity for O2{radical dot}-and OH{radical dot} radical formation in anatase and rutile TiO2suspension as the effect of H2O2addition', *Applied Catalysis A: General*. doi: 10.1016/j.apcata.2007.03.015.

Hoeben, W. (2000) *Pulsed corona-iduced degradation of organic materials in water*.

Hoigne, J. (1988) *The Chemistry of Ozone in Water. In Process Technologies for Water Treatment*. New York: Stucki, S., Ed.; Plenum Publishing Corporation.

Holleman, E. W. N. W. A. F. (2001) *Inorganic Chemistry*. Edited by Nils Wiberg. San Diego/Berlin/New York: San Diego : Academic Press ; Berlin ; New York : De Gruyter,.

Homem, V., Alves, A. and Santos, L. (2010) 'Amoxicillin degradation at ppb levels by Fenton's oxidation using design of experiments', *Science of the Total Environment*. doi: 10.1016/j.scitotenv.2010.08.058.

Houtman, C.J., Kroesbergen, J., Lekkerkerker-Teunissen, K., van der Hoek, J. P. (2014) 'Title: Human health risk assessment of the mixture of pharmaceuticals in Dutch, drinking water and its sources based on frequent monitoring data.', *Sci. Total Environ.*, 496, pp. 54-62.

Hu, A. *et al.* (2011a) 'Hydrothermal growth of free standing TiO2 nanowire membranes for photocatalytic degradation of pharmaceuticals', *Journal of Hazardous Materials*. doi: 10.1016/j.jhazmat.2011.02.033.

Hu, A. *et al.* (2011b) 'Hydrothermal growth of free standing TiO2 nanowire membranes for photocatalytic degradation of pharmaceuticals', *Journal of Hazardous Materials*. Elsevier B.V., 189(1–2), pp. 278–285. doi: 10.1016/j.jhazmat.2011.02.033.

Hua, L. and Hou, H. (2012) 'Electrochemical migration behaviors of lead-free 64Sn-35Bi-1Ag solder on FR-4 PCB board plated with Cu', *Wuhan University Journal of Natural Sciences*. doi: 10.1007/s11859-012-0808-5.

Huang, F. *et al.* (2012) 'Degradation of methyl orange by atmospheric DBD plasma: Analysis of the degradation effects and degradation path', *Journal of Electrostatics*. doi: 10.1016/j.elstat.2011.10.001.

Hummel, D., Loffler, D., Fink, G., Ternes, T. A. (2006) 'Title: Simultaneous determination of psychoactive drugs and their metabolites in aqueous matrices by liquid Chromatography mass spectrometry.', *Environ. Sci. Technol.*, 40, pp. 7321–7328.

Hyunook Kim, H. L. & M. F. C. (2007) 'Determination of chemical oxygen demand (COD) using ultrasound digestion and oxidation-reduction potential-based titration', *Journal of Environmental Science and Health*, Part A, 42(11), pp. 1665–1670. doi: 10.1080/10934520701518190.

I. Ivancev-Tumbas (2014) 'Title: The fate and importance of organics in drinking water treatment: a review', *Environ. Sci. Pollut. Res. Int.*, 21, pp. 11794 –11810.

Ince, N. H. and Tezcanh, G. (1999) 'Treatability of textile dye-bath effluents by advanced oxidation: Preparation for reuse', *Water Science and Technology*. No longer published by Elsevier, 40(1), pp. 183–190. doi: 10.1016/S0273-1223(99)00379-0.

Van Ingelgem, Y. *et al.* (2009) 'Advantages of odd random phase multisine electrochemical impedance measurements', *Electroanalysis*. doi: 10.1002/elan.200804471.

Iqbal, M., Bhatti, I. A. and Ahmad, I. (2013) 'Photo-degradation of the methyl blue: Optimization through response surface methodology using rotatable center composite design', *International Journal of Basic and Applied Sciences*. doi: 10.14419/ijbas.v2i2.707.

Irie, H., Watanabe, Y. and Hashimoto, K. (2003) 'Nitrogen-Concentration Dependence on Photocatalytic Activity of $TiO_{2-x}N_x$ Powders', *The Journal of Physical Chemistry B*. doi: 10.1021/jp030133h.

Islam, M. A. *et al.* (2015) 'Effect of microstructure on the erosion behavior of carbon steel', *Wear*. doi: 10.1016/j.wear.2014.12.004.

Jang, J. S. *et al.* (2006) 'Formation of crystalline TiO2-xNx and its photocatalytic activity', *Journal of Solid State Chemistry*. doi: 10.1016/j.jssc.2006.01.004.

Jarka, P. *et al.* (2017) 'Manufacturing and investigation of surface morphology and optical properties of composite thin films reinforced by TiO2, Bi2O3 and SiO2 nanoparticles', *Applied Surface Science*. doi: 10.1016/j.apsusc.2017.03.232.

Ji, Y. *et al.* (2013) 'Degradation of sunscreen agent 2-phenylbenzimidazole-5-sulfonic acid by TiO2photocatalysis: Kinetics, photoproducts and comparison to structurally related compounds', *Applied Catalysis B: Environmental*. doi: 10.1016/j.apcatb.2013.04.046.

Jiang, B. *et al.* (2013) 'Degradation of organic dye by pulsed discharge non-thermal plasma technology assisted with modified activated carbon fibers', *Chemical Engineering Journal*. doi: 10.1016/j.cej.2012.11.046.

Jiang, B. *et al.* (2014) 'Review on electrical discharge plasma technology for wastewater remediation', *Chemical Engineering Journal*. doi: 10.1016/j.cej.2013.09.090.

Jo, J.-O. and Mok, Y. S. (2009) 'In-situ production of ozone and ultraviolet light using a barrier discharge reactor for wastewater treatment', *J Zhejiang Univ Sci A*, 10(9), pp. 1359–1366. doi: 10.1631/jzus.A0820696.

Jones, K.W., Feng, H., Stern, E.A., Neuhausler, U., Osan, J., Marinkovic, N., and Song, Z. (2006) 'Title: Properties of New York/New Jersey Harbor Sediments.', *Acta Physica Polonica*, 109(3), pp. 279–86.

Joshi, A. A. *et al.* (1995) 'Formation of hydroxyl radicals, hydrogen peroxide and aqueous electrons by pulsed streamer corona discharge in aqueous solution', *Journal of Hazardous Materials*. Elsevier, 41(1), pp. 3–30. doi: 10.1016/0304-3894(94)00099-3.

Joshi, R. P. and Thagard, S. M. (2013) 'Streamer-like electrical discharges in water: Part II. environmental applications', *Plasma Chemistry and Plasma Processing*. doi: 10.1007/s11090-013-9436-x.

Joshi, Suresh G *et al.* (2015) 'Microarray Analysis of Transcriptomic Response of

Escherichia coli to Nonthermal Plasma-Treated PBS Solution', 6(6), pp. 49–62. doi: 10.4236/abb.2015.62006.

Junwei, W. *et al.* (2007) 'An efficient two-step technique for nitrogen-doped titanium dioxide synthesizing: Visible-light-induced photodecomposition of methylene blue', *Journal of Physical Chemistry C*. doi: 10.1021/jp066156o.

Justin Schäffer (2012) 'Immobilization of TiO2 Via different routes for photocatalytic reactions in a PDMS based microreactor. A thesis submitted for the degree of Bachelor of Science University of Twente Faculty of Science and Technology Soft Matter, Fluidics and Interfaces.'

Kanade, K. G. *et al.* (2007) 'Self-assembled aligned Cu doped ZnO nanoparticles for photocatalytic hydrogen production under visible light irradiation', *Materials Chemistry and Physics*. doi: 10.1016/j.matchemphys.2006.11.012.

Kanakaraju, D., Glass, B. D. and Oelgemöller, M. (2014) 'Titanium dioxide photocatalysis for pharmaceutical wastewater treatment', *Environmental Chemistry Letters*, 12(1), pp. 27–47. doi: 10.1007/s10311-013-0428-0.

Kanazawa, S. *et al.* (2011) 'Observation of OH radicals produced by pulsed discharges on the surface of a liquid', *Plasma Sources Science and Technology*. doi: 10.1088/0963-0252/20/3/034010.

Kenanakis, G. *et al.* (2015) 'Photocatalytic and electrooxidation properties of TiO2thin films deposited by sol-gel', *Catalysis Today*. doi: 10.1016/j.cattod.2014.05.007.

Khan, M. I. *et al.* (2017) 'Characterizations of multilayer ZnO thin films deposited by sol-gel spin coating technique', *Results in Physics*. doi: 10.1016/j.rinp.2016.12.029.

Khan, M. M. *et al.* (2014) 'Band gap engineered TiO_2 nanoparticles for visible light induced photoelectrochemical and photocatalytic studies', *J. Mater. Chem. A*. doi: 10.1039/C3TA14052K.

Khan, M. M., Adil, S. F. and Al-Mayouf, A. (2015) 'Metal oxides as photocatalysts', *Journal of Saudi Chemical Society*. doi: 10.1016/j.jscs.2015.04.003.

Khan, M. Z. R. *et al.* (2009) 'Trapped charge dynamics in a sol-gel based TiO2high- k gate dielectric silicon metal-oxide-semiconductor field effect transistor', *Journal of Physics Condensed Matter*. doi: 10.1088/0953-8984/21/21/215902.

Khetan, S.K., Collins, T.J. (2007) 'Title: Human pharmaceuticals in the aquatic environment: a challenge to green chemistry.', *Chem. Rev.*, 107, pp. 2319–2364.

Kim, H., and Yu, M. (2005) 'Title: Characterization of Natural Organic Matter in Conventional Water Treatment Processes for Selection of Treatment Processes Focused on

DBPs Control.', *Water Res.*, 39(19), pp. 4779–4789.
Kim, K., Kyu, S. and Sun, Y. (2015) 'Elucidation of the degradation pathways of sulfonamide antibiotics in a dielectric barrier discharge plasma system', *CHEMICAL ENGINEERING JOURNAL*. Elsevier B.V., 271, pp. 31–42. doi: 10.1016/j.cej.2015.02.073.
Kim, K. S., Kam, S. K. and Mok, Y. S. (2015) 'Elucidation of the degradation pathways of sulfonamide antibiotics in a dielectric barrier discharge plasma system', *Chemical Engineering Journal*. doi: 10.1016/j.cej.2015.02.073.
Kim, K. S., Yang, C. S. and Mok, Y. S. (2013) 'Degradation of veterinary antibiotics by dielectric barrier discharge plasma', *Chemical Engineering Journal*. doi: 10.1016/j.cej.2012.12.079.
Kinumoto, T. *et al.* (2015) 'Preparation of fibrous titania oxynitride - Carbon catalyst and oxygen reduction reaction analysis in both acidic and alkaline media', *Journal of Power Sources*, 273, pp. 136–141. doi: 10.1016/j.jpowsour.2014.09.069.
Kirk, R.E., Othmer, D. F. (1996) 'Encyclopedia of chemical technology', 4th ed.Vol(London:Wiley-Interscience, ISBN 0-471-52686-X, Ozone), p. ,953-994.
Kirk R.E., O. D. F. (1996) *Encyclopedia of chemical technology*. 4th ed.Vol. 17,. London: Wiley-Interscience.
Kirkland, N. T. *et al.* (2012) 'Exploring graphene as a corrosion protection barrier', *Corrosion Science*. doi: 10.1016/j.corsci.2011.12.003.
Klamerth N, Rizzo L, Malato S, Maldonado MI, Agüera A, F.-A. A. R. (2010) 'Title: Degradation of fifteen emerging contaminants at µg L-1 initial concentrations by mild solar photo-Fenton in MWTP effluents.', *Water Res*, 44, pp. 545 – 54.
Klavarioti, M., Mantzavinos, D. and Kassinos, D. (2009) 'Removal of residual pharmaceuticals from aqueous systems by advanced oxidation processes', *Environment International*. doi: 10.1016/j.envint.2008.07.009.
Klaysri, R. *et al.* (2017) 'Deposition of Visible Light-Active C-Doped Titania Films via Magnetron Sputtering Using CO2 as a Source of Carbon', *Nanomaterials*. doi: 10.3390/nano7050113.
Kochany, J. and Lipczynska-Kochany, E. (1992) 'Application of the EPR spin-trapping technique for the investigation of the reactions of carbonate, bicarbonate, and phosphate anions with hydroxyl radicals generated by the photolysis of H2O2', *Chemosphere*. doi: 10.1016/0045-6535(92)90018-M.
Kogelschatz, U. (2000) 'Fundamentals and applications of dielectric-barrier discharges'.
Kogelschatz, U. (2003) *Dielectric-barrier Discharges: Their History, Discharge Physics, and*

Industrial Applications.

Kolpin, D.W., Furlong, E.T., Meyer, M.T., Thurman, E.M., Zaugg, S.D., Barber, L. B. and Buxton, H. T. (2002) 'Title: Pharmaceuticals, hormones, and other organic wastewater contaminants in U.S. streams, 1999-2000: a national reconnaissance.', *Environ. Sci. Technol.*, 36, pp. 1202–1211.

Konelschatz U., B. E. and W. E. (1997) 'Title: Dielectric-barrier discharges. Principle and applications.', Journal de.

Konstantinou, I. K. and Albanis, T. A. (2004) 'TiO2-assisted photocatalytic degradation of azo dyes in aqueous solution: Kinetic and mechanistic investigations: A review', *Applied Catalysis B: Environmental*. doi: 10.1016/j.apcatb.2003.11.010.

Kr´ysa, J. *et al.* (2014) 'Photocatalytic and photoelectrochemical properties of sol-gel TiO 2 films of controlled thickness and porosity', *Catalysis Today*, 230, pp. 2–7. doi: 10.1016/j.cattod.2014.01.008.

Krasner, S.W., and Amy, G. (1995) 'Title: Jar Test Evaluations of Enhanced Coagulation.', *JAWW.*, 87(12), pp. 93–107.

Krugly, E. *et al.* (2015) 'Decomposition of 2-naphthol in water using a non-thermal plasma reactor', *Chemical Engineering Journal*. doi: 10.1016/j.cej.2014.08.098.

Kuang, L., Zhao, Y. and Liu, L. (2011) 'Photodegradation of Orange II by mesoporous TiO2', *Journal of Environmental Monitoring*. doi: 10.1039/c1em10361j.

Kumar, A. *et al.* (2015) 'High performance sol-gel spin-coated titanium dioxide dielectric based MOS structures', *Materials Science in Semiconductor Processing*. doi: 10.1016/j.mssp.2015.06.073.

Kuo, C. S., Lin, C. F. and Hong, P. K. A. (2015) 'Photocatalytic degradation of methamphetamine by UV/TiO2-Kinetics, intermediates, and products', *Water Research*. doi: 10.1016/j.watres.2015.01.043.

Kutschej, K. *et al.* (2005) 'Comparative study of Ti1-xAlxN coatings alloyed with Hf, Nb, and B', *Surface and Coatings Technology*. doi: 10.1016/j.surfcoat.2005.02.072.

L.S. Darken R.P. Smith (1948) 'Behaviour of Hydrogen in Steel During and After Immersion in Acid', *Corrosion*, 5, pp. 1–16. doi: doi:10.5006/0010-9312-5.1.1.

Laffont, L. *et al.* (2004) 'An EELS study of the structural and chemical transformation of PAN polymer to solid carbon', *Carbon*. doi: 10.1016/j.carbon.2004.04.043.

Lafi, W. K. and Al-Qodah, Z. (2006) 'Combined advanced oxidation and biological treatment processes for the removal of pesticides from aqueous solutions', *Journal of Hazardous Materials*. doi: 10.1016/j.jhazmat.2006.02.027.

Lallement, A. *et al.* (2018) 'First evaluation of the effect of microorganisms on steady state hydroxyl radical concentrations in atmospheric waters', *Chemosphere*. doi: 10.1016/j.chemosphere.2018.08.128.

Lam, M. W. and Mabury, S. A. (2005) 'Photodegradation of the pharmaceuticals atorvastatin, carbamazepine, levofloxacin, and sulfamethoxazole in natural waters', *Aquatic Sciences*. doi: 10.1007/s00027-004-0768-8.

Lapertot, M. *et al.* (2006) 'Enhancing biodegradability of priority substances (pesticides) by solar photo-Fenton', *Water Research*. doi: 10.1016/j.watres.2006.01.002.

Lazar, A. M. *et al.* (2014) 'Corrosion protection of 304L stainless steel by chemical vapor deposited alumina coatings', *Corrosion Science*. doi: 10.1016/j.corsci.2013.12.012.

Lazar, M., Varghese, S. and Nair, S. (2012) 'Photocatalytic Water Treatment by Titanium Dioxide: Recent Updates', *Catalysts*. doi: 10.3390/catal2040572.

Lazar M, M. A. (2014) 'Development of a stability indicating RP-HPLC method for simultaneous estimation of trimethoprim, sulfamethoxazole and methyl paraben in oral Suspension', *International Journal of Pharmaceutical Research & Analysis.*, Vol 4(Issue 2), pp. 83–89.

Ledakowicz, S., Solecka, M. and Zylla, R. (2001) 'Biodegradation, decolourisation and detoxification of textile wastewater enhanced by advanced oxidation processes', *Journal of Biotechnology*. doi: 10.1016/S0168-1656(01)00296-6.

Lee, D. Y. *et al.* (2014) 'Effect of Nb doping on morphology, crystal structure, optical band gap energy of TiO2thin films', *Current Applied Physics*. doi: 10.1016/j.cap.2013.12.025.

Lewkowicz, A. *et al.* (2012) 'Concentration-dependent fluorescence properties of rhodamine 6G in titanium dioxide and silicon dioxide nanolayers', *Journal of Physical Chemistry C*. doi: 10.1021/jp3022562.

Lewkowicz, A. *et al.* (2014) 'Thickness and structure change of titanium(IV) oxide thin films synthesized by the sol-gel spin coating method', *Optical Materials*. doi: 10.1016/j.optmat.2014.02.033.

Li, F. *et al.* (2017) 'Preparation and photocatalytic properties of porous C and N co-doped TiO2deposited on brick by a fast, one-step microwave irradiation method', *Journal of Environmental Sciences*. doi: 10.1016/j.jes.2017.03.042.

Li, H. *et al.* (2013) 'Degradation of orange II by UV-assisted advanced fenton process: Response surface approach, degradation pathway, and biodegradability', in *Industrial and Engineering Chemistry Research*. doi: 10.1021/ie401503u.

Li Puma, G., Bono, A. and Collin, J. G. (2008) 'Preparation of titanium dioxide photocatalyst

loaded onto activated carbon support using chemical vapor deposition: A review paper', *Journal of Hazardous Materials*. doi: 10.1016/j.jhazmat.2008.01.040.

Li, S. *et al.* (2015) 'Fluorescence detection of hydroxyl radicals in water produced by atmospheric pulsed discharges', *IEEE Transactions on Dielectrics and Electrical Insulation*. doi: 10.1109/TDEI.2015.005147.

Li, Shuzhen *et al.* (2015) 'Recyclable CNTs/Fe3O4magnetic nanocomposites as adsorbents to remove bisphenol A from water and their regeneration', *Chemical Engineering Journal*. doi: 10.1016/j.cej.2014.09.032.

Li, S. and Fu, J. (2013) 'Improvement in corrosion protection properties of TiO2 coatings by chromium doping', *Corrosion Science*, 68, pp. 101–110. doi: 10.1016/j.corsci.2012.10.040.

Li, X. Z. (2010) 'PCED2.0-A computer program for the simulation of polycrystalline electron diffraction pattern', *Ultramicroscopy*. doi: 10.1016/j.ultramic.2009.12.009.

Li, Y. *et al.* (2005) 'Synthesis and characterization of carbon-doped titania as an artificial solar light sensitive photocatalyst', *Chemical Physics Letters*. doi: 10.1016/j.cplett.2005.01.062.

Liang, L., and Singer, P. C. (2003) 'Title: Factors Influencing the Formation and Relative Distribution of Haloacetic Acids and Trihalomethanes in Drinking Water.', *Environ. Sci. Technol.*, 37, pp. 2920–2928.

Liao, J. *et al.* (2012) 'Photocatalytic degradation of methyl orange using a TiO2/Ti mesh electrode with 3D nanotube arrays', *ACS Applied Materials and Interfaces*. doi: 10.1021/am201220e.

Liao, Y. *et al.* (2013) 'Photocatalytic generation of multiple ROS types using low-temperature crystallized anodic TiO2 nanotube arrays', *Journal of Hazardous Materials*. Elsevier B.V., 260, pp. 434–441. doi: 10.1016/j.jhazmat.2013.05.047.

Licausi, M. P., Igual Muñoz, A. and Amigó Borrás, V. (2013) 'Influence of the fabrication process and fluoride content on the tribocorrosion behaviour of Ti6Al4V biomedical alloy in artificial saliva', *Journal of the Mechanical Behavior of Biomedical Materials*. doi: 10.1016/j.jmbbm.2013.01.019.

Lichtin, N. N. *et al.* (1994) 'Photocatalytic oxidative Degradation of vapors of some organic compounds over TiO2', *Research on Chemical Intermediates*. doi: 10.1163/156856794X00531.

Lide D.R. (1999) 'Title: Handbook of Chemistry and Physics 79th edn., Cleveland (OH):Chemical Rubber Co.', *ISBN Solubility of selected gases in water*, 8(89), pp. 8–86.

Lin, A. Y. C. *et al.* (2009) 'O3and O3/H2O2treatment of sulfonamide and macrolide

antibiotics in wastewater', *Journal of Hazardous Materials*. doi: 10.1016/j.jhazmat.2009.06.031.

Lin, H. J. *et al.* (2014) 'Optical and photocatalytic properties of Fe3+-doped TiO 2 thin films prepared by a sol-gel spin coating', *Ceramics International*. doi: 10.1016/j.ceramint.2014.03.046.

Lin, T.-F. and S.-W. H. (2000) 'Title: Inhalation exposure to THMs from drinking water in south Taiwan.', *The Science of the Total Environment*, 246, pp. 41–49.

Lin, W. De *et al.* (2015) 'Humidity sensing properties of novel graphene/TiO2composites by sol-gel process', *Sensors and Actuators, B: Chemical*. doi: 10.1016/j.snb.2014.12.013.

Lin, Y. T. *et al.* (2013) 'Effect of C content and calcination temperature on the photocatalytic activity of C-doped TiO2catalyst', *Separation and Purification Technology*. doi: 10.1016/j.seppur.2013.05.018.

Lin, Y. T. *et al.* (2014) 'Effect of oxygen, moisture, and temperature on the photo oxidation of ethylene on N-doped TiO2catalyst', *Separation and Purification Technology*. doi: 10.1016/j.seppur.2014.07.039.

Lin, Y. T., Weng, C. H. and Chen, F. Y. (2014) 'Key operating parameters affecting photocatalytic activity of visible-light-induced C-doped TiO2 catalyst for ethylene oxidation', *Chemical Engineering Journal*. doi: 10.1016/j.cej.2014.02.085.

Lindgren, T. *et al.* (2003) 'Photoelectrochemical and Optical Properties of Nitrogen Doped Titanium Dioxide Films Prepared by Reactive DC Magnetron Sputtering', *The Journal of Physical Chemistry B*. doi: 10.1021/jp027345j.

Lindstrom, H., R. Wootton, and A. I. (2007) 'High surface area titania photocatalytic microfluidic reactors', *Aiche Journal*, 53(3), pp. 695–702.

Liney, K. E. *et al.* (2006) 'Health effects in fish of long-term exposure to effluents from wastewater treatment works', *Environmental Health Perspectives*, 114(SUPPL.1), pp. 81–89. doi: 10.1289/ehp.8058.

Lister, T. E. *et al.* (2008) *General and Localized Corrosion of Borated Stainless Steels NACE Corrosion 2008 General and localized corrosion of borated stainless steels*.

Liu, C. *et al.* (2016) 'Hydrothermal synthesis of N-doped TiO2nanowires and N-doped graphene heterostructures with enhanced photocatalytic properties', *Journal of Alloys and Compounds*. doi: 10.1016/j.jallcom.2015.09.211.

Liu, J. *et al.* (2008) 'Generation of OH radicals at palladium oxide nanoparticle modified electrodes, and scavenging by fluorescent probes and antioxidants', *Journal of Electroanalytical Chemistry*. doi: 10.1016/j.jelechem.2008.03.017.

Liu, Y. *et al.* (2012) 'Carbamazepine removal from water by dielectric barrier discharge: Comparison of ex situ and in situ discharge on water', *Chemical Engineering and Processing: Process Intensification*. doi: 10.1016/j.cep.2012.03.003.
Liu, Y. *et al.* (2013) 'Removal of iopromide from an aqueous solution using dielectric barrier discharge', *Journal of Chemical Technology and Biotechnology*. doi: 10.1002/jctb.3851.
Liu, Y. and Wang, J. (2013) 'Degradation of sulfamethazine by gamma irradiation in the presence of hydrogen peroxide', *Journal of Hazardous Materials*. doi: 10.1016/j.jhazmat.2013.01.050.
Lolic, A., Paíga, P., Santos, L.H.M.L.M., Ramos, S., Correia, M., Delerue-Matos, C. (2015) 'Title: Pharmaceuticals, Assessment of non-steroidal anti-inflammatory and analgesic in seawaters of North of Portugal: occurrence and environmental risk.', *Sci.Total, Environ.*, 508, pp. 240–250.
Lomoră, M., Drăghici, C. and Eneşca, A. (2011) *Intermediary compounds in advanced oxidation processes for wastewater treatment, Bulletin of the Transilvania University of Braşov Series I: Engineering Sciences* •.
Lopez-Serna, R., Petrovic, M., Barcelo, D. (2012) 'Title: Occurrence and distribution of Transformation, multi-class pharmaceuticals and their active metabolites and products in the Ebro River basin (NE Spain).', *Sci. Total Environ*, 440, pp. 280–289.
Lopez, J. L. (2008) 'Dielectric Barrier Discharge , Ozone Generation , and their Applications'.
Loraine, G.A., Pettigrove, M.E. (2006) 'Title: Seasonal variations in concentrations of Reclaimed, pharmaceuticals and personal care products in drinking water and wastewater in Southern California.', *Environ. Sci. Technol.*, 40, pp. 687–695.
Loures, C. C. A. *et al.* (2013) 'Advanced Oxidative Degradation Processes: Fundamentals and Applications', *International Review of Chemical Engineering (I.RE.CH.E.)*, 5(2).
Lu, F. K. *et al.* (2003) *Development of Corona Discharge Apparatus for Supersonic Flow Millimeter-scaled boats and flotillas View project Blast wave attenuation View project Development of Corona Discharge Apparatus for Supersonic Flow*. Available at: https://www.researchgate.net/publication/239586580.
Lu, P.-J. *et al.* (2010) 'Azo dye degradation kinetics in TiO 2 film-coated photoreactor', *Chemical Engineering Journal*, 163, pp. 28–34. doi: 10.1016/j.cej.2010.07.022.
Luo, Y., Guo, W., Ngo, H.H., Nghiem, L.D., Hai, F.I., Zhang, J., Liang, S., Wang, X. C. (2014) 'Title: A review on the occurrence of micropollutants in the aquatic Environment and their fate and removal during wastewater treatment.', *Sci. Total Environ*, 473–474, pp. 619–

641.
Lv, K. *et al.* (2010) 'Effect of phase structures on the formation rate of hydroxyl radicals on the surface of TiO2', *Journal of Physics and Chemistry of Solids*. doi: 10.1016/j.jpcs.2009.12.026.
Ma, J. *et al.* (2006) 'Fenton degradation of organic pollutants in the presence of low-molecular-weight organic acids: Cooperative effect of quinone and visible light', *Environmental Science and Technology*. doi: 10.1021/es051657t.
Mackey, E. D. and Seacord, T. F. (2017) 'Guidelines for using stainless steel in the water and desalination industries', *Journal - American Water Works Association*. doi: 10.5942/jawwa.2017.109.0044.
Madhu, G. M. *et al.* (2009) 'Titamium oxide (TiO 2) assisted photocatalytic degradation of methylene blue', *Journal of Environmental Biology*, 30(2), pp. 259–264. Available at: http://www.jeb.co.ininfo@jeb.co.in.
Magureanu, M. *et al.* (2010) 'Degradation of pharmaceutical compound pentoxifylline in water by non-thermal plasma treatment', *Water Research*. doi: 10.1016/j.watres.2010.03.020.
Magureanu, M., Bradu, C., *et al.* (2013) 'Pulsed corona discharge for degradation of methylene blue in water', *Plasma Chemistry and Plasma Processing*. doi: 10.1007/s11090-012-9422-8.
Magureanu, M., Dobrin, D., *et al.* (2013) 'The mechanism of plasma destruction of enalapril and related metabolites in water', *Plasma Processes and Polymers*. doi: 10.1002/ppap.201200146.
Magureanu, M., Mandache, N. B. and Parvulescu, V. I. (2015) 'Degradation of pharmaceutical compounds in water by non-thermal plasma treatment', *Water Research*. doi: 10.1016/j.watres.2015.05.037.
Manoj Kumar Reddy, P. *et al.* (2013) 'Degradation and mineralization of methylene blue by dielectric barrier discharge non-thermal plasma reactor', *Chemical Engineering Journal*. doi: 10.1016/j.cej.2012.11.116.
Manoj Kumar Reddy, P., Mahammadunnisa, S. and Subrahmanyam, C. (2014) 'Catalytic non-thermal plasma reactor for mineralization of endosulfan in aqueous medium: A green approach for the treatment of pesticide contaminated water', *Chemical Engineering Journal*. Elsevier B.V., 238, pp. 157–163. doi: 10.1016/j.cej.2013.08.087.
Mansour, S. F., El-Dek, S. I. and Ahmed, M. K. (2017) 'Physico-mechanical and morphological features of zirconia substituted hydroxyapatite nano crystals', *Scientific Reports*. doi: 10.1038/srep43202.

Marković, M. *et al.* (2015) 'Application of non-thermal plasma reactor and Fenton reaction for degradation of ibuprofen', *Science of the Total Environment*. doi: 10.1016/j.scitotenv.2014.11.017.

Marotta, E. *et al.* (2011) 'Advanced oxidation process for degradation of aqueous phenol in a dielectric barrier discharge reactor', *Plasma Processes and Polymers*. doi: 10.1002/ppap.201100036.

Mason, T. J. *et al.* (1994) 'Dosimetry in sonochemistry: the use of aqueous terephthalate ion as a fluorescence monitor', *Ultrasonics - Sonochemistry*. doi: 10.1016/1350-4177(94)90004-3.

Massima, M. E. S. (2014) *Water treatment using electrohydraulic discharge system*. University of the Western Cape.

Massima Mouele, E. S. *et al.* (2018a) 'Review of the methods for determination of reactive oxygen species and suggestion for their application in advanced oxidation induced by dielectric barrier discharges', *Environmental Science and Pollution Research*. doi: 10.1007/s11356-018-1392-9.

Massima Mouele, E. S. *et al.* (2018b) 'Review of the methods for determination of reactive oxygen species and suggestion for their application in advanced oxidation induced by dielectric barrier discharges', *Environmental Science and Pollution Research*. doi: 10.1007/s11356-018-1392-9.

Mastanaiah, N., Johnson, J. A. and Roy, S. (2013) 'Effect of Dielectric and Liquid on Plasma Sterilization Using Dielectric Barrier Discharge Plasma', *PLoS ONE*. doi: 10.1371/journal.pone.0070840.

Matsubara H., Takada M., Koyama S., Hashimoto K., F. A. (1995) 'Photoactive TiO2 containing paper: preparation and its photocatalytic activity under weak UV light illumination', *Chemistry Letters*, 9, pp. 767–768.

Matsumoto, T. *et al.* (2007) 'High visible-light photocatalytic activity of nitrogen-doped titania prepared from layered titania/isostearate nanocomposite', *Catalysis Today*. doi: 10.1016/j.cattod.2006.07.047.

Mechiakh, R. *et al.* (2010) 'Correlation between microstructure and optical properties of nano-crystalline TiO2thin films prepared by sol-gel dip coating', *Applied Surface Science*. doi: 10.1016/j.apsusc.2010.08.008.

Mechiakh, R. *et al.* (2011) 'Annealing temperature effect on the properties of mercury-doped TiO2films prepared by sol-gel dip-coating technique', *Applied Surface Science*. doi: 10.1016/j.apsusc.2011.01.028.

Mededovic, S. (2007) 'Discharges : Fundamental Mechanisms and Applications To'.

Mekprasart, W. and Pecharapa, W. (2011) 'Synthesis and Characterization of Nitrogen-Doped Tio2 and Its Photocatalytic Activity Enhancement Under Visible Light', *Energy Procedia*. doi: 10.1016/j.egypro.2011.09.058.

Merajin, M. T. *et al.* (2013) 'Photocatalytic conversion of greenhouse gases (CO2 and CH4) to high value products using TiO2 nanoparticles supported on stainless steel webnet', *Journal of the Taiwan Institute of Chemical Engineers*. doi: 10.1016/j.jtice.2012.11.007.

Miao, X.-S., Yand, J.-J., Metcalfe, C. D. (2005) 'Title: Carbamazepine and its metabolites in wastewater and in biosolids in a municipal wastewater treatment Plant', *Environ. Sci.Technol.*, 39, pp. 7469–7475.

Mills, A. and Le Hunte, S. (1997) 'An overview of semiconductor photocatalysis', *Journal of Photochemistry and Photobiology A: Chemistry*. Elsevier, 108(1), pp. 1–35. doi: 10.1016/S1010-6030(97)00118-4.

Minami, T., Nishio, S. and Murata, Y. (2014) 'Periodic microstructures of Cr-O-N coatings deposited by arc ion plating', *Surface and Coatings Technology*. doi: 10.1016/j.surfcoat.2014.06.051.

Mohamed Elham Farouk (2011) 'Title: Removal of organic compounds from water by adsorption and photocatalytic oxidation.', *PhD thesis, University of Toulouse*.

Mohamed, M. A. *et al.* (2018) 'Concurrent growth, structural and photocatalytic properties of hybridized C, N co-doped TiO2mixed phase over g-C3N4nanostructured', *Scripta Materialia*. doi: 10.1016/j.scriptamat.2017.08.044.

Mohamed, R. *et al.* (2005) 'Characterisation and process optimisation of photosensitive acrylates for photonics applications', in *Science and Technology of Advanced Materials*. doi: 10.1016/j.stam.2005.03.008.

Möhring, H. C. *et al.* (2015) 'Materials in machine tool structures', *CIRP Annals - Manufacturing Technology*. doi: 10.1016/j.cirp.2015.05.005.

Mok, Y. S., Jo, J.-O. and Whitehead, J. C. (2008) 'Degradation of an azo dye Orange II using a gas phase dielectric barrier discharge reactor submerged in water', *Chemical Engineering Journal*. doi: 10.1016/j.cej.2007.11.012.

Mok, Y. S., Jo, J. O. and Whitehead, J. C. (2008) 'Degradation of an azo dye Orange II using a gas phase dielectric barrier discharge reactor submerged in water', *Chemical Engineering Journal*. doi: 10.1016/j.cej.2007.11.012.

Mompelat, S., Le Bot, B., Thomas, O. (2009) 'Title: Occurrence and fate of pharmaceutical products and by-products, from resource to drinking water.', *Environ. Int.*, 35, pp. 803–814.

Monteiro, R. A. R. *et al.* (2015) 'N-modified TiO2photocatalytic activity towards diphenhydramine degradation and Escherichia coli inactivation in aqueous solutions', *Applied Catalysis B: Environmental*. doi: 10.1016/j.apcatb.2014.06.017.

Montesinos, V. N. *et al.* (2015) 'Detection and quantification of reactive oxygen species (ROS) in indoor air'. doi: 10.1016/j.talanta.2015.02.015.

Morales-Torres, S. *et al.* (2013) 'Graphene oxide-P25 photocatalysts for degradation of diphenhydramine pharmaceutical and methyl orange dye', in *Applied Surface Science*. doi: 10.1016/j.apsusc.2012.11.157.

Morikawa, T. *et al.* (2001) 'Band-Gap Narrowing of Titanium Dioxide by Nitrogen Doping', *Japanese Journal of Applied Physics*. doi: 10.1143/JJAP.40.L561.

Mouele, Emile S.Massima *et al.* (2015) 'Degradation of organic pollutants and microorganisms from wastewater using different dielectric barrier discharge configurations—a critical review', *Environmental Science and Pollution Research*. doi: 10.1007/s11356-015-5386-6.

Mouele, Emile S Massima *et al.* (2015) 'Degradation of organic pollutants and microorganisms from wastewater using different dielectric barrier discharge configurations—a critical review', 22(23), pp. 18345–18362. doi: 10.1007/s11356-015-5386-6.

Mu, Y. *et al.* (2004a) 'TiO2-mediated photocatalytic degradation of Orange II with the presence of Mn2+ in solution', *Journal of Photochemistry and Photobiology A: Chemistry*. doi: 10.1016/j.jphotochem.2003.08.002.

Mu, Y. *et al.* (2004b) 'TiO2-mediated photocatalytic degradation of Orange II with the presence of Mn2+in solution', *Journal of Photochemistry and Photobiology A: Chemistry*. doi: 10.1016/j.jphotochem.2003.08.002.

Munter R. (2001) 'Advanced oxidation processes – current status and prospects', *Proc. Estonian Acad. Sci. Chem.*, 50, pp. 59–80.

Murgolo, S. *et al.* (2015) 'UV and solar-based photocatalytic degradation of organic pollutants by nano-sized TiO2grown on carbon nanotubes', *Catalysis Today*. doi: 10.1016/j.cattod.2014.04.021.

Murgolo, S. *et al.* (2017) 'A new supported TiO 2 film deposited on stainless steel for the photocatalytic degradation of contaminants of emerging concern', *Chemical Engineering Journal*, 318, pp. 103–111. doi: 10.1016/j.cej.2016.05.125.

Nadim, A. H. *et al.* (2015) 'Gallic acid magnetic nanoparticles for photocatalytic degradation of meloxicam: synthesis, characterization and application to pharmaceutical wastewater treatment', *RSC Adv.*, 5(127), pp. 104981–104990. doi: 10.1039/C5RA20281G.

Nakabayashi, Y. and Nosaka, Y. (2015) 'The pH dependence of OH radical formation in photo-electrochemical water oxidation with rutile TiO2 single crystals', *Physical Chemistry Chemical Physics*. doi: 10.1039/c5cp04531b.

Nakada, N. *et al.* (2007) 'Removal of selected pharmaceuticals and personal care products (PPCPs) and endocrine-disrupting chemicals (EDCs) during sand filtration and ozonation at a municipal sewage treatment plant', *Water Research*. doi: 10.1016/j.watres.2007.06.038.

Nakata, K. and Fujishima, A. (2012) 'TiO2photocatalysis: Design and applications', *Journal of Photochemistry and Photobiology C: Photochemistry Reviews*. doi: 10.1016/j.jphotochemrev.2012.06.001.

Naz, M. Y. *et al.* (2012) *Optical characterization of 50 hz atmo-spheric pressure single dielectric barrier discharge plasma, Progress In Electromagnetics Research M*.

Nehra, V., Kumar, A. and Dwivedi, H. K. (2008) 'Atmospheric Non-Thermal Plasma Sources', *International Journal of Engineering*, 2(1), pp. 53–68.

Neppolian, B. *et al.* (2002) 'Solar light induced and TiO2 assisted degradation of textile dye reactive blue 4', *Chemosphere*. Pergamon, 46(8), pp. 1173–1181. doi: 10.1016/S0045-6535(01)00284-3.

Neumann, B. *et al.* (2005) 'Electrochemical mass spectroscopic and surface photovoltage studies of catalytic water photooxidation by undoped and carbon-doped titania', *Journal of Physical Chemistry B*. doi: 10.1021/jp051339g.

Nifuku, M. *et al.* (1997) 'A study on the decomposition of volatile organic compounds by pulse corona', *Journal of Electrostatics*. doi: 10.1016/S0304-3886(97)00116-2.

Nyamukamba, Pardon *et al.* (2017) 'Plasmonic metal decorated titanium dioxide thin films for enhanced photodegradation of organic contaminants', *Journal of Photochemistry and Photobiology A: Chemistry*. doi: 10.1016/j.jphotochem.2017.04.014.

Nyamukamba, P. *et al.* (2017) 'Silver/Carbon Codoped Titanium Dioxide Photocatalyst for Improved Dye Degradation under Visible Light', *International Journal of Photoenergy*. doi: 10.1155/2017/3079276.

Okolongo, G. (2011) 'Advanced oxidative water treatment process using an electrohydraulic Prototype Design Case study Results Conclusions & Scopes', pp. 1–8.

Olcay T., Isik K., G. E. and D. O. (1996) 'Color removal from textile wastewaters', *Water Science and Technology*, 34, pp. 9–11.

Oller, I., Malato, S. and Sánchez-Pérez, J. A. (2011) 'Combination of Advanced Oxidation Processes and biological treatments for wastewater decontamination-A review', *Science of the Total Environment*. doi: 10.1016/j.scitotenv.2010.08.061.

Ozone, B. *et al.* (2011) *Optimization of operational parameters for decolorization and degradation of c. i. reactive blue 29, J. Environ. Health. Sci. Eng*.

P., B. (2004) *Title: Organic Chemistry.* 4th Ed. Pe. Upper Saddle River, N.J.

Palanivelu K., Ji Sun Im, Y.-S. L. (2007) 'Carbon Doping of TiO2 for Visible Light Photo Catalysis - A review', *Carbon Science*, Vol. 8(No. 3), pp. 214–224.

Pan X-M, Schuchmann MN, von S. C. (1993) 'Oxidation of benzene by the OH radical — a product and pulseradiolysis study in oxygenated aqueous solutions.', *J Chem Soc Perkin Trans*, 2, pp. 289–97.

Pang, Y. L. and Abdullah, A. Z. (2012) 'Comparative study on the process behavior and reaction kinetics in sonocatalytic degradation of organic dyes by powder and nanotubes TiO 2', *Ultrasonics Sonochemistry*. doi: 10.1016/j.ultsonch.2011.09.007.

Pang, Y. L., Abdullah, A. Z. and Bhatia, S. (2010) 'Effect of annealing temperature on the characteristics, sonocatalytic activity and reusability of nanotubes TiO2in the degradation of Rhodamine B', *Applied Catalysis B: Environmental*. doi: 10.1016/j.apcatb.2010.08.016.

Parau, A. C. *et al.* (2016) 'TiSiC, TiSiC-Zr, and TiSiC-Cr Coatings—Corrosion Resistance and Tribological Performance in Saline Solution', *Tribology Transactions*. doi: 10.1080/10402004.2015.1077406.

Park, H. *et al.* (2011) 'Fabrication of dye-sensitized solar cells by transplanting highly ordered TiO2 nanotube arrays', in *Solar Energy Materials and Solar Cells*. doi: 10.1016/j.solmat.2010.02.017.

Park, I. T. *et al.* (2013) 'Electrochemical reactivity of chemically roughened tungsten electrodes', in *Asian Journal of Chemistry*, pp. 7037–7040.

Park, Y. *et al.* (2009) 'Carbon-doped TiO2photocatalyst synthesized without using an external carbon precursor and the visible light activity', *Applied Catalysis B: Environmental*. doi: 10.1016/j.apcatb.2009.06.001.

Pastrana-Martínez, L. M. *et al.* (2012) 'Advanced nanostructured photocatalysts based on reduced graphene oxide-TiO2composites for degradation of diphenhydramine pharmaceutical and methyl orange dye', *Applied Catalysis B: Environmental*. doi: 10.1016/j.apcatb.2012.04.045.

Patel, N. S. *et al.* (2010) *Corrosion behavior of Ti 2 N thin films in various corrosive environments, J. Mater. Environ. Sci*.

Pavel Zinin (2009) 'Transmission Electron Microscope, HIGP, University of Hawaii, Honolulu, USA'.

Pelaez, M. *et al.* (2010) 'Synthesis, structural characterization and evaluation of sol-gel-based

NF-TiO2 films with visible light-photoactivation for the removal of microcystin-LR', *Applied Catalysis B: Environmental*. doi: 10.1016/j.apcatb.2010.06.017.

Pelentridou, K. *et al.* (2009) 'Photodegradation of the herbicide azimsulfuron using nanocrystalline titania films as photocatalyst and low intensity Black Light radiation or simulated solar radiation as excitation source', *Journal of Hazardous Materials*. doi: 10.1016/j.jhazmat.2008.07.023.

Peralta-Hernández, J. M. *et al.* (2008) 'Comparison of hydrogen peroxide-based processes for treating dye-containing wastewater: Decolorization and destruction of Orange II azo dye in dilute solution', *Dyes and Pigments*. doi: 10.1016/j.dyepig.2007.01.001.

Pérez, J. A. B. *et al.* (2017) 'Effect of ytterbium doping concentration on structural, optical and photocatalytic properties of TiO2thin films', *Ceramics International*. doi: 10.1016/j.ceramint.2017.08.141.

Pérez, M. H. *et al.* (2006) 'Degradation of pesticides in water using solar advanced oxidation processes', *Applied Catalysis B: Environmental*. doi: 10.1016/j.apcatb.2005.11.013.

Petr Lukeš (2001) *Institute of chemical technology, prague water treatment by pulsed streamer corona discharge petr lukeš*. Available at: http://www.ipp.cas.cz.

Petrik, L. *et al.* (2017) 'Desalination and seawater quality at Green Point, Cape Town: A study on the effects of marine sewage outfalls', *South African Journal of Science*, 113(11/12). doi: 10.17159/sajs.2017/a0244.

Petrovic, M., Skrbic, B., Zivancev, J., Ferrando-Climent, L., Barcelo, D. (2014) 'Title: Determination of 81 pharmaceutical drugs by high performance liquid Chromatography coupled to mass spectrometry with hybrid triple quadrupole - linear Ion trap in different types of water in Serbia.', *Sci. Total Environ.*, 468–469, pp. 415–428.

Peuravuori, J., Koivikko, R., and Pihlaja, K. (2002) 'Title: Characterization, Differentiation and Classification of Aquatic Humic Matter Separated with Different Sorbents: Synchronous Scanning Fluorescence Spectroscopy.', *Water Res.*, 36, pp. 4552–4562.

Pitwell, L. R. (1983) 'Standard COD', *Chem Brit*, 19, p. 907.

Pons, M., Bonte, S.L., and Potier, O. (2004) 'Title: Spectral Analysis and Fingerprinting for Biomedia Characterisation. Proc., Highlights from the ECB11: Building Bridges between Bioscience.', *Elsevier, Amsterdam, 1000 AE, Netherlands:*, pp. 211–230.

Porter, D. *et al.* (no date) *Formation of Hydrogen Peroxide, Hydrogen, and Oxygen in Gliding Arc Electrical Discharge Reactors with Water Spray The stoichiometric ratios of H 2 :O 2 :H 2 O 2 exhibited a range of behaviors for the different carrier gases with the highest H 2 formation in Ar and N 2 and the largest O 2 formation in CO 2*.

Postigo, C., Barcelo, D. (2015) 'Title: Synthetic organic compounds and their transformation products in groundwater: occurrence, fate and mitigation.', *Sci. Total Environ.*, 503–504, pp. 32–47.

Pressouyre, G. M. and Bernstein, I. M. (1981) 'An example of the effect of hydrogen trapping on hydrogen embrittlement', *Metallurgical Transactions A*, 12(5), pp. 835–844. doi: 10.1007/BF02648348.

Protection Agency, E. (1983) *EPAl600f4-79f020 &EPA Methods for Chemical Analysis of Water and Wastes*.

Pruncu, C. I. *et al.* (2017) 'Corrosion and tribological performance of quasi-stoichiometric titanium containing carbo-nitride coatings', *Arabian Journal of Chemistry*. doi: 10.1016/j.arabjc.2016.09.009.

Qi, C. *et al.* (2014) 'Degradation of sulfamethoxazole by microwave-activated persulfate: Kinetics, mechanism and acute toxicity', *Chemical Engineering Journal*. doi: 10.1016/j.cej.2014.03.086.

Qi, J. *et al.* (2015) 'Simultaneous removal of methylene blue and copper(II) ions by photoelectron catalytic oxidation using stannic oxide modified iron(III) oxide composite electrodes', *Journal of Hazardous Materials*. doi: 10.1016/j.jhazmat.2015.03.059.

Qiang, Z. and Adams, C. (2004) 'Potentiometric determination of acid dissociation constants (pKa) for human and veterinary antibiotics', *Water Research*. doi: 10.1016/j.watres.2004.03.017.

Qifu, L. *et al.* (2008) 'Special type of plasma dielectric barrier discharge reactor for direct ozonization of water and degradation of organic pollution Degradation of Alizarin Red by Hybrid Gas-Liquid Dielectric Barrier Discharge Treatment of Wastewater with High Conductivity by Pulsed Discharge Plasma', *J. Phys. D: Appl. Phys*, 41, p. 85207. doi: 10.1088/0022-3727/41/8/085207.

QIN, L. yuan, LIAN, J. she and JIANG, Q. (2010) 'Effect of grain size on corrosion behavior of electrodeposited bulk nanocrystalline Ni', *Transactions of Nonferrous Metals Society of China (English Edition)*. doi: 10.1016/S1003-6326(09)60101-1.

Qu, X., Kirschenbaum, L. J., & Borish, E. T. (2000) 'Hydroxyterephthalate as a Fluorescent Probe for Hydroxyl Radicals: Application to Hair Melanin. Photochemistry and Photobiology', *doi:10.1562/0031-8655(2000)0710307haafpf2.0.co2*, 71(3), pp. 307 – 313.

Rabiet, M., Togola, A., Brissaud, F., Seidel, J.L., Budzinski, H., Elbaz-Poulichet, F. (2006) 'Title: Consequences of treated water recycling as regards pharmaceuticals and drugs in surface and ground waters of a medium-sized Mediterranean Catchment.', *Environ. Sci.*

Technol., 40, pp. 5282–5288.
Rajendran, K., Senthil Kumar, V. and Anitha Rani, K. (2014) 'Synthesis and characterization of immobilized activated carbon doped TiO2thin films', *Optik*. doi: 10.1016/j.ijleo.2013.10.055.
Rajeshwar, K. *et al.* (2008) 'Heterogeneous photocatalytic treatment of organic dyes in air and aqueous media', *Journal of Photochemistry and Photobiology C: Photochemistry Reviews*. doi: 10.1016/j.jphotochemrev.2008.09.001.
Ramasundaram, S. *et al.* (2013) 'Titanium dioxide nanofibers integrated stainless steel filter for photocatalytic degradation of pharmaceutical compounds', *Journal of Hazardous Materials*. doi: 10.1016/j.jhazmat.2013.04.047.
Ramasundaram, S. *et al.* (2016) 'Highly reusable TiO2nanoparticle photocatalyst by direct immobilization on steel mesh via PVDF coating, electrospraying, and thermal fixation', *Chemical Engineering Journal*. doi: 10.1016/j.cej.2016.07.077.
Rao, C. N. R. (1989) 'Transition Metal Oxides', *Annual Review of Physical Chemistry*. doi: 10.1146/annurev.pc.40.100189.001451.
Rebholz, C. *et al.* (1999) 'Structure, mechanical and tribological properties of nitrogen-containing chromium coatings prepared by reactive magnetron sputtering', *Surface and Coatings Technology*, 115(2–3), pp. 222–229. doi: 10.1016/S0257-8972(99)00240-6.
Reddy, P. M. K. and Subrahmanyam, C. (2012) 'Green approach for wastewater treatment-degradation and mineralization of aqueous organic pollutants by discharge plasma', *Industrial and Engineering Chemistry Research*. doi: 10.1021/ie301122p.
Rehman, A. U. *et al.* (2013) 'Characterization of singlet oxygen production and its involvement in photodamage of Photosystem II in the cyanobacterium Synechocystis PCC 6803 by histidine-mediated chemical trapping', *Biochimica et Biophysica Acta - Bioenergetics*. Elsevier B.V., 1827(6), pp. 689–698. doi: 10.1016/j.bbabio.2013.02.016.
Riaz, N. *et al.* (2012) 'Photodegradation of Orange II under visible light using Cu-Ni/TiO2: Effect of calcination temperature', *Chemical Engineering Journal*. doi: 10.1016/j.cej.2012.01.052.
Riffard, F. *et al.* (2002) 'Yttrium implantation effect on 304L stainless steel high temperature oxidation at 1000°C', *Journal of Materials Science*. doi: 10.1023/A:1019667825476.
Rioja, N., Benguria, P., Peñas, F. J., & Zorita, S. (2014) 'Competitive removal of pharmaceuticals from environmental waters by adsorption and photocatalytic degradation.', *Environmental Science and Pollution Research*, 21(19), pp. 11168 –11177. doi: doi:10.1007/s11356-014-2593-5.

Rizzo, L. *et al.* (2009) 'Degradation of diclofenac by TiO2photocatalysis: UV absorbance kinetics and process evaluation through a set of toxicity bioassays', *Water Research*. doi: 10.1016/j.watres.2008.11.040.

Rocha, L. A. *et al.* (2004) 'Structural and corrosion behaviour of stoichiometric and substoichiometric TiN thin films', *Surface and Coatings Technology*. doi: 10.1016/j.surfcoat.2003.10.059.

Rong, S. P., Sun, Y. B. and Zhao, Z. H. (2014) 'Degradation of sulfadiazine antibiotics by water falling film dielectric barrier discharge', *Chinese Chemical Letters*. doi: 10.1016/j.cclet.2013.11.003.

Roy, H. E. *et al.* (2011) 'Alien arthropod predators and parasitoids: An ecological approach', *BioControl*. doi: 10.1007/s10526-011-9388-0.

Rozas, O. *et al.* (2010) 'Experimental design of Fenton and photo-Fenton reactions for the treatment of ampicillin solutions', *Journal of Hazardous Materials*, 177(1–3), pp. 1025–1030. doi: 10.1016/j.jhazmat.2010.01.023.

Ruan, J. J. *et al.* (2005) 'Decomposition of simulated odors in municipal wastewater treatment plants by a wire-plate pulse corona reactor', *Chemosphere*. doi: 10.1016/j.chemosphere.2004.10.025.

Saharudin, K. A., Sreekantan, S. and Lai, C. W. (2014) 'Fabrication and photocatalysis of nanotubular C-doped TiO2arrays: Impact of annealing atmosphere on the degradation efficiency of methyl orange', *Materials Science in Semiconductor Processing*. doi: 10.1016/j.mssp.2013.12.019.

Sahni, M. and Locke, B. R. (2006a) 'Quantification of hydroxyl radicals produced in aqueous phase pulsed electrical discharge reactors', *Industrial and Engineering Chemistry Research*. doi: 10.1021/ie0601504.

Sahni, M. and Locke, B. R. (2006b) 'Quantification of hydroxyl radicals produced in aqueous phase pulsed electrical discharge reactors', *Industrial and Engineering Chemistry Research*. doi: 10.1021/ie0601504.

Sakthivel, S., Janczarek, M. and Kisch, H. (2004) 'Visible light activity and photoelectrochemical properties of nitrogen-doped TiO2', *Journal of Physical Chemistry B*. doi: 10.1021/jp046857q.

Sakthivel, S. and Kisch, H. (2003) 'Daylight Photocatalysis by Carbon-Modified Titanium Dioxide', *Angewandte Chemie - International Edition*. doi: 10.1002/anie.200351577.

Salomon, E. *et al.* (2018) 'Enhancement of the Corrosion Resistance of 304 Stainless Steel by Cr-N and Cr(N,O) Coatings Synthesis of silver doped titanium dioxide nanocomposites and

investigating their antimicrobial effect. View project Water Treatment View project Enhancement of the Corrosion Resistance of 304 Stainless Steel by Cr-N and Cr(N,O) Coatings', *Coatings*, 8, p. 132. doi: 10.3390/coatings8040132.

Salomon, E. and Mouele, M. (2014) *Water treatment using electrohydraulic discharge system*.

Sambandam, B. *et al.* (2015) 'Rapid Synthesis of C-TiO2: Tuning the Shape from Spherical to Rice Grain Morphology for Visible Light Photocatalytic Application', *ACS Sustainable Chemistry and Engineering*. doi: 10.1021/acssuschemeng.5b00044.

Samsudin, E. M. and Abd Hamid, S. B. (2017) 'Effect of band gap engineering in anionic-doped TiO2photocatalyst', *Applied Surface Science*. doi: 10.1016/j.apsusc.2016.07.007.

Sánchez-Soto, P. J. *et al.* (2001) 'Thermal study of the effect of several solvents on polymerization of acrylonitrile and their subsequent pyrolysis', *Journal of Analytical and Applied Pyrolysis*. doi: 10.1016/S0165-2370(00)00203-5.

Santos, L.H.M.L.M., Araújo, A.N., Fachini, A., Pena, A., Delerue-Matos, C. Montenegro, M. C. B. S. M. (2010) 'Title: Ecotoxicological aspects related to the presence of pharmaceuticals in the aquatic environment.', *J. Hazard. Mater.*, 175, pp. 45–95.

Saracino, M. *et al.* (2016) *Contaminants of emerging concern and developping advanced remediation technologies*.

Saracino, M., Emmi, S. S. and Zanelli, A. (2015) 'Water remediation 2.0: Advanced Oxidation Processes', *La Chimica e l'Industria*, Anno XCVII(5), pp. 18–25. doi: 10.17374/CI.2015.97.5.18.

Saravanan, R. *et al.* (2013) 'Comparative study on photocatalytic activity of ZnO prepared by different methods', *Journal of Molecular Liquids*. doi: 10.1016/j.molliq.2013.02.023.

Sarkar, S., Chakraborty, S. and Bhattacharjee, C. (2015) 'Photocatalytic degradation of pharmaceutical wastes by alginate supported TiO<inf>2</inf> nanoparticles in packed bed photo reactor (PBPR)', *Ecotoxicology and Environmental Safety*. doi: 10.1016/j.ecoenv.2015.02.035.

Sawyer, D. T. and Valentine, J. S. (1981) 'How super is superoxide?', *Accounts of Chemical Research*, 14(12), pp. 393–400. doi: 10.1021/ar00072a005.

Sayed, E. and El-Ashtoukhy, Z. (2013) *Removal of Indigo Carmine Dye from Synthetic Wastewater by Electrochemical Oxidation in a New Cell with Horizontally Oriented Electrodes, Int. J. Electrochem. Sci*. Available at: www.electrochemsci.org.

Sayres, S. G., Ross, M. W. and Castleman, A. W. (2011) 'Influence of clustering and molecular orbital shapes on the ionization enhancement in ammonia', *Physical Chemistry*

Chemical Physics. doi: 10.1039/c1cp20612e.

Sebastiani, M., Piccoli, M. and Bemporad, E. (2013) 'Effect of micro-droplets on the local residual stress field in CAE-PVD thin coatings', *Surface and Coatings Technology*. doi: 10.1016/j.surfcoat.2012.08.094.

Sedira, S. *et al.* (2014) 'Physical deposition of carbon doped titanium nitride film by DC magnetron sputtering for metallic implant coating use', *Applied Surface Science*. doi: 10.1016/j.apsusc.2014.01.010.

Shan, A. Y., Ghazi, T. I. M. and Rashid, S. A. (2010) 'Immobilisation of titanium dioxide onto supporting materials in heterogeneous photocatalysis: A review', *Applied Catalysis A: General*. doi: 10.1016/j.apcata.2010.08.053.

Shang, J., Li, W. and Zhu, Y. (2003) 'Structure and photocatalytic characteristics of TiO2 film photocatalyst coated on stainless steel webnet', *Journal of Molecular Catalysis A: Chemical*. doi: 10.1016/S1381-1169(03)00200-0.

Shao, G. S., Zhang, X. J. and Yuan, Z. Y. (2008) 'Preparation and photocatalytic activity of hierarchically mesoporous-macroporous TiO2-xNx', *Applied Catalysis B: Environmental*. doi: 10.1016/j.apcatb.2008.01.026.

Sharma, A. K. *et al.* (1993) 'A Preliminary Study of Pulsed Streamer Corona Discharge for the Degradation of Phenol in Aqueous Solutions', *Hazardous Waste and Hazardous Materials*, 10(2), pp. 209–219. doi: 10.1089/hwm.1993.10.209.

Shen, Y., Lei, L. and Zhang, X. (2008) 'Evaluation of energy transfer and utilization efficiency of azo dye removal by different pulsed electrical discharge modes', *Chinese Science Bulletin*. doi: 10.1007/s11434-008-0251-3.

Shi, J., Bian, W. and Yin, X. (2009) 'Organic contaminants removal by the technique of pulsed high-voltage discharge in water', *Journal of Hazardous Materials*. doi: 10.1016/j.jhazmat.2009.06.134.

Shi, N., Zhang, X. and Lei, L. (2009) 'Sulfite oxidation in seawater flue gas desulfurization by a pulsed corona discharge process', *Separation and Purification Technology*. doi: 10.1016/j.seppur.2009.09.018.

Shin, E. C. and Jeong, G. H. (2012) 'Highly efficient carbon nanotube growth on plasma pretreated stainless steel substrates', in *Thin Solid Films*. doi: 10.1016/j.tsf.2012.02.043.

Shriver D. F., Atkins P. W., L. C. H. (1994) *Inorganic Chemistry 2nd ed. International student edition*. 2nd edn. Oxford Melbourne Tokyo: Oxford University press.

Sies, H. and Menck, C. F. M. (1992) 'Singlet oxygen induced DNA damage', *Mutation Research/DNAging*. Elsevier, 275(3–6), pp. 367–375. doi: 10.1016/0921-8734(92)90039-R.

Silva, A. C. *et al.* (2009) 'Ozonation of azo dyes (Orange II and Acid Red 27) in saline media', *Journal of Hazardous Materials*. doi: 10.1016/j.jhazmat.2009.04.051.

Singh, S., Mahalingam, H. and Singh, P. K. (2013) 'Polymer-supported titanium dioxide photocatalysts for environmental remediation: A review', *Applied Catalysis A: General*. doi: 10.1016/j.apcata.2013.04.039.

Sirés, I. and Brillas, E. (2012) 'Remediation of water pollution caused by pharmaceutical residues based on electrochemical separation and degradation technologies: A review', *Environment International*. doi: 10.1016/j.envint.2011.07.012.

Siuleiman, S. *et al.* (2014) 'Photodegradation of Orange II by ZnO and TiO2powders and nanowire ZnO and ZnO/TiO2thin films', *Colloids and Surfaces A: Physicochemical and Engineering Aspects*. doi: 10.1016/j.colsurfa.2014.01.010.

Sivakumar, B., Pathak, L. C. and Singh, R. (2017) 'Role of surface roughness on corrosion and fretting corrosion behaviour of commercially pure titanium in Ringer's solution for bio-implant application', *Applied Surface Science*. doi: 10.1016/j.apsusc.2017.01.033.

Slang, S., Palka, K. and Vlcek, M. (2017) 'Thermal dependence of photo-induced effects in spin-coated As20Ge12.5S67.5thin films', *Journal of Non-Crystalline Solids*. doi: 10.1016/j.jnoncrysol.2017.06.033.

Soares, O. S. G. P. *et al.* (2006) 'Ozonation of textile effluents and dye solutions under continuous operation: Influence of operating parameters', *Journal of Hazardous Materials*. doi: 10.1016/j.jhazmat.2006.05.006.

Sobczyk-Guzenda, A. *et al.* (2013) 'Photocatalytic activity of thin TiO2 films deposited using sol-gel and plasma enhanced chemical vapor deposition methods', *Ceramics International*. doi: 10.1016/j.ceramint.2012.09.046.

Sonawane, R. S., Hegde, S. G. and Dongare, M. K. (2003) 'Preparation of titanium(IV) oxide thin film photocatalyst by sol-gel dip coating', *Materials Chemistry and Physics*. doi: 10.1016/S0254-0584(02)00138-4.

Song, Z., Chouparove, E., Jones, K.W., Feng, H., and Marinkovic, N. S. (2001) 'Title: FTIR Investigation of Sediments from NY/NJ Harbor, San Diego Bay, and the Venetian Lagoon.', *NSLS Activity Report.*, 2, pp. 112–116.

Sonntag, C. von (1987) *The Chemical Basis of Radiation Biology*. London: Taylor & Francis.

Sopyan, I. (2007) 'Kinetic analysis on photocatalytic degradation of gaseous acetaldehyde, ammonia and hydrogen sulfide on nanosized porous TiO2 films', *Science and Technology of Advanced Materials*. doi: 10.1016/j.stam.2006.10.004.

Soresa M. (2011) 'Ayka Addis Textile Wastewater Treatment by the Fenton's Reagent. MSc

thesis in Chemical Engineering (Process Engineering). Addis Ababa University, institute of technology, school of graduate studies.'

Soresa, M. (2011) 'Ayka Addis Textile Wastewater Treatment by the Fenton's Reagent', pp. 1–73.

de Souza, S. M. de A. G. U., Bonilla, K. A. S. and de Souza, A. A. U. (2010) 'Removal of COD and color from hydrolyzed textile azo dye by combined ozonation and biological treatment', *Journal of Hazardous Materials*. doi: 10.1016/j.jhazmat.2010.02.053.

Souzanchi, S. *et al.* (2013) 'Performance of an Annular Sieve-Plate Column photoreactor using immobilized TiO2on stainless steel support for phenol degradation', *Chemical Engineering Journal*. doi: 10.1016/j.cej.2013.02.123.

Sresomroeng, B. *et al.* (2011) 'Performance of CrN radical nitrided tools on deep drawing of advanced high strength steel', *Surface and Coatings Technology*. doi: 10.1016/j.surfcoat.2011.03.010.

Srikanth, B. *et al.* (2017) 'Recent advancements in supporting materials for immobilised photocatalytic applications in waste water treatment', *Journal of Environmental Management*. doi: 10.1016/j.jenvman.2017.05.063.

Staehelin, J., & Hoigné, J. (1983) 'Reaktionsmechanismus und Kinetik des Ozonzerfalls in Wasser in Gegenwart organischer Stoffe', *Vom Wasser*, 61, pp. 337–348.

Staehelin, J. and Hoigne, J. (1985) 'Decomposition of ozone in water in the presence of organic solutes acting as promoters and inhibitors of radical chain reactions', *Environmental Science and Technology*, 19(12), pp. 1206–1213. doi: 10.1021/es00142a012.

Stasinakis, A. S. (2008) *Use of selected advanced oxidation processes (aops) for wastewater treatment-a mini review*, *Global NEST Journal*.

Stathatos, E. *et al.* (2012) 'TiO_2/palygorskite composite nanocrystalline films prepared by surfactant templating route: Synergistic effect to the photocatalytic degradation of an azo-dye in water', *Journal of Hazardous Materials*. doi: 10.1016/j.jhazmat.2011.11.055.

Steyer, P. *et al.* (2008) 'Influence of the nanostructuration of PVD hard TiN-based films on the durability of coated steel', *Surface and Coatings Technology*, 202(11), pp. 2268–2277. doi: 10.1016/j.surfcoat.2007.08.073.

Subramanian, B., Ananthakumar, R. and Jayachandran, M. (2011) 'Structural and tribological properties of DC reactive magnetron sputtered titanium/titanium nitride (Ti/TiN) multilayered coatings', *Surface and Coatings Technology*. doi: 10.1016/j.surfcoat.2010.12.016.

Sugiarto, A. T. *et al.* (2003) 'Oxidative decoloration of dyes by pulsed discharge plasma in

water', *Journal of Electrostatics*. doi: 10.1016/S0304-3886(02)00203-6.
Sugiarto, A. T. and Sato, M. (2001) 'Pulsed plasma processing of organic compounds in aqueous solution', *Thin Solid Films*. doi: 10.1016/S0040-6090(00)01669-2.
Suzuki, K. *et al.* (2013) 'Epitaxial Growth of Chromium Oxynitride Thin Films on Magnesium Oxide (100) Substrates and Their Oxidation Behavior'. doi: 10.2320/matertrans.MAW201310.
Swartz CD, Genthe B, Chamier J, Petrik LF, Tijani JO, Adeleye A, Coomans CJ, Ohlin A, Falk D, M. J. (2017) 'Emerging Contaminants In Wastewater Treated For Direct Potable Re-Use: The Human Health Risk Priorities In South Africa. Volume I: A Concise Research Report; Volume II: A Prioritization Framework For Monitoring Contaminants Of Emerging Concern In Reclaimed Water For Potable Use; Volume III: Occurrence, Fate, Removal And Health Risk Assessment Of Chemicals Of Emerging Concern In Reclaimed Water For Potable Reuse. Report To The Water Research Commission: Project No. K5/2369 Final report in press.'
Syam Krishna, Alan Maslani, Tomasz Izdebski, Marta Horakova, Sarka Klementova, P. S. (2016) 'Degradation of verapamil hydrochloride in water by gliding arc discharge', *Chemosphere*, 152, pp. 47–54.
T. B. Massalski (1990) *Binary Alloy Phase Diagrams*. 2nd edn. Edited by T.B. Massalski; H. Okamoto. Asm Intl.
Tait, W. S. (1994) *Teflon electrical insulators test fluid an introduction to electrochemical corrosion testing for practicing engineers and scientists electrical cap for lead through pins filling HOLE PAg-40120C4 Pil&e•414'410s4*.
Tantis, I. *et al.* (2015) 'Photocatalytic and photoelectrocatalytic degradation of the drug omeprazole on nanocrystalline titania films in alkaline media: Effect of applied electrical bias on degradation and transformation products', *Journal of Hazardous Materials*. doi: 10.1016/j.jhazmat.2015.03.042.
Tarr M. (2003) *Chemical Degradation Methods for Wastes and Pollutants*. New York, NY: Marcel Dekker Inc.
Thagard, S. M., Takashima, K. and Mizuno, A. (2009) 'Chemistry of the positive and negative electrical discharges formed in liquid water and above a gas-liquid surface', *Plasma Chemistry and Plasma Processing*. doi: 10.1007/s11090-009-9195-x.
Thompson, J.D., White, M.C., Harrington, G.W., and Singer, P. C. (1997) 'Title: Enchanced Softening: Factors Influencing DBP Precursor Removal.', *JAWWA.*, 89(6), pp. 94–105.
Tichonovas, M. *et al.* (2013) 'Degradation of various textile dyes as wastewater pollutants

under dielectric barrier discharge plasma treatment', *Chemical Engineering Journal*. doi: 10.1016/j.cej.2013.05.095.

De Tiedra, P., Martín, Ó. and San-Juan, M. (2016) 'Potentiodynamic study of the influence of gamma prime and eta phases on pitting corrosion of A286 superalloy', *Journal of Alloys and Compounds*. doi: 10.1016/j.jallcom.2016.02.261.

Tijani, J. O. *et al.* (2014) 'A review of combined advanced oxidation technologies for the removal of organic pollutants from water', *Water, Air, and Soil Pollution*. doi: 10.1007/s11270-014-2102-y.

Tijani, J. O. *et al.* (2017) 'Degradation of 2-Nitrophenol by Dielectric Barrier Discharge System: The Influence of Carbon Doped TiO2 Photocatalyst Supported on Stainless Steel Mesh', *Plasma Chemistry and Plasma Processing*. doi: 10.1007/s11090-017-9824-8.

Tijani, Jimoh O. *et al.* (2017) 'Degradation of bisphenol-A by dielectric barrier discharge system: Influence of polyethylene glycol stabilized nano zero valent iron particles', *Advances in Natural Sciences: Nanoscience and Nanotechnology*. doi: 10.1088/2043-6254/aa7714.

Tijani, J O *et al.* (2017) 'Synthesis and characterization of carbon doped TiO 2 photo-catalysts supported on stainless steel mesh by sol-gel method Original Articles', *Carbon Letters*, 22, pp. 48–59. doi: 10.5714/CL.2017.22.048.

Tilley, E. *et al.* (2014) 'Compendium of Sanitation Systems and Technologies', *Development*, p. 180. doi: SAN-12.

Tong, A. Y. C. *et al.* (2012) 'TiO2-assisted photodegradation of pharmaceuticals — a review', *Central European Journal of Chemistry*, 10(4), pp. 989–1027. doi: 10.2478/s11532-012-0049-7.

Trovó, Alam G *et al.* (2009) 'Chemosphere Photodegradation of sulfamethoxazole in various aqueous media : Persistence , toxicity and photoproducts assessment', *Chemosphere*. Elsevier Ltd, 77(10), pp. 1292–1298. doi: 10.1016/j.chemosphere.2009.09.065.

Trovó, Alam G. *et al.* (2009) 'Photodegradation of sulfamethoxazole in various aqueous media: Persistence, toxicity and photoproducts assessment', *Chemosphere*. doi: 10.1016/j.chemosphere.2009.09.065.

Trovó, A. G., Melo, S. A. S. and Nogueira, R. F. P. (2008) 'Photodegradation of the pharmaceuticals amoxicillin, bezafibrate and paracetamol by the photo-Fenton process-Application to sewage treatment plant effluent', *Journal of Photochemistry and Photobiology A: Chemistry*, 198(2–3), pp. 215–220. doi: 10.1016/j.jphotochem.2008.03.011.

Tschirch, J. *et al.* (2008) 'Photodegradation of methylene blue in water, a standard method to determine the activity of photocatalytic coatings?', *Research on Chemical Intermediates*. doi:

10.1163/156856708784040588.
Uher G., E. Gilbert, U. Siegfried, H. E. (1991) '"Determination of hydrogen peroxide in presence of organic peroxides"', *Vom Wasser*, 76, pp. 225 – 234.
Uher, J. and Hoefer, W. J. R. (1991) 'Tunable microwave and millimeter-wave band-pass filters', *IEEE Transactions on Microwave Theory and Techniques*, 39(4), pp. 643–653.
Ullmann (1991) 'Encyclopedia of Industrial Chemistry 5th Edn', VolumeA18,(einheim: Verlag Chemie,ISBN 3-527-20118-1, Ozone,), pp. 349–357.
Urbansky, E. T. (2001) 'Total organic carbon analyzers as tools for measuring carbonaceous matter in natural waters', in *Journal of Environmental Monitoring*. doi: 10.1039/b006564l.
Uwe Hubner, Urs von Gunten, M. J. (2015) 'Evaluation of the persistence of transformation products from ozonation of trace organic compounds. A critical review.', *Water Research*, 68, p. pp.150–170.
Valentin, C. Di, Pacchioni, G. and Selloni, A. (2004) 'Origin of the different photoactivity of N-doped anatase and rutile TiO 2', *PHYSICAL REVIEW B*, 70, p. 85116. doi: 10.1103/PhysRevB.
Di Valentin, C., Pacchioni, G. and Selloni, A. (2005) 'Theory of carbon doping of titanium dioxide', *Chemistry of Materials*. doi: 10.1021/cm051921h.
Valinčius, V., Grigaitienė, V. and Tamošiūnas, A. (2012) 'Report on the different Plasma Modules for Pollution Removal', *Plastep.Eu*, p. 49.
Varshney, G. *et al.* (2016) 'Nanoscale TiO<inf>2</inf> films and their application in remediation of organic pollutants', *Coordination Chemistry Reviews*. doi: 10.1016/j.ccr.2015.06.011.
Veronika R. Meyer (2010) *Practical High-Performance Liquid Chromatography*. Fifth edition. Edited by John Wiley & Sons Ltd. Swiss Federal Laboratories for Materials Testing and Research (EMPA),St. Gallen, Switzerland.: The Atrium, Southern Gate, Chichester, West Sussex, PO19 8SQ, United Kingdom.
Vignesh, A. *et al.* (2014) 'A novel approach for textile dye degradation by zinc, iron-doped tin oxide/titanium moving anode', *International Journal of Environmental Science and Technology*. doi: 10.1007/s13762-013-0318-9.
Vitelaru, C. *et al.* (2014) 'Corrosion behaviour of Ti6Al4V alloy in artificial saliva solution with fluoride content and low pH value: Korrosionsverhalten der Legierung Ti6Al4V in künstlicher Speichelflüssigkeit mit Fluoridanteilen und geringem pH-Wert', *Materialwissenschaft und Werkstofftechnik*. doi: 10.1002/mawe.201400191.
Vladescu, A. *et al.* (2013) 'Characterization of the Ti-10Nb-10Zr-5Ta alloy for biomedical

applications. Part 1: Microstructure, mechanical properties, and corrosion resistance', *Journal of Materials Engineering and Performance*. doi: 10.1007/s11665-013-0517-z.

Vladescu, A. *et al.* (2014) 'Enhancement of the mechanical properties of hydroxyapatite by SiC addition', *Journal of the Mechanical Behavior of Biomedical Materials*. doi: 10.1016/j.jmbbm.2014.08.025.

Vladescu, A. *et al.* (2016) 'In vitro biocompatibility of Si alloyed multi-principal element carbide coatings', *PLoS ONE*. doi: 10.1371/journal.pone.0161151.

Vohra, A. *et al.* (2006) 'Enhanced photocatalytic disinfection of indoor air', *Applied Catalysis B: Environmental*. doi: 10.1016/j.apcatb.2005.10.025.

Volmajer Valh, J. *et al.* (2012) 'The applicability of an advanced oxidation process for textile finishing waste streams & fate of persistent organic pollutants', *International Journal of Environmental Research*.

Volovitch, P. *et al.* (2011) 'Understanding corrosion via corrosion product characterization: II. Role of alloying elements in improving the corrosion resistance of Zn-Al-Mg coatings on steel', *Corrosion Science*. doi: 10.1016/j.corsci.2011.03.016.

Vujevic, D. *et al.* (2004) 'The removal of direct orange 39 by pulsed corona discharge from model wastewater', *Environmental Technology*. doi: 10.1080/09593330.2004.9619370.

Vujevic, D *et al.* (2004) 'The Removal of Direct Orange 39 by Pulsed Corona Discharge From Model Wastewater', *Environmental Technology*, 257(25), pp. 791–800. doi: 10.1080/09593330.2004.9619370.

Wang, A., Li, Y. Y. and Estrada, A. L. (2011) 'Mineralization of antibiotic sulfamethoxazole by photoelectro-Fenton treatment using activated carbon fiber cathode and under UVA irradiation', *Applied Catalysis B: Environmental*. doi: 10.1016/j.apcatb.2010.12.007.

Wang, J. *et al.* (2011) 'Synthesis and characterization of C, N-codoped TiO2nanotubes/nanorods with visible-light activity', *Rare Metals*. doi: 10.1007/s12598-011-0261-1.

Wang, K.-H. *et al.* (2000) 'The pH and anion effects on the heterogeneous photocatalytic degradation of o-methylbenzoic acid in TiO2 aqueous suspension', *Chemosphere*. Pergamon, 40(4), pp. 389–394. doi: 10.1016/S0045-6535(99)00252-0.

Wang, S. *et al.* (2010) 'Solubilities of ibuprofen in different pure solvents', *Journal of Chemical and Engineering Data*. doi: 10.1021/je100255z.

Wang, W. and Ku, Y. (2003) 'Photocatalytic degradation of gaseous benzene in air streams by using an optical fiber photoreactor', *Journal of Photochemistry and Photobiology A: Chemistry*. doi: 10.1016/S1010-6030(03)00111-4.

Wang, Y. *et al.* (2008) 'Enhanced sonocatalytic degradation of azo dyes by Au/TiO2', *Environmental Science and Technology*. doi: 10.1021/es800168k.

Wardman, P. (1989) 'Reduction potentials of one-electron couples involving free radicals in aqueous solution', *J. Phys Chem. Ref. Data*, 18(4), pp. 1637–1753. doi: 10.1063/1.555843.

Weirich, T. . *et al.* (2002) 'Rietveld analysis of electron powder diffraction data from nanocrystalline anatase, TiO2', *Ultramicroscopy*. doi: 10.1016/s0304-3991(99)00189-8.

Wen, Z.-H., Chen, L., Meng, X.-Z., Duan, Y.-P., Zhang, Z.-S., Zeng, E. Y. (2014) 'Title: Occurrence and human health risk of wastewater - derived pharmaceuticals in A drinking water source for Shanghai, East China.', *Sci. Total Environ.*, 490, pp. 987–993.

Von Woedtke, T. *et al.* (2004) 'Sporicidal efficacy of hydrogen peroxide aerosol', *Pharmazie*, 59(3), pp. 207–211.

Wood, R. J. K. *et al.* (2013) 'Influence of microstructure on the erosion and erosion-corrosion characteristics of 316 stainless steel', *Wear*. doi: 10.1016/j.wear.2013.08.007.

Wu, C. Y. *et al.* (2013) 'Thickness-dependent photocatalytic performance of nanocrystalline TiO2thin films prepared by sol-gel spin coating', *Applied Surface Science*. doi: 10.1016/j.apsusc.2013.05.053.

Wu, H. *et al.* (2012) 'Reactive oxygen species in a non-thermal plasma microjet and water system: Generation, conversion, and contributions to bacteria inactivation -An analysis by electron spin resonance spectroscopy', *Plasma Processes and Polymers*. doi: 10.1002/ppap.201100065.

Wu, J., Doan, H. and Upreti, S. (2008) 'Decolorization of aqueous textile reactive dye by ozone', *Chemical Engineering Journal*. doi: 10.1016/j.cej.2007.11.019.

Wu, K. *et al.* (1999) 'Photo-Fenton degradation of a dye under visible light irradiation', *Journal of Molecular Catalysis A: Chemical*. doi: 10.1016/S1381-1169(98)00354-9.

Xekoukoulotakis, N. P. *et al.* (2011) 'Kinetics of UV-A/TiO2 photocatalytic degradation and mineralization of the antibiotic sulfamethoxazole in aqueous matrices', *Catalysis Today*. doi: 10.1016/j.cattod.2010.09.027.

Xie, C. *et al.* (2016) 'C-doped mesoporous anatase TiO2comprising 10 nm crystallites', *Journal of Colloid and Interface Science*. doi: 10.1016/j.jcis.2016.01.080.

Xu, J. hua *et al.* (2008) 'Simple fabrication of thermally stable apertured N-doped TiO2microtubes as a highly efficient photocatalyst under visible light irradiation', *Catalysis Communications*. doi: 10.1016/j.catcom.2007.05.043.

Xu, T. *et al.* (2006) 'Band structures of TiO2 doped with N, C and B', *Journal of Zhejiang University SCIENCE B*. doi: 10.1631/jzus.2006.B0299.

Y.Q. Gao, N.Y. Gao, Y. Deng, Y.Q. Yang, Y. M. (2012) 'Ultraviolet (UV) light-activated persulfate oxidation of sulfamethazine in water', *Chem. Eng. J.*, 195, pp. 248– 253.

Yadav, S. and Jaiswar, G. (2017) 'Review on Undoped/Doped TiO $_2$ Nanomaterial; Synthesis and Photocatalytic and Antimicrobial Activity', *Journal of the Chinese Chemical Society*. doi: 10.1002/jccs.201600735.

Yan, J. H. *et al.* (2006) 'Degradation of phenol in aqueous solutions by gas-liquid gliding arc discharges', *Plasma Chemistry and Plasma Processing*. doi: 10.1007/s11090-005-8723-6.

Yan, J. H. *et al.* (2008) 'Degradation of gas-liquid gliding arc discharge on Acid Orange II', *Journal of Hazardous Materials*. doi: 10.1016/j.jhazmat.2008.01.007.

Yan, W. Y. *et al.* (2016) 'C-doped and N-doped reduced graphene oxide/TiO2 composites with exposed (0 0 1) and (1 0 1) facets controllably synthesized by a hydrothermal route and their gas sensing characteristics', *Sensors and Actuators, B: Chemical*. doi: 10.1016/j.snb.2016.02.133.

YANG, S. *et al.* (2009) 'A novel advanced oxidation process to degrade organic pollutants in wastewater: Microwave-activated persulfate oxidation', *Journal of Environmental Sciences*. doi: 10.1016/S1001-0742(08)62399-2.

Yetim, T. (2016) 'Corrosion Behavior of Ag-doped TiO2Coatings on Commercially Pure Titanium in Simulated Body Fluid Solution', *Journal of Bionic Engineering*. doi: 10.1016/S1672-6529(16)60311-6.

Yin, S. *et al.* (2007) 'Synthesis of visible-light responsive nitrogen/carbon doped titania photocatalyst by mechanochemical doping', *Journal of Materials Science*. doi: 10.1007/s10853-006-1231-0.

Yiruhan, Wang, Q.-J., Mo, C.-H., Li, Y.-W., Gao, P., Tai, Y.-P., Zhang, Y., Ruan, Z.-L. and Xu, J.-W. (2010) 'Title: Determination of four fluoroquinolone antibiotics in tap water in Guangzhou and Macao.', *Environ. Pollut.*, 158, pp. 2350–2358.

Yu, C. and Yu, J. C. (2009) 'A simple way to prepare C-N-codoped TiO2 photocatalyst with visible-light activity', *Catalysis Letters*. doi: 10.1007/s10562-008-9824-7.

Zabihi, F. *et al.* (2015) 'Morphology, conductivity, and wetting characteristics of PEDOT:PSS thin films deposited by spin and spray coating', *Applied Surface Science*. doi: 10.1016/j.apsusc.2015.02.128.

Zhang, H.; Zhang, Y.; Zhang, D. (2007) 'Decolorisation and mineralisation of CI Reactive Black 8 by the Fenton and ultrasound/ Fenton methods', *Color Technol.*, 123, p. 101.

Zhang, Y., Geißen, S.-U., Gal, C. (2008) 'Title: Carbamazepine and diclofenac: removal in wastewater treatment plants and occurrence in water bodies.', *Chemosphere*, 73, pp. 1151–

1161.

Zhang, C. *et al.* (2018) 'Simultaneous removal of Cr(VI) and acid orange 7 from water solution by dielectric barrier discharge plasma', *Chemosphere*. doi: 10.1016/j.chemosphere.2017.10.087.

Zhang, J. *et al.* (2012) 'Degradation of 2,4-dichorophenol by pulsed high voltage discharge in water', *Desalination*. doi: 10.1016/j.desal.2012.01.027.

Zhang, L. *et al.* (2003) 'Preparation and performances of mesoporous TiO2film photocatalyst supported on stainless steel', *Applied Catalysis B: Environmental*. doi: 10.1016/S0926-3373(02)00154-6.

Zhang, L. and Wang, J. (2014) 'Effect of dissolved oxygen content on stress corrosion cracking of a cold worked 316L stainless steel in simulated pressurized water reactor primary water environment', *Journal of Nuclear Materials*. doi: 10.1016/j.jnucmat.2013.11.027.

Zhang, Q., Gao, L. and Guo, J. (2000) *Effects of calcination on the photocatalytic properties of nanosized TiO 2 powders prepared by TiCl 4 hydrolysis, Applied Catalysis B: Environmental*.

Zhang, S., Jiang, D. and Zhao, H. (2006) 'Development of chemical oxygen demand on-line monitoring system based on a photoelectrochemical degradation principle', *Environmental Science and Technology*. doi: 10.1021/es052018l.

Zhang, S. and Song, L. (2009) 'Preparation of visible-light-active carbon and nitrogen codoped titanium dioxide photocatalysts with the assistance of aniline', *Catalysis Communications*. doi: 10.1016/j.catcom.2009.05.017.

Zhang, S. and Zhu, W. (1993) *TiN coating of tool steels: a review, Journal of Materials Processing Technology*.

Zhang, T.-H. *et al.* (2012) 'Application of TiO_2 with different structures in solar cells', *Chinese Physics B*. doi: 10.1088/1674-1056/21/11/118401.

Zhang, X. *et al.* (2016) 'Preparation of Ti mesh supported N-S-C-tridoped TiO2nanosheets to achieve high utilization of optical energy for photocatalytic degradation of norfloxacin', *RSC Advances*. doi: 10.1039/c5ra27639j.

Zhang, Y. *et al.* (2007) 'Degradation mechanisms of 4-chlorophenol in a novel gas–liquid hybrid discharge reactor by pulsed high voltage system with oxygen or nitrogen bubbling', *Chemosphere*. Pergamon, 67(4), pp. 702–711. doi: 10.1016/J.CHEMOSPHERE.2006.10.065.

Zhang, Y. and Li, Q. (2013) 'Synthesis and characterization of Fe-doped TiO2films by electrophoretic method and its photocatalytic activity toward methyl orange', *Solid State Sciences*. doi: 10.1016/j.solidstatesciences.2012.11.012.

Zhao, H. *et al.* (2004) 'Development of a Direct Photoelectrochemical Method for Determination of Chemical Oxygen Demand', *Analytical Chemistry*. doi: 10.1021/ac0302298.

Zhihui, A., Peng, Y. and Xiaohua, L. (2005) 'Degradation of 4-Chlorophenol by microwave irradiation enhanced advanced oxidation processes', in *Chemosphere*. doi: 10.1016/j.chemosphere.2005.04.027.

Zhuang, J. *et al.* (2010) 'Photocatalytic degradation of RhB over TiO2 bilayer films: Effect of defects and their location', *Langmuir*. doi: 10.1021/la100302m.

Zhuo, C. *et al.* (2014) 'Oxidative heat treatment of 316L stainless steel for effective catalytic growth of carbon nanotubes', *Applied Surface Science*. doi: 10.1016/j.apsusc.2014.05.189.

Zoita, N. C. *et al.* (2014) 'Influence of film thickness on the morphological and electrical properties of epitaxial TiC films deposited by reactive magnetron sputtering on MgO substrates', *Journal of Crystal Growth*. doi: 10.1016/j.jcrysgro.2013.11.076.

APPENDICES

Appendix 1: Preparation of 0.01M, 0.02M and 0.04M sodium carbonate (Na_2CO_3) solution: calculation of Na_2CO_3 corresponding mass that was introduced in the DBD reactor (R1) for the scavenging of OH radical at the indicated conditions.

$Mm_{Na_2CO_3} = 106\text{g/mol}$, where Mm stands for the molar mass of Na_2CO_3.

$$Molar\ concentration = \frac{mol}{L} \times Mr = {}^{g}/_{L} \quad \text{.....10.1}$$

$$1M = \frac{1mol}{L} \times \frac{106g}{mol} = 106g/L \quad \text{.....10.2}$$

$$\begin{cases} 1M \rightarrow 106g/L \\ 0.01M \rightarrow \frac{106g/L \times 0.01M}{1M} = 1.06g/L \end{cases} \quad \text{.....10.3}$$

$$\begin{cases} 1L \rightarrow 1.06g/L \\ 1.5L \rightarrow \frac{1.06g/L \times 1.5L}{1L} = 1.59g\ in\ 1.5\ L \end{cases} \quad \text{.....10.4}$$

Appendix 2: Preparation of 0.01M, 0.02M and 0.04M sodium chloride solution (NaCl): calculation of NaCl mass that was dissolved in the DBD reactor (R_1) for the scavenging of ·OH radicals.

$Mm_{NaCl} = 58\text{g/mol}$, where Mm is the molar mass of NaCl

$$Molar\ concentration = \frac{mol}{L} \times Mm = {}^{g}/_{L} \quad \text{.....10.5}$$

$$1M = \frac{1mol}{L} \times \frac{58g}{mol} = 58\ g/L \quad \text{.....10.6}$$

$$\begin{cases} 1M \rightarrow 58\ g/L \\ 0.01M \rightarrow \frac{58g/L \times 0.01M}{1M} = 0.58\ g/L \end{cases} \quad \text{.....10.7}$$

$$\begin{cases} 1L \rightarrow 0.58\ g/L \\ 1.5L \rightarrow \frac{0.58g/L \times 1.5L}{1L} = 0.87g\ in\ 1.5L \end{cases} \quad \text{.....10.8}$$

Appendix 3: Preparation of 0.01M, 0.02M and 0.04M terephthalic acid ($C_8H_6O_4$) solution: calculation of each TA corresponding mass that was dissolved in the solvent.

$Mm_{NaCl} = 166\text{g/mol}$

$$Molar\ concentration = \frac{mol}{L} \times Mm = {}^{g}/_{L} \quad \text{.....10.9}$$

$$1M = \frac{1mol}{L} \times \frac{166g}{mol} = 166g/L \quad \text{.....10.10}$$

$$\begin{cases} 1M \rightarrow 166g/L \\ 0.01M \rightarrow \frac{166g/L \times 0.01M}{1M} = 1.66g/L \end{cases} \quad \text{.....10.11}$$

$$\begin{cases} 1L \rightarrow 1.66g/L \\ 1.5L \rightarrow \frac{1.66g/L \times 1.5L}{1L} = 2.49g\ in\ 1.5L \end{cases} \quad \text{.....10.12}$$

Appendix 4 a: Absorbance of orange II solutions sampled within 60 minutes during investigation of the effect of initial concentration on orange II decolouration efficiency.Varied parameter: Orange II concentration from 10.20, 30, 40, 50 to 60 mg/L. Fixed parameters: Peak voltage 6.8 kV, pH (in between 6.04 and 6.69), air flow rate of 3 L/min, air gap 2 mm, 50 g/L NaCl electrolyte, 0.5 mm silver electrode and contact time of 60 minutes.

O.II initial concentration (mg/L)	Absorbance (A)													
	0 min		10 min		20 min		30 min		40 min		50 min		60 min	
	A_1	A_2	A_1	A_2	A_1	A_2	A_1	A_2	A_1	A_2	A_1	A_2	A_1	A_2
10	0.634	0.630	0.229	0.228	0.045	0.044	0.003	0.002	0.001	0.001	0.001	0.001	0.001	0.001
20	1.144	1.143	0.643	0.642	0.257	0.256	0.070	0.070	0.010	0.011	0.004	0.004	0.002	0.001
30	1.754	1.753	1.035	1.034	0.500	0.501	0.189	0.188	0.043	0.042	0.011	0.012	0.005	0.004
40	2.218	2.219	1.355	1.354	0.828	0.827	0.416	0.417	0.116	0.117	0.040	0.041	0.014	0.015
50	2.970	2.971	2.240	2.241	1.305	1.306	0.948	0.947	0.443	0.444	0.146	0.145	0.034	0.035
60	2.970	2.971	2.240	2.241	1.305	1.306	0.754	0.753	0.309	0.309	0.103	0.104	0.037	0.034

Appendix 4 a: Concentrations of orange II solutions sampled within 60 minutes during investigation of the effect of initial concentration on orange II decolouration efficiency. Varied parameter: Orange II concentration from 10.20, 30, 40, 50 to 60 mg/L. Fixed parameters: Peak voltage 6.8 kV, pH (in between 6.04 and 6.69), air flow rate of 3 L/min, air gap 2 mm, 50 g/L NaCl electrolyte, 0.5 mm silver electrode and contact time of 60 minutes.

O.II initial concentration (mg/L)	Concentrations (C) in mg/L within 60 minutes											
	10 min		20 min		30 min		40 min		50 min		60 min	
	C_1	C_2	C_1	C_2	C_1	C_2	C_1	C_2	C_1	C_2	C_1	C_2
10	4.362	4.342	0.857	0.838	0.057	0.038	0.019	0.019	0.019	0.019	0.019	0.019
20	12.247	12.228	4.895	4.876	1.333	1.333	0.190	0.209	0.076	0.076	0.038	0.019
30	19.71	19.695	9.524	9.541	3.6	3.581	0.82	0.80	0.209	0.228	0.095	0.076
40	25.809	25.79	15.77	15.75	7.92	7.943	2.209	2.228	0.762	0.781	0.267	0.285
50	42.67	42.68	24.85	24.85	18.057	18.038	8.438	8.457	2.781	2.80	0.647	0.670
60	42.67	42.385	24.85	24.876	14.362	14.343	5.885	5.885	1.962	1.980	0.704	0.647

Appendix 4 c: Decolouration efficiency of orange II solutions sampled within 60 minutes during investigation of the effect of initial concentration on orange II decolouration efficiency. Varied parameter: Orange II concentration from 10.20, 30, 40, 50 to 60 mg/L. Fixed parameters: Peak voltage 6.8 kV, pH (in between 6.04 and 6.69), air flow rate of 3 L/min, air gap 2 mm, 50 g/L NaCl electrolyte, 0.5 mm silver electrode and contact time of 60 minutes.

O.II initial concentration (mg/L)	Decolouration efficiency (D%) within 60 minutes											
	10 min		20 min		30 min		40 min		50 min		60 min	
	$D\%_1$	$D\%_2$	$D\%_1$	$D\%_2$	$D\%_1$	$D\%_2$	$D\%_1$	$D\%_2$	$D\%_1$	$D\%_2$	$D\%_1$	$D\%_2$
10	56.38	56.58	91.43	91.62	99.43	99.62	99.81	99.81	99.81	99.81	99.81	99.81
20	38.76	38.86	75.52	75.62	93.33	93.33	99.05	98.95	99.62	99.62	99.81	99.05
30	34.3	34.35	68.25	68.20	88	88.06	97.26	97.33	99.30	99.24	99.68	99.75
40	35.47	35.52	60.57	60.62	80.2	80.14	94.47	94.43	98.09	98.04	99.33	99.28
50	14.66	14.64	50.3	50.23	63.88	63.92	83.124	83.086	94.43	94.4	98.706	98.66
60	28.88	29.358	58.58	58.54	76.06	76.09	90.192	90.192	96.73	96.7	98.83	98.923

Appendix 5 a: Absorbance of methylene blue solutions sampled within 60 minutes during optimisation of O.II solution pH. Varied parameter: Solution volume from 500, 1000and 1500 to 2000 mL. Fixed parameters: MB concentration 5 mg/L, pH (in between 6.04 and 6.64), applied voltage 25, peak voltage 7.8 kV, air flow rate of 3 L/min, air gap 2 mm, 50 g/L NaCl electrolyte, 0.5 mm silver electrode and contact time of 60 minutes.

pH	Absorbance (A)													
	0 min		10 min		20 min		30 min		40 min		50 min		60 min	
	A_1	A_2	A_1	A_2	A_1	A_2	A_1	A_2	A_1	A_2	A_1	A_2	A_1	A_2
2.5	2.929	2.930	1.340	1.343	0.056	0.056	0.000	0.00	0.00	0.00	0.00	0.00	0.00	0.00
4.5	2.923	2.924	1.620	1.620	0.682	0.682	0.171	0.172	0.027	0.028	0.004	0.004	0.00	0.00
6.5	2.924	2.925	1.588	1.587	0.530	0.531	0.093	0.094	0.029	0.030	0.007	0.007	0.002	0.003
8.5	2.927	2.926	2.165	2.166	1.345	1.344	0.620	0.621	0.256	0.256	0.068	0.068	0.015	0.015
10.5	2.878	2.879	0.620	0.621	0.242	0.243	0.095	0.096	0.038	0.039	0.011	0.012	0.001	0.001

Appendix 5 B: Concentrations of orange II solutions sampled within 60 minutes during optimisation of O.II solution pH. Varied parameter: peak voltage from 6.8, 8 to 10 kV. Fixed parameters: orange II concentration 100 mg/L, pH (in between 6.04 and 6.69), air flow rate of 3 L/min, 50 g/L NaCl electrolyte, air gap 2 mm, 0.5 mm silver electrode and contact time of 60 mm.

pH	Concentrations (C) in mg/L within 60 minutes											
	10 min		20 min		30 min		40 min		50 min		60 min	
	C_1	C_2	C_1	C_2	C_1	C_2	C_1	C_2	C_1	C_2	C_1	C_2
2.5	25.52	25.58	1.067	1.085	0.00	0.00	0.00	0.00	0.00	0.00	0.00	0.00
4.5	30.857	30.857	12.99	12.99	3.257	3.257	0.514	0.533	0.076	0.076	0.00	0.00
6.5	1.588	1.587	10.095	10.114	1.771	1.79	0.552	0.571	0.133	0.133	0.038	0.057
8.5	41.238	41.257	25.62	25.6	11.809	11.828	4.876	4.876	1.295	1.295	0.285	0.285
10.5	11.81	11.83	4.61	4.63	1.81	1.828	0.727	0.743	0.21	0.23	0.019	0.019

Appendix 5 C: Decolouration efficiency of orange II solutions sampled within 60 minutes during optimisation of O.II solution pH. Varied parameter: peak voltage from 6.8, 8 to 10 kV. Fixed parameters: orange II concentration 100 mg/L, pH (in between 6.04 and 6.69), air flow rate of 3 L/min, 50 g/L NaCl electrolyte, air gap 2 mm, 0.5 mm silver electrode and contact time of 60 mm.

pH	Decolourization efficiency (D%) within 60 minutes											
	10 min		20 min		30 min		40 min		50 min		60 min	
	D% $_1$	D% $_2$	D% $_1$	D% $_2$	D% $_1$	D% $_2$	D% $_1$	D% $_2$	D%$_1$	D% $_2$		
2.5	57.47	57.37	98.22	98.19	99.99	99.99	99.99	99.99	99.99	99.99	99.99	99.99
4.5	48.57	48.57	78.35	78.35	94.57	94.54	99.14	99.11	99.87	99.87	99.99	99.99
6.5	49.58	49.62	83.17	83.14	97.05	97.02	99.08	99.04	99.77	99.04	99.94	99.90
8.5	31.27	31.24	57.3	57.33	80.32	80.28	91.87	91.87	97.84	97.84	99.52	99.52
10.5	80.32	80.28	92.32	92.28	96.98	96.95	98.79	98.76	99.65	99.62	99.96	99.96

Appendix 6 A: absorbance of orange II solutions sampled within 60 minutes during optimisation of air flow rate (L/min). Varied parameter: Solution volume from 500, 1000and 1500 to 2000 mL. Fixed parameters: MB concentration 5 mg/L, pH (in between 6.04 and 6.64), applied voltage 25, peak voltage 7.8 kV, air flow rate of 3 L/min, air gap 2 mm, 50 g/L NaCl electrolyte, 0.5 mm silver electrode and contact time of 60 minutes.

Air flow rate (L/min)	Absorbance (A)													
	0 min		10 min		20 min		30 min		40 min		50 min		60 min	
	A_1	A_2	A_1	A_2	A_1	A_2	A_1	A_2	A_1	A_2	A_1	A_2	A_1	A_2
3	2.920	2.621	2.036	2.035	1.037	1.036	0.364	0.365	0.083	0.084	0.019	0.018	0.009	0.008
6	2.909	2.910	2.758	2.759	2.514	2.515	2.311	2.312	2.057	2.057	1.821	1.820	1.564	1.563
9	2.916	2.918	2.700	2.701	2.484	2.484	2.271	2.271	2.073	2.073	1.881	1.881	1.744	1.744

Appendix 6 B: Concentrations of orange II solutions sampled within 60 minutes during optimisation of air flow rate (L/min). Varied parameter: peak voltage from 6.8, 8 to 10 kV. Fixed parameters: orange II concentration 100 mg/L, pH (in between 6.04 and 6.69), air flow rate of 3 L/min, 50 g/L NaCl electrolyte, air gap 2 mm, 0.5 mm silver electrode and contact time of 60 mm.

Air flow rate (L/min)	Concentrations (C) in mg/L within 60 minutes											
	10 min		20 min		30 min		40 min		50 min		60 min	
	C_1	C_2	C_1	C_2	C_1	C_2	C_1	C_2	C_1	C_2	C_1	C_2
3	38.78	38.76	19.75	19.73	6.93	6.95	1.58	1.6	0.36	0.34	0.17	0.15
6	52.53	52.55	47.88	47.90	44.02	44.038	39.18	39.18	34.68	34.66	29.79	29.77
9	51.43	51.44	47.31	47.31	43.25	43.25	39.48	39.48	35.83	35.83	32.22	32.22

Appendix 6 C: Decolouration efficiency of orange II solutions sampled within 60 minutes during optimisation of air flow rate (L/min). Varied parameter: peak voltage from 6.8, 8 to 10 kV. Fixed parameters: orange II concentration 100 mg/L, pH (in between 6.04 and 6.69), air flow rate of 3 L/min, 50 g/L NaCl electrolyte, air gap 2 mm, 0.5 mm silver electrode and contact time of 60 mm.

Air flow rate (L/min)	Decolourization efficiency (D%) within 60 minutes											
	10 min		20 min		30 min		40 min		50 min		60 min	
	$D\%_1$	$D\%_2$	$D\%_1$	$D\%_2$	$D\%_1$	$D\%_2$	$D\%_1$	$D\%_2$	$D\%_1$	$D\%_2$	$D\%_1$	$D\%_2$
3	35.37	36.61	67.083	67.12	88.45	88.42	97.37	97.33	99.4	99.43	99.72	99.75
6	12.45	12.42	20.20	20.167	26.63	26.60	34.70	34.70	42.2	42.23	50.35	50.38
9	14.44	14.28	21.15	21.15	27.92	27.92	34.2	34.2	40.198	40.198	44.63	44.63

Appendix 7 A: Absorbance of orange II solutions sampled within 60 minutes during optimisation of peak voltage (kV). Varied parameter: peak voltage from 6.8, 8 to 10 kV. Fixed parameters: O.II concentration 100 mg/L, pH (in between 6.04 and 6.69), air flow rate of 3 L/min, air gap 2 mm, 50 g/L NaCl electrolyte, 0.5 mm silver electrode and contact time of 60 minutes.

Peak voltage (kV)	Absorbance (A)													
	0 min		10 min		20 min		30 min		40 min		50 min		60 min	
	A_1	A_2	A_1	A_2	A_1	A_2	A_1	A_2	A_1	A_2	A_1	A_2	A_1	A_2
6.8	2.920	2.921	2.036	2.035	1.037	1.036	0.364	0.365	0.083	0.084	0.019	0.018	0.009	0.008
8	2.927	2.930	1.862	1.861	0.856	0.857	0.268	0.269	0.048	0.049	0.023	0.022	0.015	0.014
10			1.940	1.941	0.902	0.903	0.252	0.251	0.058	0.058	0.023	0.023	0.015	0.015

Appendix 7 B: Concentrations of orange II solutions sampled within 60 minutes during optimisation of peak voltage (kV). Varied parameter: peak voltage from 6.8, 8 to 10 kV. Fixed parameters: orange II concentration 100 mg/L, pH (in between 6.04 and 6.69), air flow rate of 3 L/min, 50 g/L NaCl electrolyte, air gap 2 mm, 0.5 mm silver electrode and contact time of 60 mm.

Peak voltage (kV)	Concentrations (C) in mg/L within 60 minutes											
	10 min		20 min		30 min		40 min		50 min		60 min	
	C_1	C_2	C_1	C_2	C_1	C_2	C_1	C_2	C_1	C_2	C_1	C_2
6.8	38.78	38.76	19.75	19.73	6.93	6.95	1.58	1.6	0.36	0.34	0.17	0.15
8	35.47	35.45	16.30	16.32	5.105	5.12	0.914	0.895	0.438	0.42	0.285	0.267
10	36.95	36.97	17.18	17.2	4.8	4.78	1.058	1.085	0.438	0.438	0.285	0.285

Appendix 7 C: Decolouration efficiency of orange II solutions sampled within 60 minutes during optimisation of peak voltage (kV). Varied parameter: peak voltage from 6.8, 8 to 10 kV. Fixed parameters: orange II concentration 100 mg/L, pH (in between 6.04 and 6.69), air flow rate of 3 L/min, 50 g/L NaCl electrolyte, air gap 2 mm, 0.5 mm silver electrode and contact time of 60 mm.

Peak voltage (kV)	Decolouration efficiency (D%) within 60 minutes											
	10 min		20 min		30 min		40 min		50 min		60 min	
	$D\%_1$	$D\%_2$	$D\%_1$	$D\%_2$	$D\%_1$	$D\%_2$	$D\%_1$	$D\%_2$	$D\%_1$	$D\%_2$	$D\%_1$	$D\%_2$
6.8	35.37	36.61	67.083	67.12	88.45	88.42	97.37	97.33	99.4	99.43	99.72	99.75
8	40.88	40.92	72.83	72.8	91.49	91.47	98.47	98.51	99.27	99.3	99.52	99.55
10	38.42	38.38	71.37	71.37	92.00	92.03	98.16	98.16	99.27	99.27	99.52	99.52

Appendix 8: Decolouration of O.II within 60 minutes at the following optimum conditions: Peak voltage 8 kV, [O.II] = 60 mg/L, V= 1500 mL, air flow rate 3 L/min, 1.5 mm silver electrode, 50 g/L NaCl inner electrode electrolyte, air gap 2 mm.

Time (min)	A_1	A_2	C_1	C_2	$D\%_1$	$D\%_2$	Average	StdeV
0	1.412	1.862	60	60	0	0	0	0
10	0.161	0.268	3.078	5.114	94.87	91.476	93.173	2.399
20	0.015	0.038	0.289	0.740	99.547	98.765	98.656	1.260
30	0.009	0.009	0.175	0.188	99.708	99.685	98.696	1.429
40	0.008	0.0098	0.156	0.186	99.74	99.688	98.714	1.450
50	0.005	0.008	0.104	0.169	99.825	99.717	98.771	1.490
60	0.003	0.007	0.066	0.142	99.889	99.761	98.825	1.504

Appendix 9 a: Effect of initial concentration on degradation of sulfamethoxazole (SMX). Experimental conditions: varied parameter: initial concentration from 20, 40, 60 to 100 mg/L. Fixed conditions: pH 5.634, solution volume 1500mL, voltage 6.8 kV, air flow rate 3L/min, 1.5 mm silver electrode, 50 g/L NaCl electrolyte and 60 minutes of treatment time.

SMX initial concentration (mg/L)	Initial concentration (mg/L) of SMX within 60 minutes of DBD run													
	0 min		10 min		20 min		30 min		40 min		50 min		60 min	
	C_1	C_2	C_1	C_2	C_1	C_2	C_1	C_2	C_1	C_2	C_1	C_2	C_1	C_2
20	6.728	8.32	5.17	7.25	3.722	5.54	2.13	4.56	0.28	0.01	0	0	0	0
40	9.101	11.23	6.774	8.45	3.38	5.49	0.151	2.35	0	0	0	0	0	0
60	16.915	18.56	14.63	16.23	12.08	14.58	6.668	8.79	2.081	4.89	0	0	0	0
100	32.856	34.89	27.283	29.89	20.37	22.59	7.895	9.45	0.565	2.65	0.278	2.46	0	0

Appendix 9 b: Effect of initial concentration on degradation of sulfamethoxazole (SMX). Experimental conditions: varied parameter: initial concentration from 20, 40, 60 to 100 mg/L. Fixed conditions: pH 5.634, solution volume 1500mL, voltage 6.8 kV, air flow rate 3L/min, 1.5 mm silver electrode, 50 g/L NaCl electrolyte and 60 minutes of treatment time.

SMX initial concentration (mg/L)	Degradation efficiency of SMX within 60 minutes of DBD run													
	0 min		10 min		20 min		30 min		40 min		50 min		60 min	
	C_1	C_2	C_1	C_2	C_1	C_2	C_1	C_2	C_1	C_2	C_1	C_2	C_1	C_2
20	0	0	23.15	12.86	44.67	33.41	68.34	45.19	95.89	99.87	100	100	100	100
40	0	0	25.56	24.75	62.86	51.11	98.34	79.07	100	100	100	100	100	100
60	0	0	13.49	12.55	28.56	21.44	60.57	52.64	87.69	73.65	100	100	100	100
100	0	0	16.96	14.33	37.97	35.25	75.97	72.91	98.28	92.40	99.15	92.94	100	100

Appendix 10 a: Effect of solution pH on degradation of sulfamethoxazole (SMX). Experimental conditions: varied parameter: solution pH from 2.5, 6.5, 8.5 to 10.5. Fixed conditions: [SMX] 40 mg/L, solution volume 1500mL, voltage 6.8 kV, air flow rate 3L/min, 1.5 mm silver electrode, 50 g/L NaCl electrolyte and 60 minutes of treatment time.

Solution pH	Initial concentration (mg/L) of SMX within 60 minutes of DBD run													
	0 min		10 min		20 min		30 min		40 min		50 min		60 min	
	C_1	C_2	C_1	C_2	C_1	C_2	C_1	C_2	C_1	C_2	C_1	C_2	C_1	C_2
2.5	53.52	55.36	31.87	33.86	13.87	15.95	2.684	4.56	0.668	2.98	0	0	0	0
6.5	22.614	24.56	4.223	6.23	0	0	0	0	0	0	0	0	0	0
8.5	16.03	18.56	14.62	16.59	10.88	12.85	4.792	6.89	0.217	2.56	0	0	0	0
10.5	25.88	27.5	23.58	25.89	18.76	20.8	13.15	15.56	9.94	11.89	6.42	8.78	3.78	5.98

Appendix 10 b: Effect of solution pH on degradation of sulfamethoxazole (SMX). Experimental conditions: varied parameter: solution pH from 2.5, 6.5, 8.5 to 10.5. Fixed conditions: [SMX] 40 mg/L, pH 6.5, solution volume 1500mL, voltage 6.8 kV, air flow rate 3L/min, 1.5 mm silver electrode, 50 g/L NaCl electrolyte and 60 minutes of treatment time.

Solution pH	Degradation efficiency of SMX within 60 minutes of DBD run													
	0 min		10 min		20 min		30 min		40 min		50 min		60 min	
	C_1	C_2	C_1	C_2	C_1	C_2	C_1	C_2	C_1	C_2	C_1	C_2	C_1	C_2
2.5	0	0	40.45	38.84	74.07	71.19	94.98	91.76	98.75	94.61	100	100	100	100
6.5	0	0	81.32	74.63	100	100	100	100	100	100	100	100	100	100
8.5	0	0	8.758	10.61	32.10	30.76	70.10	62.87	98.64	86.20	100	100	100	100
10.5	0	0	8.892	5.85	27.50	24.36	49.20	43.41	61.56	56.76	75.19	68.07	85.36	78.25

Appendix 11 a: Effect of air flow rate (L/min) on degradation of sulfamethoxazole (SMX). Experimental conditions: varied parameter: air flow rate from 3, 6 to 9 L/min. Fixed conditions: [SMX] 40 mg/L, pH 6.5, solution volume 1500mL, voltage 6.8 kV, 1.5 mm silver electrode, 50 g/L NaCl electrolyte and 60 minutes of treatment time.

Air flow rate (L/min)	Initial concentration (mg/L) of SMX within 60 minutes of DBD run													
	0 min		10 min		20 min		30 min		40 min		50 min		60 min	
	C_1	C_2	C_1	C_2	C_1	C_2	C_1	C_2	C_1	C_2	C_1	C_2	C_1	C_2
3	58.53	62.3	31.52	35.23	4.13	7.12	0.63	0.14	0	0	0	0	0	0
6	66.01	69.23	39.42	42.12	14.9	16.32	1.04	0.52	0	0	0	0	0	0
9	77.43	80.12	0	2.12	15.05	18.02	0	0	0	0	0	0	0	0

Appendix 11 b: Effect of air flow rate (L/min) on degradation of sulfamethoxazole (SMX). Experimental conditions: varied parameter: air flow rate from 3, 6 to 9 L/min. Fixed conditions: [SMX] 40 mg/L, pH 6.5, solution volume 1500mL, voltage 6.8 kV, 1.5 mm silver electrode, 50 g/L NaCl electrolyte and 60 minutes of treatment time.

Air flow rate (L/min)	Degradation efficiency of SMX within 60 minutes of DBD run													
	0 min		10 min		20 min		30 min		40 min		50 min		60 min	
	C_1	C_2	C_1	C_2	C_1	C_2	C_1	C_2	C_1	C_2	C_1	C_2	C_1	C_2
3	0	0	46.14	43.45	92.94	88.57	98.92	99.77	100	100	100	100	100	100
6	0	0	40.28	39.15	77.42	76.42	98.42	99.24	100	100	100	100	100	100
9	0	0	100	97.35	80.56	77.50	100	100	100	100	100	100	100	100

Appendix 12 a: Effect of voltage (kV) on degradation efficiency of sulfamethoxazole (SMX). Experimental conditions: varied parameter: voltage from 6.8 kV, 8 kV to 10 kV. Fixed conditions: [SMX] 40 mg/L, pH 6.5, solution volume 1500mL, voltage 6.8 kV, 1.5 mm silver electrode, 50 g/L NaCl electrolyte and 60 minutes of treatment time.

Applied voltage (kV)	Initial concentration (mg/L) of SMX within 60 minutes of DBD run													
	0 min		10 min		20 min		30 min		40 min		50 min		60 min	
	C_1	C_2	C_1	C_2	C_1	C_2	C_1	C_2	C_1	C_2	C_1	C_2	C_1	C_2
6.8	189.08	185.2	178.0	174.0	158.4	154.0	123.4	120.3	60.56	58.6	37.92	34.86	10.42	8.82
8	169.18	165.0	158.4	155.5	137.2	134.5	95.69	92.35	69.43	65.65	36.15	33.54	6.67	4.12
10	153.97	151.0	146.0	142.2	134.2	131.2	87.2	86.1	37.57	34.21	3.81	1.62	1.6	0.23

Appendix 12 b: Effect of voltage (kV) on degradation efficiency of sulfamethoxazole (SMX). Experimental conditions: varied parameter: voltage from 6.8 kV, 8 kV to 10 kV. Fixed conditions: [SMX] 40 mg/L, pH 6.5, solution volume 1500mL, voltage 6.8 kV, 1.5 mm silver electrode, 50 g/L NaCl electrolyte and 60 minutes of treatment time.

Applied voltage (kV)	Degradation efficiency (%) of SMX within 60 minutes of DBD run													
	0 min		10 min		20 min		30 min		40 min		50 min		60 min	
	C_1	C_2	C_1	C_2	C_1	C_2	C_1	C_2	C_1	C_2	C_1	C_2	C_1	C_2
6.8	0	0	5.844	6.035	16.19	16.83	34.72	35.03	67.97	68.36	79.94	81.18	94.48	95.23
8	0	0	6.342	5.76	18.84	18.47	43.43	44.04	58.96	60.22	78.63	79.67	96.05	97.50
10	0	0	5.150	5.82	12.82	13.09	43.36	42.98	75.59	77.34	97.52	98.92	98.96	99.84

Appendix 13: Degradation of SMX in DBD at optimum conditions; Peak voltage 8 kV, SMX concentration 40 mg/L, pH 6.5, solution volume 1500 mL, 1.5 mm silver electrode, 50 g/L NaCl electrolyte and 60 minutes of treatment time.

Time (min)	C_1	C_2	$D\%_1$	$D\%_2$	Average	StdeV
0	100	100	0	0	0	0
10	43.934	45.56	56.065	54.44	55.252	1.149
20	11.524	13.86	88.475	86.14	87.307	1.651
30	1.759	3.57	98.240	96.43	97.335	1.279
40	1.307	3.65	98.692	96.35	97.521	1.656
50	1.220	3.49	98.779	96.51	97.644	1.604
60	0.978	2.987	99.021	97.013	98.017	1.419

Appendix 14: Comprehensive summary of chapter five

Unique number	Varied parameters	Fixed parameters	Comments
	Chemical parameters		
O2C	O.II concentration (mg/L)	Peak voltage 6.8 kV, O.II volume 1 500 mL, pH (5.04 – 6.03), solution, air flow rate 3 L/min, 50 g/L NaCl, 1.5 mm silver electrode, air gap 2 mm and treatment time of 60 min.	The degradation of O.II decreased with increase of O.II initial concentration. Nevertheless, 60 m/L was chosen as the optimum concentration value that was used throughout all experiments. This parameter significantly affected the removal of O.II.
Range	10 - 60		
SMXC	SMX concentration (g/L)	Peak voltage 6.8 kV, SMX volume 1500 mL, pH (4.04 -5.06), air flow rate 3 L/min, 50 g/L NaCl, 1.5 mm silver electrode, air gap 2 mm and treatment time of 60 min.	No constant trend was depicted; however, complete degradation of SMX was achieved with 40 mg/L at all sampling times. This parameter significantly impacted up on SMX decomposition.
SMXC1	20		
SMXC2	40		
SMXC3	60		
SMXC4	100		

Appendix 14: Comprehensive summary of chapter five (cont.)

Unique number	Varied parameters	Fixed parameters	Comments
	Physical parameters		
SPHO	Solution initial pH of O.II dye		
SPHO1	2.5	Peak voltage 6.8 kV, O.II concentration 60 mg/L, O.II volume 1500 mL, air flow rate 3 L/min, 50 g/L NaCl, air gap 2 mm, 1.5 mm silver electrode and contact time of 60 min	The removal of O.II increased with a decrease in pH. Hence, pH 2.5 was selected as the optimum pH at which O.II solution was set in all experiments. This factor significantly affected the decomposition of O.II dye.
SPHO2	4.5		
SPHO3	6.5		
SPHO4	8.5		
SPHO5	10.5		
SMXPH	Solution initial pH of SMX drug		
SMXPH1	2.5	Peak voltage 6.8 kV, SMX concentration 40 mg/L, solution volume 1500 mL, air flow rate 3 L/min, 50 g/L NaCl, air gap 2 mm, 1.5 mm silver electrode and contact time of 60 min	No uniform trend was observed, however, total degradation of SMX was achieved at 2.5 at all sampling times. This factor significantly affected the removal efficiency of SMX drug.
SMXPH2	6.5		
SMXPH3	8.5		
SMXPH4	10.5		
AFRO	Air flow rate (L/min) for O.II dye		
AFRO1	3	Peak voltage 6.8 kV, O.II concentration 60 mg/L, O.II volume 1500 mL, air flow rate 3 L/min, 50 g/L NaCl, air gap 2 mm, 1.5 mm silver electrode and contact time of 60 min	No continuous trend was observed. However, the best degradation of O.II was achieved at an air flow rate of 3 L/min.
AFRO2	6		
AFRO3	9		
AFRS	Air flow rate (L/min) for SMX drug		
AFR1	3	Peak voltage 6.8 kV, SMX concentration 40 mg/L, solution volume 1500 mL, air flow rate 3 L/min, 50 g/L NaCl, air gap 2 mm, 1.5 mm silver electrode and contact time of 60 min	No constant trend was noted, however, the highest degradation of SMX was achieved at a flow rate of 3L/min, and this factor significantly affected SMX removal efficiency.
AFR2	6		
AFR3	9		

Appendix 14: Comprehensive summary of chapter five (cont.)

Electrical parameter			
Unique number	Varied parameters	Fixed parameters	Comments
APVO	Voltage (V) with O.II		The degradation of O.II rose with an increase of voltage.
APVO1	6.8	[O.II] 60 mg/L, solution volume 1500 mL, pH (6.04 – 6.64),	In order to minimise sparking constraint, 6.8 kV was
APVO2	8	air flow rate 3 L/min, 50 g/L NaCl, air gap 2 mm,1.5 mm	chosen as the optimum voltage value that was employed
APVO3	10.5	silver electrode and contact time of 60 min.	in all experiments.
APVS	Voltage (V) with SMX		Comments
APVS1	6.8	[SMX] 40 mg/L, solution volume 1500 mL, pH (4.04 -	A slight increase of SMX degradation efficiency with
APVS2	8	5.06), air flow rate 3 L/min, 50 g/L NaCl, air gap 2 mm,1.5	increase of peak voltage was observed. Nevertheless 6.8
APVS3	10.5	mm silver electrode and contact time of 60 min.	kV was selected as the optimum voltage value to minimise
			the risks of sparkling during DBD run.

Appendix 14: Comprehensive summary of chapter five (cont.)

Pollutants	**Optimum parameters**	**Comments**
DBD experiment performed at optimum conditions for O.II dye	Peak voltage 6.8 kV, O.II volume 1 500 mL, pH 2.5, air flow rate 3 L/min, 50 g/L NaCl and air gap 2 mm, 1.5 mm electrode and fixed time of 60 minutes.	Full decolouration of O.II was achieved within 20 minutes. Its degradation induced by O_3 and $\cdot OH$ led to six abundant by-products that were further mineralised to H_2O, CO_2 and simpler inorganics
DBD experiment performed at optimum conditions for SMX pharmaceutical drug	Peak voltage 6.8 kV, SMX volume 1 500 mL, pH 2.5, air flow rate 3 L/min, 50 g/L NaCl and air gap 2 mm, 1.5 mm electrode and fixed time of 60 minutes.	Complete degradation of SMX was reached within 30 minutes. Its deactivation mainly initiated by O_3 and $\cdot OH$ resulted in six degradation intermediate by-products that were recalcitrant but later converted into CO_2, H_2O and small inorganic entities.

Appendix 15 a: UV-vis results for the photocatalytic degradation of orange II by grounded C-N-TiO_2 Nano composite (***M_{cat} = 0.08 g***) pyrolysed with N_2 gas at 350 ^oC, 50 ^oC/min ramping rate for 105 min and Kinetics studies. Experimental conditions [O.II] 5 mg/L, volume 500 mL, pH 2.5, catalyst dosage 0.08 g and irradiation time of 120 min.

Time (min)	Absorbance		Concentration (mg/L)		Degradation efficiency		Ct/Co	L(Ct/Co)
	A_1	A_2	C_1	C_2	$D\%_1$	$D\%_2$		
0	0.301	0.301	5	5	0	0	1	0
30	0.258	0.258	3.733	3.733	25.34	25.34	0.746	0.292
60	0.191	0.191	2.764	2.764	44.72	44.72	0.552	0.552
90	0.140	0.141	2.026	2.026	59.48	59.48	0.405	0.903
120	0.090	0.090	1.302	1.302	73.96	73.96	0.260	1.345

Appendix 15 b: UV-vis results for the photocatalytic degradation of orange II by grounded C-N-TiO_2 Nano composite (***M_{cat} = 0.08 g***) pyrolysed with N_2 gas at 350 ^oC, 50 ^oC/min ramping rate for 120 min and Kinetics studies. Experimental conditions [O.II] 5 mg/L, volume 500 mL, pH 2.5, catalyst dosage 0.08 g and irradiation time of 120 min.

Time (min)	Absorbance		Concentration (mg/L)		Degradation efficiency		Ct/Co	L(Ct/Co)
	A_1	A_2	C_1	C_2	$D\%_1$	$D\%_2$		
0	0.304	0.304	5	5	0	0	1	0
30	0.254	0.250	3.675	3.675	26.5	26.5	0.735	0.307
60	0.185	0.185	2.67	2.67	46.6	46.6	0.534	0.627
90	0.138	0.138	1.997	1.997	60.06	60.06	0.399	0.92
120	0.104	0.104	1.505	1.505	69.9	69.9	0.301	1.20

Appendices 15 c: UV-vis results for the photocatalytic degradation of orange II by grounded C-N-TiO_2 nano composite (***M_{cat} = 0.08 g***) pyrolysed with N_2 gas at 350 ^oC, 50 ^oC/min ramping rate for 135 min and Kinetics studies. Experimental conditions [O.II] 5 mg/L, volume 500 mL, pH 2.5, catalyst dosage 0.08 g and irradiation time of 120 min.

Time (min)	Absorbance		Concentration (mg/L)		Degradation efficiency		Ct/Co	L(Ct/Co)
	A_1	A_2	C_1	C_2	$D\%_1$	$D\%_2$		
0	0.304	0.304	5	5	0	0	1	0
30	0.284	0.284	4.12	4.12	17.6	17.6	0.88	0.13
60	0.259	0.259	3.748	3.748	25.04	25.04	0.749	0.288
90	0.231	0.231	3.343	3.343	33.14	33.14	0.668	0.402
120	0.199	0.199	2.879	2.879	42.404	42.104	0.575	0.575

Appendix 15 d: UV-vis results for the effect of pyrolysis time on the photocatalytic degradation of orange II by C-N-TiO_2 nano composite pyrolysed with N_2 gas at 350 ^oC, 50 ^oC/min ramping rate at 3 different holding times (105, 120 and 35 min) and Kinetics studies. Experimental conditions [O.II] 5 mg/L, volume 500 mL, pH 2.5, catalyst dosage 0.08 g and irradiation time of 120 min.

Degradation efficiency (D%) of O.II within 60 minutes of DBD experiment										
Time (min)	0 min		30 min		60 min		90 min		120 min	
System	$D\%_1$	$D\%_2$	$D\%_1$	$D\%_2$	$D\%_1$	$D\%_2$	$D\%_1$	$D\%_2$	$D\%_1$	$D\%_2$
UV alone	0	0	2	4	2.6	4.23	4	6	4.8	6.56
UV+ TiO_2 Degussa	0	0	13	15	20.23	22.06	26.814	29.002	39.7	41.32
UV + C-N-TiO_2 135 min	0	0	17.6	20.12	25.04	27.123	33.14	35.25	42.4	44.24
UV+ C-N-TiO_2 120 min	0	0	23.1	25.23	41.6	43.123	57.06	59.12	69.9	72.24
UV+ C-N-TiO_2 135 min	0	0	25.34	27.12	44.72	46.23	59.48	62.12	73.96	76.123

Appendix 16: UV-vis results for the effect of catalysts dosage on the photocatalytic degradation of orange II by C-N-TiO_2 Nano composite pyrolysed with N_2 gas at 350 ^oC, 50 ^oC/min ramping rate for 105 min and Kinetics studies. Experimental conditions [O.II] 5 mg/L, volume 500 mL, pH 2.5, catalyst dosage varied from 0.02, 0.08 to 0.14g and irradiation time of 120 min.

Degradation efficiency of O.II (D%) within 60 minutes of DBD experiment										
Time (min)	0 min		30 min		60 min		90 min		120 min	
System	D% $_1$	D% $_2$	D% $_1$	D% $_2$	D% $_1$	D% $_2$	D% $_1$	D% $_2$	D% $_1$	D% $_2$
UV alone	0	0	2	4	2.6	4.53	4	6	4.8	6.98
UV+ 0.02g C-N-TiO_2	0	0	11.2	13.4	11.8	14.005	15.2	17.23	17.8	20.012
UV + 0.08g C-N-TiO_2	0	0	25.34	27.26	44.72	47.023	59.48	61.12	73.96	76.132
UV+ 0.14g C-N-TiO_2	0	0	30.8	33.02	50.22	52.32	65.8	68.024	91.6	93.26

Appendix 17: HPLC results for the degradation of orange II sodium salt dye by combined DBD and C-N-TiO_2 immobilized on SS (C-N-TiO_2/SS) and pure Ti mesh (C-N-TiO_2/Ti) at the following optimum conditions: Peak voltage 8 kV, [O.II] 60 mg/L, solution volume 1500 mL, solution pH 2.5, 50 g/L NaCl inner electrode electrolyte, air gap 2 mm, 1.5 mm silver electrode, experimental time 60 min, (8 cm long x 2 cm large) x 4 uncoated and coated meshes enfolded around the outer tube of the DBD reactor.

Degradation efficiency of O.II (D%) within 60 minutes of DBD experiment														
Time (min)	0 min		10 min		20 min		30 min		40 min		50 min		60 min	
System	D% $_1$	D% $_2$	D% $_1$	D% $_2$	D% $_1$	D% $_2$	D% $_1$	D% $_2$	D% $_1$	D% $_2$	D% $_1$	D% $_2$	D%$_1$	D% $_2$
DBD + C-N-TiO_2/Ti	0	0	34.732	36.35	59.285	61.565	80.450	82.575	90.029	91.892	96.299	98.786	98.526	99.989
DBD alone	0	0	94.87	96.562	99.547	98.235	99.708	98.123	99.74	98.325	99.825	98.123	99.889	98.281
DBD + C-N-TiO_2/SS	0	0	99.904	98.02	99.992	98.23	99.999	98.12	99.197	97.580	100	98.001	100	98.002

Appendix 18: HPLC results for the degradation of SMX by C-N-TiO_2/SS and C-N-TiO_2/Ti mesh in DBD at optimum conditions: Applied voltage 8 kV, SMX concentration 40 mg/L, solution volume 1500 mL, solution pH 6.5, air flow rate 3 L/min, 1.5 mm silver electrode, 50 g/L NaCl inner electrode electrolyte, air gap 2 mm, (8 cm long x 2 cm large) x 4 coated meshes enfolded around the outer tube of the DCDBD reactor and an experimental time of 60 min.

Degradation efficiency of SMX (D%) within 60 minutes of DBD experiment														
Time (min)	0 min		10 min		20 min		30 min		40 min		50 min		60 min	
System	D% $_1$	D% $_2$	D% $_1$	D% $_2$	D% $_1$	D% $_2$	D% $_1$	D% $_2$	D% $_1$	D% $_2$	D% $_1$	D% $_2$	D%$_1$	D% $_2$
DBD + C-N-TiO_2/Ti	0	0	19.345	22.563	38.987	41.896	51.697	54.996	68.298	71.263	76.486	79.985	84.658	87.622
DBD alone	0	0	26.277	28.366	66.5737	68.255	73.777	75.555	78.960	80.824	85.486	87.456	89.645	91.694
DBD + C-N-TiO_2/SS	0	0	56.065	58.014	88.475	90.255	98.052	100	98.002	100	98.012	100	98.021	100

Appendix 19: UV-vis results for the photocatalytic activity of glass coated with C-N-TiO_2 nano composites at catalyst to solvent volume ratio altered from 3:5, 4:5 to 5:5 at the following experimental conditions: [O.II] 5 mg/L, volume 500 mL, pH 2.5, Mega-Ray 160 W/240 V MR160 UV lamp, and irradiation time of 120 min.

Degradation efficiency of O.II (D%) within 120 minutes of DBD experiment										
Time (min)	0 min		30 min		60 min		90 min		120 min	
System	D% $_1$	D% $_2$	D% $_1$	D% $_2$	D% $_1$	D% $_2$	D% $_1$	D% $_2$	D% $_1$	D% $_2$
UV alone	0	0	2	3.5	2.6	4.22	4	5.6	4.8	6.5
UV + coating with catalyst to solvent ratio 5:5	0	0	5.325	7.423	8.7120	10.525	9.117	10.563	8.509	10.078
UV + coating with 4:5 ratio	0	0	7.843	9.5130	10.390	12.158	10.790	12.265	11.417	13.054
UV + coating with 3:5 ratio	0	0	8.7120	10.256	15.426	16.895	12.677	14.098	12.839	14.585

Appendix 20: UV-vis results for the photocatalytic activity of glass coated with C-N-TiO_2 nano composites at catalyst to solvent volume ratio altered from 3:5, 4:5 to 5:5 at the following experimental conditions: [O.II] 5 mg/L, volume 500 mL, pH 2.5, Mega-Ray 160 W/240 V MR160 UV lamp, and irradiation time of 120 min.

Degradation efficiency of O.II (D%) within 120 minutes of DBD experiment										
Time (min)	0 min		30 min		60 min		90 min		120 min	
System	D% $_1$	D% $_2$	D% $_1$	D% $_2$	D% $_1$	D% $_2$	D% $_1$	D% $_2$	D% $_1$	D% $_2$
UV alone	0	0	2	3.5	2.6	4.063	4	5.56	4.8	6.252
UV + coating @ 2300 rpm	0	0	3.849	5.556	4.196	6.056	5.325	7.086	6.946	8.462
UV + coating @ 2600 rpm	0	0	8.712	10.156	15.426	17.031	12.677	14.231	12.839	14.452
UV + coating @ 2900 rpm	0	0	5.238	7.026	7.612	9.326	8.133	9.862	9.7250	11.456